STATE OF CALIFORNIA • DEPARTMENT OF TRANSPORTATION

TECHNICAL REPORT DOCUMENTATION PAGE

DRISI-2011 (REV 10/1998)

1. REPORT NUMBER	2. GOVERNMENT ASSOCIATION NUMBER	3. RECIPIENT'S CATALOG NUMBER
CA18-2880		

4. TITLE AND SUBTITLE Development of Performance-based Seismic Design of Ordinary Standard Bridges	5. REPORT DATE December 2018 6. PERFORMING ORGANIZATION CODE UCSD
7. AUTHOR Angshuman Deb, Alex L. Zha, Zachary Caamaño-Withall, Joel P. Conte, José I. Restrepo	8. PERFORMING ORGANIZATION REPORT NO. UCSD / CA 18-2880 SSRP 18-06
9. PERFORMING ORGANIZATION NAME AND ADDRESS Jacobs School of Engineering University of California, San Diego 9500 Gilman Drive La Jolla, CA 92093-0403	10. WORK UNIT NUMBER 11. CONTRACT OR GRANT NUMBER 65A0594
12. SPONSORING AGENCY AND ADDRESS California Department of Transportation Engineering Service Center 1801 30th Street, MS 9-2/5i Sacramento, California 95816 California Department of Transportation Division of Research and Innovation, MS-83 1727 30th Street, 2nd Floor Sacramento CA 95816	13. TYPE OF REPORT AND PERIOD COVERED Final Report 5/1/2016-4/30/2018 14. SPONSORING AGENCY CODE 913

15. SUPPLEMENTARY NOTES

Prepared in cooperation with the State of California Department of Transportation.

16. ABSTRACT

Driven by the necessity to meet changing public expectations in the wake of natural disasters, such as earthquakes, the structural engineering community is moving towards more rational, risk-informed, and transparent approaches to structural design, amidst which probabilistic performance-based seismic design (PBSD) has emerged as the most scientific and promising one. However, performance-based earthquake engineering (PBEE), owing to its esoteric nature, has faced issues of impeded implementation in seismic design practice, especially in the area of bridge engineering. The main objective of this research is to lay the groundwork for the formulation of a simplified, yet rigorous, framework for risk-targeted PBSD of Ordinary Standard Bridges (OSBs) in California. Rooted in the formulation of this design framework is the PBEE assessment methodology, developed at the Pacific Earthquake Engineering Research (PEER) Center, integrating site-specific seismic hazard analysis, structural demand analysis, and damage analysis in a comprehensive and consistent probabilistic framework. Following an implementation of the PEER PBEE methodology, incorporating various improvements from the state-of-the-art literature related to its various steps, and an application of it for the damage hazard assessment of four distinct OSBs in California, a parametric full-blown probabilistic seismic performance assessment of the testbed bridges is carried out to investigate the effects of varying key, or primary, structural design parameters on the estimated damage hazard. The parametric study indicates irregular levels of conservativeness exhibited by the as-designed testbed bridges and illustrates the need for a PBSD framework for OSBs such that explicitly stated risk-targeted performance objectives are consistently satisfied by the population of OSBs in California. Finally, a simplified risk-targeted PBSD methodology is distilled out of this project which can be used to: (i) locate a feasible design point in the primary design parameter space of a bridge being designed for multiple risk-based performance objectives; and (ii) delineate a feasible design domain containing other acceptable design options in the primary design parameter space thereby facilitating risk-informed design decisions/adjustments. It is believed that the adoption of the proposed PBSD methodology, although non-traditional in its format, will be extremely beneficial in the medium and long-term. This initial venture will also prove to be crucial in supporting and fostering future research work and innovative technological developments in bridge infrastructure engineering.

17. KEYWORDS	18. DISTRIBUTION STATEMENT	
	No restrictions. This document is available to the public through the National Technical Information Service, Springfield, VA 22161	
19. SECURITY CLASSIFICATION (*of this report*)	20. NUMBER OF PAGES	21. COST OF REPORT CHARGED
Unclassified	384	

Disclaimer

This document is disseminated in the interest of information exchange. The contents of this report reflect the views of the authors who are responsible for the facts and accuracy of the data presented herein. The contents do not necessarily reflect the official views or policies of the State of California or the Federal Highway Administration. This publication does not constitute a standard, specification or regulation. This report does not constitute an endorsement by the California Department of Transportation of any product described herein.

For individuals with sensory disabilities, this document is available in Braille, large print, audiocassette, or compact disk. To obtain a copy of this document in one of these alternate formats, please contact: The Division of Research and Innovation, MS-83, California Department of Transportation, P.O. Box 942873, Sacramento, CA 94273-0001.

STRUCTURAL SYSTEMS

RESEARCH PROJECT

Report No.

SSRP–18/06

Performance-based Seismic Design of Ordinary Standard Bridges

by

Angshuman Deb

Alex L. Zha

Zachary Caamaño-Withall

Joel P. Conte

José I. Restrepo

Final Report

December 2018

Department of Structural Engineering
University of California, San Diego
La Jolla, California 92093-0085

University of California, San Diego
Department of Structural Engineering
Structural Systems Research Project

Report No. SSRP-18/06

Performance-based Seismic Design of Ordinary Standard Bridges

by

Angshuman Deb
Graduate Researcher

Alex L. Zha
Graduate Researcher

Zachary Caamaño-Withall
Graduate Researcher

Joel P. Conte
Professor of Structural Engineering

José I. Restrepo
Professor of Structural Engineering

Final Report submitted to the California Department of Transportation
Under Contract No. 65A0594

Department of Structural Engineering
University of California, San Diego
La Jolla, California 92093-0085

December 2018

Acknowledgments

Support of this research by the California Department of Transportation under Contract no. 65A0594, Task No. 2880 is gratefully acknowledged. Opinions and findings in this report are those of the authors and do not necessarily reflect the views of the sponsor.

Abstract

Driven by the necessity to meet changing public expectations in the wake of natural disasters, such as earthquakes, the structural engineering community is moving towards more rational, risk-informed, and transparent approaches to structural design, amidst which probabilistic performance-based seismic design (PBSD) has emerged as the most scientific and promising one. However, performance-based earthquake engineering (PBEE), owing to its esoteric nature, has faced issues of impeded implementation in seismic design practice, especially in the area of bridge engineering. The main objective of this research is to lay the groundwork for the formulation of a simplified, yet rigorous, framework for risk-targeted PBSD of Ordinary Standard Bridges (OSBs) in California. Rooted in the formulation of this design framework is the PBEE assessment methodology, developed at the Pacific Earthquake Engineering Research (PEER) Center, integrating site-specific seismic hazard analysis, structural demand analysis, and damage analysis in a comprehensive and consistent probabilistic framework. Following an implementation of the PEER PBEE methodology, incorporating various improvements from the state-of-the-art literature related to its various steps, and an application of it for the damage hazard assessment of four distinct OSBs in California, a parametric full-blown probabilistic seismic performance assessment of the testbed bridges is carried out to investigate the effects of varying key, or primary, structural design parameters on the estimated damage hazard. The parametric study indicates irregular levels of conservativeness exhibited by the as-designed testbed bridges and illustrates the need for a PBSD framework for OSBs such that explicitly stated risk-targeted performance objectives are consistently satisfied by the population of OSBs in California. Finally, a simplified risk-targeted PBSD methodology is distilled out of this project which can be used to: (i) locate a feasible design point in the primary design parameter space of a bridge being designed for multiple risk-based performance objectives; and (ii) delineate a feasible design domain containing other acceptable design options in the primary design parameter space thereby facilitating risk-informed design decisions/adjustments. It is believed that the adoption of the proposed PBSD methodology, although non-traditional in its format, will be extremely beneficial in the medium and long-term. This initial venture will also prove to be crucial in supporting and fostering future research work and innovative technological developments in bridge infrastructure engineering.

Table of Contents

List of Figures

List of Tables

1 Introduction

1.1 Background

Traditional seismic design philosophy for earthquake resistant structures permits them to deform beyond elastic limits and thereby yield, incur damage, and dissipate energy as long as collapse is prevented. The main requirements of such a design philosophy can be summarized as:

(i) No, or unnoticeable damage to structural and non-structural elements should be incurred in the event of small earthquakes;

(ii) Minor and repairable damage to structural and non-structural elements is admissible in the event of an earthquake of moderate intensity; and

(iii) Severe structural damage is allowed for strong earthquakes, if collapse is prevented.

With the above being the overarching requirement of seismic design codes to date, all design codes can be considered performance-based, although partially. The idea has always been to design structures such that a performance objective, usually that of collapse prevention, is achieved. Traditionally, this fulfilment of structural performance goals along with certain functional requirements has been carried out by means of prescriptive measures, primarily empirical. A deterministic approach to the design of structural systems, wherein loads and resistances are considered deterministically quantifiable without any uncertainty, has been predominant until recently. According to this approach, structural members are designed to have their capacities exceed the demands expected to be imposed on them by a certain margin. The capacity-to-demand ratio, also known as safety factor, is considered to be a measure of structural reliability. Experience and engineering judgment have dictated the prescription of values for structural loads/demands, capacities, and safety factors in codes of practice.

The structural engineering profession's realization of uncertainties inherent in structural loads and strengths has led to the advent of structural reliability and risk analysis in structural design. A reflection of this can be seen in the form of *Load and Resistance Factor Design* (LRFD) in newer design codes wherein partial safety factors are applied to characteristic values of uncertain loads and resistances to ensure the safety of a structural member. LRFD aims to ensure that a factored load is less than or equal to the factored strength, where the partial safety factors are derived based on calibration to desired measures of reliability obtained by probabilistic methods.

Due to the large uncertainty associated with seismic loads by virtue of random occurrence time and space (source-to-site distance), magnitude, seismic wave transmission path (seismic wave attenuation), local site/soil condition, etc., and hence the structural response under the same owing to uncertain structural properties (e.g., material and geometric properties) and structural capacity to withstand such loads, seismic design and evaluation of structures calls for the inclusion of methods of probability and statistics in order that these uncertainties be properly quantified, and their effects adequately taken into account. However, the handling of uncertain seismic loads to date has primarily been limited to the selection of design ground motion parameters based on a certain return period (i.e., seismic hazard level). Henceforth, the treatment becomes tacit by way of designing conservative structural systems to ensure that structural capacities are not exceeded by the demands. A lack of explicit consideration of the uncertainties prevalent in structural loads (which themselves depend on structural properties) and resistances deem such a design to be one of questionable reliability.

Also, from experiences of severe damage and losses incurred during recent earthquakes, such as the 1994 Northridge, 1995 Kobe, 1999 Kocaeli Turkey and Chi-Chi Taiwan earthquakes, 2010 Maule Chile, 2010 Canterbury and 2011 Christchurch New Zealand earthquakes, an urgent need to amend the seismic design framework has arisen (Wen 2004). An important observation from these recent earthquake events is that structures complying with seismic codes based on traditional design philosophy, although having performed satisfactorily as per their design objectives, did not perform equally well in terms of resiliency and public expectation, and thereby failed to serve the community (Günay and Mosalam 2013). This realization highlighted the need for refining the definition of performance goals such that they hold reliably well for the stakeholders and society as a whole. Societal expectations of structural performance can only be met by explicit statements of performance objectives in terms of the risk associated with well-defined performance levels, rather than ambiguous and misleading statements of "collapse prevention" that is assumed, and not directly checked, to be engendered upon satisfaction of prescriptive measures. Performance objectives stated in terms of the risk associated with performance levels (e.g., exceedance of damage/limit-states and/or specific values of monetary loss/deaths etc.) will not only allow an active participation of the public/stakeholders in the design/decision making process thereby 2 making it more rational, scientific, and transparent, but also lead to greater societal awareness of earthquake risk and consequences (May 2001). Consistent incorporation, quantification, and propagation of the inherent uncertainties involved at various stages of the design process are therefore inevitably called for. The necessity of having quantitative methods ensuring adequate performance of structures, i.e., satisfaction of multiple risk-targeted performance objectives within a confidence level, laid the path towards the development of performance-based earthquake engineering and design.

Identification and filling of knowledge gaps in earthquake engineering, accelerated through advancement in technology and the availability of tremendous computational power has made it possible for researchers to make substantial progress in the domain of performance-based earthquake engineering and design whereby prescriptive measures have become more and more conceptual, rather than empirical. Fueled by the societal demands of improved life safety, economy and resiliency, the structural engineering community has made some considerable advancement in the realm of performance-based earthquake engineering over the last few decades, consistently improving over time and culminating in the fully probabilistic, rigorous and advanced assessment framework (Krawinkler and Miranda 2004; Moehle and Deierlein 2004; Porter 2003; etc.) developed by the researchers at the Pacific Earthquake Engineering Research (PEER) Center.

The PEER performance-based earthquake engineering (PBEE) methodology has been mainly developed for analysis and assessment and not directly for design, except for some initial efforts (Cornell et al. 2002; Mackie and Stojadinović 2007), but has recently been recommended as a future alternative for bridge seismic design (NCHRP 2013). The inherent theoretical complexity of the full-blown PEER PBEE methodology also adds to its hampered implementation in engineering and design practice. The proposed research to be conducted in this project will thus focus on bridging the gap existing between the theoretical rigor of the PEER PBEE framework and its practical implementation in the design of bridges, which is also a less trodden area in terms of performance-based earthquake engineering applications as compared to building structures.

1.2 Research Objectives and Scope

This project is aimed to deliver performance-based seismic design (PBSD) guidance for Ordinary Standard Bridges (OSBs) in California. OSBs, i.e., conventional, multiple span, skewed reinforced concrete bridges, are the most common bridges in California. They are designed in-house by the

California Department of Transportation (Caltrans) and are chosen as bridge testbeds in this project to determine whether the reported benefits of using a performance-based design approach over the current bridge design procedure used by Caltrans are significant or not.

Rooted in the formulation of the targeted PBSD framework is the four-step PEER PBEE assessment methodology integrating (1) site-specific seismic hazard analysis, (2) structural demand analysis, (3) damage analysis, and (4) loss analysis in a comprehensive and consistent probabilistic framework. This assessment methodology involves a sequential execution of the four above mentioned analytical steps pieced together (integrated) using the Total Probability Theorem of probability theory to arrive at an estimate of a performance measure, e.g., the mean annual rate (MAR) at which a damage/limit-state is exceeded, and/or the MAR at which a decision variable (e.g., monetary loss, deaths, etc.) exceeds a value of interest. Performance measures considered in this study are the MARs or, equivalently, their reciprocals which are the mean return periods (RPs) of limit-state exceedances for a selected set of limit-states. The task of probabilistically predicting the future seismic performance (in terms of damage) of a bridge is, therefore, broken down into the following three steps: Probabilistic Seismic Hazard Analysis (PSHA) in terms of a ground motion intensity measure (IM), Probabilistic Seismic Demand Hazard Analysis (PSDemHA) in terms of engineering demand parameters $(EDP\text{s})$, and Probabilistic Seismic Damage Hazard Analysis (PSDamHA) for various limit-states of interest. It is noted that the fourth and final step of the PEER PBEE assessment methodology, i.e., probabilistic seismic loss hazard analysis, is kept outside the scope of this work.

While moving towards accomplishing the central objective of a PBSD framework for OSBs, completion of the following tasks is achieved during this project:

(i) Selection of testbed bridges for this study based on previous Caltrans funded research projects, revisiting inherited finite element models of these testbed bridges, and incorporation of improvements in the finite element modeling approach employed for these bridges.

(ii) Incorporation of improvements of several aspects in the various stages of the state-of-the-art PEER PBEE assessment methodology. This includes: (1) introduction of an improved earthquake to account for structural period elongation caused by damage during an earthquake, and the lack of certainty in identifying the period of the predominant mode of vibration of a reinforced concrete OSB; (2) conditional mean spectrum-based hazard-consistent site-specific ground motion selection for the ensemble nonlinear time-history analyses involved in the PSDemHA stage; (3) introduction of material strain-based *EDP*s which are better correlated to damage (Priestley et al. 2007) than are traditionally used displacement based *EDP*s (e.g., column drift, plastic hinge rotation); (4) identification of material strain-based limit-states of interest, viz., concrete cover crushing/spalling, initiation (onset) of longitudinal rebar buckling and initiation (onset) of longitudinal bar fracture, which are pertinent to the seismic evaluation of bridge structures and physically meaningful to practicing bridge engineers, and finally (5) development of strain-based normalized fragility functions, required in the PSDamHA stage, for the considered limit-states through proper identification of previous experimental/numerical research programs, experimental/numerical data, and appropriate capacity prediction equations for normalization.

(iii) Documenting a comprehensive treatise on the first three steps, i.e., PSHA, PSDemHA, and PSDamHA, of the PEER PBEE assessment methodology. This exposition of the PEER PBEE assessment framework revisited and applied to a set of testbed OSBs is expected to serve in the interest of the structural engineering community and bridge any knowledge gap, whatsoever, that is holding back a full-fledged PBSD method from being implemented in bridge design practice.

(iv) A fully automated and portable (in terms of computational platform, i.e., easily scalable from a desktop computing environment to cloud-based supercomputing environments) implementation of the improved version of the PEER PBEE assessment methodology for probabilistic performance assessment of OSBs.

(v) Numerical seismic performance-based assessment of the selected testbed bridges using the implemented improved PEER PBEE assessment methodology.

(vi) Conceptualization of a generalized workflow for a full-blown parametric probabilistic seismic performance assessment applied to OSBs (i.e., probabilistic performance-based assessment of parametrically redesigned versions of the testbed OSBs) and a fully automated and computationally portable implementation of the same making use of high-throughput computing to solve an embarrassingly parallelizable problem.

(vii) Development and formulation of a simplified, risk-targeted PBSD framework for OSBs accommodating multiple risk-based design objectives with target levels of risk to be specified based on risk tolerance of the engineering community and society.

Risk-targeted performance-based design is undoubtedly the most advanced design methodology that will shape the seismic design philosophy of future design codes (Cornell and Krawinkler 2000; Ellingwood 2008; NCHRP 2013). PBSD also presents a novel way of approaching design and construction technologies, allowing the tailoring of structural design to meet changing public expectations in the wake of natural disasters such as earthquakes (Ellingwood 2008). The targeted PBSD framework will provide a more rational, scientific, consistent, and transparent design process, thus resulting in more reliable estimates of bridge safety against various limit-states of interest. It is believed that the adoption of the targeted PBSD framework will equip practicing bridge engineers with scientific and risk-informed approaches towards building economic and safe bridge structures, especially with regard to the seismic hazard. This will be extremely beneficial to Caltrans in the medium to long-term. This initial venture will also prove to be crucial in supporting and fostering future research work and innovative technological developments in bridge infrastructure engineering that might lead to significant financial savings in the long term.

1.3 Organization of Report

Details of this research work has been comprehensively documented in the form of this technical report which consists of eleven chapters. Brief accounts of the contents of these chapters are outlined below.

Chapter 1 serves as an introduction by posing the need to revise the traditional seismic design philosophy and solve problems of structural design in a rigorous probabilistic, risk-targeted, performance-based context. The research objectives of this work are also outlined in this chapter.

A thorough literature review on the history and development of performance-based engineering, particularly applicable to structural – and especially bridge – engineering practice is presented in **Chapter 2**. This chapter also familiarizes the reader with the PEER PBEE assessment methodology by succinctly going over each analytical step of this methodology.

Chapter 3 introduces four distinct ordinary standard bridge structures in California located in regions with disparate levels of seismicity. A brief description of these OSBs, selected as testbed structures for this project and the remainder of the report, is also presented in Chapter 3.

Chapter 4 elaborates on the details of inherited and subsequently improved (during this project) nonlinear finite element computational models of the selected testbed OSBs and the analysis setup for nonlinear response-history analysis of these bridge models

The following four chapters expound on the first three steps of the PEER PBEE framework revisited and applied to the set of selected testbed OSBs. **Chapter 5** presents the details of Probabilistic Seismic Hazard Analysis which produces a probabilistic description of the seismic hazard at the site of each selected testbed bridge in terms of an improved ground motion intensity measure. Based on the results of PSHA, discrete seismic hazard levels of interest are identified and the probability structures of target ground motion response spectra corresponding to these seismic hazard levels are derived. A novel ground motion selection algorithm is then invoked to select ensembles of risk-consistent site-specific ground motion records corresponding to the seismic hazard levels of interest.

Before moving on to Probabilistic Seismic Demand Hazard Analysis, deterministic seismic response analyses of the testbed bridge models are conducted, the details of which are discussed in **Chapter 6**. Results of nonlinear time-history analyses of the finite element models of these bridges subjected to a single ground motion record, rather than an ensemble of records, at a few seismic hazard levels are reported and compared.

Probabilistic Seismic Demand Hazard Analysis, the second step of the PEER PBEE framework, is deliberated in **Chapter 7**. Practical limit-states of interest, which are pertinent to the seismic evaluation of bridge structures and meaningful to practicing bridge engineers, are identified and corresponding to each limit-state, a novel strain-/deformation-based engineering demand parameter is defined. Details of PSDemHA and the probabilistic characterization of the imposed seismic demand, in terms of the chosen engineering demand parameters, are presented.

Chapter 8 describes the third step of the PEER PBEE framework, i.e., Probabilistic Seismic Damage Hazard Analysis, which is also the final step considered in this work. Predictive capacity models and fragility functions corresponding to the selected set of limit-states are defined and the mean annual rates (or mean return periods (RPs)) of exceeding each of the limit-states of interest are evaluated for the considered testbed bridges.

Chapter 9 elaborates on the assembly, implementation, and automation of a parametric full-blown probabilistic seismic performance assessment framework for OSBs in California. Parametric probabilistic seismic performance assessment of the testbed OSBs (i.e., probabilistic performance-based assessment of parametrically redesigned versions of the testbed OSBs) are carried out to investigate the effects of varying key, or primary, structural design parameters on the mean RPs of LS exceedances. A two-dimensional design space is defined in terms of two primary design variables to which the exceedances of the selected set of limit-states are believed to be most sensitive. Feasible design domains, i.e., collection of design points in the two-dimensional design parameter space with mean RPs of limit-state exceedances higher than or equal to respective specified target mean RPs, are identified. Seismic performances of the as-designed versions of the considered testbed bridges are compared with those of the parametrically re-designed versions of these bridges. This framework forms the basis for the simplified risk-targeted performance-based seismic design procedure distilled out of this project (discussed in the next chapter) for OSBs in California.

A simplified risk-targeted performance-based seismic design methodology is proposed in **Chapter 10** in lieu of the parametric full-blown method presented and discussed in Chapter 9. The purpose of the simplified methodology is to provide an alternative method to the full-blown one in obtaining: (1) a final design point in the primary design parameter space of a bridge being designed for multiple risk-targeted performance objectives, and (2) a feasible design domain in the primary design parameter space of the bridge, while requiring much lower and practicable computational cost than that of the full-blown parametric method.

Finally, a concluding chapter, **Chapter 11**, summarizes the work performed, provides a highlight of the results obtained, and throws light on several avenues for future research work in this area.

2 Literature Review of Performance-based Design with Application to Bridge Engineering

2.1 Introduction

The Pacific Earthquake Engineering Research (PEER) Center is not the only organization that has worked towards the development of performance-based engineering, in general. The PEER performance-based earthquake engineering (PBEE) methodology is the culmination of years of research, implementation and progress made in multi-disciplinary branches of engineering by various researchers and numerous organizations. Performance-based engineering lies in the heart of all fields of engineering that entail decision making under uncertainties, risk analysis, and structural reliability. Whenever a system is to be designed or assessed in an environment where there is an uncertain hazard leading to uncertain demands on the system, which in turn has an uncertain resistance, thereby leading to uncertain levels of damage, performance-based engineering provides the most scientific and rational way towards a design and assessment process.

Being rooted in the broader area of structural reliability and quantitative risk assessment, performance-based engineering is not restricted to earthquake engineering only. It has been in practice in the nuclear industry (Cornell and Newmark 1978; Kennedy et al. 1980; Kennedy and Ravindra 1984; Shinozuka et al. 1984; etc.), and offshore/marine engineering (De 1990; Guenard 1984; Marshall 1969; Moan 1994; Moan and Holand 1981; etc.) for quite some time now, where quantitative risk assessment plays a significant role. Earlier works in probabilistic risk assessment of civil engineering facilities (Ellingwood 2001; Ellingwood and Ang 1974; etc.) are also worth mentioning in this regard.

This Chapter provides a brief account of performance-based engineering, particularly as it relates to the history and current state-of-the-art of earthquake engineering assessment and design practice of structural systems, in general. The discussion in this Chapter is gradually narrowed down to the applicability of PBEE in the seismic design of the testbed structural systems to be considered in this research work, i.e., ordinary or conventional bridges in California.

2.2 History and Development of Performance-based Earthquake Engineering

Before being shaped by PEER in its most scientific and rigorous form, performance-based seismic engineering had evolved over a period of decades in the building industry. Advancement in seismic hazard analysis (Cornell 1968) started showing up in the evolution process of PBEE as the seismic input began to be rationally and probabilistically considered, although partially, by way of introducing the concept of a design earthquake associated with a certain return period (ATC-3-06 1978). Over a few years, the description of seismic input became more elaborate with the introduction of a more severe hazard level, viz. the Maximum Considered Earthquake (ASCE-7-02 2002), however, the design and assessment of structures continued to be followed based on a deterministic structural behavior. The first generation PBEE, although implemented with the correct intention, thus fell short of a thorough and exhaustive quantitative implementation by disregarding the various uncertainties associated with the entire design and assessment process.

A sudden and more recent (during early 90's) spike in the advancement of PBEE occurred with the need to assess existing structures for safety. The Structural Engineering Association of California (SEAOC) came up with the Vision 2000 report where structural performance objectives were defined in terms of performance levels (see Figure 2.1), viz. Fully Operational, Operational, Life Safety, and Near Collapse at different levels of seismic hazard, for example, Frequent (43 yr. return period), Occasional (72 yr. return period), Rare (475 yr. return period) and Very Rare (970 yr. return period). Other documents like FEMA-273 (1997) and FEMA-356 (2000) followed a similar approach to develop a performance-based framework by associating discrete levels of performance with discrete hazard levels, the difference with Vision 2000 (SEAOC 1995) lying in the definition of these levels. However, all throughout these stages of development of the framework, performance evaluation was primarily done deterministically by comparing element forces and deformation to prescriptive limits and acceptance criteria. These criteria were derived based on laboratory tests, simplified analytical models, or plain engineering judgment. Furthermore, element or component performance was assumed to be indicative of a global system performance which is not necessarily always true. Also, the performance measures, in terms of element forces and deformations, used in the 1st generation PBEE were not of direct interest to the stakeholders which led to a gap in the process of decision making between engineers and the public.

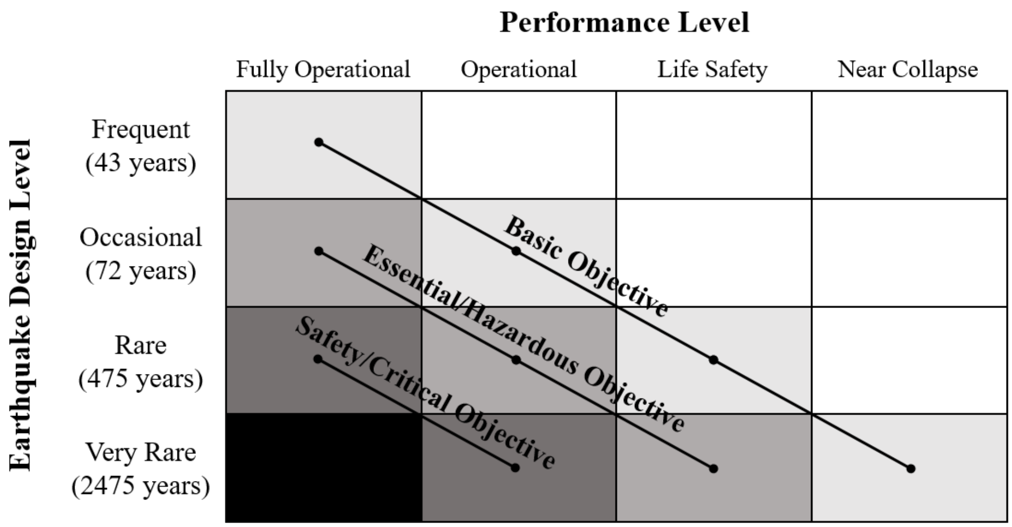

Figure 2.1 Vision 2000 (SEAOC 1995) performance matrix

These shortcomings of the 1st generation PBEE were attempted to be resolved through the development of a more robust, and technically sound framework at PEER. The performance-based framework developed at PEER provides a more transparent process in which performance objectives are explicitly stated as measures of monetary losses, downtime, and deaths, that make more sense to stakeholders, and all pertinent sources of uncertainty are included in the analysis procedure. As the structural engineering community aims to move toward more rational, risk-informed approaches to structural design and assessment, the paradigm of performance-based engineering is expected to provide technical support for this move and a novel way to tailor structural design to meet the changing public expectation after disasters (public's risk tolerance). The placement of structural performance classification on the basis of acceptable risk is the key feature of this methodology developed at PEER.

The PEER PBEE methodology has been used extensively by the United States Federal Emergency Management Agency (FEMA) and the Applied Technology Council (ATC) to develop a new generation of performance-based seismic design (PBSD) guidelines (FEMA-445 2006) for structural engineering practice. In recent years, PBEE has been followed in designing the seismic force resisting system of a number of tall buildings in the western U.S. (Ellingwood 2008). PBEE will continue to shape the core of future seismic design codes. Design methodologies for port structures are moving towards performance-based (PIANC 2001). This trend has also been followed by port owners and code developers who have issued design guidelines for seafront structures (Johnson et al. 2013; Port of Long Beach 2009; Port of Los Angeles 2010) and has now reached a national level with the publication of the Seismic Design of Piers and Wharves Code issued by ASCE/COPRI (2014). This code incorporates elements of PBSD and, in prescriptive language, states performance objectives as well as damage limit-states.

The PEER PBEE formulation has also been extended to other engineering fields such as blast engineering (e.g., Whittaker et al. 2003), fire engineering (e.g., Rini and Lamont 2008), tsunami engineering (e.g., Keon et al. 2016; Riggs et al. 2008), wind engineering (e.g., Augusti and Ciampoli 2008; Ciampoli and Petrini 2012; Ciampoli et al. 2011; van de Lindt and Dao 2009), hurricane engineering (e.g., Barbato et al. 2013; Masters et al. 2010), offshore engineering (e.g., Nezamian and Morgan 2014) and aerospace engineering (e.g., Gobbato et al. 2012; Gobbato et al. 2014).

2.3 PEER PBEE Assessment Framework

This section aims to present the PEER PBEE framework in detail elucidating all the steps included therein (Krawinkler and Miranda 2004; Moehle and Deierlein 2004; Porter 2003; etc.). Firstly, the forward analysis/assessment side of the framework is presented followed by its application to design which is basically an inverse probabilistic performance-based assessment.

2.3.1 Performance-based Analysis and Assessment of New and Existing Structures

The PEER PBEE methodology breaks down the task of predicting probabilistically the future seismic performance of a structure into four analytical steps pieced together (integrated) using the Total Probability Theorem (TPT) as shown in Figure 2.2. These steps are: (1) probabilistic seismic hazard analysis in terms of a ground motion intensity measure (IM), (2) probabilistic seismic demand analysis given , in terms of engineering demand parameters $(EDP\text{s})$, (3) probabilistic capacity analysis (or fragility analysis) and probabilistic damage analysis for various limit-states associated with the critical potential failure modes of the structure in concern, and (4) probabilistic loss analysis for decision variables $(DV\text{s})$, that are of great interest to stakeholders.

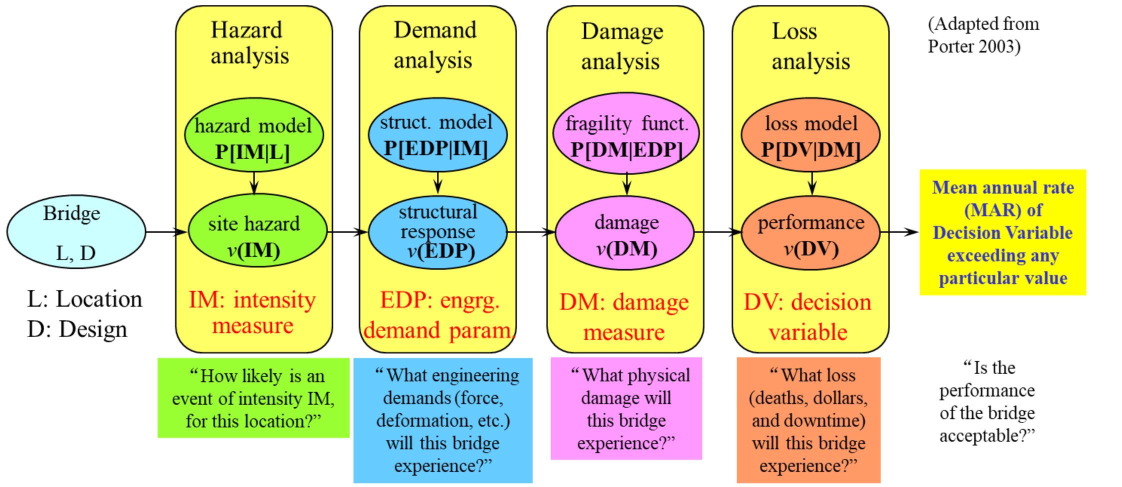

$$\therefore \nu_{DV} = \int_{dm}\int_{edp}\int_{im} G_{DV|DM}\left(dv \mid DM = dm\right) \cdot \left|dG_{DM|EDP=edp}\left(dm \mid EDP = edp\right)\right| \cdot \left|dG_{EDP|IM=im}\left(edp \mid IM = im\right)\right| \cdot \left|d\nu_{IM}\left(im\right)\right|$$

Figure 2.2 PEER performance-based earthquake engineering methodology (adapted from Porter (2003)). Notation: $G_{X|Y}\left(x \mid Y = y\right)$ = conditional complementary CDF of X given Y.

2.3.1.1 Probabilistic Seismic Hazard Analysis (PSHA)

The objective of PSHA is to compute for the site of the considered structure, the mean annual rate (MAR) $\nu_{IM}(x)$ (or annual probability) of exceeding any specified value x of a specified ground motion Intensity Measure (IM). The latter is usually taken as a structure-independent ground motion parameter (e.g., peak ground acceleration (PGA), peak ground velocity (PGV), Arias intensity, Housner's spectrum intensity) or more often as a structure-dependent ground motion parameter such as the first-mode pseudo-spectral acceleration, $S_a(T_1,\xi)$, or the spectral displacement $S_d(T_1,\xi)$ at the expected predominant period. For a given site, PSHA integrates the contribution of all possible seismic sources to calculate the MAR of random events $\{IM > x\}$ according to the TPT as

$$\nu_{IM}\left(x\right) = \sum_{i=1}^{N_{\text{flt}}} \nu_i \int_{R_i}\int_{M_i} P\left[IM > x \mid M_i = m, R_i = r\right] \cdot f_{M_i}\left(m\right) \cdot f_{R_i}\left(r\right) \cdot dm \cdot dr \qquad (2.1)$$

where N_{flt} = number of causative faults; ν_i = MAR of occurrence of earthquakes on fault (or seismic source) i. The functions $f_{M_i}(m)$ and $f_{R_i}(r)$ denote the probability density functions (PDFs) of the magnitude (M_i) and source-to-site distance (R_i), respectively, given the occurrence of an earthquake on fault i. The conditional probability $P\left[IM > x \mid M_i = m, R_i = r\right]$ in Eq. (2.1) is referred to as attenuation relationship (predictive relationship of given seismological variables M and R), is typically developed by applying statistical regression analyses to recorded earthquake ground motion data. The seismic hazard curve at a given site accounts for the uncertainty of due to the randomness of the time and spatial occurrences of future earthquakes affecting the site, as well as the uncertainties related to the seismic wave propagation path and the local site conditions. The random occurrence of earthquake in time is commonly modeled using the Poisson model. For small values of $\nu_{IM}(x)$, typical of large earthquakes of interest to structural engineers, the value of the MAR and the corresponding annual probability of occurrence almost coincide.

2.3.1.2 Probabilistic Seismic Demand Hazard Analysis (PSDemHA)

The next step in the PEER PBEE methodology is to estimate in probabilistic terms the seismic demand that future possible earthquake ground motions will impose on the structure. The objective of PSDemHA is to compute the MAR, $\nu_{EDP}(\delta)$, that a given structural response parameter (referred to Engineering Demand Parameter, EDP) exceeds any specified value δ as (Zhang 2006)

$$\nu_{EDP}\left(\delta\right) = \int_{IM} P\left[EDP\left(\bar{\boldsymbol{y}}, IM, \varepsilon_I\right) > \delta \mid IM = x\right] \cdot \left|d\nu_{IM}\left(x\right)\right| \tag{2.2}$$

where $EDP(\bar{\boldsymbol{y}}, IM, \varepsilon_I)$ denotes the dependence of EDP on the best estimates (expected values) $\bar{\boldsymbol{y}}$ of the system properties $\mathbf{Y}$, the ground motion intensity measure , and the record-to-record variability ε_I. Thus, according to Eq. (2.2), the demand hazard curve $\nu_{EDP}(\delta)$ is obtained as the convolution of the conditional complementary CDF (CCDF) of the EDP given , $P\left[EDP > \delta \mid IM = x\right]$, with the seismic hazard curve $\nu_{IM}\left(x\right)$. The conditional CCDF $P\left[EDP > \delta \mid IM = x\right]$ is obtained through subjecting the FE model of the considered structure through ensembles of scaled earthquake records.

2.3.1.3 Probabilistic Seismic Damage Hazard Analysis (PSDamHA)

The objective of the third step of the PEER PBEE methodology is to compute the MAR of exceedance of a specified damage/limit-state LS, ν_{LS}. Although in reality, there is a continuous progression of physical damage in a structure subjected to a damaging load, we typically focus on discretely observed (Veletzos et al. 2008) or prescribed (ASCE 2013) damage-states. For example, discrete damage-states for reinforced concrete bridge piers include the onset of concrete cracking, concrete spalling, bar buckling, fracture of transverse and longitudinal reinforcement. The MAR of exceedance of a specified damage/limit-state can be obtained as (Conte and Zhang 2007; Zhang 2006):

$$\nu_{LS} = \int_{EDP} P\left[LS \mid EDP = \delta\right] \cdot \left|d\nu_{EDP}\left(\delta\right)\right| \tag{2.3}$$

where $P\left[LS \mid EDP = \delta\right]$ denotes the probability that the damage/limit-state LS is reached or exceeded given that the associated EDP is equal to the specific value δ. This probability quantity, $P\left[LS \mid EDP = \delta\right]$, viewed as a function of δ is referred to as a *fragility function* or *fragility curve* in the literature. Thus, according to Eq. (2.3), the MAR of exceedance of a specified damage/limit-state LS, ν_{LS}, is obtained mathematically as the convolution of the corresponding fragility curve, $P\left[LS \mid EDP = \delta\right]$, and the seismic demand hazard curve $\nu_{EDP}\left(\delta\right)$ of the associated EDP. A fragility curve is typically developed based on the joint use of a simplified (design code type) analytical, semi-analytical or empirical predictive capacity model for this limit-state and experimental data collected from an ensemble of specimens for this limit-state (e.g., Berry and Eberhard 2004; Berry and Eberhard 2005). In the absence of experimental data for a given limit-state (e.g., structural system limit-states), fragility curves are obtained through numerical simulation of the structural response behavior using reliable (e.g., validated at the component level) FE structural models (e.g., Mackie and Stojadinović 2004; Nielson 2005)

2.3.1.4 Probabilistic Seismic Loss Hazard Analysis (PSLHA)

In the PEER PBEE methodology, the probabilistic performance assessment results reviewed above can be propagated further to decision variables (DVs) that relate to loss of life, cost (direct and indirect), and downtime and are of great interest to property owners. The objective of probabilistic seismic loss analysis is to assess DVs probabilistically (e.g., compute the MAR that the total repair/replacement cost due to seismic damage exceeds any specified dollar amount) for a given structure at a given location. The probabilistic assessment of these DVs, which are random variables, accounts for the uncertainties in the seismic hazard at the site or in , in the seismic demand (EDPs), in the structural capacity and damage/limit-states, and in the cost associated with the repair of individual structural components or replacement of the entire structure. The outcome of a probabilistic loss analysis is the seismic loss hazard curve $\nu_{DV}(v)$, which expresses the MAR of the DV (e.g., total repair/replacement cost) exceeding any specified threshold value v.

In the case of global failure of the structure, a new structure will be constructed, and the total repair cost is defined by the construction cost of the new structure. In the case of "no global collapse", it is assumed that all damage occurs at the component level and the total repair cost L_T of the structure (in a year) is equal to the summation of the repair costs of all components damaged during that year, i.e.,

$$L_T = \sum_{j=1}^{n} L_j \tag{2.4}$$

where L_j is the repair cost of the j^{th} damaged component, and n is the number of damaged components in the structure. The repair cost of a damaged component is generally associated with a specified repair scheme, which is associated with the damage state of the component. Basic ingredients to probabilistic loss assessment are repair actions and probability distributions of their costs given the component damage state. A multi-layer Monte Carlo simulation approach can be used to compute very efficiently the seismic loss hazard curve related to L_T (Conte and Zhang 2007; Zhang 2006).

The loss hazard curve incorporates the effects of the uncertainties related to earthquake occurrences in space and time, ground motion intensity, ground motion time history (record-to-record variability), structural capacity, damage/limit-states, and repair costs. The relative importance of these various sources of uncertainty in regard to the loss hazard results can be investigated through parametric studies.

2.4 Current Bridge Design Practice

Current practices of seismic design for ordinary or conventional bridges primarily includes two design methodologies. The first is a force-based approach incorporated into the AASHTO LRFD Bridge Design Specifications (AASHTO 2012), while the second one is a displacement-based approach, originating partly from the Caltrans Seismic Design Criteria (SDC) version 1.4 (Caltrans 2006), and on which the AASHTO Guide Specifications for Seismic Bridge Design (AASHTO 2011) is predicated. Ordinary or conventional bridges are subjects of concern in this proposed research because these are the most common bridges designed in-house by Caltrans and it is aimed to determine whether the reported benefits of using a design approach corresponding to the PEER PBEE framework over the current design procedure used by Caltrans are significant. This section briefly discusses both methodologies with an aim to primarily highlight the weak points of the current seismic bridge design practice and how PBSD can serve to bolster it.

2.4.1 Force-based Approach

The force-based approach, with capacity design as its underlying philosophy, relies on providing adequate resistance to structural elements of the bridge that are selected to dissipate energy by way of yielding when subjected to an earthquake. This is done by selecting a design ground motion (with a probability of exceedance of 5% in 50 years or 1000-year return period) and subjecting a linear elastic model of the bridge to the same. The forces generated in the critical locations of the energy-dissipating (yielding) elements are obtained and these regions are designed to resist only a fraction (called design forces) of the originally calculated forces by multiplying response modification factors (called R-factors) to them. These R-factors are selected primarily based on structure geometry, and anticipated ductility. Adequate detailing is provided at the locations of yielding to get desired inelastic action through ductility. Having designed for ductility, all other members are then protected against overstrength forces so as to make sure that they remain linear elastic.

Apart from the usual problem of incomplete incorporation of uncertainty by only considering it in determining the seismic hazard, that too for a single hazard level, this approach has the added disadvantage of assuming that prescriptive requirements of detailing will do their job of ensuring bridge performance without any firsthand scrutiny been made.

2.4.2 Displacement-based Approach

The displacement-based approach differs from its force-based counterpart in that a direct check of the displacement capacity of the system is made. The present Caltrans SDC v1.7 (Caltrans 2013) uses this approach for the design of bridge systems. Still rooted in capacity design philosophy, this approach involves the selection of a trial design that is detailed for suitable inelastic action and ductility, followed by checking for the displacement capacity directly. The system displacement capacity is controlled by prescribing material strain limit states which can be related to global system displacements through element curvature and rotations. The inelastic displacement capacity is then compared to the elastic displacement demand generated due to the action of the design earthquake (with a probability of exceedance of 5% in 50 years or 1000-year return period).

This approach has the merit of a firsthand quantitative check of displacement capacity being made. Additionally, it is welcoming of the complete PBSD framework, because it already follows a partial 1st generation performance-based procedure by allowing prescriptive strain limits (related to various damage states and hence performance levels) to control the system displacement capacity. However, it has the drawbacks, similar to that of the 1st generation PBEE procedures mentioned earlier, of having inadequately accounted for uncertainty only in the seismic input, that too for a single hazard level. Element performance evaluation is considered to be void of uncertainties and prescriptive strain limits, based on laboratory tests, simplified analytical models, and engineering judgment are assumed to be representative of system behavior. Also, metrics of structural performance being based on element forces and deformation, does not allow the public and/or owners to participate in risk-informed decision making, unlike what is promised by the PEER PBEE framework.

Prescriptive design methodologies form the heart of current seismic bridge design practice in the US. With a latent objective of collapse prevention and life safety under a design earthquake event, these prescriptive measures do the job of evaluating the seismic performance of bridges only to a limited extent as there is no direct control over the seismic performance of bridges in the hands of the designer. Although this has proved to be a satisfactory design methodology for the bridge engineering profession till date (NCHRP 2013), the application of PBSD in bridge design, nonetheless, does not become less promising in this regard. With a significantly better comprehension and quantification of seismic demand and response of bridges due to the incorporation of all the sources of inherent uncertainties, PBSD will allow designers and the owners/public to make collective and risk-informed decisions regarding the performance of bridges during a seismic event, thereby leading to a more efficient and rational design practice.

2.5 Recent Performance-based Design Developments in Bridge Engineering

The fully probabilistic PBSD is the most advanced design methodology and is expected to provide the foundation for future design codes (Cornell and Krawinkler 2000; Ellingwood 2008; NCHRP 2013). Although not in its all-inclusive form, PBSD has already started to be implemented in practice (ASCE-7-10 2010; FEMA-445 2006; FHWA Retrofit Manual 2006; ICC-PC 2012; NCHRP 2013) by the structural engineering profession and several design and retrofit projects have also been undertaken by various organizations. Significant work has been done and progress is being made in both spheres of building and bridge engineering, albeit the latter has seen relatively less advancement as compared to the former (NCHRP 2013).

A recent investigation (NCHRP 2013) led by the Transportation Research Board of the National Academies under the National Cooperative Highway Research Program (NCHRP) regarding the current state of seismic design practice in the area of bridge engineering, made the necessity and significance of the implementation of PBSD in bridge design quite evident. This synthesis brings out the fact that the current bridge design practice considers safety and risk associated with seismic performance of bridges as mere ramifications of the fulfillment of prescriptive measures. May's argument (May 2001) of explicit consideration of safety and risk, in order that public and engineers participate in the decision-making process in tandem, is emphasized. This process of collective decision-making, however, will require an unambiguous definition of performance objectives that will facilitate its smooth working and will also help to keep post-hazard, performance-related, political and/or legal issues at bay.

The synthesis also covers the 4 analytical stages of PEER PBEE framework discussed before highlighting the areas where special attention is the need of the hour as per the current state of practice in the bridge engineering profession. With the current tools of seismic hazard analyses and nonlinear structural analyses, the implementation of the first two steps of the framework seems to be a little less demanding and more feasible than the last two steps, via a probabilistic treatment of the seismic hazard and structural response. A noteworthy highlight of the synthesis is that the field of damage and loss prediction, in a rigorous probabilistic manner, has yet to see significant advancement. The complexity of predicting the highly uncertain phenomenon of damage has so far been underestimated by its treatment based on deterministic strain-limits. A complete probabilistic treatment of damage requires extensive laboratory testing and analytical investigations (Berry and Eberhard 2004; Mackie and Stojadinović 2004), thereby leading to development of fragility functions which relate an engineering demand parameter or a response quantity to the probability of exceedance of a specific damage state. The final and the most important step, novel to the PEER PBEE framework, is the explicit probabilistic consideration of loss metrics, which are of interest to owners and stakeholders. Loss prediction, till date, has largely been qualitative and has lacked objectivity. Thus, the need to explicitly consider this, in a probabilistic manner, whereby the risk of incurring losses pertaining to decision variables, viz., deaths, dollars, downtime, etc., can be accurately evaluated is expressed. For this purpose, loss models (Baker and Cornell 2003; Mander et al. 2012; Miranda et al. 2004; Moehle and Deierlein 2004, etc.) relating damage to the probability of exceeding various levels of losses are required. Once equipped with all the tools required for a rigorous implementation of the framework, wherein all sources of uncertainty are accounted for, it can be applied to the design (inverse assessment problem) of new bridges. As mentioned earlier, the works of Cornell and coworkers (2002) and Mackie and Stojadinović (2007) can be cited as premises to such an effort.

More recently, research conducted at the University of Nevada, Reno, led to the development of the Probabilistic Damage Control Approach (PDCA) (Saini and Saiidi 2014) for seismic design of bridge columns. This research, funded by Caltrans, is a significant step forward toward the implementation of a probabilistic PBSD in the bridge engineering industry. In this approach, the uncertainties in seismic demand and structural response are taken into account explicitly. A displacement-based representative parameter of bridge-column response, called Damage Index (DI), defined as the ratio of plastic deformation demand to the plastic deformation capacity, is used to measure the seismic performance of columns. Fragility functions correlating Damage States (DSs) to DIs were used from a previous experimental study (Vosooghi and Saiidi 2012) at University of Nevada, Reno to come up with a probabilistic resistance/capacity model. The probabilistic load/demand model was developed using extensive analytical modeling of columns designed to have a desired probability of exceedance of a certain DS, and nonlinear time history analyses of the same subjected to a suite of ground motions conducted thereafter. In order to have a realistic load/demand model, uncertainties in seismic demand were incorporated through the inclusion of different site classes, ground motion parameters, bent properties and earthquake return period. Structural performance was evaluated based on the reliability indices (βs) associated with different DSs. Finally, a non-iterative, approximate, yet direct design method is forwarded so as to design a column bent for a target DI in order that a desired reliability index is achieved for a specific damage state.

Research studies and implementations of PBSD, as such, have served to expose the difficulties and challenges it entails, thereby helping to fill the knowledge gaps and move forward towards the goal of a convenient implementation of the framework in its most rigorous form.

3 Testbed Bridges

3.1 Introduction

For this study, four as built bridges located in California were selected for analysis and are described in this chapter. The selected bridges conform to the definition of ordinary standard bridges as described in Caltrans SDC and repeated in Section 3.2.1. Multiple testbed bridges are required to cover a spectrum of design characteristics of ordinary bridges in California to ensure the overall methodology utilized in this project can be reproduced for a variety of design scenarios.

Each testbed bridge will be used to generate a corresponding design matrix where multiple key design parameters can be varied from the as-designed case. Practical combinations of design parameters encountered in the field and its effects on the performance of each bridge are analyzed using this design matrix. The utilization of these testbed bridges and subsequent findings are investigated and described more comprehensively later in this report.

The testbed bridges selected for this study are based on bridges studied in recent research projects funded by Caltrans and PEER (Beckwith et al. 2015; Kaviani et al. 2012; Kaviani et al. 2014; Omrani et al. 2015). The selected set of testbed bridges comprises of representative modern Ordinary Standard Bridges (OSBs) in California constructed after year 2000, viz., Bridge A, Bridge B, Bridge C and Bridge MAOC. A comprehensive explanation behind the recommendation of these bridges are described in their respective reports.

Bridge A is the Jack Tone Road Overcrossing in Ripon, California consisting of two spans with a single column bent. Bridge B is the La Veta Avenue Overcrossing in Tustin, California also consisting of two spans but supported on a two-column bent. Bridge C is the Jack Tone Road Overhead in Ripon, California (located adjacent to Bridge A) consisting of three spans on three-column bents. The last bridge is the Massachusetts Avenue Overcrossing, Bridge MAOC, located in San Bernardino, California consisting of five spans on four-column bents. Selected characteristics of each of these bridges obtained from the National Bridge Inventory (NBI) database are listed in Table 3-1. A detailed description of the geometrical characteristics and structural properties of each bridge can be found in Section 3.2.

Table 3-1 Selected characteristics of testbed bridges in accordance with the 2017 archived NBI database

NBI Item Name	Bridge A	Bridge B	Bridge C	Bridge MAOC
Structure number	29 0320	55 0938	29 0318	54 1265
Features intersected	STATE ROUTE 99	STATE ROUTE 55	UPRR, SB99 ONRP, KAMPS WY	INTERSTATE 215 & BNSF RY
Facility carried by structure	Jack Tone Road	La Veta Avenue	Jack Tone Road	Massachusetts Avenue
Location	10-SJ-099-2.34-RIP	12-ORA-055-13.20-TUS	10-SJ-099-2.32-RIP	08-SBD-215-9.03-SBD
Latitude	37450851	33465032	37450217	34075676
Longitude	121083108	117495371	121083077	117183123
Year built	2001	2001	2001	2012
Lanes on structure	1	4	4	2
Lanes under structure	7	14	3	10
Average daily traffic	20000	10000	5000	9000
Skew	33	0	36	8
Type of service	11 (highway on bridge, highway w/wo pedestrian)	51 (highway-pedestrian on bridge, highway w/wo pedestrian under bridge)	18 (highway on bridge, highway-waterway-railroad under bridge)	54 (highway-pedestrian on bridge, highway-railroad under bridge)
Number of spans in main unit	2	2	3	5
Structure type, main	606 (prestressed concrete continuous, box beam or girders - single or spread)	605 (prestressed concrete continuous, box beam or girders - multiple)	606 (prestressed concrete continuous, box beam or girders - single or spread)	205 (concrete continuous, box beam or girders - multiple)
Deck (physical condition)	5 (fair condition, minor section loss)	8 (very good condition)	5 (fair condition, minor section loss)	7 (good condition, minor problems)
Superstructure (physical condition)	7 (good condition, minor problems)	8 (very good condition)	7 (good condition, minor problems)	7 (good condition, minor problems)
Substructure (physical condition)	5 (fair condition, minor section loss)	7 (good condition, minor problems)	5 (fair condition, minor section loss)	7 (good condition, minor problems)
Inspection date	1016 (October 2016)	0616 (June 2016)	1016 (October 2016)	1016 (October 2016)

3.2 Description of Selected Bridges

Although specific requirements must be met for bridges to be classified as Ordinary Standard Bridges, as defined in Caltrans SDC v1.7 (repeated below), nevertheless considerable variations and combinations of designs are still possible. The selected testbed bridges, therefore, should attempt to cover a spectrum of design parameters commonly found in practice such that a range of possible designs can be accounted for to increase the robustness of the developed methodology. Such variations include the number of spans, columns per supporting bent, diameter of columns, height of columns, cap beam, skew, deck width and geometry, number of bearing pads shear key type etc. A detailed description of each bridge is given below focusing on the above-mentioned properties as well as derived geometrical and structural parameters pertinent for the construction of finite element models of these bridges (discussed in the next chapter).

3.2.1 Definition of an Ordinary Standard Bridge per Caltrans SDC v1.7 (Caltrans 2013)

A structure meeting all the following requirements below, where applicable, is classified as an Ordinary Standard Bridge (taken directly from Caltrans SDC, Version 1.7, April 2013):

- Each span length is less than 300 feet.
- Bridges with single superstructures on either a horizontally curved, vertically curved, or straight alignment.
- Constructed with precast or cast-in-place concrete girder, concrete slab superstructure on pile extensions, column or pier walls, and structural steel girders composite with concrete slab superstructure which are supported on reinforced concrete substructure elements.
- Horizontal members either rigidly connected, pin connected, or supported on conventional bearings.
- Bridges with dropped bent caps or integral bent caps.
- Columns and pier walls supported on spread footings, pile caps with piles or shafts.
- Bridges supported on soils which may or may not be susceptible to liquefaction and/or scour.
- Spliced precast concrete bridge system emulating a cast-in-place continuous structure • Fundamental period of the bridge system is greater than or equal to 0.7 seconds in the transverse and longitudinal directions of the bridge.

3.2.2 Jack Tone Road Overcrossing (Bridge A)

The Jack Tone Road Overcrossing is located in Ripon, California (south of Sacramento), spanning over California State Route 99. The bridge was constructed in 2001 and consists of a single lane serving as an onramp to the main Jack Tone Road. The bridge consists of two spans at 108.58 ft and 111.82 ft for a total length of 220.4 ft and is supported on a single column bent. Each column is supported on 25 HP 305x79 steel piles. The column has a diameter of 5.51 ft and a longitudinal reinforcement ratio of 2.0%. The deck of the bridge is a three-cell continuous prestressed reinforced-concrete box girder with a total width of 27.13 ft. The bridge abutment is at a skew of 33° and supported vertically on elastomeric bearings and restrained horizontally by monolithic shear keys. A detailed description of the Jack Tone Road Overcrossing can be found in Table 3-2.

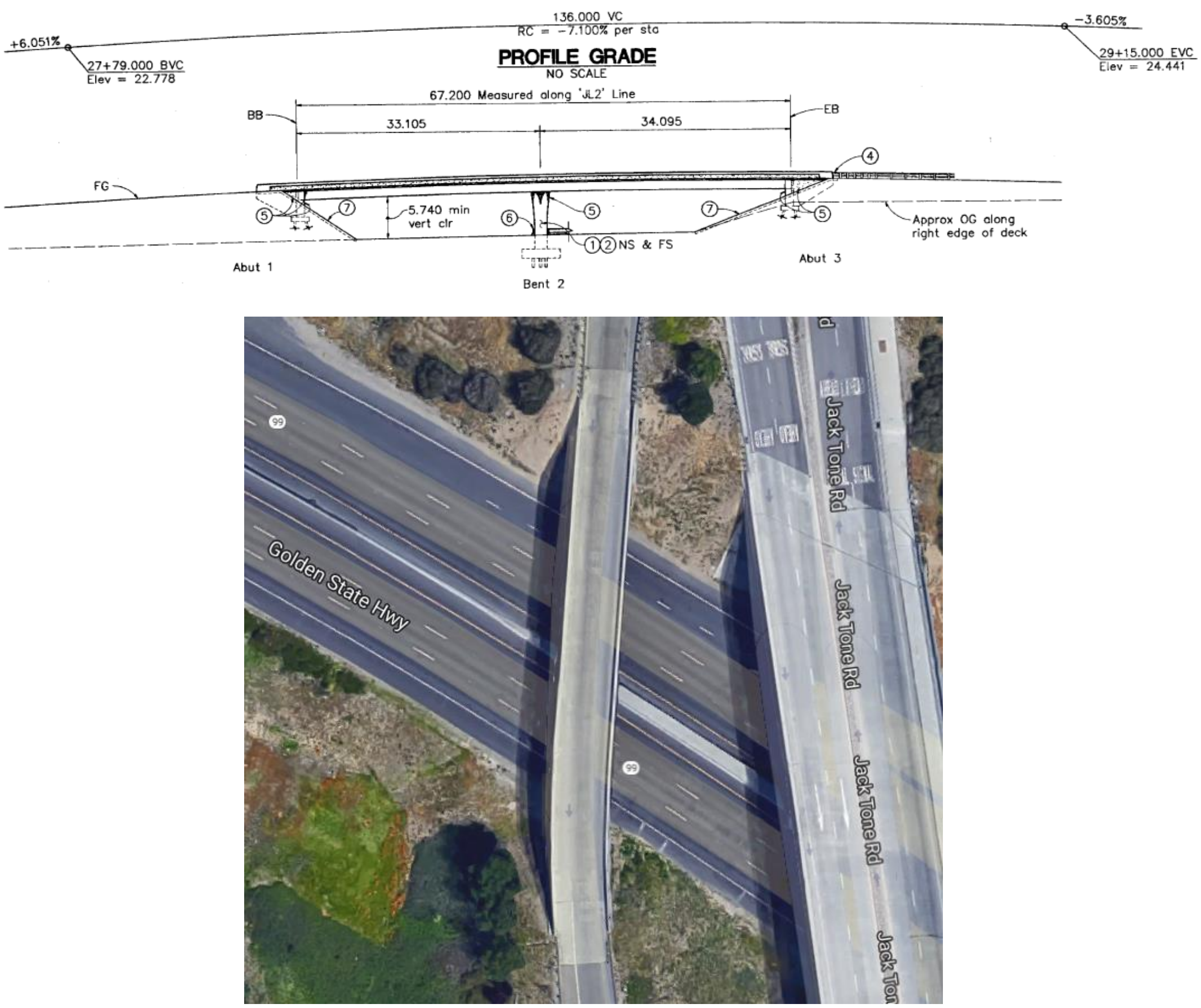

Figure 3.1 Profile and aerial overview of Bridge A on left (adjacent to main Jack Tone Road)

Table 3-2 Geometrical and structural properties of Bridge A

Parameter/Feature	**Value/Description**
Number of spans	2
Length of spans	108.58 ft (33.10 m) and 111.82 ft (34.08 m)
Total length of bridge (L_{tot})	220.4 ft (67.18 m)
Total width of deck (w_d)	27.13 ft (8.27 m)
Depth of deck (d_d)	4.64 ft (1.14 m)
Deck cross-sectional properties (Area, Torsional constant, Second moments of area)	A = 97.55 ft^2 (9.06 m^2); J = 341 ft^4 (2.94 m^4); I_y = 180.33 ft^4 (1.56 m^4); I_z = 3, 797.9 ft^4 (32.78 m^4)
Height of each bent	19.68 ft (6.0 m)
Number of columns in each bent	1
Column cross-sectional properties (Diameter, Area, Torsional constant, Second moments of area)	D_{col} = 5.51 ft (1.68 m); A_{col} = 23.84 ft^2 (2.21 m^2); J_{col} = 90.49 ft^4 (0.78 m^4); $I_{y,col}$ = 45.24 ft^4 (0.39 m^4); $I_{z,col}$ = 45.24 ft^4 (0.39 m^4)
Column reinforcement details	Longitudinal reinforcement (2.0%): 22×2#11 Transverse reinforcement: Spiral, #6 @ 3.34 in c/c
Column base hinge diameter	No base hinge
Concrete material properties of elastic superstructure (nominal) (Compressive strength, Elastic modulus)	f'_c = 5 ksi (34.5 MPa) E_c = 4, 030.5 ksi (27, 789.3 MPa)
Concrete material properties of columns (nominal) (Compressive strength, Elastic modulus)	f'_c = 5 ksi (34.5 MPa) E_c = 4, 030.5 ksi (27, 789.3 MPa)
Steel reinforcement material properties	Grade 60, ASTM A706
Bridge skew angle	33°
Shear key type	Non-isolated (monolithic) shear keys
Number of bearing pads per abutment	4 elastomeric bearings
Bearing pad dimensions (Height, Area)	h_{bp} = 2.56 in (.065 m); A_{bp} = 139.5 in^2 (0.09 m^2)

3.2.3 La Veta Avenue Overcrossing (Bridge B)

The La Veta Avenue Overcrossing is located in Tustin, California (south of Los Angeles), spanning over California State Route 55. The bridge was constructed in 2001 and consists of two lanes in each direction running east-west. The bridge consists of two spans at 154.82 ft and 144.98 ft for a total length of 299.8 ft and is supported on a two-column bent. Each column is supported by 20 23.6 in diameter cast-in-drilled hole (CIDH) piles. The columns have a diameter of 5.58 ft and a longitudinal reinforcement ratio of 1.95%. The deck of the bridge is a six-cell continuous reinforced-concrete box girder with a total width of 75.5 ft. The bridge abutment is supported vertically on elastomeric bearings and restrained horizontally by monolithic shear keys. There is no skew in the bridge abutment. A detailed description of the La Veta Avenue Overcrossing can be found in Table 3-3.

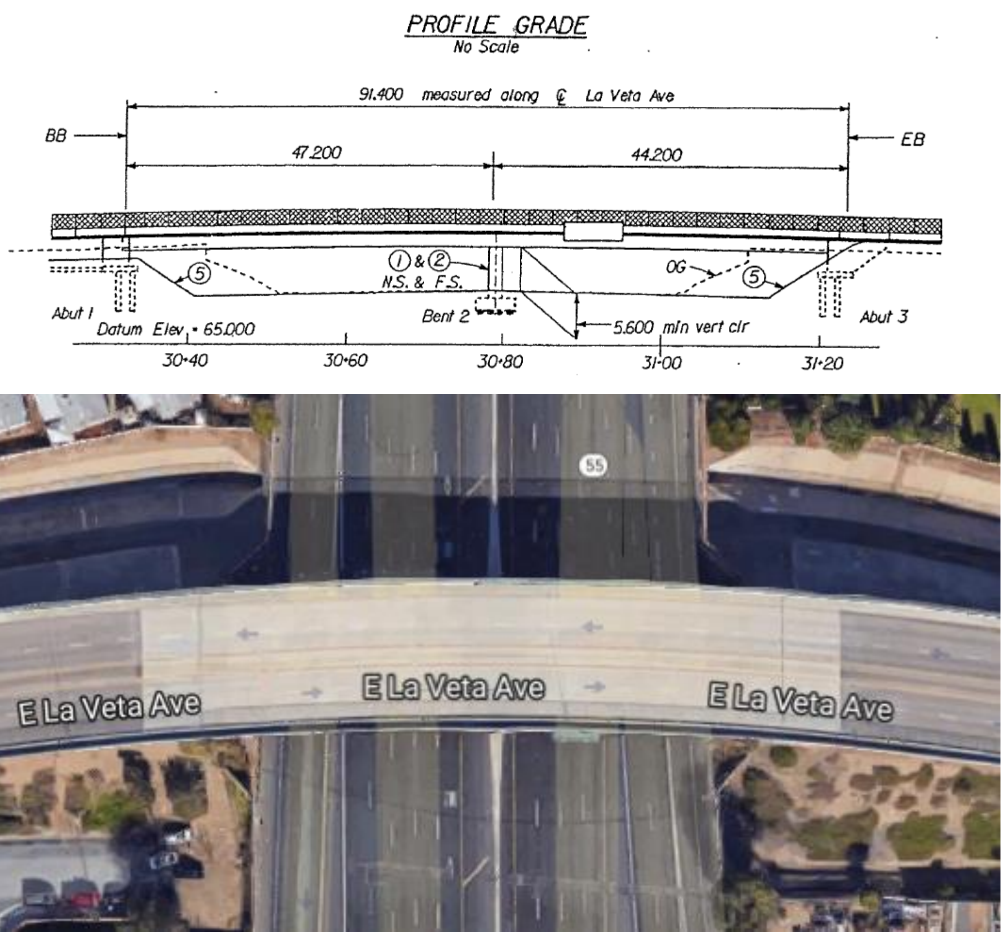

Figure 3.2 Profile and aerial overview of Bridge B

Table 3-3 Geometrical and structural properties of Bridge B

Parameter/Feature	**Value/Description**
Number of spans	2
Length of spans	154.82 ft (47.19 m) and 144.98 ft (44.19 m)
Total length of bridge (L_{tot})	299.8 ft (91.38 m)
Total width of deck (w_d)	75.5 ft (23.01 m)
Depth of deck (d_d)	6.23 ft (1.9 m)
Deck cross-sectional properties (Area, Torsional constant, Second moments of area)	A = 129.13 ft^2 (12.0 m^2); J = 2532 ft^4 (21.85 m^4); I_y = 791.76 ft^4 (6.83 m^4); I_z = 58, 352 ft^4 (503.64 m^4)
Height of each bent	22 ft (6.71 m)
Number of columns in each bent	2
Column cross-sectional properties (Diameter, Area, Torsional constant, Second moments of area)	D_{col} = 5.58 ft (1.70 m); A_{col} = 23.84 ft^2 (2.21 m^2); J_{col} = 90.49 ft^4 (0.78 m^4); $I_{y,col}$ = 45.25 ft^4 (0.39 m^4); $I_{z,col}$ = 45.25 ft^4 (0.39 m^4)
Column reinforcement details	Longitudinal reinforcement (1.95%): 22×2#11 Transverse reinforcement: Spiral, #4 @ 6 in c/c
Column base hinge diameter	3.94 ft (1.2 m)
Concrete material properties of elastic superstructure (nominal) (Compressive strength, Elastic modulus)	f'_c = 5 ksi (34.5 MPa) E_c = 4, 030.5 ksi (27, 789.3 MPa)
Concrete material properties of columns (nominal) (Compressive strength, Elastic modulus)	f'_c = 5 ksi (34.5 MPa) E_c = 4, 030.5 ksi (27, 789.3 MPa)
Steel reinforcement material properties	Grade 60, ASTM A706
Bridge skew angle	0^o
Shear key type	Non-isolated (monolithic) shear keys
Number of bearing pads per abutment	7 elastomeric bearings
Bearing pad dimensions (Height, Area)	h_{bp} = 3.74 in (.095 m); A_{bp} = 558.0 in^2 (0.36 m^2)

3.2.4 Jack Tone Road Overhead (Bridge C)

The Jack Tone Road Overhead is located in Ripon, California (south of Sacramento), spanning over California State Route 99. The bridge was constructed in 2001 and consists of two lanes in each direction running north-south and is located adjacent to Bridge A. The bridge consists of three spans at 156.12 ft, 144 ft and 118.08 ft for a total length of 418.2 ft and is supported on three-column bents. The columns have a diameter of 5.51 ft and a longitudinal reinforcement ratio of 2.20%. Each column is supported on 24 HP 305x79 steel piles. The deck of the bridge is a seven-cell continuous reinforced-concrete box girder with a total width of 77 ft. The bridge abutment is at a skew of 36° and supported vertically on elastomeric bearings and restrained horizontally by monolithic shear keys. A detailed description of the Jack Tone Road Overhead can be found in Table 3-4.

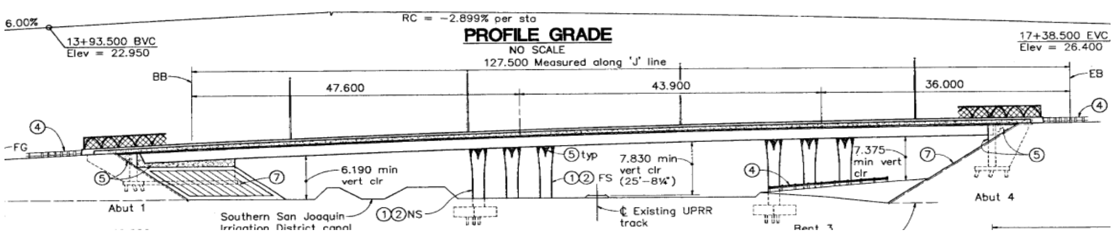

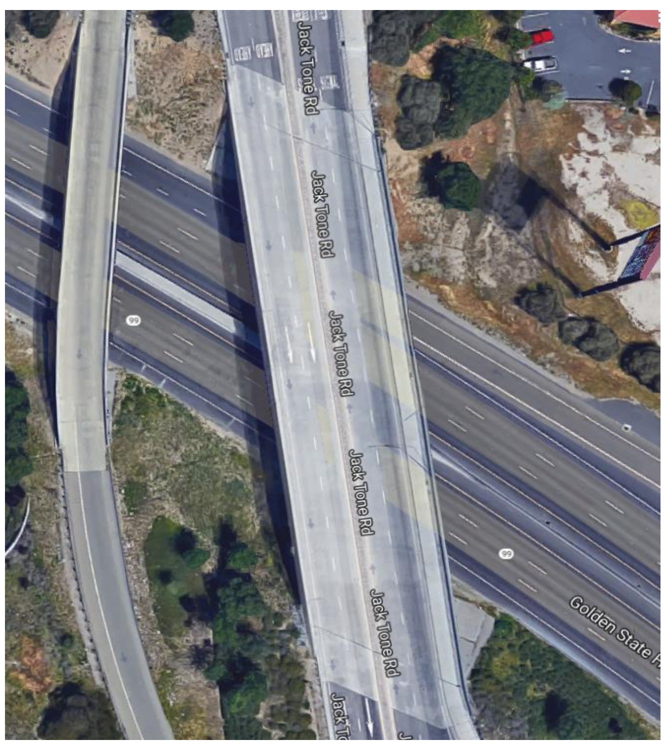

Figure 3.3 Profile and aerial overview of Bridge C (right)

Table 3-4 Geometrical and structural properties of Bridge C

Parameter/Feature	**Value/Description**
Number of spans	3
Length of spans	156.12 ft (47.59 m), 144 ft (43.89 m), and 118.08 ft (36.0 m)
Total length of bridge (L_{tot})	418.2 ft (127.47 m)
Total width of deck (w_d)	77 ft (23.47 m)
Depth of deck (d_d)	6.3 ft (1.92 m)
Deck cross-sectional properties (Area, Torsional constant, Second moments of area)	A = 131.65 ft^2 (12.0 m^2); J = 2563 ft^4 (22.12 m^4); I_y = 788.90 ft^4 (6.81 m^4); I_z = 59, 761 ft^4 (515.80 m^4)
Height of each bent	24.6 ft (7.5 m)
Number of columns in each bent	3
Column cross-sectional properties (Diameter, Area, Torsional constant, Second moments of area)	D_{col} = 5.51 ft (1.68 m); A_{col} = 23.84 ft^2 (2.21 m^2); J_{col} = 90.49 ft^4 (0.78 m^4); $I_{y,col}$ = 45.25 ft^4 (0.39 m^4); $I_{z,col}$ = 45.25 ft^4 (0.39 m^4)
Column reinforcement details	Longitudinal reinforcement (2.2%): 17×2#14 Transverse reinforcement: Spiral, #6 @ 3.34 in c/c
Column base hinge diameter	3.41 ft (1.04 m)
Concrete material properties of elastic superstructure (nominal) (Compressive strength, Elastic modulus)	f'_c = 5 ksi (34.5 MPa) E_c = 4, 030.5 ksi (27, 789.3 MPa)
Concrete material properties of columns (nominal) (Compressive strength, Elastic modulus)	f'_c = 5 ksi (34.5 MPa) E_c = 4, 030.5 ksi (27, 789.3 MPa)
Steel reinforcement material properties	Grade 60, ASTM A706
Bridge skew angle	36^o
Shear key type	Non-isolated (monolithic) shear keys
Number of bearing pads per abutment	9 elastomeric bearings
Bearing pad dimensions (Height, Area)	h_{bp} = 4.53 in (.115 m); A_{bp} = 327.98 in^2 (0.212 m^2)

3.2.5 Massachusetts Avenue Overcrossing (Bridge MAOC)

The Massachusetts Avenue Overcrossing is located in San Bernandino, California (east of Los Angeles), spanning over Interstate 215. The bridge was constructed in 2012 and consists of two lanes running in the northeast-southwest direction. The bridge consists of five spans at 49.21 ft, 94.49 ft, 91.86 ft, 99.74 and 78.08 ft for a total length of 413.39 ft and is supported on four-column bents. Each bent is supported on either 8 or 4 HP 360×132 steel piles. The columns have a diameter of 4.00 ft and a longitudinal reinforcement ratio of 1.90%. The deck of the bridge is a five-cell continuous reinforced-concrete box girder with a total width of 48.72 ft. The bridge abutment is at a skew of 8.1° and supported vertically on elastomeric bearings and restrained horizontally by isolated shear keys. A detailed description of Massachusetts Avenue Overcrossing can be found in Table 3-5.

Figure 3.4 Profile and aerial overview of Bridge MAOC

Table 3-5 Geometric and structural properties of Bridge MAOC

Parameter/Feature	**Value/Description**
Number of spans	5
Length of spans	49.21 ft (15.0 m), 94.49 ft (28.8 m), 91.86 ft (28.0 m), 99.74 ft (30.4 m), and 78.08 ft (23.8 m)
Total length of bridge (L_{tot})	413.39 ft (126.0 m)
Total width of deck (w_d)	48.72 ft (14.8 m)
Depth of deck (d_d)	4.49 ft (1.37 m)
Deck cross-sectional properties (Area, Torsional constant, Second moments of area)	A = 72.44 ft^2 (6.73 m^2); J = 724 ft^4 (6.25 m^4); I_y = 210.87 ft^4 (1.82 m^4); I_z = 12, 698 ft^4 (109.60 m^4)
Height of each bent	29.53 ft (9.0 m), 31.50 ft (9.6 m), 30.71 ft (9.4 m), and 27.43 ft (8.4 m)
Number of columns in each bent	4
Column cross-sectional properties (Diameter, Area, Torsional constant, Second moments of area)	D_{col} = 4.00 ft (1.22 m); A_{col} = 12.57 ft^2 (1.17 m^2); J_{col} = 22.34 ft^4 (0.19 m^4); $I_{y,col}$ = 11.17 ft^4 (0.096 m^4); $I_{z,col}$ = 11.17 ft^4 (0.096 m^4)
Column reinforcement details	Longitudinal reinforcement (1.9%): 22×#11 Transverse reinforcement: Circular, #7 @ 5.91 in c/c
Column base hinge diameter	2.13 ft (0.65 m)
Concrete material properties of elastic superstructure (nominal) (Compressive strength, Elastic modulus)	f'_c = 5 ksi (34.5 MPa) E_c = 4, 030.5 ksi (27, 789.3 MPa)
Concrete material properties of columns (nominal) (Compressive strength, Elastic modulus)	f'_c = 5 ksi (34.5 MPa) E_c = 4, 030.5 ksi (27, 789.3 MPa)
Steel reinforcement material properties	Grade 60, ASTM A706
Bridge skew angle	8.1°
Shear key type	Isolated shear keys
Number of bearing pads per abutment	6 elastomeric bearings
Bearing pad dimensions (Height, Area)	h_{bp} = 3.54 in (.09 m); A_{bp} = 144.19 in^2 (0.093 m^2)

4 Computational Models of Testbed Bridges

4.1 Introduction

Earthquake-resistant structural design and/or assessment requires analysis of structural systems subjected to seismic loads to predict the induced internal forces and deformations. A well-posed structural analysis problem for a reliable prediction of the seismic response of a structural system requires:

(i) An appropriate analytical/numerical model of the structure providing a realistic representation of the structure both at the component-level and at the system-level;
(ii) An accurate representation of the earthquake ground motion and/or its effects; and
(iii) A robust analytical/numerical procedure to construct and solve the governing equations

Structural analysis can range from being simple to intricate depending on the level of sophistication implemented in each of the above three requirements.

Prevailing approaches for the modeling of structural systems based on the principles of mechanics cover the gamut from being theoretical, computational, or experimental. Computational mechanics-based models are typically used for the simulation of large-scale real-world structural systems, such as bridges. Computational/numerical approaches to modeling of structural systems involve idealizations mainly distinguishable into either phenomenological (i.e., describing the empirical/observed relationships between phenomena in a way which is consistent with the relevant theory but not directly derived from it) or fundamental (i.e., based/derived directly from first principles). Fundamental approaches to modeling have become increasingly popular as ample computational power is made available with the advent of computers. Standing the test of accuracy, feasibility and practicability, finite element modeling has emerged as an effective tool for modeling and simulation of structural systems.

An earthquake ground motion and/or its effects on structural systems are represented, typically in practice, by an equivalent lateral load, an earthquake ground motion response spectrum, or the ground motion history itself. Based on such a representation, and the assumption of the nature of relationship between forces and deformations in structures, several methods of analyses are used in the field of earthquake-resistant structural design and/or assessment. These methods include the relatively simple linear static analysis, linear response spectrum analysis, and linear dynamic response history analysis, in one hand, while the somewhat involved nonlinear static analysis, and nonlinear dynamic response history analysis, on the other.

The level of sophistication employed in this project for the structural analysis of Ordinary Standard Bridges (OSBs) is predicated on the purpose of the analysis. Keeping in mind the overarching goal of developing a simplified and practicable, yet rigorous, performance-based seismic design (PBSD) methodology for OSBs, achievement of a middle ground between accuracy, feasibility and practicability of the chosen structural analysis procedure is desirable. Thus, the analysis method implemented in this project involves nonlinear dynamic response history analyses of bridge models consisting of frame/beam-column elements combined with springs. A convenient, yet reasonably accurate, depiction of nonlinear structural behavior of OSBs can be obtained by using highly detailed fiber-section Euler-Bernoulli beam-column elements with distributed plasticity in conjunction with the $P-\Delta$/Corotational nonlinear geometric transformation. Analytical/empirical nonlinear force-deformation relationships can be used to represent the behavior of structural components modeled with springs. This type of modeling, common for both buildings and bridges in current earthquake engineering practice, is chosen to benefit from a finite element modeling technique that:

(i) is reasonably accurate in terms of representing nonlinear structural behavior;
(ii) is numerically robust to the implicit integration of the governing equation of motion for multiple seismic inputs; and
(iii) leads to acceptable computational workload and runtime.

To apply and evaluate the PEER PBEE assessment framework, lying at the heart of the proposed PBSD methodology, a set of four testbed OSBs, described in Chapter 3, are selected in this project. This chapter elaborates on the nonlinear finite element modeling technique and the response-history analysis setup employed for the probabilistic seismic performance assessment of these selected testbed bridges.

4.2 Finite Element Model Description

The selected set of testbed OSBs is comprised of bridges with prestressed concrete box-girder decks supported by column-bent(s) and seat-type abutments. Three-dimensional nonlinear finite element models (consisting of beam-column elements and zero-length elements) of these bridges are constructed in OpenSees (Mazzoni et al. 2006; McKenna 2011), the open-source finite element computational platform for research in PBEE developed at PEER. OpenSees has advanced capabilities for modeling and analyzing the nonlinear seismic response of structural systems using an abundant library of material models, elements, and solution algorithms. The software enables script-based automated execution of ensemble nonlinear response history analyses which can also be parallelized (across multiple-cores in a desktop computer or a supercomputer) thus providing resources deemed extremely valuable for probabilistic performance assessment of structures and/or parametric studies.

Initially inherited Tcl input files of the OpenSees models of these bridges from previous Caltrans/PEER funded projects (Beckwith et al. 2015; Kaviani et al. 2014; Omrani et al. 2015) are revisited, parameterized, and improved based on experimental validation and/or literature review as required while adhering to the recommendations of Omrani et al. (2015) and the Caltrans Seismic Design Criteria (SDC) version 1.7 (Caltrans 2013). Schematic representations of the computational models of the four testbed bridges (Bridge A, Bridge B, Bridge C, and Bridge MAOC), with splines drawn along the section centroid of respective elements, are shown Figure 4.1 through Figure 4.4. The following sections provide an in-depth account of the modeling technique employed for various components of the testbed OSBs including model attributes such as chosen material properties, inertial properties and damping model.

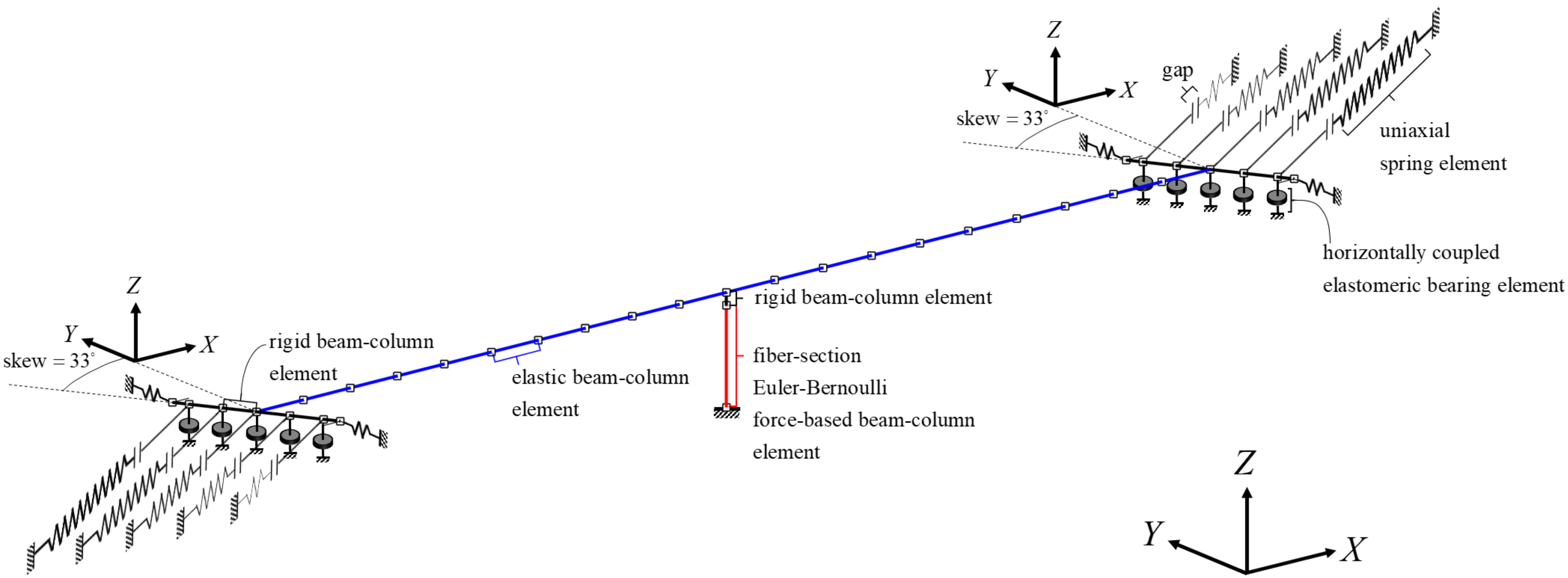

Figure 4.1 Schematic representation of the finite element model of Bridge A

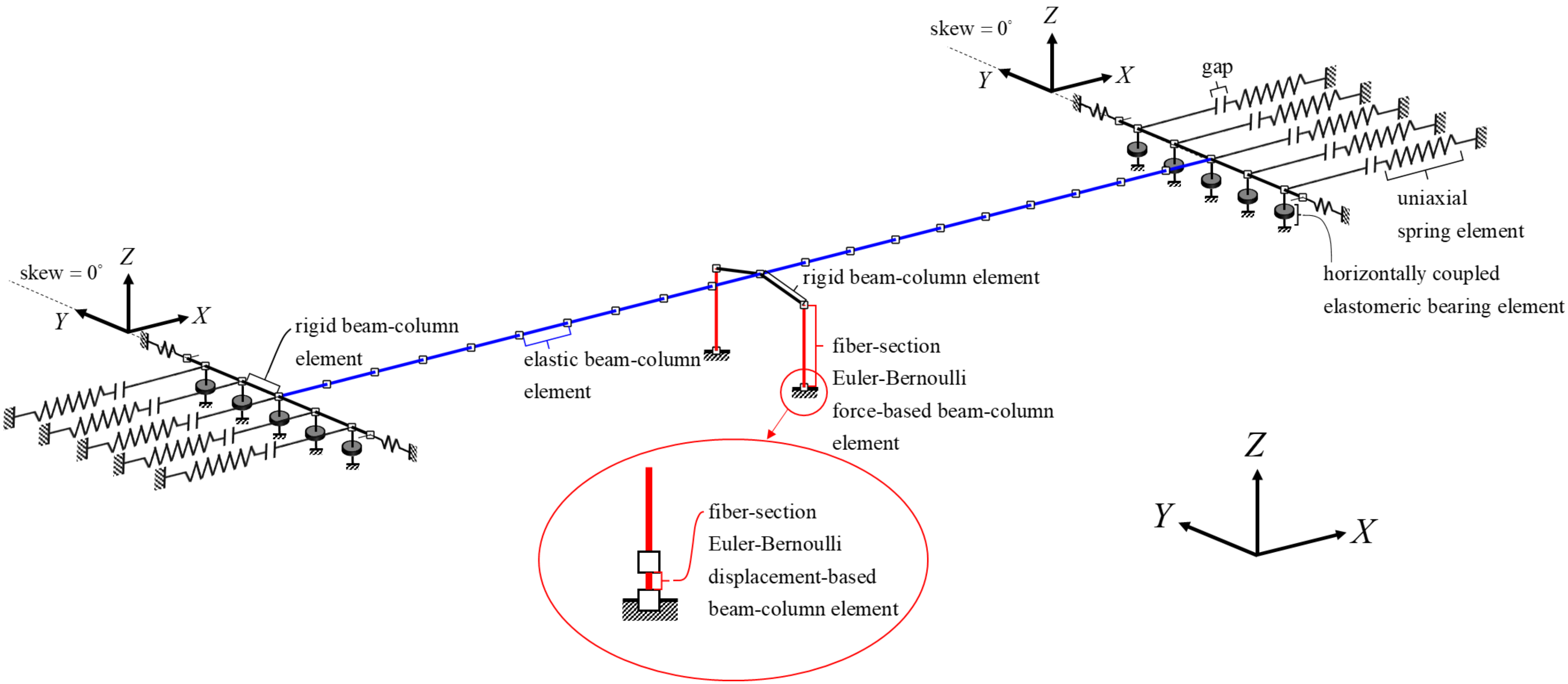

Figure 4.2 Schematic representation of the finite element model of Bridge B

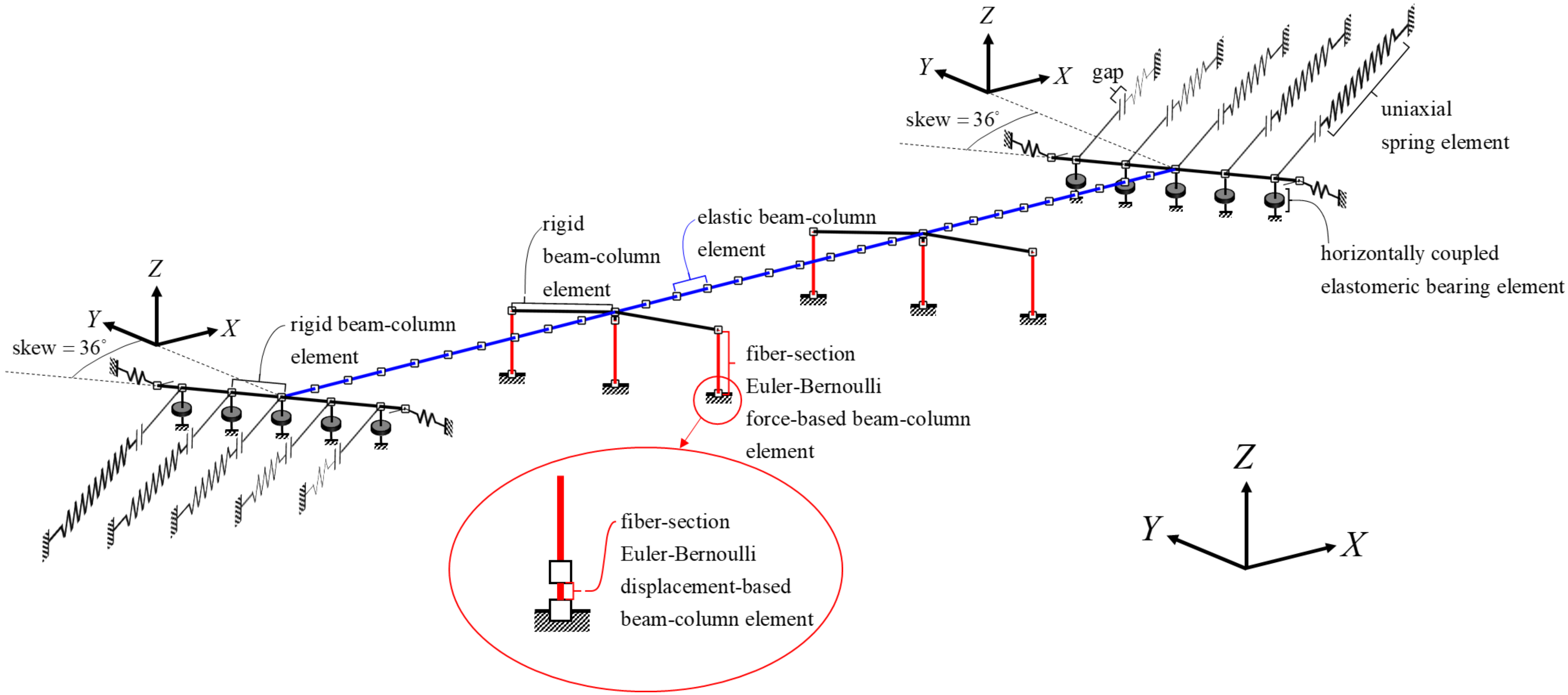

Figure 4.3 Schematic representation of the finite element model of Bridge C

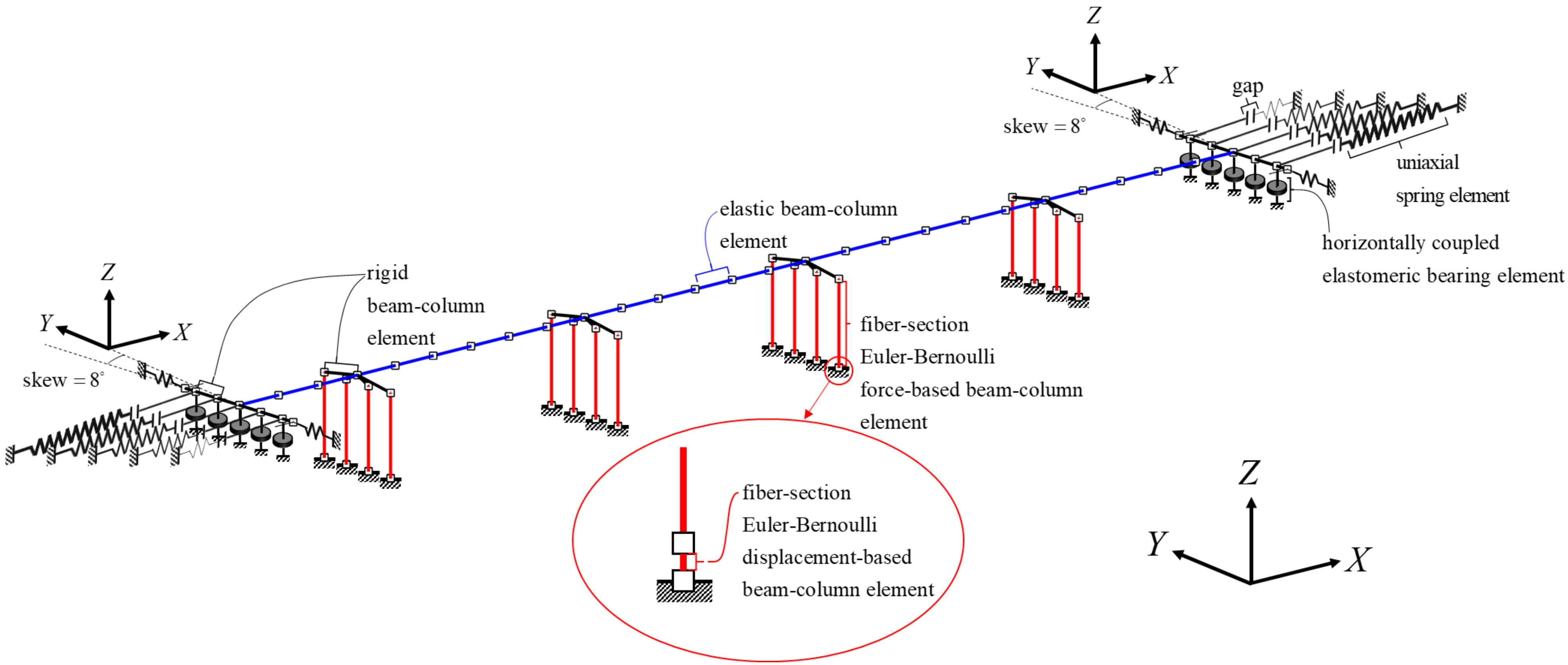

Figure 4.4 Schematic representation of the finite element model of Bridge MAOC

4.2.1 Deck

Bridge decks of the considered testbed bridges are designed as pre-stressed concrete box girders. Bridge decks are typically capacity-protected elements which are not meant to undergo flexural yielding and dissipate energy over the entire duration of the seismic ground motion input in the event of an earthquake. As such, the deck of a testbed bridge is modeled using elastic beam-column elements (implemented as *elasticBeamColumn* element in OpenSees) laid along the centroid of the deck section. To evenly capture the mass distribution across the entire length of a bridge deck via a lumped mass model, each span of the deck is further sub-divided in several (10) elements.

Section properties, as per the original design drawings of the testbed bridges, and material properties, characteristic of normal-weight concrete, are assigned to the deck elements. The assigned material and section properties for the deck elements of each testbed bridge are given in Table 4-1. It is noted that to obtain realistic predictions of structural periods and seismic demands, cracked section properties are typically assigned to elastic elements. However, Caltrans SDC v1.7 recommends that no stiffness reductions be applied for pre-stressed concrete box girder sections. Therefore, gross-section properties of the as-designed bridge decks are used in the *elasticBeamColumn* element definition in OpenSees. It is to be noted that the inherited model input files for Bridge C, in particular, used the gross area of the as-designed box girder deck section without excluding the areas of the hollow enclosed tubes. This is corrected in the current implementation of the finite element model of Bridge C in OpenSees.

Table 4-1 Material and section properties for elastic bridge deck elements

Bridge	**Modulus of Elasticity (E),**	**Shear Modulus (G),**	**Area of cross section (A), [ft^2]**	**Moment of inertia (I_Y), [ft^4]**	**Moment of inertia (I_Z), [ft^4]**	**Torsional constant (J), [ft^4]**
A	4262	1776	98	180	3798	341
B	4262	1776	129	792	58352	2532
C	4262	1776	132	789	59761	2536
MAOC	4262	1776	72.4	211	12698	724

4.2.2 Bent Group Components

Bent groups of the testbed bridges comprise of single (in case of Bridge A) or multiple (in case of Bridge B, Bridge C, and Bridge MAOC) columns supported on pile foundations. Schematic diagrams of the bent groups of the considered testbed bridges are shown (not to scale) in Figure 4.5 through Figure 4.8 along with spline representations of their finite element models developed in this project. Modeling details of individual components of a bent group are presented next. It is to be noted that modeling of pile shafts and soil-structure interaction at/beneath the foundations of bent groups are kept outside the scope of this study.

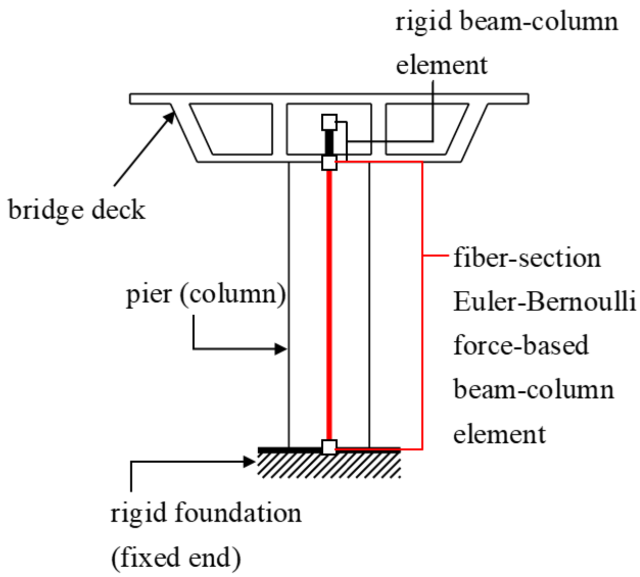

Figure 4.5 Schematic diagram of the finite element model of the single-column bent of Bridge A

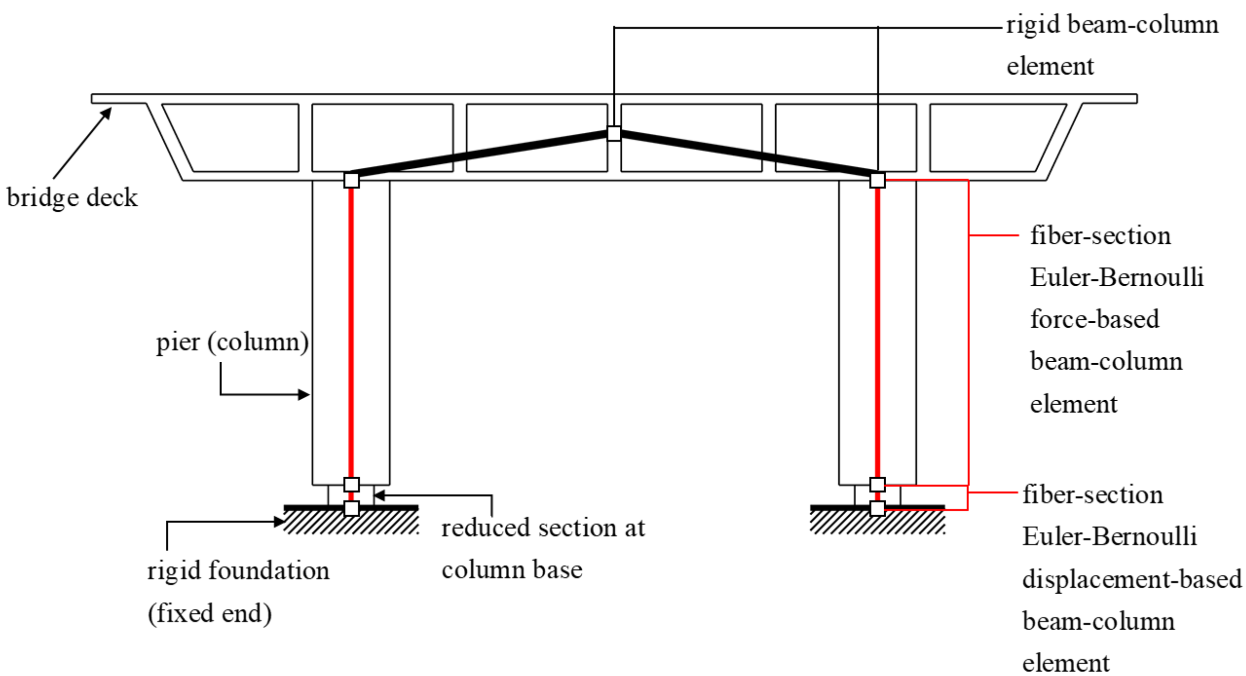

Figure 4.6 Schematic diagram of the finite element model of the two-column bent of Bridge B

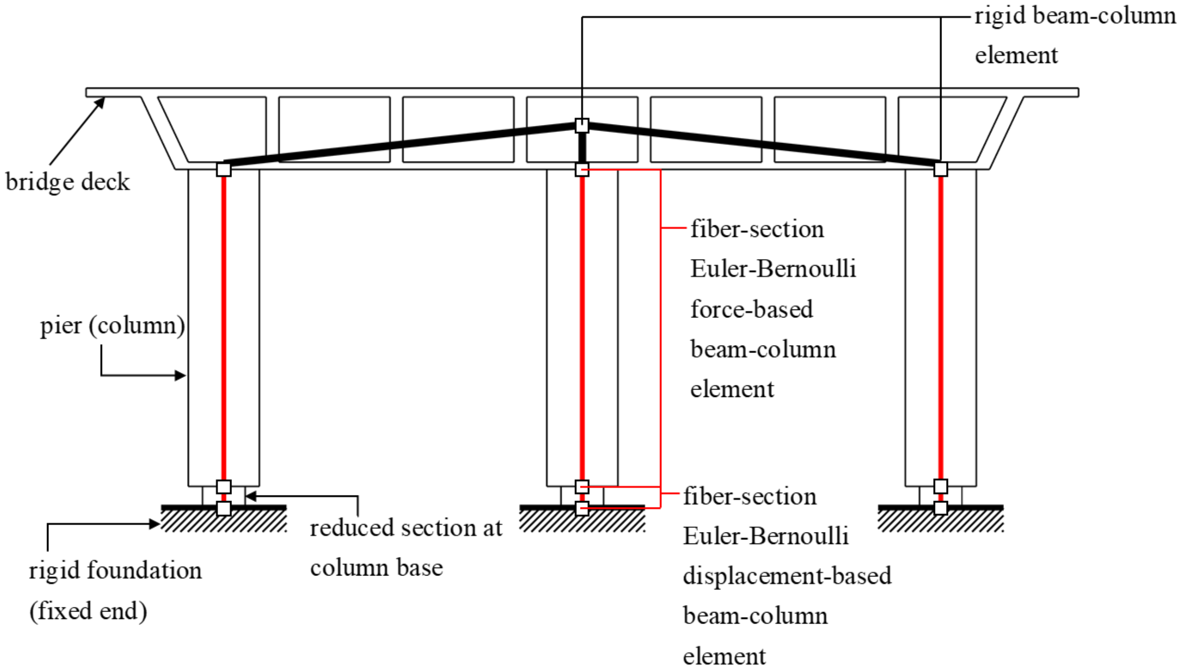

Figure 4.7 Schematic diagram of the finite element model of a three-column bent of Bridge C

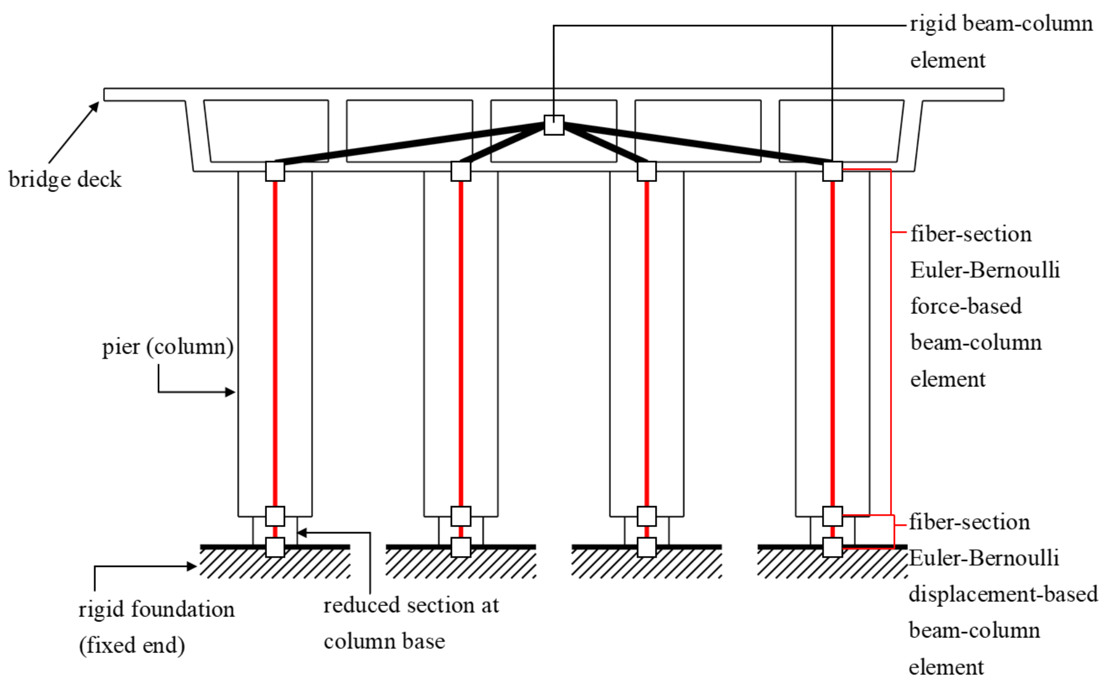

Figure 4.8 Schematic diagram of the finite element model of a four-column bent of Bridge MAOC

4.2.2.1 Bent Cap

Columns of the testbed bridges are constructed monolithically with the deck. Hence, each column element in a bent is attached to the deck using a rigid link, implemented as *rigidLink beam* in OpenSees, to simulate the bent cap. This is done by slaving the top node of each column in a bent to a "master" node specific to that bent. The master node for a bent corresponds to the deck node at the location of the bent. The rigid link connecting a column to the deck, as shown in Figure 4.1 through Figure 4.4 and Figure 4.5 through Figure 4.8, includes the vertical deck offset from the column top to the deck centroid and the horizontal offset (for multiple-column bents) from the deck center.

4.2.2.2 Column

Fiber-section Euler-Bernoulli force-based beam-column elements with distributed plasticity (implemented as *forceBeamColumn* element in OpenSees) are used to model the clear length of reinforced concrete columns of the considered testbed bridges. The force-based element formulation relies on the availability of a theoretically "exact" solution (based on the satisfaction of equilibrium between element-end forces and section forces) to a classical beam problem. The exactness of the force-based element formulation holds even in the range of material constitutive nonlinearity. Therefore, only one force-based element per bridge column is used which considerably reduces the total number of degrees of freedom (DOFs) in the structural model. Geometric nonlinearities due to large deformations (i.e., second-order effects) are accounted for using the $P-\Delta$ geometric transformation.

Element integrals, involved in the force-based element formulation (Neuenhofer and Filippou 1998; Taucer et al. 1991), to compute element flexibility matrices and element-end displacement vectors are numerically evaluated with integration points (sections) placed along the length of the element. These elements allow highly detailed fiber-section definitions with cover concrete (unconfined), core concrete (confined), and reinforcing steel fibers. Associated with each fiber is a nonlinear hysteretic law relating uniaxial stresses and strains thereby modeling the coupled interaction of nonlinear axial and flexural behavior of a Euler-Bernoulli beam.

The Kent-Scott-Park (Kent and Park 1971; Mander et al. 1988; Scott et al. 1982) concrete material stress-strain law with degraded linear unloading/reloading stiffness and no tensile strength is used to model the cover and core concrete fibers of a column section. This material model is implemented in OpenSees as the uniaxial material object *Concrete01*. Table 4-2 and Table 4-3, respectively, show the expected constitutive material model parameters for cover (unconfined) and core (confined) concrete fibers used in the *Concrete01* material definition in OpenSees. Confined concrete properties for the specific column designs of the considered testbed bridges are estimated using the theoretical stress-strain model for confined concrete by Mander et al. (1988).

Reinforcing steel fibers of a column section are modeled using the uniaxial stress-strain law proposed by Menegotto and Pinto (1973) and extended by Filippou et al. (1983). This material model is implemented in OpenSees as the uniaxial material object *SteelMPF*. The expected constitutive material model parameters for steel reinforcing fibers used in the *SteelMPF* material definition in OpenSees are shown in Table 4-4. These parameters correspond to the properties (as suggested by Caltrans SDC v1.7) of ASTM A706 Grade 60 reinforcing steel used in the original design of the considered testbed bridges.

Figure 4.9 through Figure 4.12 show the fiber-section definitions corresponding to the columns of each testbed bridge. Also shown in Figure 4.9 through Figure 4.12 are the concrete and reinforcing steel material hysteretic stress-strain laws assigned to respective fibers. Figure 4.13 shows the cyclic moment-curvature response of the bridge column sections under an axial load ratio of 10%, a rather conservative representation of the action of real-world gravity loads.

The numerical evaluation of element integrals in the force-based element formulation is usually carried out by using the Gauss-Lobatto integration scheme. This is because it places the first and the last integration points at the element end sections which are typically the most-critical sections in flexure. A commonly encountered numerical localization issue with the implementation of the Gauss-Lobatto integration scheme in the force-based element formulation leads to non-objectivity of computed local/global structural response due to formation of plastic hinges, i.e., regions of concentrated plastic deformations at/near critical sections, in force-based elements. Depending on the section constitutive behavior, force-based elements are found to lose objectivity of plastic response. For elements with sections exhibiting softening behavior, the computed local/global response changes as a function of the total number of element integration points (i.e., sections) used. The latest OpenSees implementation of the *forceBeamColumn* element incorporates a numerically consistent regularized plastic hinge integration scheme (Scott and Hamutçuoğlu 2008) in order to get rid of such localization issues. Eight integration points per element along with the plastic hinge length (L_p) defined according to Eq. (4.1), proposed by Paulay and Priestley (1992) and shown in Figure 4.9 through Figure 4.12, are used in the regularized *forceBeamColumn* element definition in OpenSees.

$$L_p = 0.08L + 0.15 f_{ye} d_{bl} \quad \text{(in, ksi)} \tag{4.1}$$

where, L is the total length of the column, f_{ye} is the expected yield stress for A706 reinforcement, and d_{bl} is the nominal bar diameter of longitudinal column reinforcement. Ratios of plastic hinge lengths to the total lengths of the considered testbed bridge columns are shown in Table 4-5.

Table 4-2 Expected material properties for unconfined concrete fibers

Bridge	**Compressive strength** ,	**Strain at** ,	**Crushing strength** ,	**Strain at** ,
A	6.5	0.002	1.3	0.006
B	6.5	0.002	1.3	0.006
C	6.5	0.002	1.3	0.006
MAOC	6.5	0.002	1.3	0.006

Table 4-3 Expected material properties for confined concrete fibers

Bridge	**Compressive strength** (f'_{cc}),	**Strain at** f'_{cc} (ε'_{cc}),	**Crushing strength** $(f'_{ccu} = 0.2 f'_{cc})$,	**Strain at** f'_{ccu} ,
A	8.4	0.003	1.68	0.06
B	8.4	0.003	1.68	0.06
C	8.4	0.003	1.68	0.06
MAOC	8.36	0.003	1.67	0.06

Table 4-4 Expected material properties for reinforcing steel fibers

Bridge	**Yield strength** (f_{ye}),	**Modulus of Elasticity** (E_s) ,	**Post-yield stiffness ratio,** (b)
A	68.0	29000	0.02
B	68.0	29000	0.02
C	68.0	29000	0.02
MAOC	68.0	29000	0.02

$= 0.2 f'_{ce})$

Table 4-5 Ratios of plastic hinge lengths to total lengths of testbed bridge columns

Bridge	**Maximum column length (L), [ft]**	**Yield strength of rebar (f_{ye}),**	**Nominal rebar diameter, (d_{bl}) [in]**	**Plastic hinge length as a fraction of L (L_p / L),**
A	19.68	68.0	1.410	0.14
B	22.0	68.0	1.410	0.14
C	24.6	68.0	1.693	0.14
MAOC	31.50	68.0	1.410	0.12

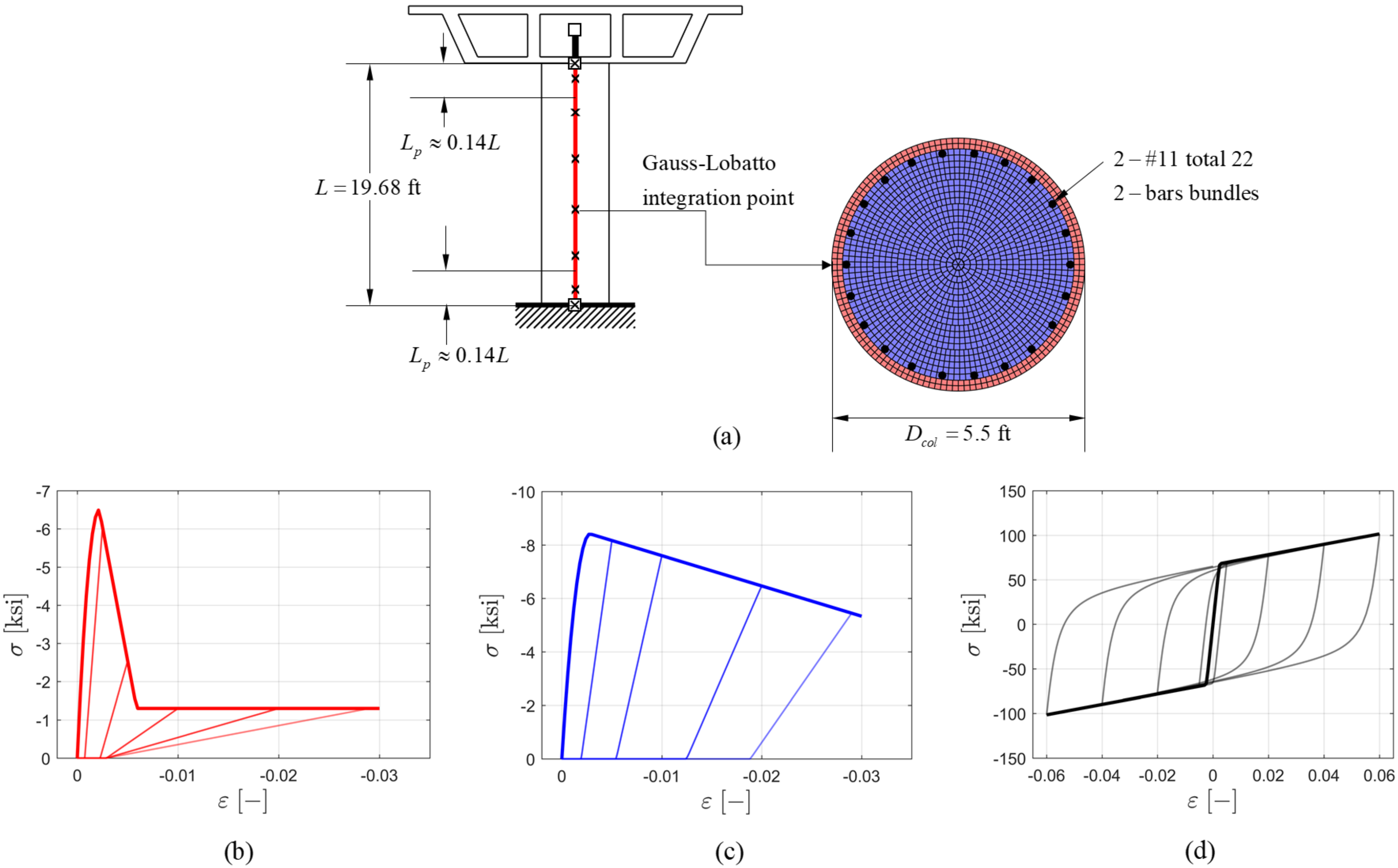

Figure 4.9 Details of force-based beam-column element for the column of Bridge A (a) Gauss-Lobatto integration points and fiber-section definition; Material hysteretic stress-strain laws (backbone curves in bold) for: (b) unconfined concrete fibers; (c) confined concrete fibers; and (d) reinforcing steel fibers

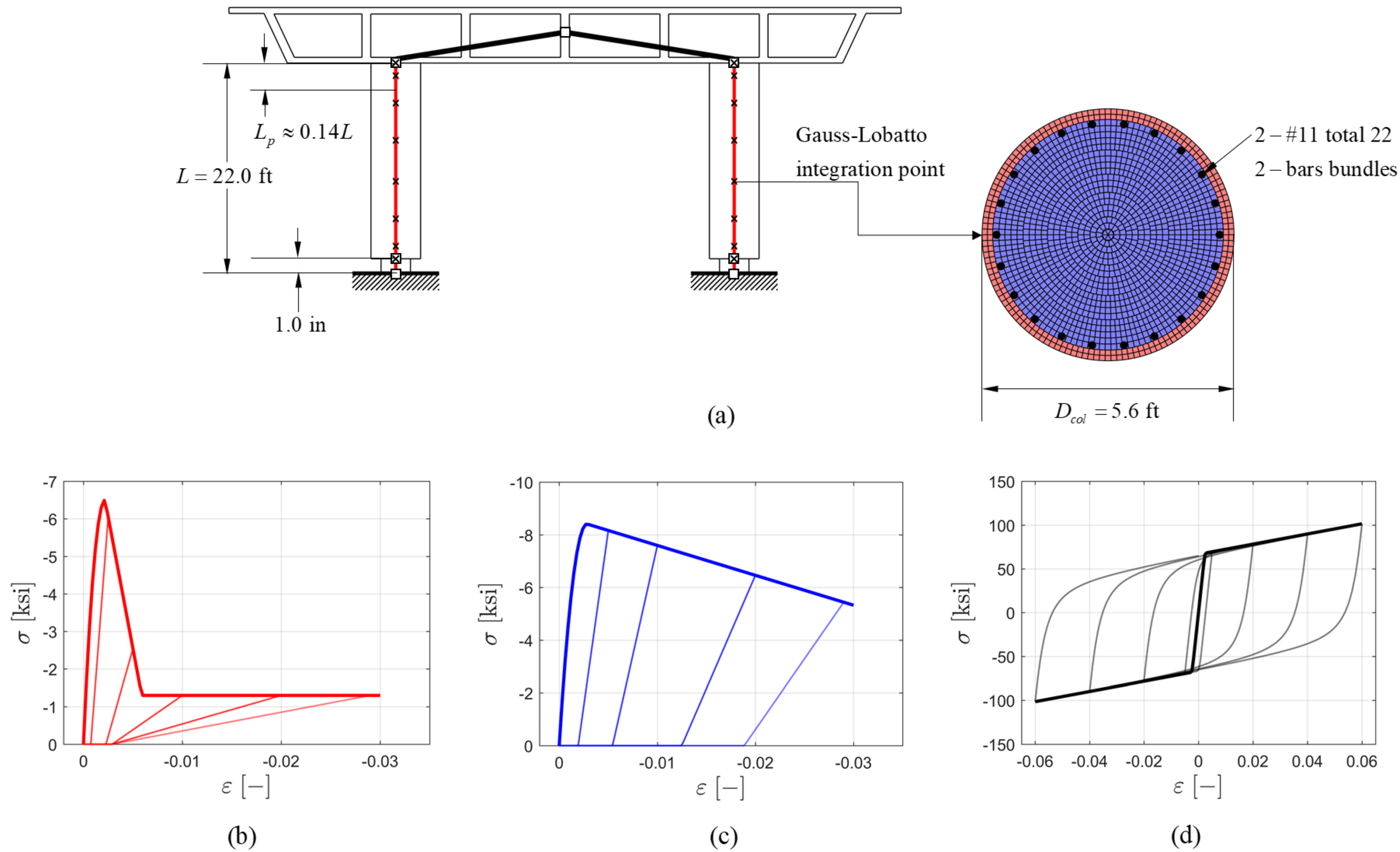

Figure 4.10 Details of force-based beam-column element for a column of Bridge B: (a) Gauss-Lobatto integration points and fiber-section definition; Material hysteretic stress-strain laws (backbone curves in bold) for: (b) unconfined concrete fibers; (c) confined concrete fibers; and (d) reinforcing steel fibers

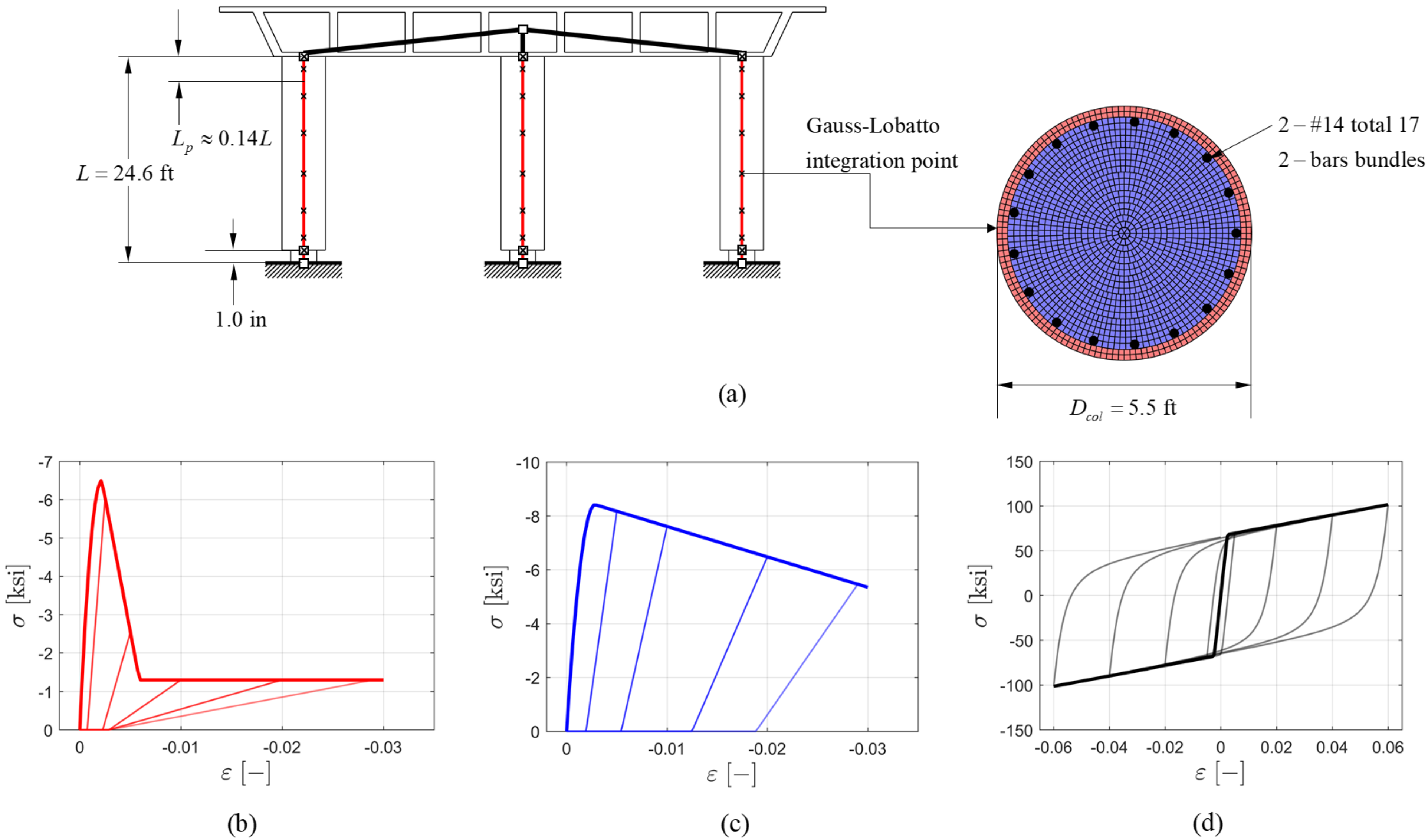

Figure 4.11 Details of force-based beam-column element for a column of Bridge C: (a) Gauss-Lobatto integration points and fiber-section definition; Material hysteretic stress-strain laws (backbone curves in bold) for: (b) unconfined concrete fibers; (c) confined concrete fibers; and (d) reinforcing steel fibers

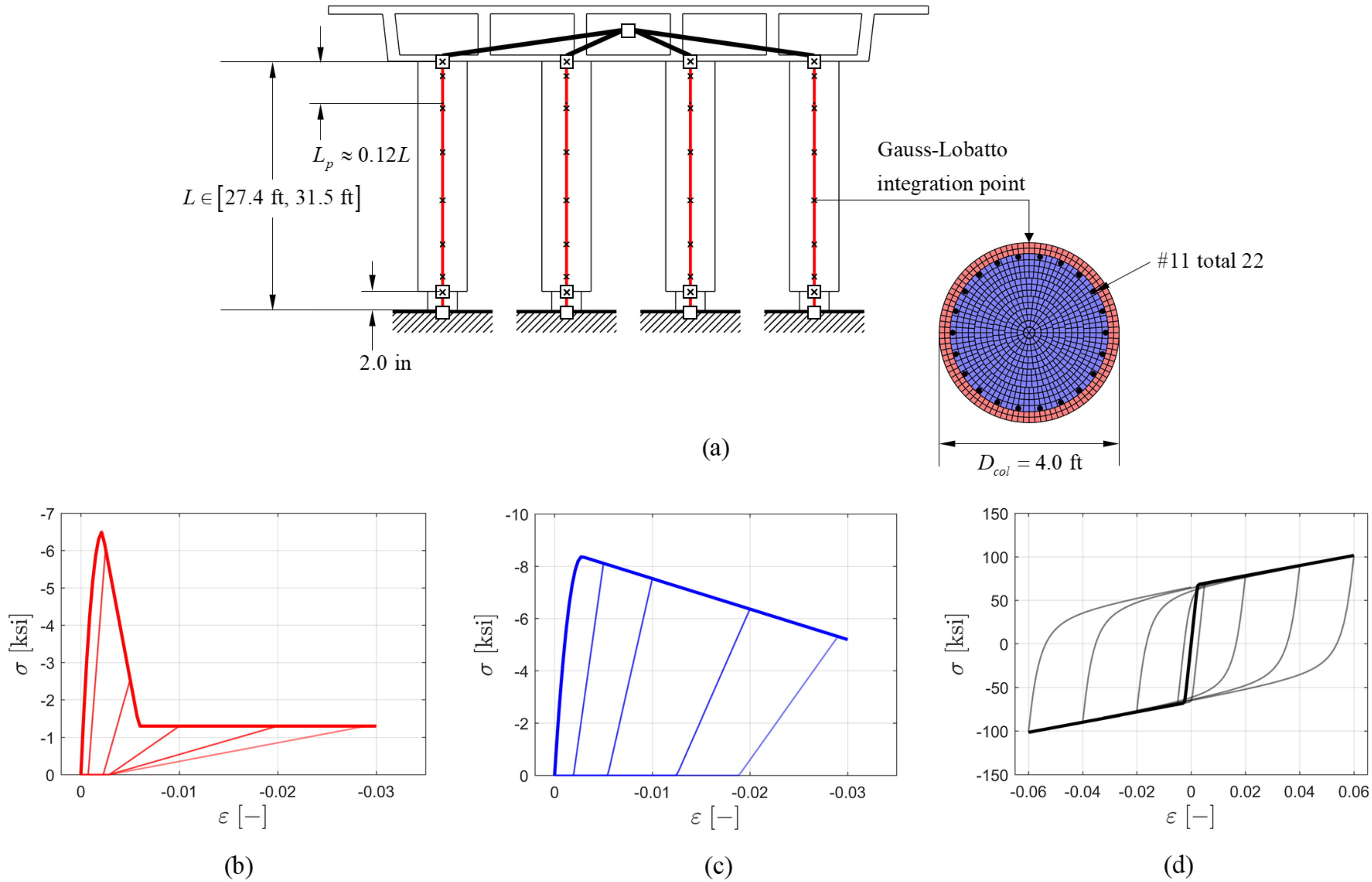

Figure 4.12 Details of force-based beam-column element for a column of Bridge MAOC: (a) Gauss-Lobatto integration points and fiber-section definition; Material hysteretic stress-strain laws (backbone curves in bold) for: (b) unconfined concrete fibers; (c) confined concrete fibers; and (d) reinforcing steel fibers

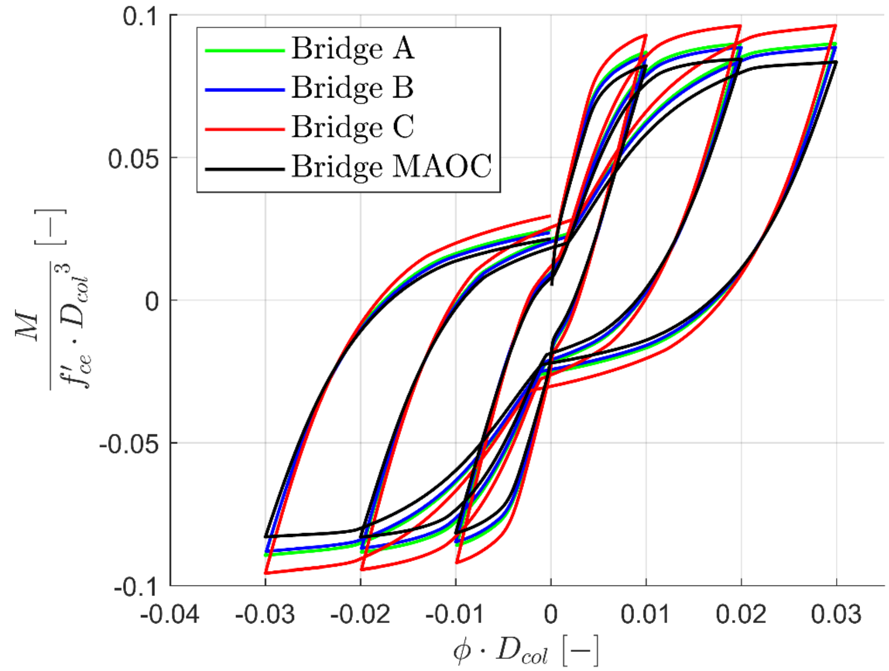

Figure 4.13 Normalized moment-curvature responses of testbed bridge column sections

4.2.2.3 Column Base Hinge for Multiple-column Bents

The bridge column in a single-column bent is monolithically attached to the foundation cap surface. The boundary condition of the column base in a single-column bent is therefore aptly modeled as a fixed-base connection. This technique is employed for Bridge A, the only testbed bridge with a single-column bent. However, a bridge column in a multiple-column bent is attached to the foundation cap surface, although monolithically, via a very short reduced section between the column base and the foundation cap. This is done to mimic a hinge at the column base thereby significantly lowering the moment demand on the foundation cap and, in turn, leading to economic design of foundations. Traditionally, the boundary condition of the column base in a multiple-column bent is modeled as a pinned-base connection as the moment capacity of the base hinge, i.e., the reduced section between the column base and the foundation cap, is supposedly assumed to be negligible as compared to the original column section. This presumptive approach is supplanted by explicitly modeling, without any notable increase in complexity and/or computational cost, the base hinge using a fiber-section Euler-Bernoulli displacement-based beam-column element (implemented as *dispBeamColumn* element in OpenSees) for the testbed bridges with multiple-column bents (i.e., Bridge B, Bridge C, and Bridge MAOC). A single nonlinear fiber-section displacement-based element is used to connect the column element to a fixed support representing the rigid foundation. Geometric nonlinearities are accounted for using the $P-\Delta$ geometric transformation.

Displacement-based beam-column elements, like their force-based counterpart, also admit the distribution of plasticity with highly detailed fiber-sections placed along the length of the element at integration point locations. Fiber-sections for base hinges are defined with concrete and reinforcing steel fibers with a nonlinear hysteretic uniaxial stress-strain law assigned to each fiber. The base hinge is highly confined by the rigid footing surface and the column core section. In the absence of available literature/data corroborating the estimation of confinement characteristics for such a section, concrete fibers of the base hinge section are assumed to have identical properties as that of the core (confined) concrete fibers of the respective column section. The Kent-Scott-Park material model (Kent and Park 1971; Mander et al. 1988; Scott et al. 1982), i.e., *Concrete01* in OpenSees, is used to model the concrete fibers of the base hinge section. Expected confined concrete material properties as listed in Table 4-3 for the testbed bridges in question are used in defining the material model in OpenSees. Reinforcing steel fibers of the base hinge section are modeled, like those of the respective column section, using the material model by Menegotto and Pinto (1973) and extended by Filippou et al. (1983), i.e., *SteelMPF* in OpenSees with expected material properties and parameters as shown in Table 4-4.

Figure 4.14 through Figure 4.16 show the fiber-section definitions corresponding to the column base hinges of the testbed bridges with multiple-column bents (i.e., Bridge B, Bridge C, and Bridge MAOC). Also shown in Figure 4.14 through Figure 4.16 are the concrete and reinforcing steel material hysteretic stress-strain laws assigned to the respective fibers. The cyclic moment-curvature response of these base hinge sections under the influence of axial loads corresponding to the respective column-axial load ratio of 10% are shown in Figure 4.17. Comparison of the moment-curvature responses of these base hinge sections with that of the respective column sections indicate that the moment capacities of these reduced section base hinges are indeed not negligible as compared to that of the respective column sections. Thus, the explicit modeling of a column base hinge, in contrast to modeling the column base connection as a perfect pin, is deemed justified.

Unlike the "exact" formulation of the force-based element within classical beam theories, the displacement-based element formulation involves some simplifying theoretical approximations. Thus, many displacement-based elements per structural member are typically required to capture the structural response with a level of accuracy comparable to that achieved by a single "exact" force-based element. However, in this case, a single displacement-based element with 2 Gauss-Lobatto integration points is used to model the base hinge of a column. This is firstly because the length of the base hinge is very small compared to the entire length of the column. Secondly, structural response, in case of displacement-based elements with sections exhibiting softening of constitutive behavior, localizes and loses objectivity at the element level rather than at the section (integration point) level as in case of force-based elements. Since the entire length of the base hinge is expected to undergo tremendous amounts of concentrated plastic deformations, an element-level localization (non-objectivity of response) is prevented by using a single displacement-based element along the entire region of concentrated plastic deformations.

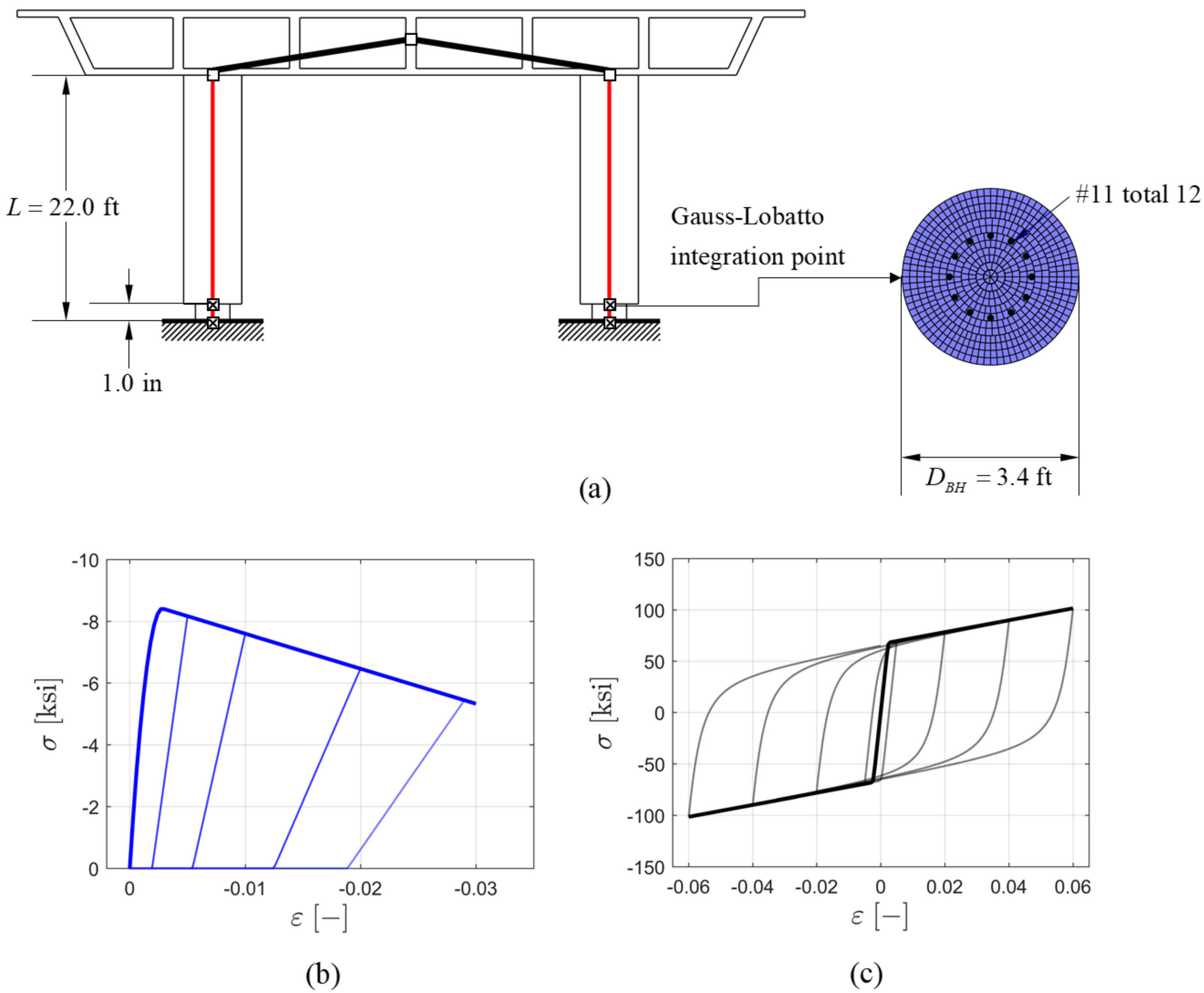

Figure 4.14 Details of displacement-based beam-column element for a column base hinge of Bridge B: (a) Gauss-Lobatto integration points and fiber-section definition; Material hysteretic stress-strain laws (backbone curves in bold) for: (b) confined concrete fibers; and (c) reinforcing steel fibers

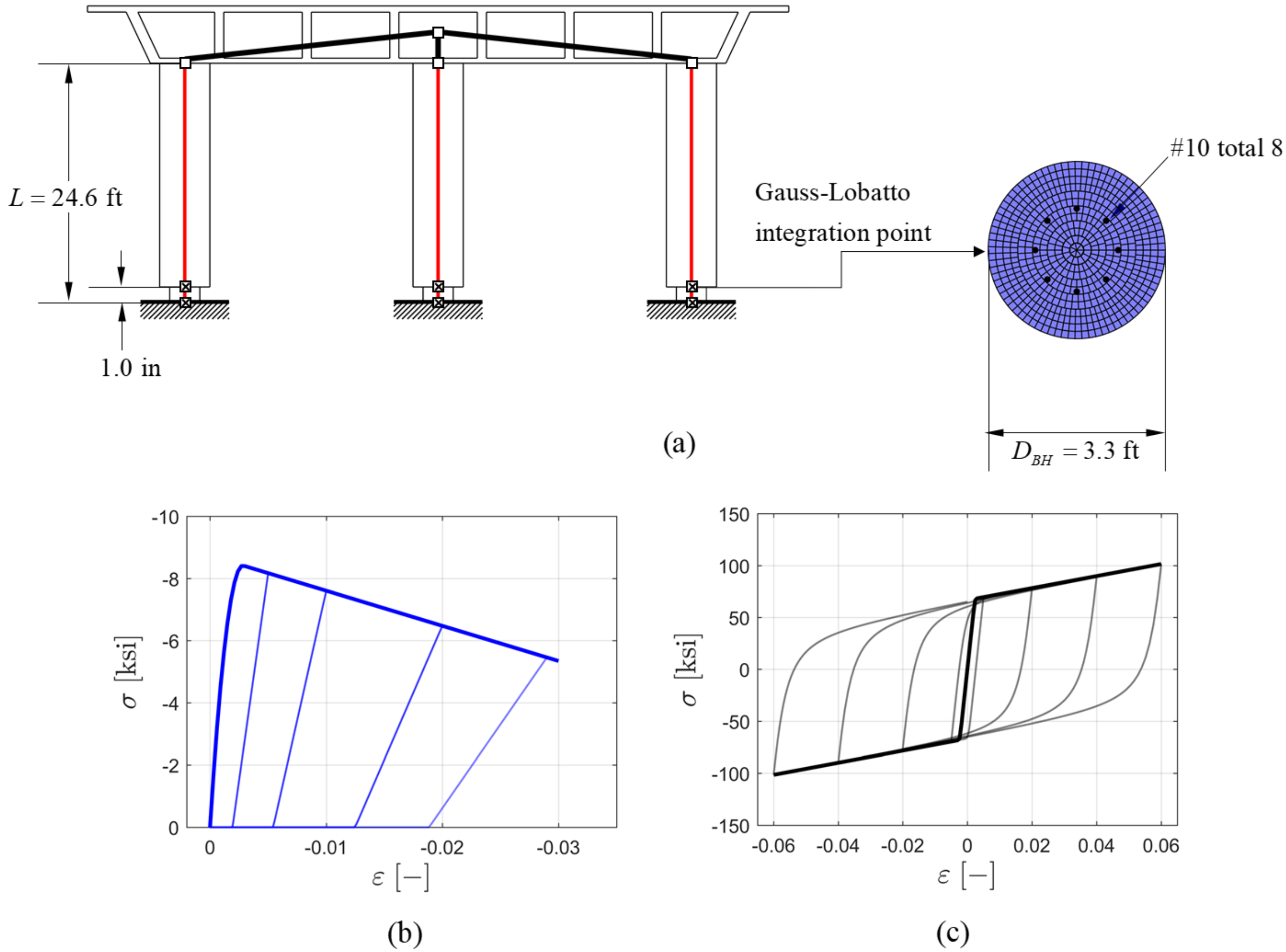

Figure 4.15 Details of displacement-based beam-column element for a column base hinge of Bridge C: (a) Gauss-Lobatto integration points and fiber-section definition; Material hysteretic stress-strain laws (backbone curves in bold) for: (b) confined concrete fibers; and (c) reinforcing steel fibers

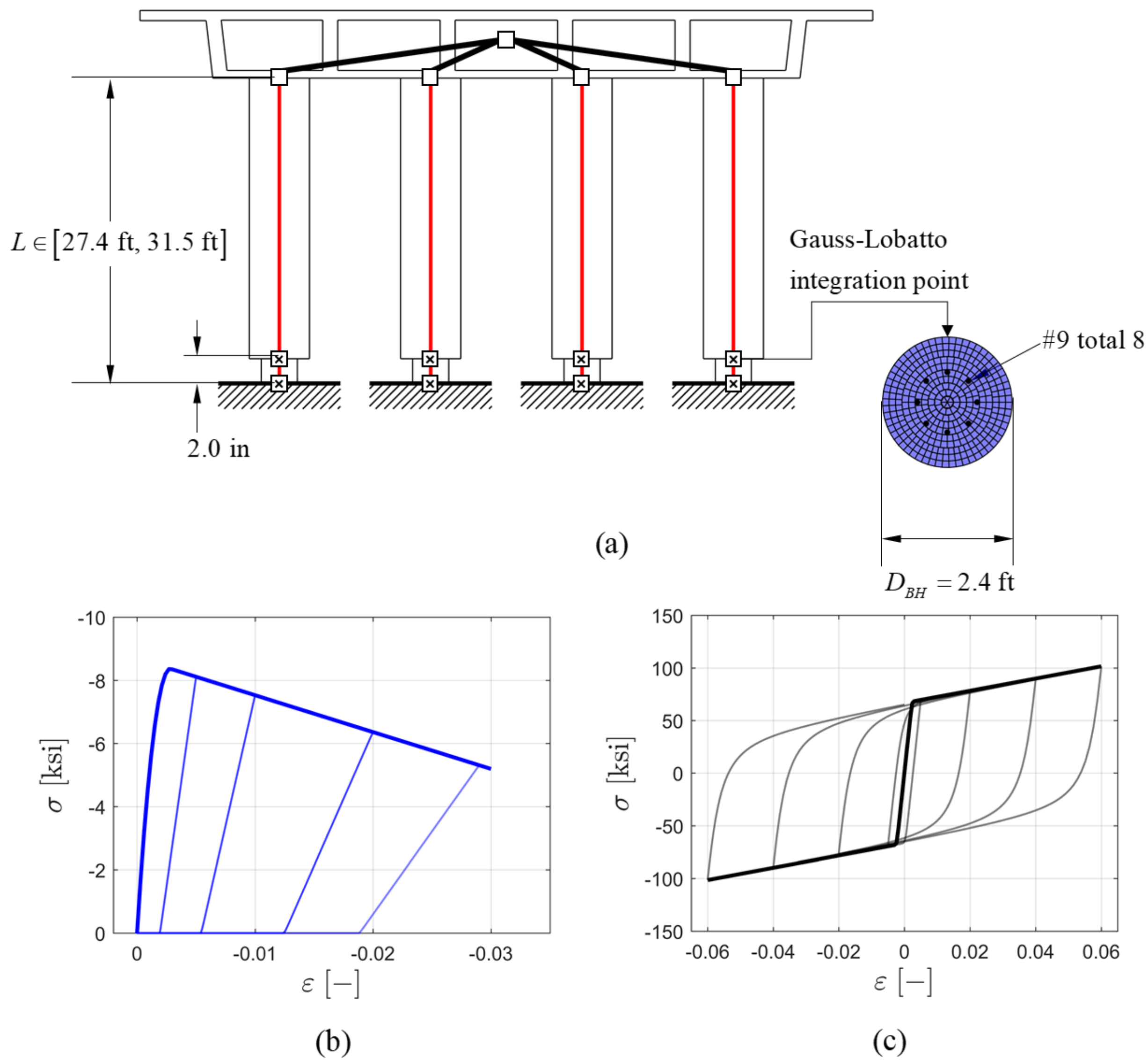

Figure 4.16 Details of displacement-based beam-column element for a column base hinge of Bridge MAOC: (a) Gauss-Lobatto integration points and fiber-section definition; Material hysteretic stress-strain laws (backbone curves in bold) for: (b) confined concrete fibers; and (c) reinforcing steel fibers

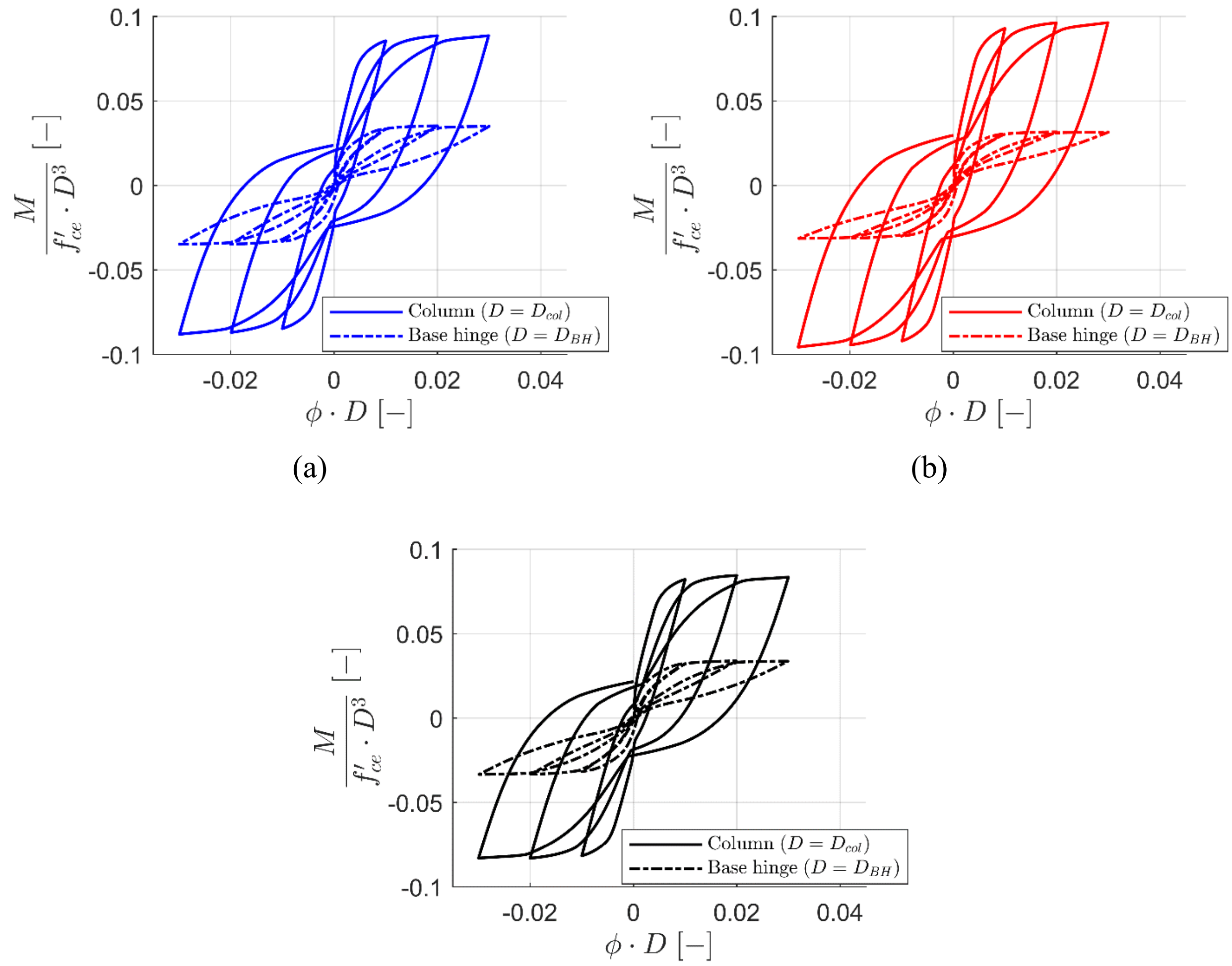

(a) (b) (c)

Figure 4.17 Normalized moment-curvature responses of testbed bridge column and base-hinge sections: (a) Bridge B; (b) Bridge C; and (c) Bridge MAOC

4.2.2.4 Experimental Validation of Bent Group Modeling Technique

Nada et al. (2003) conducted a series of tests on reinforced concrete bent group specimens with columns, architecturally flared, like the ones in the considered testbed bridges. The primary objective of this Caltrans sponsored study was to verify the seismic behavior of such bent groups detailed according to current Caltrans requirements relating to the design of architectural flares. To this end, the specimens were subjected to progressive dynamic shake table tests with increasingly scaled versions of the 1994 Northridge earthquake ground motion recorded at the Sylmar station. These tests were conducted in the Large-scale Structures Laboratory at the University of Nevada, Reno.

Four 1/5th scaled specimens, viz., LFCD1, LFCD2, SFCD1 and SFCD2, were constructed. The first two specimens had the same layout each with a column clear height of 64 in. However, different flare reinforcement details were called for in the design of these two specimens. The other two specimens, SFCD1 and SFCD2, had the same reinforcement detailing as LFCD1 and LFCD2, respectively, but with a shorter clear height of 39 in each. For a detailed description of the geometrical, material, and mechanical parameters of the experimental specimens and loading procedures involved in their testing, the reader is referred to the original report by Nada et al. (2003). Figure 4.18 shows details of the finite element models developed for these specimens. It is to be noted that accounting for the differences between specimens LFCD1 and LFCD2, and that between specimens SFCD1 and SFCD2, are beyond the scope of the modeling technique employed in this project. Hence, two distinct finite element models, one applicable to LFCD1 and LFCD2 while the other to SFCD1 and SFCD2, are developed.

Researchers of the original study provided successfully measured lateral load-displacement curves enveloping the accumulative lateral load-displacement responses of three (LFCD1, LFCD2, and SFCD2) out of the four tested specimens. These experimentally obtained envelope lateral load-displacement curves are used to validate the numerical lateral load-displacement response of the finite element models of these specimens developed using the modeling technique outlined previously. A displacement-controlled pushover analysis, preceded by a load-controlled gravity analysis, is conducted to push each numerical model up to a value of lateral drift equal to 4% past which the gap between the column flare and the bent cap was found to close in the conducted experiments. It is to be noted that the numerical models of bent groups developed for this experimental validation study and this project, in general, are unable to capture any such gap closure. Figure 4.19 shows the comparison of experimental and numerical lateral load-displacement responses for the specimens considered. Also shown in Figure 4.19 are the responses of numerical models of these specimens with the boundary condition at the column base modeled as perfect pinned-connections.

It is noted from Figure 4.19 that explicitly modeling the base hinge as a displacement-based element, with coupled nonlinear axial-flexural interaction, does affect the lateral load-displacement relationship of a bent group. Numerical models of column-bents with columns perfectly pinned at the base are found to underpredict the transverse pushover resistance of such bents when compared to experimental data for the same imposed lateral displacement time history.

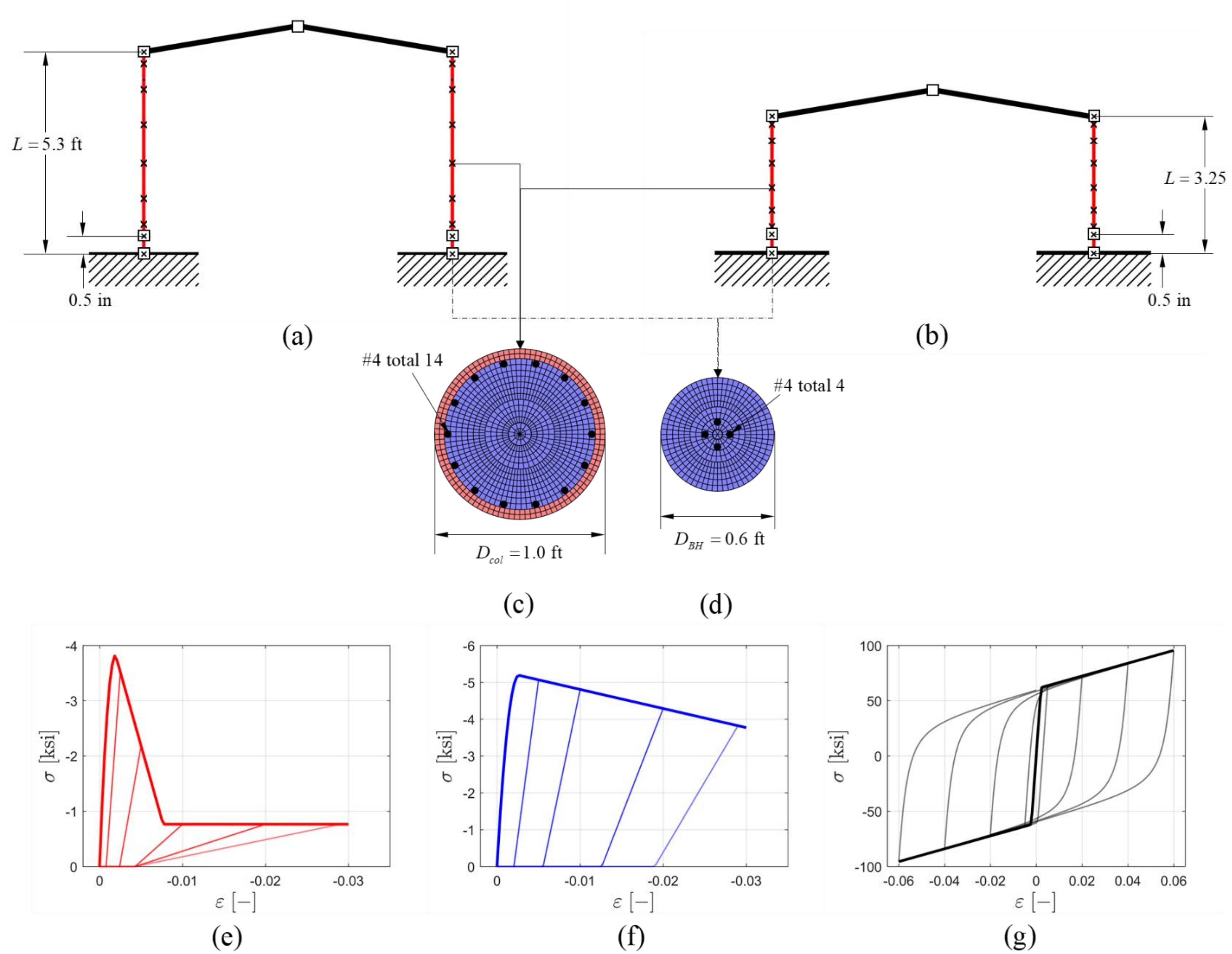

Figure 4.18 Details of finite element models of experimental column bent specimens: (a) specimens LFCD1 and LFCD2; (b) specimens SFCD1 and SFCD2; Fiber-section definitions for: (c) column section; (d) column base hinge; Material hysteretic stress-strain laws (backbone curves in bold) for: (e) unconfined concrete fibers; (f) confined concrete fibers; and (g) reinforcing steel fibers

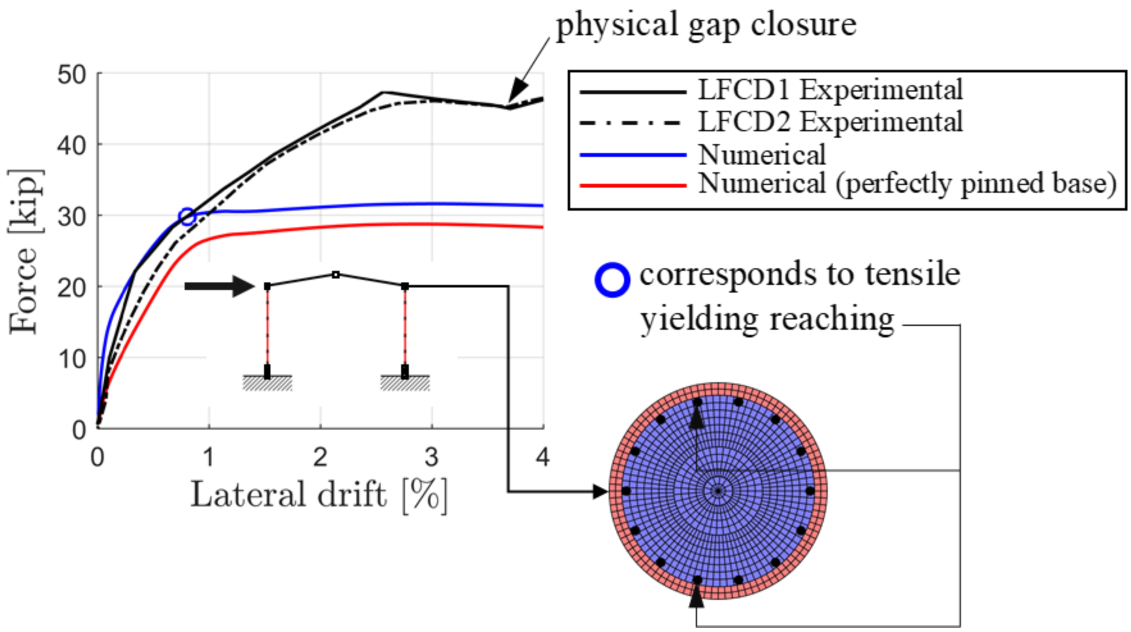

(a)

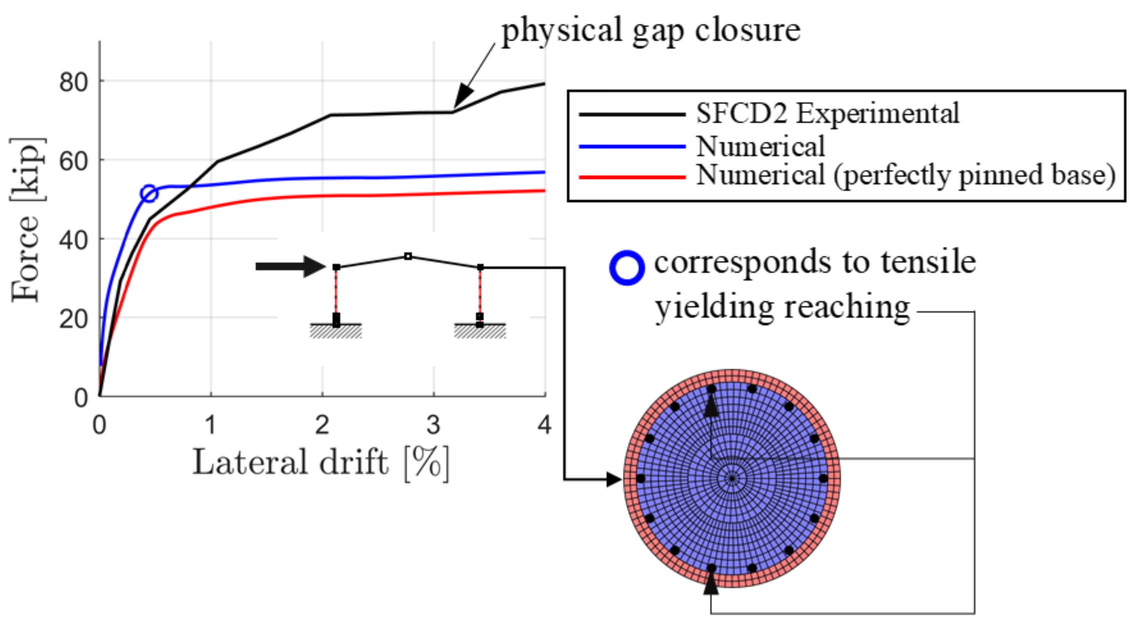

(b)

Figure 4.19 Comparison of experimental and numerical lateral load-displacement responses for (a) LFCD1 and LFCD2; and (b) SFCD2

Numerical and experimental responses of a bent group are found to noticeably deviate past a point on the load-displacement equilibrium path much before a physical closure of the flare gap is experimentally recorded. This point, upon investigation, is found to correspond to the state at which tensile yielding of rebars in the most critical column section (i.e., at the top) has reached more than halfway through the section, i.e., rebars near the middle of the section lying along a plane normal to the direction of loading have reached yielding in tension. Past this state, the lateral force, required to achieve a specific level of drift, computed using the numerical model is significantly underpredicted as compared to that measured in case of the respective experimental specimen. It is believed that nearing this, somewhat damaged, state of the most critical column section, a redistribution of internal forces takes place in the column. As a result, the flared region, near the concrete core of sections below the topmost one, starts actively participating in resisting the applied loads. This is substantiated by strut-and-tie models proposed by the researchers of the original study (Nada et al. 2003) following detailed full-blown nonlinear finite element analyses of bent groups with flared columns. Two strut-and-tie models, one applicable before flare gap closure and the other after, were proposed. The presence of compressive struts in the flared region of the former strut-and-tie model, does indicate some flare participation in the lateral load resisting mechanism of such bent groups before flare gap closure is encountered. The absence of flares in the numerical model of a bent group specimen is believed to lead to the above-mentioned underprediction of numerically evaluated lateral forces as compared to the experimentally measured ones given specific levels of drift.

4.2.3 Abutment Components

The selected testbed bridges are supported on seat-type skewed (depending on the bridge skew angle) abutments supported on pile foundations. A typical seat type skewed abutment is shown in Figure 4.20 (a). Such an abutment system comprises of a backwall interacting with the backfill soil, wingwalls, shear keys, bearing pads, a stemwall, expansion joints, and a pile group supporting the system. Kaviani et al. (2012; 2014) implemented a simplified, yet effective and numerically robust, skewed abutment model by explicitly considering, in a phenomenological sense, the interaction between the bridge superstructure (i.e., the deck) and specific components of the bridge abutment, viz, the backfill, shear keys and bearing pads. An explicit consideration of the responses of other components is omitted because their contributions to the overall response of an OSB and their effects on relevant failure modes were deemed insignificant by the researchers. Figure 4.20 (b) and Figure 4.20 (c) show schematic diagrams (top-view and perspective view, respectively) of the simplified finite element model of a generic seat-type skewed abutment. Relevant details of modeling each of the aforementioned components, as implemented in this project, are presented in the following sub-sections. It is to be noted that modeling of pile groups and soil-structure interaction at/beneath the abutment foundations are kept outside the scope of this study.

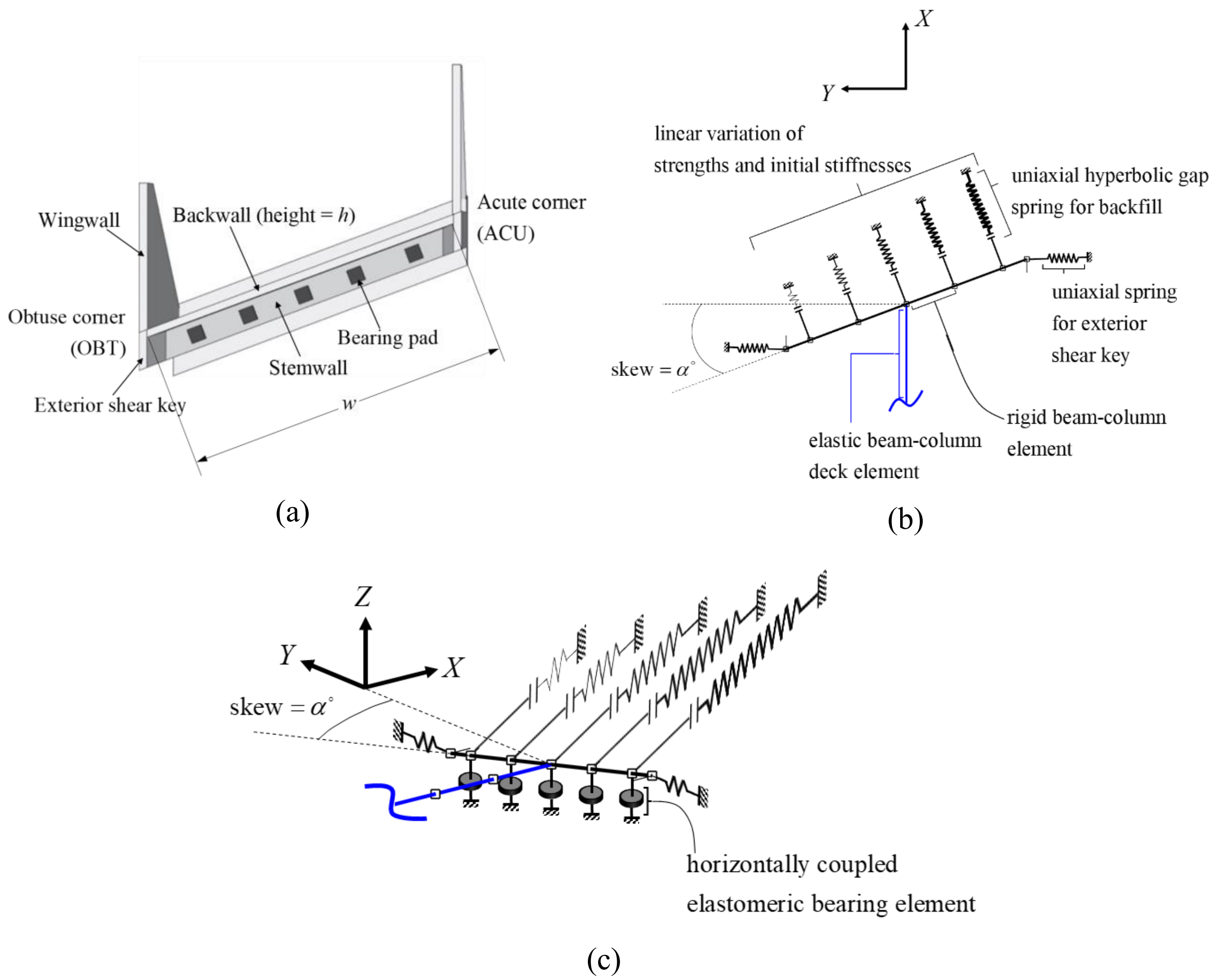

Figure 4.20 A typical seat-type skewed abutment: (a) general configuration (top-view) (Kaviani et al. 2012); (b) simplified finite element model (top view); and (c) simplified finite element model (perspective view)

4.2.3.1 Backfill

Kaviani et al. (2012; 2014) modeled the longitudinal interaction of the bridge superstructure (i.e., the deck) with the abutment backwall and the ensuing passive resistance of the backfill soil using several (five) translational compressive gap springs evenly distributed over the skewed length of the backwall as shown in Figure 4.20 (b) and Figure 4.20 (c). The gaps represent the expansion joint between the deck and the backwall. Modeling of springs in OpenSees is achieved by means of a specialized element, referred to as the *zeroLength* element, defined by two nodes at the same location. The nodes are connected by uniaxial material object(s) to represent the uncoupled unidirectional force-deformation relationships for the element. A quasi-rigid element, i.e., an exceedingly stiff elastic beam-column element with highly amplified material properties, is used to geometrically capture the physical dimension of the deck at each end of the bridge.

A nonlinear hysteretic force-deformation relationship with a hyperbolic backbone curve, implemented in OpenSees as the uniaxial material model *HyperbolicGapMaterial*, is used to model the passive resistance of each backfill spring activated upon closure of the expansion joint gap. This material model is based on the work by Duncan and Mokwa (2001) and Shamsabadi et al. (2007) with parameters calibrated from large-scale abutment tests (Wilson and Elgamal 2006) performed on the large high-performance outdoor shake table facility (LHPOST) at the University of California, San Diego. The parameters of this model primarily include the initial stiffness, K_{init}^{bf}, and the ultimate passive resistance, F_{ult}^{bf}. The following empirical equations, recommended by Caltrans SDC v1.7, are used to estimate the values of K_{init}^{bf} and F_{ult}^{bf} (shown in Table 4-6) for the backfill springs of the selected testbed bridges.

$$K_{init}^{bf} = 25\,\frac{\text{kip/in}}{\text{ft}} \times w \times \left(\frac{h}{5.5\text{ ft}}\right) \times \frac{1}{n_{bf}} \quad \text{(ft, kip)} \tag{4.2}$$

$$F_{ult}^{bf} = h \times w \times 5.0\text{ ksf} \times \left(\frac{h}{5.5}\right) \times \frac{1}{n_{bf}} \quad \text{(ft, kip)} \tag{4.3}$$

where h and w represent the height and the skewed length of the backwall, respectively. n_{bf} represents the number of backfill springs used per abutment and is taken as 5 (as per Kaviani et al. (2012; 2014)). It is to be noted that the skewed, rather than the projected, length of the backwall is used in Eq.s (4.2) and (4.3) because the passive resistances of the backfill springs are assumed to be aligned perpendicular to the skewed backwall. The *HyperbolicGapMaterial* material model definition in OpenSees also allows for the inclusion of a compression gap representing the expansion joint ($\approx$ 1 in wide) between the deck and the backwall. Figure 4.21 shows, for each testbed bridge, the resulting nonlinear (hyperbolic envelope) hysteretic force-deformation $(F-\Delta)$ relationship (obtained using values of K_{init}^{bf} and F_{ult}^{bf} in Table 4-6) corresponding to the backfill spring located midway along the skewed length of the abutment backwall.

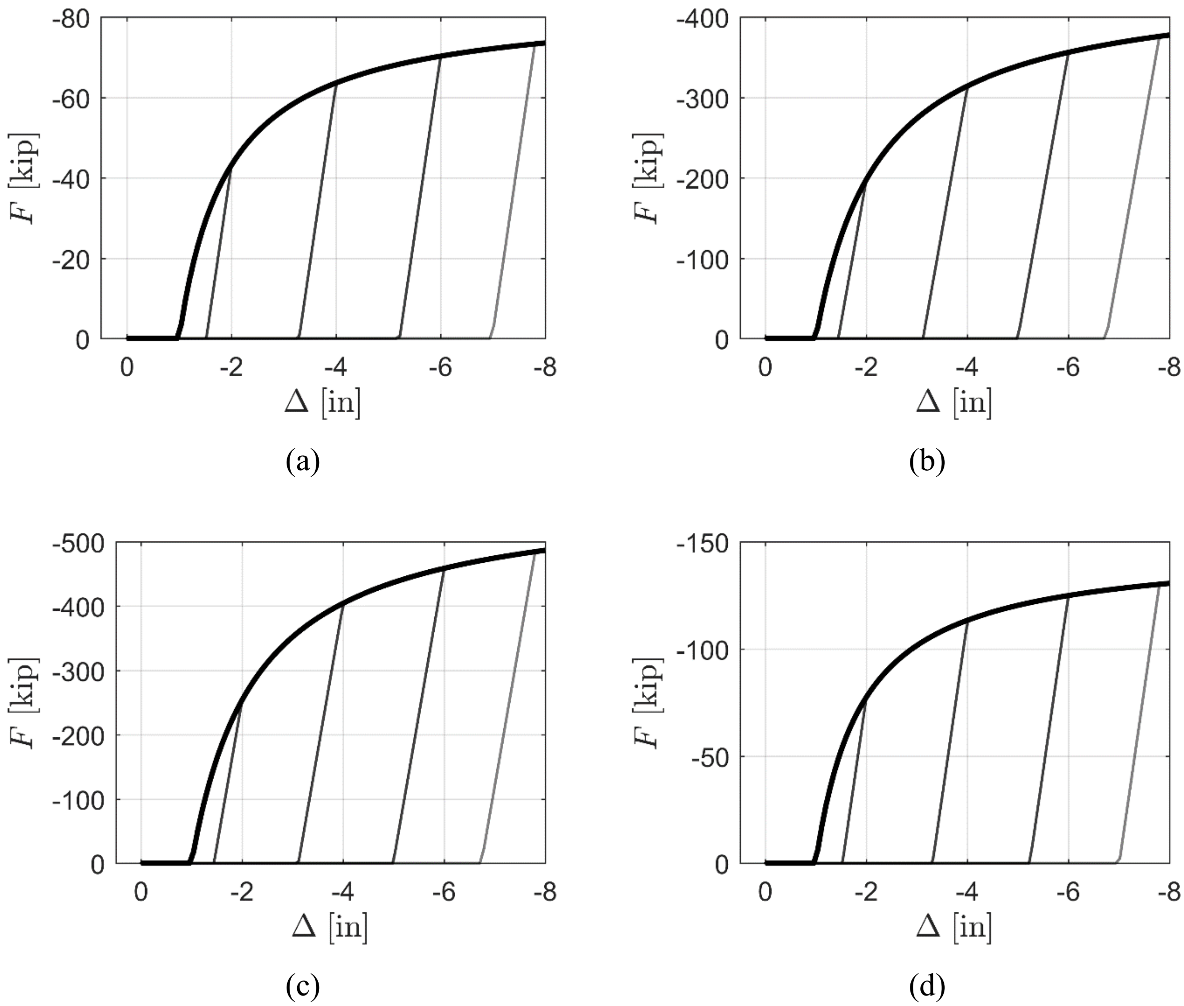

Figure 4.21 Nonlinear hysteretic force-deformation relationship (hyperbolic backbone curve in bold) used to model the longitudinal passive resistance of a single backfill spring (out of a total of 5 equally spaced backfill springs per abutment) placed midway along the skewed length of the abutment backwall: (a) Bridge A; (b) Bridge B; (c) Bridge C; and (d) Bridge MAOC

Table 4-6 Material properties for uniaxial backfill springs

Bridge	**Backwall height (h), [ft]**	**Backwall skewed length (w), [ft]**	**Number of backfill springs (n_{bf})**	**Initial stiffness of backfill spring (K_{init}^{bf}), [kip / in]**	**Ultimate passive resistance of backfill spring (F_{ult}^{bf}), [kip]**
A	4.6	21.3	5	89.8	83.3
B	6.2	63.0	5	357.0	444.8
C	6.3	79.6	5	455.9	574.4
MAOC	4.5	40.1	5	164.0	147.4

Kaviani et al. (2012; 2014) also accounted for the effect of abutment skew angle on the passive resistance of the abutment backfill by assuming a linear variation (schematically shown in Figure 4.20 (b) and Figure 4.20 (c)) of the initial stiffness and the ultimate strength of the backfill springs over the skewed length of the backwall between the obtuse (OBT) and acute (ACU) corners (marked in Figure 4.20 (a)). The lower and upper bounds of the coefficient of linear variation are defined as $1-\beta$ and $1+\beta$, respectively, with the former applied to the stiffness and strength (given by Eq. (4.2) and Eq. (4.3) respectively) of the spring near OBT while the latter applied to that of the spring near ACU. With parameter β defined by Eq. (4.4) (Kaviani et al. 2012; Kaviani et al. 2014), wherein α is the value of bridge skew in degrees, the researchers of the original study postulated that for the largest abutment skew angle of 60 degrees, a maximum variation of 30% occurs between the stiffness/strength of backfill springs located at the obtuse and acute corners.

$$\beta = 0.3 \times \frac{\tan \alpha^{\circ}}{\tan 60^{\circ}} \tag{4.4}$$

This variation was hypothesized to phenomenologically account for the increase in the available volume of engineered backfill soil that can be mobilized per unit length of the backwall in going from point OBT towards the point ACU. Figure 4.22 shows the hyperbolic backbone curves assigned to the backfill springs of the selected testbed bridges linearly varying in stiffness/strength in going from points OBT to ACU.

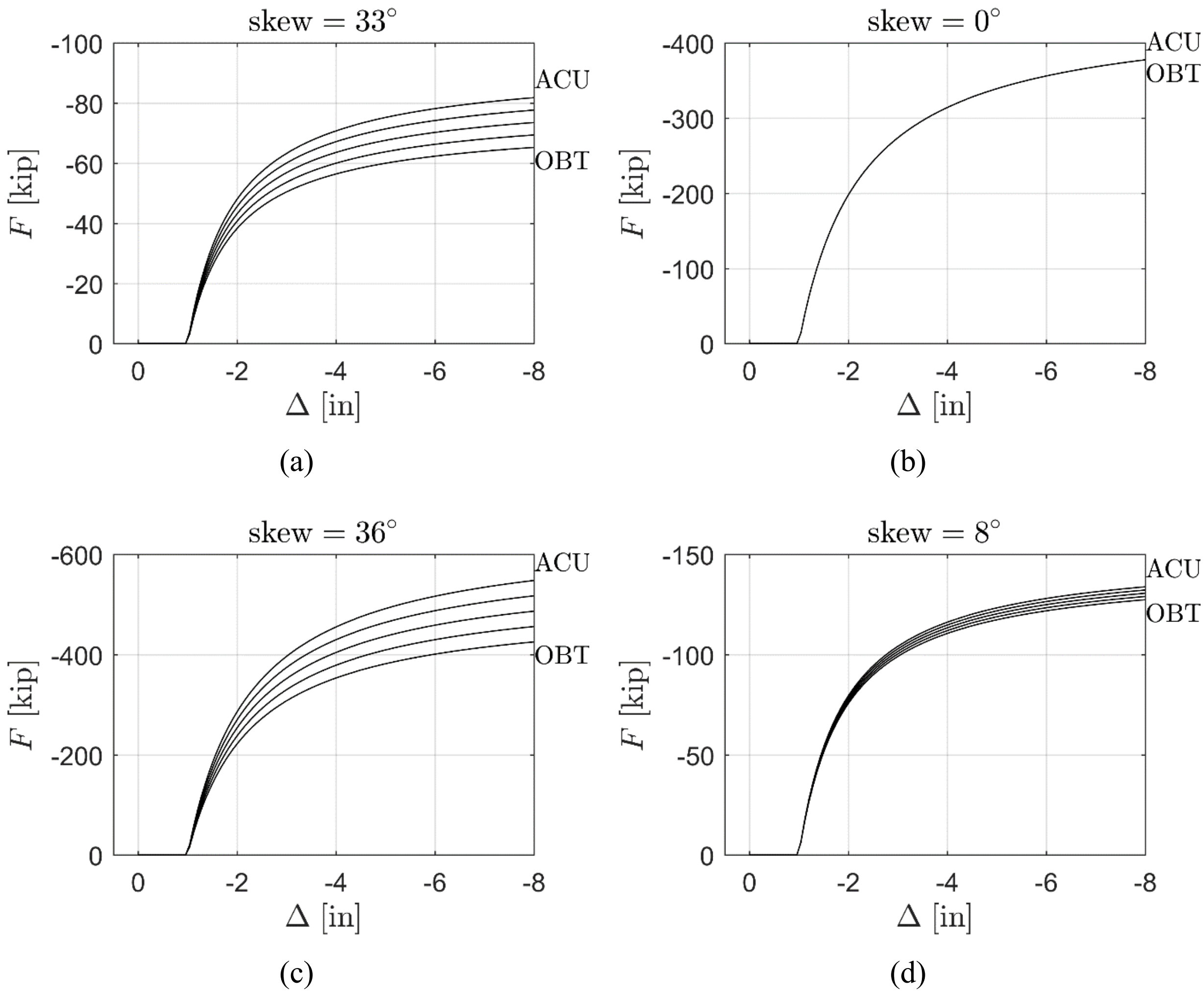

Figure 4.22 Hyperbolic backbone curves of the force-deformation relationships used to model the longitudinal passive resistances of five equally spaced backfill springs (per bridge abutment) with linearly varying strengths and initial stiffnesses: (a) Bridge A; (b) Bridge B; (c) Bridge C; and (d) Bridge MAOC

4.2.3.2 Bearing Pad

Steel reinforced elastomeric bearing pads evenly laid on top of abutment stemwalls are used to support both ends of the testbed bridge decks. These fairly strong, yet pliable, bearing pads allow slight horizontal movements of the deck after construction. Allowing such necessary movements in irregular environmental conditions prevent the development of unwanted/harmful residual stresses in bridge components. As schematically shown in Figure 4.20 (c), the combined vertical, longitudinal, and transverse resistances of the total number, say n_{bp}^{actual}, of bearing pads per abutment are modeled using n_{bp}^{model} specialized zero-length bearing elements implemented in OpenSees as the *elastomericBearingPlasticity* element. Note that n_{bp}^{actual} corresponds to the total number of bearing pads per abutment used in the actual design of the testbed bridges while n_{bp}^{model} refers to that used in the finite element model, conveniently taken equal to the number of backfill springs used. The *elastomericBearingPlasticity* element uses a plasticity-based (rate-independent) phenomenological model to describe the coupled bidirectional nonlinear shear force-deformation response of bearing pads. A bilinear hardening force-deformation backbone curve, with a post-yield stiffness ratio of 0.1, is assigned to both translational directions of an elastomeric bearing element as shown in Figure 4.23. Coupling between the two horizontal resistances of a bearing pad element is described by a circular, rotationally symmetric, yield surface as shown in Figure 4.23. Nonlinear hardening effects, also captured by the *elastomericBearingPlasticity* element, are not included in this project for simplicity. Each bearing pad is supported vertically on the essentially rigid stemwall (represented by a fixed connection at the base of the element), thus allowing the vertical (uncoupled with respect to the two horizontal directions) response of the bearing pad element to be modeled as exceeding stiff (quasi-rigid).

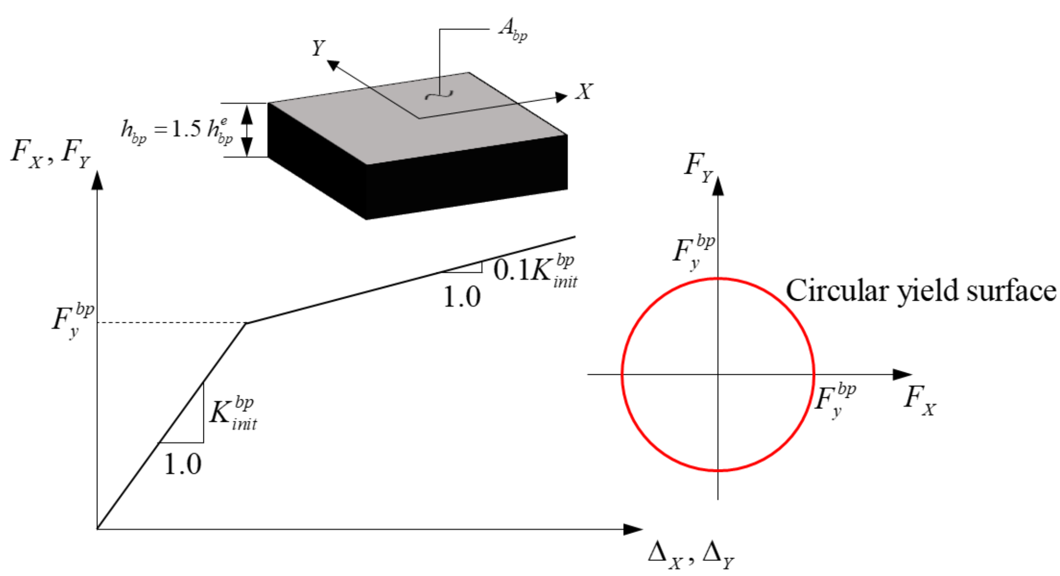

Figure 4.23 Bilinear backbone curve of the force-deformation relationship used to model the coupled bidirectional (longitudinal and transverse) resistance of an elastomeric bearing pad element. The circular yield surface, shown in red, describes coupling between the resistances in the two horizontal directions

The initial stiffness, K_{init}^{bp}, and, the yield resistance, F_y^{bp}, of a single bearing pad are evaluated as follows:

$$K_{init}^{bp} = \frac{G_{bp} A_{bp}}{h_{bp}^{e}} \times \frac{n_{bp}^{\text{actual}}}{n_{bp}^{\text{model}}} \tag{4.5}$$

$$F_y^{bp} = K_{init}^{bp} \times \frac{h_{bp}^{e}}{2} \tag{4.6}$$

where, G_{bp}, A_{bp}, and h_{bp}^{e} refer to the shear modulus, the cross-sectional area, and the total elastomer height/thickness of a single bearing pad, respectively. Assuming the total thickness of reinforcing steel shims to be approximately 50% of the elastomer height, the latter can be taken as $0.67\,h_{bp}$, where h_{bp} is the total height of the bearing pad. The yield resistance, F_y^{bp}, is calculated by limiting the maximum elastic shear deflection of the bearing pad to half the total elastomer height (Caltrans 2000). Table 4-7 shows the geometric properties of elastomeric bearing pads used in the original design of the selected testbed bridges and their corresponding material properties obtained as per Eq.s (4.5) and (4.6). Figure 4.24 shows the resulting hysteretic force-deformation relationships, given the values of K_{init}^{bp} and F_y^{bp} in Table 4-7, each corresponding to any one (out of $n_{bp}^{\text{model}} = 5$ per abutment) elastomeric bearing element in the finite element model of a testbed bridge.

Table 4-7 Material properties for elastomeric bearing elements

Bridge	**Elastomer shear modulus (G_{bp}),**	**Bearing pad cross-sectional area (A_{bp}), [in × in]**	**Elastomer thickness (h_{bp}^{e}), [in]**	$\frac{n_{bp}^{\text{actual}}}{n_{bp}^{\text{model}}}$	**Initial stiffness (K_{init}^{bp}), [kip / in]**	**Yield resistance (F_y^{bp}), [kip]**
A	0.10	11.8 × 11.8	1.7	4/5	6.54	5.58
B	0.10	23.6 × 23.6	2.5	7/5	31.34	39.10
C	0.10	18.1 × 18.1	3.0	9/5	19.57	29.53
MAOC	0.10	12.0 × 12.0	2.4	6/5	7.33	8.66

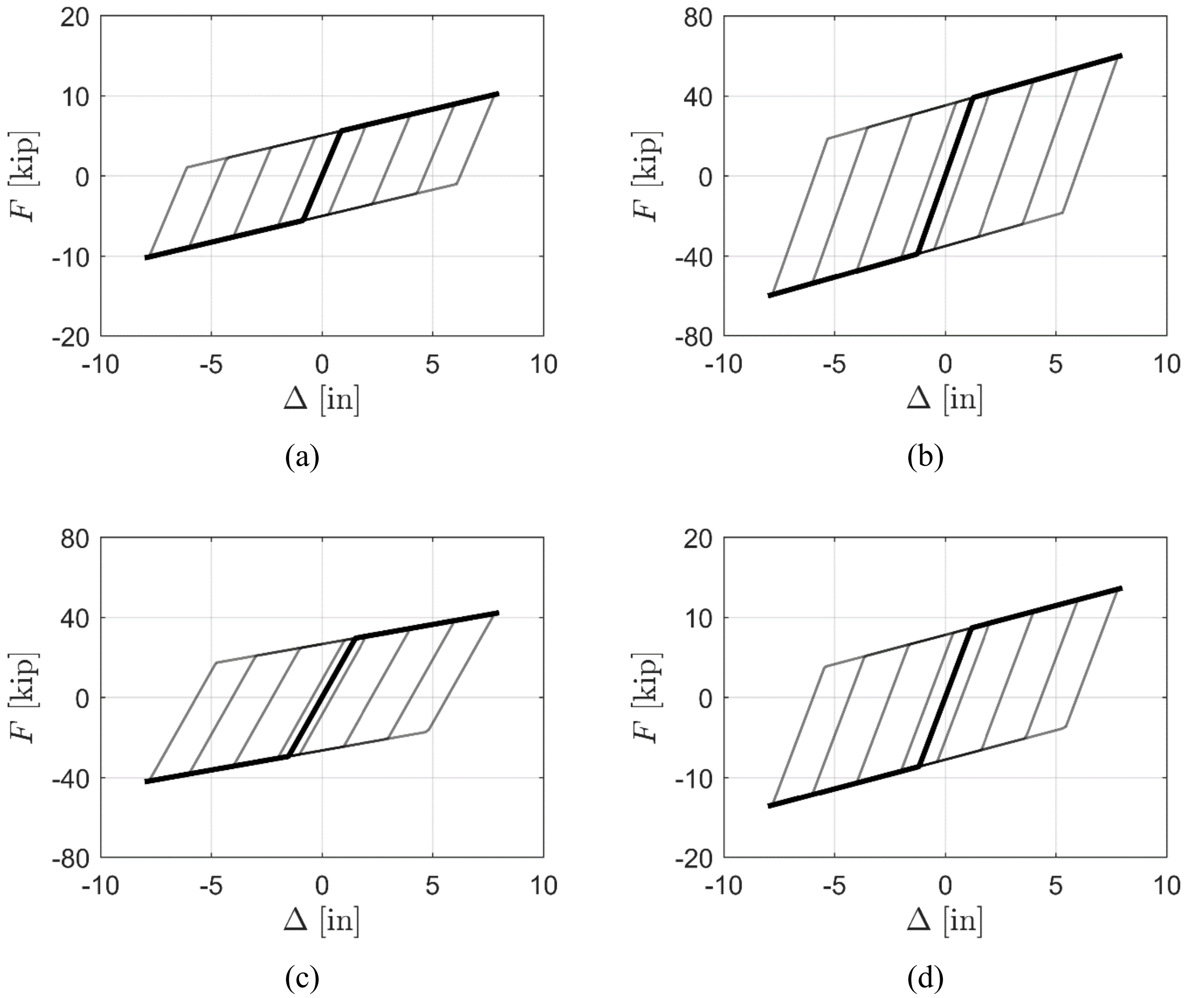

Figure 4.24 Nonlinear hysteretic force-deformation relationships (bilinear backbone curve in bold) used to model the coupled horizontal (longitudinal and transverse) resistance of a single bearing pad element (out of a total of 5 equally spaced bearing pad elements per abutment): (a) Bridge A; (b) Bridge B; (c) Bridge C; and (d) Bridge MAOC

4.2.3.3 Shear Keys

Bridge abutments of each of the testbed bridges comprise of exterior shear keys to provide transverse support to the superstructure (deck). Transverse shear forces imparted by the deck are transmitted to the stemwall primarily through vertical reinforcement between the shear key and the stemwall. Such keys are intended to act as structural fuses that break off in the event of a strong earthquake to prevent the propagation of damage to the stemwall and the supporting piles. However, two prevalent approaches (Caltrans 2013) to the design and detailing of shear keys have been historically found, and experimentally corroborated, to engender different damage/failure modes in the seismic aftermath depending on the reinforcement detailing and the type of construction joint between the shear key and the abutment stemwall. One approach, called the isolated shear key method, involves a smooth construction joint between the shear key and the stemwall with vertical reinforcement detailed so as to ensure an easily repairable brittle failure based on a sliding shear mechanism through a well-defined horizontal plane. The other approach, referred to as the non-isolated shear key method, involves a rough, or no, construction joint between the shear key and the stemwall. Reinforcing details for non-isolated shear keys have been shown to result in a rather undesirable strut-and-tie failure mechanism accompanied by diagonal tension that engages the stemwall reinforcement and subsequently damages the stemwall significantly. Reinforcement details of generic shear keys designed according to both design approaches and their corresponding failure mechanisms are shown in Figure 4.25. Original designs of three of the selected testbed bridges, i.e., Bridge A, Bridge B, and Bridge C, utilize non-isolated shear keys. The fourth testbed bridge, i.e., Bridge MAOC, on the other hand, calls for isolated shear keys in its original design. The transverse resistance of an exterior shear key is modeled using a translational compressive spring, by means of the *zeroLength* element in OpenSees, on each side of an abutment as shown in Figure 4.20 (b) and Figure 4.20 (c).

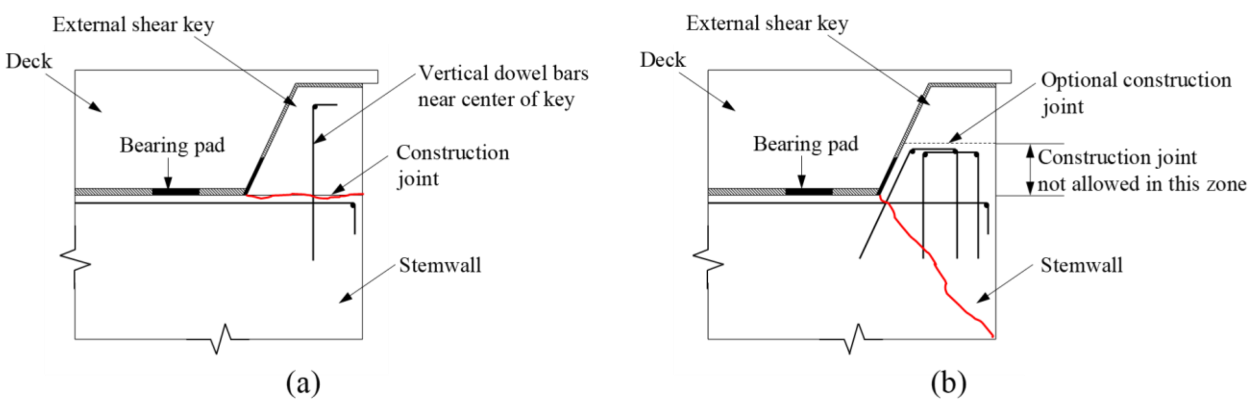

Figure 4.25 Exterior shear key reinforcement details (based on Caltrans SDC v1.7) and observed failure mechanisms (shown in red): (a) Isolated shear key (brittle failure in sliding shear mechanism along a horizontal plane; shear key slides along construction joint without engaging the stemwall); and (b) Non-isolated shear key (ductile failure in diagonal tension along a diagonal plane thereby engaging and damaging the stemwall)

Megally et al. (2002) proposed a semi-empirical mechanics- and deformation-based shear force-deformation hysteretic macro-model (shown in Figure 4.26) for non-isolated shear keys validated based on the experimental force-deformation data obtained from destructive testing of reduced-scale physical specimens of exterior shear keys. The complete model is constructed by superimposing the hysteretic contributions from steel and concrete components as shown in Figure 4.26. The original authors related each branch of the proposed quinque-linear (branches AB, BC, CD, DE, and EF shown in Figure 4.26) backbone force-deformation curve to distinct damage levels/mechanisms observed in the conducted experiments. Level-I (contained in branch AB) corresponds to initiation of diagonal cracking at the intersection of the shear key's sloped surface with the top of the stemwall. Level-II (point B) is the onset of yielding of shear key reinforcement. Level-III (point C) corresponds to the peak load with significant crack width opening at the shear key-stemwall interface. Level-IV (point D) is the point at which concrete contribution to the resistance falls to zero while Level-V (point E) is the initiation of failure of the steel resisting component. Kaviani et al. (2014) suggested the use of *Concrete02*, a material model from the library of uniaxial materials in OpenSees, for a numerically robust implementation of the proposed model for exterior shear keys. The backbone curve of the force-deformation hysteresis described by *Concrete02* can be adjusted to approximately agree with that of the proposed quinque-linear model. To define the *Concrete02* material model in OpenSees, only three parameters, viz., V_{III}, Δ_{III}, and Δ_D, of the quinque-linear model are required. To this end, force-deformation coordinates corresponding to three damage levels, i.e., Level-III, Level-IV, and Level-V, need to be evaluated.

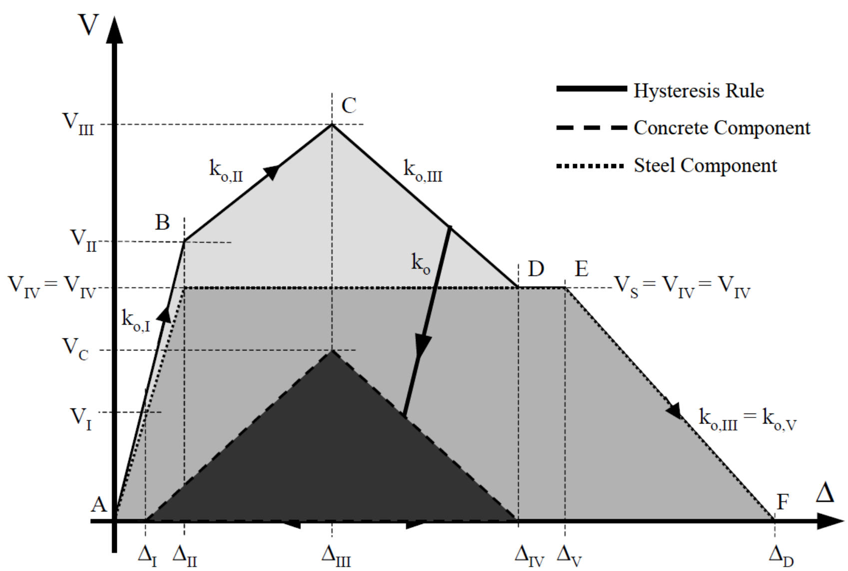

Figure 4.26 Quinque-linear backbone curve (Megally et al. 2002) and hysteresis rule for non-isolated exterior shear keys obtained as a superposition of a concrete component and a steel component

Level-III corresponds to the shear key capacity for a non-isolated shear key. This can be obtained by aggregating the contributions from concrete and reinforcing steel (i.e., $\mathrm{V_C}$ and $\mathrm{V_S}$, respectively) to the shear resistance as follows (Megally et al. 2002):

$$\mathrm{V_{III}} = \mathrm{V_C} + \mathrm{V_S} \tag{4.7}$$

$$\mathrm{V_C} = 2.4\sqrt{f_c'} \times b \times h \quad \text{(in, psi)} \tag{4.8}$$

$$\mathrm{V_S} = \left[A_{s1} f_y h + A_{s2} f_y \left(d_2 \sin\theta + h \cos\theta \right) + n_h A_{ssh} f_y \frac{h^2}{2s_h} + n_v A_{ssv} f_y \frac{d_2^2}{2s_v} \right] \left(\frac{1}{h + d_1} \right) \tag{4.9}$$

where, d_1 is the height of the shear key, d_2 is the length of the shear key-stemwall interface, b is the width of the stemwall; and h is the height of the stemwall. A_{s1} is the area of horizontal reinforcement at the top of the stemwall, A_{s2} is the area of inclined hanger reinforcement near the intersection of the shear key's sloped surface with the top of the stemwall, A_{ssh} is the area of stemwall horizontal side reinforcement, and A_{ssv} is the area of stemwall vertical side reinforcement. n_h and n_v are the numbers of horizontal and vertical side reinforcement layers in the stem wall, respectively, with s_h and s_v representing the respective rebar spacing. Finally, f_c' and f_y represent the nominal characteristic compressive strength of concrete and the nominal yield strength of steel reinforcing bars, respectively. Figure 4.27 schematically shows the diagonal failure mechanism of an exterior non-isolated shear key along with the parameters involved in the above equations. It is noted that the steel contribution, $\mathrm{V_S}$, is calculated based on the rotational equilibrium of the diagonally cracked shear key about the point A (in Figure 4.27). The shear key top displacement at this level is computed by assuming that the bottommost rebars near the toe of the stemwall crossing the diagonal crack have reached yielding in tension. The displacement capacity, Δ_{III}, of a non-isolated shear key is accordingly given by (Megally et al. 2002):

$$\Delta_{\mathrm{III}} = \sqrt{2}\varepsilon_y \left(L_d + b \right) \frac{h + d_1}{s} \tag{4.10}$$

where, ε_y is the yield strain of steel reinforcing bars, and s is the larger of the horizontal and vertical rebar spacing of the stemwall side reinforcement. L_d represents the reinforcement development length given by (Megally et al. 2002):

$$L_d = \frac{d_b f_y}{25\sqrt{f_c'}} \quad \text{(in, psi)} \tag{4.11}$$

where d_b represents the rebar diameter of the bottommost reinforcing bars in the stemwall.

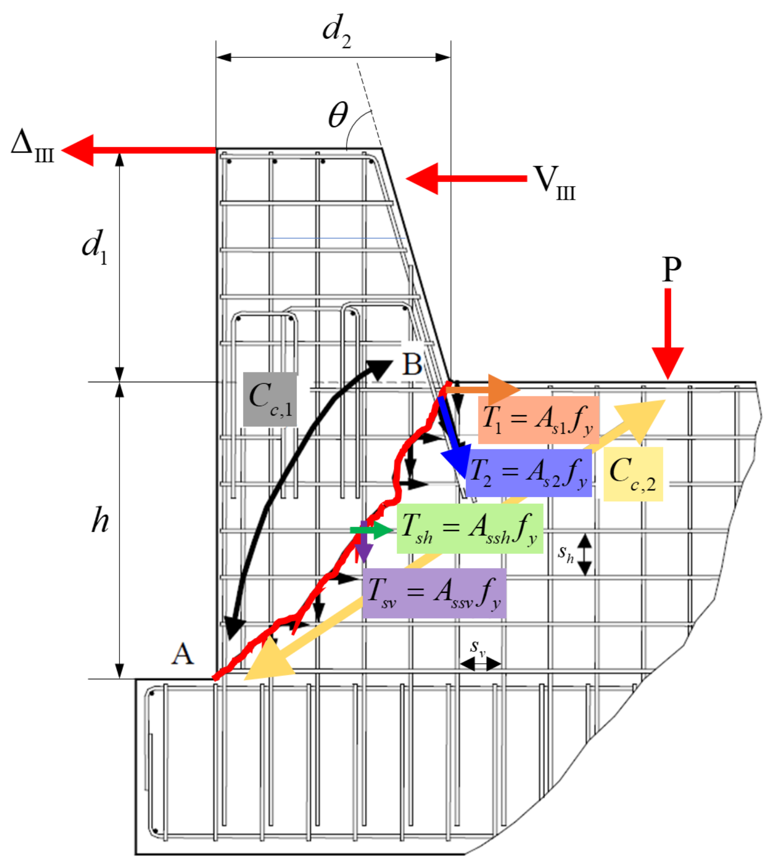

Figure 4.27 Schematic diagram of the strut-and-tie model capturing the failure mechanism involving diagonal tension in a non-isolated exterior shear key (Megally et al. 2002)

The force and displacement coordinates at Level-IV, corresponding to full degradation of concrete contribution to the shear resisting mechanism, are given by Eq.s (4.12) and (4.13) respectively (Megally et al. 2002). A tensile strain of 0.005 in the bottommost rebars (near the toe of the stemwall crossing the diagonal crack) is assumed to be reached at this damage level upon experimental corroboration.

$$V_{IV} = V_S \tag{4.12}$$

$$\Delta_{IV} = \sqrt{2} \times 0.005 \times \left(L_d + b\right)\frac{h + d_1}{s} \tag{4.13}$$

Finally, the force and displacement coordinates at Level-V are given by Eq.s (4.14) and (4.15) respectively (Megally et al. 2002). Level-V, corresponding to the initiation of fracture of rebars crossing the crack at the shear key-stemwall interface, is experimentally found to be accompanied by the tensile strain in the bottommost rebars (crossing the diagonal crack near the toe of the stemwall) reaching 0.007.

$$V_V = V_S \tag{4.14}$$

$$\Delta_V = \sqrt{2} \times 0.007 \times \left(L_d + b\right)\frac{h + d_1}{s} \tag{4.15}$$

The shear key top displacement, Δ_D, corresponding to complete failure of the shear key can be computed as (Megally et al. 2002):

$$\Delta_D = \Delta_V + V_V \frac{\Delta_{IV} - \Delta_{III}}{V_{III} - V_{IV}} \tag{4.16}$$

Table 4-8 shows the material parameters obtained for the shear keys of Bridge A, Bridge B, and Bridge C. Eq.s (4.7) through (4.16), along with the shear key details given in the original design drawings of these testbed bridges are utilized in arriving at the values shown in Table 4-8. Figure 4.28 (a) through Figure 4.28 (c) show the resulting hysteretic force-deformation relationships obtained for the shear keys of these testbed bridges.

Table 4-8 Material properties for exterior shear key springs

Bridge	$\mathbf{V_{III}}$ **[kip]**	$\mathbf{\Delta_{III}}$ **[in]**	$\mathbf{\Delta_D}$ **[in]**
A	1425.16	1.2	5.4
B	2103.90	3.6	19.3
C	1895.00	1.7	6.6
MAOC	406.12	3.7	4.7

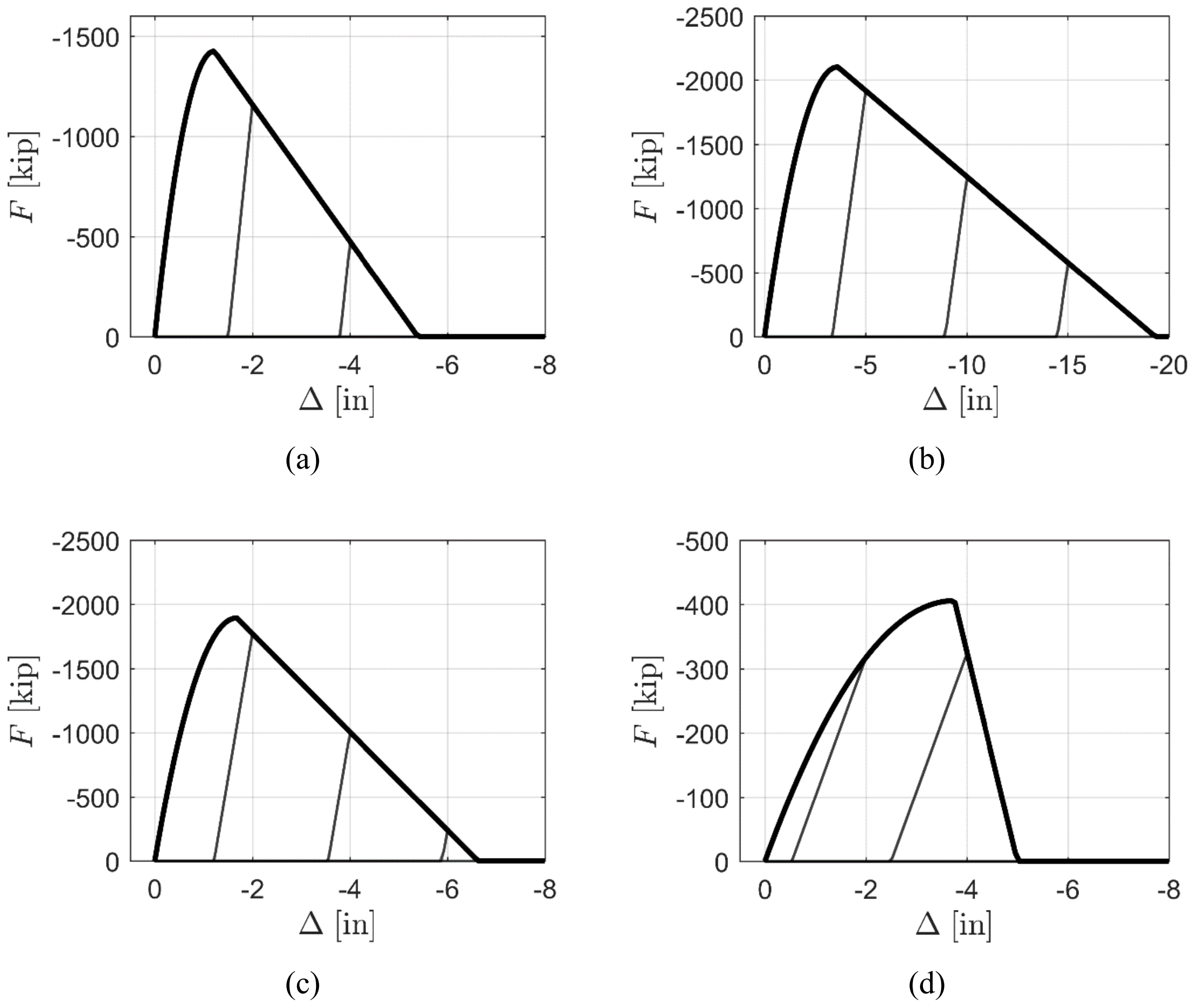

Figure 4.28 Nonlinear hysteretic force-deformation relationships (backbone curve in bold) used to model the transverse resistance of an exterior abutment shear key spring: (a) Bridge A (non-isolated shear key); (b) Bridge B (non-isolated shear key); (c) Bridge C (non-isolated shear key); and (d) Bridge MAOC (isolated shear key)

In the absence of an experimentally validated and well documented force-deformation hysteretic rule for isolated shear keys, the type used in Bridge MAOC, the original developers (Beckwith et al. 2015) of the finite element model of this bridge, calibrated experimental backbone curves corresponding to isolated shear key specimens tested at 40% scale (Bozorgzadeh et al. 2007) to model the force-deformation hysteretic response of the actual bridge shear keys. Beckwith et al. (2015) originally used the *Pinching4* uniaxial material in OpenSees to model a trilinear backbone curve for the shear keys of Bridge MAOC. However, to maintain consistency of modeling approach in this project, the uniaxial material *Concrete02* (same as that used for the three other testbed bridges) with parameters given in Table 4-8 (as obtained from Beckwith et al. (2015)) is used. The resulting hysteretic force-deformation relationship obtained for the shear keys of Bridge MAOC is shown in Figure 4.28 (d).

4.2.4 Inertial Properties, Gravity Loads, and Modal Analysis

Translational masses based on the unit weight of reinforced concrete are assigned to the global translational, i.e., longitudinal (x), transverse (y), and vertical (z), DOFs corresponding to the nodes associated with the superstructure (i.e., the deck) and the columns of each testbed bridge. Normal weight concrete, specified by Caltrans SDC v1.7, with a unit weight (w_c) of 143.96 pcf (lb/ft^3) and, therefore, a mass density (ρ_c) of 4.471 $\text{lb-sec}^2/\text{ft}^4$ is used for the specification of gravity loads and translational masses respectively. Any deck/column node is assigned its respective translational masses and gravity load, as per Eq.s (4.17) and (4.18) respectively, lumped based on the tributary lengths and section properties of the total number of non-rigid frame elements meeting at that node.

$$m_x^{(i)} = m_y^{(i)} = m_z^{(i)} = \sum_{j=1}^{N_{el}^{(i)}} \rho_c \times A_j \times L_j^{trib} \tag{4.17}$$

$$w_z^{(i)} = -\sum_{j=1}^{N_{el}^{(i)}} w_c \times A_j \times L_j^{trib} \tag{4.18}$$

where $m_x^{(i)}$, $m_y^{(i)}$, and $m_z^{(i)}$ are the translational masses assigned to node i; $w_z^{(i)}$ is the gravity (along z direction) load assigned to node i; A_j and L_j^{trib} are the cross-sectional area and tributary length, respectively, of the j^{th} (out of $N_{el}^{(i)}$ total) non-rigid frame element meeting at node i; and $N_{el}^{(i)}$ is the total number of non-rigid frame elements meeting at node i.

A load-controlled static gravity analysis is conducted to reflect service conditions of each testbed bridge subjected to gravity loads. Post-gravity modal analyses of these bridges are then carried out to obtain periods of vibration corresponding to the first few (four) participating modes of the bridges. Mode shapes of the testbed bridge models are shown in Figure 4.29 through Figure 4.32.

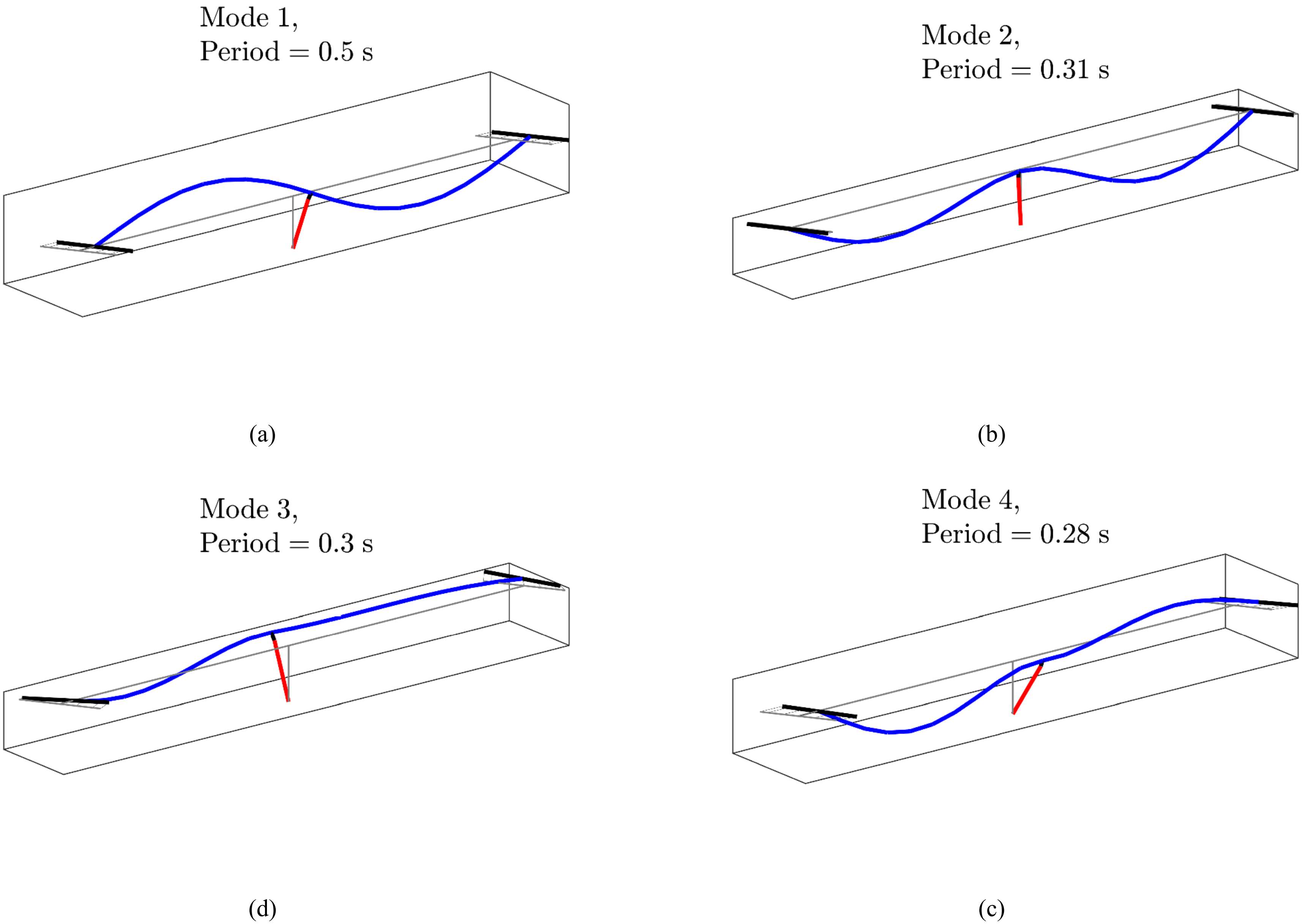

Figure 4.29 Mode shapes (post-gravity load analysis) of Bridge A: (a) Mode 1; (b) Mode 2; (c) Mode 3; and (d) Mode 4

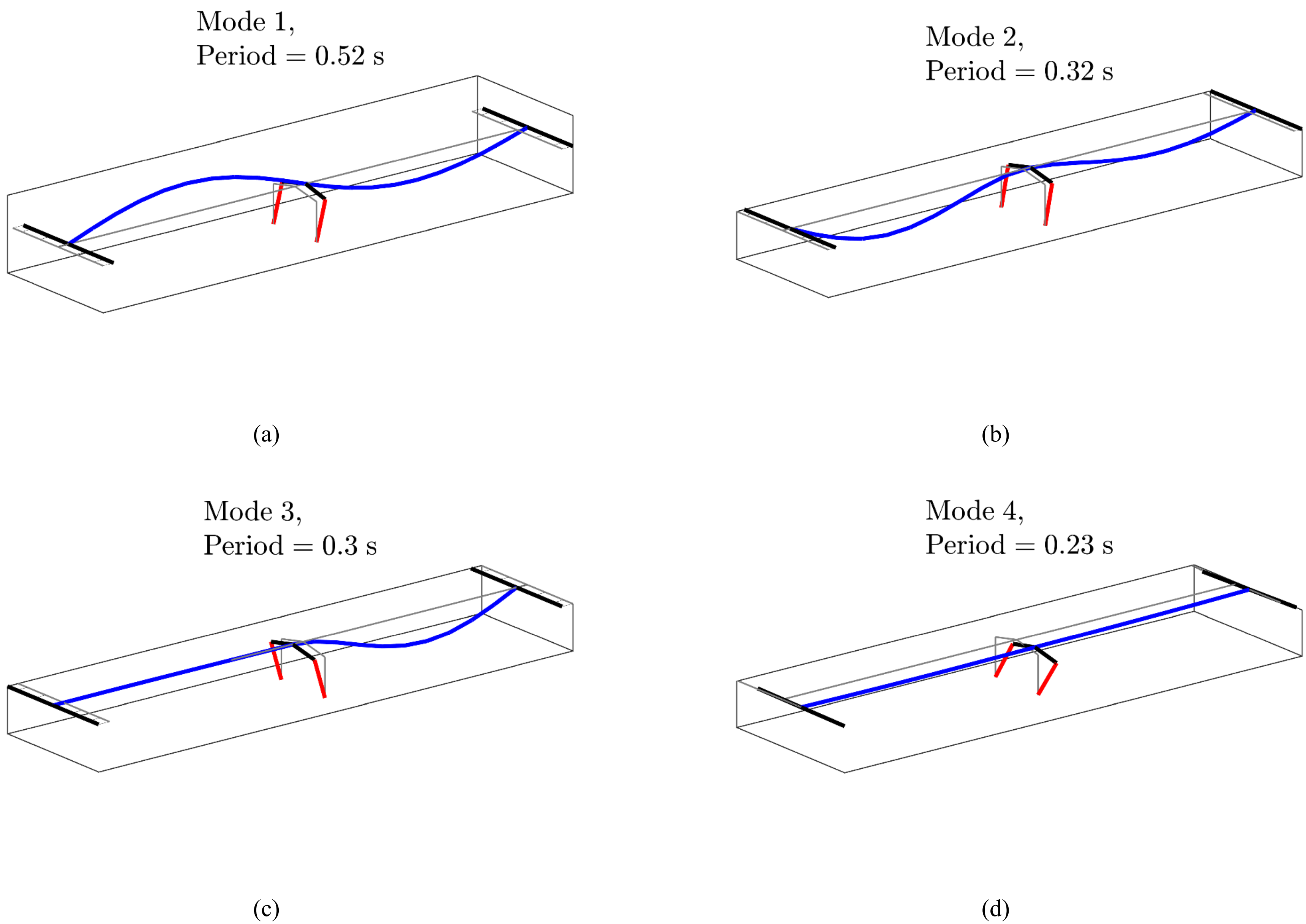

Figure 4.30 Mode shapes (post-gravity load analysis) of Bridge B: (a) Mode 1; (b) Mode 2; (c) Mode 3; and (d) Mode 4

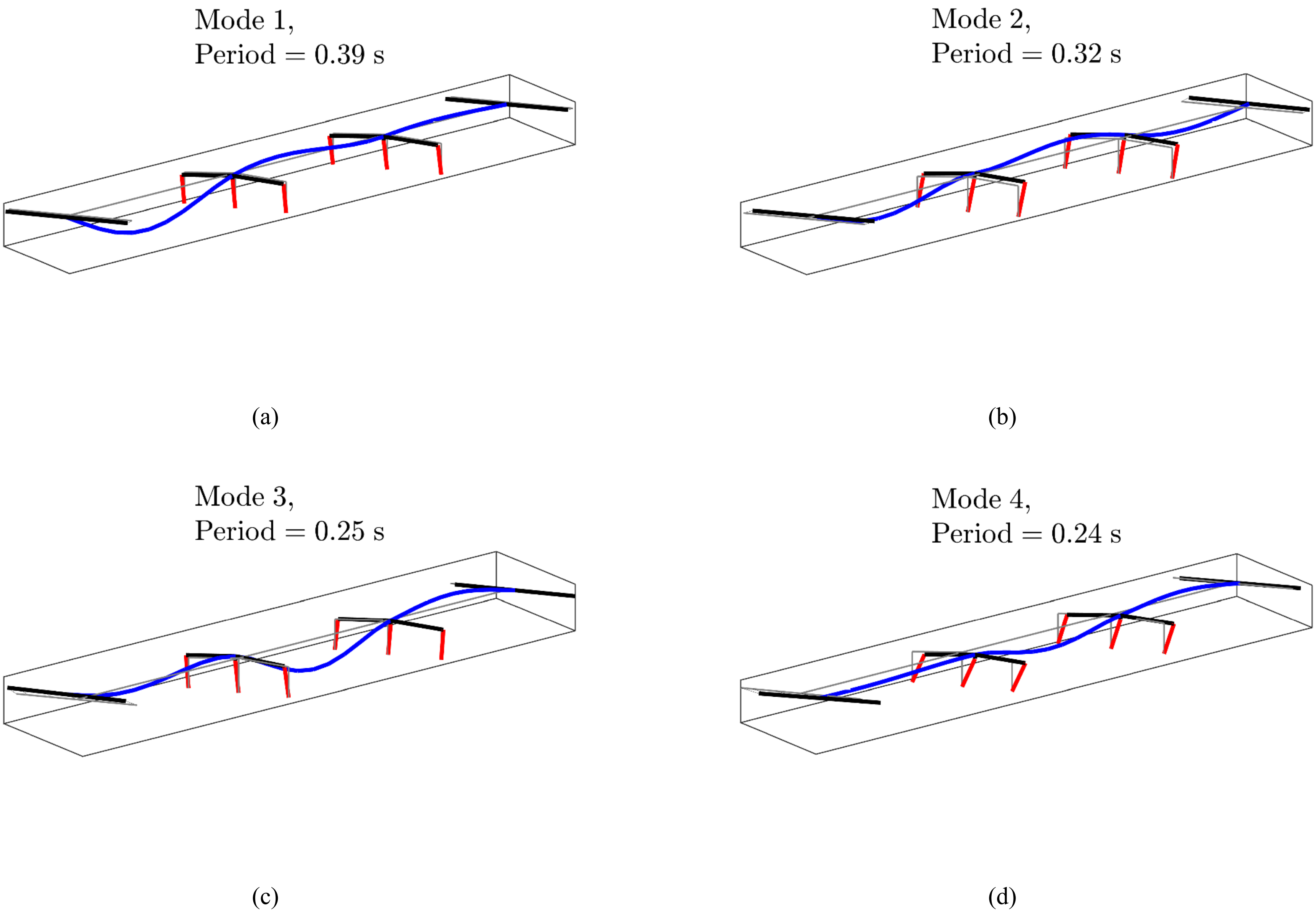

Figure 4.31 Mode shapes (post-gravity load analysis) of Bridge C: (a) Mode 1; (b) Mode 2; (c) Mode 3; and (d) Mode 4

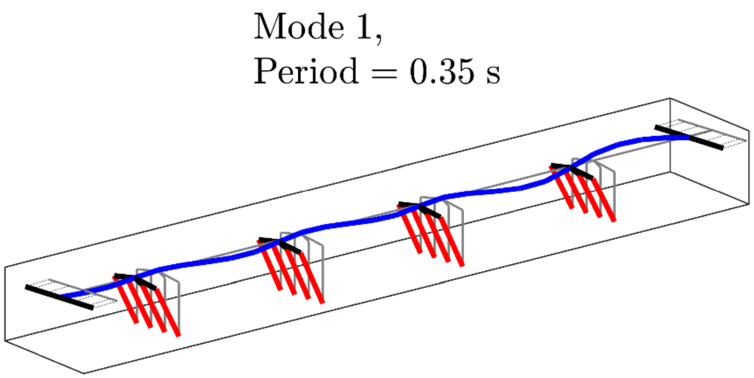

(a)

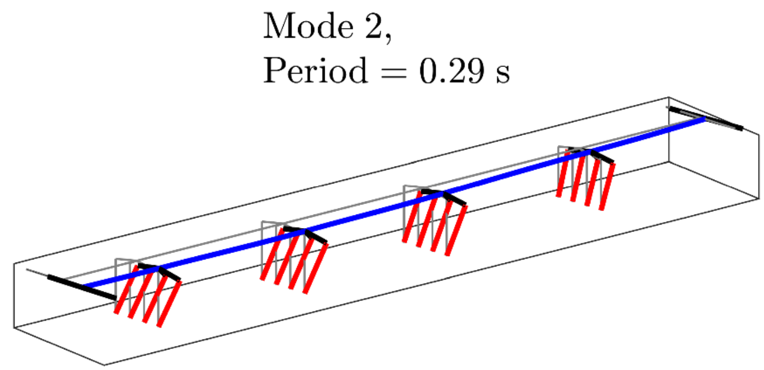

(b)

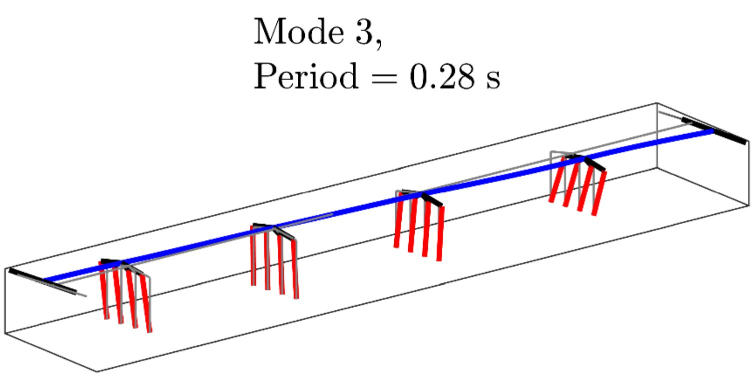

(c)

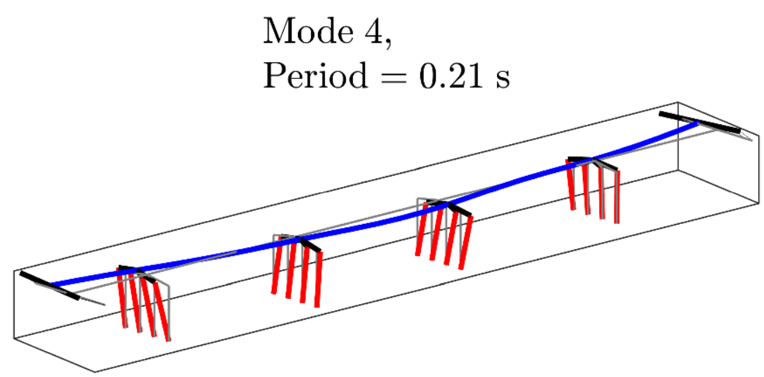

(d)

Figure 4.32 Mode shapes (post-gravity load analysis) of Bridge MAOC: (a) Mode 1; (b) Mode 2; (c) Mode 3; and (d) Mode 4

4.2.5 Damping Model

A part of the total seismic energy imparted to a structural system subjected to an earthquake ground motion is dissipated by the hysteretic response of the inherently inelastic structure. This phenomenon is captured by carrying out a dynamic time-history analyses of the finite element model of the structure thoroughly developed with an in-depth consideration of material constitutive nonlinearity. However, an inelastic structural model provides only an approximation of the myriad phenomena that actually contribute to the actual seismic energy dissipation in the structure. The Rayleigh damping model, a mass- and stiffness- proportional damping model and conceived to account for energy dissipation in elastic structural models with significant mathematical convenience, is commonly used in practice to capture such additional and unknown sources of seismic energy dissipation for inelastic structures as well. The popularity of Rayleigh damping, despite its arguable lack of physical consistency, emerges from the fact that it rules out an explicit construction of a damping matrix for an inelastic structural model whose mass and stiffness matrix have already been assembled.

Rayleigh damping defines the structural damping matrix, $\mathbf{C}$, as a linear combination of the mass matrix, $\mathbf{M}$, and the stiffness matrix (post-gravity-initial/current), $\mathbf{K}$, of the structure as follows:

$$\mathbf{C} = \alpha \mathbf{M} + \beta \mathbf{K} \tag{4.19}$$

where α and β are parameters to be determined. The above coupled (in general) matrix equation can be diagonalized or uncoupled following a pre- and post- multiplication of the above equation on both sides with the matrix of mass-normalized mode shapes (post-gravity-initial/current). Hence, Eq. (4.19) reduces to the following modal equation expressed in terms of the critical damping ratio, ξ_i, and the natural frequency, ω_i, of the i^{th} mode (post-gravity-initial/current).

$$\xi_i = \alpha \frac{1}{2\omega_i} + \beta \frac{\omega_i}{2} \tag{4.20}$$

The Rayleigh parameters, α and β, can be computed as follows such that predefined values of critical damping ratios, ξ_m and ξ_n, are respectively observed at specific values of modal frequencies, ω_m and ω_n $(\omega_m < \omega_n)$.

$$\begin{bmatrix} \alpha \\ \beta \end{bmatrix} = \begin{bmatrix} \dfrac{1}{2\omega_m} & \dfrac{\omega_m}{2} \\ \dfrac{1}{2\omega_n} & \dfrac{\omega_n}{2} \end{bmatrix}^{-1} \cdot \begin{bmatrix} \xi_m \\ \xi_n \end{bmatrix} \tag{4.21}$$

Eq. (4.21) gives

$$\alpha = \frac{2\omega_m\omega_n\left(\xi_m\omega_n - \xi_n\omega_m\right)}{\omega_n^2 - \omega_m^2} \tag{4.22}$$

$$\beta = \frac{2\left(\xi_n\omega_n - \xi_m\omega_m\right)}{\omega_n^2 - \omega_m^2} \tag{4.23}$$

Three different approaches of implementing Rayleigh damping, as listed below, are brought about based on the choice of the state of the structure (i.e., post-gravity-initial/current) in the above definitions.

(i) The damping model is based on the post-gravity-initial stiffness matrix with Rayleigh parameters based on the post-gravity-initial modal frequencies corresponding to the post-gravity-initial stiffness matrix

(ii) The damping model is based on the current stiffness matrix with Rayleigh parameters based on the post-gravity-initial modal frequencies corresponding to the post-gravity-initial stiffness matrix

(iii) The damping model is based on the current stiffness matrix with Rayleigh parameters based on the updated modal frequencies corresponding to the current stiffness matrix

Although the third approach appears to be the most appropriate and scientific way to implement Rayleigh damping, the benefit entailed by it can be far outweighed by the computational cost of successive modal analyses required at different time steps of an already demanding nonlinear dynamic time-history analysis. Either of the two other approaches, on the other hand, can be readily applied with the current implementation of the *rayleigh* command in OpenSees. However, contrasting opinions, regarding these approaches, exist among researchers and practitioners in the current literature with some advocating the use of one over the other and vice-versa. Without any further investigation of such equally prevalent schools of thoughts, the first approach is selected in this project as a neutral choice. In this approach, the damping matrix for the structural model of a testbed bridge is constructed following the application of gravity loads and, thereafter, held constant for the remainder of the analysis.

Rayleigh damping must be sparingly and cautiously applied to an inelastic structural model in order to prevent the structure from being over-damped and develop non-physical damping forces (Charney 2008; Jehel et al. 2014). As such, the assignment of Rayleigh damping in the finite element model of a testbed bridge is limited (using the $\textit{region} < -\textit{rayleigh} >$ command in OpenSees) to the elastic beam-column elements used to model the bridge deck and the force-based beam-column elements used to model the bridge columns. Elements in a bridge model expected to undergo localized yielding in areas of concentrated plasticity, e.g., displacement-based beam-column elements modeling the column base hinges and nonlinear springs/zero-length elements used to phenomenologically capture the nonlinear hysteretic response of various bridge abutment components, are precluded to dissipate energy via Rayleigh damping.

Although the first transverse mode of vibration of any given testbed bridge appears as a relatively higher mode of vibration, as compared to the first longitudinal mode, its participation in the simulated seismic response of the bridge is expected to be more pronounced. This is because the longitudinal response of the bridge is eventually going to be stabilized by the passive resistance of the hyperbolic backfill springs, initially separated by physically modeled gaps. As such, a value of critical damping ratio, ξ_m, equal to 0.01 (1%) is applied to the modal frequency, ω_m, corresponding to the first mode (post-gravity-initial) of vibration of a testbed bridge in the transverse direction. This somewhat frugal choice for the value of critical damping ratio is based on the ground that damping/energy dissipation is already partially captured by an inelastic structural model via hysteresis of material constitutive behavior.

The second value of critical damping ratio, ξ_n, is selected to be relatively large, i.e., 0.05 (5%), and is applied to a higher value of frequency, ω_n, representative of a higher structural mode as compared to the predominant modes of vibration. This is done with the intention of suppressing spurious higher mode contributions to the seismic response of an OSB. This value of ω_n is calculated such that the following inequality is satisfied.

$$\omega_n > \frac{\xi_n \omega_m}{\xi_m} \tag{4.24}$$

Satisfaction of Eq. (4.24) is required to ensure that a positive value of the Rayleigh parameter α is obtained (see Eq. (4.22)). Computed values of Rayleigh parameters for the selected testbed bridges are shown in Table 4-9. The corresponding Rayleigh damping curves (i.e., ξ versus ω relationships given by Eq. (4.20)) obtained for these bridges are shown in Figure 4.33.

Table 4-9 Rayleigh damping parameters for the testbed bridge models

Bridge	ω_m **[Hz]**	ξ_m **[%]**	ω_n **[Hz]**	ξ_n **[%]**	α **[rad s^{-1}]**	β **[rad^{-1} s]**
A	3.4 (Mode 3)	1.0	18.5	5.0	0.0397	0.00086
B	4.3 (Mode 4)	1.0	23.6	5.0	0.0508	0.00067
C	4.2 (Mode 4)	1.0	23.0	5.0	0.0493	0.00069
MAOC	3.5 (Mode 2)	1.0	19.3	5.0	0.0414	0.00082

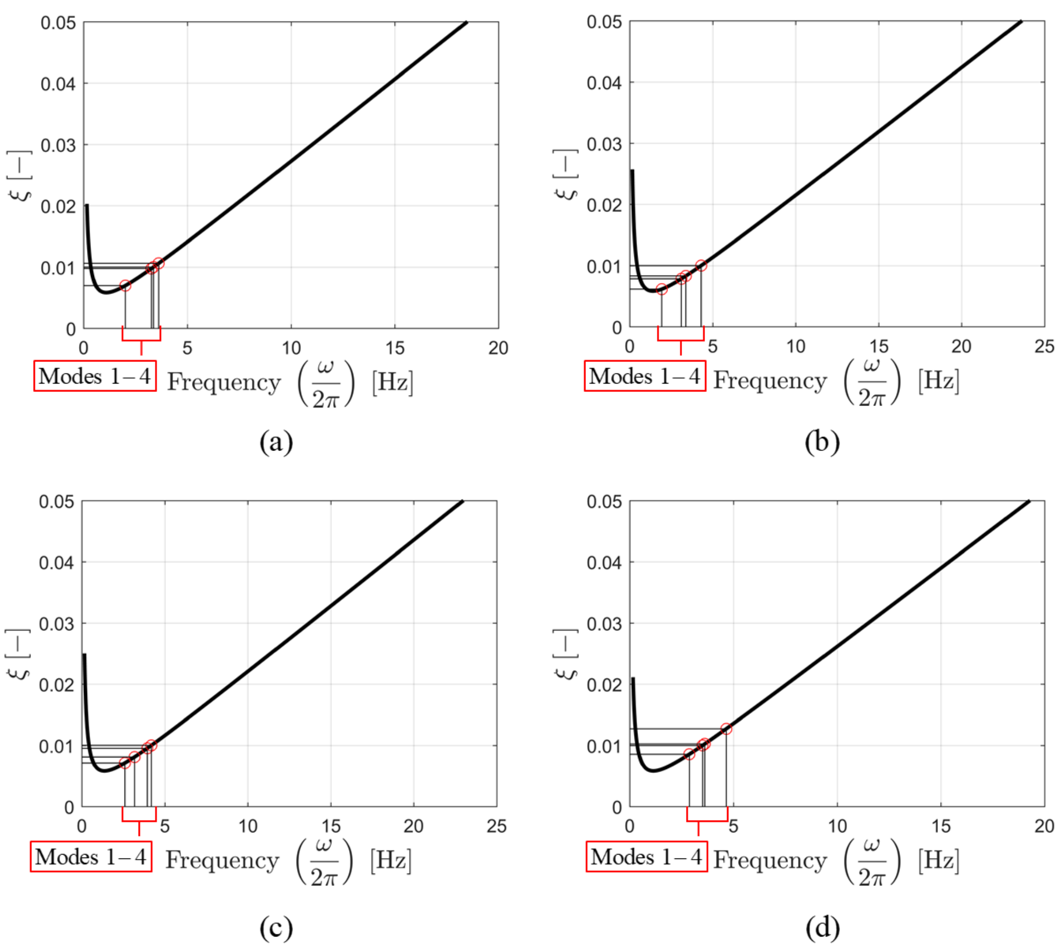

Figure 4.33 Rayleigh damping curves for the considered testbed bridges:(a) Bridge A; (b) Bridge B; (c) Bridge C; and (d) Bridge MAOC

4.3 Nonlinear Time History Analysis Setup

Computational models of the testbed bridges are subjected to seismic excitation by means of rigid body ground motion histories uniformly prescribed to all supports (bases). This approach relies on a relative displacement-based formulation wherein response histories of deformation quantities (such as relative displacement, relative velocity, and relative acceleration with respect to the support/base/ground) corresponding to the global DOFs of the finite element model of a bridge are evaluated under dynamic seismic loading. Dynamic seismic loads are defined in the form of equivalent inertial forces (proportional to the spatial mass distribution in the bridge model) resulting from the prescribed rigid body base motions. This method of performing nonlinear time history analysis is implemented in OpenSees using the *UniformExcitation* loading pattern.

The mathematical model describing the system of governing differential equations (generally coupled) of motion of an inelastic multi-DOF bridge structural system subjected to uniformly prescribed dynamic seismic excitation at all support/base/ground nodes is given by (Clough and Penzien 1993; Filippou and Fenves 2004):

$$\mathbf{M}\,\ddot{\mathbf{U}}(t)+\mathbf{C}\,\dot{\mathbf{U}}(t)+\mathbf{P}_{\mathbf{R}}\left(\mathbf{U}(\tau),\ 0\le\tau\le t\right)=-\mathbf{M}\,\mathbf{R}\,\ddot{\mathbf{U}}^{g}(t) \tag{4.25}$$

where $\ddot{\mathbf{U}}$, $\dot{\mathbf{U}}$, and $\mathbf{U}$ refer to vectors of deformation quantities, i.e., relative acceleration, relative velocity, and relative displacement with respect to the ground, corresponding to the global DOFs in the bridge model. $\mathbf{M}$ and $\mathbf{C}$ are the mass and damping matrices of the bridge model, respectively. $\mathbf{P}_{\mathbf{R}}(\mathbf{U}(\tau),\ 0\le\tau\le t)$ denotes the displacement history dependent resisting force vector of the bridge structural model. The vector $\ddot{\mathbf{U}}^{g}$ is, in general, a six-dimensional vector of ground accelerations corresponding to the six (three translational and three rotational) DOFs of a support node. $\mathbf{R}$ is referred to as the influence coefficient matrix with R_{ij}, its $i-j^{\text{th}}$ component, giving the displacement at the structural DOF i corresponding to a slow uniform movement of all support nodes along DOF j (≤ 6). Time-dependence of the above system of equations is indicated by t.

Dimensionality of the applied loading function, i.e., the ground motion acceleration history, accommodated by the system of equations described in Eq. (4.25) is general and can be easily extended to all six DOFs corresponding to rigid-body ground/support movement. However, restricted by the sparse availability of recorded multi-DOF free-field ground motion records from past seismic events and to maintain the simplicity and practicability of analyses to be conducted in this project, a testbed bridge model is subjected to a two-dimensional seismic input corresponding to the two horizontal-translational (i.e., longitudinal and transverse) directions of the bridge. Following the selection of site-specific risk-consistent ensembles of unrotated two-component ground motion records for a bridge, as will be discussed in the next Chapter, ground acceleration histories corresponding to the two horizontal directions of each record are arbitrarily (without any loss of generality) assigned to the two horizontal-translational directions of the bridge model.

The Newmark-Beta family of transient integrators are commonly used to numerically integrate the system of second-order continuous-time differential equations (Eq. (4.25)) governing the dynamic response of structural systems by employing discrete time-stepping techniques. The Newmark-Beta constant average acceleration method, with values of Newmark parameters, γ and β, set equal to 0.5 and 0.25, respectively, is used in this project to solve the governing equations of motion of the testbed bridge models developed herein. The constant average acceleration time-stepping scheme is implicit in the sense that it leads to a coupled system of equations with respect to dependent and independent variables (i.e., the solution to the state of the structure at a future time $t+\Delta t$ depends on the future state of the structure at time $t+\Delta t$ itself). This, when applied to nonlinear systems, necessitates the use of specialized solution algorithms meant to iteratively solve the incremental equations of dynamic equilibrium for such systems. Numerical robustness of such solution algorithms is the key to mitigate the occurrence of non-convergence of the iterative scheme used to integrate the nonlinear equations of motion over an integration time-step. In the case of non-convergence during a nonlinear time-history analysis, it is important to distinguish between the onset of physical collapse or a numerical, non-collapse related convergence issue. In other words, non-converged nonlinear time-history analyses cannot be discarded. Thus, the nonlinear solution strategy is made adequately robust to minimize the number of non-converged nonlinear time-history analyses. In case a non-collapse-related numerical convergence issue is encountered, convergence of the numerical solution is ensured mainly through adaptive switching between available iterative methods (e.g., Newton, modified-Newton, BFGS, Newton-Krylov) in OpenSees used to solve the incremental equations of dynamic equilibrium over a time step.

It is also essential to ensure that numerical results obtained from employing such discrete time-stepping numerical techniques to solve continuous-time differential equations are not sensitive to the integration time-step (Δt_{int}) used. With values of Newmark parameters, γ and β, respectively taken as 0.5 and 0.25, consistency, second-order accuracy, and unconditional stability of numerically obtained results are engendered. This, however, is strictly valid only for linear systems in which numerical stability, consistency, and second-order accuracy is guaranteed irrespective of the integration time-step used in the constant average acceleration method. For nonlinear problems involving inelastic structural models, the constant average acceleration method does not promise numerical stability and consistency of results, which is why the sensitivity of results needs to be assessed with respect to the integration time-step used. Time-histories of response quantities such as column drift-ratio and absolute acceleration at the column top, corresponding to the testbed bridge models subjected to arbitrarily chosen bi-directional earthquake ground acceleration histories, are shown in Figure 4.34 through Figure 4.37 wherein results obtained using three different values of Δt_{int} are compared. Each earthquake ground motion input assigned to a testbed bridge model (shown in Table 4-10) is arbitrarily picked from a set of ground motion records, scaled and selected such that these records, as an ensemble, are consistent with the site-specific seismic hazard (elaborated in Chapter 5). Results corresponding to each bridge model are found to converge to a stable solution with increasingly small values of the integration time-step thereby establishing the adequacy of the nonlinear time history analysis setup implemented in this project. A middle ground between accuracy of results and feasibility of computational runtime is achieved with a value of Δt_{int} taken equal to 0.005 s. However, for future analyses, the value of Δt_{int} can be adaptively incremented or decremented, in conjunction with adaptive switching between available iterative methods, as and when numerical issues are encountered in the convergence of the iterative scheme used to solve the incremental equations of dynamic equilibrium over an integration time-step.

Table 4-10 Earthquake ground motion records for preliminary nonlinear time-history analyses

Bridge	Earthquake Event (Year)	Station	Magnitude	Duration (s)	Scale factor	Ground motion component assigned to bridge direction	
						Long.	Trans.
A	Loma Prieta (1989)	Treasure Island	6.93	39.9	2.87	0	90
B	Northridge-01 (1994)	Pasadena - N Sierra Madre	6.69	19.9	2.56	180	270
C	Imperial Valley-06 (1979)	Coachella Canal #4	6.53	28.5	3.47	45	135
MAOC	Landers (1992)	Coolwater	7.28	27.9	2.83	LN (Fault Parallel)	TR (Fault Normal)

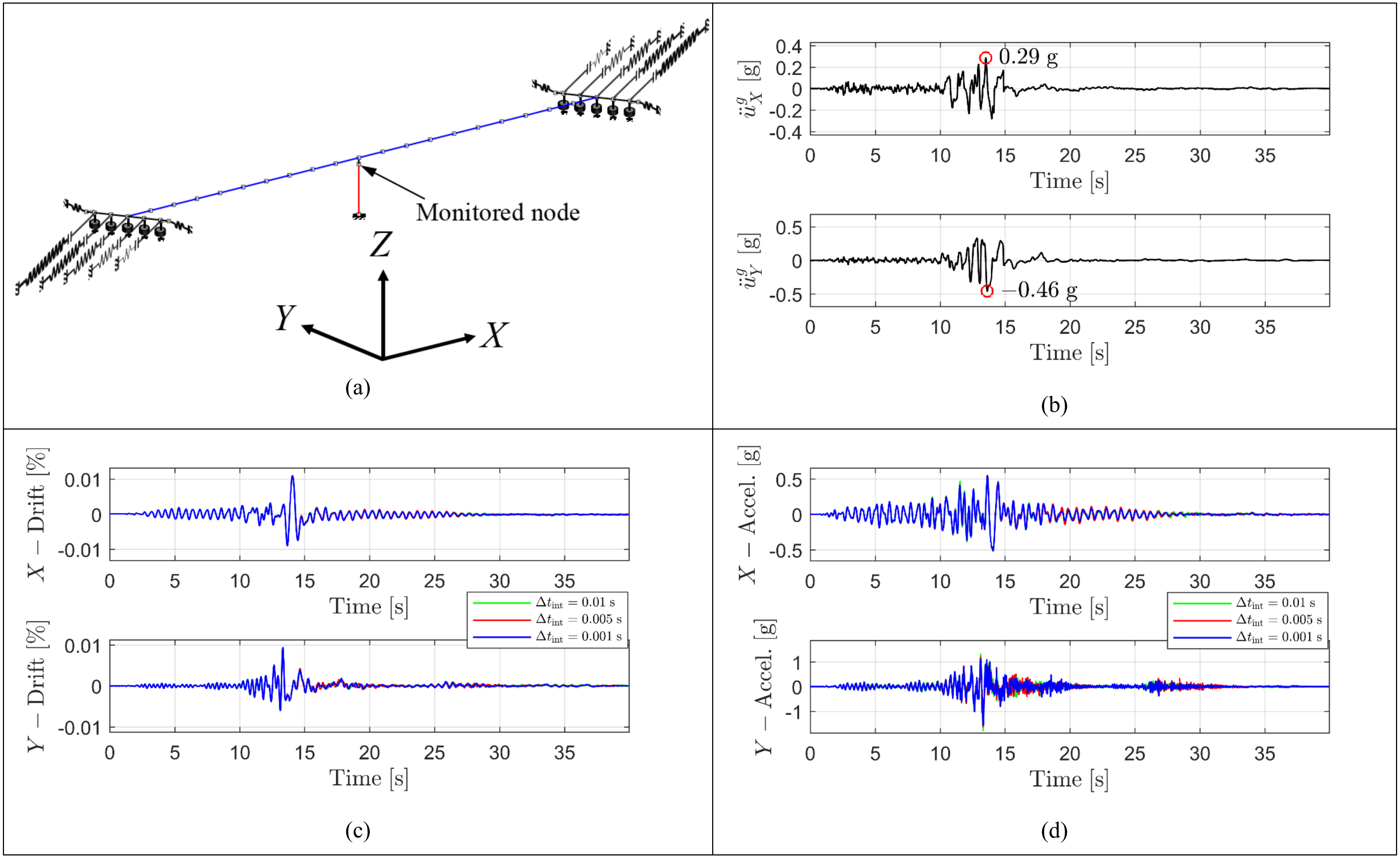

Figure 4.34 Convergence of nonlinear time-history analyses results of Bridge A with respect to integration time-step (Δt_{int}): (a) finite element model and monitored node; (b) Input bi-directional earthquake ground acceleration record; (c) lateral drift response history recorded at monitored node; and (d) absolute acceleration response history recorded at monitored node

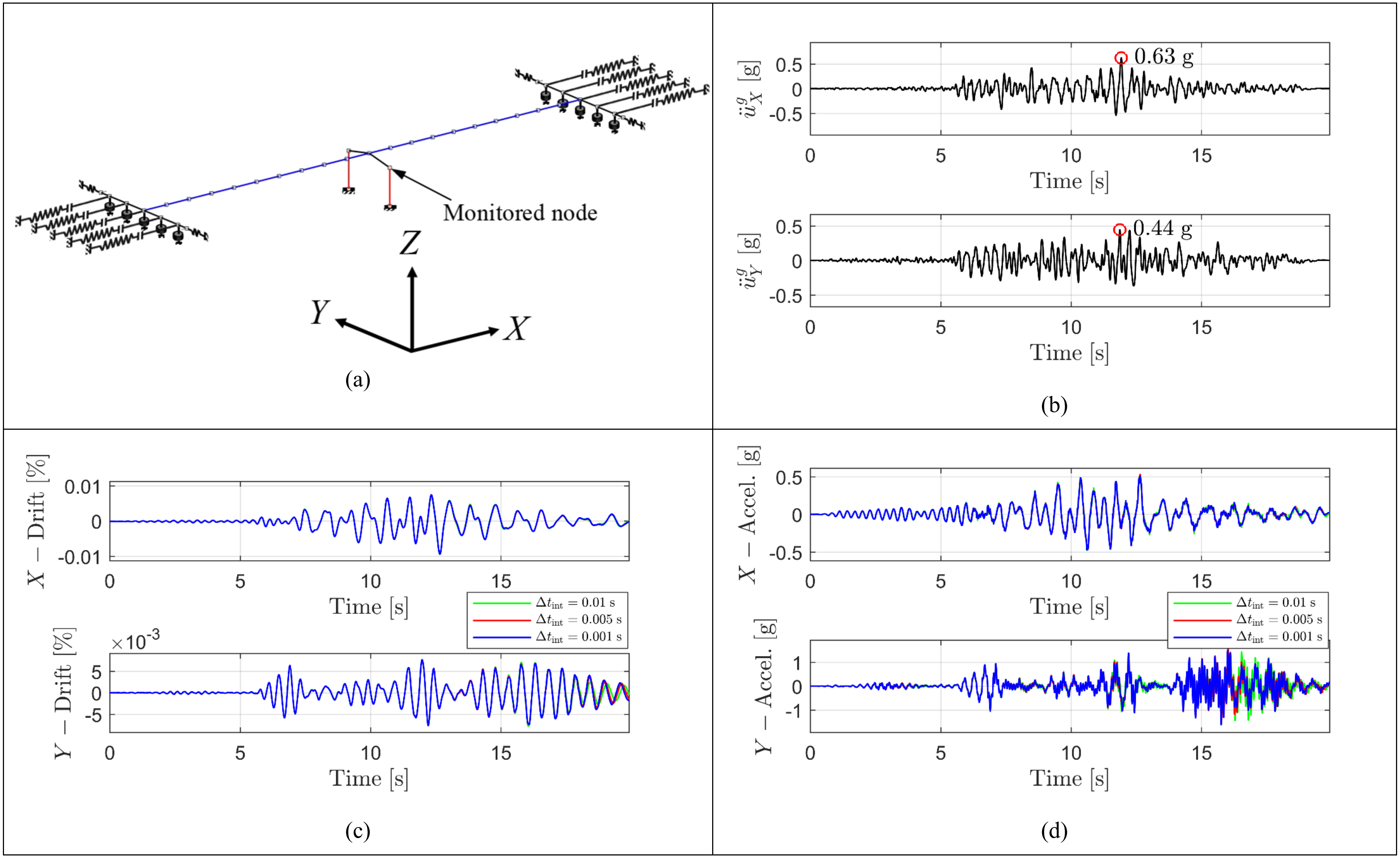

Figure 4.35 Convergence of nonlinear time-history analyses results of Bridge B with respect to integration time-step (Δt_{int}): (a) finite element model and monitored node; (b) Input bi-directional earthquake ground acceleration record; (c) lateral drift response history recorded at monitored node; and (d) absolute acceleration response history recorded at monitored node

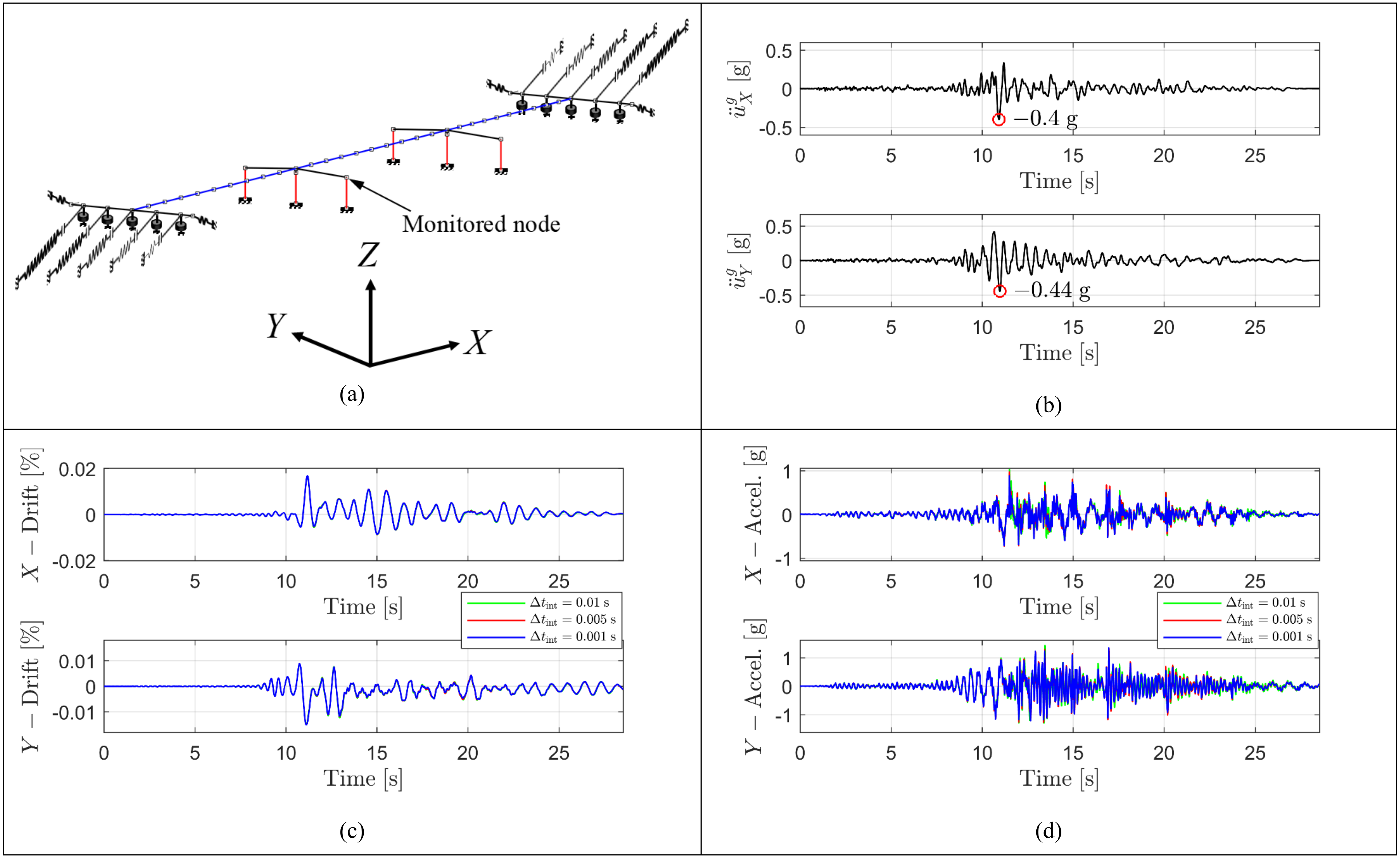

Figure 4.36 Convergence of nonlinear time-history analyses results of Bridge C with respect to integration time-step $(\Delta t_{\rm int})$: (a) finite element model and monitored node; (b) Input bi-directional earthquake ground acceleration record; (c) lateral drift response history recorded at monitored node; and (d) absolute acceleration response history recorded at monitored node

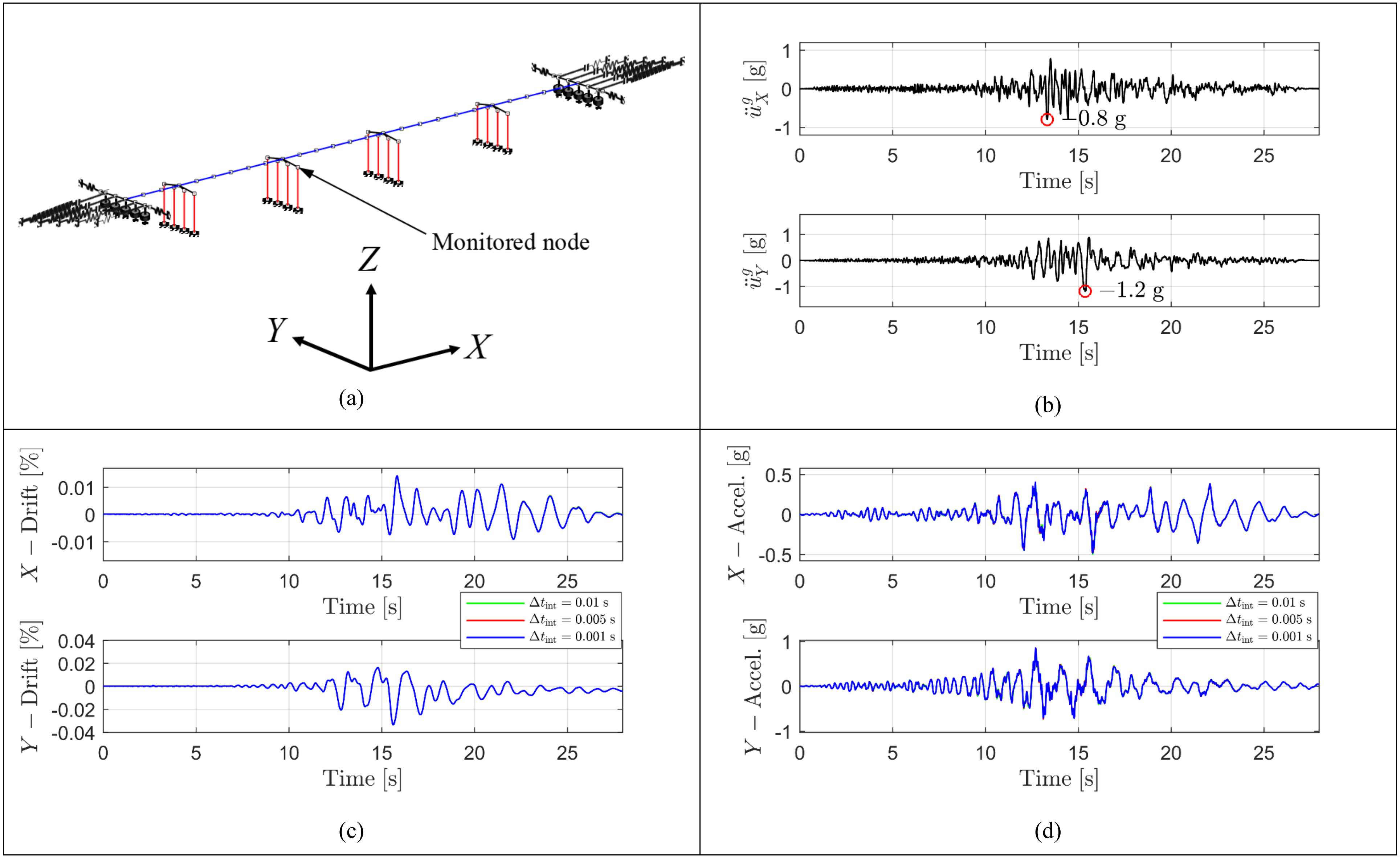

Figure 4.37 Convergence of nonlinear time-history analyses results of Bridge MAOC with respect to integration time-step (Δt_{int}): (a) finite element model and monitored node; (b) Input bi-directional earthquake ground acceleration record; (c) lateral drift response history recorded at monitored node; and (d) absolute acceleration response history recorded at monitored node

5 Probabilistic Seismic Hazard Analysis

5.1 Introduction

Seismic response evaluation of structures is an integral part of performance-based seismic assessment and/or design. Seismic performance assessment and/or design of structures requires predictions of risk-levels associated with structural performance in the event of an earthquake. To obtain reliable risk predictions, the level of ground shaking to be considered for evaluating the seismic response of structures should be consistent with the seismic hazard at the site of the structure. This necessitates an explicit description of the seismic hazard in terms of a ground motion parameter that correlates well with structural response and, in turn, with damage due to an earthquake.

The occurrence of an earthquake is a highly random phenomenon and there is large uncertainty associated with seismic loads and ground motion parameters due to random occurrence time, variability in magnitude, source-to-site distance, seismic wave attenuation, etc. Therefore, seismic hazard assessments must inevitably involve a treatment of uncertainties. Uncertainties can be categorized as aleatory and epistemic. Aleatory uncertainty, also known as natural variability, is inherent to the considered phenomenon and hence classified as irreducible. Epistemic uncertainty, however, arises due to lack of completeness in the chosen model of the considered phenomenon and is primarily due to insufficient knowledge and/or data. Epistemic uncertainty promises to reduce with more information, knowledge, and/or research. An explicit account of epistemic uncertainties is kept outside the scope of this project.

Probabilistic Seismic Hazard Analysis (PSHA), originally proposed and developed by Cornell (1968) aims to identify and quantify the pertinent sources of uncertainties to rigorously characterize the seismic hazard in a probabilistic sense.

5.2 Seismic Hazard Integral

The essence of PSHA is to identify and aggregate the contribution of all possible seismic events (characterized by pairs of earthquake magnitudes and source-to-site distances that could potentially affect the considered structure) to arrive at an estimate of the mean annual rate (MAR) at which specific values of a ground motion intensity measure (IM) are exceeded. An reflects the intensity of the earthquake ground motion and can be taken as a structure-independent ground motion parameter (e.g., peak ground acceleration (PGA), peak ground velocity (PGV), Arias intensity, Housner's spectrum intensity) or more often as a structure-dependent ground motion parameter such as the 5% damped pseudo-spectral acceleration, $S_a(T_1, \xi = 5\%)$, or the spectral displacement, $S_d(T_1, \xi = 5\%)$, at the expected predominant period T_1. The level of damping associated in the definition of damped pseudo-spectral acceleration and/or displacement is assumed to be 5% and the explicit indication of $\xi = 5\%$ is dropped hereafter for the sake of brevity and ease of notation. Furthermore, pseudo-spectral accelerations, henceforth are referred to as spectral accelerations.

The basic underlying assumption in probabilistic seismic hazard computations is that of a random earthquake occurrence model in time. The homogenous Poisson process is a reasonable model for this purpose (Cornell 1968). The time to first occurrence of a Poisson event and the interarrival times between such events are distributed according to the exponential distribution with the parameter ν, where ν is the mean annual rate (MAR) of occurrence of the Poisson event. The mean interarrival time, popularly known as the mean return period (RP), of Poisson events is given by the reciprocal of ν. An important property of the Poisson process, exploited at all stages of the PEER PBEE framework and illustrated in Figure 5.1, is that the occurrence of an event following or resulting from that of a basic Poisson event also admits a Poisson description. The resulting process, known as a censored Poisson process, has a mean annual rate of occurrence equal to the product of the MAR of occurrence of the basic Poisson event and the probability of the consequential event.

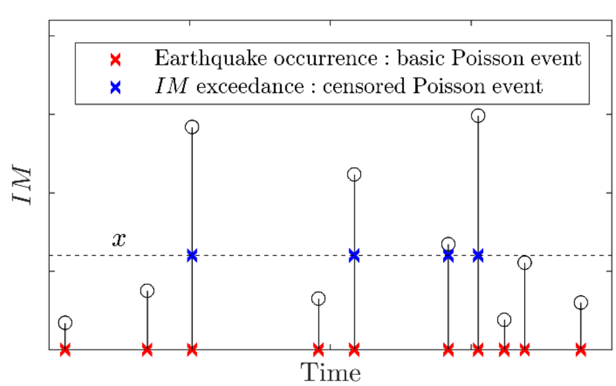

Figure 5.1 Basic and censored Poisson events

Hence, the MAR at which an exceeds a given value x due to an earthquake is given by

$$\nu_{IM}\left(x\right)=\nu\cdot P\left[IM>x\right] \tag{5.1}$$

where ν is the MAR of occurrence of earthquakes with magnitude/intensity greater than a lower bound threshold value such that earthquakes with magnitude/intensity lower than this threshold do not cause any significant damage to the considered structure. The Poisson model for earthquake occurrence in time also allows for computation of the probability of exceedance in an exposure time of t years in terms of the MAR of exceedance, $\nu_{IM}(x)$, as follows

$$P\left[IM>x \text{ in } t \text{ years}\right]=1-e^{-\nu_{IM}(x)\times t} \tag{5.2}$$

An exposure time of 50 years is common in structural engineering practice, and MAR (or mean RP) of exceedance is sometimes equivalently expressed as the probability of exceedance in 50 years using the relation given by Eq. (5.2).

The exceedance of a specific value of a ground motion is influenced by a number of factors. For a given earthquake-prone site, there are several faults or seismic sources nearby (see Figure 5.2). Each seismic source has a distinct seismic activity rate i.e., an MAR of earthquake occurrence, a range of possible earthquake magnitude values and depending on where the rupture occurs on the fault, a range of possible source-to-site distance values. When an earthquake of a given magnitude (M) and source-to-site distance (R) occurs, seismic waves propagate from the source to the site. It has been observed that even with the same M and R values for an earthquake, regional seismic wave attenuation and local site-effects produce a significant scatter or uncertainty in the values of IMs recorded at the site. With simplifying yet reasonable assumptions of (1) mutual exclusivity of simultaneous earthquake occurrences near the site; (2) statistical independence of M and R given the occurrence of an earthquake from a certain source; and (3) the Poisson description of earthquake occurrence in time, Eq. (5.1) can be expanded invoking the Total Probability Theorem as follows:

$$\nu_{IM}\left(x\right)=\sum_{i=1}^{N_{\text{flt}}}\nu_i\int_{R_i}\int_{M_i}P\left[IM>x\,|\,M_i=m,R_i=r\right]\cdot f_{M_i}\left(m\right)\cdot f_{R_i}\left(r\right)\cdot dm\cdot dr \tag{5.3}$$

where N_{flt} = number of causative seismic sources/faults; ν_i = MAF of occurrence of earthquakes on seismic source i. The functions $f_{M_i}(m)$ and $f_{R_i}(r)$ denote the probability density functions (PDFs) of the magnitude (M_i) and source-to-site distance (R_i), respectively, given the occurrence of an earthquake on seismic source i.

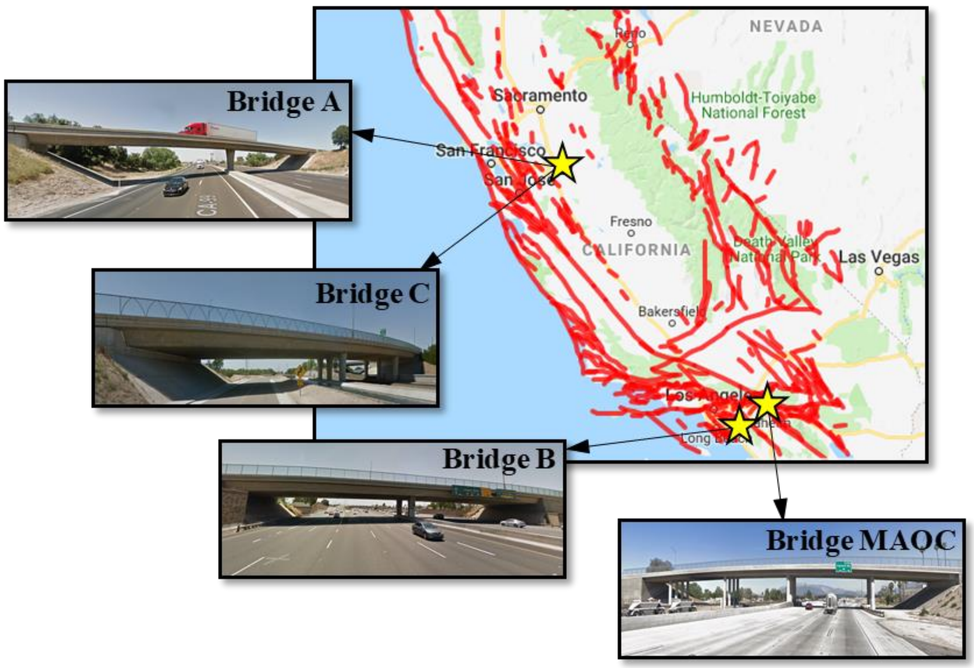

Figure 5.2 Location of testbed bridges shown on a map of California with seismic sources/faults shown in red. Image courtesy: Caltrans ARS Online (v2.3.09) and Google Maps

The conditional probability $P\left[IM > x \mid M_i = m, R_i = r\right]$ in Eq. (5.3) is given by attenuation relations or ground motion prediction equations (GMPEs) which are predictive relationships of , accounting for local site effects, given seismological variables M and R. These are typically developed by applying statistical regression analyses to recorded earthquake ground motion data. Ground motion intensity is closely related to the shear wave velocity profile of the soil/rock at the site. For prediction of site-specific ground motion intensity, the time-averaged shear wave velocity to 30 m depth, also known as V_{S30}, is used in GMPEs as an index of local site effects. Numerous GMPEs developed by various researchers in the past (Abrahamson and Silva 2008; Boore and Atkinson 2008; etc.) are commonly used for PSHA computations.

The seismic hazard integral (Eq. (5.3)) thus provides a probabilistic characterization of the seismic hazard at the site in terms of the MAR of exceeding a specific value of the chosen . In doing so, it explicitly accounts for the uncertainty of due to randomness in temporal and spatial occurrence of future earthquakes affecting the site, as well as the uncertainties related to the seismic wave propagation path and local site conditions.

5.3 Seismic Intensity Measure: Average Spectral Acceleration over a Period Range

As stated in the previous section, the results of PSHA are expressed as the MAR of exceedance of a specific value of a seismic intensity measure (IM). Depending on the results of PSHA, earthquake ground motion records producing desired levels of are selected for response assessment of structures subjected to seismic loading. Thus, an connects seismological characteristics of earthquakes (magnitude (M), source-to-site distance (R), regional seismic wave attenuation, local site-effects, etc.) to structural behavior. A proper choice of is therefore crucial to have a true picture of structural performance against earthquakes.

Ideally, an earthquake and its effects on the considered structure should be completely represented by the chosen . However, to date, there exists no such single, or scalar, ground motion in the literature that can characterize ground motions and their effects on structural response completely. A reasonable choice of should therefore exhibit desirable properties of "efficiency" and "sufficiency" (Luco and Cornell 2007). An "efficient" results in small dispersion/variability of peak structural responses obtained using different ground motion records with the same level of intensity as measured by the . A "sufficient" leads to statistical independence of structural response, given , from ground motion characteristics, such as M and R. Numerous studies and research have been conducted in the past focusing on evaluation and comparison of the performance of different IMs based on their efficiency and sufficiency (Aslani and Miranda 2005; Baker and Cornell 2004; Baker and Cornell 2005a; Baker and Cornell 2005b; Baker and Cornell 2006a; Baker and Cornell 2006b; Luco and Cornell 2007; Riddell 2007; Shome et al. 1998; Tothong and Luco 2007). The elastic first-mode 5% damped spectral acceleration, $S_a(T_1)$, is a commonly used . However, it has been shown not to be an efficient and sufficient predictor of structural response, especially for (1) structures exhibiting highly nonlinear response which leads to significant period elongation; (2) structures that have significantly different fundamental periods in two orthogonal directions; and (3) structures with significant contribution to dynamic response from higher modes (Baker and Cornell 2005b; Barbosa 2011; Faggella 2008; Luco and Cornell 2007; Shome et al. 1998). Ordinary standard bridges (OSBs), the kind of bridges considered in this study, typically fall under the first two categories of structures mentioned above, thereby ruling out the choice of $S_a(T_1)$ as a potential candidate .

Vector-valued IMs can be used to address the issue of efficiency and sufficiency to an extent. But vector-valued PSHA (VPSHA) (Bazzurro 1998; Bazzurro and Cornell 2002) comes at the price of theoretical and computational complexity. It requires the daunting task of integrating joint probability density functions of the IMs which are correlated in general. Although simplified and computationally efficient methods for performing VPSHA computations exist in the literature (Barbosa 2011; Bazzurro et al. 2009; Wang et al. 2016), vector-valued IMs are not opted for in this study to maintain the practicability of the aimed performance-based seismic design framework for OSBs.

To achieve a middle ground between rigor and practicability, researchers have introduced scalar IMs which are meaningful functional combinations of multiple IMs (Bianchini et al. 2009; Bojórquez and Iervolino 2011; Cordova et al. 2000; Fajfar et al. 1990; Kohrangi et al. 2016; Luco and Cornell 2007; Mehanny 2009; Vamvatsikos and Cornell 2005). One such , originally IM proposed by Baker and Cornell (2005a; 2006a) which has been demonstrated to exhibit higher levels of efficiency in the prediction of displacement-based nonlinear structural response (Bianchini et al. 2009; Bojórquez and Iervolino 2011; De Biasio et al. 2014; Eads et al. 2015; Kennedy et al. 1984; Tsantaki et al. 2012; Vamvatsikos and Cornell 2005) and that of sufficiency (Bojórquez and Iervolino 2011; De Biasio et al. 2014; Eads et al. 2015) as compared to $S_a(T_1)$, is the spectral acceleration averaged over a period range $(S_{a,\,\mathrm{avg}})$. The average spectral acceleration is defined as the geometric mean of spectral accelerations at different periods and is given by

$$S_{a,\,\mathrm{avg}}\left(T_1,\ldots T_n\right) = \left[\prod_{p=1}^{n} S_a\left(T_p\right)\right]^{1/n} \tag{5.4}$$

To remove any ambiguity in notation, the index $p \in [1, n]$ in Eq. (5.4) refers to the number of periods in the averaging period range and not to structural vibration modes. Although studies relating to the efficiency and sufficiency of $S_{a,\,\mathrm{avg}}$ have primarily focused on buildings, this is selected in this study to account for the following phenomena not captured by the traditionally used *IM*, i.e., the spectral acceleration at a single predominant period of the structure:

(a) Lack of certainty in predicting the natural period of the pre-dominant mode of vibration for reinforced concrete structures such as OSBs;

(b) Change in natural periods of reinforced concrete structures in going from pristine conditions to cracked states under service loads;

(c) Structural period elongation due to accumulation of damage during an earthquake which leads to higher correlation of structural response with spectral accelerations at longer periods; and

(d) Difference in computed periods of fundamental modes of vibration in two orthogonal directions of the bridge.

During an earthquake, an OSB is supposedly going to be in a more precarious state in the transverse direction as compared to that in the longitudinal direction. This is because, in the latter direction, the backfill eventually stabilizes the longitudinal response of the bridge. However, shear keys, the primary force-resisting mechanism of bridge abutments in the transverse direction, show a deteriorating response once their peak strengths are reached (Bozorgzadeh et al. 2007; Megally et al. 2002). Hence, the transverse seismic response of an OSB is more likely to govern and result in severe damage. Therefore, the range of periods used in the definition of $S_{a,\,\mathrm{avg}}$ for the OSBs considered in this study span from the first transverse mode of vibration, i.e., $T_{1,\mathrm{trans}}$, to $2.5T_{1,\mathrm{trans}}$. Ten discrete points logarithmically spaced within the extremes of the period range (Bianchini et al. 2009) are used to calculate the average spectral acceleration. This choice of the period range also happens to include the first mode period in the longitudinal direction of the considered OSBs. Table 5-1 lists the first mode vibration periods of the considered OSBs in the transverse and longitudinal directions along with the period range chosen for each bridge to compute the average spectral acceleration. The reported periods are calculated post gravity load application using uncracked section properties. The effects of cracking and period elongation under service, as well as, design loads are captured with the range of periods considered.

Table 5-1 First mode periods of vibration and period ranges for

Bridge	$T_{1,\text{trans}}$ [s]	$T_{1,\text{long}}$ [s]	Period Range: $\left[T_{1,\text{trans}}, 2.5T_{1,\text{trans}}\right]$
A	0.29	0.50	[0.29, 0.73]
B	0.23	0.53	[0.23, 0.60]
C	0.24	0.40	[0.24, 0.60]
MAOC	0.28	0.35	[0.28, 0.70]

The choice of a geometric mean in the definition of $S_{a,\text{ avg}}$ (Eq. (5.4)) over an arithmetic mean is firstly because the geometric mean is relatively less sensitive to extreme (i.e., very high or very low) values. Secondly, and more importantly, the multivariate lognormal distribution, which is found to appropriately model the variability in a random vector of correlated spectral accelerations (Jayaram and Baker 2008), is closed under the log-linear transformation given by the definition of the geometric mean (Eq. (5.4)). Hence, the lognormality of $S_{a,\text{ avg}}$ is preserved which facilitates the computation of its GMPE (probabilistic characterization of $S_{a,\text{ avg}}$ given an earthquake scenario, i.e., a pair of M and R values), required in PSHA calculations, from existing GMPEs of spectral accelerations at single periods. The lognormal random variable $S_{a,\text{ avg}}$, given a scenario, can be completely characterized by two parameters, viz., the mean (μ) and standard deviation (σ) of the natural logarithm of the random variable, as follows

$$\mu_{\ln S_{a,\text{ avg}}|\text{scenario}} = \left(\frac{1}{n}\right)\cdot\sum_{p=1}^{n}\mu_{\ln S_a\left(T_p\right)|\text{scenario}} \tag{5.5}$$

$$\sigma_{\ln S_{a,\text{ avg}}|\text{scenario}} = \left(\frac{1}{n}\right)\cdot\sqrt{\sum_{p=1}^{n}\sum_{q=1}^{n}\rho_{\ln S_a\left(T_p\right)\ln S_a\left(T_q\right)|\text{scenario}}\cdot\sigma_{\ln S_a\left(T_p\right)|\text{scenario}}\cdot\sigma_{\ln S_a\left(T_q\right)|\text{scenario}}} \tag{5.6}$$

$\mu_{\ln S_a(T_p)|\text{scenario}}$ and $\sigma_{\ln S_a(T_p)|\text{scenario}}$ in Eq.s (5.5) and (5.6) can be obtained from existing GMPEs (e.g., Boore and Atkinson 2008) for spectral accelerations at single periods. The correlation structure between pairs of spectral accelerations at two different periods has been previously studied by researchers and predictive models available in the literature can be used to compute the correlation coefficient $\rho_{\ln S_a(T_p)\ln S_a(T_q)|\text{scenario}}$ in Eq. (5.6). The well-known correlation model by Baker and Jayaram (2008) that assumes the correlation coefficient to be independent of earthquake scenario (Baker and Cornell 2005a), i.e., a pair of M and R values, is used in this study. Thus, Eq. (5.6) can be rewritten as

$$\sigma_{\ln S_{a,\,\text{avg}}|\text{scenario}} = \left(\frac{1}{n}\right)\cdot\sqrt{\sum_{p=1}^{n}\sum_{q=1}^{n}\rho_{\ln S_a\left(T_p\right)\ln S_a\left(T_q\right)}\cdot\sigma_{\ln S_a\left(T_p\right)|\text{scenario}}\cdot\sigma_{\ln S_a\left(T_q\right)|\text{scenario}}} \tag{5.7}$$

Eq.s (5.5) and (5.7) define the GMPE for $S_{a,\,\text{avg}}$ which can be used in the computation of seismic hazard at the site as per Eq. (5.3). Details of PSHA using $S_{a,\,\text{avg}}$, an improved measure of seismic intensity as compared to the traditionally used $S_a(T_1)$, are provided in the next section.

5.4 Seismic Hazard Analysis

Seismic hazard analysis involves evaluation of the seismic hazard integral given by Eq. (5.3). Standard open-source tools (e.g., OpenSHA (Field et al. 2003)) readily provide results of PSHA given a site and a choice of . However, owing to the novelty of the chosen , these tools do not include seismic hazard assessments in terms of $S_{a,\,\text{avg}}$. Therefore, the seismic hazard integral (Eq. (5.3)), rewritten in terms of $S_{a,\,\text{avg}}$ as follows, needs to be evaluated while keeping things as simple and practicable as possible.

$$\nu_{S_{a,\,\text{avg}}}\left(x\right) = \sum_{i=1}^{N_{\text{flt}}}\nu_i\int_{R_i}\int_{M_i}P\left[\underbrace{\left[\prod_{p=1}^{n}S_a\left(T_p\right)\right]^{1/n}}_{S_{a,\,\text{avg}}} > x \mid M_i = m, R_i = r\right]\cdot f_{M_i}\left(m\right)\cdot f_{R_i}\left(r\right)\cdot dm\cdot dr \tag{5.8}$$

In the above equation, x is a specific value of average spectral acceleration. Analytical evaluation of the integrals in Eq. (5.8) is an impracticable problem. Hence, these integrals need to be evaluated numerically. One approach is to treat the continuous random variables M_i and R_i as discrete and thereby divide the possible ranges of these random variables into N_M and N_R segments, respectively (Kramer 1996). This leads to the following simplification of the hazard integral which is now expressed as a summation.

$$\nu_{S_{a,\,\text{avg}}}(x) = \sum_{i=1}^{N_{\text{flt}}} \nu_i \sum_{j=1}^{N_M} \sum_{k=1}^{N_R} P\left[\underbrace{\left[\prod_{p=1}^{n} S_a\left(T_p\right) \right]^{1/n}}_{S_{a,\,\text{avg}}} > x \mid m_j^i, r_k^i \right] \cdot P\left[m_j^i\right] \cdot P\left[r_k^i\right] \tag{5.9}$$

Where $P\left[m_j^i\right]$ and $P\left[r_k^i\right]$ are the probabilities of the random variables M_i and R_i, related to seismic source i, taking the discrete values m_j^i and r_k^i respectively. Defining an earthquake scenario on fault i as a magnitude and source-to-site distance pair, i.e., (m_j^i, r_k^i), Eq. (5.9) becomes

$$\nu_{S_{a,\,\text{avg}}}(x) = \sum_{i=1}^{N_{\text{flt}}} \nu_i \underbrace{\sum_{s=1}^{N_S}}_{\sum_{j=1}^{N_M}\sum_{k=1}^{N_R}} P\left[\underbrace{\left[\prod_{p=1}^{n} S_a\left(T_p\right) \right]^{1/n}}_{S_{a,\,\text{avg}}} > x \mid \underbrace{\text{scenario}_s^i}_{m_j^i,\, r_k^i} \right] \cdot \underbrace{P\left[\text{scenario}_s^i\right]}_{P\left[m_j^i\right] \cdot P\left[r_k^i\right]} \tag{5.10}$$

where N_S, equal to $N_M \times N_R$, is the number of possible earthquake scenarios. The probability of $S_{a,\,\text{avg}}$ exceeding a specific value x, given an earthquake scenario on fault i can be computed based on the lognormality of $S_{a,\,\text{avg}}$ and using Eq.s (5.5) and (5.7). The remaining terms, ν_i and $P\left[\text{scenario}_s^i\right]$, are results of seismic source characterization involved in standard PSHA calculations. These results, although computed and used in standard PSHA tools (e.g., OpenSHA), are not readily available as an output of such tools. For the sake of simplicity, seismic source characterization and related calculations are avoided, and a workaround is developed based on the results of standard PSHA for spectral accelerations at single periods such that the hazard given by Eq. (5.10) can be reasonably approximated.

The seismic source dependence of the term $P\left[S_{a,\,\text{avg}} > x \mid \text{scenario}_s^i\right]$ can be conveniently dropped if the GMPE by Boore and Atkinson (2008), which allows for unspecified fault, is used. With this simplification, Eq. (5.10) can be rewritten as

$$\nu_{S_{a,\,\text{avg}}}(x) = \sum_{s=1}^{N_S} \underbrace{\nu_{\text{scenario}_s}}_{\sum_{i=1}^{N_{\text{flt}}} \nu_i \cdot P\left[\text{scenario}_s^i\right]} \cdot P\left[\underbrace{\left[\prod_{p=1}^{n} S_a\left(T_p\right) \right]^{1/n}}_{S_{a,\,\text{avg}}} > x \mid \text{scenario}_s \right] \tag{5.11}$$

Eq. (5.11) gives a more tractable form of the seismic hazard integral in terms of $S_{a,\,\mathrm{avg}}$ where $\nu_{\mathrm{scenario}_s}$, defined as the MAR of occurrence of scenario s from any seismic source affecting the considered site, is the only term yet to be determined. This is done by resorting to the results of standard PSHA for spectral accelerations at single periods.

The seismic hazard integral in terms of spectral acceleration at a single period T, in a form similar to Eq. (5.11), is given by

$$\nu_{S_a(T)}(x) = \sum_{s=1}^{N_S} \underbrace{\nu_{\mathrm{scenario}_s}}_{\sum_{i=1}^{N_{\mathrm{flt}}} \nu_i \cdot P\left[\mathrm{scenario}_s^i\right]} \cdot P\left[S_a(T) > x \mid \mathrm{scenario}_s\right] \tag{5.12}$$

Seismic hazard curves, for each of the considered testbed bridges, in terms of $S_a(T)$ for each period in the averaging period range are shown in Figure 5.3. These hazard curves are obtained from OpenSHA (Field et al. 2003) using the Boore and Atkinson (2008) GMPE.

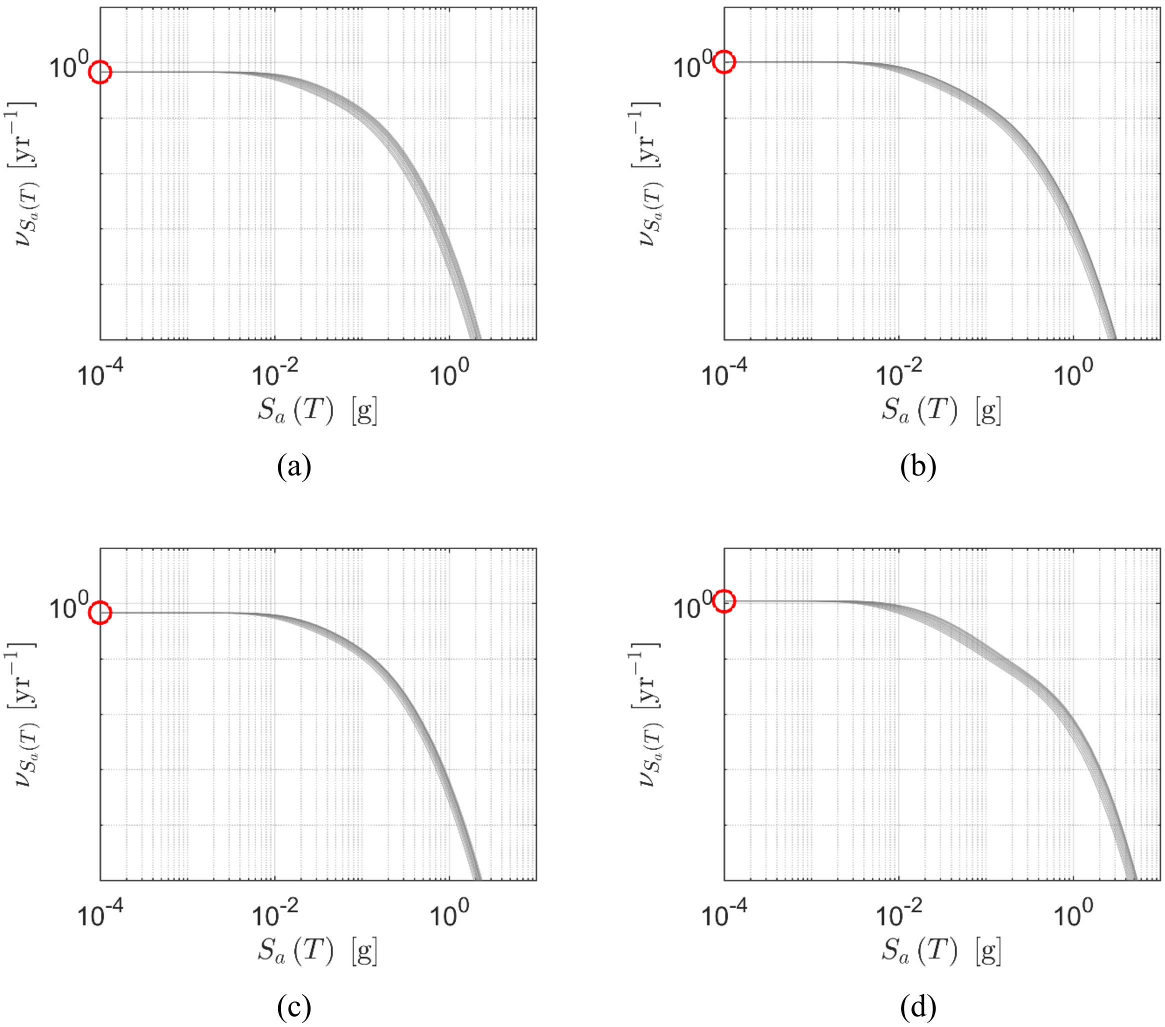

Figure 5.3 Seismic hazard curves in terms of $S_a(T)$ for each period in the averaging period range for (a) Bridge A; (b) Bridge B; (c) Bridge C; and (d) Bridge MAOC

An important observation from Figure 5.3, that facilitates determination of ν_{scenario_s} to be used in Eq. (5.11), is that all seismic hazard curves for spectral accelerations at single periods, irrespective of the period, converge to a single value (indicated by the red markers) of MAR of exceedance at very small spectral acceleration values. Very small values of $S_a(T)$, e.g., 10^{-4} g, are almost certainly exceeded given any earthquake scenario or any period T (i.e., $P[S_a(T) > 10^{-4} \,|\, \text{scenario}_s] \approx 1.0$). Hence, the MAR of exceeding this value of $S_a(T)$ is, per Eq. (5.12), equal to the sum of the rates of all possible scenarios contributing to the seismic hazard at the site, i.e.,

$$\nu_{S_a(T)}\left(x=10^{-4}\right)=\sum_{s=1}^{N_S}\nu_{\text{scenario}_s} \tag{5.13}$$

A routinely available output from standard PSHA tools is the $M-R$ scenario disaggregation of seismic hazard (Bazzurro and Cornell 1999).It gives the relative contribution to a specific value of seismic hazard for a fixed intensity level x of spectral acceleration $S_a(T)$, from each earthquake scenario (a pair of M and R) that could possibly affect the considered site. Hence,

$$\%\text{ contribution of scenario}_s=\frac{\nu_{\text{scenario}_s}\cdot P\left[S_a(T)>x\,|\,\text{scenario}_s\right]}{\nu_{S_a(T)}(x)}\times 100 \tag{5.14}$$

An example disaggregation of one point (corresponding to a RP of 975 yrs.) of the seismic hazard curve (Figure 5.4 (a)) for Bridge B in terms of $S_a(T=T_{1,\text{ trans}}=0.23\text{ s})$, with respect to M and R, is shown in Figure 5.4 (b) where the percentage (%) contribution of each earthquake scenario (an $M-R$ pair) is indicated as the height (and color) of the bar associated with the corresponding $M-R$ bin.

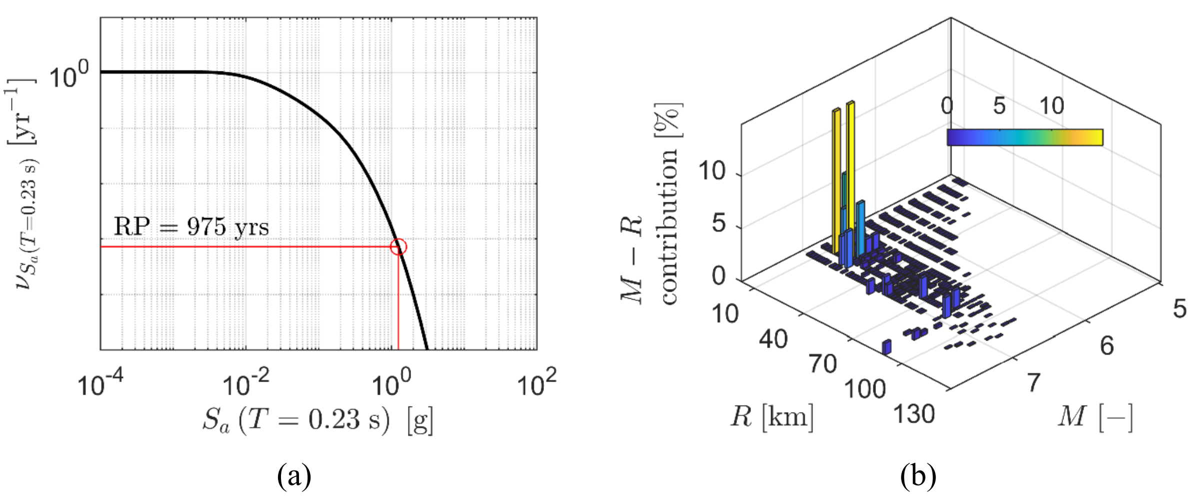

Figure 5.4 (a) Seismic hazard curve for Bridge B in terms of $S_a(T=0.23\text{ s})$; (b) $M-R$ disaggregation of seismic hazard for a mean RP of 975 yrs. associated with $S_a(T=0.23\text{ s})$ exceeding 1.26 g.

Thus, in order to obtain ν_{scenario_s} for a specific site, the disaggregation results corresponding to the points marked in red in Figure 5.3 come to aid. The extremely small spectral acceleration value of

10^{-4} g is almost certainly exceeded, i.e., $P\left[S_a(T) > 10^{-4} \text{ g} \mid \text{scenario}_s\right] \approx 1.0$ given any earthquake scenario for any period T at the considered site. Therefore, Eq. (5.14), for $x = 10^{-4}$ g, can be rewritten as

$$\nu_{\text{scenario}_s} = \frac{\left(\% \text{ contribution of scenario}_s\right) \times \nu_{S_a(T)}\left(x = 10^{-4}\right)}{100} \tag{5.15}$$

where the percentage (%) contribution of scenario_s is obtained from the disaggregation output from OpenSHA corresponding to an intensity level given by $S_a(T)$ equal to 10^{-4} g for each testbed bridge. The choice of T here is arbitrary, since the hazard as well as the associated $M-R$ disaggregation for such a small value of $S_a(T)$ are identical, irrespective of T. $\nu_{S_a(T)}(x = 10^{-4})$ is just the value of the hazard (given by the red markers in Figure 5.3) at that intensity level. The MAR of occurrence of pertinent earthquake scenarios, per Eq. (5.15), for each testbed bridge considered in this project are shown in Figure 5.5.

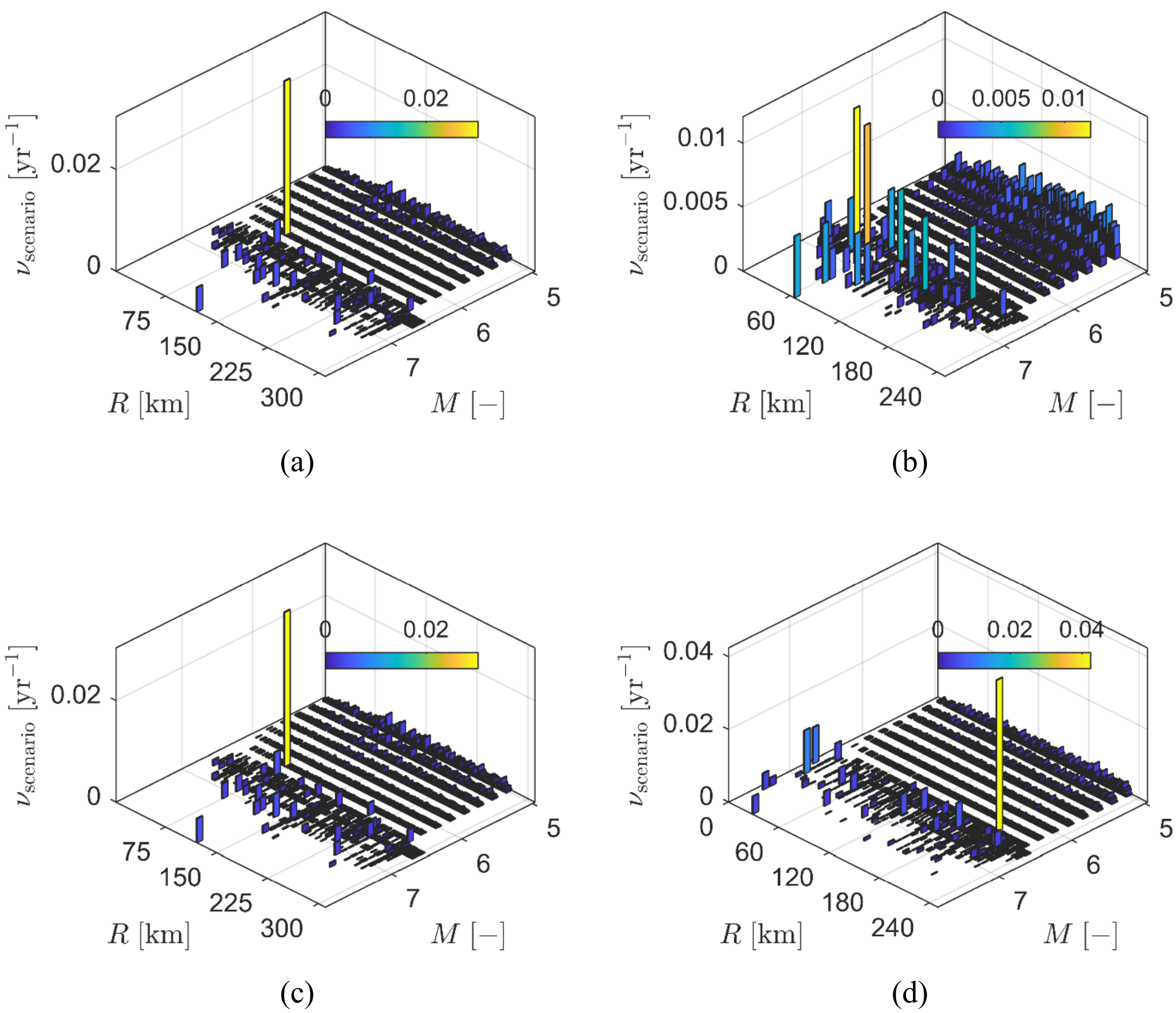

Figure 5.5 MAR of occurrence of all pertinent scenarios for (a) Bridge A; (b) Bridge B; (c) Bridge C; and (d) Bridge MAOC

With ν_{scenario_s}, given by Eq. (5.15), and the GMPE for $S_{a,\,\text{avg}}$, given by Eq.s (5.5) and (5.7) in hand, obtaining seismic hazard curves for the testbed bridges in terms of $S_{a,\,\text{avg}}$ merely reduces to a straightforward evaluation of Eq. (5.11). Figure 5.6 shows the seismic hazard curve for each testbed bridge in terms of $S_{a,\,\text{avg}}$, and how it compares to the hazard curves in terms of $S_a(T)$ for each period T in the averaging period range.

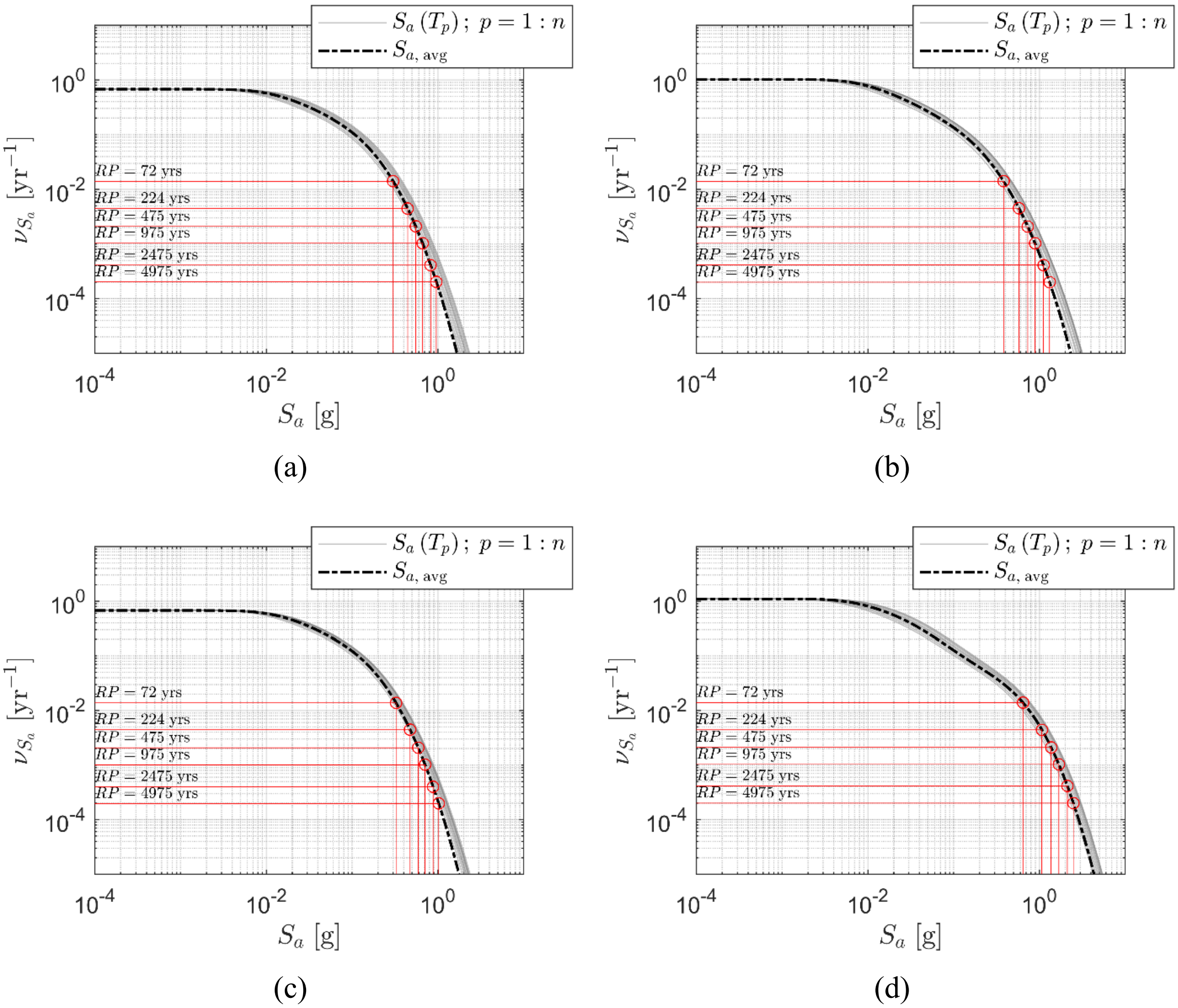

Figure 5.6 Seismic hazard curves in terms of $S_{a,\,\mathrm{avg}}$ for (a) Bridge A; (b) Bridge B; (c) Bridge C; and (d) Bridge MAOC

These hazard curves can now be used to define seismic hazard levels that correspond to different MARs, or equivalently mean RPs, of exceedance (also shown in Figure 5.6) which are of interest to practicing engineers. Six different seismic hazard levels corresponding to mean RPs of 72 years (or 50 percent probability of exceedance in 50 years), 224 years (or 20 percent probability of exceedance in 50 years), 475 years (or 10 percent probability of exceedance in 50 years), 975 years (or 5 percent probability of exceedance in 50 years), 2475 years (or 2 percent probability of exceedance in 50 years), and 4975 years (or 1 percent probability of exceedance in 50 years) are chosen for the purpose of this project. These hazard levels are numbered I through VI, respectively. Earthquake ground motion records matching these desired levels of seismic intensity can now be selected for evaluating structural response to earthquakes, via nonlinear response history analyses, to consistently quantify the seismic demand on the structure of interest. Earthquake record selection is typically done by matching their 5% damped spectral acceleration response spectra to a target response spectrum corresponding to a hazard level. The next section presents, in detail, the definition of a realistic target spectrum for ground motion selection and scaling.

5.5 Target Spectrum: Conditional Mean Spectrum

Ground motion record selection serves as the link between probabilistic seismic hazard analysis and probabilistic seismic response assessment of structures. This imposes a need for hazard- or risk-consistency of earthquake ground motion records to be used for ensemble nonlinear response history analyses of the considered structure. One method of selecting risk-consistent ground motion records is to match individual acceleration response spectra of earthquake records to a target response spectrum corresponding to a specific hazard level (i.e., a specific MAR or mean RP of exceedance).

The uniform hazard spectrum (UHS) has traditionally been used as a target spectrum. The UHS is constructed such that at any period, the MAR (or mean RP) of exceeding the respective spectral acceleration is equal. It is, therefore, an envelope over the spectral acceleration amplitudes of several ground motion records, pertaining to the relevant earthquake scenarios and site conditions, such that spectral accelerations at all periods are exceeded with the same MAR. This makes the UHS equally hazardous/severe at all defining periods and makes it contradict with actual spectral shapes of individual earthquake ground motion records. The frequency content of an earthquake record is not usually as broad as that required to match the UHS. An earthquake record that leads to a severe (i.e., one with low MAR or high mean RP) spectral acceleration value at one period usually does not produce equally severe spectral accelerations at all other periods. Hence, to select UHS-compatible ground motions records, one might have to resort to frequency modification of accelerograms which, in turn, tends to produce records that are unrealistically aggressive leading to conservative estimates of structural response (Baker and Cornell 2006a). The UHS, therefore, falls short of qualifying as a realistic target spectrum for ground motion selection.

A target spectrum, for a given hazard level, should be representative of: (1) the seismic events or scenarios leading to the specific level of hazard associated with the considered ; (2) the joint probability distribution of spectral accelerations at different periods, conditioned on this specific level of and the contributing earthquake scenarios; and (3) the spectral shape of real ground motion records. The conditional mean spectrum (CMS), originally proposed by Baker and Cornell (2006a), stands out as a more suitable target based on the above-mentioned requirements. Baker and Cornell (2006a) defined the CMS, at a hazard level, as the expected response spectrum conditioned on the specific value of at the same hazard level and its associated mean causal earthquake scenario, $\bar{s}$. The mean causal scenario is given by the pair of mean magnitude $(\bar{M})$ and mean source to site distance $(\bar{R})$, obtained from $M-R$ disaggregation of seismic hazard. By definition, the CMS is based on the conditional joint probability structure of spectral accelerations at different periods, given the specific level and the mean causal scenario. Hence, unlike the UHS and as will be illustrated later, it preserves the natural spectral shape of real earthquake ground motions. The term mean in CMS refers to the conditional mean of the natural logarithm of spectral accelerations at different periods defining the spectrum, given the specific level and $\bar{s}$.

Baker and Cornell (2006a) originally defined the conditioning in the CMS as the spectral acceleration at a single period of interest, say T^*. They also introduced formulations of the conditional mean and standard deviation of log spectral acceleration at any period, T_i, of the spectrum. These formulations, based on the joint normality of a vector of log spectral accelerations (or equivalently, the joint lognormality of a vector of spectral accelerations) at different periods, are given by

$$\mu_{\ln S_a(T_i)|\ln S_a(T^*)=\ln x,\bar{s}} = \mu_{\ln S_a(T_i)|\bar{s}} + \rho_{\ln S_a(T_i),\ln S_a(T^*)} \cdot \frac{\left(\ln x - \mu_{\ln S_a(T^*)|\bar{s}}\right)}{\sigma_{\ln S_a(T^*)|\bar{s}}} \cdot \sigma_{\ln S_a(T_i)|\bar{s}} \tag{5.16}$$

$$\sigma_{\ln S_a(T_i)|\ln S_a(T^*)=\ln x,\bar{s}} = \sigma_{\ln S_a(T_i)|\bar{s}} \sqrt{1-\rho^2_{\ln S_a(T_i),\ln S_a(T^*)}} \tag{5.17}$$

where x is the value of the , i.e., (* , corresponding to the hazard level for which the CMS is defined. $\mu_{\ln S_a(T_i)|\bar{s}}$ and $\sigma_{\ln S_a(T_i)|\bar{s}}$ are obtained from a standard GMPE, e.g., Boore and Atkinson (2008), and $\rho_{\ln S_a(T_i),\ln S_a(T^*)}$ is given by, for example, the correlation model by Baker and Jayaram (2008).

The probability normalized deaggregation of the contribution of M and R to the MAR at which $S_a(T^*)$ exceeds the threshold value x can be viewed as a bivariate probability mass function (PMF) of discretized random variables M and R, or equivalently a univariate PMF of a random variable S representing possible (M, R) scenarios, given the specific MAR of exceedance. The mean causal scenario, $\bar{s}$, the center of gravity of this conditional PMF of S, may correspond to an unrealistic causative earthquake scenario at the site in case there are widely varying contributing scenarios leading to a multimodal PMF of S (Bazzurro and Cornell 1999). To address this issue, a more complete version of the CMS, called the "exact" CMS, incorporating all causative earthquake scenarios has been introduced by Lin et al. (2013a).

The formulation of the "exact" CMS relies on deriving the unconditional (with respect to S) PDF of the log spectral acceleration at any period, T_i, as

$$f_{\ln S_a(T_i)}\left(a\right) = \sum_{q=1}^{N_S} f_{\ln S_a(T_i)|S=s}\left(a \mid S = s_q\right) \cdot P\left[S = s_q\right] \tag{5.18}$$

where a is a specific value of $\ln S_a(T_i)$. The exact mean and standard deviation of the unconditional log spectral acceleration at any period, T_i, are obtained as

$$\mu_{\ln S_a(T_i)} = E_S\left[E_{\ln S_a(T_i)|S}\left[\ln S_a\left(T_i\right) \mid S = s\right]\right] = \sum_{q=1}^{N_S} \mu_{\ln S_a(T_i)|S=s_q} \cdot P\left[S = s_q\right] \tag{5.19}$$

and

$$\begin{aligned}\sigma_{\ln S_a(T_i)} &= \sqrt{E_S\left[Var_{\ln S_a(T_i)|S}\left[\ln S_a\left(T_i\right) \mid S = s\right]\right] + Var_S\left[E_{\ln S_a(T_i)|S}\left[\ln S_a\left(T_i\right) \mid S = s\right]\right]} \\ &= \sqrt{\sum_{q=1}^{N_S} \sigma^2_{\ln S_a(T_i)|S=s_q} \cdot P\left[S = s_q\right] + \sum_{q=1}^{N_S}\left(\mu_{\ln S_a(T_i)|S=s_q} - \mu_{\ln S_a(T_i)}\right)^2 \cdot P\left[S = s_q\right]}\end{aligned} \tag{5.20}$$

respectively. Note that $E_S\left[\cdots\right]$ and $Var_S\left[\cdots\right]$ refer to the expectation and variance, respectively, of the operand with respect to S, and $P[S = s_q]$ is the deaggregation weight, or the fractional contribution of the (M, R) scenario s_q to the considered level of seismic hazard.

The normality of the conditional distribution $f_{\ln S_a(T_i)|S=s}\left(a \mid S = s_q\right)$ is lost upon "unconditioning" with respect to S as per Eq. (5.18). The unconditional random variable $\ln S_a(T_i)$ is, therefore, no longer necessarily normally distributed. However, for practical purposes and usability in ground motion record selection procedures, the vector of unconditional log spectral accelerations across different periods can be assumed to follow a multivariate normal distribution (Lin et al. 2013b). The exact mean and standard deviation of $\ln S_a(T_i)$ (Eqs. (5.19) and (5.20)) can therefore be used to rewrite Eqs. (5.16) and (5.17), now incorporating all causative (M, R) scenarios and thereby defining the "exact" CMS as

$$\mu_{\ln S_a(T_i)|\ln S_a\left(T^*\right)=\ln x} = \mu_{\ln S_a(T_i)} + \rho_{\ln S_a(T_i),\ln S_a\left(T^*\right)} \cdot \frac{\left(\ln x - \mu_{\ln S_a\left(T^*\right)}\right)}{\sigma_{\ln S_a\left(T^*\right)}} \cdot \sigma_{\ln S_a(T_i)} \tag{5.21}$$

$$\sigma_{\ln S_a(T_i)|\ln S_a\left(T^*\right)=\ln x} = \sigma_{\ln S_a(T_i)} \sqrt{1-\rho^2_{\ln S_a(T_i),\ln S_a\left(T^*\right)}} \tag{5.22}$$

Eq. (5.21) defines the "exact" CMS, to be referred to as just the CMS hereafter, and Eq. (5.22) gives the conditional variability of spectral accelerations at all periods of the spectrum. The exponent of Eq. (5.21) gives the conditional median (used for plotting the target spectrum) of the lognormal random variable $S_a(T_i)$ given the specific value of (* .

For illustration purposes, say T^* is chosen as $T_{1,\text{ trans}}$ for one of the testbed bridges, i.e., Bridge B. The seismic hazard curve for Bridge B in terms of spectral acceleration at this period of interest, was previously shown in Figure 5.4 (a). Figure 5.4 (b) showed the $M-R$ disaggregation results obtained from OpenSHA corresponding to the hazard level given by a mean RP of (* exceedance equal to 975 years (i.e., hazard level IV). These disaggregation results are used to compute the weights $P[S=s_q]$, i.e., the fractional contribution of each causative scenario to the seismic hazard, required in Eq.s (5.19) and (5.20). Eq.s (5.19) and (5.20) define the probability structure (incorporating all associated causative scenarios) of spectral accelerations across different periods, given the exceedance of this specific level (1.26 g) of (* .

Figure 5.7 (a) shows the probability density functions of spectral accelerations at five arbitrarily chosen periods (including T^* = 0.23s). These probability density functions are predicted using the Boore and Atkinson (2008) GMPE along with Eq.s (5.19) and (5.20). The median values of these distributions are joined by the dashed-dotted blue line, thus giving the median spectrum corresponding to a mean RP of exceedance equal to 975 years. The red line, in Figure 5.7 (a), denotes the UHS corresponding to a mean RP of 975 years, constructed such that the spectral accelerations across all periods are also exceeded every 975 years. As depicted in Figure 5.7 (a), the UHS is indeed an overly-conservative target spectrum since it is very unlikely that the spectral shapes of real ground motions will be equally above the median at all spectral periods.

Figure 5.7 (b) shows the conditional probability density functions (predicted using Eq.s. (5.21) and (5.22)) of spectral accelerations at the same periods as in Figure 5.7 (a), given the random variable $(^{*}$ takes the value 1.26 g that is exceeded every 975 years. The probability density function of $(^{*}$, at the conditioning period, is shown as a dirac-delta function centered at 1.26 g, implying that the random variable $(^{*}$ can only take this value. The exponent of Eq. (5.21), shown as the black dashed-dotted line in Figure 5.7 (b), gives the conditional median target spectrum for hazard level IV defined by a mean RP of $(^{*}$ exceedance equal to 975 years. As shown in Figure 5.7 (b), the target spectrum obtained using the CMS approach drops in magnitude away from the conditioning period thereby reflecting credible spectral shapes which are peaked only in limited periods and/or period ranges and not uniformly throughout.

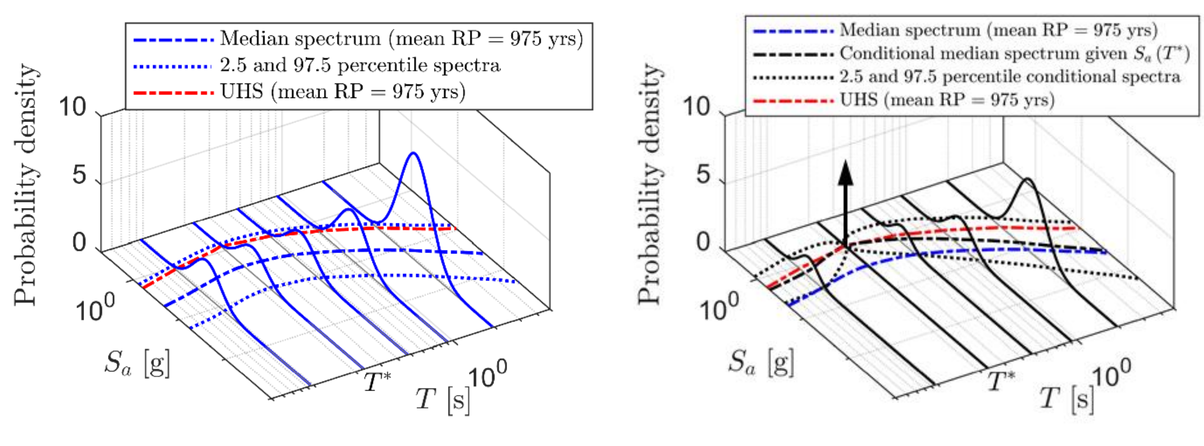

(a) (b)

Figure 5.7 (a) Probability structure of $S_a(T_i)$ incorporating all causative scenarios and corresponding to a 975 year mean RP of $(^{*}$ exceeding a value equal to 1.26 g for Bridge B; (b) conditional probability structure of $S_a(T_i)$ given $S_a(T^*) = 1.26$ g for Bridge B

Baker and Cornell (2006a) also extended their definition of CMS to include $S_{a,\,\mathrm{avg}}(T_1,\ldots,T_n)$, the improved considered in this project, as the conditioning . Based on the log-linear transformation that defines $S_{a,\,\mathrm{avg}}$, joint normality of the natural logarithm of $S_{a,\,\mathrm{avg}}$ with a vector of jointly normal log spectral acceleration accelerations at different periods is ensured. Therefore, the CMS, conditioned on a specific level of average spectral acceleration is given by

$$\mu_{\ln S_a(T_i)|\ln S_{a,\,\mathrm{avg}}=\ln x} = \mu_{\ln S_a(T_i)} + \rho_{\ln S_a(T_i),\ln S_{a,\,\mathrm{avg}}} \cdot \frac{\left(\ln x - \mu_{\ln S_{a,\,\mathrm{avg}}}\right)}{\sigma_{\ln S_{a,\,\mathrm{avg}}}} \cdot \sigma_{\ln S_a(T_i)} \tag{5.23}$$

$$\sigma_{\ln S_a(T_i)|\ln S_{a,\,\mathrm{avg}}=\ln x} = \sigma_{\ln S_a(T_i)} \sqrt{1-\rho^2_{\ln S_a(T_i),\ln S_{a,\,\mathrm{avg}}}} \tag{5.24}$$

where x is the value of $S_{a,\,\mathrm{avg}}$, corresponding to the hazard level for which the CMS is defined. $\mu_{\ln S_a(T_i)}$ and $\sigma_{\ln S_a(T_i)}$ are given by Eq.s (5.19) and (5.20), respectively, which require a standard GMPE, e.g., Boore and Atkinson (2008), and the results of $M-R$ disaggregation of the specific level of seismic hazard. The correlation coefficient between any $\ln S_a(T_i)$ and $\ln S_{a,\,\mathrm{avg}}(T_1,\ldots,T_n)$, i.e., $\rho_{\ln S_a(T_i),\ln S_{a,\,\mathrm{avg}}}$ in Eq.s (5.23) and (5.24), is given by (Baker and Cornell 2006a)

$$\rho_{\ln S_a(T_i),\ln S_{a,\,avg}} = \frac{\sum_{p=1}^{n} \rho_{\ln S_a(T_i),\ln S_a(T_p)} \cdot \sigma_{\ln S_a(T_p)}}{\sqrt{\sum_{p=1}^{n}\sum_{q=1}^{n} \rho_{\ln S_a(T_p),\ln S_a(T_q)} \cdot \sigma_{\ln S_a(T_p)} \cdot \sigma_{\ln S_a(T_q)}}} \tag{5.25}$$

For the purpose of illustration and comparison of the CMS conditioned on $S_{a,\,\mathrm{avg}}$ with that conditioned on (* , the same testbed bridge as before, i.e., Bridge B is considered. The seismic hazard curve for Bridge B in terms of $S_{a,\,\mathrm{avg}}$, and the $M-R$ disaggregation for hazard level IV defined by a mean RP of $S_{a,\,\mathrm{avg}}$ exceedance equal to 975 years are shown in Figure 5.8 (a) and (b) respectively. Using Eq.s (5.19) and (5.20) along with the disaggregation results shown in Figure 5.8 (b) and the GMPE by Boore and Atkinson (2008), the probability structure of spectral accelerations across different periods, given the exceedance of this specific level (0.89 g) of the average spectral acceleration $(S_{a,\,\mathrm{avg}})$ is determined.

Figure 5.9 (a) shows the probability density functions (predicted using the Boore and Atkinson (2008) GMPE along with Eq.s (5.19) and (5.20)) of spectral accelerations at five arbitrarily chosen periods (same as before in Figure 5.7). The median values of these probability distributions of $S_a(T_i)$ at different periods, i.e., the median spectrum, and the UHS, both corresponding to a mean RP of 975 years, are shown as the blue dashed-dotted line and the red line, respectively, in Figure 5.9 (a).

Figure 5.9 (b) shows the conditional probability density functions (predicted using Eq.s. (5.23) and (5.24)) of spectral accelerations at the same periods as in Figure 5.9 (a), given the random variable $S_{a,\,\mathrm{avg}}$ takes the value 0.89 g that is exceeded every 975 years. The exponent of Eq. (5.23), shown as the black dashed-dotted line in Figure 5.9 (b), gives the conditional median target spectrum associated with hazard level IV defined by a mean RP of $S_{a,\,\mathrm{avg}}$ exceedance equal to 975 years. The light green patch in Figure 5.9 (b) represents the averaging period range starting from $T_{1,\,\mathrm{trans}}$ to $2.5T_{1,\,\mathrm{trans}}$.

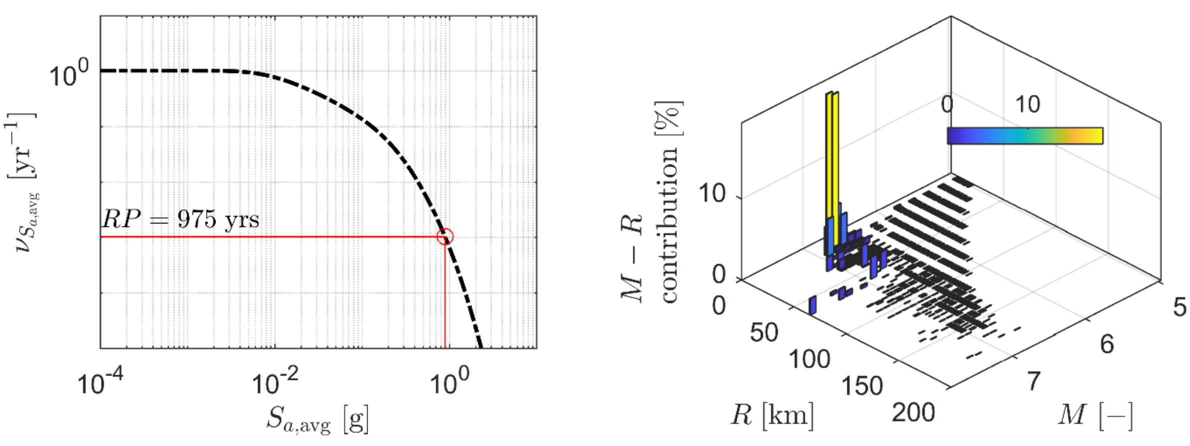

Figure 5.8 (a) Seismic hazard curve for Bridge B in terms of $S_{a,\,\mathrm{avg}}$; (b) $M-R$ disaggregation of seismic hazard for a mean RP of 975 yrs. associated with $S_{a,\,\mathrm{avg}}$ exceeding 0.89 g

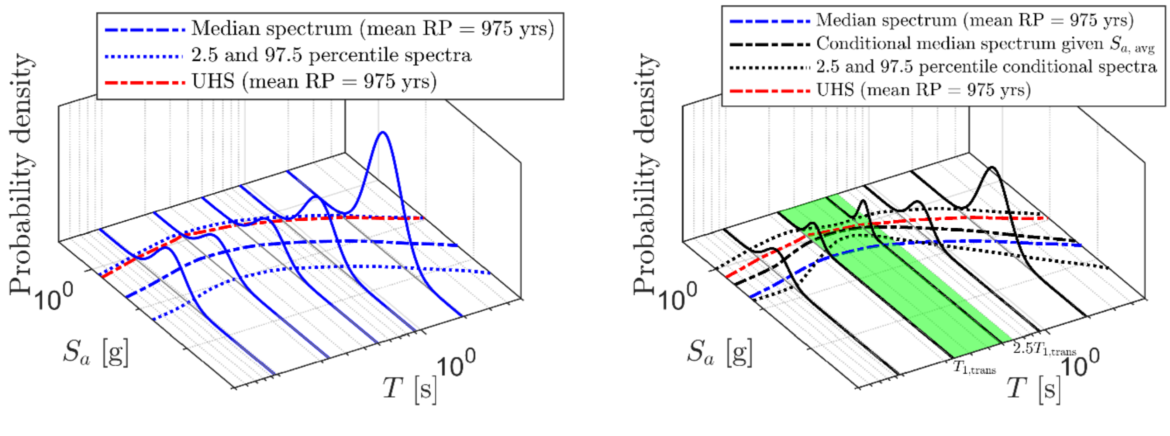

(a) (b)

Figure 5.9 (a) Probability structure of $S_a(T_i)$ incorporating all causative scenarios and corresponding to a 975 year mean RP of $S_{a,\,\mathrm{avg}}$ exceeding a value equal to 0.89 g for Bridge B; (b) conditional probability structure of $S_a(T_i)$ given $S_{a,\,\mathrm{avg}} = 0.89$ g for Bridge B

A remarkable difference in the conditional probability structure of spectral accelerations at different periods given $S_{a,\,\mathrm{avg}}$ with that given (* is the absence of a period where the spectral acceleration value is fixed thereby allowing no variability in spectral acceleration at that period. Instead, the spectral accelerations within the averaging period range (the light green patch) are allowed to vary, with reduced variability, such that the geometric mean of spectral accelerations at the periods in this range is fixed.

A comparison between the target spectrum as obtained from the CMS conditioned on (* and that conditioned on $S_{a,\,\mathrm{avg}}$ for the considered illustrative example corresponding to hazard level IV for Bridge B is shown in Figure 5.10. Figure 5.10 (a) compares the target conditional median spectrum obtained in each case while Figure 5.10 (b) compares the standard deviations of log spectral accelerations at different periods of the spectrum, given the specific value of the conditioning , in each case (i.e., of (* and of $S_{a,\,\mathrm{avg}}$), at hazard level IV.

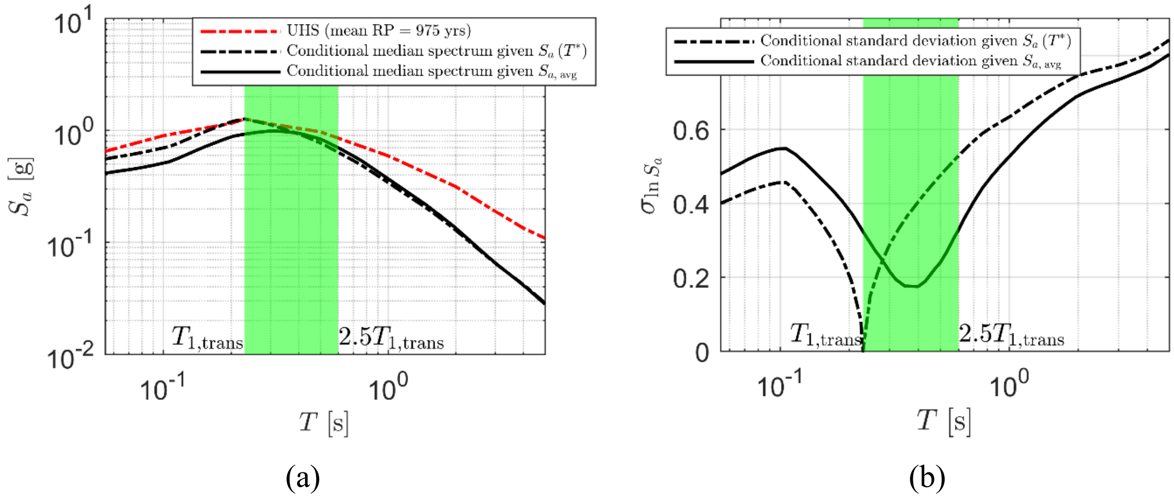

Figure 5.10 Comparison between target spectra based on CMS given $S_a(T^*)$ and CMS given $S_{a,\,\mathrm{avg}}$ for hazard level IV for Bridge B: (a) target conditional median spectra; and (b) target conditional standard deviations of log spectral accelerations

As can be observed from Figure 5.7 (b), Figure 5.9 (b), and Figure 5.10 (a), the median target spectrum conditioned on $S_a(T^*)$, unlike the one conditioned on $S_{a,\,\mathrm{avg}}$, is peaked at a single period T^*, touching the UHS corresponding to hazard level IV. As Baker and Cornell (2006a) pointed out, instead for posing a target spectrum that is "very" strong at a single period of interest, T^*, which might elongate due to structural damage during an earthquake and is difficult to accurately identify in the first place, a target spectrum that is "somewhat" strong at several relevant structural periods seems more sensible. This is in agreement with the rationale behind defining and choosing $S_{a,\,\mathrm{avg}}$ as the seismic intensity measure. Ground motion records selected based on the target spectrum conditioned on $S_{a,\,\mathrm{avg}}$, therefore, will have the trait of being neither very aggressive nor very benign in the range of relevant structural periods (Kohrangi et al. 2017). Figure 5.10 (b) brings out another positive aspect of using $S_{a,\,\mathrm{avg}}$ as the conditioning to define the target spectrum for ground motion record selection. As will be discussed in the next section, a novel way of selecting ensemble of ground motions based on a target spectrum is to capture the natural conditional variability at different periods associated with the target spectrum. The target spectrum conditioned on $S_{a,\,\mathrm{avg}}$ has moderate conditional variability at different periods of the spectrum. This is in contrast with the conditional variability associated with the target spectrum conditioned on

(* which has no (or zero) variability at a single period and relatively large variability at periods farther away.

Target spectra corresponding to each identified hazard level for all considered testbed bridges are obtained using the CMS approach conditioned on $S_{a,\,\mathrm{avg}}$. The next section describes the use of a novel algorithm (originally proposed by Jayaram et al. (2011) and subsequently modified by Kohrangi et al. (2017)) to select ensembles of ground motion records consistent with the risk-level of the target spectra.

5.6 Site-specific Risk-consistent Ground Motion Selection

As a final step of PSHA, ensembles of site-specific risk-consistent ground motions need to be selected to perform response history analyses of the considered structure. Three-dimensional structural finite element models require two components of ground motions to be selected. Given a target CMS, i.e., the mean of log spectral accelerations at different periods conditioned on a target value of the considered , ground motions can be selected via least squared error-based matching between logarithms of the geometric mean (of each horizontal component) response spectra of individual ground motions and the target spectrum. The spectra should be matched over a range of periods broad enough to capture all relevant structural periods and to ensure a reasonably smooth match. For a specific hazard level, the CMS is given by the mean (μ) of $\ln S_a(T_i)$, conditioned on a value of $\ln S_{a,\,\mathrm{avg}}$. The sum of squared error (SSE) for a single ground motion record is calculated as

$$\mathrm{SSE} = \sum_{i=1}^{N_P} \left(\ln S_a^{\mathrm{REC}}\left(T_i\right) - \mu_{\ln S_a(T_i) | \ln S_{a,\,\mathrm{avg}}} \right)^2 \tag{5.26}$$

where $S_a^{\mathrm{REC}}(T_i)$ is the geometric mean of spectral ordinates of a two-component ground motion record at a period, T_i. N_P is the number of periods over which the SSE is calculated. Baker (2011a) suggested the use of 50 periods in calculating the SSE. Ground motion records from a database can therefore be chosen based on the least deviation (i.e., SSE) from the target spectrum.

Ground motion records selected to match the CMS only, as described above, have artificially suppressed variability at different periods of the spectrum (Baker 2011a). The CMS is a mean (of log spectral accelerations) spectrum and ensemble of records selected to match only the mean spectrum fail to exhibit the associated natural conditional variability at other spectral periods. Jayaram et al. (2011) examined the importance of capturing the natural conditional variability associated with the target spectrum and found that considering target response spectrum variance in ground motion selection tends to increase the mean structural response and the dispersion in the response. This can conceivably influence the estimates of risk associated with structural seismic performance and hence signifies the importance of capturing response spectrum variance. Jayaram et al. (2011), in the same paper, proposed a ground motion selection algorithm that selects a suite of ground motions whose logarithmic response spectra match not only a specified target mean spectrum, but also the natural variability at different periods of the spectrum. In other words, ground motions are selected such that they match a complete target conditional probability structure given a hazard level. The algorithm, originally proposed by Jayaram et al. (2011), allowed for the conditioning in the CMS to be the spectral acceleration at a single period. This has been recently modified by Kohrangi et al. (2017) to include $S_{a,\,\text{avg}}$ as the conditioning .

The ground motion selection algorithm is based on a complete characterization of the probability structure of the multivariate normal random vector, say $\mathbf{X}$, of log spectral accelerations at different periods conditional on a target value of the normally distributed random variable $\ln S_{a,\,\text{avg}}$.

$$\mathbf{X} \mid \ln S_{a,\,\text{avg}} = \begin{bmatrix} \ln S_a\left(T_1\right) \mid \ln S_{a,\,\text{avg}} \\ \vdots \\ \ln S_a\left(T_{N_P}\right) \mid \ln S_{a,\,\text{avg}} \end{bmatrix}_{N_P \times 1} \sim N\left(\boldsymbol{\mu}, \boldsymbol{\Sigma}\right) \tag{5.27}$$

where $\boldsymbol{\mu}$ is the mean vector and $\boldsymbol{\Sigma}$ is the covariance matrix, of the N_P dimensional conditional random vector $\mathbf{X} \mid \ln S_{a,\,\text{avg}}$. The conditional mean vector, $\boldsymbol{\mu}$, and the conditional covariance matrix, $\boldsymbol{\Sigma}$, can be obtained from the statistical parameters $(\boldsymbol{\mu_0}, \boldsymbol{\Sigma_0})$ of the unconditional multivariate normal $N_P + 1$ dimensional random vector $\mathbf{X_0}$ defined as follows

$$\mathbf{X_0} = \begin{bmatrix} \ln S_a(T_1) \\ \vdots \\ \ln S_a(T_{N_P}) \\ \hdashline \ln S_{a,\,\text{avg}} \end{bmatrix}_{(N_P+1)\times 1} \sim N(\boldsymbol{\mu_0}, \boldsymbol{\Sigma_0}) \tag{5.28}$$

$\ln S_{a,\,\text{avg}}$, by definition, is just a linear transformation on a set of jointly normal log spectral accelerations over a certain period range. Hence, the random vector $\mathbf{X_0}$ follows a multivariate normal distribution which is closed under linear transformation. The mean vector, $\boldsymbol{\mu_0}$, and the covariance matrix, $\boldsymbol{\Sigma_0}$, of the N_P+1 dimensional random vector $\mathbf{X_0}$ is given by

$$\boldsymbol{\mu_0} = \begin{bmatrix} \mu_{\ln S_a(T_1)} \\ \vdots \\ \mu_{\ln S_a(T_{N_P})} \\ \hdashline \mu_{\ln S_{a,\,\text{avg}}} \end{bmatrix} = \begin{bmatrix} \boldsymbol{\mu_1} \\ \hdashline \mu_{\ln S_{a,\,\text{avg}}} \end{bmatrix} \tag{5.29}$$

$$\begin{aligned} \boldsymbol{\Sigma_0} &= \left[\begin{array}{ccc:c} \sigma^2_{\ln S_a(T_1)} & \cdots & \rho_{\ln S_a(T_1)\ln S_a(T_{N_P})}\sigma_{\ln S_a(T_1)}\sigma_{\ln S_a(T_{N_P})} & \rho_{\ln S_a(T_1)\ln S_{a,\,\text{avg}}}\sigma_{\ln S_a(T_1)}\sigma_{\ln S_{a,\,\text{avg}}} \\ \vdots & \cdots & \vdots & \vdots \\ \rho_{\ln S_a(T_{N_P})\ln S_a(T_1)}\sigma_{\ln S_a(T_{N_P})}\sigma_{\ln S_a(T_1)} & \cdots & \sigma^2_{\ln S_a(T_{N_P})} & \rho_{\ln S_a(T_{N_P})\ln S_{a,\,\text{avg}}}\sigma_{\ln S_a(T_{N_P})}\sigma_{\ln S_{a,\,\text{avg}}} \\ \hdashline \rho_{\ln S_{a,\,\text{avg}}\ln S_a(T_1)}\sigma_{\ln S_{a,\,\text{avg}}}\sigma_{\ln S_a(T_1)} & \cdots & \rho_{\ln S_{a,\,\text{avg}}\ln S_a(T_{N_P})}\sigma_{\ln S_{a,\,\text{avg}}}\sigma_{\ln S_a(T_{N_P})} & \sigma^2_{\ln S_{a,\,\text{avg}}} \end{array}\right] \\ &= \left[\begin{array}{c:c} \boldsymbol{\Sigma_1} & \boldsymbol{\Sigma_2} \\ \hdashline \boldsymbol{\Sigma_2'} & \sigma^2_{\ln S_{a,\,\text{avg}}} \end{array}\right] \end{aligned}$$

(5.30)

The conditional mean vector, $\boldsymbol{\mu}$, and the conditional covariance matrix, $\boldsymbol{\Sigma}$ of the random vector, $\mathbf{X}$, of log spectral accelerations at different periods conditional on a target value, say $\ln x$, of $\ln S_{a,\,\text{avg}}$ are given by

$$\boldsymbol{\mu} = \boldsymbol{\mu_1} + \boldsymbol{\Sigma_2}\frac{\left(\ln x - \mu_{\ln S_{a,\,\text{avg}}}\right)}{\sigma^2_{\ln S_{a,\,\text{avg}}}} \tag{5.31}$$

$$\boldsymbol{\Sigma} = \boldsymbol{\Sigma_1} - \frac{1}{\sigma^2_{\ln S_{a,\,\text{avg}}}}\boldsymbol{\Sigma_2}\boldsymbol{\Sigma_2'} \tag{5.32}$$

Eq. (5.31) is equivalent to, the previously defined CMS given $\ln S_{a,\,\text{avg}}$ in Eq. (5.23). The square root of the diagonal entries of the covariance matrix given by Eq. (5.32) is also equivalent to the previously defined conditional standard deviation (Eq. (5.24)) of log spectral accelerations at different periods given $\ln S_{a,\,\text{avg}}$.

Having completely characterized the multivariate normal distribution of the target spectrum given a hazard level (Eq.s (5.31) and (5.32)), Monte Carlo simulation is used to generate random realizations of this target spectrum. This is done by sampling random vectors from the multivariate normal distribution with mean vector and covariance matrix defined by Eq.s (5.31) and (5.32). The response spectra are simulated at 50 periods logarithmically spaced between 0.05 s and 5 s to ensure a good match of individual ground motion spectra with the target over a wide range of periods. The number of target spectrum realizations generated is equal to the number of ground motions to be selected. For each simulated spectrum, the SSE is calculated, as follows, for optionally scaled geometric mean (of two horizontal components) response spectra of each ground motion in a database.

$$\text{SSE} = \sum_{i=1}^{N_P} \left(\ln\left(\alpha \cdot S_a^{\text{REC}}\left(T_i\right)\right) - \ln S_a^{\text{SIM}}\left(T_i\right)\right)^2 \tag{5.33}$$

where, $\ln S_a^{\text{SIM}}(T_i)$ is the simulated spectral ordinate at the period T_i. The scale factor, α , to be applied to the ground motion record in question, is given by

$$\alpha = \frac{x}{\left[\prod_{p=1}^{n} S_a^{\text{REC}}\left(T_p\right) \right]^{1/n}} \tag{5.34}$$

where x is the target value of $S_{a,\,\text{avg}}$ at the considered hazard level. The scale factor α , as per Eq. (5.34), is determined such that the geometric mean of S_a^{REC} over the averaging period range of $S_{a,\,\text{avg}}$ is equal to the desired value, x , of $S_{a,\,\text{avg}}$. The scaling is applied to the geometric mean response spectra of the two horizontal components of the recording. The same scale factor is applied to both horizontal components of the ground motion record to be used as input to nonlinear dynamic time-history analyses. For every simulated target spectrum, the ground motion in a database having the smallest SSE, given by Eq. (5.33), is selected. It is also ensured that no ground motion record is repeated in a particular suite of selected records. The procedure is illustrated in Figure 5.11 which shows two such simulated target spectra at hazard level IV for Bridge B, and the corresponding spectra of real ground motion records chosen from the NGA database (Chiou et al. 2008).

The sample mean and variance of the suite of ground motions selected using this algorithm may deviate slightly from the target values, especially for smaller sets of ground motions. Jayaram et al, also suggested an optimization technique to improve the match between sample and target means and variances. The technique relies on replacing a ground motion from an initially selected suite with one from the database if such a replacement leads to improvement in the match between sample and target statistics. For a detailed description of the optimization technique, the reader is asked to refer to the original paper by Jayaram et al. (2011). Suites of ground motions selected using the algorithm described is able to accurately

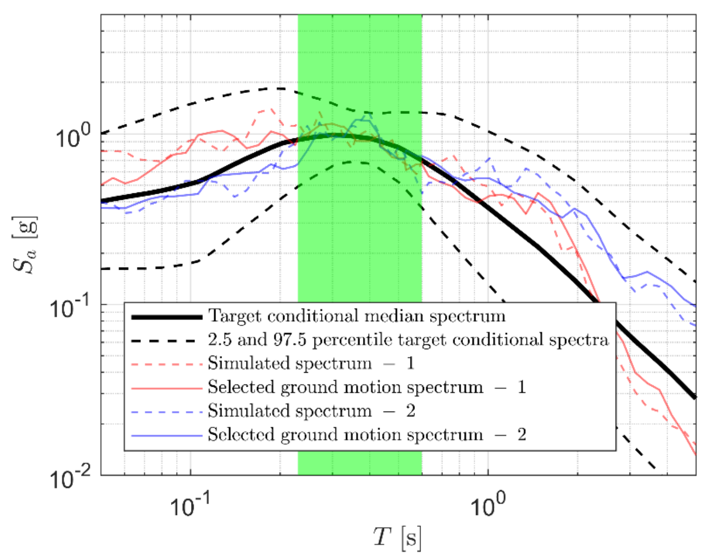

Figure 5.11 Example of simulated and selected ground motion spectra for Bridge B at hazard level IV

reproduce, not only the target mean spectrum, but also the natural variability and correlation across different periods. MATLAB scripts, originally developed by Baker (2011b) and recently modified by Kohrangi (2015), implementing the complete algorithm, including the optimization technique, discussed so far are made available online. These scripts are used for selecting ensembles of ground motions from the NGA database (Chiou et al. 2008) at different hazard levels (i.e., hazard levels I through VI) for the testbed bridges considered in this project.

The match between achieved/sample and target spectrum statistics depends on the size of the ensemble, i.e., on the number of ground motions, n_{GM}, chosen. To arrive at a conclusive value of n_{GM}, ensembles of size varying from $n_{GM} = 1$ to $n_{GM} = 100$ are selected for hazard levels I through VI for Bridge B. The square root of the mean squared (RMS) deviation over the most significant period range (i.e., the averaging period range from $T_{1,\text{ trans}}$ to $2.5T_{1,\text{ trans}}$) between the sample median, 16th percentile, and 84th percentile; and the corresponding targets, i.e, $(e^{\mu_{\ln S_a|\ln S_{a,\text{ avg}}}})$, $(e^{\mu_{\ln S_a|\ln S_{a,\text{ avg}}}-\sigma_{\ln S_a|\ln S_{a,\text{ avg}}}})$, and $(e^{\mu_{\ln S_a|\ln S_{a,\text{ avg}}}+\sigma_{\ln S_a|\ln S_{a,\text{ avg}}}})$ are plotted as a function of n_{GM} in Figure 5.12. It can be seen from Figure 5.12 that the RMS error tends to reduce and becomes almost stationary as n_{GM} is increased. A value of $n_{GM} = 100$ per hazard level, for which the error is shown to be reasonably low, is chosen for a forward performance-based assessment of the considered testbed bridges to be described in the following chapters. The premise of this, rather expensive, choice of n_{GM} is to enhance, as part of a forward performance-based seismic assessment, the reliability of risk estimates associated with structural performance as much as possible. Thus, it is desired to have a large enough ground motion ensemble, given , so that record-to-record variability is well propagated to uncertainty in structural response which can, in turn, be adequately quantified.

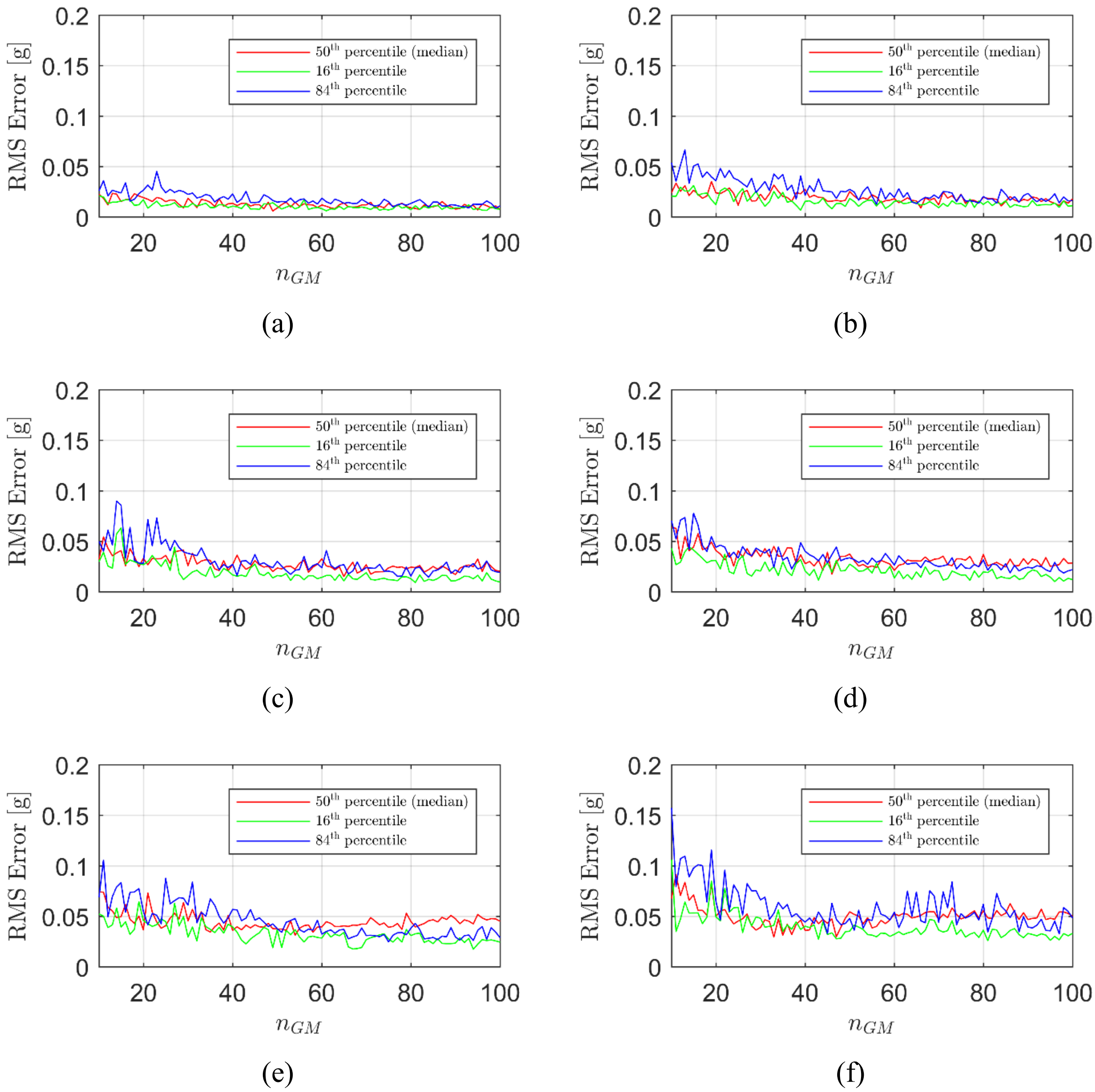

Figure 5.12 RMS error between sample and target spectrum percentiles versus n_{GM} calculated over the averaging period range for ensembles of ground motions selected at (a) hazard level I; (b) hazard level II; (c) hazard level III; (d) hazard level IV; (e) hazard level V; and (f) hazard level VI for Bridge B;

Figure 5.13 through Figure 5.16 show the response spectra of selected ground motions for each testbed bridge at different hazard levels, along with the respective UHS, the conditional median spectrum, and the 2.5th and 97.5th percentile conditional spectra. As can be qualitatively seen from these figures, the spectrum of an individual selected ground motion, at a hazard level, may deviate from the target median spectrum. However, the selected suite of ground motions, as an ensemble, matches the complete probability structure, i.e., the measures of central tendency, the variability, and the correlation structure, of the target response spectrum.

A few remarks regarding the selected ensembles of ground motion records need to be made. Firstly, the values of scale factors applied to the selected earthquake ground motions are bounded between 0.3 to 4.0 to have realistic records for response assessment of the testbed bridges. Secondly, it is to be noted that although computation of the target CMS at each hazard level requires identification of causative scenarios from disaggregation of seismic hazard, no restriction whatsoever is imposed on the causal magnitudes and source-to-site distances of the selected ground motion records. Finally, an explicit consideration of near fault effects and consistent incorporation of velocity pulses in the selected ensembles of ground motions are beyond the scope of this project. However, following the selection of a ground motion ensemble, the number of records selected, per hazard level, with pulse-like characteristics (Baker 2007) are counted and listed in Table 5-2 for each testbed bridge

Table 5-2 Fraction of pulse-like ground motion records selected per hazard level

Bridge	**Hazard Level**					
	I	**II**	**III**	**IV**	**V**	**VI**
A	4/100	3/100	4/100	8/100	7/100	8/100
B	5/100	7/100	7/100	9/100	9/100	11/100
C	5/100	4/100	4/100	4/100	6/100	7/100
MAOC	16/100	20/100	21/100	26/100	33/100	39/100

As a part of the next step in the PEER PBEE framework, i.e., Probabilistic Seismic Demand Hazard Analysis (PSDemHA), the selected ensembles of site-specific risk-consistent ground motions are used in seismic response assessment of the considered testbed bridges, the results of which will be discussed in the subsequent chapters.

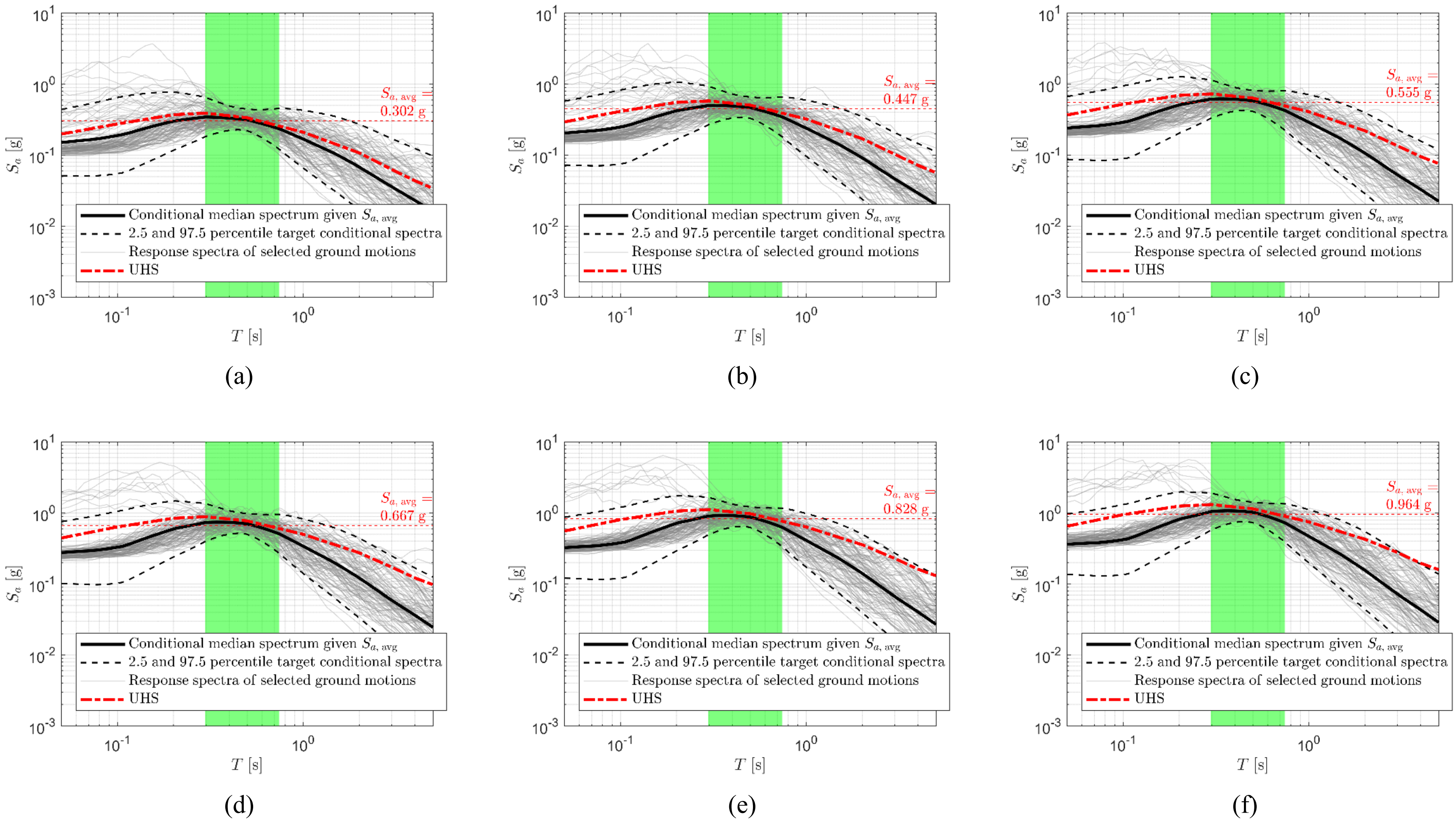

Figure 5.13 Risk-consistent ground motion ensembles for Bridge A at (a) hazard level I; (b) hazard level II; (c) hazard level III; (d) hazard level IV; (e) hazard level V; (f) hazard level VI

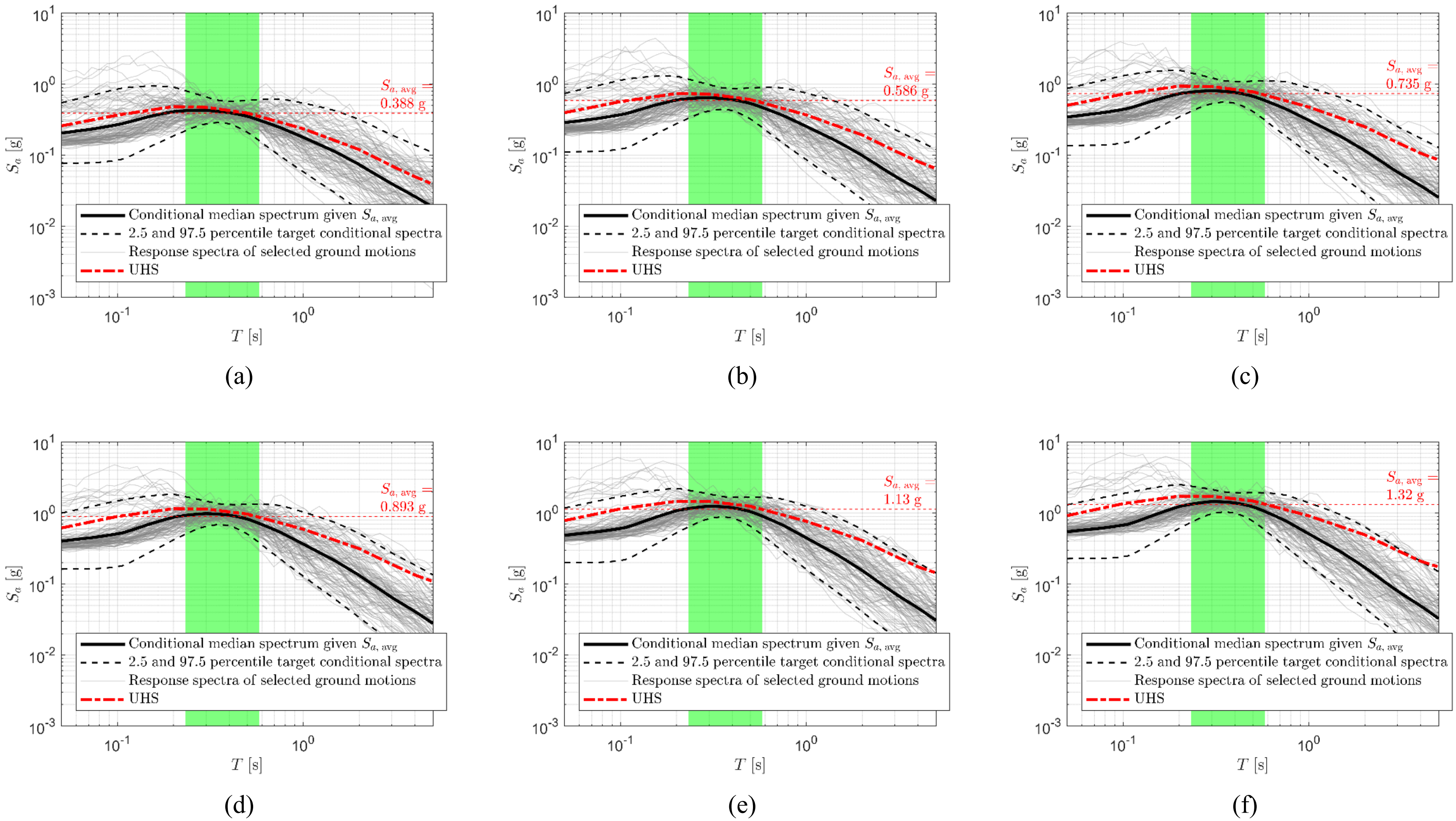

Figure 5.14 Risk-consistent ground motion ensembles for Bridge B at (a) hazard level I; (b) hazard level II; (c) hazard level III; (d) hazard level IV; (e) hazard level V; (f) hazard level VI

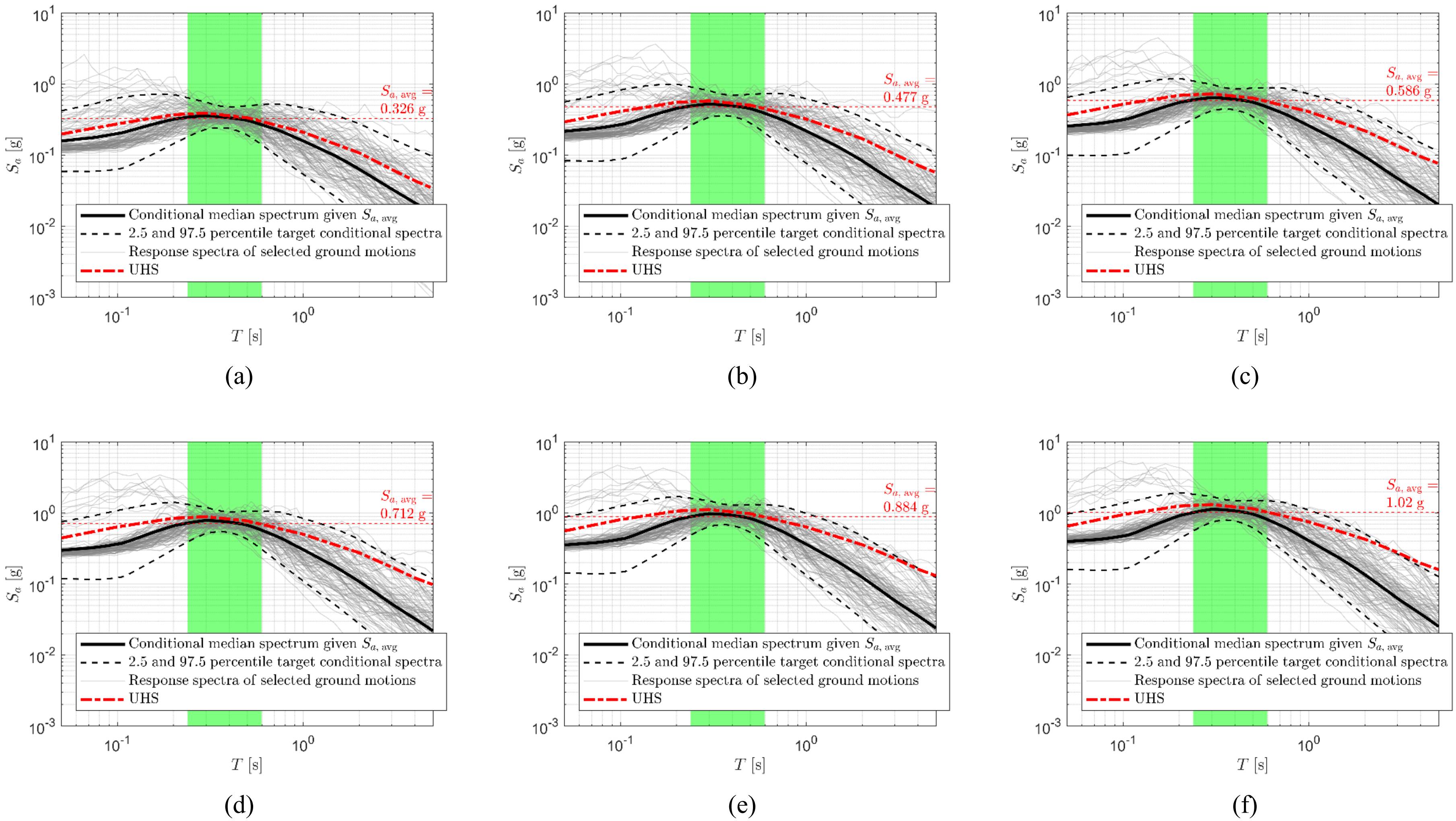

Figure 5.15 Risk-consistent ground motion ensembles for Bridge C at (a) hazard level I; (b) hazard level II; (c) hazard level III; (d) hazard level IV; (e) hazard level V; (f) hazard level VI

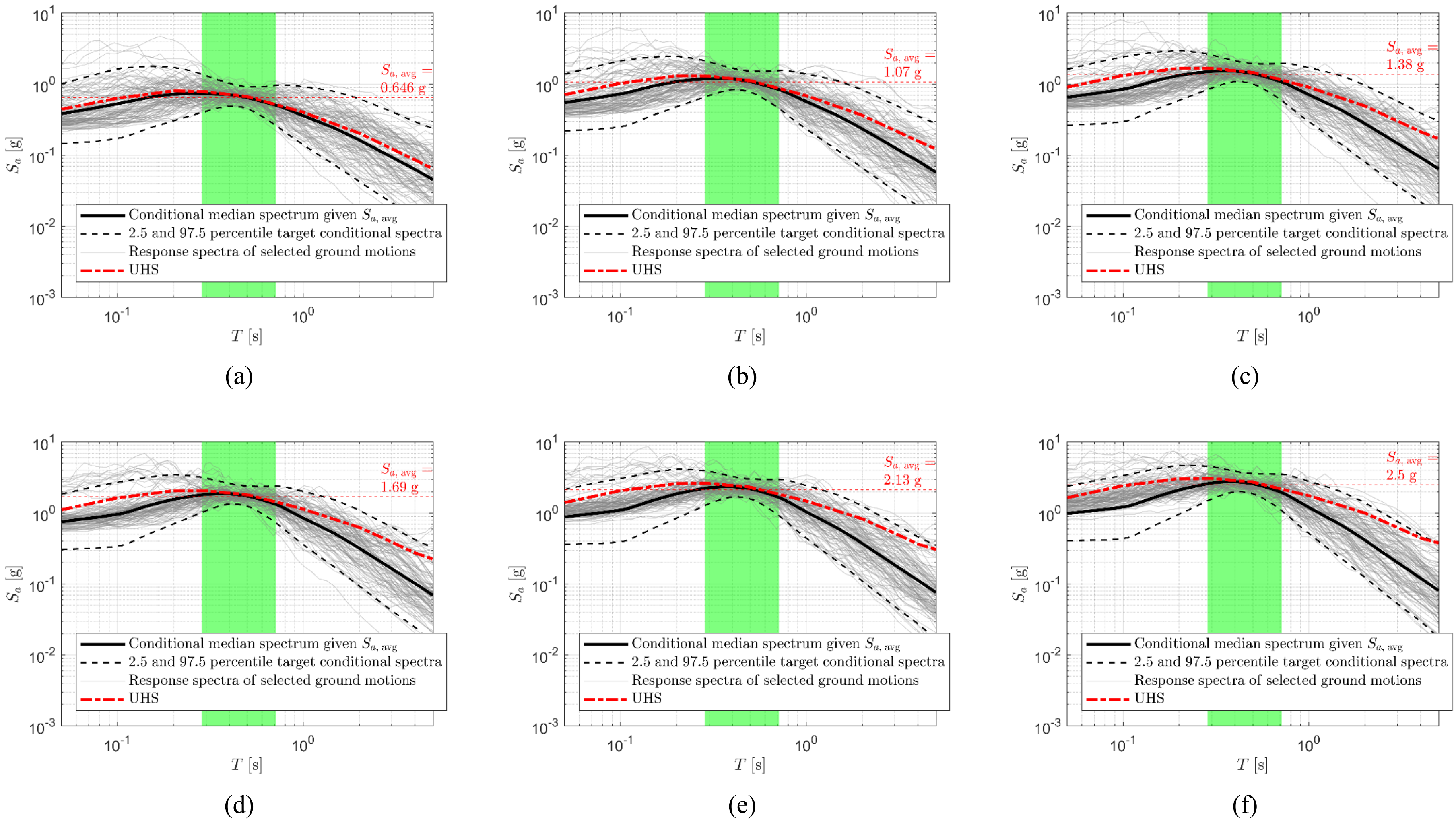

Figure 5.16 Risk-consistent ground motion ensembles for Bridge MAOC at (a) hazard level I; (b) hazard level II; (c) hazard level III; (d) hazard level IV; (e) hazard level V; (f) hazard level VI

6 Deterministic Seismic Response Analysis

6.1 Introduction

Utilizing the detailed three-dimensional nonlinear finite element models of the considered testbed bridges developed in OpenSees (described in Chapter 4), a series of dynamic time history analyses is carried out to assess the structural behavior of these bridges subjected to seismic loading. Each testbed bridge model is subjected to a few ground motion records, each associated with a distinct level of seismic hazard. These analyses are conducted to gauge the seismic behavior of the as-designed testbed bridges and to assess the extent of inelastic/nonlinear responses of various structural components of these bridges resulting from subjecting the bridge models to ground motion records corresponding to increasing levels of seismic hazard.

In particular, structural responses relating to the column(s) and abutments of the testbed bridges are evaluated and compared. Evaluated responses relating to reinforced concrete bridge columns include the moment-curvature response of the most critical section in a column, the material hysteretic stress-strain responses of reinforcing steel and concrete (unconfined and confined) fibers in the most critical column section, and the history of column-axial load ratio. The backfill-superstructure passive interaction, and the force-deformation hysteresis of bearing pads and exterior shear keys are the evaluated responses pertaining to seat-type abutments of the testbed bridges.

The primary focus of this chapter is merely to evaluate and compare the deterministic seismic responses of the selected testbed bridges at different seismic hazard levels via nonlinear time-history analysis of the finite element models (corresponding to expected values and/or best-estimates of material and/or geometric properties) of these bridges subjected to a single record at each hazard level. It is important to note that the results shown in this chapter give no information, whatsoever, relating to the statistics of seismic response/demand and/or its associated hazard in terms of the annual probability/MAR of exceedance. Such a probabilistic characterization of seismic demand and subsequent damage, requiring an explicit account of all pertinent sources of uncertainties and their consistent propagation through various stages of the PEER PBEE analytical framework, are elaborated in the chapters to follow.

6.2 Analysis Setup

The selected set of bridge testbeds are multi-span OSBs supported on one or more single/multiple-column bent(s) and seat-type abutments. Schematic spline representations of the finite element models of these bridges, each subjected to a generic two-component earthquake ground motion record, are shown in Figure 6.1 (a) through Figure 6.4 (a). Also marked in Figure 6.1 (a) through Figure 6.4 (a) are specific structural members/components of each bridge model chosen for a concise presentation of seismic response analyses results. These members are singled out from damageable groups of similar structural components for the sole purpose of brevity and succinctness of presentation without any loss of generality.

Three ground motion records, each belonging to an ensemble of records previously selected (described in Chapter 5) to represent a distinct seismic hazard level at a specific bridge site, are chosen for the deterministic seismic response evaluation of a bridge. Seismic hazard levels II, IV, and VI, encompassing a wide range of seismic hazard characterized by mean RPs of exceedance equal to 224 years, 975 years, and 4975 years, respectively are considered. As previously stated in Chapter 5, it is noted that all earthquake records belonging to an ensemble of records selected to represent a specific level of seismic hazard follow, as a joint set rather than individually, the complete probability structure of the target conditional spectrum defined for that hazard level. A ground motion record, corresponding to one of the three hazard levels mentioned, is singled out from the already selected ensemble of records such that the geometric mean response spectrum of the two-component record (i.e., the geometric mean of the spectral ordinates of the two horizontal components of the record at different spectral periods) closely follows the conditional median spectrum defined for that hazard level, especially in the averaging period range.

Response spectra of the three individual ground motion records chosen for deterministic earthquake response analyses of the testbed bridges are shown in Figure 6.1 (b)-(i), (c)-(i), and (d)-(i), through Figure 6.4 (b)-(i), (c)-(i), and (d)-(i). As stated before, the records chosen for the response analyses of a bridge individually belong to ensembles of previously selected records (whose response spectra are also shown in Figure 6.1 (b)-(i), (c)-(i), and (d)-(i), through Figure 6.4 (b)-(i), (c)-(i), and (d)-(i)) corresponding to seismic hazard levels II, IV, and VI. Also shown in Figure 6.1 (b)-(ii), (c)-(ii), and (d)-(ii), through Figure 6.4 (b)-(ii), (c)-(ii), and (d)-(ii), are the two-component horizontal ground acceleration time-histories of these records arbitrarily assigned as seismic excitation inputs to the finite element models of the testbed bridges in the longitudinal and transverse directions. Table 6-1 shows pertinent details of the chosen seismic ground motion inputs for response analyses of the testbed bridges considered.

Each finite element model of a testbed bridge is subjected to its respective set of three earthquake ground motion input excitations, individually corresponding to hazard levels II, IV, and VI. Recorded responses of key structural components of these bridges (marked in Figure 6.1 (a) through Figure 6.4 (a)) obtained from nonlinear time-history analyses of their finite element models at three different levels of seismic input are presented next. Needless to explicitly mention here is that these analyses are performed using the analysis setup previously outlined in Chapter 4.

Table 6-1 Earthquake ground motion records for deterministic nonlinear time-history analyses

Bridge	Hazard Level	Earthquake Event (Year)	Station	Magnitude	Duration (s)	Scale factor	Ground motion component assigned to bridge direction	
							Longitudinal	Transverse
A	II	Coalinga-01 (1983)	Parkfield - Cholame 2WA	6.36	40.0	1.59	0	90
	IV	Coalinga-01 (1983)	Parkfield - Cholame 4AW	6.36	32.0	3.80	0	90
	VI	Taiwan SMART1(45) (1986)	SMART1 O02	7.3	44.0	1.75	EW	NS
B	II	Kobe, Japan (1995)	Takatori	6.9	40.96	0.38	0	90
	IV	Loma Prieta (1989)	Anderson Dam (Downstream)	6.93	39.60	1.58	250	340
	VI	Taiwan SMART1(45) (1986)	SMART1 O01	7.3	44.0	2.98	EW	NS
C	II	Chi-Chi, Taiwan-06 (1999)	HWA2	6.30	44.95	2.81	N	E
	IV	Chi-Chi, Taiwan-05 (1999)	CHY052	6.2	55.0	3.66	N	W
	VI	Northridge-01 (1994)	San Pedro - Palos Verdes	6.69	32.0	3.89	0	90
MAOC	II	Chi-Chi, Taiwan (1999)	ILA067	7.62	90.0	2.90	E	N
	IV	Northridge-01 (1994)	Canyon Country - W Lost Cany	6.69	19.99	1.57	0	270
	VI	Northridge-01 (1994)	Canyon Country - W Lost Cany	6.69	19.99	2.32	0	270

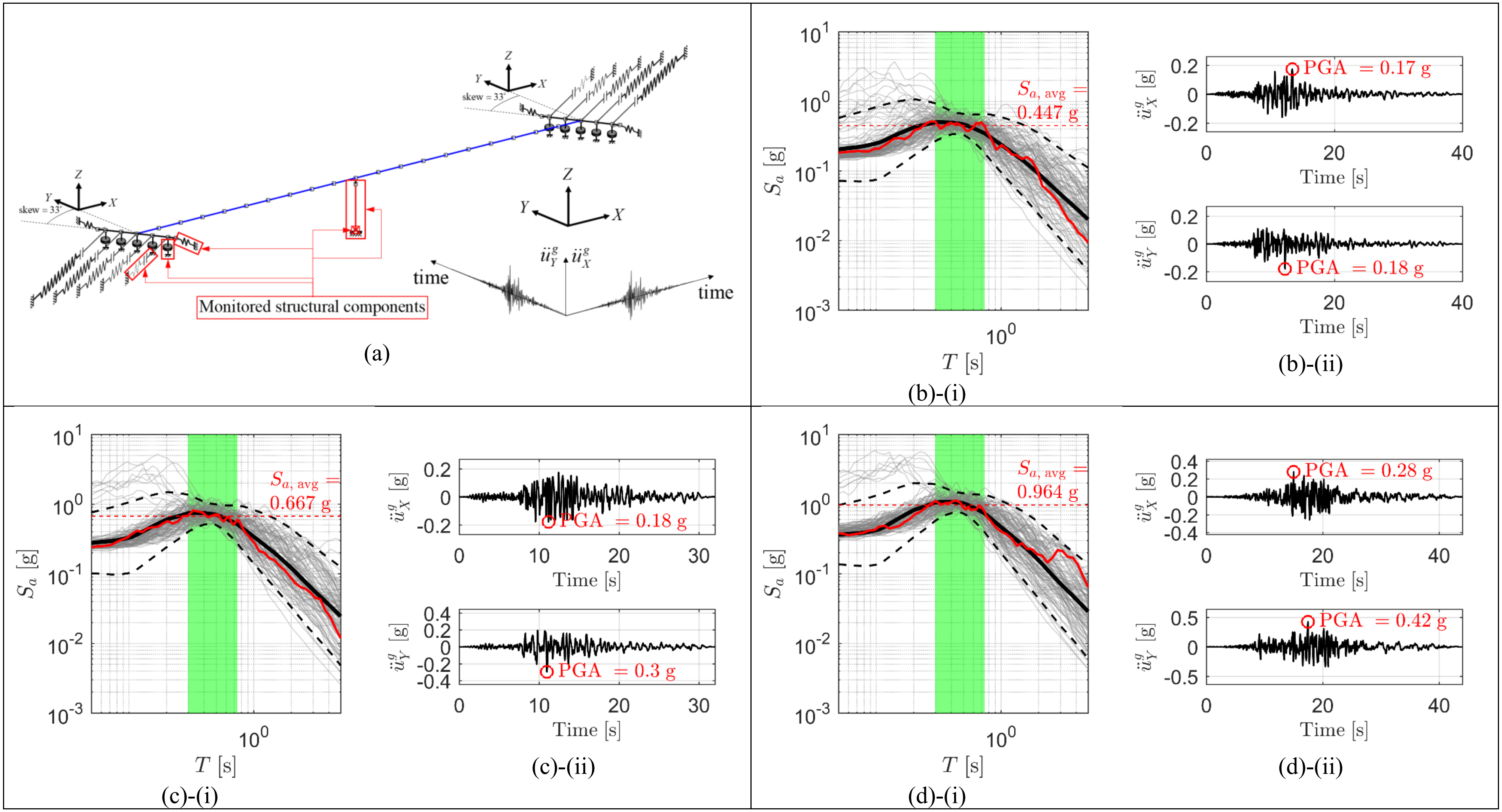

Figure 6.1 Deterministic seismic response analysis setup for Bridge A: (a) schematic representation of the finite element model with structural components to be monitored; (i) Geometric mean (of two horizontal components) response spectra; and (ii) bi-directional ground acceleration history of ground motion record selected for deterministic response analysis at: (b) hazard level II; (c) hazard level IV; and (d) hazard level VI

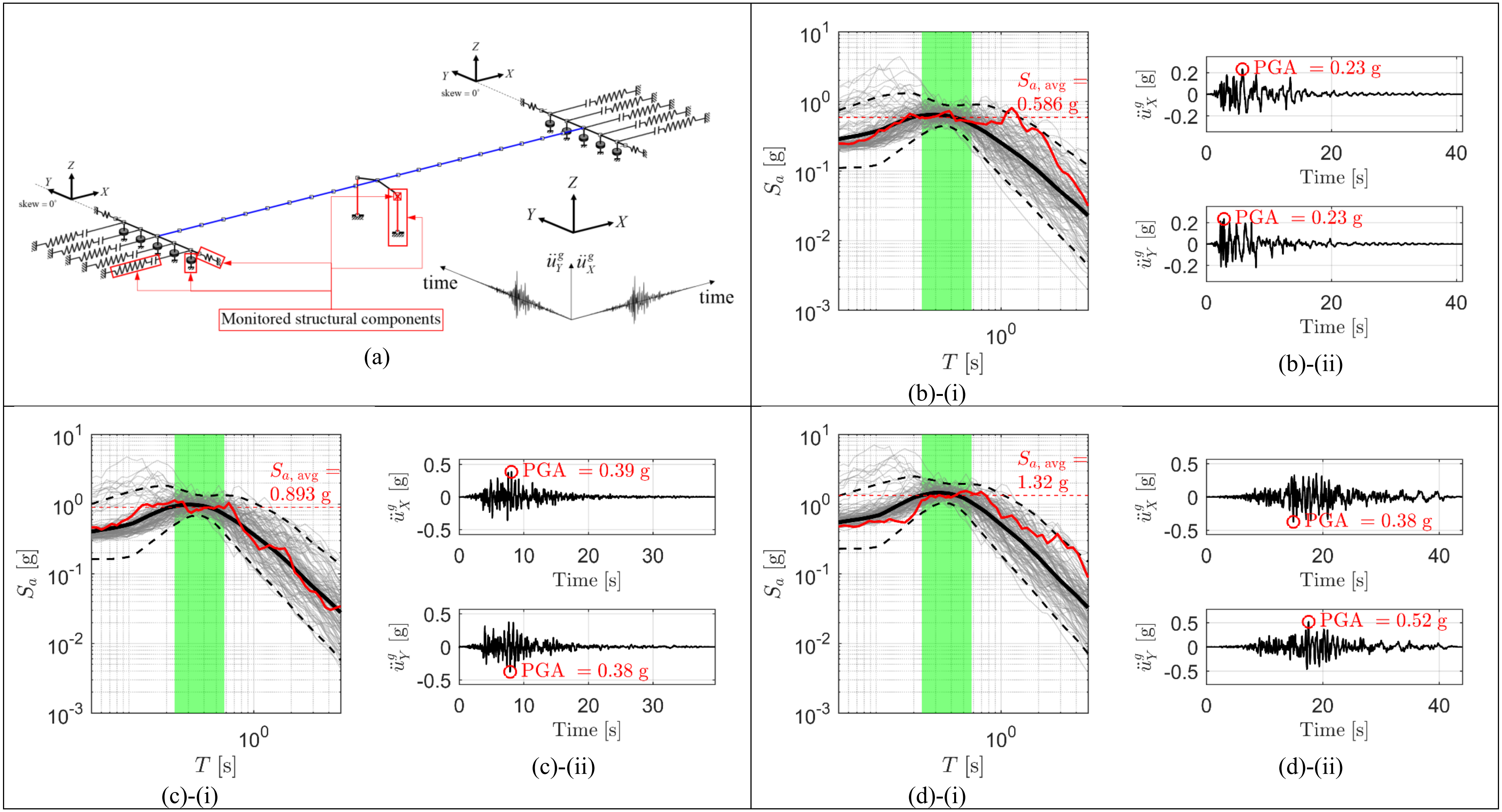

Figure 6.2 Deterministic seismic response analysis setup for Bridge B: (a) schematic representation of the finite element model with structural components to be monitored; (i) Geometric mean (of two horizontal components) response spectra; and (ii) bi-directional ground acceleration history of ground motion record selected for deterministic response analysis at: (b) hazard level II; (c) hazard level IV; and (d) hazard level VI

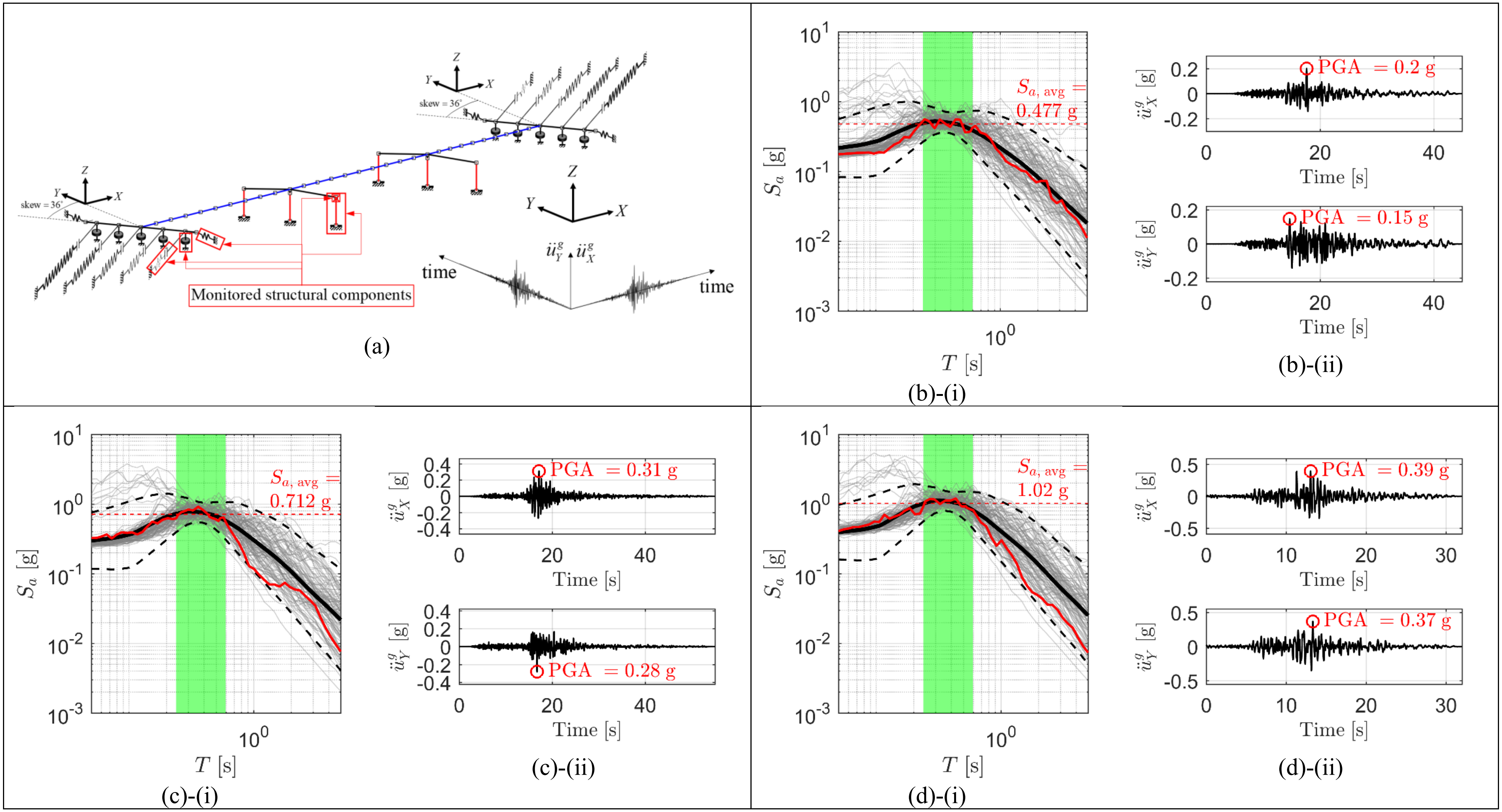

Figure 6.3 Deterministic seismic response analysis setup for Bridge C: (a) schematic representation of the finite element model with structural components to be monitored; (i) Geometric mean (of two horizontal components) response spectra; and (ii) bi-directional ground acceleration history of ground motion record selected for deterministic response analysis at: (b) hazard level II; (c) hazard level IV; and (d) hazard level VI

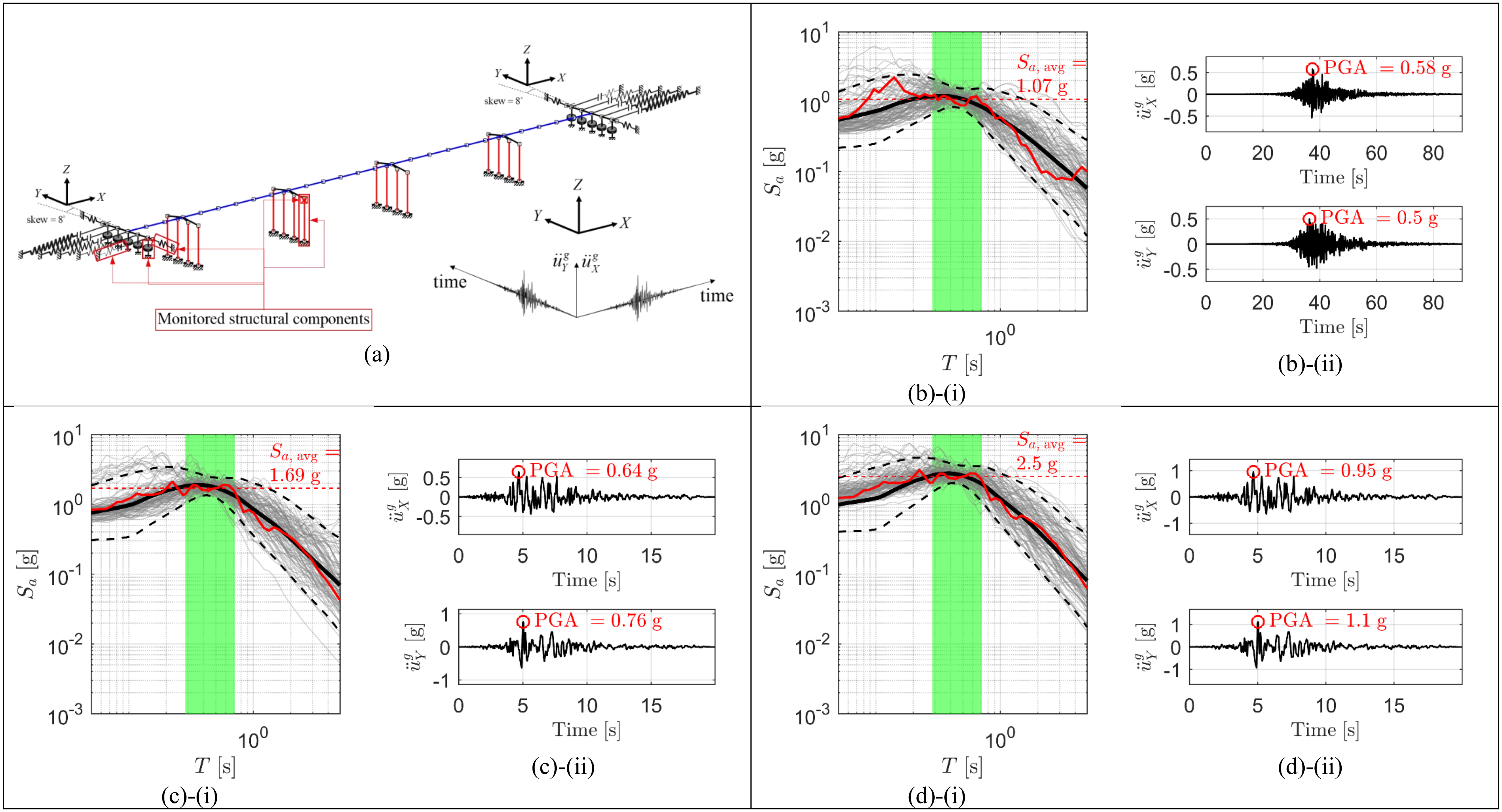

Figure 6.4 Deterministic seismic response analysis setup for Bridge MAOC: (a) schematic representation of the finite element model with structural components to be monitored; (i) Geometric mean (of two horizontal components) response spectra; and (ii) bi-directional ground acceleration history of ground motion record selected for deterministic response analysis at: (b) hazard level II; (c) hazard level IV; and (d) hazard level VI

6.2.1 Bridge Column Response

The longitudinal and transverse moment-curvature (normalized) responses recorded at the bottommost section of the single column in the finite element model of Bridge A, and the topmost sections (closest to the deck) of the monitored columns of each of the finite element models of Bridge B, Bridge C, and Bridge MAOC, are shown in Figure 6.5 (b)-(i), (c)-(i), and (d)-(i), through Figure 6.8 (b)-(i), (c)-(i), and (d)-(i), for the considered set of seismic ground motion inputs. As noted from these figures, the longitudinal or transverse moment-curvature response of a bridge column intuitively amplifies with increasing levels of seismic hazard associated with the input ground motion. The moment-curvature response of any column section, in general, is found to qualitatively range from being more or less linear, characterized by small hysteretic cycles, at hazard level II to exceedingly nonlinear, described by large plastic deformations and extensive hysteresis, at hazard level VI.

Plotted alongside the moment-curvature responses of the monitored column sections of each testbed bridge model are the material stress-strain responses of individual fibers (shown in Figure 6.5 (a) through Figure 6.8 (a)) corresponding to the cover (unconfined) concrete, core (confined) concrete, and reinforcing steel in these sections. Material strains, directly relatable to structural damage (ref), are found to vary proportionally with levels of seismic hazard associated with the input ground motions. Highest extents of nonlinear hysteretic material stress-strain responses are recorded for the seismic input corresponding to hazard level VI. Fiber stress-strain responses resulting from ground motion inputs corresponding to lower hazard levels, i.e., hazard levels II and IV, show proportionally reduced levels of nonlinear material hysteresis.

Temporal variations of axial load ratio recorded in the monitored columns of each testbed bridge model for the considered seismic inputs are shown in Figure 6.9 (b), (c), and (d), through Figure 6.12 (b), (c), and (d). Axial load ratio is expressed as the ratio of axial load in the column to the axial load capacity (defined as $A_g f'_{ce}$, where A_g is the gross area of the column cross-section and f'_{ce} is the expected compressive strength of the design concrete mix) of the column section. From gravity loading alone, the bridge columns of the testbed bridge models are found to experience low initial axial load ratios (ranging from 4.0-8.0%) shown as the starting point of the axial load ratio time-histories. It is noted from Figure 6.9 (b), (c), and (d), through Figure 6.12 (b), (c), and

(d) that the maximum axial load ratios reached in the columns due to the considered set of input ground motions do not vary significantly at different seismic hazard levels and are found to remain considerably low (less than 15.0%).

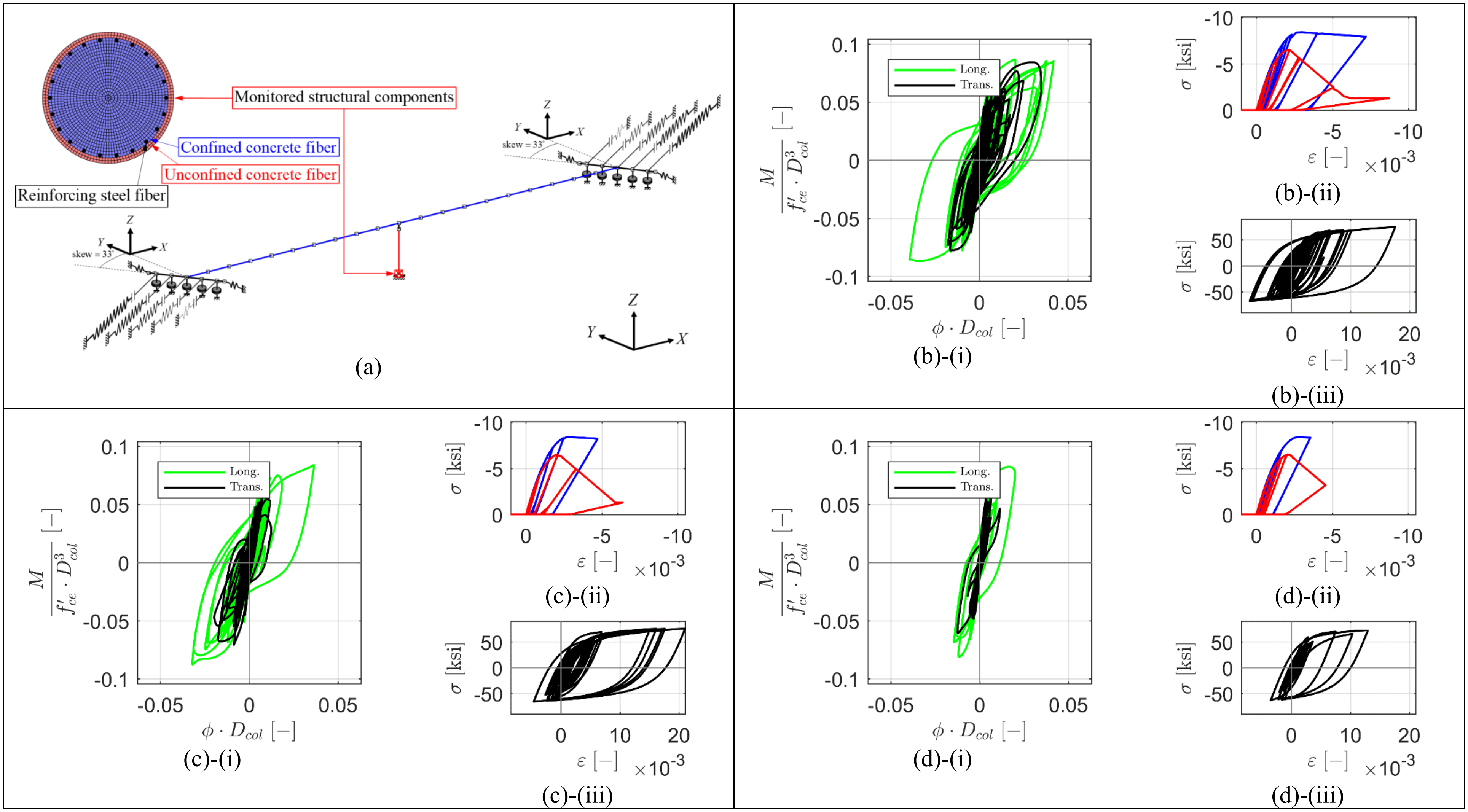

Figure 6.5 Seismic response of various components of the single column of Bridge A: (a) schematic representation of the finite element model with column structural components being monitored; (i) normalized moment-curvature section response; (ii) material hysteretic stress strain response of a single confined (in blue) and unconfined (in red) concrete fiber; and (iii) material hysteretic stress strain response of a reinforcing steel fiber recorded at: (b) hazard level II; (c) hazard level IV; and (d) hazard level VI

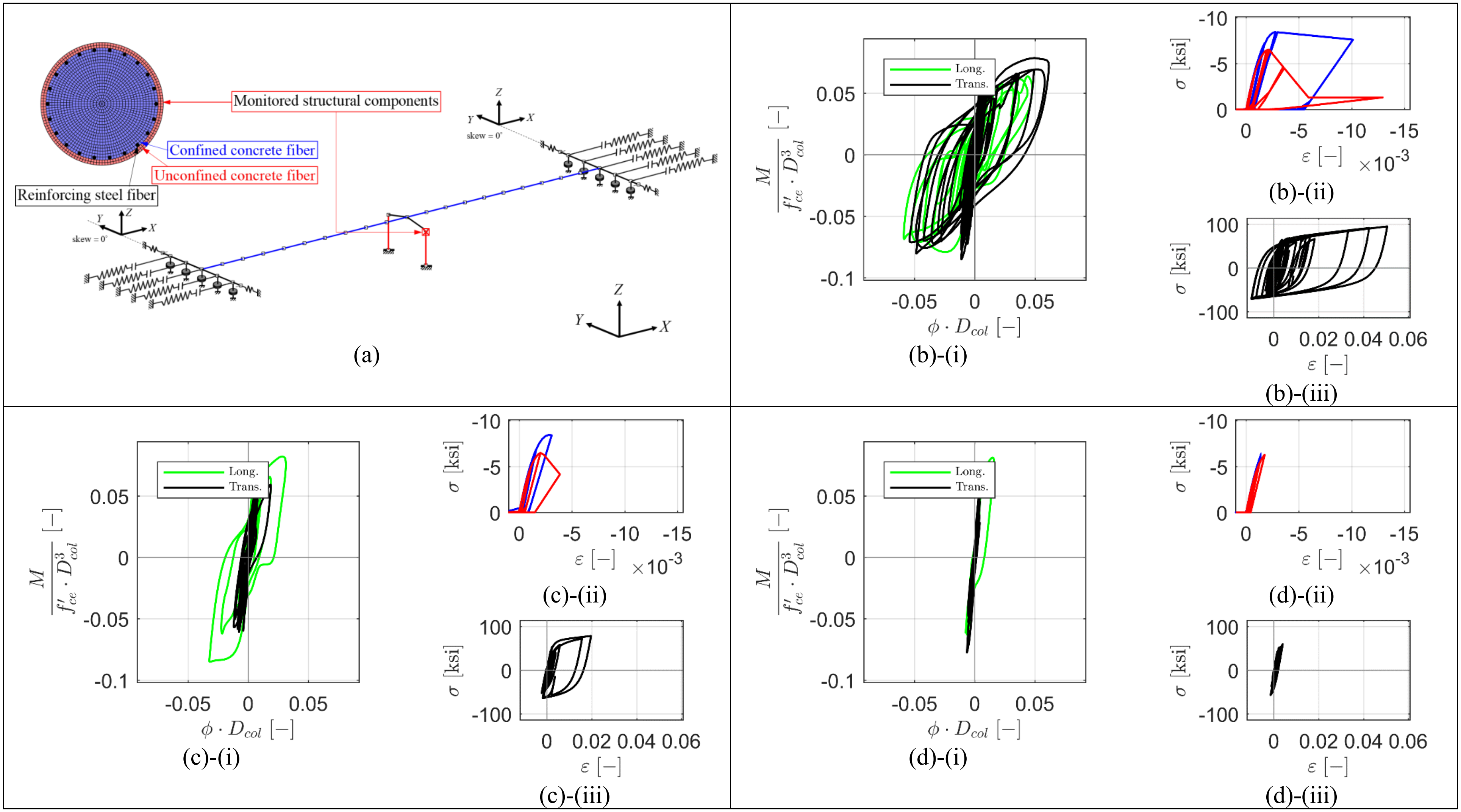

Figure 6.6 Seismic response of various components of the monitored column of Bridge B: (a) schematic representation of the finite element model with column structural components being monitored; (i) normalized moment-curvature section response; (ii) material hysteretic stress strain response of a single confined (in blue) and unconfined (in red) concrete fiber; and (iii) material hysteretic stress strain response of a reinforcing steel fiber recorded at: (b) hazard level II; (c) hazard level IV; and (d) hazard level VI

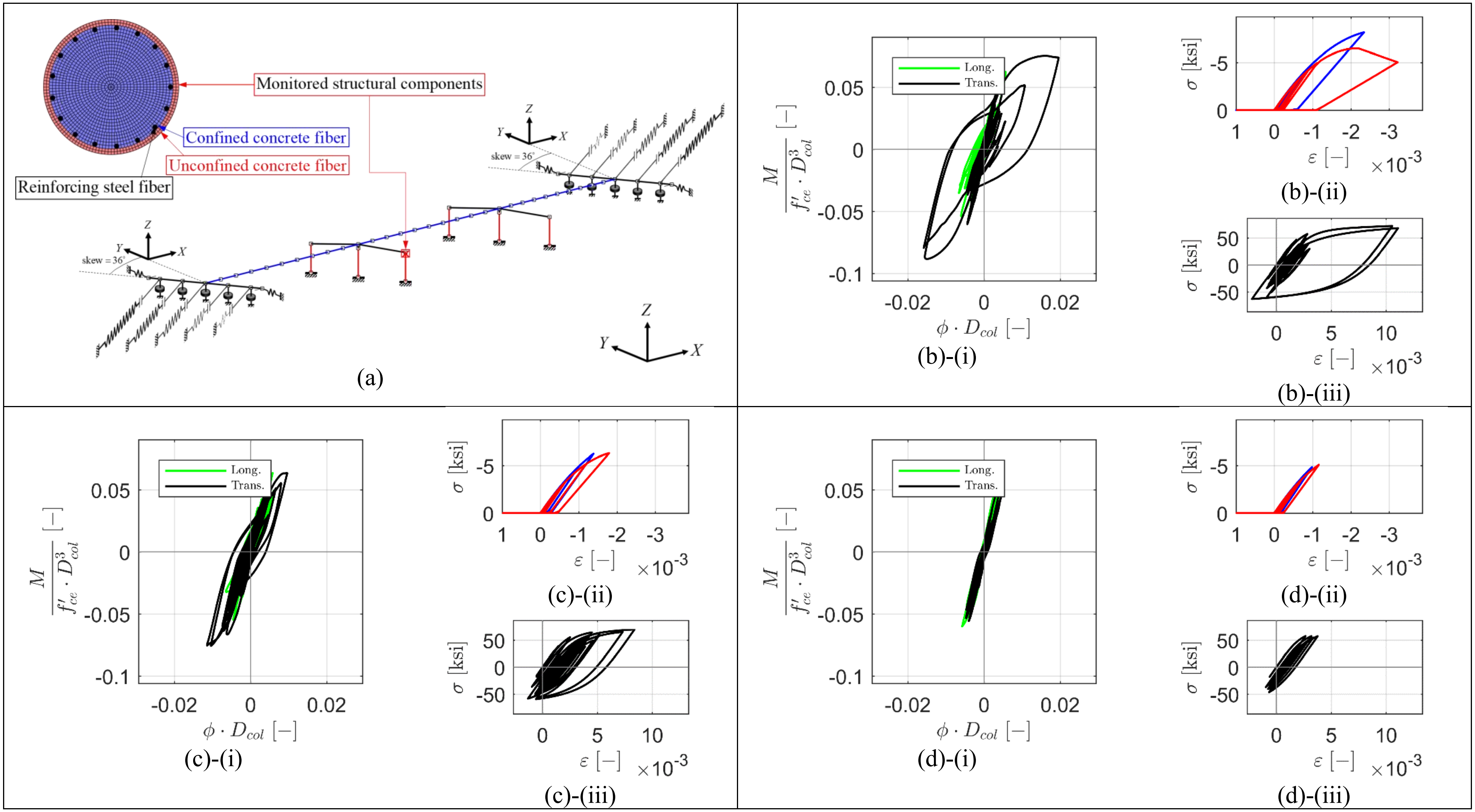

Figure 6.7 Seismic response of various components of the monitored column of Bridge C: (a) schematic representation of the finite element model with column structural components being monitored; (i) normalized moment-curvature section response; (ii) material hysteretic stress strain response of a single confined (in blue) and unconfined (in red) concrete fiber; and (iii) material hysteretic stress strain response of a reinforcing steel fiber recorded at: (b) hazard level II; (c) hazard level IV; and (d) hazard level VI

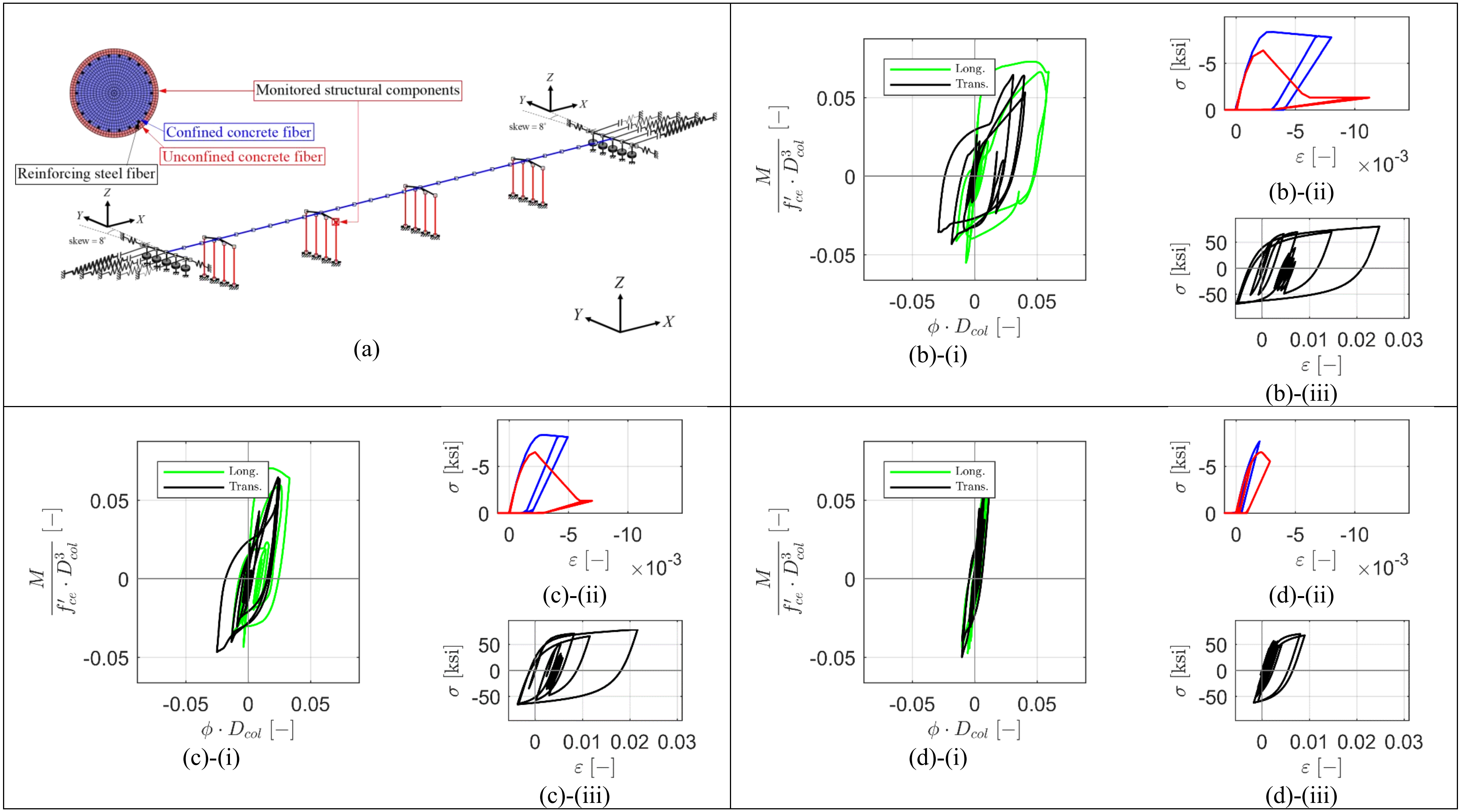

Figure 6.8 Seismic response of various components of the monitored column of Bridge MAOC: (a) schematic representation of the finite element model with column structural components being monitored; (i) normalized moment-curvature section response; (ii) material hysteretic stress strain response of a single confined (in blue) and unconfined (in red) concrete fiber; and (iii) material hysteretic stress strain response of a reinforcing steel fiber recorded at: (b) hazard level II; (c) hazard level IV; and (d) hazard level VI

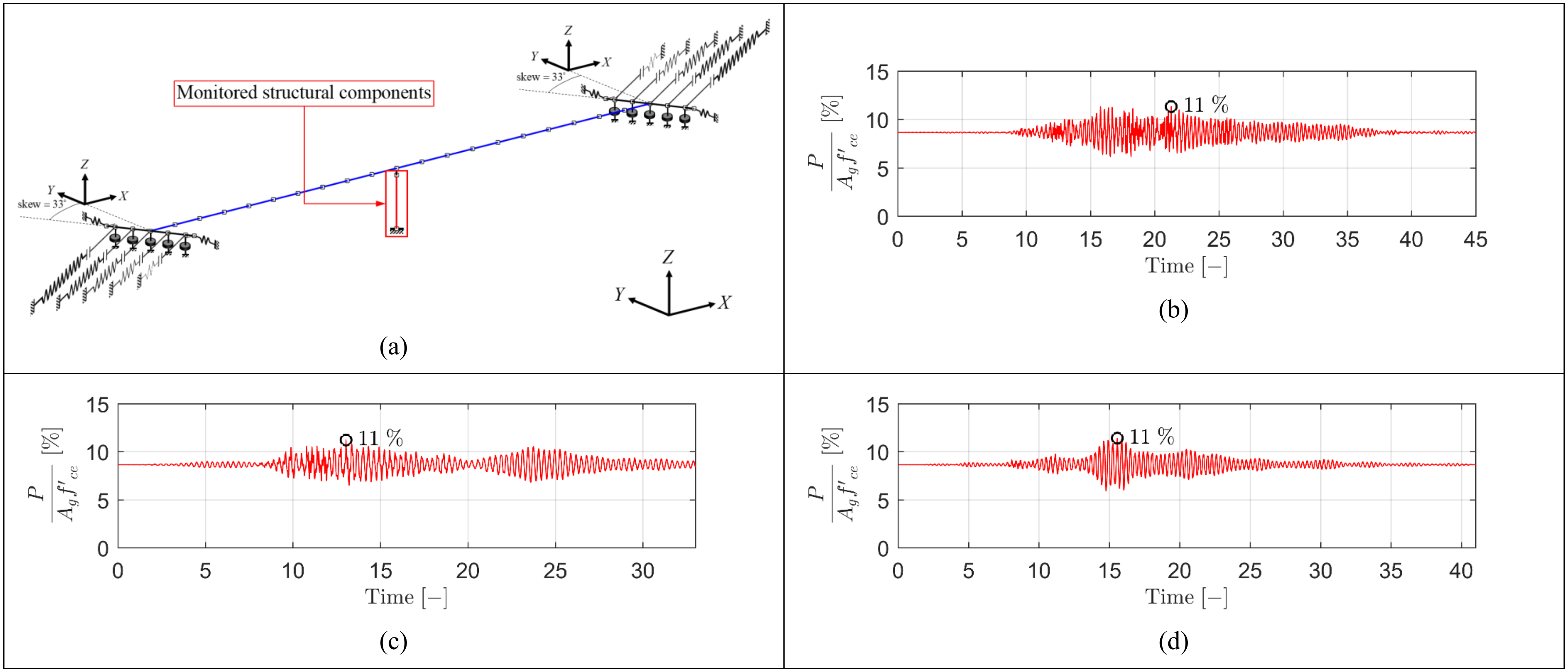

Figure 6.9 Seismic response history of the single column of Bridge A: (a) schematic representation of the finite element model with column being monitored; temporal variation of axial load ratio recorded in the monitored column at: (b) hazard level II; (c) hazard level IV; and (d) hazard level VI

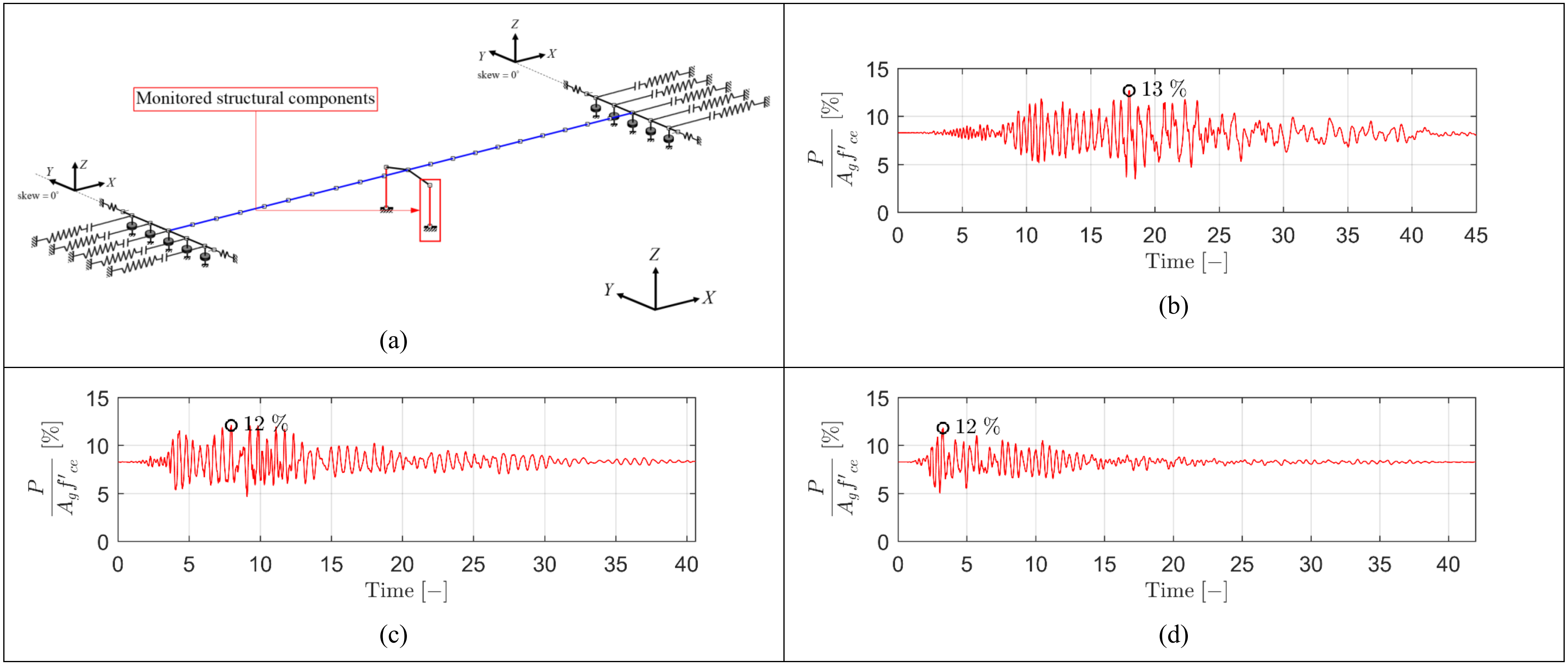

Figure 6.10 Seismic response history of the monitored column of Bridge B: (a) schematic representation of the finite element model with column being monitored; temporal variation of axial load ratio recorded in the monitored column at: (b) hazard level II; (c) hazard level IV; and (d) hazard level VI

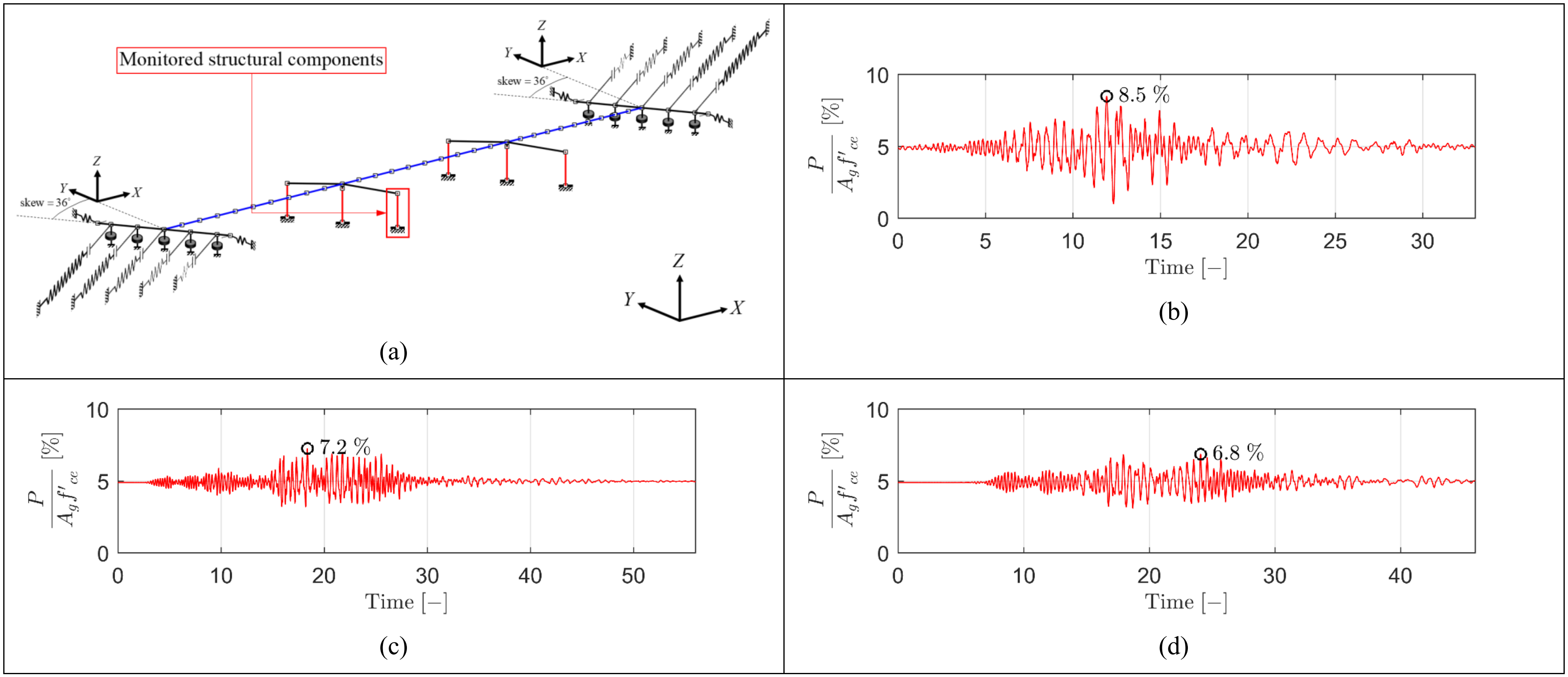

Figure 6.11 Seismic response history of the monitored column of Bridge C: (a) schematic representation of the finite element model with column being monitored; temporal variation of axial load ratio recorded in the monitored column at: (b) hazard level II; (c) hazard level IV; and (d) hazard level VI

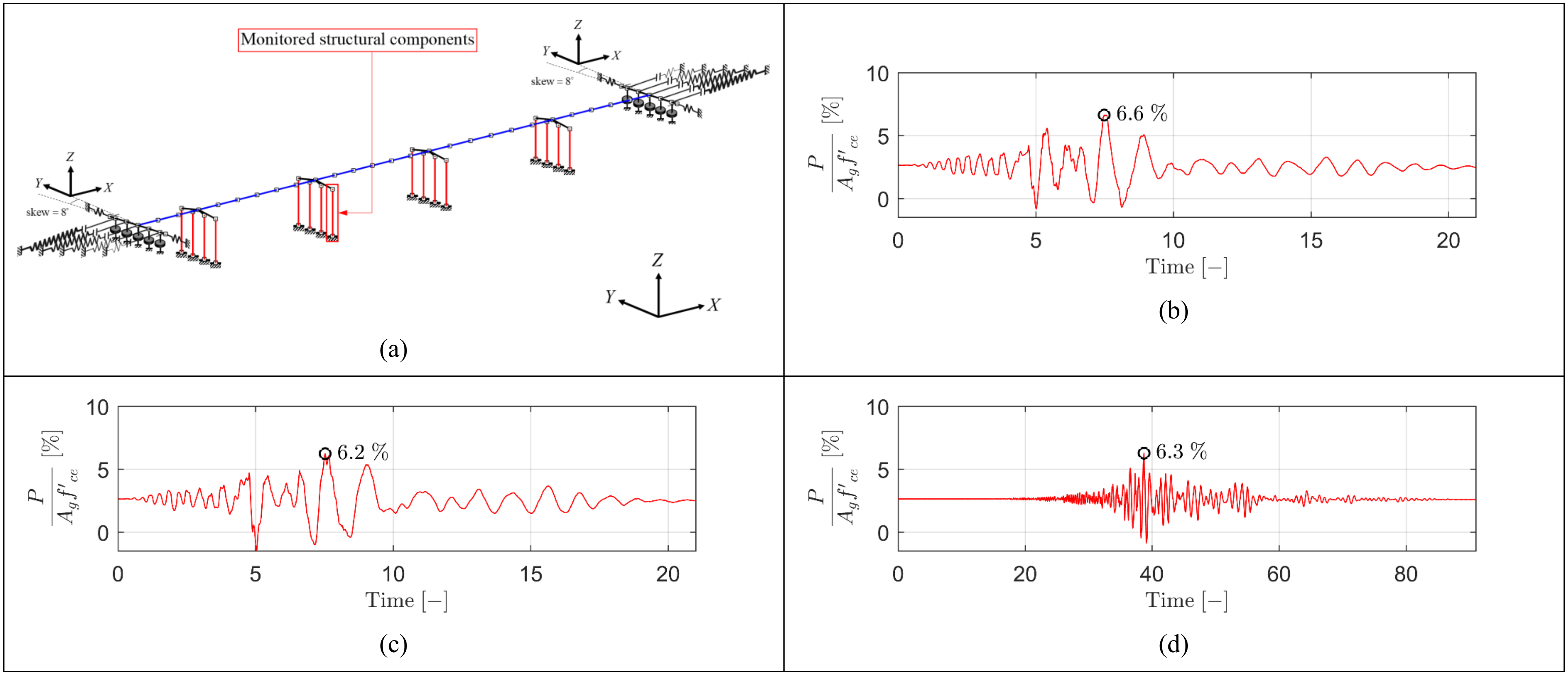

Figure 6.12 Seismic response history of the monitored column of Bridge MAOC: (a) schematic representation of the finite element model with column being monitored; temporal variation of axial load ratio recorded in the monitored column at: (b) hazard level II; (c) hazard level IV; and (d) hazard level VI

6.2.2 Bridge Abutment Response

Recorded force-deformation longitudinal responses, corresponding to the considered seismic inputs, of the backfill springs (marked in Figure 6.13 (a) through Figure 6.16 (a)) placed near the obtuse corners of the, in general, skewed bridge abutments on one end of each testbed bridge model are shown in Figure 6.13 (b)-(i), (c)-(i), and (d)-(i), through Figure 6.16 (b)-(i), (c)-(i), and (d)-(i). With increasing levels of hazard associated with the seismic inputs, progressively amplified levels of the passive response of the backfill spring, mobilized upon closure of the abutment expansion joint gap, of a testbed bridge model are observed.

Transverse responses of the non-isolated (for Bridge A, Bridge B, and Bridge C) and isolated (for Bridge MAOC) exterior shear keys (marked in Figure 6.13 (a) through Figure 6.16 (a)) of the testbed bridge models resulting from the considered seismic inputs are shown in Figure 6.13 (b)-(ii), (c)-(ii), and (d)-(ii), through Figure 6.16 (b)-(ii), (c)-(ii), and (d)-(ii). Shear keys are found to respond in a progressively amplified manner thereby resulting in worsening levels of inflicted damage as the bridge models are subjected to ground motion inputs corresponding to successively higher levels of seismic hazard. The isolated shear key of Bridge MAOC, unlike the non-isolated shear keys of Bridge A, Bridge B, and Bridge C, is found to completely break off at higher seismic hazard levels, thus playing the role of a sacrificial structural fuse that is meant to prevent the propagation of damage to the abutment stemwall.

Horizontally coupled longitudinal and transverse responses of the chosen bearing pad elements (marked in Figure 6.13 (a) through Figure 6.16 (a)) recorded in the seismic response analyses of the testbed bridge models at the considered seismic hazard levels are shown in Figure 6.13 (b)-(iii), (c)-(iii), and (d)-(iii), through Figure 6.16 (b)-(iii), (c)-(iii), and (d)-(iii). The coupling between the two horizontal translational force responses of the chosen bearing pad elements at the three seismic hazard levels considered are shown in Figure 6.13 (b)-(iv), (c)-(iv), and (d)-(iv), through Figure 6.16 (b)-(iv), (c)-(iv), and (d)-(iv). It is again noted that, like in the case of every other structural component assessed, increasingly hazardous seismic ground motion inputs engender increasing levels of inelastic bearing pad deformations.

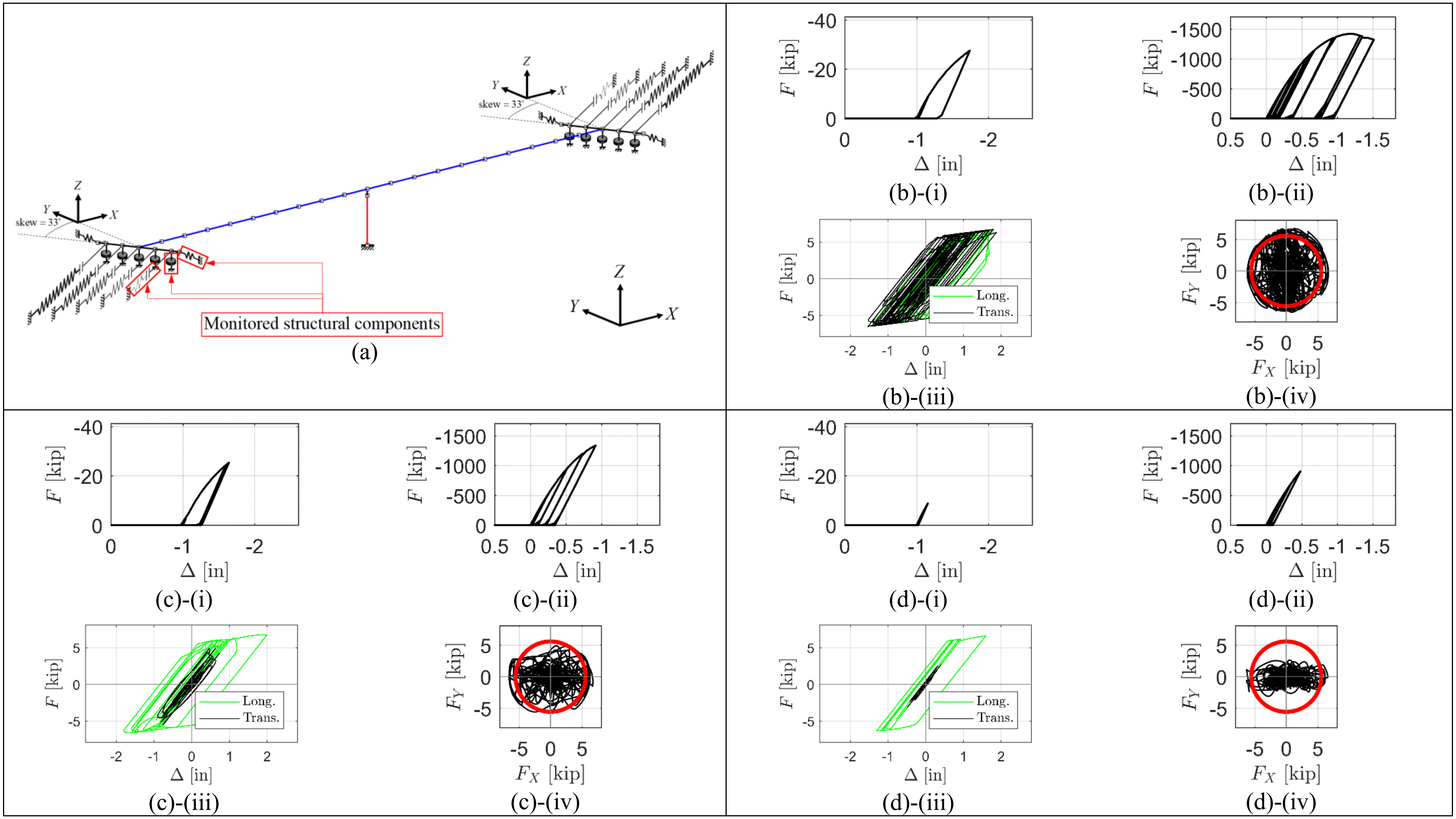

Figure 6.13 Seismic response of various components of an abutment of Bridge A: (a) schematic representation of the finite element model with abutment structural components being monitored; (i) force-deformation hysteretic response of a backfill spring; (ii) force-deformation hysteretic response of an exterior shear key; (iii) force-deformation hysteretic response of a bearing pad; and (iv) bi-directional coupled force response along with circular yield surface of a bearing pad recorded at: (b) hazard level II; (c) hazard level IV; and (d) hazard level VI

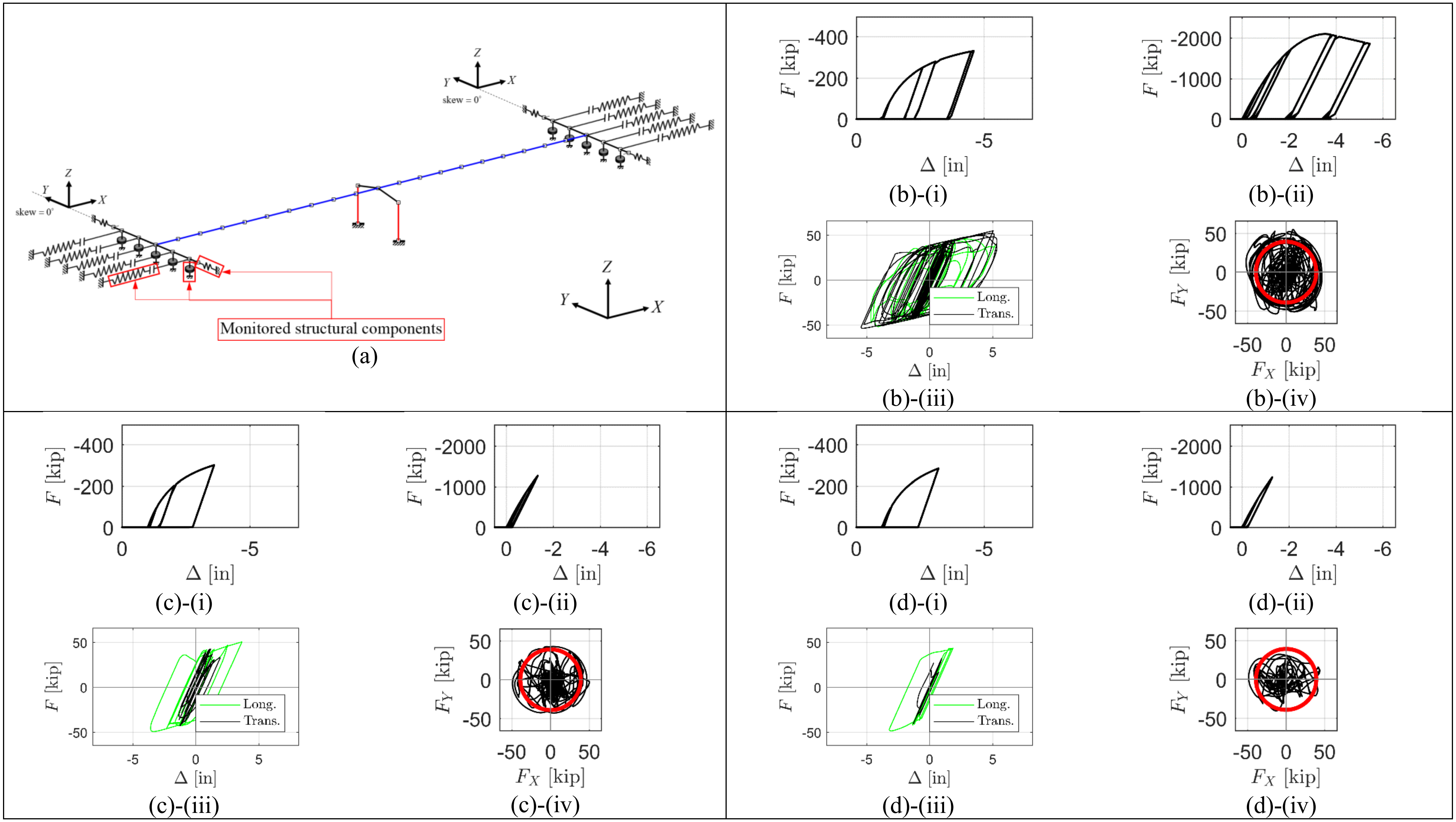

Figure 6.14 Seismic response of various components of an abutment of Bridge B: (a) schematic representation of the finite element model with abutment structural components being monitored; (i) force-deformation hysteretic response of a backfill spring; (ii) force-deformation hysteretic response of an exterior shear key; (iii) force-deformation hysteretic response of a bearing pad; and (iv) bi-directional coupled force response along with circular yield surface of a bearing pad recorded at: (b) hazard level II; (c) hazard level IV; and (d) hazard level VI

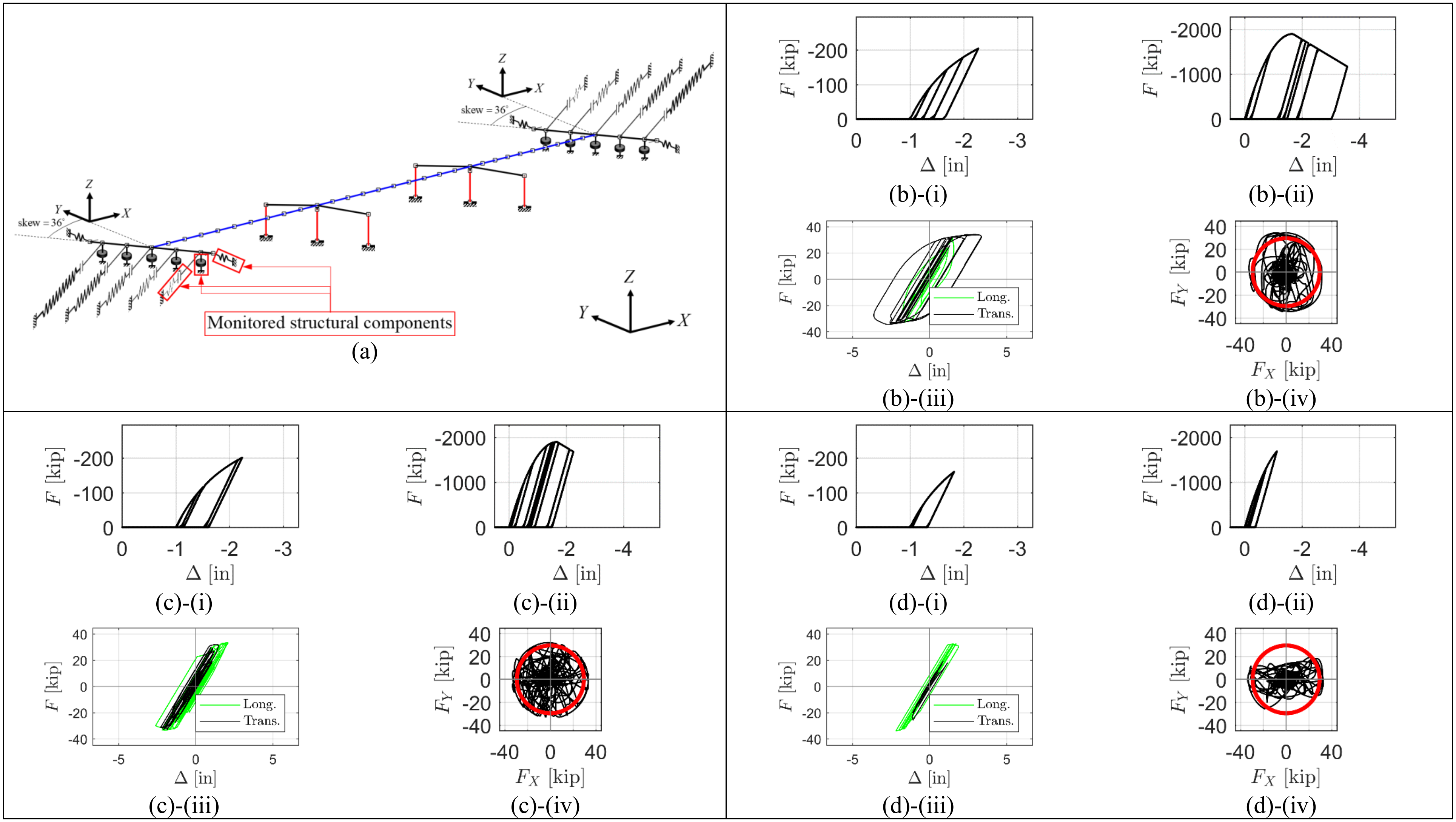

Figure 6.15 Seismic response of various components of an abutment of Bridge C: (a) schematic representation of the finite element model with abutment structural components being monitored; (i) force-deformation hysteretic response of a backfill spring; (ii) force-deformation hysteretic response of an exterior shear key; (iii) force-deformation hysteretic response of a bearing pad; and (iv) bi-directional coupled force response along with circular yield surface of a bearing pad recorded at: (b) hazard level II; (c) hazard level IV; and (d) hazard level VI

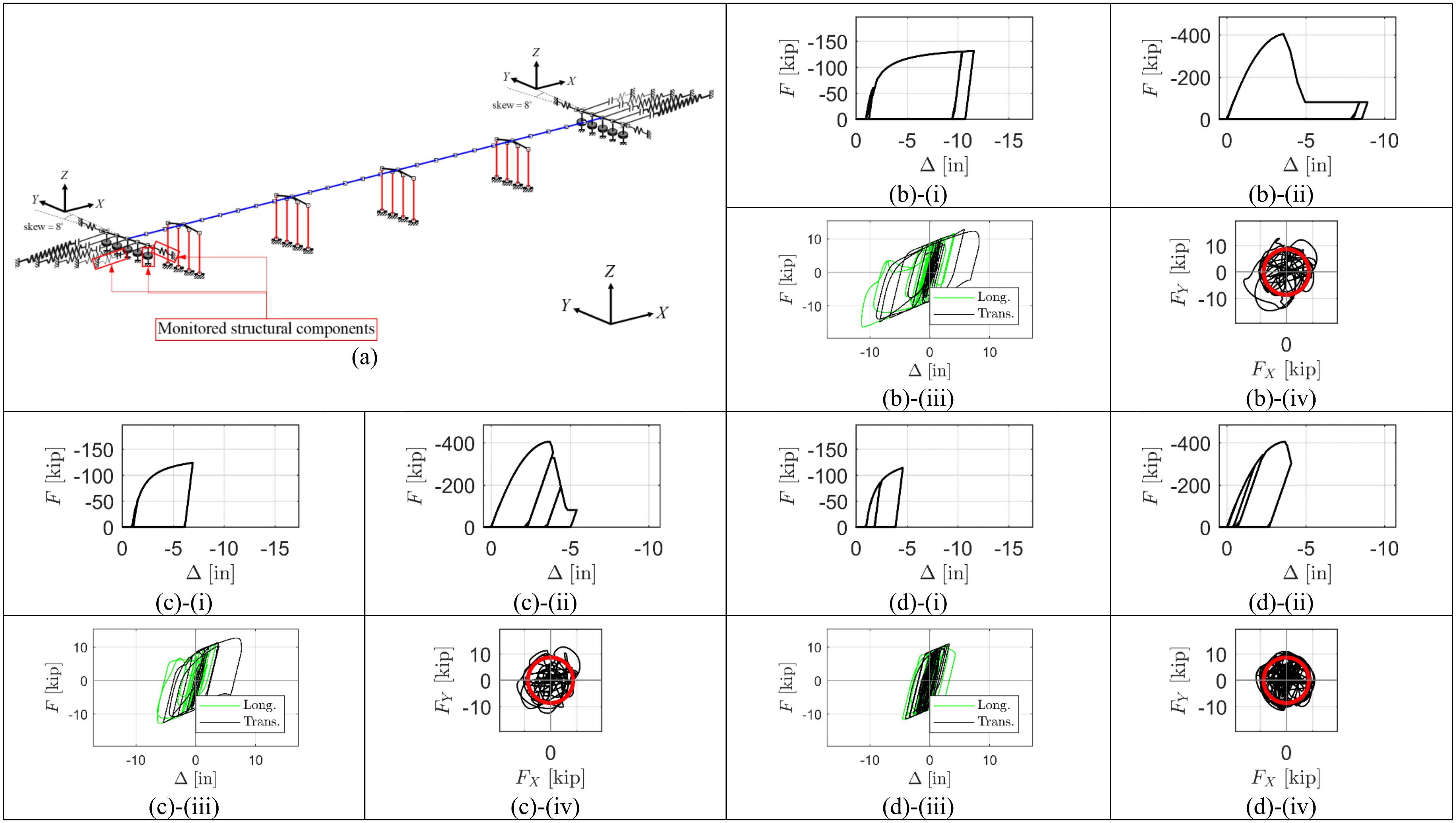

Figure 6.16 Seismic response of various components of an abutment of Bridge MAOC: (a) schematic representation of the finite element model with abutment structural components being monitored; (i) force-deformation hysteretic response of a backfill spring; (ii) force-deformation hysteretic response of an exterior shear key; (iii) force-deformation hysteretic response of a bearing pad; and (iv) bi-directional coupled force response along with circular yield surface of a bearing pad recorded at: (b) hazard level II; (c) hazard level IV; and (d) hazard level VI

7 Probabilistic Seismic Demand Hazard Analysis

7.1 Introduction

Following a thorough probabilistic treatment of the seismic hazard at a given site which enables the selection of representative ensembles of site-specific risk-consistent ground motion records, the next pivotal step in the PEER PBEE framework is to evaluate the structural seismic response, i.e., the seismic demand imposed on the considered structure, due to these earthquakes. Structural seismic response assessment is not devoid of uncertainties. In addition to the uncertainty associated with occurrence/exceedance of the earthquake itself propagating to the response of the structure, there is extensive variability in the amplitudes of structural response quantities recorded from nonlinear response history analyses of finite element structural models subjected to earthquake excitations corresponding to the same level of intensity. Such variability in structural response, given , is due to:

(a) the aleatory record-to-record variability of ground motion histories with the same level of intensity as measured by the ;
(b) the aleatory uncertainty in the finite element model parameters (e.g., constitutive material model parameters, damping model parameters, etc.);
(c) the epistemic parameter estimation uncertainty associated with using finite datasets to estimate the parameters of the aleatory probability distributions characterizing the FE model parameters;
(d) the epistemic modeling uncertainty characterizing the overall numerical models of the structural systems considered and resulting from the inability of idealized (due to numerous simplifying assumptions) numerical models of structural systems to predict the actual response of the structure to earthquake ground motions.

Out of the listed sources, ground motion record-to-record variability has been found to primarily contribute to the dispersion in structural response given an intensity level. Record-to-record variability is exhibited by ground motions, given , because the is usually not able to perfectly gauge an entire ground motion history, which for every earthquake is unique. Although not negligible, contributions of the three other sources of uncertainty listed above are not considered in this project for simplicity.

The objective of Probabilistic Seismic Demand Hazard Analysis (PSDemHA) is to probabilistically characterize the seismic demand on the considered structure through a rigorous quantification of the relevant sources of uncertainties.

7.2 Demand Hazard Integral

PSDemHA aims to predict the mean annual rate (MAR) at which specific values of seismic response parameter amplitudes, called engineering demand parameters $(EDP\text{s})$, are exceeded at the given site for the considered structure. This is done by aggregating the contribution to the rate of EDP exceedance from different levels of corresponding to different hazard levels specific to the site of the structure. Dependence of EDPs on other ground motion characteristics (e.g., magnitude and source-to-site distance) is neglected by relying on "sufficiency" (defined in Chapter 5) of the considered . EDPs are defined to characterize the structural response in terms of deformations (strains/displacements), accelerations, induced forces, and/or other quantities relevant to damage and/or losses incurred by the structure and its components.

The exceedance of a specific value, δ, of an EDP in time, due to an earthquake occurrence (Poisson event) admits a censored Poisson description with the MAR of EDP exceedance given by

$$\nu_{EDP}(\delta) = \nu \cdot P[EDP > \delta] \tag{7.1}$$

where ν, the seismic activity rate, is the MAR of occurrence of earthquakes with magnitude/intensity greater than a lower bound threshold value such that earthquakes with magnitude/intensity lower than this threshold do not cause any significant damage to the considered structure. Different levels of , resulting from earthquake occurrences, contribute to the exceedance of a specific value of an EDP. These levels are assumed to be mutually exclusive owing to the basic assumption of mutual exclusivity of simultaneous earthquake occurrences in time. As a result, the Total Probability Theorem can be used to rewrite Eq. (7.1) as follows

$$\nu_{EDP}(\delta) = \nu \cdot \int_{IM} P[EDP > \delta \mid IM = x] \cdot f_{IM}(x) \cdot dx \tag{7.2}$$

where x is a specific value of the , conditional on which, the uncertainty in EDP is primarily due to ground motion record-to-record variability, which is the only source considered. $f_{IM}(x) \cdot dx$ is the probability that the continuous random variable takes a value between x and $x + dx$, where dx is an infinitesimally small increment. Thus, the seismic activity rate ν, taken inside the integral, and multiplied by $f_{IM}(x) \cdot dx$ can be written as

$$\begin{aligned} \nu \cdot f_{IM}\left(x\right) \cdot dx &= \nu \cdot P\left[x < IM < x + dx\right] \\ &= \nu \cdot \left|P\left[IM > x + dx\right] - P\left[IM > x\right]\right| \\ &= \left|\nu_{IM}\left(x + dx\right) - \nu_{IM}\left(x\right)\right| \\ &= \left|d\nu_{IM}\left(x\right)\right| \end{aligned} \tag{7.3}$$

where $\left|d\nu_{IM}(x)\right|$ is the absolute differential of the seismic hazard curve giving the MAR of occurrence, and not exceedance, of a specific value, x, of . The final form of the seismic demand hazard integral is obtained as follows by substituting Eq. (7.3) into Eq. (7.2).

$$\nu_{EDP}\left(\delta\right) = \int_{IM} P\left[EDP > \delta \mid IM = x\right] \cdot \left|d\nu_{IM}\left(x\right)\right| \tag{7.4}$$

Eq. (7.4) probabilistically characterizes the seismic demand imposed on the considered structure at a given site, in terms of the MAR at which specific values of an EDP are exceeded. The curve representing $\nu_{EDP}(\delta)$ versus δ is called the demand hazard curve of the EDP of interest. A set of EDPs, each corresponding to a discrete state of damage in the structure, is identified for PSDemHA. Damage limit-states considered and their associated EDPs, pertinent to the seismic evaluation of ordinary standard reinforced concrete bridge structures and meaningful to practicing engineers, are discussed in detail in the next section.

7.3 Damage/Limit-states Considered and Associated Engineering Demand Parameters

The damage/limit-states considered in this project to evaluate the performance of ordinary standard bridges (OSBs) are classified into serviceability limit-states and ultimate-limit states. Serviceability limit-states deemed important for a reinforced concrete OSB are: (i) crushing of the cover concrete in a bridge column; and (ii) damage of any shear key in the abutment. These represent superficial damage to the bridge and require significant repairs to be conducted, especially in the case of shear key damage. However, a bridge is not designed to rely on the concrete cover and/or shear keys for primary load resistance and support under any type of loading. Therefore, structural integrity is not significantly affected due to the exceedance of serviceability limit-states. Ultimate limit-states pertinent to seismic performance of a reinforced concrete OSB are (i) buckling of the first longitudinal reinforcement bar (rebar); and (ii) subsequent rupture of a longitudinal rebar. Buckling of a rebar represents serious compromise to the structural integrity of a bridge structure and extreme damage of the core concrete characterizing the limit of economical repair (Goodnight et al. 2016). Rupture or fracture of a previously buckled rebar leads to rapid loss of strength in the supporting column which may cause structural collapse.

Associated with each of the four limit-states described above, representative engineering demand parameters (EDPs) need to be defined to gauge the level of imposed seismic demand on OSBs. Displacement-based EDPs have been found to correlate better to structural damage as compared to force-based EDPs (Priestley et al. 2007). Traditionally, measures of deformation such as displacements, curvatures, drift ratios etc. have been used as EDPs. However, for reinforced concrete flexural members, such as columns, deformations can be directly and most reliably related to structural damage through material strains (Priestley et al. 2007). Despite being good indicators of damage, material strains have not been readily used in the past as EDPs because they are often difficult to predict objectively in finite element models that exhibit softening of section response. Nevertheless, for this project, EDPs relating to the damage/limit-states affecting reinforced concrete bridge columns are defined to be strain-based. This is supported by the finding that localization or softening behavior (leading to loss of objectivity in strain prediction) is not observed for reinforced concrete columns with low expected axial load ratios (typically less than 15% under combined gravity and earthquake loading) which are characteristic of OSBs in

California (Coleman and Spacone 2001). For the EDP relating to damage of shear keys in a bridge, a conventional displacement ratio is used. An EDP is defined to represent the amplitude, i.e., the maximum value in the entire time-history, of the response quantity being monitored for a single earthquake. Therefore, a single value of EDP_k associated with the k^{th} limit-state, LS_k, is recorded from every nonlinear time-history analysis performed.

For the limit state of concrete cover crushing, defined as LS_1, EDP_1 is the maximum value of absolute compressive (negative) strain of any longitudinal rebar in any column.

$$EDP_1 = \max_{col}\left(\max_{bar}\left(\max_{t}\left|\varepsilon_{comp}^{bar}\left(t\right)\right|\right)\right) \tag{7.5}$$

In the above definition, $\varepsilon_{comp}^{bar}(t)$ represents the compressive (negative) strain recorded in a single bar among the outermost layer of rebars in a column (col) at time t. The choice of this EDP comes from experimental observations by Goodnight et al. (2016) corroborating the adequacy of this parameter in prediction of concrete cover crushing (Section 8.3.1).

For LS_2, i.e., the initiation of longitudinal rebar buckling, EDP_2 is the maximum tensile (positive) strain of any longitudinal reinforcement in any column.

$$EDP_2 = \max_{col}\left(\max_{bar}\left(\max_{t}\varepsilon_{tensile}^{bar}\left(t\right)\right)\right) \tag{7.6}$$

$\varepsilon_{tensile}^{bar}(t)$, here, represents the tensile (positive) strain recorded in a single bar in a column (col) at time t. In the same set of experiments as before, Goodnight et al. (2016) also demonstrated that the initiation of, or equivalently a precursor to, buckling of a rebar can be related to the value of the peak tensile strain experienced by the rebar (Section 8.3.2).

For LS_3 representing longitudinal rebar fracture, EDP_3 is the maximum excursion or difference between the maximum tensile (positive) strain and the minimum compressive (negative) strain, the latter following the former, of any longitudinal reinforcement in any column.

$$EDP_3 = \max_{col}\left(\max_{bar}\left(\max_{t}\varepsilon_{tensile}^{bar}\left(t\right) - \min_{t'>t}\varepsilon_{comp}^{bar}\left(t'\right)\right)\right) \tag{7.7}$$

$\varepsilon_{tensile}^{bar}(t)$ and $\varepsilon_{comp}^{bar}(t')$ represent the tensile (positive) strain recorded at time t and the compressive (negative) strain recorded at time t' $(>t)$ in a single bar in a column (col). Duck et al. (2018) (discussed in Section 8.3.3) found that strain excursions encountered by rebars in circular columns during a complete cyclic loading history can be used to predict Plastic Buckling Straightening Fatigue (PBSF), a phenomenon leading to potential fracture of buckled rebars.

A conventional displacement-based EDP is defined for the limit-state, LS_4, representing shear key damage. EDP_4 is the maximum horizontal displacement, Δ^{SK}, recorded at the top of any shear key (SK).

$$EDP_4 = \max_{SK}\left(\max_{t} \Delta^{SK}\left(t\right)\right) \tag{7.8}$$

This choice is dictated by the load-displacement relationships of exterior shear keys, extracted from the experimental work by Megally et al. (2002). These relationships, used to model the hysteretic response of shear keys in the finite element models of the considered bridges (Chapter 4), show distinct branches separated by different levels of horizontal displacement of the top of shear keys. Each such branch corresponds to a level of damage inflicted and/or the formation of a damage mechanism.

The rationale behind the specific choice of an EDP associated with a limit-state is based on a deterministic predictive capacity model (explained later in the report in Chapter 8) for that limit-state. Table 7-1 summarizes the associated EDPs for the four considered limit-states. Figure 7.1 visually describes the chosen EDPs with Bridge B as an example.

Table 7-1 Summary of limit states used in project with associated engineering demand parameters

Limit-state	**Associated Engineering Demand Parameter (*EDP*)**	
LS_1 : Concrete cover crushing	Maximum absolute compressive strain of any longitudinal rebar in any column.	$EDP_1 = \max_{col}\left(\max_{bar}\left(\max_{t}\left\|\varepsilon^{bar}_{comp}(t)\right\|\right)\right)$
LS_2 : Longitudinal rebar buckling	Maximum tensile strain of longitudinal rebar in any column.	$EDP_2 = \max_{col}\left(\max_{bar}\left(\max_{t}\varepsilon^{bar}_{tensile}(t)\right)\right)$
LS_3 : Longitudinal rebar fracture	Maximum difference of tensile (positive) and compressive (negative) strain, the latter following the former, of any longitudinal rebar in any column	$EDP_3 = \max_{col}\left(\max_{bar}\left(\max_{t}\varepsilon^{bar}_{tensile}(t) - \min_{t'>t}\varepsilon^{bar}_{comp}(t')\right)\right)$
LS_4 : Shear key damage	Maximum horizontal displacement of any shear key normalized by the displacement at peak strength.	$EDP_4 = \max_{SK}\left(\max_{t}\Delta^{SK}(t)\right)$

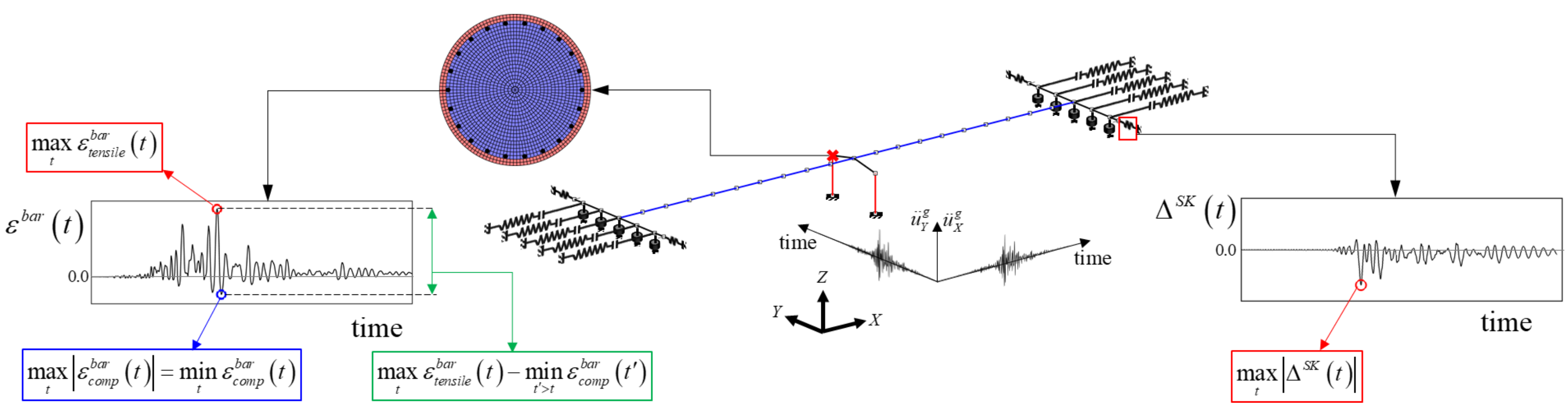

Figure 7.1 Illustration of recorded engineering demand parameters for each limit-state based on Bridge B

7.4 Demand Hazard Analysis

For the k^{th} damage/limit-state and its associated engineering demand parameter, EDP_k, Probabilistic Seismic Demand Hazard Analysis (PSDemHA) involves evaluation of the demand hazard integral given by Eq. (7.4), rewritten as follows

$$\nu_{EDP_k}(\delta) = \int_{IM} P\left[EDP_k > \delta \mid IM = x\right] \cdot \left|d\nu_{IM}(x)\right| \tag{7.9}$$

PSDemHA is mainly carried out in two steps: (i) probabilistic quantification of the conditional seismic demand on the structure given a hazard level that allows computation of the conditional probability, $P\left[EDP_k > \delta \mid IM = x\right]$; and (ii) convolution of the conditional probability of EDP_k exceedance with the site-specific seismic hazard curve $\nu_{IM}(x)$ for the considered structure.

The first step of PSDemHA is accomplished by subjecting the nonlinear finite-element model of the considered structure to selected ensembles of site-specific risk-consistent ground motion records. At each hazard level, response histories of relevant strain/deformation measures (discussed in Section 7.3) resulting from nonlinear time-history analyses of the considered testbed bridges are recorded and the values of each EDP_k associated with the considered set of k limit-states are determined. To predict the structural response, EDP_k, based on a given value, x, of the chosen earthquake intensity measure, , a statistical model is established by fitting a probability distribution to the data of EDP_k, given each hazard level. The two-parameter $(\mu_{\ln EDP_k|IM}, \sigma_{\ln EDP_k|IM})$ lognormal distribution is commonly used to model the scatter in the values of EDP_k conditional on .

The estimated probability distributions of EDP_k at discrete levels are then interpolated/extrapolated over a wide range of values. For this purpose, functional forms capturing the observed growth (versus) of statistics of the lognormal distribution of EDP_k, given , are assumed and least square fitted. Cornell et al. (2002) assumed the following power law growth function for the lognormal median, $\eta_{EDP_k|IM}$, i.e., $e^{\mu_{\ln EDP_k|IM}}$, with respect to .

$$\eta_{EDP_k|IM}(x) = a \cdot x^b \tag{7.10}$$

where a and b are positive constants determined from regression by method of least squares, and x represents values of . The power law assumption is found to accurately capture the growth of the lognormal median in the case of each EDP_k for all considered testbed bridges (shown in Figure 7.2 (a) through Figure 7.17 (a)). Another assumption, forwarded by Cornell et al. (2002) and traditionally used in PBEE, is that of a constant measure of dispersion, $\zeta_{EDP_k|IM}$, i.e., $\sigma_{\ln EDP_k|IM}$, with respect to . However, in the case of each EDP_k for all considered testbed bridges, $\zeta_{EDP_k|IM}$ is observed to consistently decrease, following an initial increase, with increasing levels of (Figure 7.2 (b) through Figure 7.17 (b)). The following functional form is found to reasonably describe this trend and is, therefore, used to predict $\zeta_{EDP_k|IM}$ as a function of (represented by x).

$$\zeta_{EDP_k|IM}\left(x\right)=\frac{c\cdot x}{d}\cdot\frac{f}{f-1+\left(\frac{x}{d}\right)^{f}} \tag{7.11}$$

where, c , d , and f are positive constants obtained by least square fitting. In Eq. (7.11), c and d refer to the maximum value and the argument of the maximum value of $\zeta_{EDP_k|IM}$ respectively, and f controls the post-peak decay of the function. Note that $\zeta_{EDP_k|IM}$ is not the standard deviation of EDP_k given . It is close to the coefficient of variation of EDP_k given for small values of $\zeta_{EDP_k|IM}$. Although $\zeta_{EDP_k|IM}$ is found to first increase and then decrease with increasing , the standard deviation of EDP_k given consistently increases with increasing levels of .

Figure 7.2 (c) through Figure 7.17 (c) show a probabilistic quantification of the conditional seismic demand (characterized by values of EDP_k corresponding to the k^{th} limit-state) imposed on the four testbed bridges given six discrete hazard levels. These figures also show the extrapolation/interpolation of the conditional probability distribution of seismic demand, given any , based on regression analysis (Eq.s (7.10) and (7.11)). The extrapolation/interpolation of the conditional probability distribution of EDP_k is based on the regression model fitted to data available at six discrete hazard levels. The error associated with the predictive models of EDP_k, given , over the range of values spanning these hazard levels is therefore minimum. These ranges of values, for the considered testbed bridges, where EDP_k, given , is most confidently predicted are indicated by the light blue patches in Figure 7.2 (c) through Figure 7.17 (c).

As the second step of PSDemHA, the demand hazard curve of EDP_k is obtained by convolving the conditional probabilities of EDP_k exceeding a specific value (δ), given different levels of , with the corresponding rates of occurrences, $d\nu_{IM}(x)$ (also shown in Figure 7.2 (c) through Figure 7.17 (c)), of these values of at the considered site. The convolution is done numerically over a wide range of , i.e., $S_{a,\,\mathrm{avg}}$, values (10^{-4} g to 5 g) and is not restricted to the light blue range of most confidence. Demand hazard curves, hence obtained, of all considered EDPs are shown in Figure 7.18 through Figure 7.21.

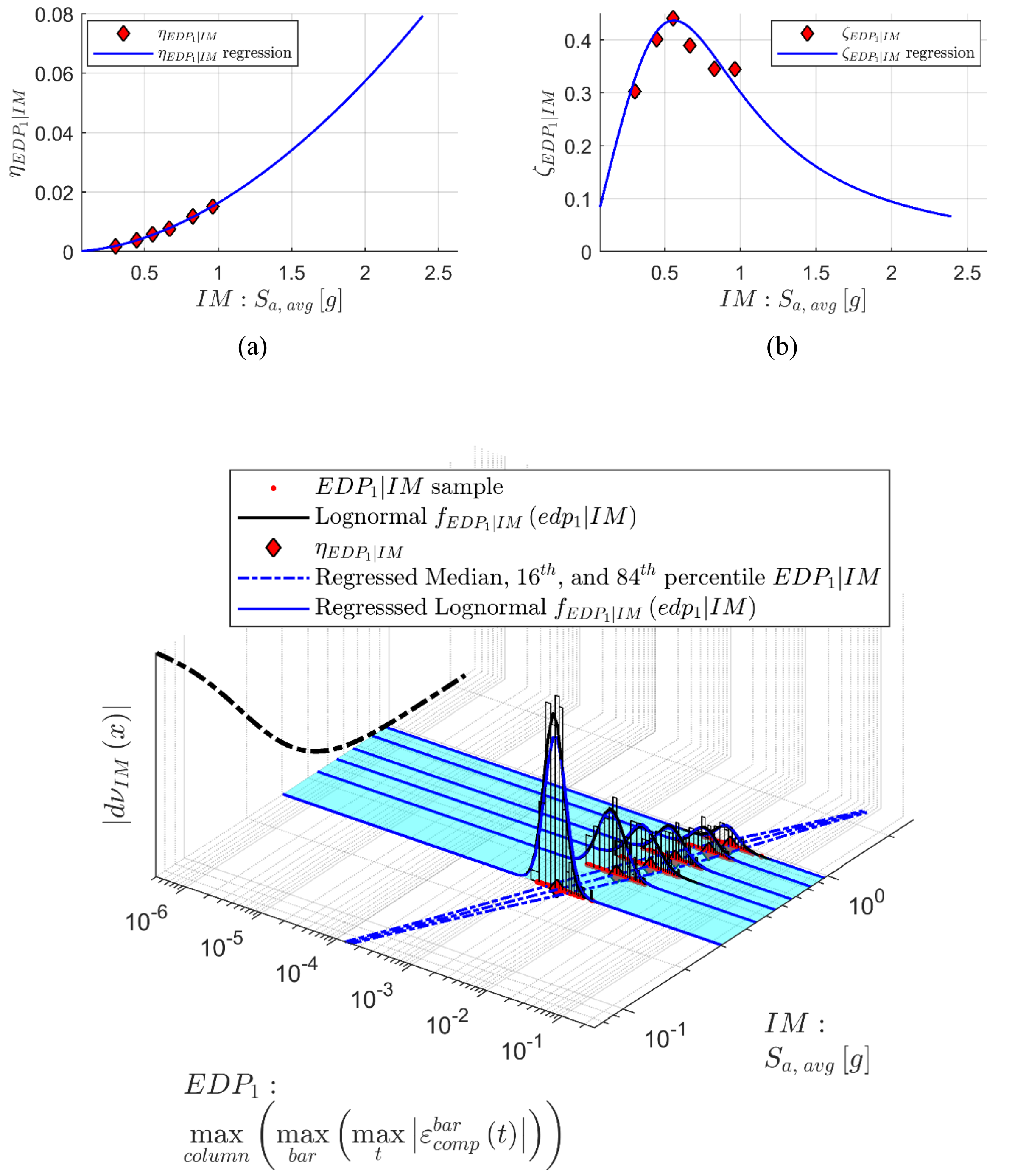

Figure 7.2 Conditional seismic demand on Bridge A, in terms of EDP_1: (a) Regression model for $\eta_{EDP_1|IM}$ versus ; (b) Regression model for $\zeta_{EDP_1|IM}$ versus ; and (c) Conditional probability distributions of EDP_1 given

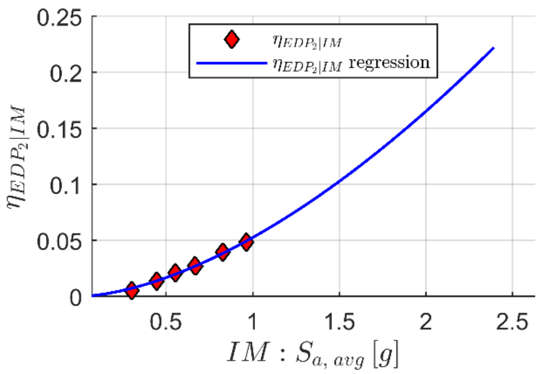

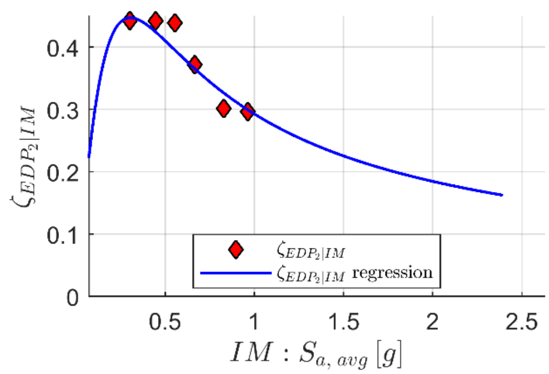

(a)

(b)

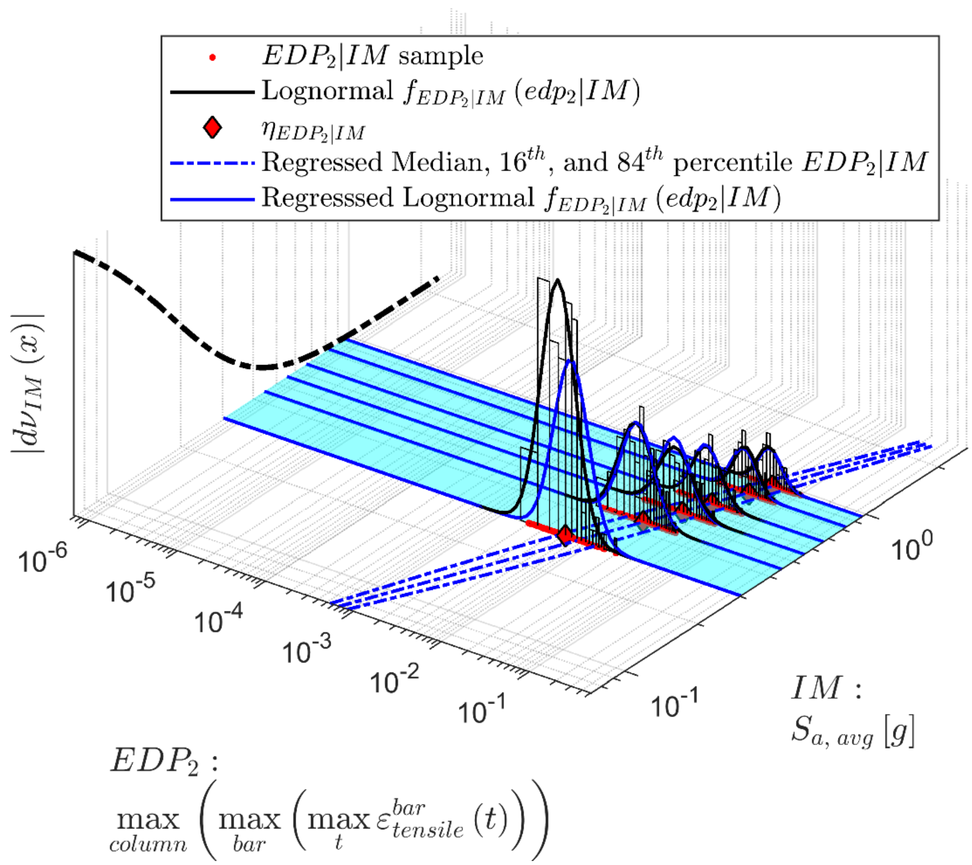

(c)

Figure 7.3 Conditional seismic demand on Bridge A, in terms of EDP_2: (a) Regression model for $\eta_{EDP_2|IM}$ versus ; (b) Regression model for $\zeta_{EDP_2|IM}$ versus ; and (c) Conditional probability distributions of EDP_2 given

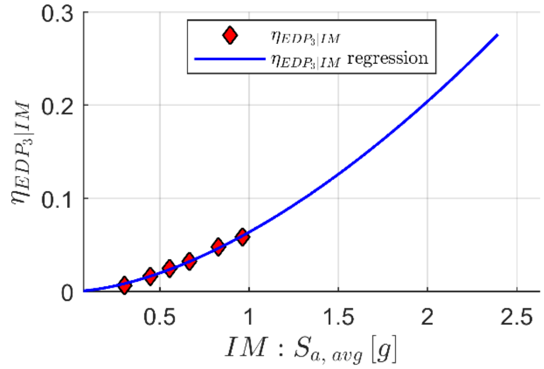

(a)

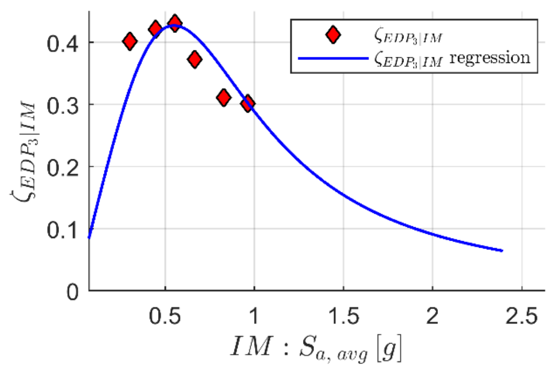

(b)

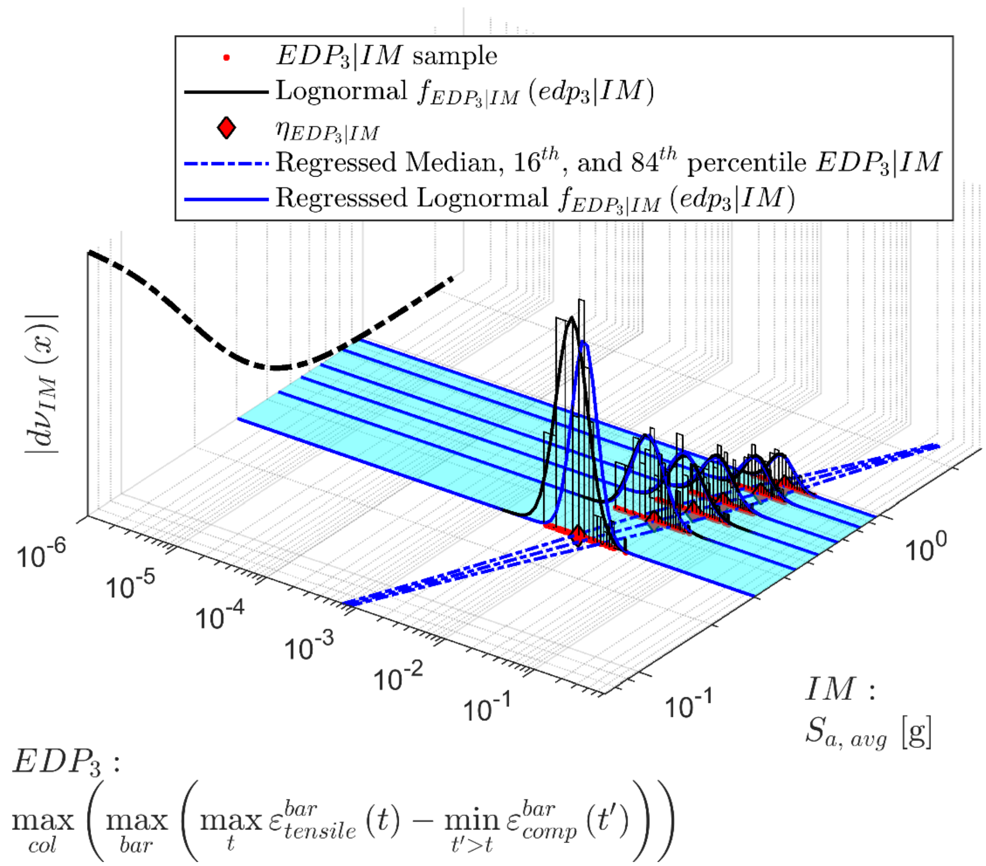

(c)

Figure 7.4 Conditional seismic demand on Bridge A, in terms of EDP_3: (a) Regression model for $\eta_{EDP_3|IM}$ versus ; (b) Regression model for $\zeta_{EDP_3|IM}$ versus ; and (c) Conditional probability distributions of EDP_3 given

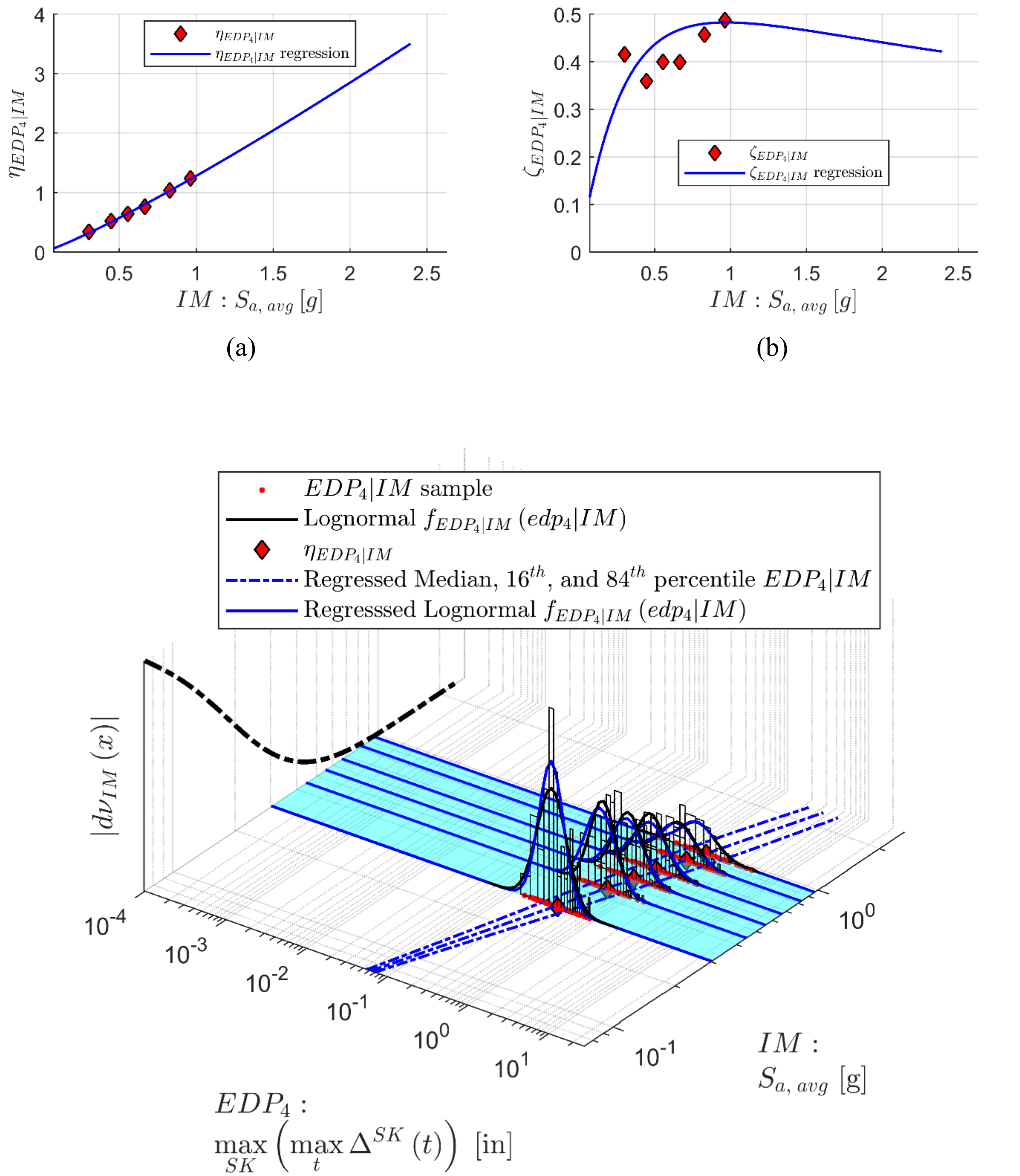

Figure 7.5 Conditional seismic demand on Bridge A, in terms of EDP_4: (a) Regression model for $\eta_{EDP_4|IM}$ versus ; (b) Regression model for $\zeta_{EDP_4|IM}$ versus ; and (c) Conditional probability distributions of EDP_4 given

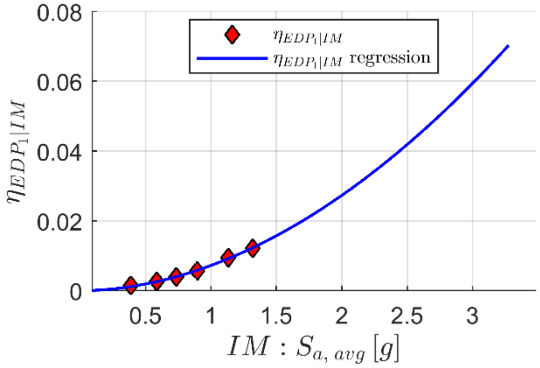

(a)

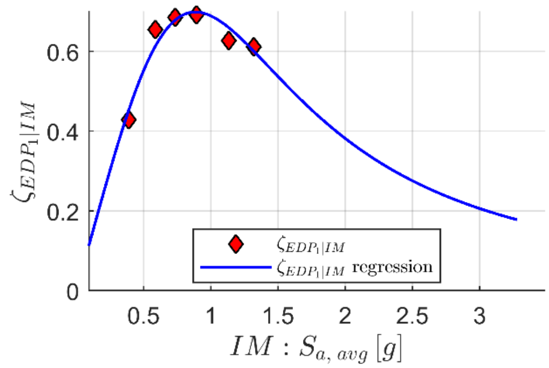

(b)

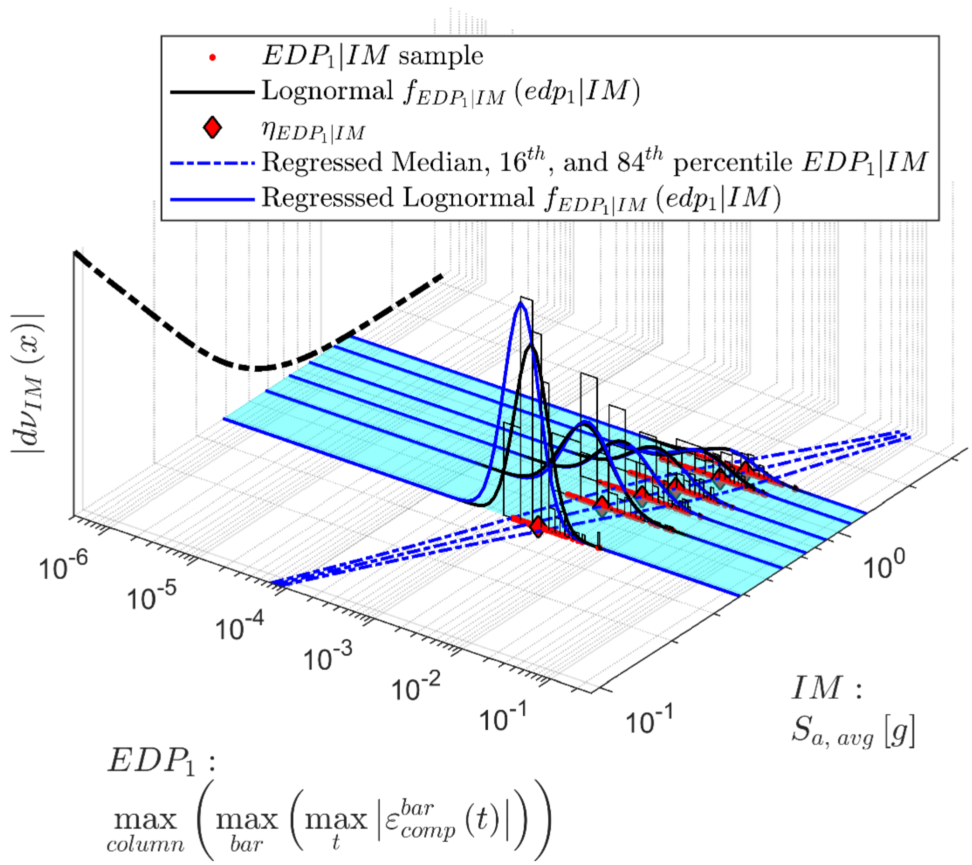

(c)

Figure 7.6 Conditional seismic demand on Bridge B, in terms of EDP_1: (a) Regression model for $\eta_{EDP_1|IM}$ versus ; (b) Regression model for $\zeta_{EDP_1|IM}$ versus ; and (c) Conditional probability distributions of EDP_1 given

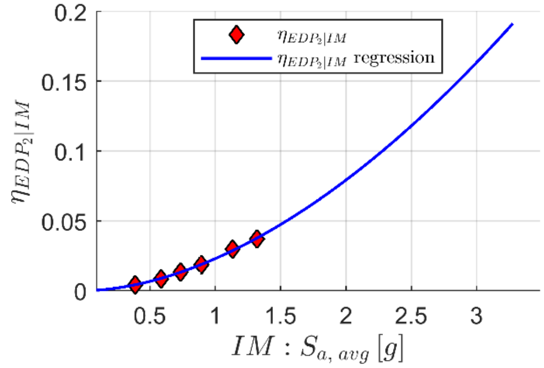

(a)

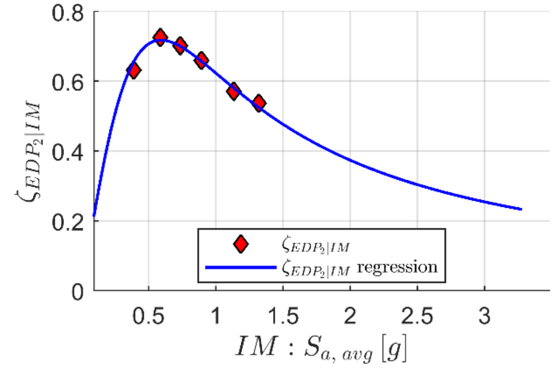

(b)

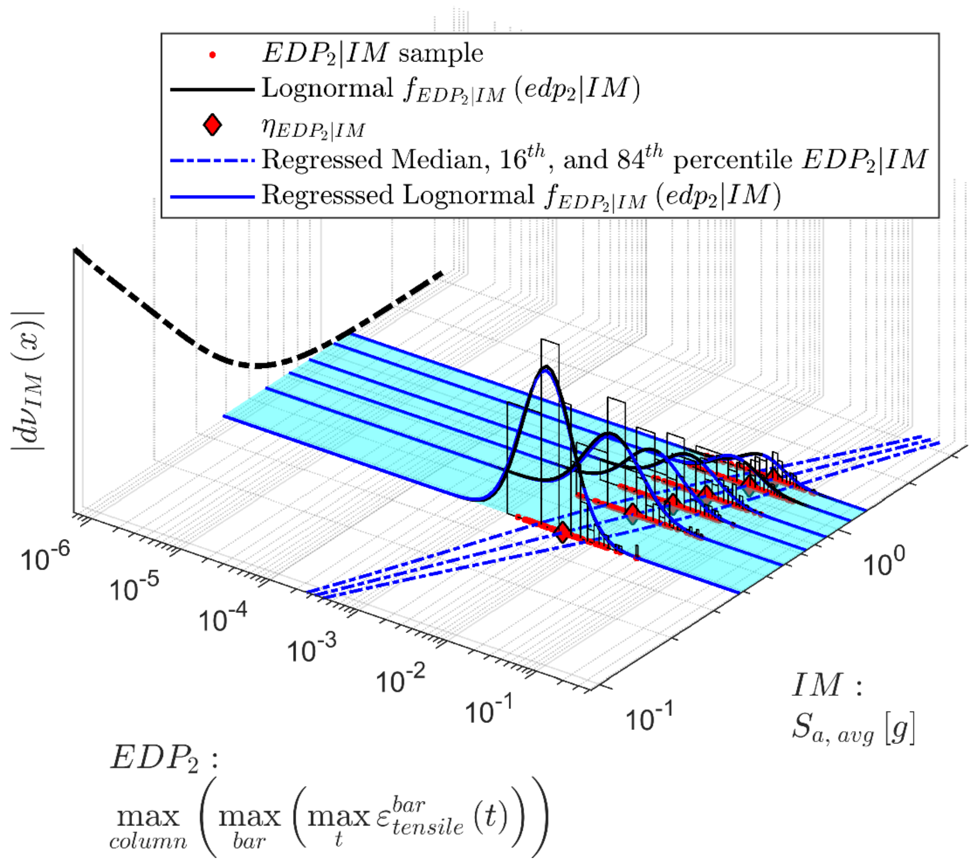

(c)

Figure 7.7 Conditional seismic demand on Bridge B, in terms of EDP_2: (a) Regression model for $\eta_{EDP_2|IM}$ versus ; (b) Regression model for $\zeta_{EDP_2|IM}$ versus ; and (c) Conditional probability distributions of EDP_2 given

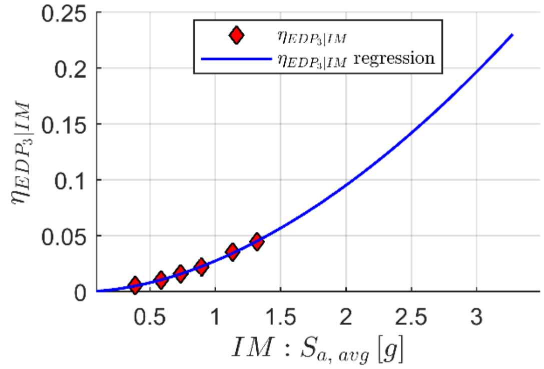

(a)

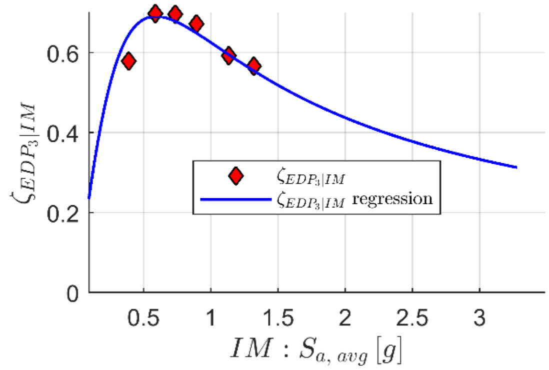

(b)

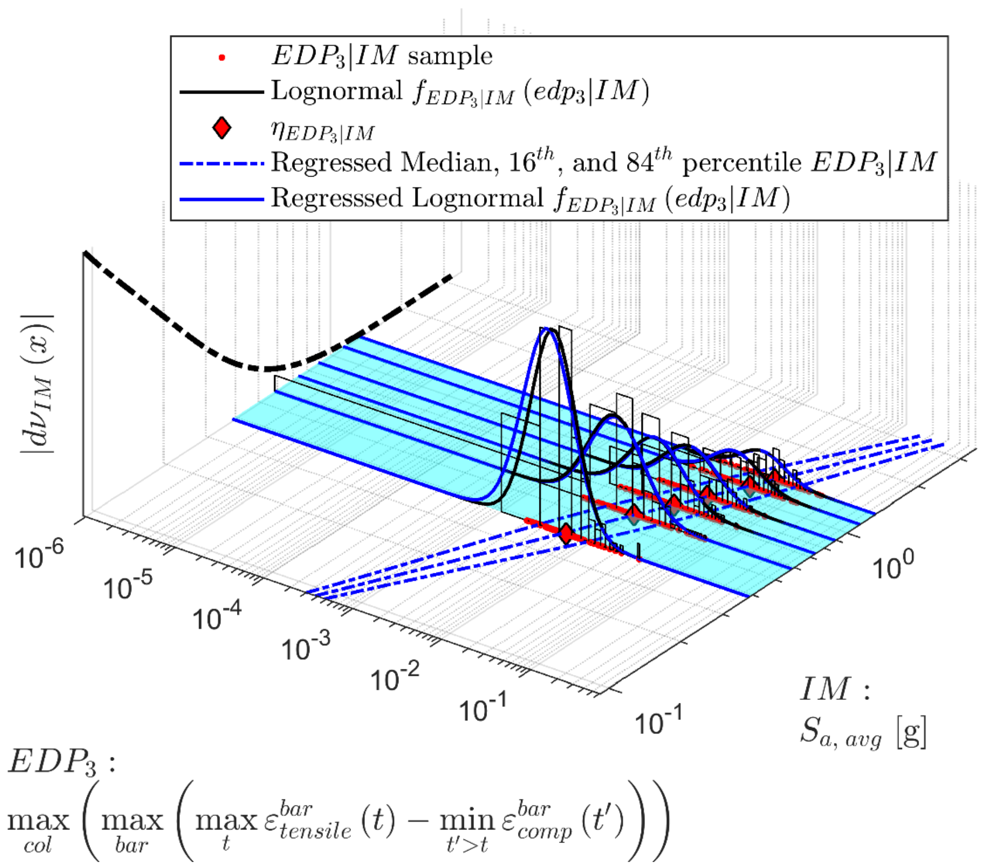

(c)

Figure 7.8 Conditional seismic demand on Bridge B, in terms of EDP_3: (a) Regression model for $\eta_{EDP_3|IM}$ versus ; (b) Regression model for $\zeta_{EDP_3|IM}$ versus ; and (c) Conditional probability distributions of EDP_3 given

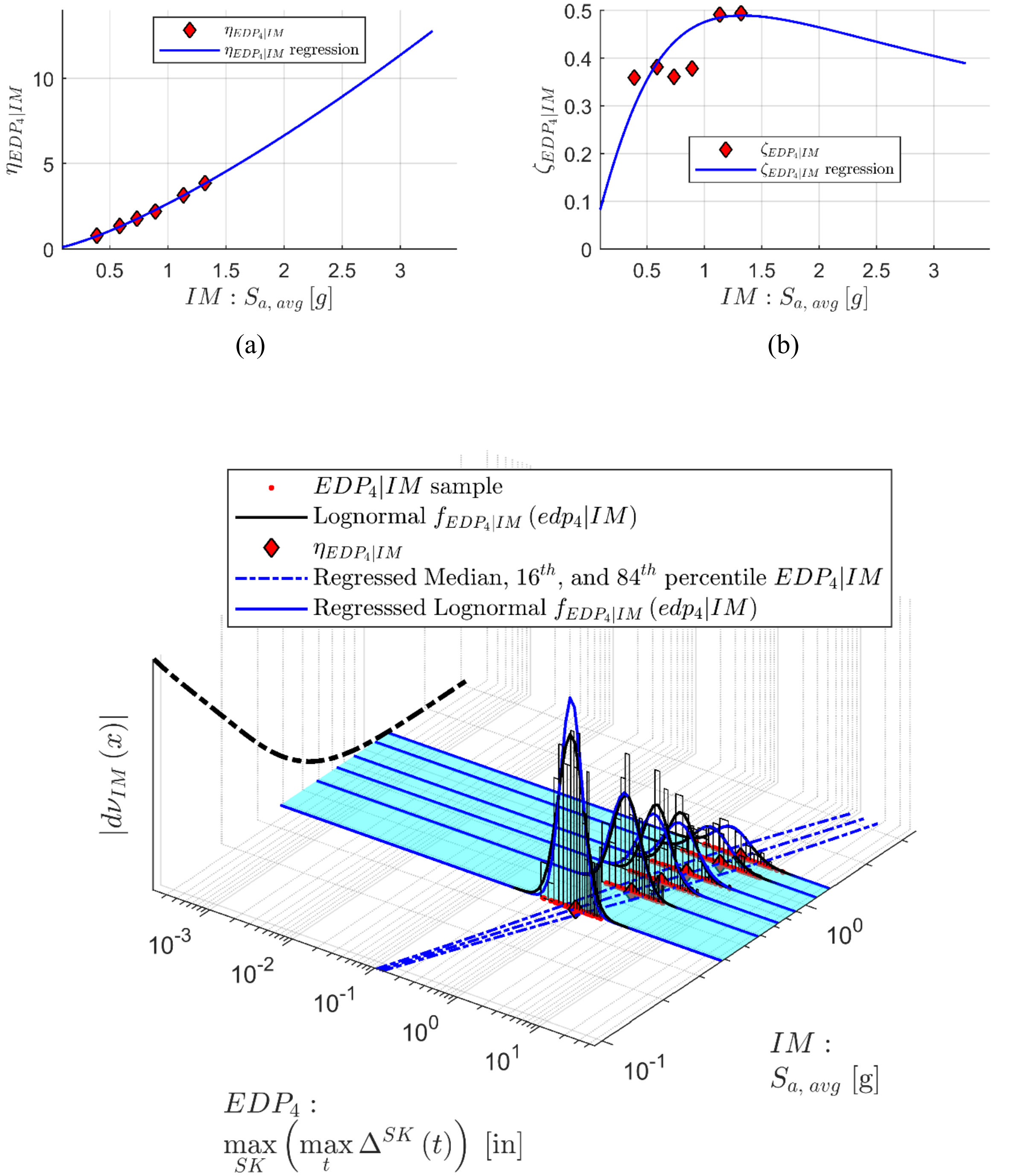

(c)

Figure 7.9 Conditional seismic demand on Bridge B, in terms of EDP_4: (a) Regression model for $\eta_{EDP_4|IM}$ versus ; (b) Regression model for $\zeta_{EDP_4|IM}$ versus ; and (c) Conditional probability distributions of EDP_4 given

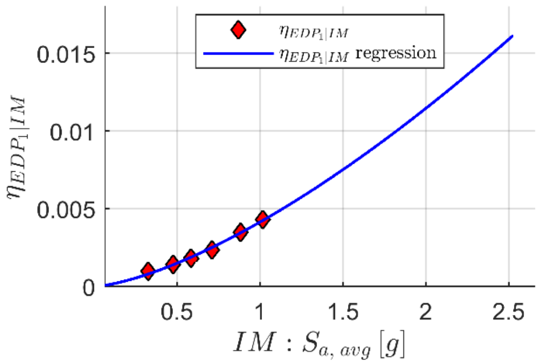

(a)

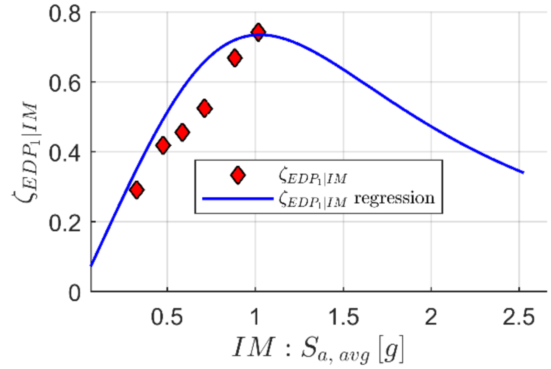

(b)

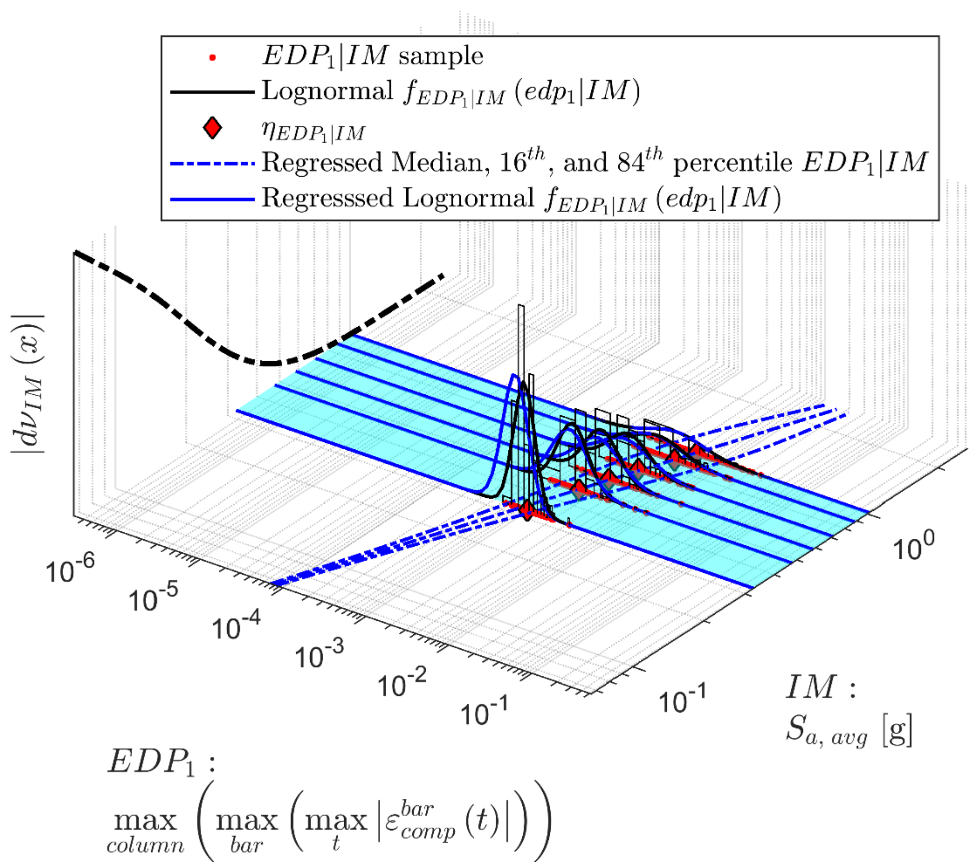

(c)

Figure 7.10 Conditional seismic demand on Bridge C, in terms of EDP_1: (a) Regression model for $\eta_{EDP_1|IM}$ versus ; (b) Regression model for $\zeta_{EDP_1|IM}$ versus ; and (c) Conditional probability distributions of EDP_1 given

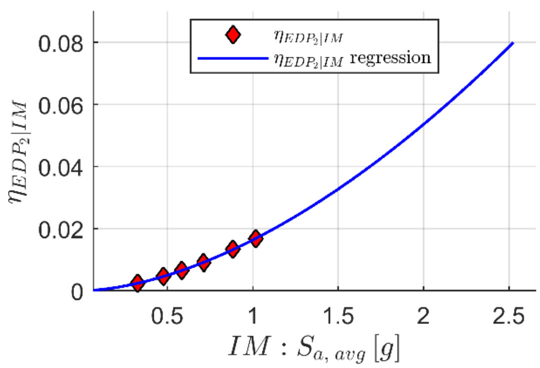

(a)

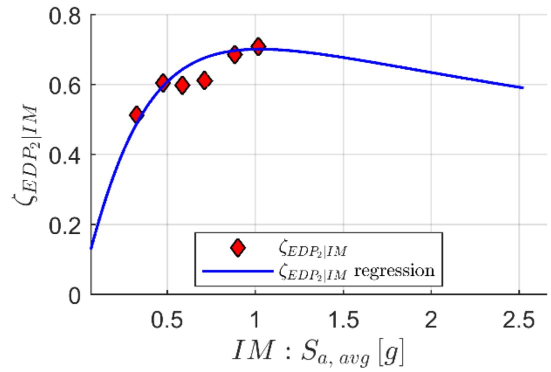

(b)

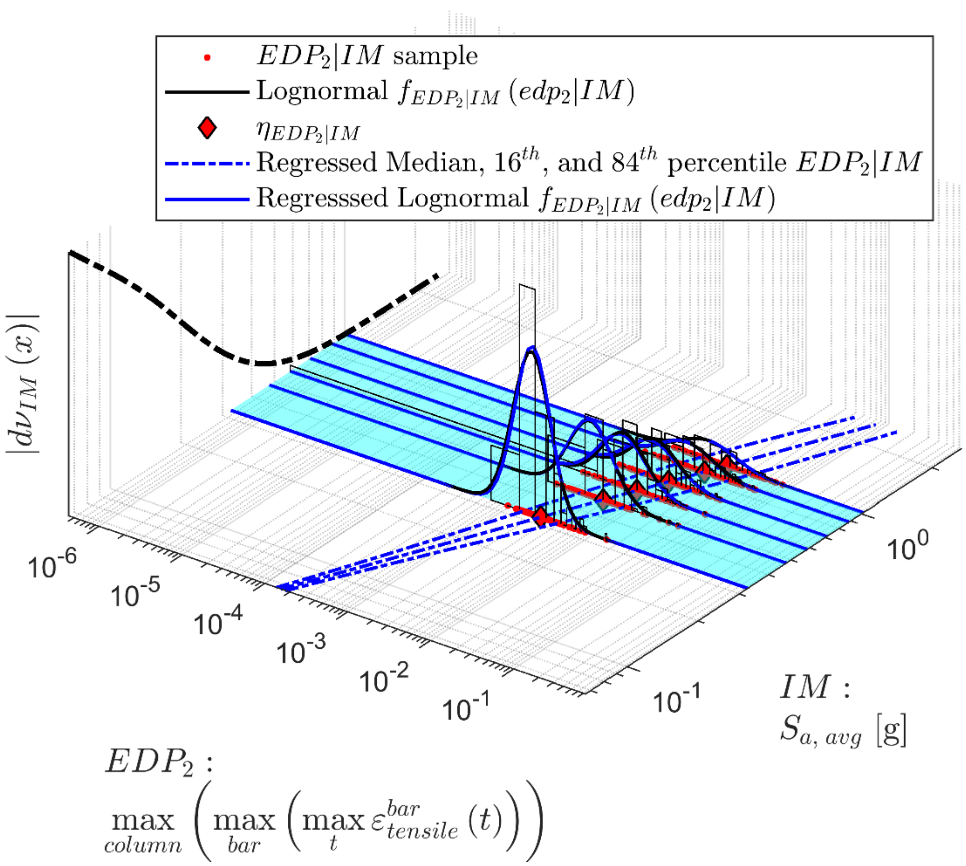

(c)

Figure 7.11 Conditional seismic demand on Bridge C, in terms of EDP_2: (a) Regression model for $\eta_{EDP_2|IM}$ versus ; (b) Regression model for $\zeta_{EDP_2|IM}$ versus ; and (c) Conditional probability distributions of EDP_2 given

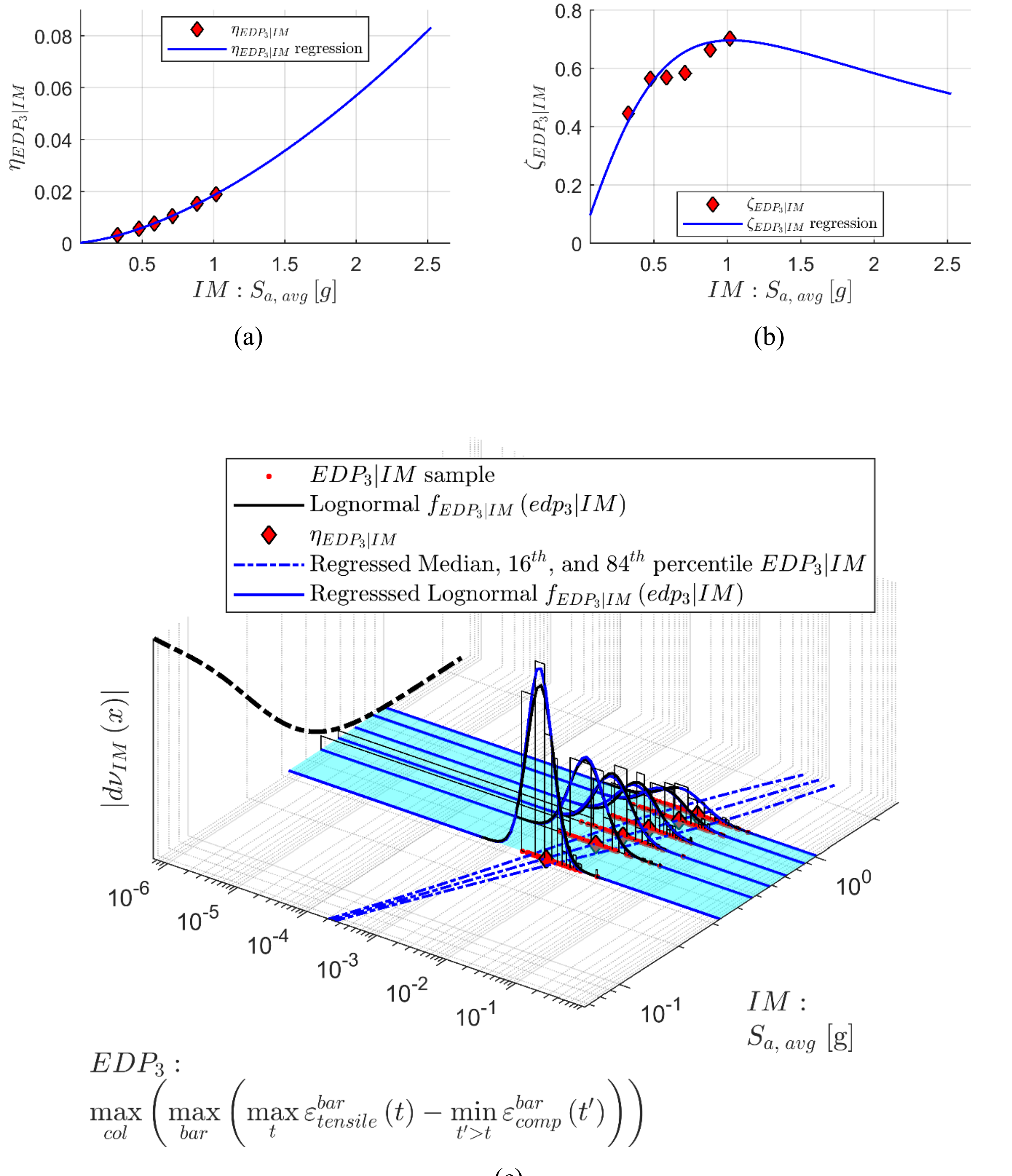

Figure 7.12 Conditional seismic demand on Bridge C, in terms of EDP_3: (a) Regression model for $\eta_{EDP_3|IM}$ versus ; (b) Regression model for $\zeta_{EDP_3|IM}$ versus ; and (c) Conditional probability distributions of EDP_3 given

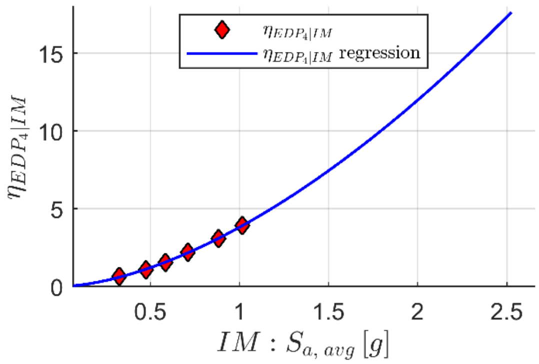

(a)

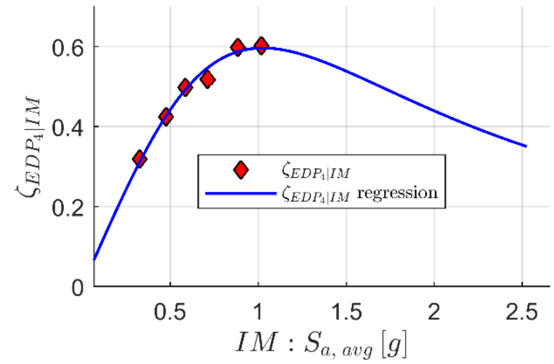

(b)

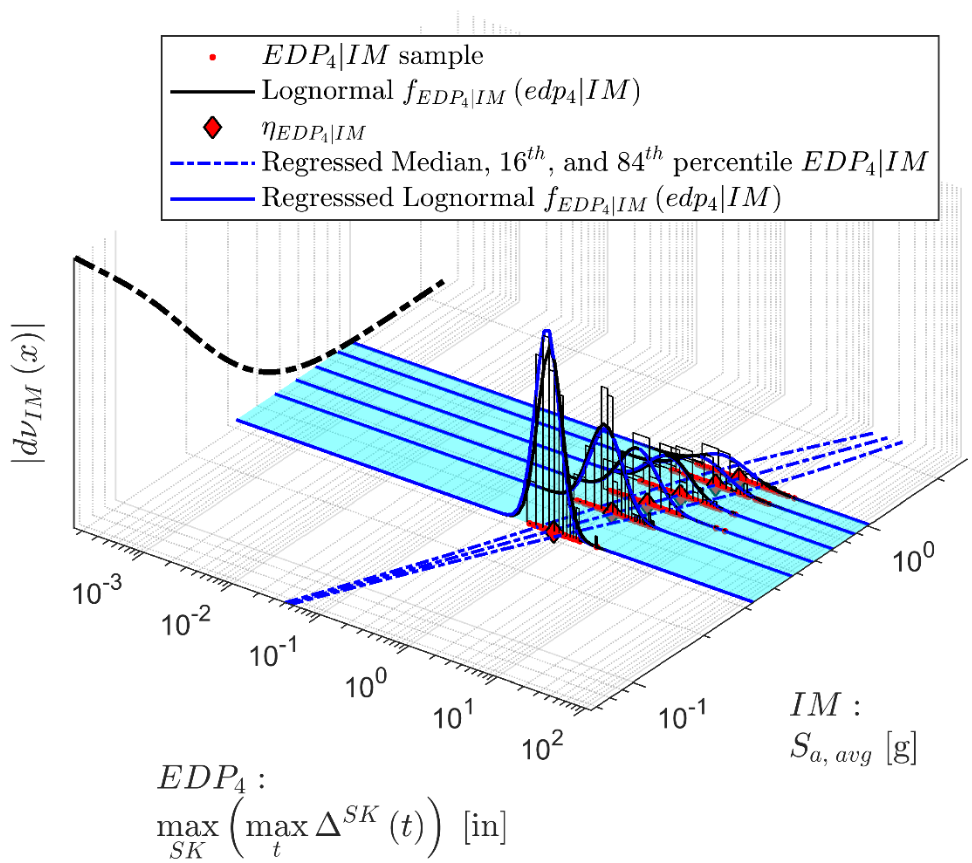

(c)

Figure 7.13 Conditional seismic demand on Bridge C, in terms of EDP_4: (a) Regression model for $\eta_{EDP_4|IM}$ versus ; (b) Regression model for $\zeta_{EDP_4|IM}$ versus ; and (c) Conditional probability distributions of EDP_4 given

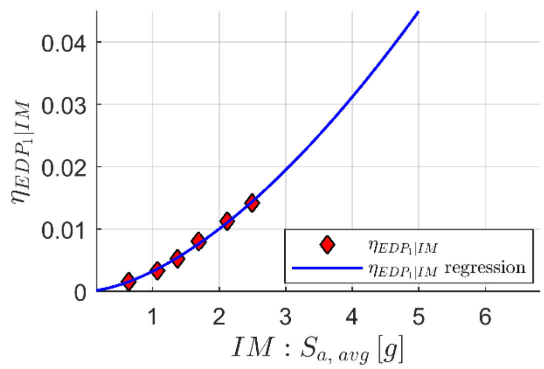

(a)

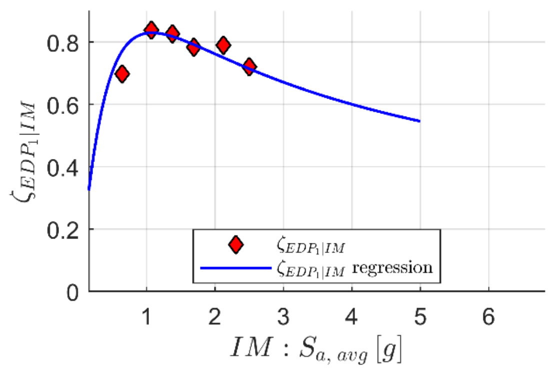

(b)

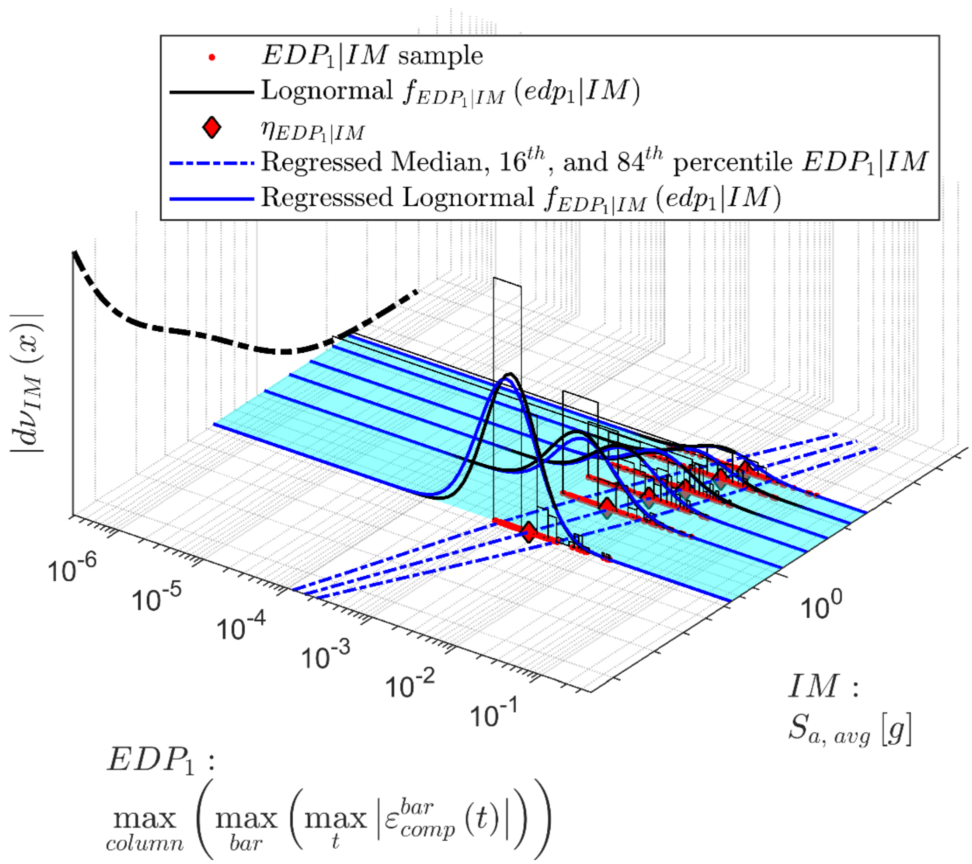

(c)

Figure 7.14 Conditional seismic demand on Bridge MAOC, in terms of EDP_1: (a) Regression model for $\eta_{EDP_1|IM}$ versus ; (b) Regression model for $\zeta_{EDP_1|IM}$ versus ; and (c) Conditional probability distributions of EDP_1 given

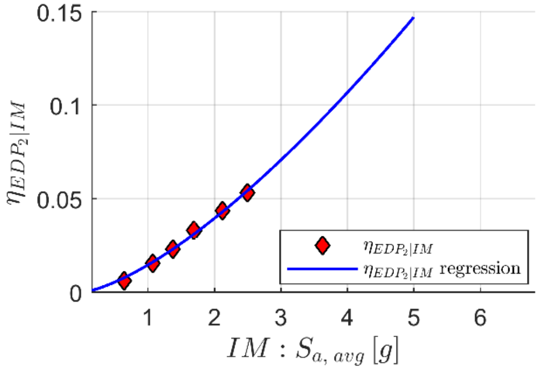

(a)

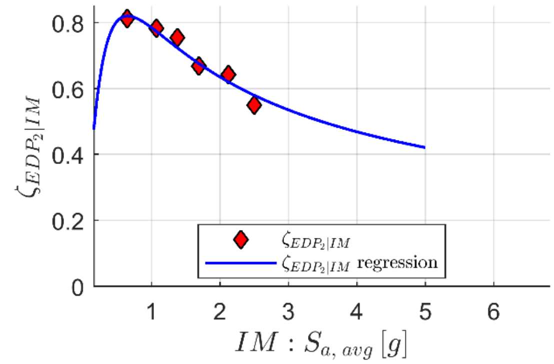

(b)

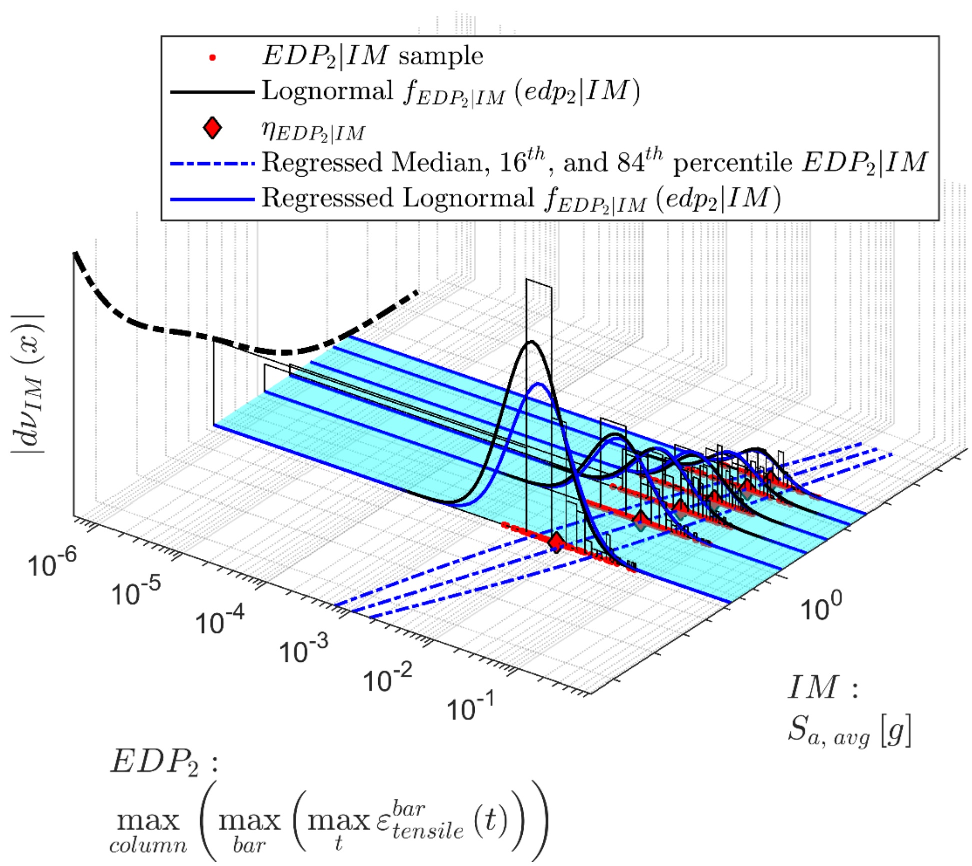

(c)

Figure 7.15 Conditional seismic demand on Bridge MAOC, in terms of EDP_2: (a) Regression model for $\eta_{EDP_2|IM}$ versus ; (b) Regression model for $\zeta_{EDP_2|IM}$ versus ; and (c) Conditional probability distributions of EDP_2 given

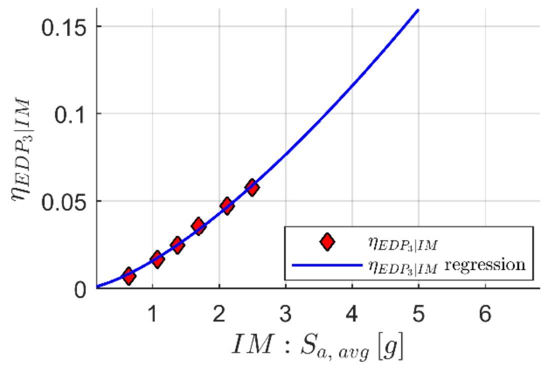

(a)

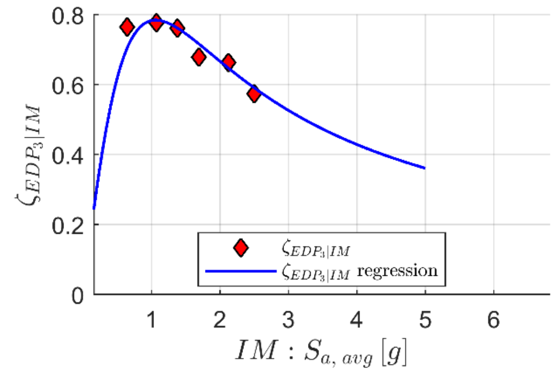

(b)

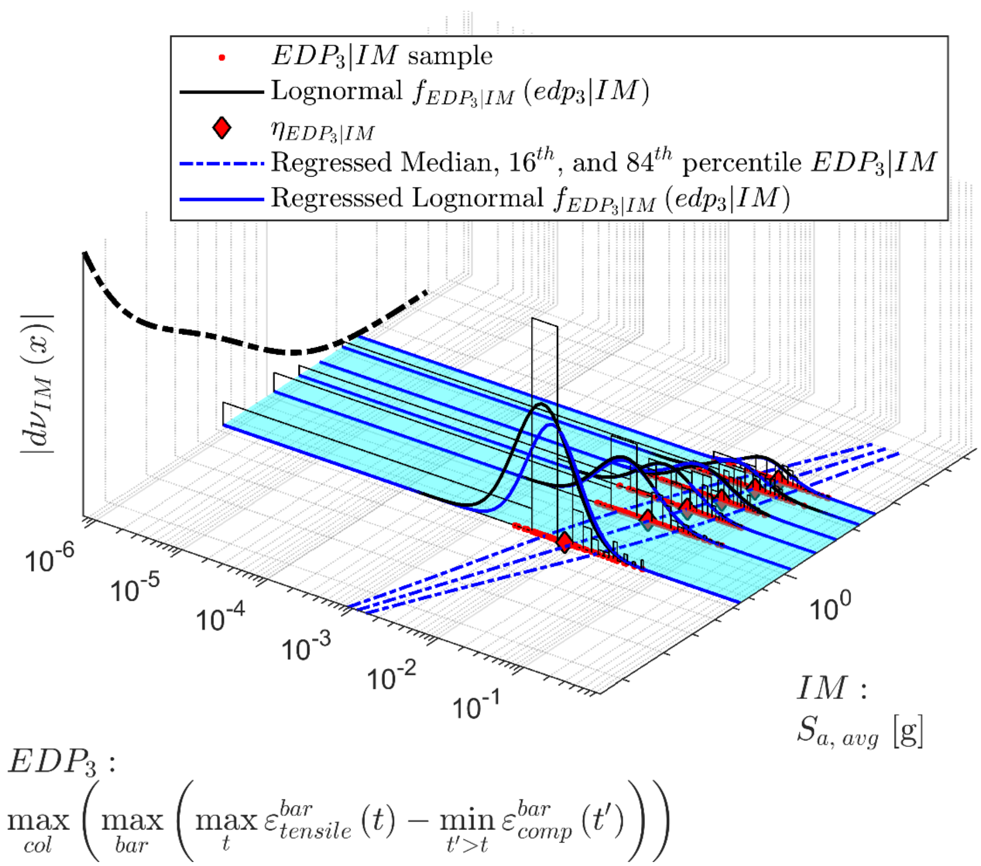

(c)

Figure 7.16 Conditional seismic demand on Bridge MAOC, in terms of EDP_3: (a) Regression model for $\eta_{EDP_3|IM}$ versus ; (b) Regression model for $\zeta_{EDP_3|IM}$ versus ; and (c) Conditional probability distributions of EDP_3 given

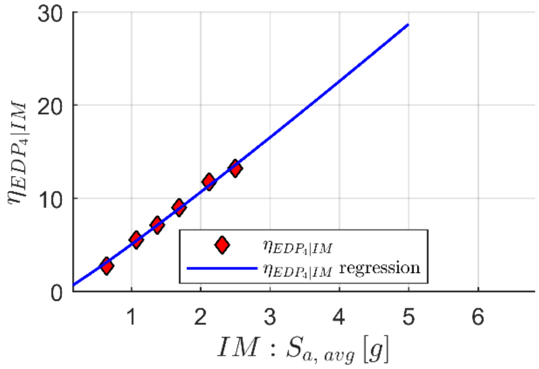

(a)

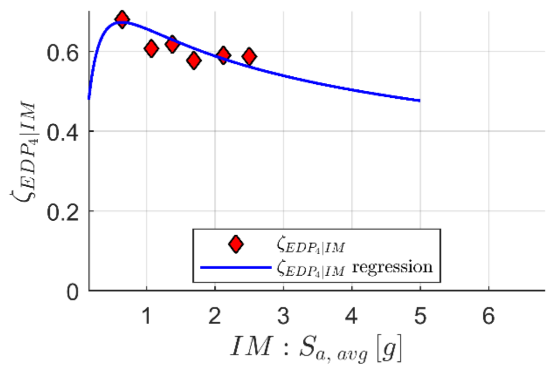

(b)

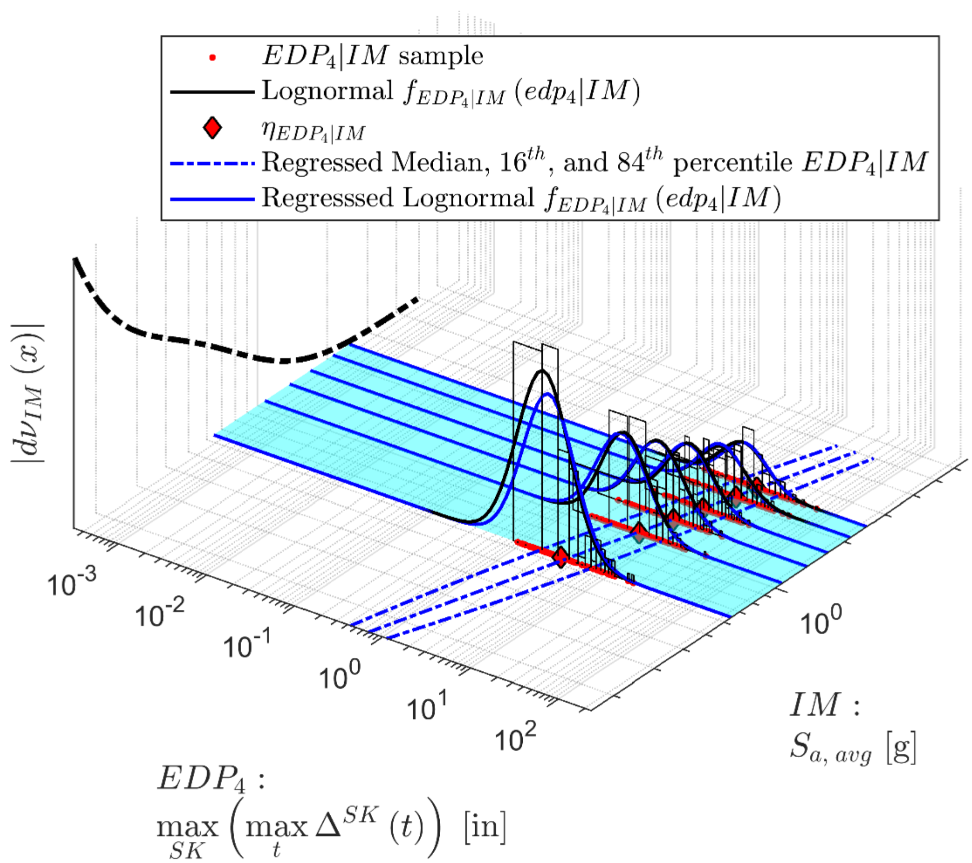

(c)

Figure 7.17 Conditional seismic demand on Bridge MAOC, in terms of EDP_4: (a) Regression model for $\eta_{EDP_4|IM}$ versus ; (b) Regression model for $\zeta_{EDP_4|IM}$ versus ; and (c) Conditional probability distributions of EDP_4 given

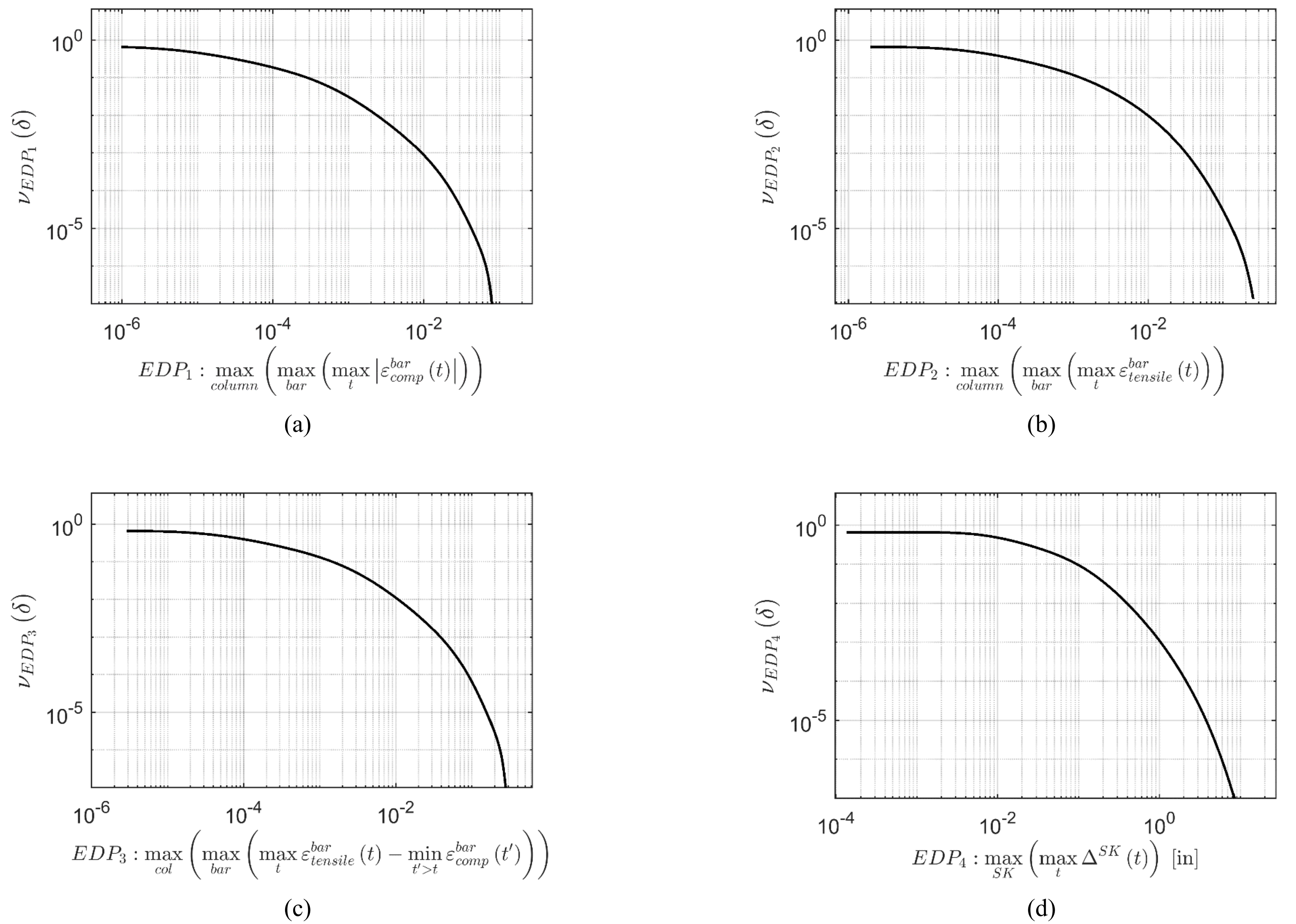

Figure 7.18 Demand hazard curves for Bridge A: (a) EDP_1; (b) EDP_2; (c) EDP_3; and (d) EDP_4

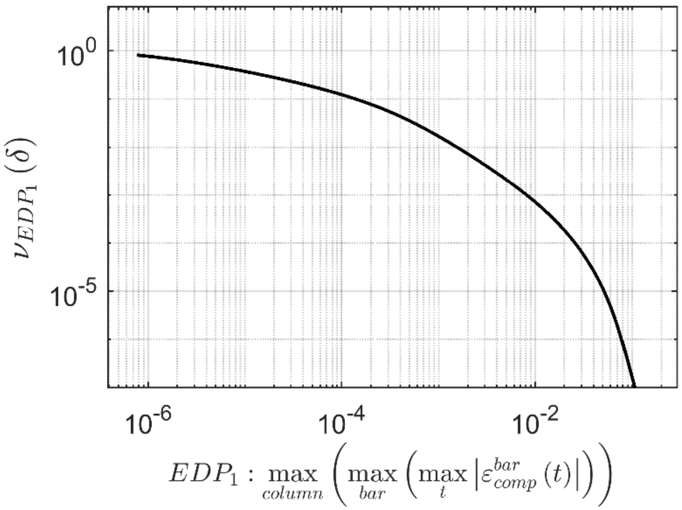

(a)

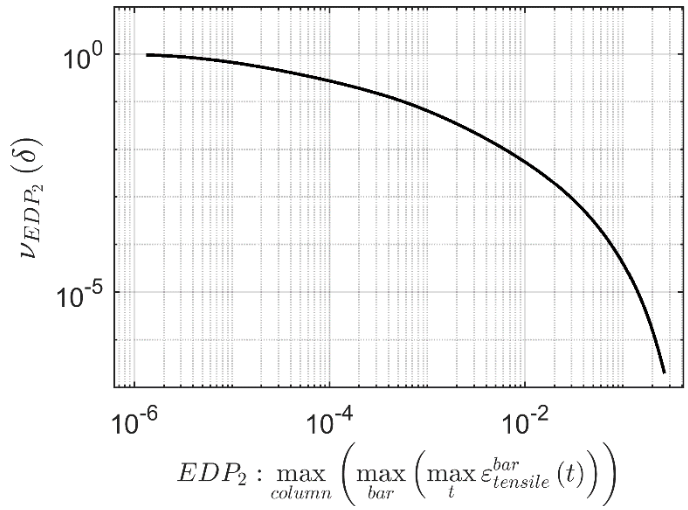

(b)

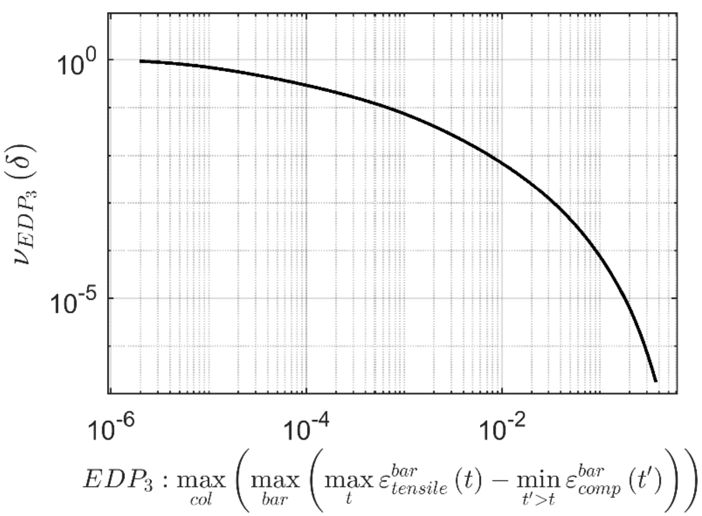

(c)

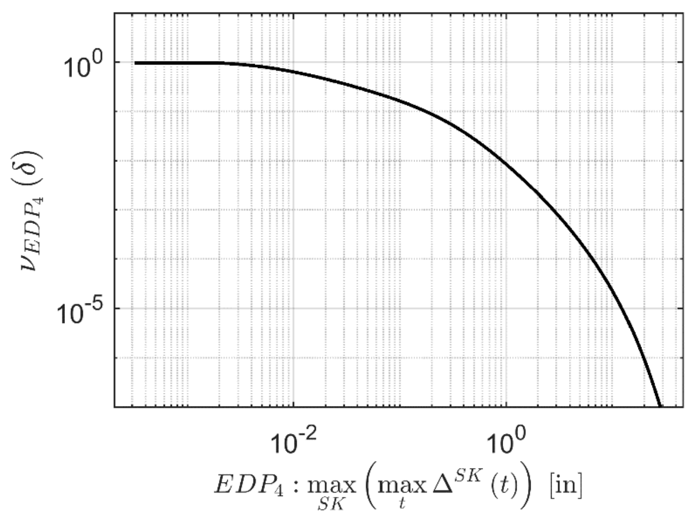

(d)

Figure 7.19 Demand hazard curves for Bridge B: (a) EDP_1; (b) EDP_2; (c) EDP_3; and (d) EDP_4

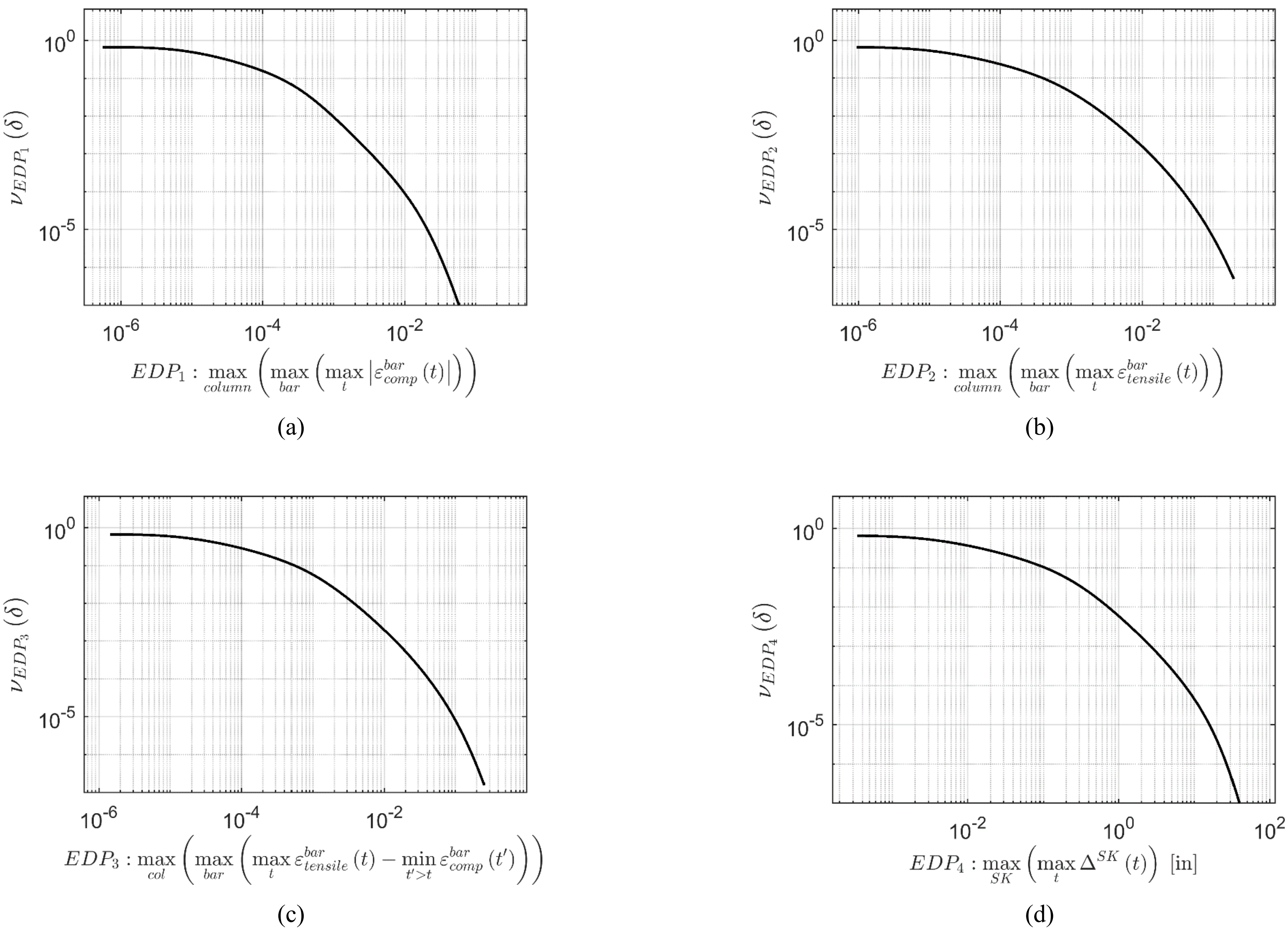

Figure 7.20 Demand hazard curves for Bridge C: (a) EDP_1; (b) EDP_2; (c) EDP_3; and (d) EDP_4

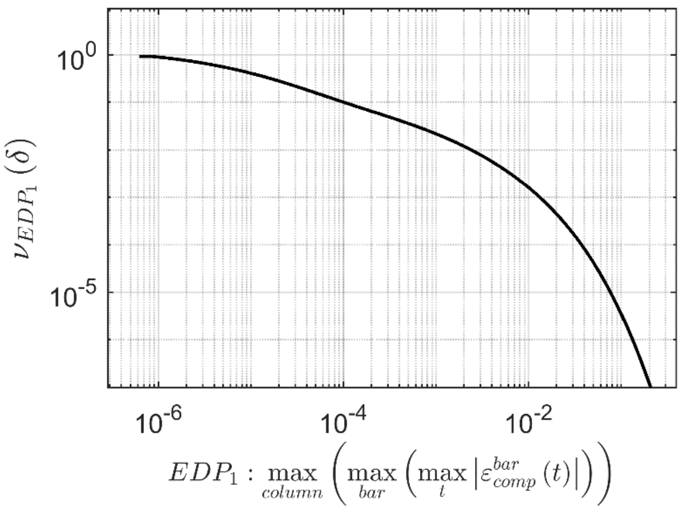

(a)

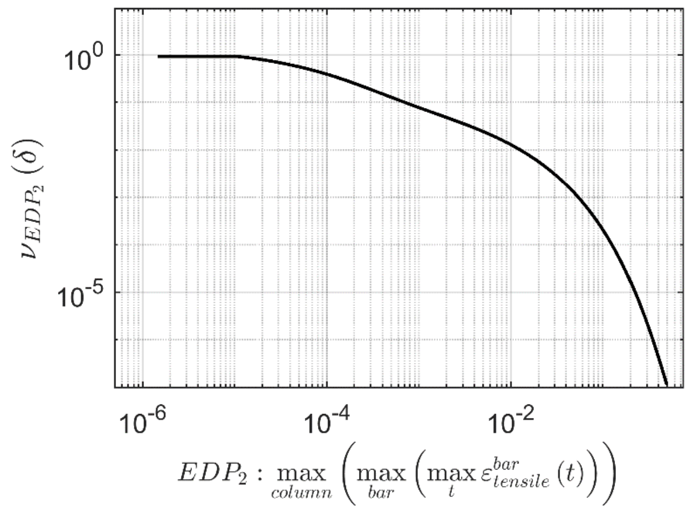

(b)

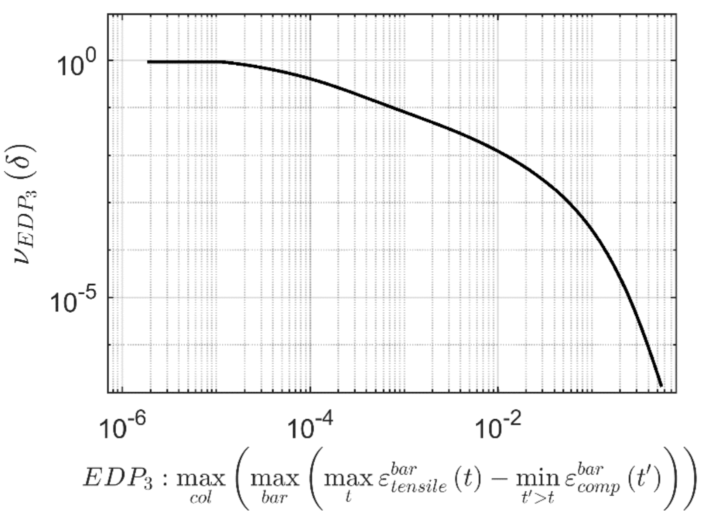

(c)

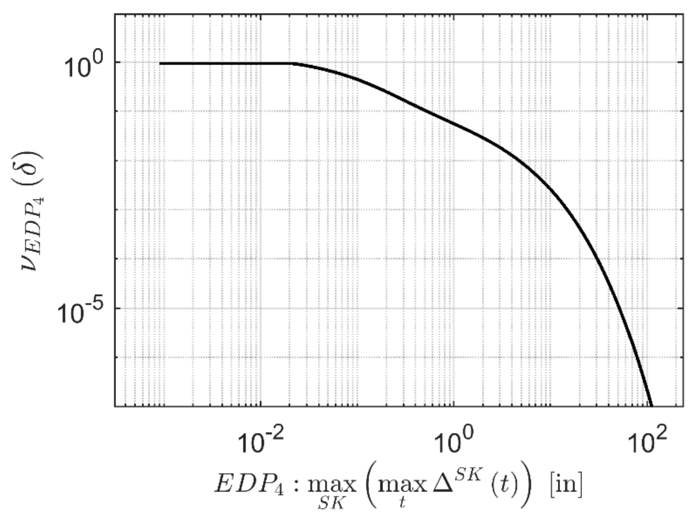

(d)

Figure 7.21 Demand hazard curves for Bridge MAOC: (a) EDP_1; (b) EDP_2; (c) EDP_3; and (d) EDP_4

7.5 Disaggregation of Seismic Demand Hazard w.r.t. Seismic Intensity Measure

Seismic demand hazard associated with the EDPs of interest for the testbed bridges are computed by aggregating, as per Eq. (7.9), the contributions from all possible levels. The MAR of exceeding a specific value, δ, of any EDP can consequently be disaggregated into the contributions from different levels of . Such a disaggregation provides additional insight into the distribution of causative values leading to a specific level of demand hazard. The conditional probability distribution of , given an EDP, say EDP_k, exceeds a value, δ, with a specific MAR, $\nu_{EDP_k}(\delta)$, is computed as follows

$$f_{IM|EDP_k>\delta}\left(x\,|\,\delta\right)=\frac{P\left[EDP_k>\delta\,|\,IM=x\right]\cdot\left|d\nu_{IM}\left(x\right)\right|}{\nu_{EDP_k}\left(\delta\right)} \tag{7.12}$$

Figure 7.22 through Figure 7.25 present disaggregation results for three points on the demand hazard curves of the EDPs of interest for all considered testbed bridges. These three points correspond to mean RPs (reciprocal of MARs) of EDP exceedance equal to 72 years, 975 years, and 4975 years. The three points are chosen to span a reasonably wide range of probabilities of EDP exceedance starting from 50 % to 1 % in an exposure time of 50 years. The ordinate of each disaggregation plot on the right-hand-side shows the conditional probability distribution, i.e., Eq. (7.12), of , given a specific level of EDP_k exceedance. The ordinate along the left-hand-side of the same plot shows the site-specific seismic hazard curve. Also marked in each of these plots is the value of corresponding to the same MAR of exceedance as given by $\nu_{EDP_k}(\delta)$.

The shape of the conditional distribution of , given a specific level of demand hazard for any EDP_k, is a result of the competing effects between the two terms in the numerator of Eq. (7.12) as a function of . "Very" small values of , despite having "high" rates of occurrence, $|\,d\nu_{IM}(x)\,|$, make negligible contributions to the demand hazard associated with a "not-too-small" value, δ, of EDP_k. Values of EDP_k generated at these "low" levels of earthquake intensity are much smaller than the specific demand value δ. Thus, the conditional probability of EDP_k exceeding δ, given "very" small values of , is almost zero, i.e., $P\left[EDP_k>\delta\,|\,IM\right]\approx 0$. As levels are increased, their rates of occurrence, $|\,d\nu_{IM}(x)\,|$, decrease. On the other hand, structural response amplification due to increasing levels of leads to increase in $P\left[EDP_k > \delta \mid IM\right]$. At first, this increase in the conditional probability of EDP_k exceedance outweighs the decrease in $|d\nu_{IM}(x)|$. As a result, contribution to demand hazard increases with increase in . This continues up to a point where values of start becoming "somewhat" rare, and the decrease in $|d\nu_{IM}(x)|$ starts to subdue the growth in $P\left[EDP_k > \delta \mid IM\right]$. Although structural seismic response is greatly amplified with increasing levels of seismic intensity, the rates of occurrence of "very" large values are "too" small, i.e., $|d\nu_{IM}(x)| \approx 0$. As a result, the contribution to demand hazard from "very" large and "too" rare values of also becomes negligible.

Also, as noted from the disaggregation curves, higher levels of earthquake intensity contribute more to the exceedance of larger values of any EDP_k. This is shown by the gradual shift of the center-of-mass of the conditional probability distributions of causative towards higher values of , as the hazard associated with increasing values of EDP_k are disaggregated. These probability distributions of causative also get fatter with an increase in the value of EDP_k, implying more variability in earthquake intensity leading to higher levels of seismic demand.

Furthermore, it is observed that contribution to a specific level of demand hazard comes from a certain range of values. It is important to note that contribution to a given MAR (or mean RP) of EDP exceedance comes not only from the value with the same MAR (or mean RP) of exceedance, but also from values with lower MARs and from those with higher MARs. It is also worthwhile to notice and appreciate that, for the considered testbed bridges, a significant part of the contribution to the considered levels of demand hazard of all EDPs in question does come from the range of most confidence (indicated by the light blue patch in Figure 7.22 through Figure 7.25).

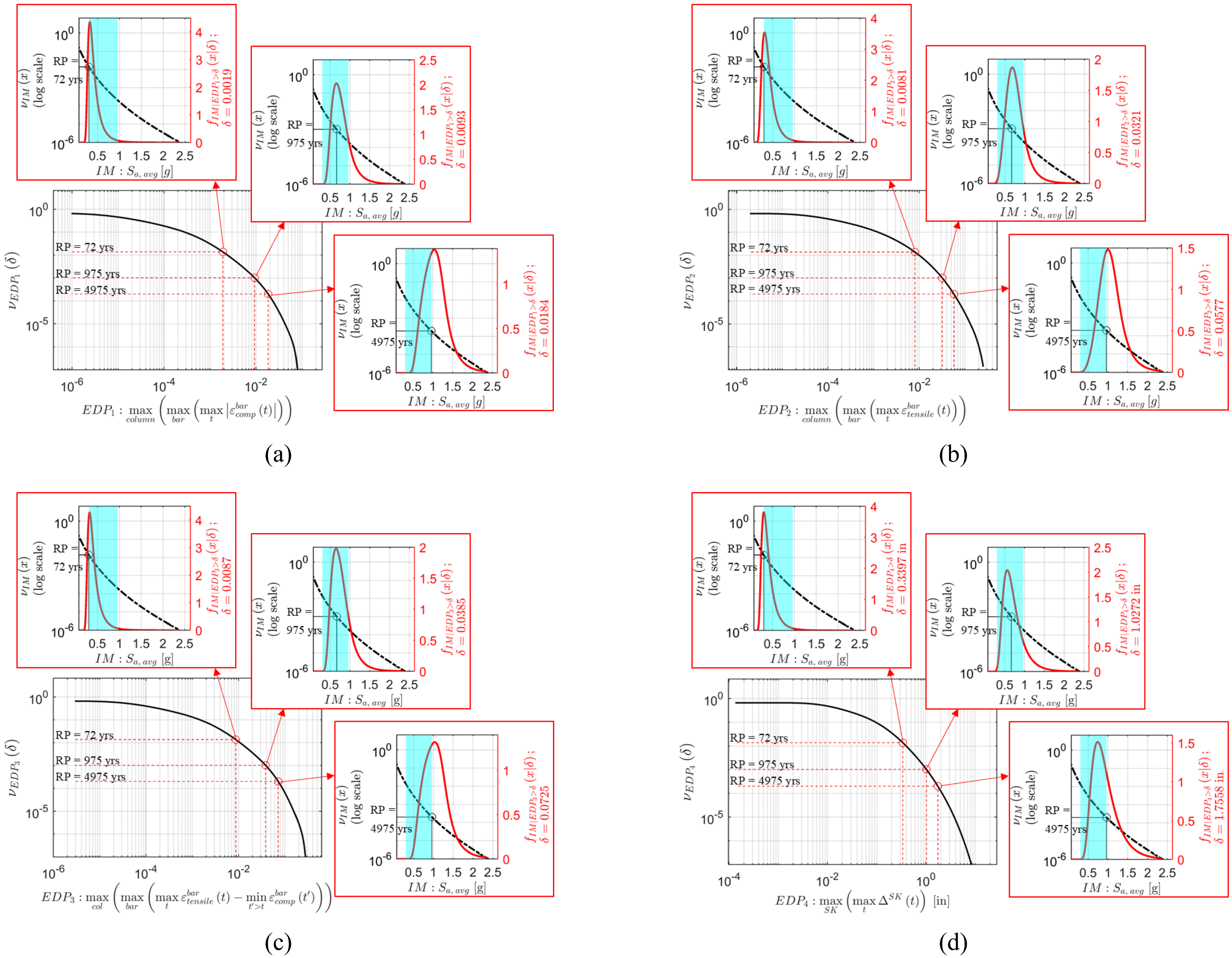

Figure 7.22 disaggregation of demand hazard for Bridge A: (a) EDP_1; (b) EDP_2; (c) EDP_3; and (d) EDP_4

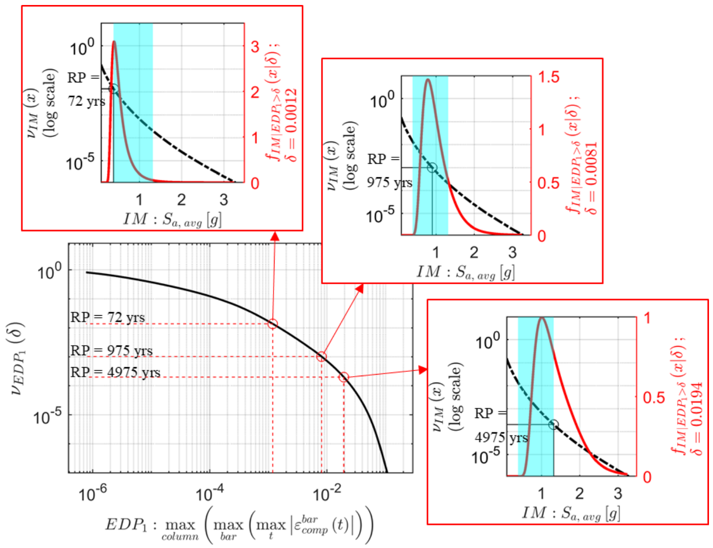

(a)

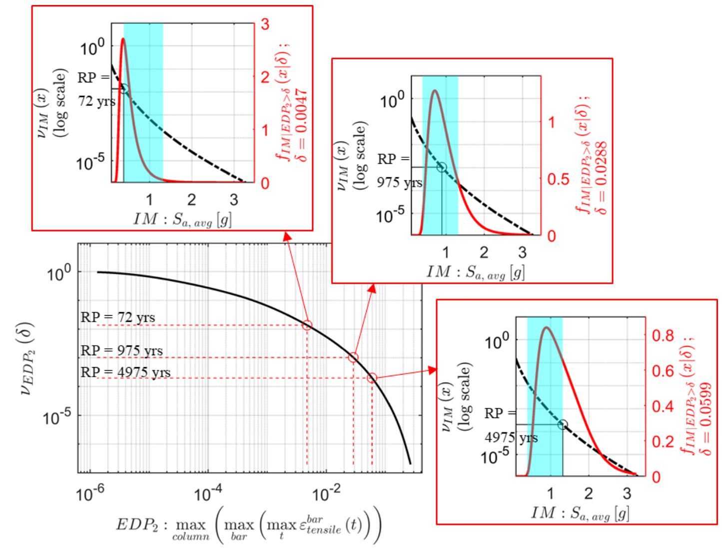

(b)

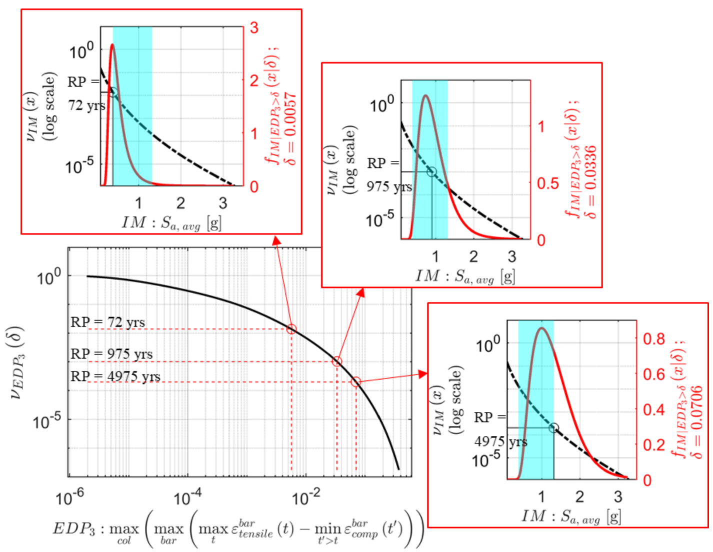

(c)

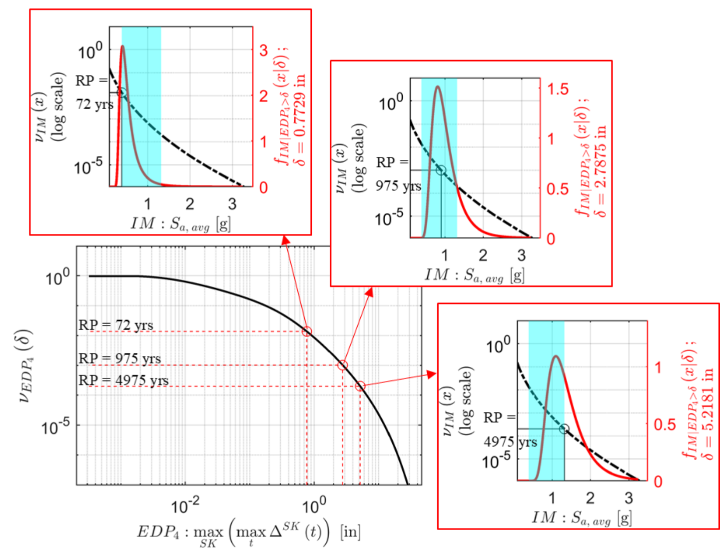

(d)

Figure 7.23 disaggregation of demand hazard for Bridge B: (a) EDP_1; (b) EDP_2; (c) EDP_3; and (d) EDP_4

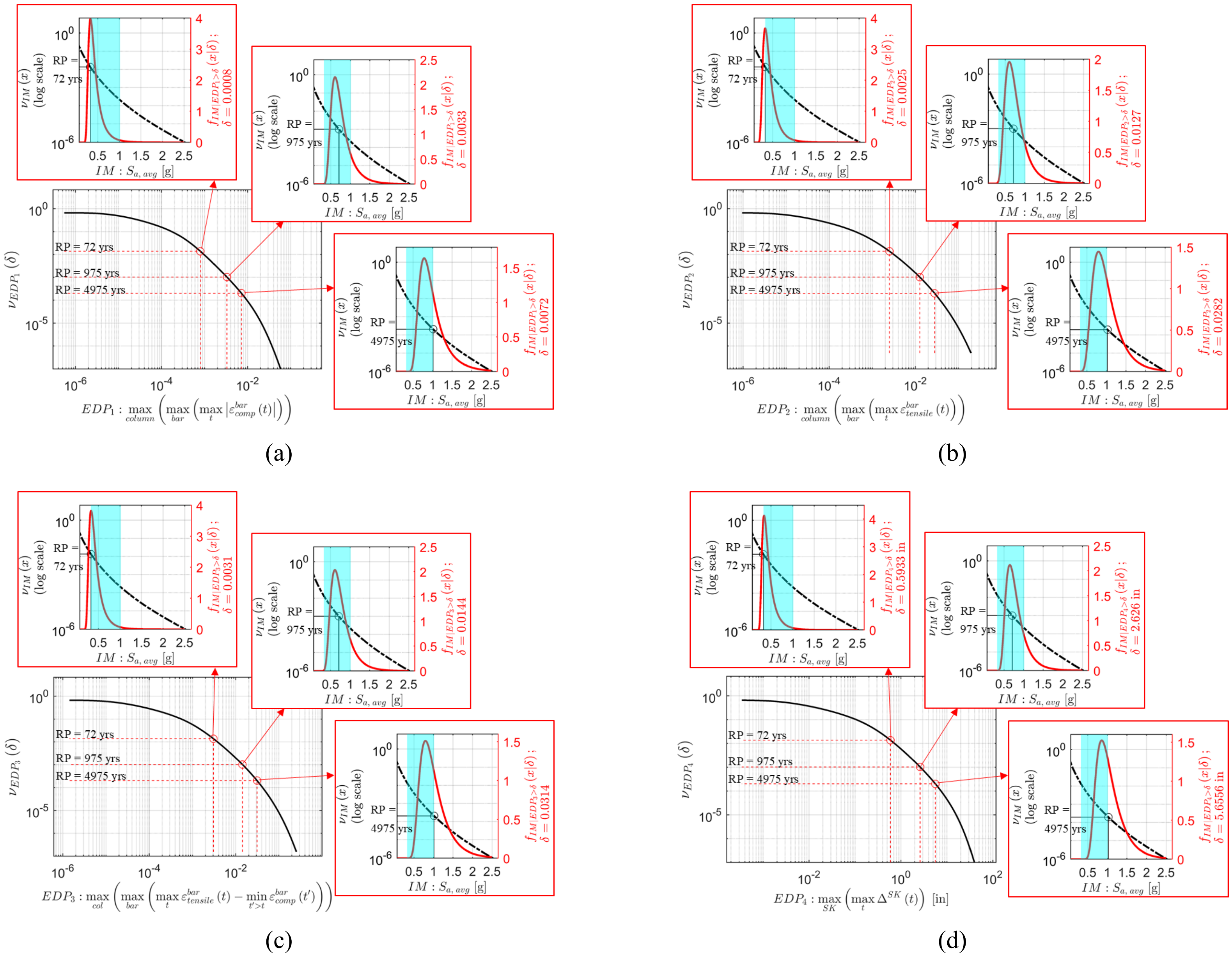

Figure 7.24 disaggregation of demand hazard for Bridge C: (a) EDP_1; (b) EDP_2; (c) EDP_3; and (d) EDP_4

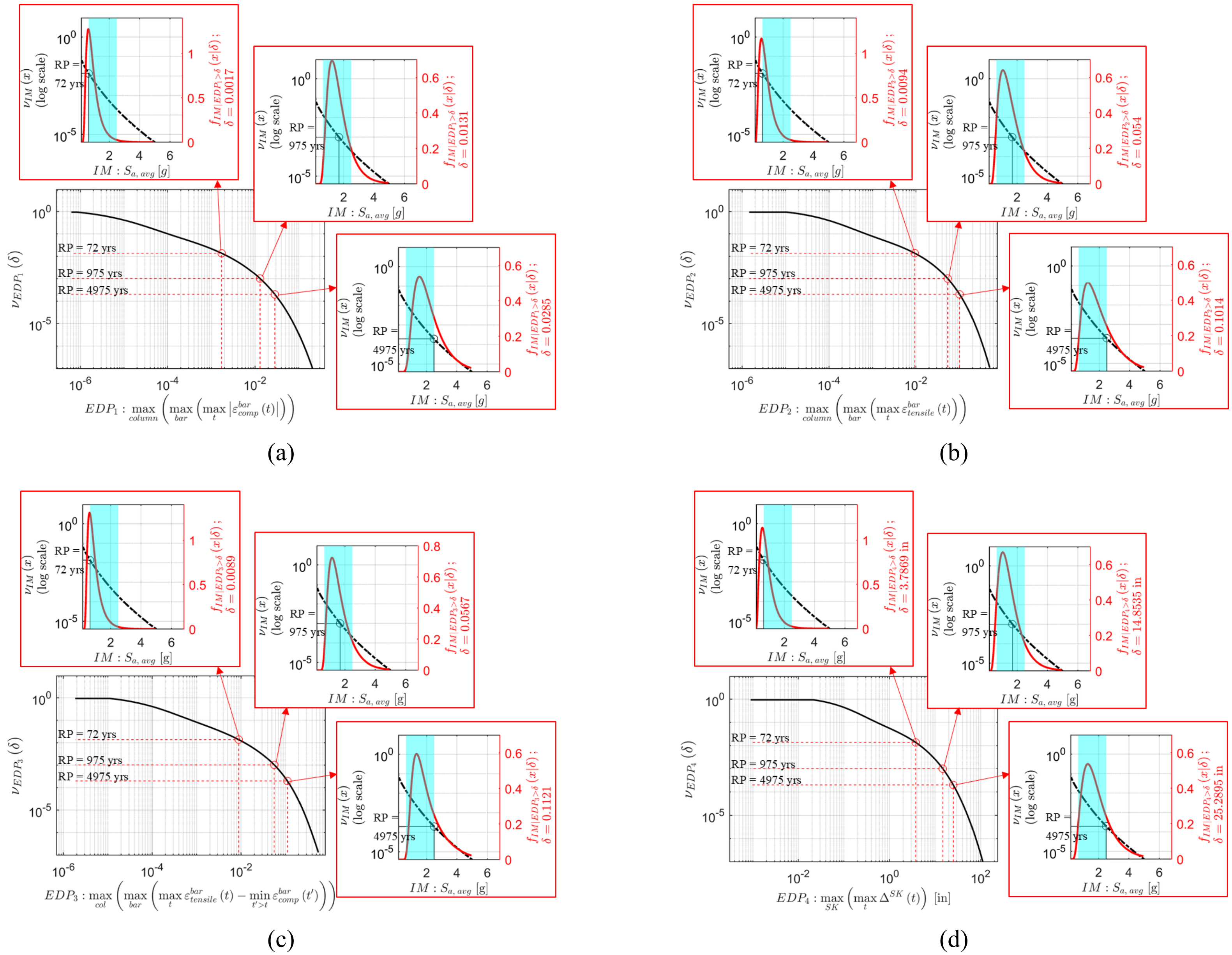

Figure 7.25 disaggregation of demand hazard for Bridge MAOC: (a) EDP_1; (b) EDP_2; (c) EDP_3; and (d) EDP_4

8 Probabilistic Seismic Damage Hazard Analysis

8.1 Introduction

To evaluate the seismic performance/adequacy/reliability of structures in terms of risk-levels associated with the exceedance of a pre-defined set of damage/limit-states, a probabilistic treatment of structural seismic demand and capacity is essential. Probabilistic Seismic Demand Hazard Analysis (Chapter 7) characterizes the uncertainties in seismic demand imposed on structures emanating primarily from underlying uncertainties in seismic source characterization (e.g., temporal and spatial occurrence of earthquakes, earthquake magnitudes, etc.), seismic wave propagation path and hence the seismic intensity measure recorded at the site, local site/soil conditions, and record-to-record variability exhibited by ground motions with the same level of seismic intensity. In doing so, all epistemic sources of uncertainties and the aleatory structural model parameter uncertainty are not considered in this project for simplicity.

Ideally, a "perfect" finite element structural model would be able to capture real physical damage (e.g., concrete cover crushing, longitudinal bar buckling, longitudinal bar fracture, etc.) and the effects of damage accumulation as the structural model is subjected to an earthquake ground motion. In such an ideal situation, computation of an estimate of the probability of exceeding specific damage/limit-states would have been possible through nonlinear response history analyses alone by merely counting the number of cases where specific damage/limit-states are encountered and/or exceeded. In the absence of "perfect" physics-based finite element structural models, seismic reliability or risk associated with the exceedance of damage/limit-states of interest is computed by bringing in the notion of structural capacity.

Structural capacity against a specific limit-state is defined as the maximum value of the physical quantity representing the associated seismic demand parameter, i.e., EDP, that the structure can withstand without exceeding or being in the specific damage/limit-state. Structural capacity can be predicted by the joint use of a simplified (design code type) analytical, semi-analytical or empirical predictive capacity model for the specific limit-state and experimental data collected from an ensemble of specimens tested for the considered limit-state (Berry and Eberhard 2004; Berry and Eberhard 2005). In the absence of experimental data for a given limit-state, predictions of structural capacity can be obtained through numerical simulation of the structural response using reliable (e.g., validated at the component level) finite-element structural models (Mackie and Stojadinović 2004; Nielson 2005). There is significant uncertainty associated with predictions of structural capacity due to a myriad of reasons which primarily include path- or history-dependence of cyclic structural response, uncertainty in material properties, difference in geometric properties and/or system configurations of experimental specimens, use of imperfect predictive methods/models, etc.

Probabilistic Seismic Damage Hazard Analysis (PSDamHA) is aimed towards a rigorous quantification of the various sources of uncertainties associated with predictions of structural capacities and a consistent and coherent propagation of the same to make probabilistic predictions of structural damage/limit-states exceedance.

8.2 Damage Hazard Integral

The objective of PSDamHA is to evaluate the mean annual rate (MAR) of the structure or its components exceeding a given damage/limit-state due to the occurrence of an earthquake. For a set of discrete limit-states, a limit-state function, also known as a performance function, is mathematically expressed as

$$Z_k = C_k - EDP_k \begin{cases} < 0 \text{ damage/limit-state exceedance} \\ = 0 \text{ damage/limit-state boundary} \\ > 0 \text{ no damage} \end{cases} \tag{8.1}$$

where C_k and EDP_k represent the random variables corresponding to the capacity and the engineering demand parameter associated with the k^{th} limit-state. The homogenous Poisson assumption of earthquake occurrences in time allows a censored Poisson description of the temporal exceedance of limit-states due to earthquakes with the MAR of limit-state exceedance given by

$$\nu_{LS_k} = \nu \cdot P\left[Z_k < 0\right] \tag{8.2}$$

where ν, the seismic activity rate, is the MAR of occurrence of earthquakes with magnitude/intensity greater than a lower bound threshold value. Earthquakes with magnitude/intensity lower than this threshold do not cause any significant damage to the considered structure. Given the joint probability distribution of C_k and EDP_k, the probability of limit-state exceedance can be evaluated by integrating the joint probability density function over the unsafe domain, i.e., $C_k < EDP_k$. Due to numerous factors affecting structural capacity and demand and significant levels of uncertainties associated with these factors, the task of formulating joint probability density functions of C_k and EDP_k, and their integration, in general, becomes a very challenging task. This can be circumvented by making numerical approximations, e.g., First-Order Reliability Method (FORM) and Second-Order Reliability Method (SORM), or by breaking down the problem into more tractable steps involving conditional and/or marginal probability distributions of the individual random variables in the limit-state function.

Numerous researchers have focused on the development of methodologies to evaluate the seismic reliability of structures (Esteva and Ruiz 1989; Kennedy et al. 1980; Song and Ellingwood 1999a; Song and Ellingwood 1999b; Tzavelis and Shinozuka 1988; Wen 1995). The formal probabilistic framework for evaluating the MARs at which specific limit-states are exceeded, originally developed by Cornell and co-workers (Bazzurro and Cornell 1994; Cornell et al. 2002; Shome et al. 1998; Yun et al. 2002) culminated into the state-of-the-art framework for PBEE developed at PEER (Krawinkler and Miranda 2004; Moehle and Deierlein 2004; Porter 2003). According to the PEER PBEE framework, the task of predicting the MAR of exceedance of a set of discrete limit-states is broken down into two major steps by invoking the Total Probability Theorem on Eq. (8.2). With the basic underlying assumption of mutual exclusivity of simultaneous earthquake occurrences in time, thereby deeming different values of EDP_k mutually exclusive, Eq. (8.2) is rewritten as

$$\nu_{LS_k} = \nu \cdot \int_{EDP_k} P\left[Z_k < 0 \mid EDP_k = \delta\right] \cdot f_{EDP_k}\left(\delta\right) \cdot d\delta \tag{8.3}$$

where δ is a specific value of EDP_k, conditional on which, the uncertainty in Z_k is solely due to that in C_k, the structural capacity against the k^{th} limit-state. Uncertainty quantification of conditional limit-state exceedance given a specific value of demand is typically done using predictive models for the specific limit-state and comparing such predictions with reliable experimental and/or numerical data. Uncertainty associated with such predictions stem from path- or history-dependence of cyclic structural response, uncertainty in material and/or geometric properties, difference in geometric properties and/or system configurations of experimental specimens, use of idealized predictive methods/models with missing explanatory variables, use of a single demand parameter to predict the exceedance of a limit-state, etc. The probabilistic analysis involved in computing the conditional probability of exceeding the k^{th} limit-state conditioned on the value of the associated engineering demand parameter, EDP_k is called fragility analysis. Details of fragility analyses conducted as a part of this project are discussed in detail in Section 8.4.

The term $f_{EDP_k}(\delta)\cdot d\delta$, in Eq. (8.3), is the probability that the continuous random variable EDP_k takes a value between δ and $\delta + d\delta$, $d\delta$ being an infinitesimally small increment. The seismic activity rate ν, taken inside the integral, and multiplied by $f_{EDP_k}(\delta)\cdot d\delta$ gives

$$\begin{aligned} \nu \cdot f_{EDP_k}(\delta)\cdot d\delta &= \nu \cdot P\left[\delta < EDP_k < \delta + d\delta\right] \\ &= \nu \cdot \left| P\left[EDP_k > \delta + d\delta\right] - P\left[EDP_k > \delta\right] \right| \\ &= \left| \nu_{EDP_k}(\delta + d\delta) - \nu_{EDP_k}(\delta) \right| \\ &= \left| d\nu_{EDP_k}(\delta) \right| \end{aligned} \tag{8.4}$$

where $\left| d\nu_{EDP_k}(\delta) \right|$ is the absolute differential of the demand hazard curve of EDP_k giving the MAR of occurrence, and not exceedance, of a specific value, δ, of EDP_k. Substituting Eq. (8.4) into Eq. (8.3), the seismic damage hazard integral for the k^{th} limit-state is written as follows

$$\nu_{LS_k} = \int_{EDP_k} P\left[Z_k < 0 \mid EDP_k = \delta\right] \cdot \left| d\nu_{EDP_k}(\delta) \right| \tag{8.5}$$

Eq. (8.5) expresses the damage hazard integral for the k^{th} limit-state as a direct convolution of the corresponding fragility function with the demand hazard curve of the associated engineering demand parameter, EDP_k. Detailed descriptions of the deterministic predictive capacity models used, and fragility analyses conducted for the considered damage/limit-states to adequately quantify the uncertainty in limit-state capacity are presented in Sections 8.3 and 8.4.

8.3 Deterministic Capacity Models for Considered Damage/Limit-States

To evaluate the performance or capacity of any structure against various damage-states or limit-states of interest, predictive capacity models are required. A capacity model attempts to relate a combination of structural properties, such as strain, displacement, material strength or geometrical properties etc. to a specific apparent damage. The models are typically empirical or semi-empirical and derived from experimental data and/or engineering judgement. Consequently, capacity models are often found in the form of equations with variables which are deemed pertinent to the damage-states of interest. The predictive capacity model for the k^{th} limit-state establishes the threshold value $(EDP_{C_k}^{\mathrm{PRED}})$ of the associated EDP, which, upon crossing, will determine if the k^{th} limit-state has been reached or exceeded. The predictive capacity models for the four considered limit-states, as defined in Section 7.3, are discussed below.

8.3.1 Predictive Capacity Model for Limit-state 1: Concrete Cover Crushing

The limit-state of concrete cover crushing is predicted to occur based solely on the absolute value of the compressive strain, $|\varepsilon_{comp}^{bar}|$, of the extreme longitudinal reinforcement. From experimental data by Goodnight et al. (2015; 2016), Eq. (8.6) was observed to minimize the sum of the squared error between the predicted strain and the observed strain for concrete cover crushing. A comparison between the experimental data and the prediction provided by Eq. (8.6) is shown in Figure 8.1. The reaching/exceeding of the concrete cover crushing limit-state is indicated by the first signs of concrete flaking between spiral layers (Goodnight et al. 2015; Goodnight et al. 2016). Experiments conducted by Goodnight et al. (2015; 2016) were cyclic pushovers. Therefore, the measured data is based on the maximum compressive strain achieved at the peak of each cycle. As discussed in their report, Eq. (8.7) should be adopted for design/assessments of new/existing structures, instead, as the measured strain at the peak of each cycle would inevitably have exceeded the actual strain which initiated the cover crushing. If the absolute value of the maximum compressive strain in a longitudinal bar is found to exceed the value given by Eq. (8.7), the concrete cover is deemed to have crushed.

$$|\varepsilon_{comp}^{bar}| = 0.00475 \tag{8.6}$$

$$EDP_{C_1}^{\mathrm{PRED}} = |\varepsilon_{comp}^{bar}| = 0.004 \tag{8.7}$$

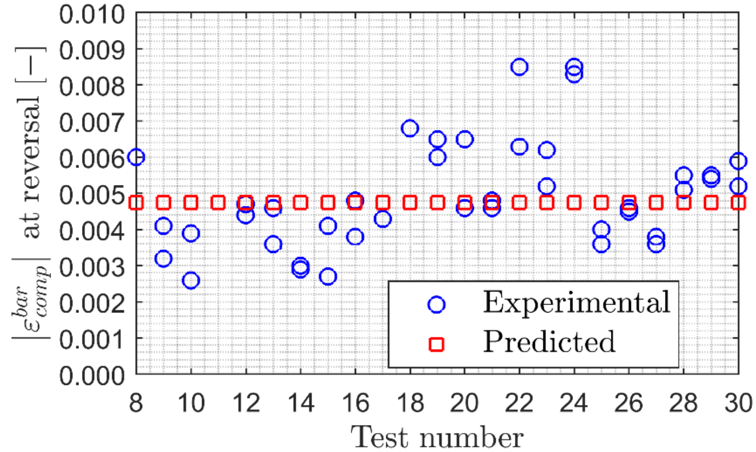

Figure 8.1 Experimental data (Goodnight et al. 2015) of recorded compressive strength at concrete cover crushing plotted with the strain obtained by minimizing the sum of the squared error between the prediction strain and observed strain.

8.3.2 Predictive Capacity Model for Limit-state 2: Longitudinal Bar Buckling

The capacity model for longitudinal bar buckling is also obtained from the same set of experiments as for concrete cover crushing. In the experiments conducted it was observed that bar buckling occurred following a reversal from a peak tensile strain while the bar is under net elongation (Goodnight et al. 2015; Goodnight et al. 2016). Therefore, the researchers concluded that the capacity of a column to bar buckling can be related to a peak tensile strain, $\varepsilon^{bar}_{tensile}$, of the longitudinal reinforcement which will cause severe instability upon reversal (Goodnight et al. 2015; Goodnight et al. 2016). The prediction equation was found to depend on structural and geometrical properties of the column, namely it is a function of the transverse volumetric steel ratio, yield strain of the transverse reinforcement and axial load ratio. The adopted capacity equation for this project, given as the peak tensile strain following which a strain reversal will cause bar buckling, is given in Eq. (8.8) (Goodnight et al. 2015; Goodnight et al. 2016). The exceedance of this threshold value of the tensile strain of a longitudinal bar in a column is deemed to be a precursor to longitudinal bar buckling upon strain reversal. A comparison between the experimental data and the prediction provided by Eq. (8.8) is shown in Figure 8.2.

$$EDP^{\mathrm{PRED}}_{C_2} = \varepsilon^{bar}_{tensile} = 0.03 + 700\rho_s \frac{f_{yhe}}{E_s} - 0.1\frac{P}{f'_{ce}A_g} \tag{8.8}$$

In Eq. (8.8), ρ_s is the volumetric transverse reinforcement ratio, f_{yhe} is the expected yield stress of transverse reinforcement, E_s is the elastic modulus of the transverse reinforcement, P is the axial load, f'_{ce} is the expected compressive yield stress of the concrete in the column, and A_g is the cross-sectional area of the column. It is noted here that, for a time-history analysis, the axial load will vary while the other components on the right-hand side of the equation will remain constant for each column. To simplify the approach such that a single value of tensile strain can be assigned to each column as its capacity for bar buckling, the axial load will also be taken as a constant. The axial load used to assess the capacity of a column is taken from the end of the gravity analysis prior to the start of the earthquake time history. In this way the capacity of a column is independent of the seismic time history.

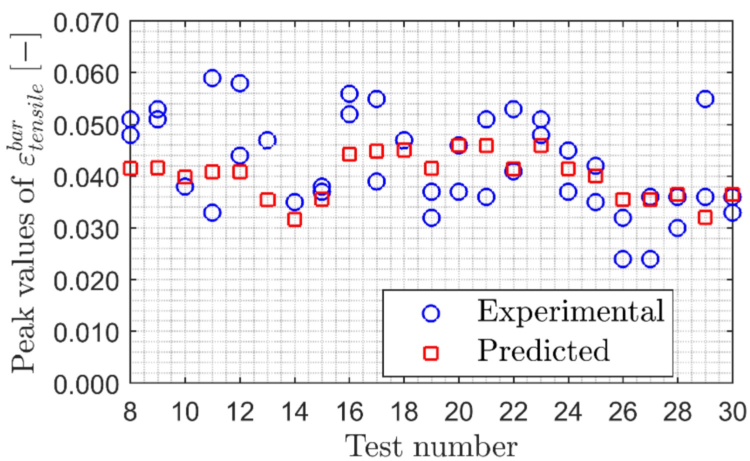

Figure 8.2 Comparison of experimental data set (Goodnight et al. 2015) of recorded tensile strengths at reversal prior to bar buckling with predicted tensile capacity from Eq. (8.8).

8.3.3 Predictive Capacity Model for Limit-state 3: Longitudinal Bar Fracture

The capacity model for longitudinal bar fracture is taken from the recent Caltrans work by Duck et al. (2018). The capacity equation is derived from comprehensive finite element analyses as part of efforts in the investigation of Plastic Buckling Straightening Fatigue (PBSF) of longitudinal bars in circular columns. The prediction of PBSF of a longitudinal bar in a circular column depends on the strain excursion encountered by the rebar during a complete loading cycle. Strain excursion is defined as the difference between the maximum tensile strain (positive) and the minimum compressive strain (negative), the latter following the former, in the strain time-history of a longitudinal reinforcement bar. The threshold value below which the strain excursion of a longitudinal bar should be kept under to prevent PBSF is termed as the von Karman strain. The researchers found that once the strain excursion in a bar has reached t fhe von Karman strain, large concentrations of strain occur between centers of rotation in the buckled shape of the reinforcement bar leading to potential fracture. The von Karman strain, $\Delta\varepsilon_{VK}$, is given in Eq. (8.9) and is used as the predictor of capacity of longitudinal bars against bar fracture. If the maximum strain excursion encountered is greater than $\Delta\varepsilon_{VK}$, the bar in the column is deemed to have fractured. For a detailed explanation and its derivation, the reader is referred to the original Caltrans report (Duck et al. 2018).

$$EPD_{C_3}^{\mathrm{PRED}} = \Delta\varepsilon_{VK} = 0.11 + \min(0.054, 0.032\rho_s(\%)) - 0.0175\left|\sqrt[3]{n_{bar}} - 2.93\right| - 0.054\frac{T}{Y} \quad (8.9)$$

In the above equation, $\rho_s(\%)$ is the volumetric transverse reinforcement ratio expressed as a percentage, n_{bar} is the number of bars in a column, and $\frac{T}{Y}$ is the ratio of the ultimate stress to yield stress of the longitudinal steel. Where bundles of bars are used, n_{bar} is to be the number of bundles rather than the total number of longitudinal reinforcement bars as this term is used to consider the "polygon effect". The polygon effect is the phenomenon where the number of bars or bundles affect the deformed shape and efficiency of the transverse reinforcement in restraining lateral deformations (Duck et al. 2018). In consultation with the researchers of the PBSF study, the ratio of the ultimate stress to yield stress of the longitudinal bar, $\frac{T}{Y}$, was taken as 1.4 for this project. Note that for bridges of identical column design, the value of $\Delta\varepsilon_{VK}$ is constant across all columns.

8.3.4 Predictive Capacity Model for Limit-state 4: Shear Key Damage

A predictive model for the displacement capacity of monolithic shear keys is extracted from the work by Megally et al. (2002) which in part focuses on the seismic response of exterior monolithic (non-isolated) shear keys, as found in three of the four testbed bridge structures (Bridge A, Bridge B and Bridge C). Megally's work attempts to model the hysteretic rule of exterior shear keys using a strut-and-tie mechanism and through observations from experimental load-displacement results. This hysteretic rule was also used in modeling the shear key in the finite element model as described in Chapter 4. The complete model is constructed by superimposing the hysteretic contributions from steel and concrete components as shown in Figure 8.3. The experimental load-displacement curves showed distinct branches that were related to five damage levels, also used in the definition of the quinque-linear hysteresis rule, by the original authors. Level-I corresponds to initiation of diagonal cracking at the intersection of the shear key's sloped surface with the top of the stemwall. Level-II is the onset of yielding of shear key reinforcement. Level-III corresponds to the peak load with significant crack width opening at the shear key-stemwall interface. Level-IV is the point at which concrete contribution to the resistance falls to zero while Level-V is the initiation of failure of the steel resisting component.

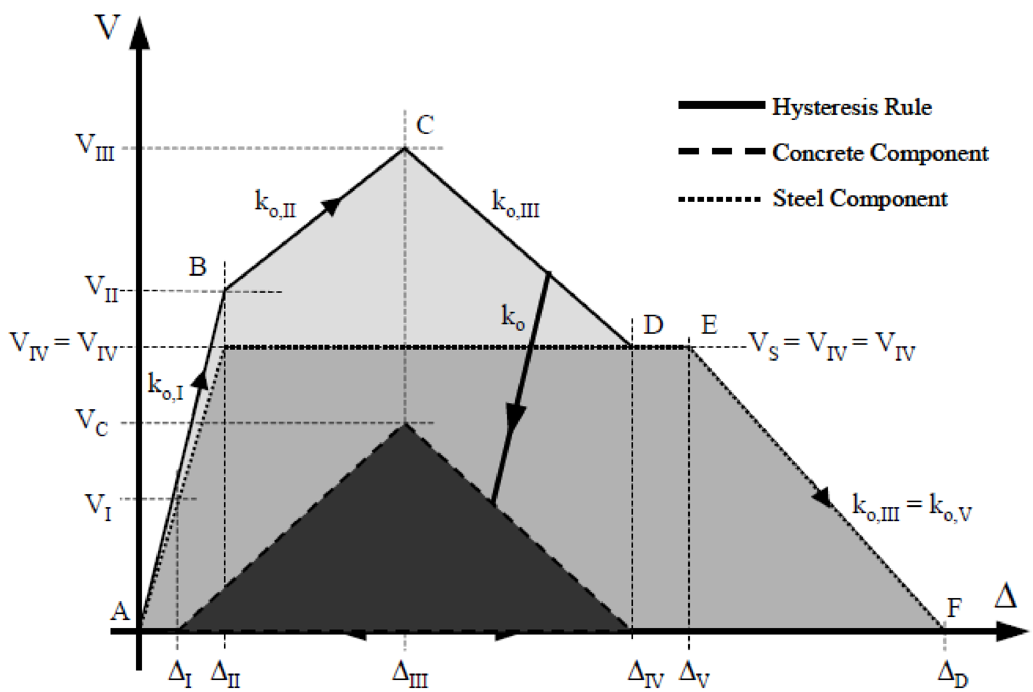

Figure 8.3 Hysteresis rule for monolithic exterior shear keys obtained from Megally et al. (2002) as a superposition of a concrete component and a steel component.

Out of the five different damage-states in the hysteretic model of exterior monolithic shear keys summarized above, the lateral displacement at the top of the shear key corresponding to damage Level-III was selected to denote the displacement capacity of the shear key for this project. This was chosen as it represented the maximum load of the shear key and the point beyond which the concrete begins to degrade causing significant damage. The lateral displacement at the top of the shear key, Δ_{III} (in its original format), corresponding to the peak load is given in Eq. (8.10)

(Megally et al. 2002). If the recorded displacement exceeds Δ_{III} the shear key is deemed to have been damaged.

$$EDP_{C_4}^{\text{PRED}} = \Delta_{III} = \sqrt{2}\varepsilon_y (L_d + b) \frac{(h + d_1)}{s} \tag{8.10}$$

where, ε_y is the yield strain of steel reinforcing bars, s is the larger of the horizontal and vertical rebar spacing of the stemwall side reinforcement, d_1 is the height of the shear key above the stemwall, b is the width of the stemwall, and h is the height of the stemwall. L_d represents the reinforcement development length given by (Megally et al. 2002).

$$L_d = \frac{d_b f_y}{25\sqrt{f_c'}} \quad \text{(psi, in)} \tag{8.11}$$

where d_b represents the rebar diameter of the bottommost reinforcing bars in the stemwall and f_c' and f_y represent the nominal characteristic compressive strength of concrete and the nominal yield strength of steel reinforcing bars, respectively.

Note that the model proposed by Megally et al. (2002) described above is applicable only to Bridge A, Bridge B and Bridge C as these bridges are designed using the same type of monolithic, i.e., non-isolated, shear keys as those tested in the experimental investigation. For Bridge MAOC, however, sacrificial type isolated shear keys are called for in the design. The displacement capacity of this type of shear keys is taken as the displacement at peak strength obtained from a scaled backbone curve calibrated using experimental data corresponding to a single specimen (Beckwith et al. 2015; Bozorgzadeh et al. 2007). This backbone curve is also used in modeling the force-displacement relationship of isolated shear keys in the finite element model of Bridge MAOC described in Chapter 4. The predictive displacement capacity model in this case is given by Eq. (8.12) (Beckwith et al. 2015).

$$EDP_{C_4}^{\text{PRED}} = \Delta_{III} = 3.75 \text{ in} \tag{8.12}$$

8.4 Fragility Analysis and Experimental/Numerical Data Sources

As previously mentioned, capacity models are used to quantify the resistance to certain damage-states of interest. However, the capacity models described are deterministic and therefore do not take into account any uncertainty related to the capacity of the structural components. To quantify uncertainty related to a limit-state capacity, fragility functions are adopted. Fragility functions are obtained by making use of the deterministic capacity models and comparing the predictions of limit-state exceedance with reliable experimental data from tests conducted in the laboratory and/or numerical results from analyses of high-fidelity finite element models. The sources of uncertainty captured through fragility curves are related to:

(a) Use of idealized/simplified predictive limit-state capacity model (e.g., missing variables)
(b) Unknown material properties
(c) A single predictive demand parameter is insufficient to perfectly predict whether a limit-state is reached or exceeded (i.e., other demand parameters play a role)

Fragility functions, defined as cumulative probability distribution functions, expresses the probability of reaching or exceeding a system or component-based limit-state (damage-state) given a specific value of a predictive demand parameter associated with this limit-state (ATC 2007), e.g., PGA, $S_a(T_1, \xi = 5\%)$, EDP, etc. In this project, fragility functions are developed to take in values of EDPs as the input for all considered limit-states and are in the form of the two-parameter lognormal cumulative distribution functions. The fragility function for the k^{th} limit-state is defined as follows

$$P\left[Z_k < 0 \mid EDP_k = \delta\right] = \Phi\left(\frac{\ln(\delta) - \lambda_k}{\zeta_k}\right) \tag{8.13}$$

where Φ is the cumulative distribution function of the standard normal distribution. λ_k and ζ_k are the parameters of the fitted lognormal distribution representing the mean and standard deviation of the natural logarithm of experimentally and/or numerically measured values of the associated EDP for which the k^{th} limit-state is exceeded.

As previously mentioned, fragility curves are constructed using experimental data from laboratory tests and/or high-fidelity numerical analyses. Typically, these fragility curves pertain to specimens/numerical models of varying design parameters. For a reinforced concrete column, for example, parameters such as the diameter, column height, material properties, longitudinal and transverse reinforcement ratio etc. can vary greatly. These fragility curves, therefore, provide a good estimate of average uncertainties and limit-state exceedance for a large population of specimens given an EDP. However, to be a good predictor for a specific design, fragility curves should ideally be constructed using data corresponding to specimens/models of the same design. This necessitates "normalization" of fragility curves to ensure that fragility curves, constructed using available experimental/numerical data pertaining to specimens/models of varying parameters, can be used for new and specific designs of the considered bridges. To create a normalized fragility curve for the k^{th} limit-state, experimentally/numerically measured values of the associated demand parameter for which the limit-state is reached or exceeded, referred to as EDP_k^{MEAS}, are recorded for each specimen tested/analyzed and divided by the predicted capacity, $EDP_{C_k}^{\text{PRED}}$, using the appropriate capacity model. The horizontal axis of the normalized fragility curve for the k^{th} limit-state is therefore the ratio of the experimentally/numerically measured value of the relevant EDP at which the limit-state of interest is reached or exceeded to the predicted (using a deterministic capacity model) value of the EDP at which the limit-state is reached or exceeded. In this way, a normalized fragility curve contains a unitless horizontal axis whereas a non-normalized fragility curve has a horizontal axis dependent on the units of the selected EDP. The normalized fragility function constructed for the k^{th} limit-state is, therefore, defined as

$$P\left[Z_k < 0 \mid \frac{EDP_k^{\text{MEAS}}}{EDP_{C_k}^{\text{PRED}}} = \delta \right] = \Phi\left(\frac{\ln(\delta) - \lambda_k'}{\zeta_k'} \right) \tag{8.14}$$

where λ_k' and ζ_k' are the parameters of the fitted lognormal distribution representing the mean and standard deviation of the natural logarithm of the ratio of experimentally/numerically measured to predicted values of EDP_k for which the k^{th} limit-state is exceeded. The value of the ratio of the experimentally/numerically measured value of EDP at limit-state exceedance to the predicted value of the same EDP would have been equal to unity in case a "perfect" deterministic capacity model were used (Zhang 2006). In such a case, the fragility function would have taken the form of a step function at a value of unity. However, in reality, a scatter of ratios is typically found due to idealized/simplified predictive models, unknown material properties, missing explanatory variables, etc. The uncertainty of the measure-to-predicted capacity ratio can be visualized as inversely proportional to the steepness of the fragility curve, i.e., a steep slope infers a lower level of uncertainty and vice versa. In addition, the bias of the deterministic capacity model can be determined based on the median value of the measured-to-predicted capacity ratio, i.e., the value of the ratio corresponding to 50% probability of exceedance.

A normalized fragility curve provides an estimate of the probability of limit-state exceedance given a value of normalized measured-to-predicted capacity ratio. To use this fragility curve for a new design, the constructed curve must be denormalized. Denormalization is done by scaling the horizontal axis of the normalized fragility curve though multiplication by the predicted capacity for that specific design using the appropriate deterministic capacity equation. This denormalized fragility curve, for the k^{th} limit-state, therefore, has a horizontal axis of EDP_k^{MEAS} and is equivalent to the definition given by Eq. (8.13) with parameters λ_k and ζ_k given by

$$\lambda_k = \lambda_k' + \log EDP_{C_k}^{\text{PRED}} \tag{8.15}$$

$$\zeta_k = \zeta_k' \tag{8.16}$$

With values of EDP_k as input, the denormalized fragility can be used to determine the MAR of limit-state exceedance by convolution with the corresponding demand hazard curve of EDP_k.

To construct reliable fragility curves specific experimental/numerical sources were used. Sources selected in this project are from modern experimental data where strain or displacement *EDPs* are recorded while, at the same time, observations are made for the exceedance of limit-states of interest. Experimental/numerical sources used in this project are listed in Table 8-1. Note that specimens from multiple sources are used in the development of some fragility curves. Also note that, the data corresponding to the limit-state of rebar fracture comes solely from a series of finite element analyses. A more detailed overview of each source is provided in the following sections.

Table 8-1 Experimental sources for constructing fragility curves for all considered limit-states

Sources	Specimen Scale	Specimens	Limit-State
Schoettler et al. (2015)	full scale	1	2
Trejo et al. (2014)	half scale	6	1
Goodnight et al. (2015)	half scale	23	1, 2
Murcia-Delso et al. (2013)	full scale	4	1, 2
Duck et al. (2018)	FE	36	3
Megally et al. (2002)	half scale	4	4

8.4.1 Fragility Curve for Limit-state 1: Concrete Cover Crushing

Normalized fragility curve for concrete cover crushing is constructed partly using data from reinforced concrete column experiments conducted by Goodnight et al. (2015) in which the strains of longitudinal reinforcement bars were recorded. These columns were constructed to represent single degree of freedom bridge columns each consisting of a footing, a column and a loading cap. The specimens were subjected to unidirectional top-column displacement histories and the strains at the end of each half cycle were recorded along with any damage observed on both sides of the column. A total of 23 columns in this dataset are utilized in forming the fragility curve for the limit-state of concrete cover crushing. It is noted that in most cases, concrete cover crushing was observed on both sides of a single column thus making a single column contribute two data points to the construction of the fragility curve. Data also came from experiments conducted by Trejo et al. (2014) and Murcia-Delso et al. (2013). The former consisted of experiments performed on single reinforced concrete cantilever columns, with a mixture of Grade 60 and Grade 80 steel reinforcement, with footings subjected to unidirectional top-column displacement time histories. The latter consisted of unidirectional top-column displacement history tests where the columns are embedded in enlarged (Type II) shafts. A total of six columns are utilized from Trejo et al. (2014) and four from Murcia-Delso et al. (2013) for the construction of the fragility curve.

The predicted capacity for concrete cover crushing is an absolute compressive strain of 0.004 in the extreme longitudinal reinforcement. As explained previously in Section 8.3.1, this is the recommended strain capacity for design/assessment of new/existing structures. However, as the normalized fragility curve is to be constructed from experimental data where the recorded/observed strain is always higher than the actual strain which initiated the crushing, the experimental data is normalized by the originally observed strain capacity of 0.00475 (Eq. (8.6)) instead of the recommended value of 0.004 (Eq. (8.7)). The recommended strain capacity is used for denormalization of the constructed normalized fragility curve such that it can be used for specific designs of the considered bridges. The relevant experimental data used in the fragility curve is provided in Table 8-2. The table does not show the corresponding predicted value of the capacity using the deterministic model. The normalized fragility curve for concrete cover crushing is provided in Figure 8.4. It can be seen that all data points lie in the vicinity of the fitted cumulative lognormal distribution function with only small deviations at the upper and lower tails of the CDF. The value of the normalized strain at 50% probability of exceedance is approximately 1.02

indicating a small bias. The fitted lognormal distribution for the normalized fragility function corresponding to limit-state 1 has parameters λ_1' and ζ_1' of 0.0174 and 0.3264 respectively.

Table 8-2 Experimental data used for fragility curve of limit-state 1

Specimen	Strain at LS 1		Specimen	Strain at LS 1	
Goodnight 8	N/A	0.0060	Goodnight 25	0.0036	0.0040
Goodnight 9	0.0041	0.0032	Goodnight 26	0.0045	0.0046
Goodnight 10	0.0026	0.0039	Goodnight 27	0.0036	0.0038
Goodnight 11	N/A	N/A	Goodnight 28	0.0051	0.0055
Goodnight 12	0.0047	0.0044	Goodnight 29	0.0055	0.0054
Goodnight 13	0.0460	0.0360	Goodnight 30	0.0052	0.0059
Goodnight 14	0.0029	0.0030	Trejo 1	0.0030	N/A
Goodnight 15	0.0027	0.0041	Trejo 2	0.0015	N/A
Goodnight 16	0.0048	0.0038	Trejo 3	0.0050	N/A
Goodnight 17	0.0043	0.0043	Trejo 4	0.0047	N/A
Goodnight 18	0.0680	0.0000	Trejo 5	0.0054	N/A
Goodnight 19	0.0060	0.0065	Trejo 6	0.0032	N/A
Goodnight 20	0.0065	0.0046	Murcia-Delso 1	0.0068	N/A
Goodnight 21	0.0046	0.0048	Murcia-Delso 2	0.0064	N/A
Goodnight 22	0.0063	0.0085	Murcia-Delso 3	0.0040	N/A
Goodnight 23	0.0052	0.0062	Murcia-Delso 4	0.0036	N/A
Goodnight 24	0.0085	0.0083			

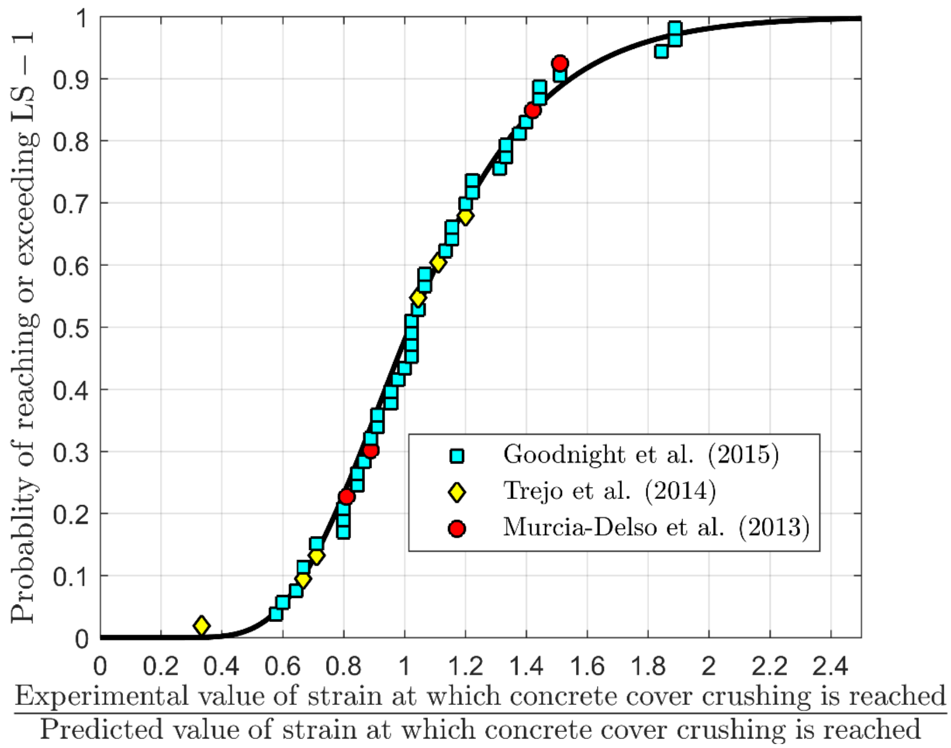

Figure 8.4 Fragility curve for limit-state 1

8.4.2 Fragility Curve for Limit-state 2: Longitudinal Bar Buckling

The fragility curve for the limit-state of longitudinal rebar buckling is developed based on experimental data from Goodnight et al. (2015), Murcia-Delso et al. (2013), and Schoettler et al. (2015). The same set of column experiments from Goodnight et al. (2015) and Murcia-Delso et al. (2013) used in obtaining the fragility curve for concrete cover crushing were used for the construction of the fragility curve for longitudinal rebar buckling. In addition, a single full-scale column from Schoettler et al. (2015) subjected to dynamic loading was included in this fragility analysis. The peak tensile strains of rebars in the tested column specimens were recorded prior to rebar buckling observation and used as the measured capacity of the column corresponding to this limit-state. The recorded strains are normalized by the predictive capacity model given by Eq. (8.8) . The data points used in the construction of the fragility curve are shown in Table 8-3. The table does not show the corresponding predicted value of the capacity. The normalized fragility curve for longitudinal rebar buckling is shown in Figure 8.5. It can be seen that all data points lie very close to the fitted cumulative lognormal distribution function with only small deviations at the upper and lower tails of the CDF. The value of the measured-to-predicted strain capacity ratio at 50% probability of exceedance is approximately 1.05 indicating a small bias. The fitted values of lognormal distribution parameters, i.e., λ_2' and ζ_2', for the normalized fragility function corresponding to limit-state 2 are 0.0451 and 0.2011 respectively.

Table 8-3 Experimental data used for fragility curve of limit-state 2

Specimen	Strain at LS 2		Specimen	Strain at LS 2	
Goodnight 8	0.0510	0.0480	Goodnight 22	0.0410	0.0530
Goodnight 9	0.0530	0.0510	Goodnight 23	0.0510	0.0480
Goodnight 10	N/A	0.0380	Goodnight 24	0.0370	0.0480
Goodnight 11	0.0590	0.0330	Goodnight 25	0.0420	0.0350
Goodnight 12	0.0580	0.0440	Goodnight 26	0.0320	0.0240
Goodnight 13	0.0470	0.0470	Goodnight 27	0.0360	0.0240
Goodnight 14	0.0350	0.0350	Goodnight 28	0.0360	0.0300
Goodnight 15	0.0370	0.0380	Goodnight 29	0.0550	0.0360
Goodnight 16	0.0560	0.0520	Goodnight 30	0.0360	0.0330
Goodnight 17	0.0550	0.0390	Murcia-Delso 1	0.0264	N/A
Goodnight 18	N/A	0.0470	Murcia-Delso 2	0.0410	N/A
Goodnight 19	0.0370	0.0320	Murcia-Delso 3	0.0321	N/A
Goodnight 20	0.0460	0.0370	Schoettler 1	0.0440	N/A
Goodnight 21	0.0510	0.0360			

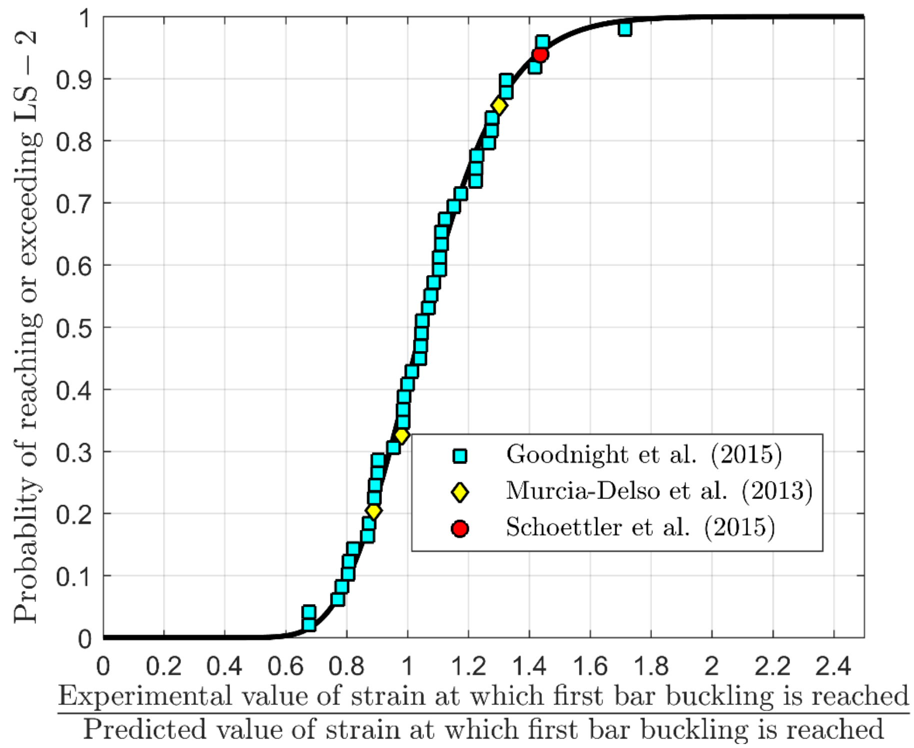

Figure 8.5 Fragility curve for limit-state 2

8.4.3 Fragility Curve for Limit-state 3: Longitudinal Bar Fracture

For longitudinal rebar fracture, the measured capacity at the limit-state is obtained from an ensemble of finite element analyses conducted by Duck et al. (2018) rather than a set of experimental data. The structural properties assigned to the columns in the finite element analyses attempt to comprehensively cover the gamut of practical structural properties found in the field. Each column is modeled in OpenSees with every longitudinal bar and hoop modeled as a single displacement-based beam-column element discretized along its length. The material properties of the steel are modeled after Dodd and Restrepo-Posada (1995). The structural characteristics evaluated in the analyses include: column diameter, rebar size, reinforcement ratio, transverse hoop spacing, yield and ultimate strengths of reinforcement and loading histories. An imperfection of 0.01 in. in the bars is initially modelled to induce buckling. For a comprehensive description of the finite element model, design parameters and loading procedures, the reader is referred to the original report by Duck et al. (2018).

Recall that the capacity of the column rebars to fracture is determined from a strain excursion following a maximum tensile strain, i.e., the difference between the maximum tensile strain (positive) and the minimum compressive strain (negative), the latter following the former, in the strain time-history of a longitudinal rebar. The predicted capacity of this excursion is called the von Karman strain evaluated using Eq. (8.9). For the normalized fragility curve corresponding to LS 4, the authors of the original work provided values of the fitted lognormal distribution parameters, i.e., λ_3' and ζ_3', as -0.0083 and 0.1088 respectively. The resulting fragility curve is shown in Figure 8.6. The value of the measured-to-predicted strain excursion capacity ratio at 50% probability of exceedance is approximately 0.99 indicating a minimal bias.

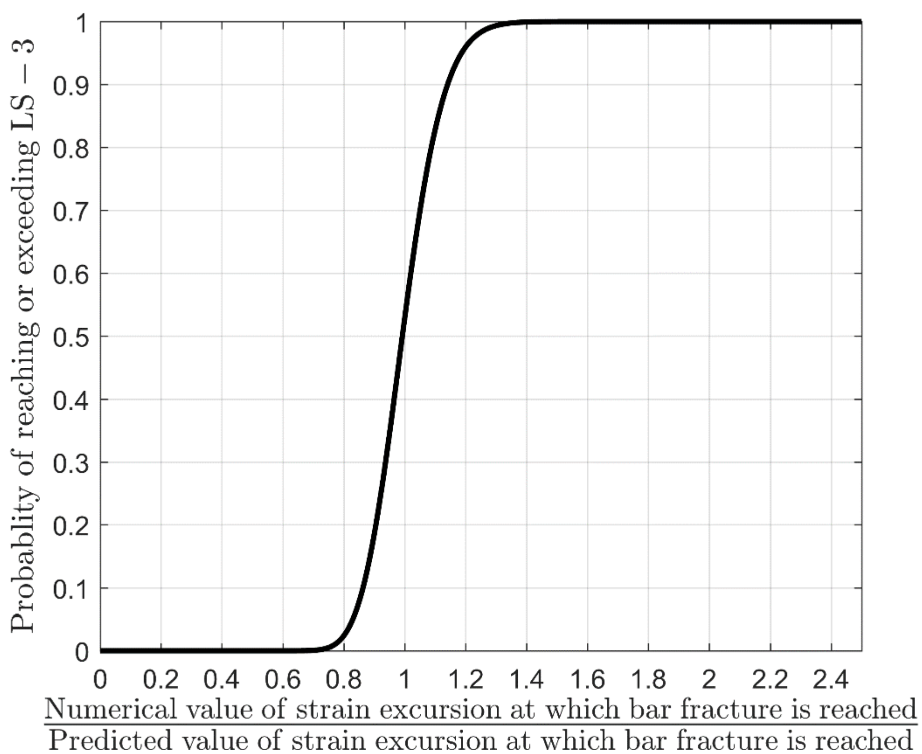

Figure 8.6 Fragility curve for limit-state 3

8.4.4 Fragility Curve for Limit-state 4: A Shear Key reaching its Shear Strength Capacity

The experimental data for constructing the fragility curve for the limit-state of a shear key reaching its shear strength capacity comes from four specimens tested in the work by Megally et al. (2002). The specimens are all exterior type non-isolated shear keys and therefore only apply to Bridge A, Bridge B and Bridge C as they have the same type of shear keys. The deformations recorded correspond to damage Level III as defined in Section 8.3.4, i.e., the deformation at peak strength of the shear key. Both the recorded and the predicted deformations (the latter given by Eq. (8.10)) for each specimen along with the ratios of measured-to-predicted deformations are provided in Table 8-4. The corresponding normalized fragility curve for limit-state 4 for a non-isolated shear key is shown in Figure 8.7. It can be seen that all data points lie close to the fitted cumulative lognormal distribution function. As there are few points used in the fragility analysis, little can be said about the fit near the tails of the CDF. The value of the measured-to-predicted displacement ratio at 50% probability of exceedance is approximately 1.15 indicating a moderate bias. The fitted lognormal distribution for the normalized fragility function corresponding to limit-state 4 has parameters λ_4' and ζ_4' equal to 0.1316 and 0.1107 respectively. For Bridge MAOC with isolated shear keys in its design, the backbone curve of the shear key is calibrated using results from a single experimental specimen (Bozorgzadeh et al. 2007). Therefore, the predicted displacement capacity, given by Eq. (8.12) in this case, is equal to the single measured displacement capacity. The normalized fragility function for limit-state 4 for an isolated shear key, also shown in Figure 8.7, is hence defined as a step function at a value of unity.

Table 8-4 Experimental data and deterministic capacity used for fragility curve of limit-state 4

Specimen	Shear key deformation at peak strength		
	Experimental (in)	**Predicted (in)**	**Ratio**
Megally 1 (non-isolated)	1.5	1.2	1.25
Megally 2 (non-isolated)	1.3	1.2	1.08
Megally 3 (non-isolated)	1.5	1.2	1.25
Megally 4 (non-isolated)	1.3	1.3	1.00
Bozorgzadeh 1 (isolated)	3.75	3.75	1.00

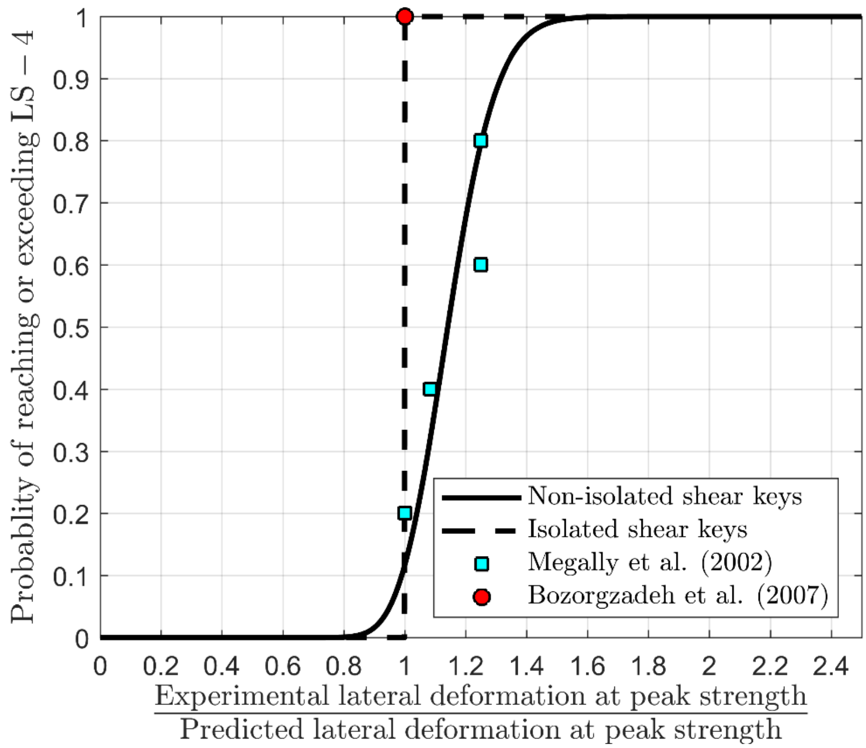

Figure 8.7 Fragility curves for limit-state 4

8.5 Seismic Damage Hazard Analysis

PSDamHA for the k^{th} limit-state is mainly carried out in two steps: (i) probabilistic quantification of the conditional limit-state capacity of the structure given a specific value, δ, of the associated engineering demand parameter, EDP_k, thereby allowing computation of the conditional probability, $P\left[Z_k < 0 \mid EDP_k = \delta\right]$; and (ii) convolution of the conditional probability of limit-state exceedance with the corresponding demand hazard curve $\nu_{EDP_k}(\delta)$ of EDP_k.

The first step of PSDamHA involves development of fragility functions as discussed in Section 8.4. Each fragility function pertaining to a limit-state of interest gives the probability of limit-state exceedance for a specific value of the associated EDP normalized with respect to the corresponding predictive capacity model. The normalization of the engineering demand parameter is essential to ensure the practicability of fragility functions obtained from experimental/numerical data coming from tests/analyses conducted on specimens of varying relevant structural parameters. Normalized fragility functions can therefore by used for new and/or specific designs of a structure with values of relevant structural parameters different from that of the experimental/numerical specimens used in the development of the fragility functions. For the specific designs of the testbed bridges considered, the normalized fragility function developed for a limit-state of interest is denormalized using the corresponding deterministic predictive capacity model in conjunction with Eq.s (8.15) and (8.16). This is required to correctly compute the conditional probability of limit-state exceedance given a specific value of the associated EDP.

Secondly, for a testbed bridge, the MAR of limit-state exceedance for the k^{th} limit-state is obtained by numerically convolving the conditional probabilities of limit-state exceedance given specific values of EDP_k with the corresponding rates of occurrences, $d\nu_{EDP_k}(\delta)$, of these values of EDP_k. Results of PSDamHA conducted for each testbed bridge are shown in Table 8-5 where the mean RP (= 1/MAR) of exceedance of each limit-state considered is reported.

Table 8-5 Mean RPs of limit-state exceedance for as-designed testbed bridges

	Mean RP of exceedance			
LS_k:	Concrete cover crushing	Longitudinal rebar buckling	Longitudinal rebar fracture3	Shear ke y damage
A	199	1378	3290	2269
B	322	1621	3654	2513
C	1202	10793	28975	525
MAOC	168	617	1152	85

It is noted from the results of PSDamHA of the testbed bridges that increasingly critical limit-states, i.e., limit-state 1 through limit-state 3, concerning reinforced concrete bridge columns for OSBs are associated with increasing values of mean RPs of exceedance. The mean RP of exceeding the 4$^{\text{th}}$ limit-state of shear key damage depends on the type of shear key used in the bridge. Bridges A, B, and C, having monolithic non-isolated type shear keys show high mean RPs of exceeding limit-state 4, while the mean RP of exceedance associated with this limit-state is found to be relatively small for Bridge MAOC with sacrificial isolated type shear keys in its design.

8.6 Deaggregation of Seismic Damage Hazard w.r.t Associated Engineering Demand Parameter

Seismic damage hazard corresponding to a limit-state of interest for a testbed bridge is computed by aggregating, as per Eq. (8.5), the contributions from all possible values of the associated EDP consistent with the seismic demand hazard at the considered site. The MAR of exceeding a limit-state can consequently be disaggregated into the contributions from different values of the associated EDP. Such a disaggregation provides additional insight into the distribution of causative EDP_k values leading to a specific level of damage hazard for the k^{th} limit-state. The conditional probability distribution of EDP_k, given exceedance of the k^{th} limit-state, i.e., $Z_k < 0$, with a specific MAR, ν_{LS_k}, is computed as per Eq. (7.12). Figure 8.8 through Figure 8.11 present results of EDP disaggregation of damage hazard corresponding to the limit-states of interest for all considered testbed bridges. The ordinate of each disaggregation plot on the right-hand-side shows the conditional probability distribution, i.e., Eq. (7.12), of EDP_k, given $Z_k < 0$. The ordinate along the left-hand-side of the same plot shows the demand hazard curve of EDP_k. Also shown in red, in its own independent ordinates in each of these plots, is the corresponding fragility function, i.e., $P\left[Z_k < 0 \mid EDP_k = \delta\right]$

$$f_{EDP_k|Z_k<0}\left(\delta \mid z\right) = \frac{P\left[Z_k < 0 \mid EDP_k = \delta\right] \cdot \left|d\nu_{EDP_k}\left(\delta\right)\right|}{\nu_{LS_k}} \tag{8.17}$$

The shape of the conditional distribution of EDP_k, given a specific level of damage hazard for the k^{th} limit-state, is a result of the competing effects between the two terms in the numerator of Eq. (7.12) as a function of EDP_k. "Very" small values of EDP_k, despite having "high" rates of occurrence, $|d\nu_{EDP_k}(\delta)|$, make negligible contributions to the damage hazard of limit-state k. The conditional probability of $Z_k < 0$, given "very" small values of EDP_k, is almost zero, i.e., $P\left[Z_k < 0 \mid EDP_k = \delta\right] \approx 0$. As values of EDP_k are increased, their rates of occurrence, $|d\nu_{EDP_k}(\delta)|$, decrease. On the other hand, direct proportionality of the chances of incurring damage with values of EDP_k leads to increase in $P\left[Z_k < 0 \mid EDP_k = \delta\right]$. At first, this increase in the conditional probability of limit-state exceedance outweighs the decrease in $|d\nu_{EDP_k}(\delta)|$. As a result, EDP_k contribution to damage hazard increases with increase in EDP_k. This continues up to a point where values of EDP_k start becoming "somewhat" rare, and the decrease in $|d\nu_{EDP_k}(\delta)|$ starts to subdue the growth in $P\left[Z_k < 0 \,|\, EDP_k = \delta\right]$. Although the chance of exceeding the k^{th} limit-state greatly increases with "very" large values of EDP_k, the rates of occurrence of these "very" large EDP_k values are "too" small, i.e., $|d\nu_{EDP_k}(\delta)| \approx 0$. This results in negligible contribution to damage hazard from "very" large and "too" rare values of EDP_k.

Furthermore, it is observed that contribution to a specific MAR of exceedance of limit-state k comes from a certain range of EDP_k values. It is important to note that EDP_k contribution to a given MAR (or mean RP) of exceedance of the k^{th} limit-state comes not only from the EDP_k value with the same MAR (or mean RP) of exceedance, but also from EDP_k values with lower MARs and from those with higher MARs.

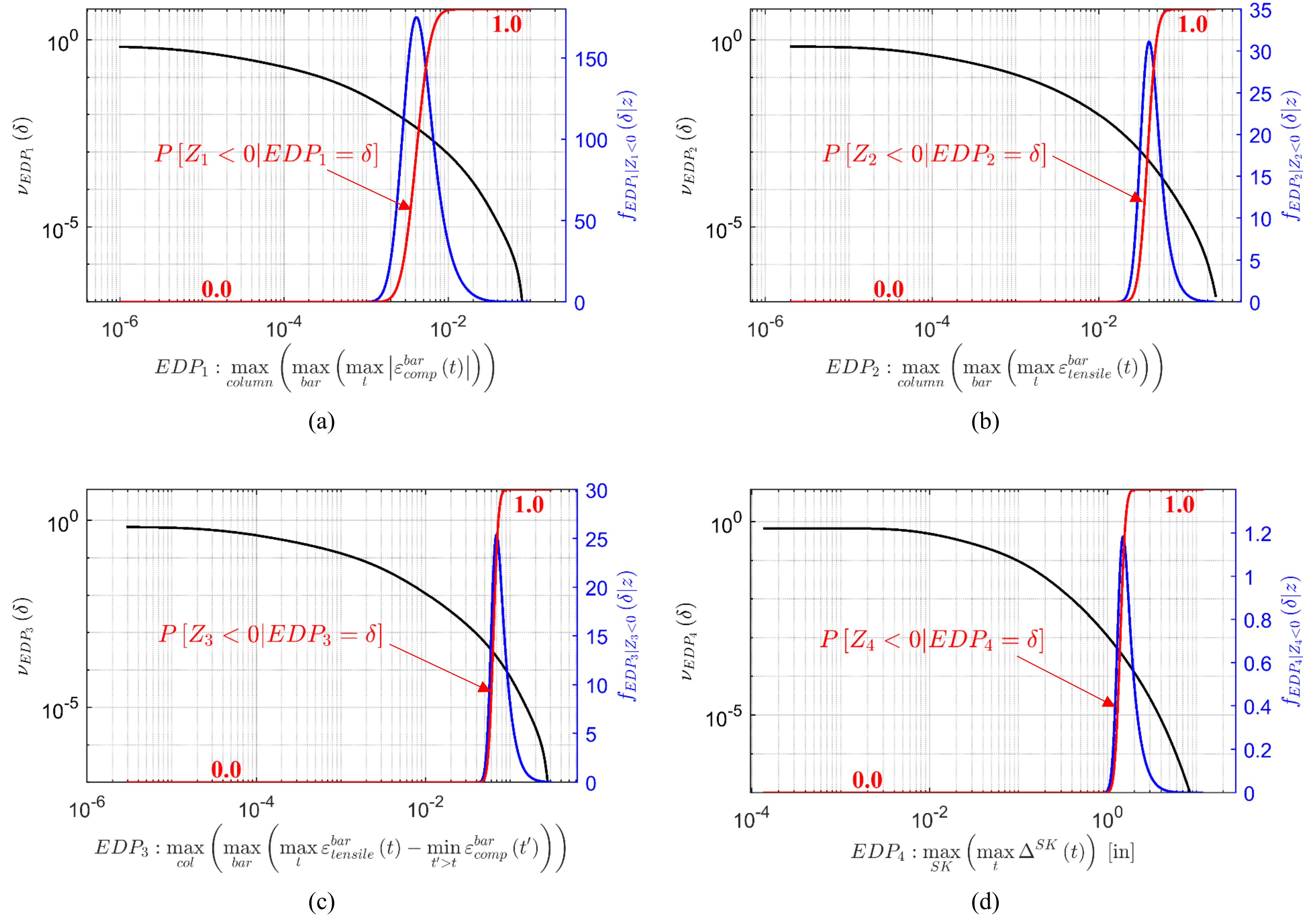

Figure 8.8 *EDP* disaggregation of damage hazard for Bridge A: (a) Limit-state 1 (b) Limit-state 2 (c) Limit-state 3 (d) Limit-state 4

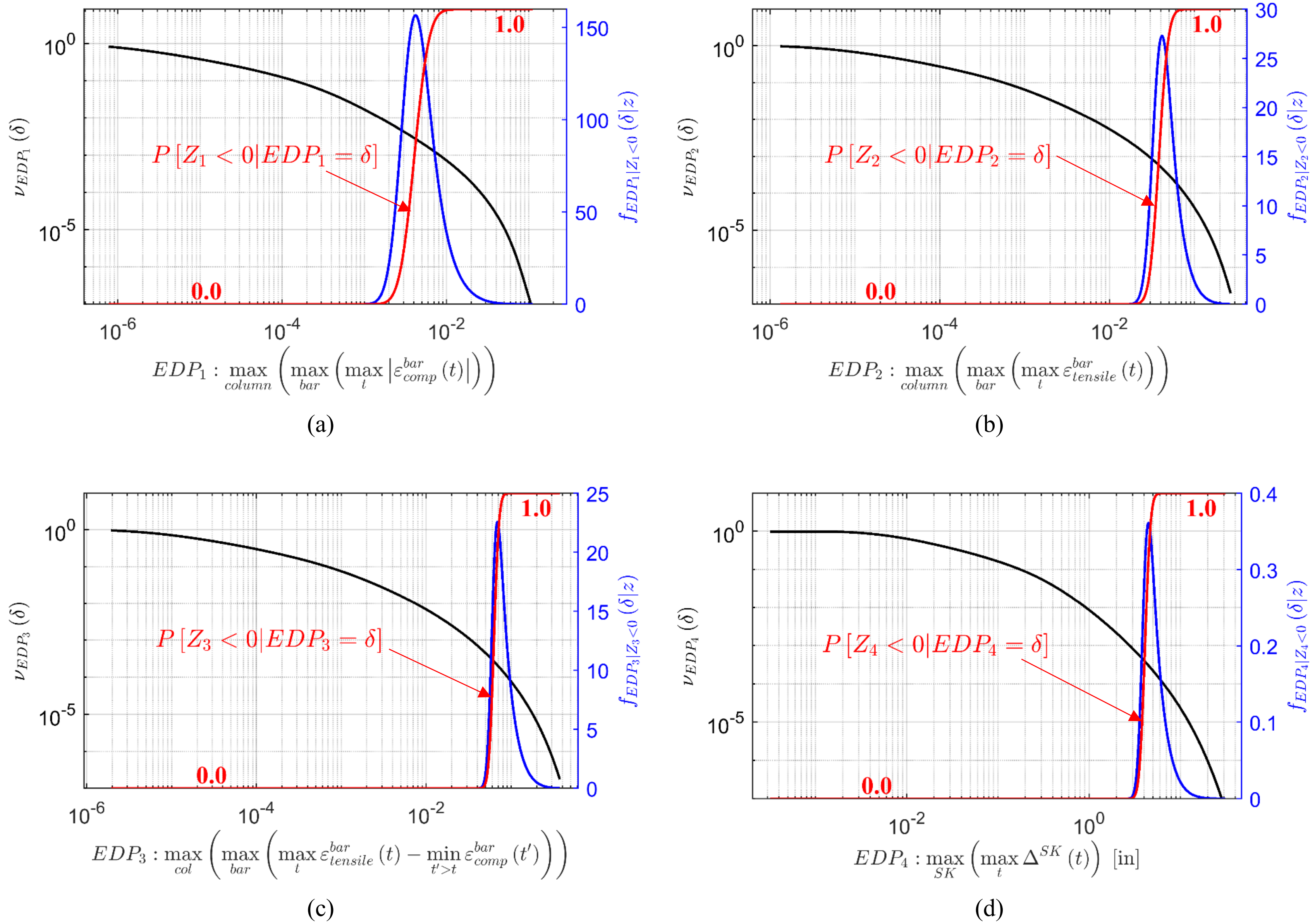

Figure 8.9 *EDP* disaggregation of damage hazard for Bridge B: (a) Limit-state 1 (b) Limit-state 2 (c) Limit-state 3 (d) Limit-state 4

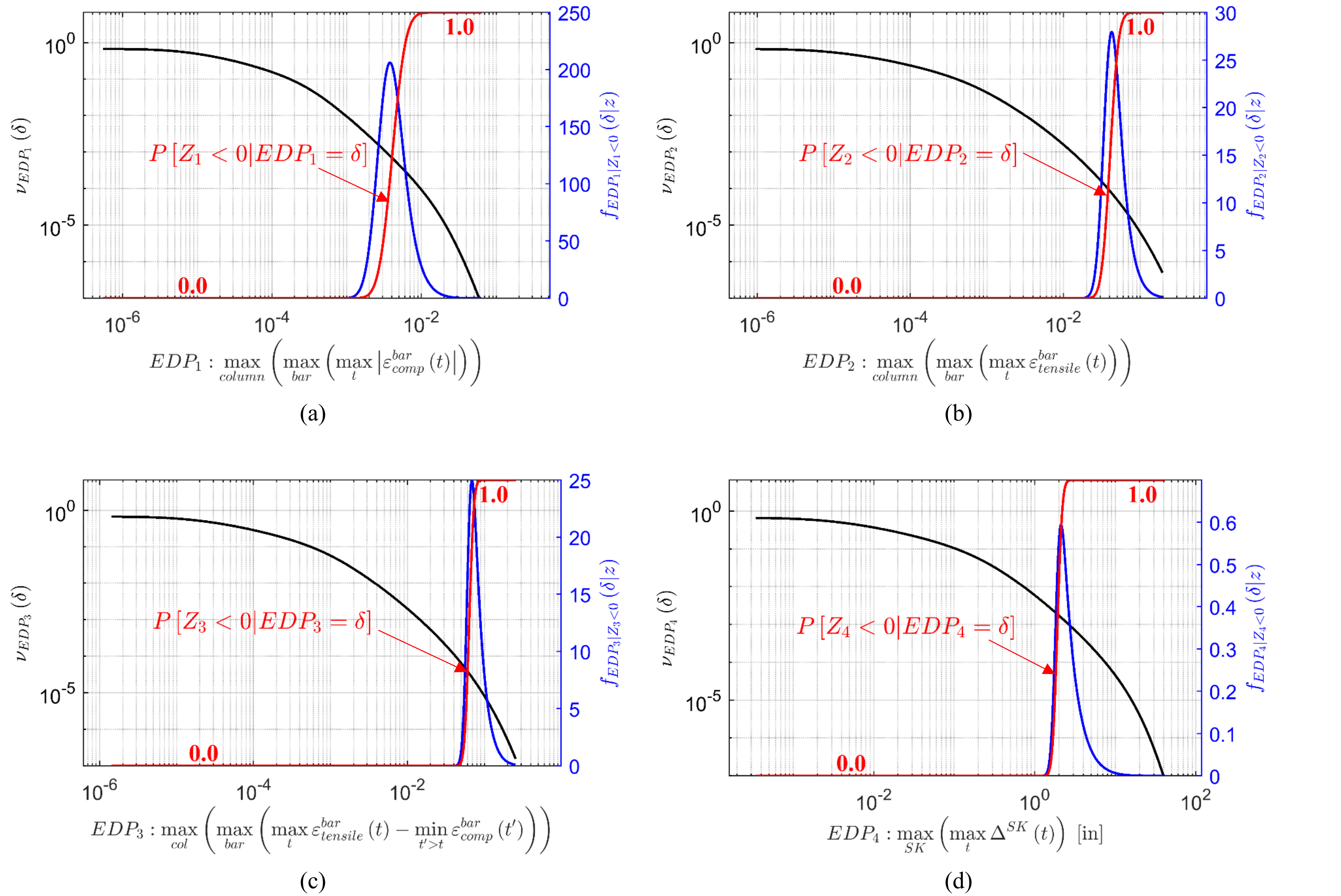

Figure 8.10 *EDP* disaggregation of damage hazard for Bridge C: (a) Limit-state 1 (b) Limit-state 2 (c) Limit-state 3 (d) Limit-state 4

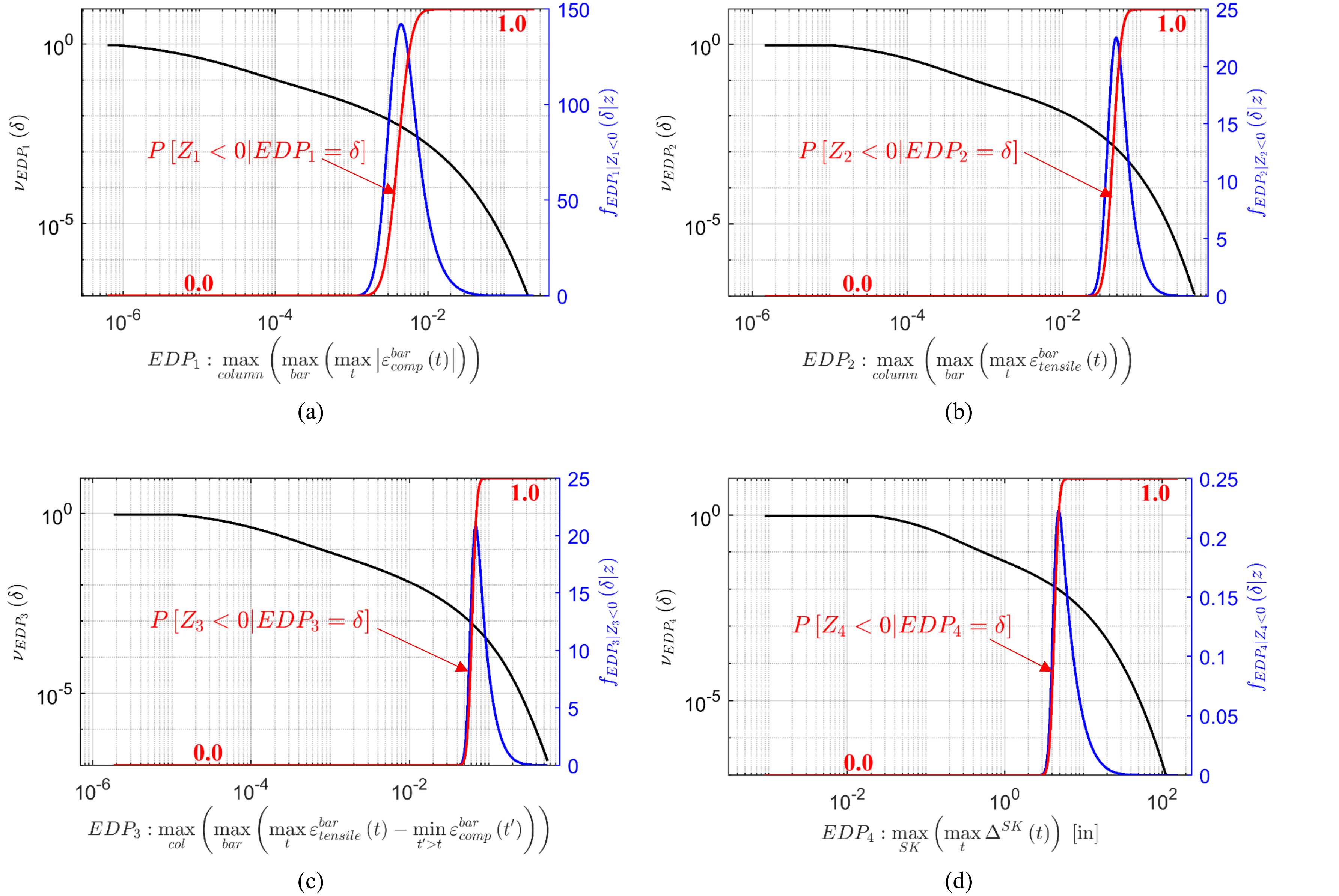

Figure 8.11 *EDP* disaggregation of damage hazard for Bridge MAOC: (a) Limit-state 1 (b) Limit-state 2 (c) Limit-state 3 (d) Limit-state 4

8.7 Deaggregation of Seismic Damage Hazard w.r.t Seismic Intensity Measure

An alternative expression of the damage hazard integral corresponding to the k^{th} limit-state of interest can be obtained by rewriting $f_{EDP_k}(\delta)$, the probability distribution function of EDP_k, in Eq. (8.3), as follows

$$f_{EDP_k}(\delta) = \int_{IM} f_{EDP_k|IM}(\delta \mid x) \cdot f_{IM}(x) \cdot dx \tag{8.18}$$

Substitution of Eq. (8.18) into Eq. (8.3) gives

$$\nu_{LS_k} = \nu \cdot \int_{IM} \int_{EDP_k} P\left[Z_k < 0 \mid EDP_k = \delta\right] \cdot f_{EDP_k|IM}(\delta \mid x) \cdot f_{IM}(x) \cdot d\delta \cdot dx \tag{8.19}$$

which is mathematically equivalent to

$$\nu_{LS_k} = \int_{IM} \underbrace{P\left[Z_k < 0 \mid IM = x\right]}_{\int_{EDP_k} P\left[Z_k < 0 \mid EDP_k = \delta\right] \cdot f_{EDP_k|IM}(\delta|x) \cdot d\delta} \cdot \underbrace{\left|d\nu_{IM}(x)\right|}_{\nu \cdot f_{IM}(x) \cdot dx} \tag{8.20}$$

Eq. (8.20), in contrast to Eq. (8.5), computes the MAR of limit-state exceedance for the k^{th} limit-state by convolving the fragility function given , i.e., $P\left[Z_k < 0 \mid IM = x\right]$, with the seismic hazard curve. This fragility function is obtained by a separate convolution of the originally defined fragility function, given EDP_k, with the conditional probability distribution of EDP_k given already quantified in the PSDemHA phase (Chapter 7) of the framework. The MARs of limit-state exceedance, for the selected set of limit-states for the testbed bridges considered, obtained using Eq. (8.20) match exactly with those obtained using Eq. (8.5).

Seismic damage hazard corresponding to the selected set of limit-states for the considered testbed bridges are computed by aggregating, as per Eq. (8.20), the contributions from all possible levels. The MAR of exceeding a limit-state can now be disaggregated into the contributions from different levels of , thereby providing additional insight into the distribution of causative values leading to a specific level of damage hazard. The conditional probability distribution of , given exceedance of the k^{th} limit-state, i.e., $Z_k < 0$, with a specific MAR, ν_{LS_k}, is given by Eq. (8.21). Figure 8.12 through Figure 8.15 present results of disaggregation of damage hazard corresponding to the limit-states of interest for all considered testbed bridges. The ordinate of each disaggregation plot on the right-hand-side shows the conditional probability distribution, i.e., Eq. (8.21), of , given $Z_k < 0$. The ordinate along the left-hand-side of the same plot shows the site-specific seismic hazard curve. Also marked in each of these plots is the value of corresponding to the same MAR of exceedance as given by ν_{LS_k}.

$$f_{IM|Z_k<0}\left(x \mid z\right) = \frac{P\left[Z_k < 0 \mid IM = x\right] \cdot \left|d\nu_{IM}\left(x\right)\right|}{\nu_{LS_k}} \tag{8.21}$$

The shape of the conditional distribution of , given a specific level of damage hazard for the k^{th} limit-state, is again due to the competing effects between the two terms in the numerator of Eq. (8.21) as a function of . "Very" small and "frequent" (having "high" rates of occurrence, $|d\nu_{IM}(x)|$) values of make negligible contributions to the damage hazard of limit-state k. This is because the conditional probability of $Z_k < 0$, given "very" small values of resulting in "very" small values of EDP_k, is almost zero, i.e., $P\left[Z_k < 0 \mid IM = x\right] \approx 0$. The contribution to damage hazard from increases with increasing values of because of the direct proportionality of with EDP_k and as a result with $P\left[Z_k < 0 \mid IM = x\right]$. Contributions to damage hazard from increasing levels of gradually start to saturate and eventually decrease. The rarity of large values of increases thereby making the drop in $|d\nu_{IM}(x)|$ outweigh the growth in $P\left[Z_k < 0 \mid IM = x\right]$. For "very" large and "too" rare (i.e., $|d\nu_{IM}(x)| \approx 0$) values of , the contribution to damage hazard therefore becomes negligible.

It is again important to notice that contribution to a specific MAR of exceedance of a limit-state comes not only from the value with the same MAR, but also from a certain range of values having lower and/or higher MARs of exceedance. As can be seen from Figure 8.12 through Figure 8.15, an appreciable part of the contribution to the achieved levels of damage hazard corresponding to the selected set of limit-states does come from the range of most confidence (indicated by the light blue patch) where predictions of EDP given are the least erroneous.

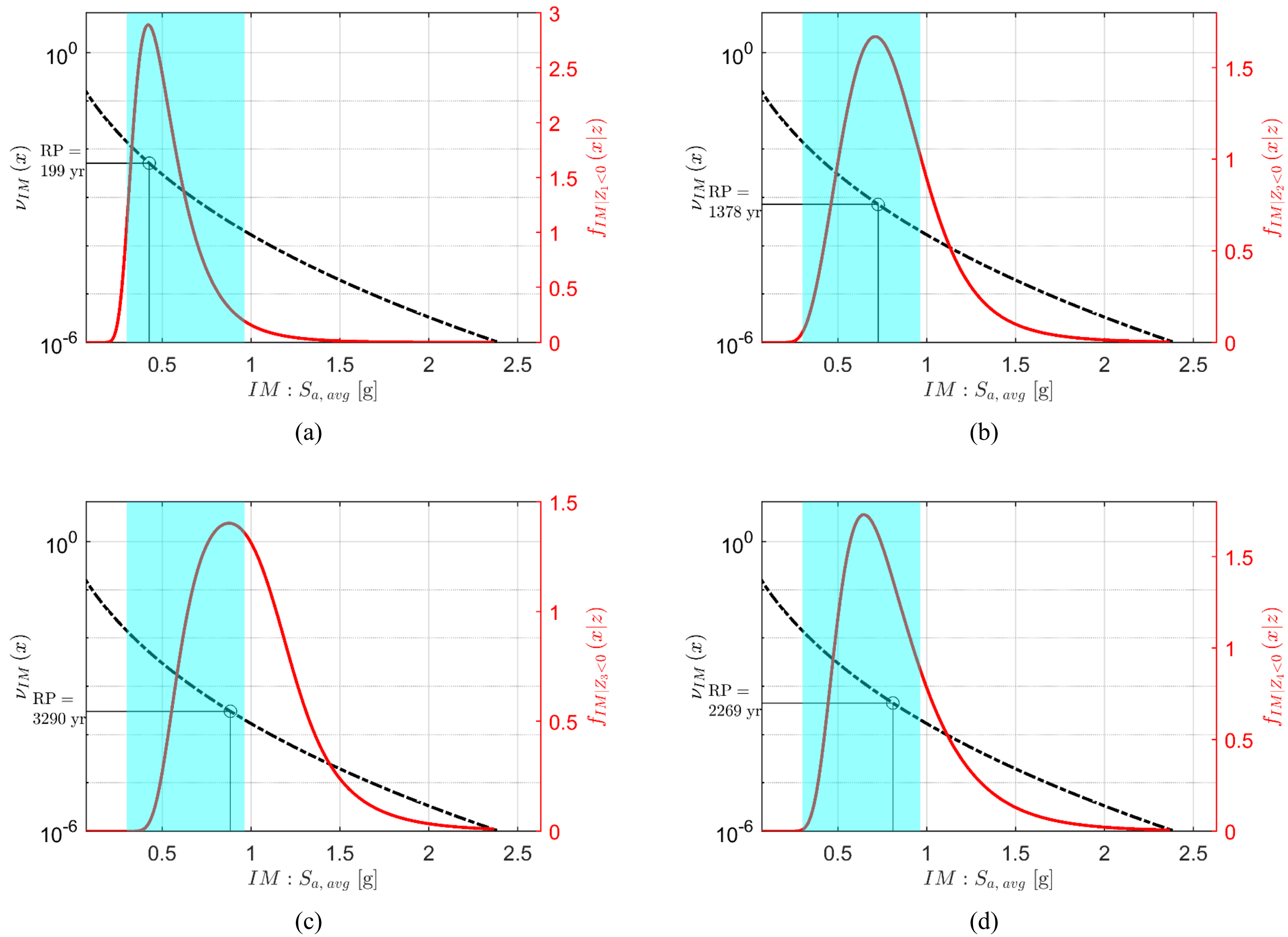

Figure 8.12 disaggregation of damage hazard for Bridge A: (a) Limit-state 1 (b) Limit-state 2 (c) Limit-state 3 (d) Limit-state 4

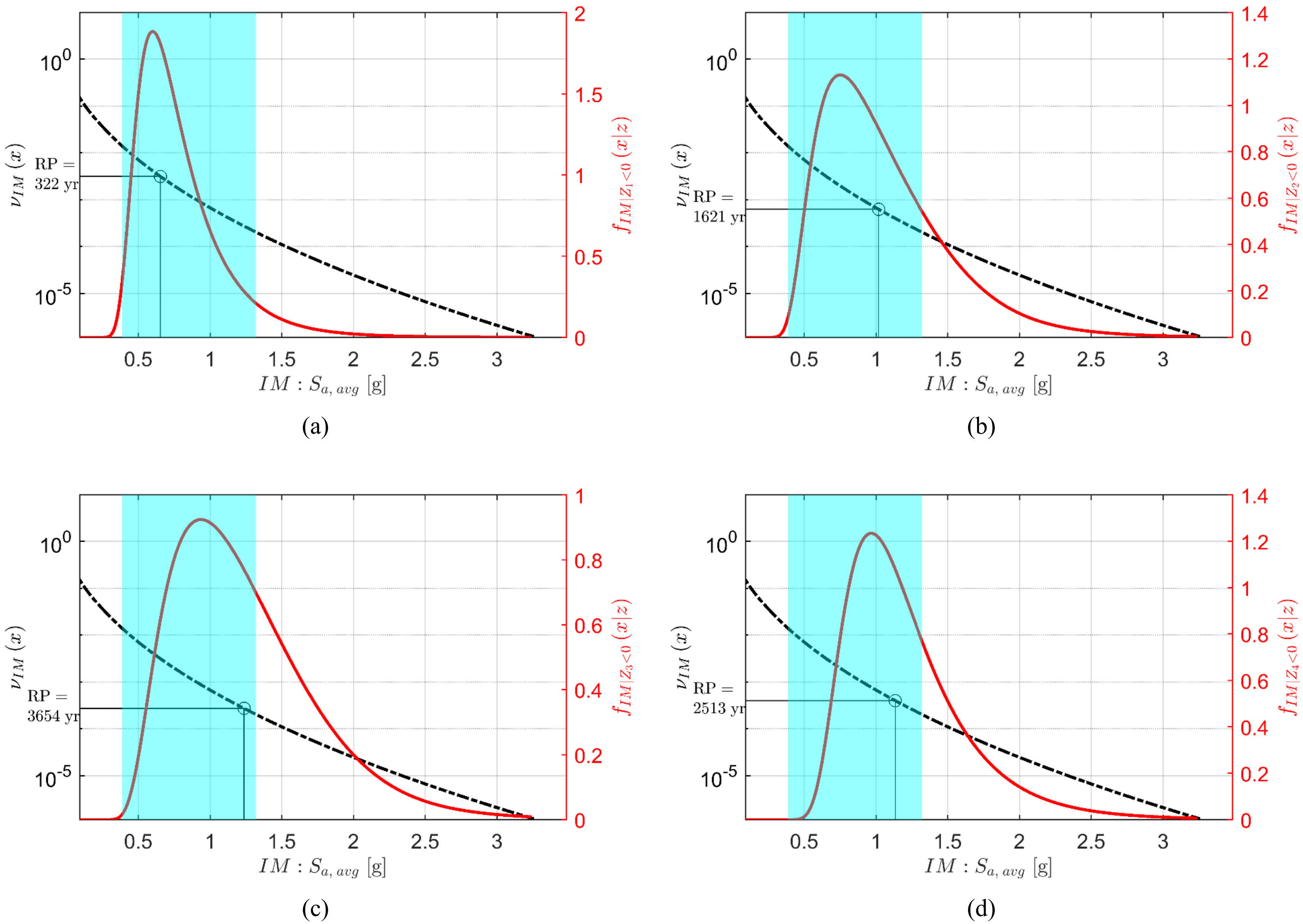

Figure 8.13 disaggregation of damage hazard for Bridge B: (a) Limit-state 1 (b) Limit-state 2 (c) Limit-state 3 (d) Limit-state 4

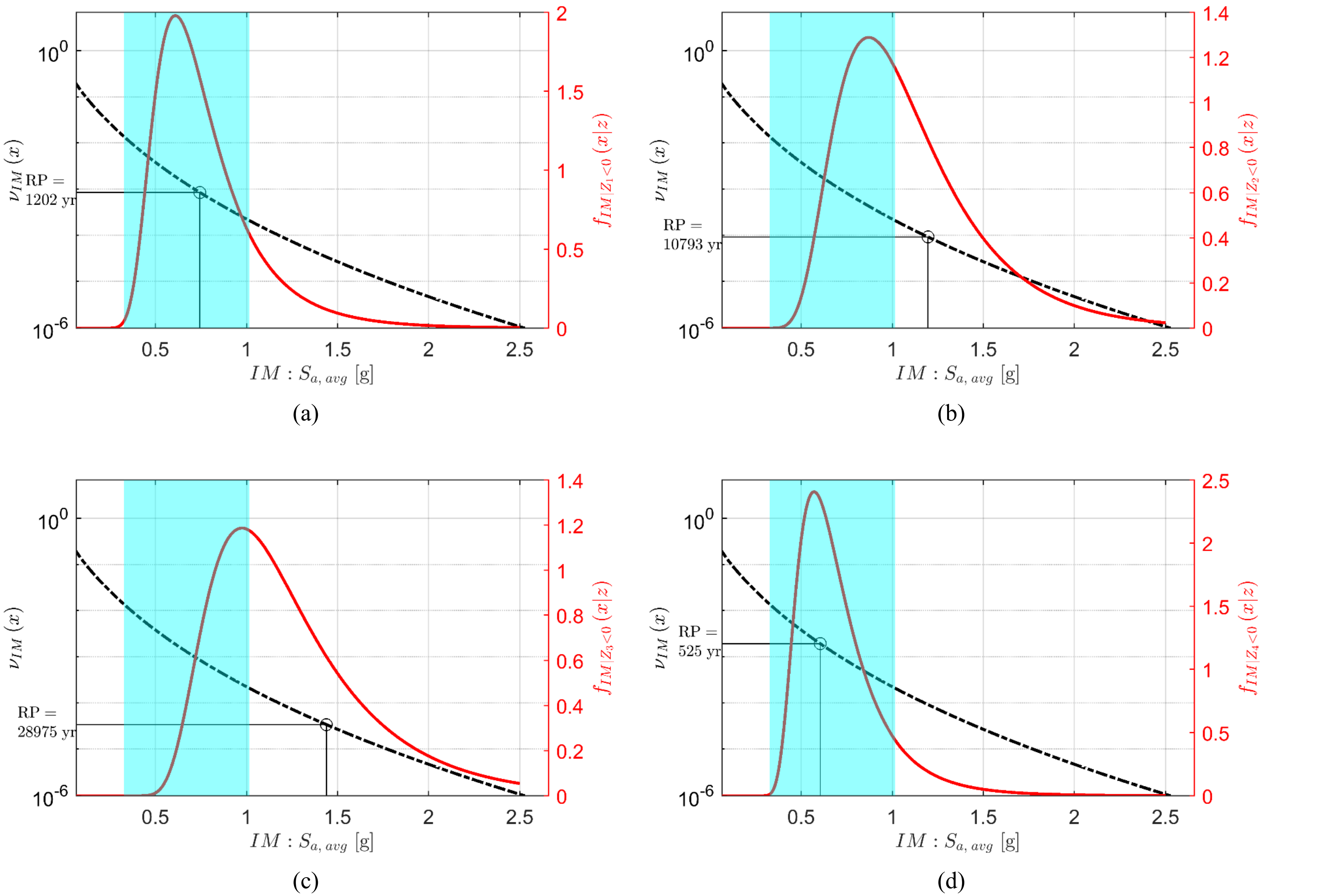

Figure 8.14 disaggregation of damage hazard for Bridge C: (a) Limit-state 1 (b) Limit-state 2 (c) Limit-state 3 (d) Limit-state 4

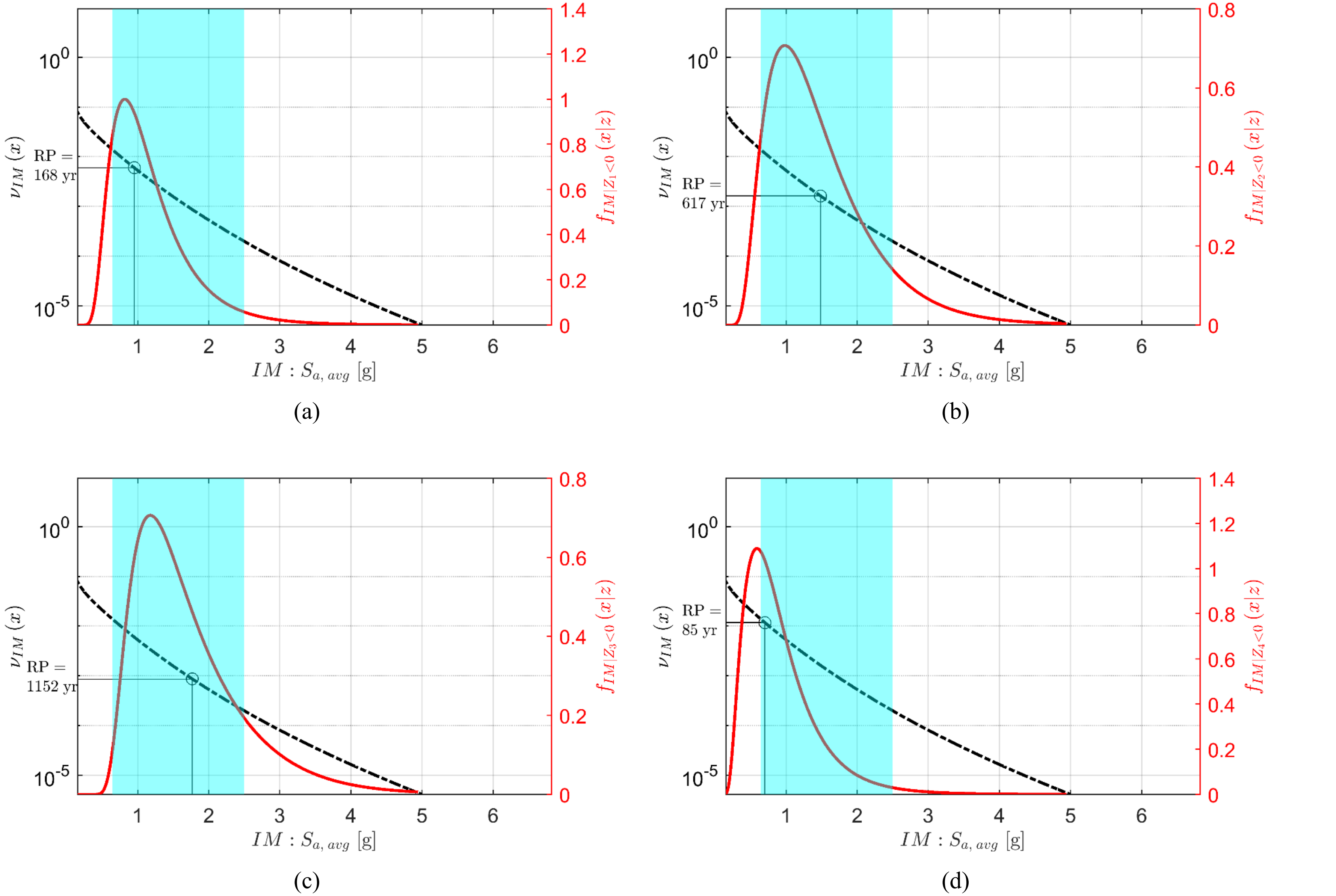

Figure 8.15 disaggregation of damage hazard for Bridge MAOC: (a) Limit-state 1 (b) Limit-state 2 (c) Limit-state 3 (d) Limit-state 4

9 Parametric Probabilistic Seismic Performance Assessment Framework

9.1 Introduction

As a part of the stated objectives of this project, the development of a rigorous performance-based seismic assessment framework for ordinary standard bridges (OSBs) in California, implementing several state-of-the-art improvements relating to various stages of the PEER PBEE framework, is achieved. However, the overarching goal of this project is the development and formulation of a performance-based seismic design framework for OSBs accommodating multiple risk-based design objectives. The essence of structural design is to select values of critical structural design parameters/variables such that a predetermined target specification of a performance measure is met. The performance measure used in this study is the MAR of limit-state exceedance or, equivalently, the mean return period (RP) of limit-state exceedance evaluated for the specific limit-states defined in Chapter 8 using the improved version of the PEER PBEE framework.

Multiple sets of structural design parameter values can satisfy the target performance objectives. The ensemble of all these possible sets with mean RPs of limit-states exceedance greater than or equal to the specified targets constitute a feasible design domain in the design parameter space. For multiple risk-targeted design objectives, the selected values of critical structural design parameters/variables should satisfy the target mean RP of one of the limit-states exactly while ensuring that the mean RPs of the other limit-states are more than satisfied. Exploring the design parameter space via a parametric probabilistic assessment can help investigate and visualize the effect of varying key structural design parameters on the mean RPs of limit-states exceedance. Feasible design domains obtained, as a result, can be used to make risk-informed design decisions.

This chapter elaborates on the assembly, implementation, and automatization of a full-blown parametric probabilistic seismic performance assessment framework for OSBs in California. This framework forms a basis for the simplified risk-targeted performance-based seismic design procedure distilled out of this project for OSBs in California.

9.2 Design Variables

The choice of design variables should cover a spectrum of meaningful structural design parameters, commonly found in seismic bridge design practice. Design variables can be classified into two categories, viz., primary design variables and secondary design variables. Primary design variables refer to design parameters to which the exceedance of the selected set of limit-states are most sensitive. A range of possible designs corresponding to different sets of primary design parameter values can be assessed to investigate the effects of varying primary design variables on the mean RPs of exceedance of the selected set of limit-states. Performance-based seismic design of OSBs, therefore, involves determining the values of primary design variables such that specified performance objectives, stated in terms of mean RPs of limit-state exceedance, are met. All other bridge design parameters determined by meeting requirements of capacity design, minimum ductility limitations, reinforcement ratio restrictions, etc., and/or restricted by the geometry of the bridge, available real estate, traffic requirements, etc. are referred to as secondary design variables. In this chapter, the effects of varying the primary design variables on the mean RPs of exceedance of the selected set of limit-states are investigated while most secondary design variables are held constant.

9.2.1 Primary Design Variables

The primary design variables deemed critical to the seismic performance of an OSB are the column diameter, D_{col}, and the column longitudinal reinforcement ratio, ρ_{long}. These two variables constitute the design parameter space to be explored such that feasible design domains can be delineated following a parametric probabilistic assessment of the testbed bridges. Columns in a bridge are the primary lateral load resisting structural components. Due to the seismic importance of bridge columns and because design parameters of columns are one of the few structural parameters that an engineer can readily vary, the primary design variables chosen in this project revolve around the design of reinforced concrete bridge columns.

Values of the chosen primary design variables are subject to practical constraints. Based on the recommendations of expert practitioners in Caltrans, the diameter of a bridge column is varied in increments of 6 in. due to the availability of existing prefabricated formwork while the longitudinal steel reinforcement ratio, although a continuous variable, is varied in increments of 0.005. Column diameters for this project vary from 4 ft to 8 ft depending on the bridge while the steel reinforcement ratio varies from 0.01 (1.0 %) to 0.03 (3.0 %). In addition, due to the fact that strain based *EDPs* are utilized in this project, the minimum value of D_{col} to be assessed for a bridge is selected so as to prevent softening of column section response. A softening behavior produces nonobjective curvatures in the column sections which consequently leads to unreliable and nonphysical predictions of strains in the finite element analyses.

Re-designs of each testbed bridge corresponding to different combinations of column diameter and longitudinal reinforcement ratio, subject to the practical limitations mentioned, are assessed in this project to obtain the mean RPs of exceedance for the selected set of limit-states. The design parameter space for each of the four testbed bridges are shown in Figure 9.1 with each combination of parameters analyzed labelled as red circles; also shown as a red star is the as-designed primary design parameters for each bridge.

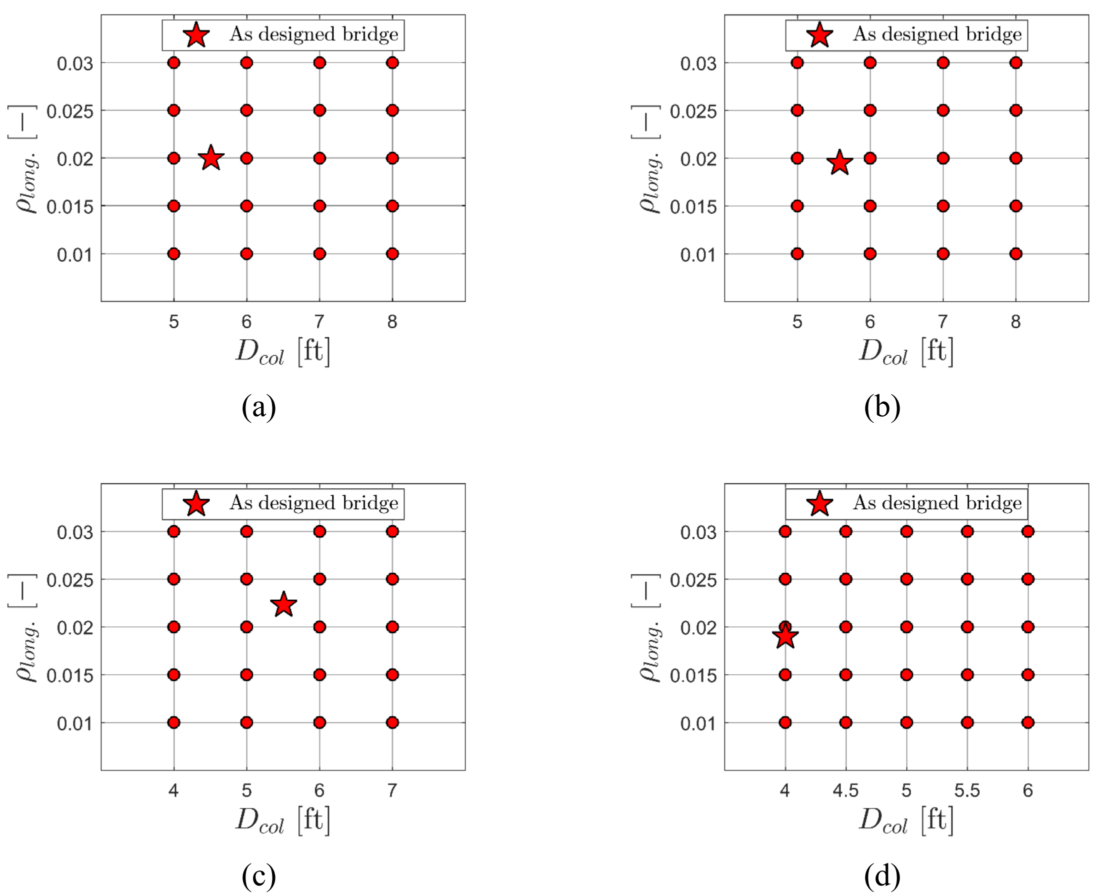

Figure 9.1 Design space for (a) Bridge A; (b) Bridge B; (c) Bridge C; and (d) Bridge MAOC

9.2.2 Secondary Design Variables

Structural design variables, pertaining to the design of OSBs, that are

(a) designed, after the primary design variables have been determined, so as to capacity protect the bridge against other undesirable failure modes thereby forcing energy dissipation to occur due to yielding of the primary load resisting components, i.e., bridge columns, only,
(b) determined by meeting requirements of minimum ductility, minimum reinforcement, distribution of reinforcement, etc. specified by the code, and/or
(c) restricted by the geometry of the bridge, available real estate, traffic requirements, etc.

are grouped into the category of secondary design variables. Secondary variables do not impact the performance of the bridge significantly in terms of mean RPs of exceeding the selected set of limit-states considered in this study and as such are not included in the design parameter space. These variables include column transverse reinforcement ratio, spacing of transverse hoops in a column, diameter and distribution of rebars in a column, height of a column, number of columns in a bent, skew of column bent(s), number of bents, along with variables involving the design of other bridge components such as the bridge deck, bent cap, abutment (shear keys, backwall, stem wall, etc.), and foundations (shallow foundations and/or piles and pile cap). For the seismic performance assessment of any re-design of a testbed bridge, values of all secondary design variables, except the column transverse reinforcement ratio (ρ_{trans}), are taken as per the original design of the as-designed bridge.

For columns with low axial load ratios, typical of OSBs, the transverse reinforcement ratio minimally affects the compressive strength of the concrete core, thereby marginally impacting seismic demand hazard assessment of OSBs. Therefore, a constant value (1.0 %) of ρ_{trans} is used for development of the finite element models of the testbed bridges and their re-designs corresponding to different values of the chosen primary design variables, subsequent structure-specific ground motion selection and demand hazard analyses. However, because the transverse reinforcement affects the capacity of the column corresponding to the limit-states of rebar buckling and rebar fracture, i.e., limit-state 2 and 3, as noted in the capacity equation Goodnight et al. (2016) and Duck et al. (2018), respectively, a sensitivity analysis is performed for these two limit-states by varying the transverse reinforcement ratio as a fraction of the longitudinal reinforcement ratio. For a design point in the primary design parameter space of a testbed bridge, mean RPs of exceeding limit-states 2 and 3 are calculated corresponding to the following cases: Case I: $\rho_{trans} = 0.01$, Case II: $\rho_{trans} = 0.5\rho_{long}$; and Case III: $\rho_{trans} = 0.75\rho_{long}$. In doing so, a constant value (1.0 %) of ρ_{trans} is used until the demand hazard analyses step of the framework. It is only in the damage hazard analysis step, different capacity predictors corresponding to the three cases of ρ_{trans} mentioned are used.

As far as ductility requirements, impacted by the column transverse reinforcement ratio, are concerned, the designer can check whether these requirements are met after the primary design variables have been determined and accordingly adjust the transverse reinforcement ratio to meet these criteria. The distribution of reinforcement bars in a column is also determined by the designer following requirements and recommendations specified by the code and may be adjusted if necessary. It is important to keep in mind that after all primary and secondary design variables have been determined following all adjustments, a final check of structural performance is required to ensure that the final design still meets the specified performance objectives.

9.3 Workflow for Parametric Full-blown Probabilistic Seismic Performance Assessment

Following the identification of primary design variables, i.e., the column diameter (D_{col}) and the column longitudinal reinforcement ratio (ρ_{long}), a rectangular grid in the design space is constructed by varying the primary design variables subject to the practical constraints defined for each testbed bridge. The seismic performance of the resulting re-designs of each testbed bridge is assessed using the improved PEER PBEE framework assembled as a part of this project. Figure 9.2 illustrates the overall workflow for the parametric full-blown probabilistic seismic performance assessment of the considered testbed bridges using Bridge B, the two-span, single-column bent bridge, located in Tustin, California, as a case in point.

For each re-design of a testbed bridge, a new nonlinear finite-element model is generated by updating the primary design parameters, and their associated geometric, material, and damping properties in OpenSees. Modal analysis is performed following the application of gravity loads on the structure and the averaging period range used in the definition of the chosen earthquake intensity measure, i.e., $S_{a,\,\mathrm{avg}}$, is identified. Probabilistic seismic hazard analysis (PSHA) (outlined in Chapter 5) is performed to obtain the site-specific seismic hazard curve in terms of $S_{a,\,\text{avg}}$. This gives the values of $S_{a,\,\text{avg}}$ corresponding to the MARs (or mean RPs) of exceedance defining the six hazard levels considered in this project. Conditional on these values of $S_{a,\,\text{avg}}$, the target response spectra at the considered hazard levels are determined for site-specific risk-consistent ground motion record selection. Ensembles of 100 ground motions at six hazard levels are selected and nonlinear time-history analyses of the re-designed bridge subjected to these ground motions are performed using the nonlinear OpenSees model. As a part of probabilistic seismic demand hazard analysis (PSDemHA) (presented in Chapter 7), an empirical conditional probability distribution of EDP_k, for the k^{th} limit-state, given is established using the two-parameter lognormal distribution. This is done for all EDPs corresponding to the considered set of limit-states. The two primary parameters of the lognormal distribution, i.e., the median $(\eta_{EDP_k|IM})$ and dispersion $(\zeta_{EDP_k|IM})$, are regressed as functions of as previously described in Chapter 7. The demand hazard curve for each EDP_k is obtained by numerically convolving the conditional probability distribution of EDP_k, given , with the site-specific seismic hazard curve. Finally, for probabilistic seismic damage hazard analysis (PSDamHA) (discussed in detail in Chapter 8), normalized fragility curves corresponding to the considered limit-states are accordingly denormalized for the current re-design of the testbed bridge and convolved with the respective demand hazard curves to arrive at estimates of the mean RPs at which different limit-states are exceeded. The entire process is repeated for all re-designs of the considered testbed bridges which define their respective design parameter spaces as shown in Figure 9.1

Implementation of the parametric full-blown risk-targeted seismic performance assessment framework for the considered bridges might seem computationally prohibitive. However, with a well-managed workflow and an efficient utilization of available computing resources, different steps involved in the framework can be smoothly and seamlessly executed. A general description of management of the overall workflow, available computing resources, and their effective utilization is provided in the next section.

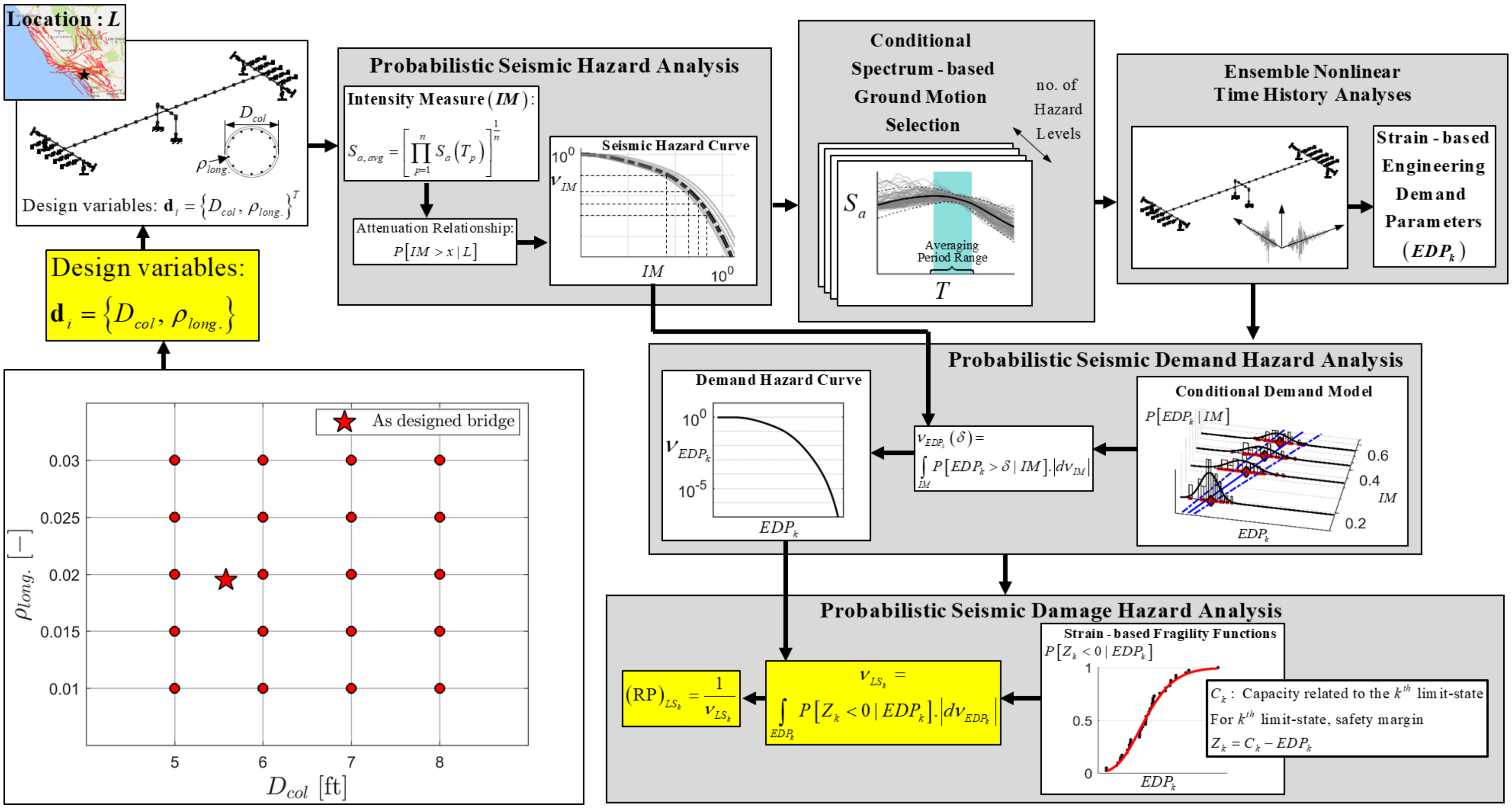

Figure 9.2 Overall workflow for parametric full-blown risk-targeted seismic performance assessment

9.4 Workflow Management and Computing Resources

To efficiently execute different steps involved in the parametric full-blown risk-targeted probabilistic seismic performance assessment framework, a well-organized management of the overall workflow is of paramount importance. To this end, the Tcl input files for the OpenSees models of the benchmark bridges used in this project are revisited for an improved and effective parameterization of the OpenSees models. This is done to facilitate the automated generation of OpenSees models corresponding to multiple re-designed versions of the actual testbed bridges. MATLAB scripts and functions previously developed to carry out individual steps of the framework, including the orchestration of performing ensemble nonlinear time-history analyses in OpenSees, are also parameterized such that changes in the primary design variables can be easily and correctly accommodated.

The Tcl input files were also modified to mitigate the occurrence of non-convergence of the iterative scheme used to integrate the nonlinear equations of motion over an integration time-step. In the case of non-convergence during a nonlinear time-history analysis, it is important to distinguish between the onset of physical collapse or a numerical, non-collapse related convergence issue. In other words, non-converged nonlinear time-history analyses cannot be discarded. Thus, the nonlinear solution strategy is made adequately robust to minimize the number of non-converged nonlinear time-history analyses. In case a non-collapse related numerical convergence issue is encountered, convergence of the numerical solution is ensured mainly through adaptive switching between iterative methods (e.g., Newton, modified-Newton, BFGS, Newton-Krylov) and/or convergence test types and tolerances used to solve the incremental equations of dynamic equilibrium over a time step. Another strategy employed is to slightly vary the number of element integration points used in numerical integration of the element stiffness matrices and element resisting force vectors.

Computationally intensive steps, i.e., selection of site-specific risk-consistent ensembles of ground motion records and subsequent ensemble nonlinear time-history analyses, of the workflow are parallelized using parallel for-loops ("parfor"-loops) in MATLAB. The parallel computing toolbox in MATLAB allows users to exploit the full-processing power of multicore computers by executing jobs on several local workers the number of which, by default, is equal to the number of physical cores available in the computer. For a smooth and seamless parametric probabilistic seismic performance assessment of the considered testbed bridges, sequential execution of different components of the overall workflow is automatized for each re-design of the testbed bridges defining their respective design parameter spaces.

A parent directory is first created for each testbed bridge, i.e., Bridge A, Bridge B, Bridge C, and Bridge MAOC. The parent directory for a testbed bridge contains parameterized Tcl input files for the considered bridge. A MATLAB script is run to feed a pair of values for the two primary design variables from the design space of a testbed bridge to the Tcl input files. OpenSees is invoked through MATLAB for a preliminary post-gravity modal analysis thereby spitting out the averaging period range to be used in the definition of $S_{a,\,\text{avg}}$, the average spectral acceleration over a period range. A MATLAB function is called thereafter which takes in relevant bridge information and performs PSHA computations. Subsequently, the hazard information is fed into another MATLAB function implementing the ground motion selection algorithm, previously described in Chapter 5. The task of ensemble ground motion record selection at a hazard level is computationally independent of any other hazard level. Therefore, a parallel execution of these tasks using a parfor-loop in MATLAB significantly speeds up the process of selecting 600 ground motions (100 per hazard level) for a single design point. Individual sub-directories containing selected ensembles of ground motion records at six different hazard levels for a specific design point are created and accordingly populated in the parent directory of a testbed bridge. Thereafter, the most computationally intensive task of performing ensemble nonlinear time-history analyses of a design point in OpenSees is orchestrated through MATLAB and executed parallelly via another parfor-loop. Inside the parent directory for a testbed bridge, results of ensemble nonlinear time-history analyses and recorded *EDP*s for a specific design point are stored in individual sub-directories for each ground motion record corresponding to a hazard level. The level of parallelization achieved at this step of the workflow is limited in a desktop computing environment and is tremendously enhanced in a supercomputing environment, as is discussed in the next sections. In a desktop computing environment, the two different parfor-loops (one for the selection of ensembles of ground motion records at six hazard levels for a design point, and the other for the orchestration of ensemble nonlinear time-history analyses of a design point in OpenSees) are nested inside a sequential for-loop that runs over all pairs of primary design parameter values defining the respective design space of a testbed bridge. As discussed later in Section 9.4.2, this flow of operations is slightly modified in the supercomputing environment to greatly utilize its tremendous parallel computing capabilities.

To avoid unnecessary computation of the subsequent steps of the workflow with *EDP* data coming from numerically non-converged analyses, the sequential for-loop running over each design point in the design space of a testbed bridge is broken at this stage. Once all ensemble nonlinear time-history analyses for all design points has finished running, an automated check is made for convergence issues encountered. With alterations made to the analysis parameters (e.g., order of switching between solution algorithms and convergence test types, values of tolerance, integration time step size) and/or model parameters (e.g., number of element integration points) subsequent runs, barring the already converged cases, are made until the number of non-collapse related numerical non-converged cases is reduced to zero. Based on the design parameter spaces defined for the testbed bridges, the number of nonlinear time-history analyses to be performed using OpenSees amounts to a total of 12000 (= 20 re-designs × 6 seismic hazard levels × 100 nonlinear time history analyses per seismic hazard level) for Bridge A, Bridge B, and Bridge C, and a total of 15000 (= 25 re-designs × 6 seismic hazard levels × 100 nonlinear time history analyses per seismic hazard level) for Bridge MAOC. This leads to a total of 51000 nonlinear time history analyses for the entire study. It is noteworthy to mention that for each of these analyses, the numerical integration of the equations of motion converged over the entire duration of the seismic input.

With available numerically converged *EDP* data for all design points in the design space of a testbed bridge, a sequential for-loop over each design point is re-initiated to carry out the remaining relatively low-cost computational tasks of the overall workflow i.e., PSDemHA and PSDamHA. For a single design point, these tasks primarily involve numerical evaluation of hazard integrals thereby leading to estimates of mean RPs of limit-state exceedance for the selected set of limit-states.

9.4.1 Desktop Computing Environment

Dell Precision T7810, a high-performance workstation, is used to execute different steps involved in the parametric full-blown risk-targeted seismic performance assessment of the four testbed bridges considered. Specifications for the workstation include a dual Intel Xeon E5-2650 v4 processor with 12 cores each, a clock rate of 2.2GHz, and 128 GB DDR4 RAM. Although the parallel computing toolbox in MATLAB imposes no limit to the number of local workers to be specified in a desktop computing environment, the default value for the chosen computer, i.e., 24 (= 2 processors × 12 cores each), is used. Thus, 24 individual jobs which are essentially independent of each other can be parallelized on the local desktop computing environment.

The entire workflow, as outlined previously, is executed in the desktop computing environment without any modification. It is only in the supercomputing environment, as will be discussed in the next section, the outlined flow of operations is slightly modified to achieve a higher level of parallelization. With the specifications of the desktop computer mentioned above, the task of selecting 600 ground motions (100 per hazard level) for a single design point is finished in about 15-20 minutes with a parallel execution of the task using a parfor-loop in MATLAB. The parfor-loop engages 6, out of 24 available, workers in the desktop computing environment to select six independent ensembles (one ensemble per worker) of ground motions at six different hazard levels. This is in significant contrast to a runtime of about 2.5-3 hours when the same task is performed sequentially for six hazard levels for a single design point.

In terms of computational cost and runtime, a significant bottleneck is encountered while performing ensemble nonlinear time-history analyses of design points defining the design space of a testbed bridge in OpenSees. Since a sequential for-loop over the number, $n_{\mathbf{D}}$, of design points of a testbed bridge drives the parametric full-blown assessment of the bridge in the desktop computing environment, only 24 out of the $600 \times n_{\mathbf{D}}$ essentially independent nonlinear time-history analyses can be carried out in parallel. This leads to significantly long runtimes (e.g., about 75-150 hours depending on the bridge model) for the ensemble nonlinear time-history analyses phase involved in the full-blown assessment of a bridge. As discussed in the next section, a remarkable improvement, primarily in terms of runtime, is achieved by switching to available supercomputing resources for the step of performing ensemble nonlinear time-history analyses of all design points of a testbed bridge.

9.4.2 Supercomputing Environment

Stampede2, the flagship supercomputer at the University of Texas at Austin's Texas Advanced Computing Center (TACC), is chosen for the parallel execution of ensemble nonlinear time-history analyses. Stampede2 provides high-performance computing resources to thousands of researchers, comprised primarily of 4,200 Intel Knight's Landing (KNL) compute nodes and 1,736 Intel Xeon Skylake (SKX) compute nodes. The KNL nodes have 96GB of DDR RAM, a clock rate of 1.4 GHz, and can parallelize 68 processes (analyses) while the SKX nodes have 192GB of RAM, a clock rate of 2.1 GHz, and can parallelize 48 processes. Researchers remotely login to one of the system's login nodes and submit jobs to a job queue where they wait to be assigned to compute nodes. The assignment of jobs is controlled by SLURM, a job scheduling software for Linux/Unix systems. SLURM job files written by the researcher provide key job information necessary for the system to process requests, including a time limit, the number of nodes and parallel processes required, and which research allocation to charge. A maximum of 50 jobs can be submitted to the KNL queue at once by any one research allocation with a maximum time limit of 48 hours. The maximum number of jobs that can be submitted to the SKX queue is restricted to 25 with the same allowable time limit of 48 hours. Therefore, in one batch of 50 jobs, the KNL compute nodes can process 3,400 (= (50 Jobs) × (1 Node per Job) × (68 processes per Node)) parallel nonlinear time-history analyses at 1.4 GHz clock rate, while the SKX compute nodes can process 1,200 (= (25 Jobs) × (1 Node per Job) × (48 processes per Node)) parallel nonlinear time-history analyses at 2.1 GHz clock rate.

The process is initiated in the desktop computing environment where the workspace outlined previously is created and the workflow is executed up to the selection of $600 \times n_{\mathbf{D}}$ ground motion records for all $n_{\mathbf{D}}$ design points in the design space of a testbed bridge. MATLAB scripts, functions, and the parent directory of a testbed bridge containing parameterized bridge model Tcl input files and selected sets of ground motion records for each design point are compressed and secure copied to a personal storage space on Stampede2 where it is subsequently extracted. Once the primary workspace has been extracted, an automated initialization script is run in MATLAB on Stampede2 that divides the total workload, i.e., $600 \times n_{\mathbf{D}}$ jobs, into batches of jobs subject to the job queue constraints previously described. The initialization script also creates respective SLURM job submission files. Thereafter, the SLURM job files are individually executed in a sequential manner as they cannot run concurrently. When a job is assigned to a compute node, the node is assigned an identification number that prescribes a unique set of time-history analyses to complete (generally a set of 68 on KNL nodes or 48 on SKX nodes) with the aim of maximizing the utility of each node. The assignment of jobs in a batch to KNL nodes and respective CPUs is illustrated in Figure 9.3.

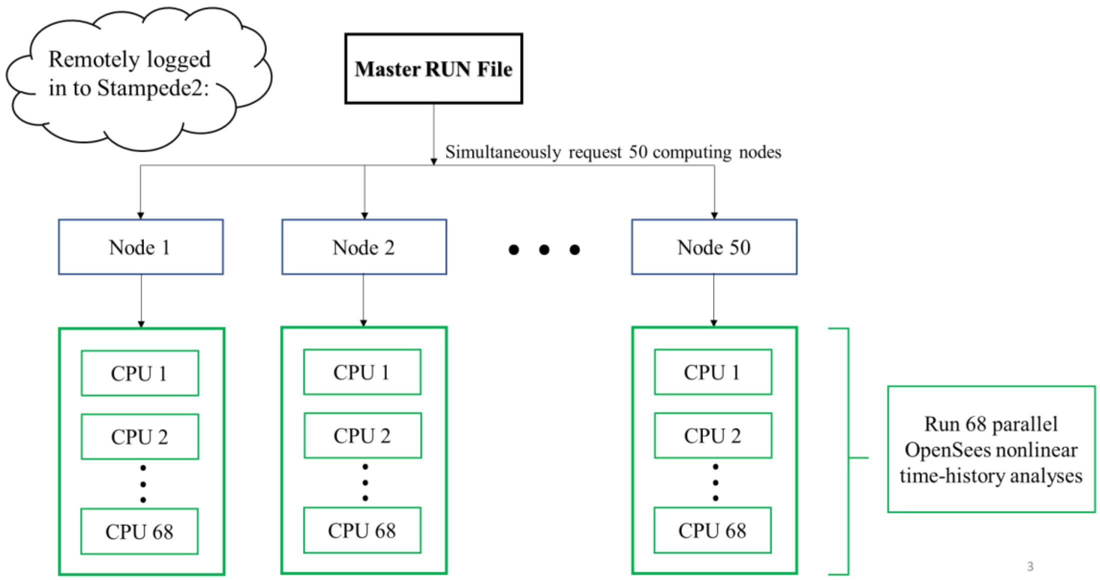

Figure 9.3 Parallel assignment of ensemble time-history analyses in a batch to KNL nodes on Stampede2

After all batches of jobs have been submitted and all analyses within a batch are complete, a second automated process is run to assess which analyses did not converge or complete in the allotted time limit and then reinitializes the workspace for a subsequent run. This reinitializing process also flags every analysis that has converged such that it is never selected on a future run and its results overwritten. Due to the high number of initial analyses (10,000+ for each bridge), the KNL nodes are typically used for the first batch of jobs due to their higher throughput (3,400 parallel processes vs. 1,200 on the SKX nodes) to reduce the number of non-converged or incomplete analyses down to a number that the SKX nodes can efficiently handle in a subsequent run. Between runs, alterations are made to analysis parameters (e.g., order of switching between solution algorithms and convergence test types, values of tolerance, integration time step size), model parameters (e.g., number of element integration points) and/or SLURM job file parameters (e.g. job queue, time limit) to increase the likelihood of converging and/or completing future analyses.

Using supercomputing resources, exorbitant desktop computing runtimes of performing ensemble nonlinear time-history analyses of all design points in the design space of a testbed bridge is remarkably brought down to about 15-20 hours. Once all analyses have converged, the analysis results are compressed and secure copied to the desktop computing environment for post-processing. The remaining relatively low-cost computational steps of the overall workflow, i.e., PSDemHA and PSDamHA, are subsequently performed in the desktop computing environment.

9.5 Mean Return Period Surfaces for Considered Limit-states and Feasible Design Domains

Results of the parametric full-blown probabilistic seismic performance assessment, in terms of mean return periods (RPs) of limit-state exceedance, obtained for the selected set of limit-states for each re-design of the considered testbed bridges are shown in Figure 9.4 (a) through Figure 9.19 (a). Figures corresponding to limit-states 2 and 3, i.e., the limit-state of longitudinal rebar buckling and longitudinal rebar fracture, include results of the sensitivity analysis performed with respect to ρ_{trans} which is assumed to vary as: Case I: $\rho_{trans} = 0.01$, Case II: $\rho_{trans} = 0.5\rho_{long}$; and Case III: $\rho_{trans} = 0.75\rho_{long}$. For each limit-state, a piecewise linear surface is least-square fitted to the mean RPs computed at the re-design points as shown in Figure 9.4 (b) through Figure 9.19 (b). Although the overall topology of the fitted mean RP surfaces over the design space is accurate, some topology details are by-products of the fitted surface (here, piecewise linear) assumed. It is important to notice that the mean RP results obtained for the as-designed bridges, in each case, remarkably agree with the topology of the fitted surfaces despite being excluded from the data used for fitting these surfaces. Contour plots of the mean return period surfaces over the design space are shown in Figure 9.4 (c) through Figure 9.19 (c).

Visual inspection, and corroboration by contours, of mean RP surfaces show an increasing trend of mean RP of exceedance values corresponding to the limit-states pertaining to bridge columns (i.e., LS_1, LS_2, and LS_3), as any one, or both, of the primary design variables in the design space of a testbed bridge are increased. Increasing values of primary design variables (both relating to design of bridge columns) result in stronger, and thereby translating to safer (characterized by low MAR or high mean RP of limit-state exceedance), designs of columns in a bridge. In an average sense, the non-zero or nor-singular slopes of the seemingly parallel contour-lines of these surfaces indicate non-trivial sensitivity of the mean RPs of exceeding limit-states concerning bridge columns to the chosen primary design variables thereby justifying the choice.

As shown in Figure 9.4 (c) through Figure 9.19 (c), contours of the mean RP surface fitted for the limit-state of shear key damage in any testbed bridge are, on an average, almost parallel to the ρ_{long} axis thereby being suggestive of low sensitivity of the exceedance of this limit-state to different values of longitudinal reinforcement ratio. With larger column diameter (D_{col}) values, however, the shear keys are found to exhibit more safety (i.e., higher mean RP of limit-state exceedance). As mentioned earlier, the design of shear keys is not intended to be achieved as a primary goal of this project. Therefore, a discussion with regard to the exceedance of this limit-state and how it relates to the primary design variables is dropped hereafter.

For a specific limit-state (1-3), design points with mean RP of exceeding a limit-state greater than or equal to a specified target for that limit-state can be deemed “safe”, while classifying those with mean RP of limit-state exceedance lower than the specified target as “unsafe”. Information as such can be used to construct and delineate regions of safety and/or feasibility over the design parameter space. For each testbed bridge, the mean RP surfaces for the considered set of limit-states (1-3) are intersected by horizontal planes corresponding to the respective specified target mean RPs enlisted in Table 9-1. Target mean RPs of limit-state exceedance adopted for this project are based on discussions with and feedback from expert Caltrans engineers thereby reflecting the risk tolerance of the bridge engineering community in general. Figure 9.4 (b) through Figure 9.19 (b), with the exception of figures corresponding to limit-state 4, show this intersection of each of these mean RP surfaces with a horizontal red plane corresponding to the respective specified target mean RP. The contour lines corresponding to these target return periods are indicated by bold lines in the contour plots shown in Figure 9.4 (c) through Figure 9.19 (c). In each of the contour plots, the feasible domain in the design space (i.e., design points corresponding to a mean RP larger than the target mean return period) is colored in green. Contour lines of the mean RP surfaces corresponding to target mean RPs of individual limit-states are superimposed in the design space to delineate the overall feasible design domains and to identify the governing limit-states along the boundaries of the feasible design domains. Seismic performance of the as-designed version of a testbed bridge can be gauged by the relative location of the corresponding design point (denoted by a red star in Figure 9.20 through Figure 9.23) in the design parameter space with respect to the feasible design domain outlined (i.e., does the as-designed bridge belong to the feasible design domain). Feasible design domains obtained for the four testbed bridges considered are shown in Figure 9.20 through Figure 9.23.

Table 9-1 Target mean RPs of limit-state exceedance

Limit-state	Target Mean RP of Exceedance (years)
1. Concrete cover crushing	225
2. Longitudinal rebar buckling	1000
3. Longitudinal rebar fracture	2500

It is observed from Figure 9.20 that Bridge A, as-designed, lies just outside the feasible design domain. The performance of the as-designed bridge is found to be considerably well with regard to the ultimate limit-states of longitudinal rebar buckling and longitudinal rebar fracture, as depicted by its proximity with respect to the corresponding target RP contour lines on the “safe” side. The as-designed bridge, however, just falls short of satisfying the target for the serviceability limit-state of concrete cover crushing with only a minimal difference between the calculated and the target mean RP value (199 years versus a target of 225 years). The feasible design domain, in this case, is controlled by the limit-state of concrete cover crushing for column designs with small D_{col} and large ρ_{long} values. For designs with large D_{col} values coupled with small values of ρ_{long}, the limit-states of longitudinal rebar buckling and longitudinal rebar fracture, are found to almost equally govern the definition of the feasible design domain.

As seen from Figure 9.21, Bridge B, as-designed, performs remarkably well with respect to all three limit-states. It lies well inside the feasible design domain while not being too far from the demarcating target mean RP contour lines. Governing the definition of the feasible design domain, in this case, is mostly found to be the limit state of longitudinal bar fracture.

Given the seismic hazard at the site of Bridge C and secondary design variables set as per the original design of this three-span, three-column bent bridge, the feasible design domain obtained and shown in Figure 9.22 is found to encompass, almost entirely, the considered design parameter space. The as-designed version of Bridge C is found to be too conservative in terms of seismic performance as measured by the mean RPs of exceeding the considered set of limit-states. The target mean RP contour for the limit-state of concrete cover crushing is not shown in Figure 9.22 because all design points in the considered design parameter space are found to have mean RPs of exceedance greater than the specified target. The feasible design domain is completely controlled by the limit-state of longitudinal rebar fracture.

In contrast to the favorable performances of the the as-designed versions of Bridge A and Bridge B, and the overly conservative performance of Bridge C, as-designed, the as-designed version of Bridge MAOC is found to underperform in terms of damage hazard associated with the selected set of limit-states. As shown in Figure 9.23, the design point corresponding to Bridge MAOC, as-designed, lies outside the feasible design domain which, in this case, is partly controlled by different limit-states. Similar to the observation made in case of Bridge A, the feasible design domain is controlled by the limit-state of concrete cover crushing for bridge designs having small D_{col} and large ρ_{long} values. On the other hand, the limit-state of longitudinal rebar fracture is found to control the feasible design domain for designs with large D_{col} and small ρ_{long} values.

Comparison of feasible design domains obtained for each of the three cases of ρ_{trans} assumed in the sensitivity analysis conducted for each testbed bridge are also shown in Figure 9.20 through Figure 9.23, (a), (b), and (c) respectively. As noted from these figures, the feasible design domains obtained for a testbed bridge in each case differ from each other to some extent. The feasible design domain obtained for Case II, i.e., $\rho_{trans} = 0.5\rho_{long}$, for a testbed bridge is found to be slightly smaller than that obtained for Case III, i.e., $\rho_{trans} = 0.75\rho_{long}$. Case I, with a constant value of ρ_{trans} equal to 0.01 (1%) is found to yield feasible design domains comparable to the other two cases. It is to be noted that the parametric probabilistic seismic performance assessment framework, subject to several simplifying and/or empirical assumptions made at its various stages, is ultimately an approximate tool for gauging the seismic performance of a structure. Given the approximate nature of this numerical assessment framework, the observed level of sensitivity of its results with respect to ρ_{trans} is not significant. For reasons of simplicity, without compromising accuracy, the choice of ρ_{trans} as a secondary design variable is hence deemed justified. Discussion hereafter, although equally applicable to all three cases, is restricted to Case I, i.e., $\rho_{trans} = 0.01$.

The full-blown parametric probabilistic seismic performance assessment framework, although computationally expensive, can be very well used for the design of a new OSB. The concept of a feasible design domain in the design parameter space can be utilized to make risk-informed design decisions while trying to satisfy multiple risk-based objectives. Values of primary design variables are determined first such that multiple risk-based objectives are met. This involves selection of a design point in the primary design parameter, i.e., $D_{col} - \rho_{long}$, space either lying on the boundary of or located inside the feasible design domain. In doing so, standardized and/or predetermined values of secondary design variables are used. Upon selection of primary design variables, secondary design variables are determined and adjusted to meet requirements of capacity design, code-based requirements of ductility, minimum reinforcement, etc., and/or other restrictions imposed by available real estate, traffic flow, etc. As mentioned earlier, after all primary and secondary design variables have been determined following all adjustments, a final check of structural performance is required to ensure that the final design still meets the specified performance objectives.

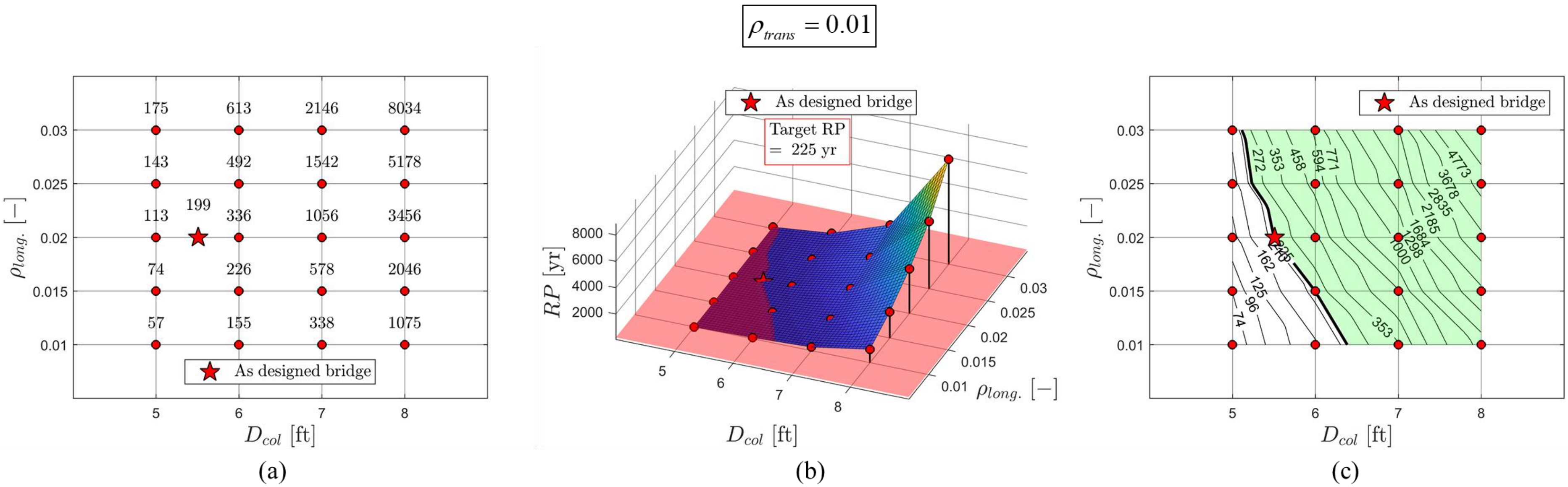

Figure 9.4 Results of parametric probabilistic seismic performance assessment of Bridge A in terms of limit-state 1, i.e., concrete cover crushing: (a) mean RPs (in years) of limit-state exceedance of all design points; (b) fitted mean RP surface; and (c) contours of mean RP surface (target RP contour line in bold) and feasible domain (in green)

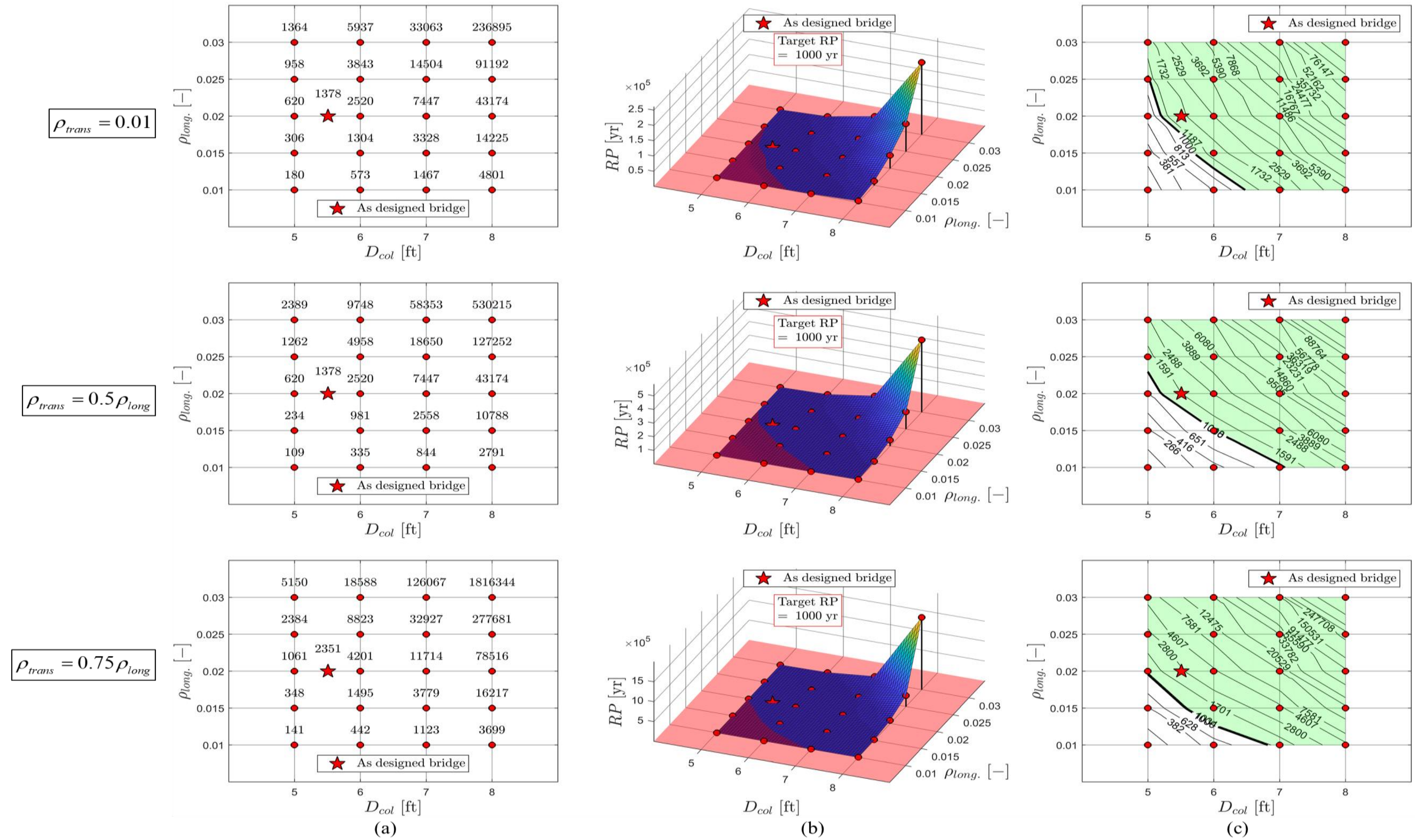

Figure 9.5 Results of parametric probabilistic seismic performance assessment of Bridge A in terms of limit-state 2, i.e., longitudinal rebar buckling: 1st row: $\rho_{trans.} = 0.01$; 2nd row: $\rho_{trans.} = 0.5\rho_{long.}$; 3rd row: $\rho_{trans.} = 0.75\rho_{long.}$; (a) mean RPs (in years) of limit-state exceedance of all design points; (b) fitted mean RP surface; and (c) contours of mean RP surface (target RP contour line in bold) and feasible domain (in green)

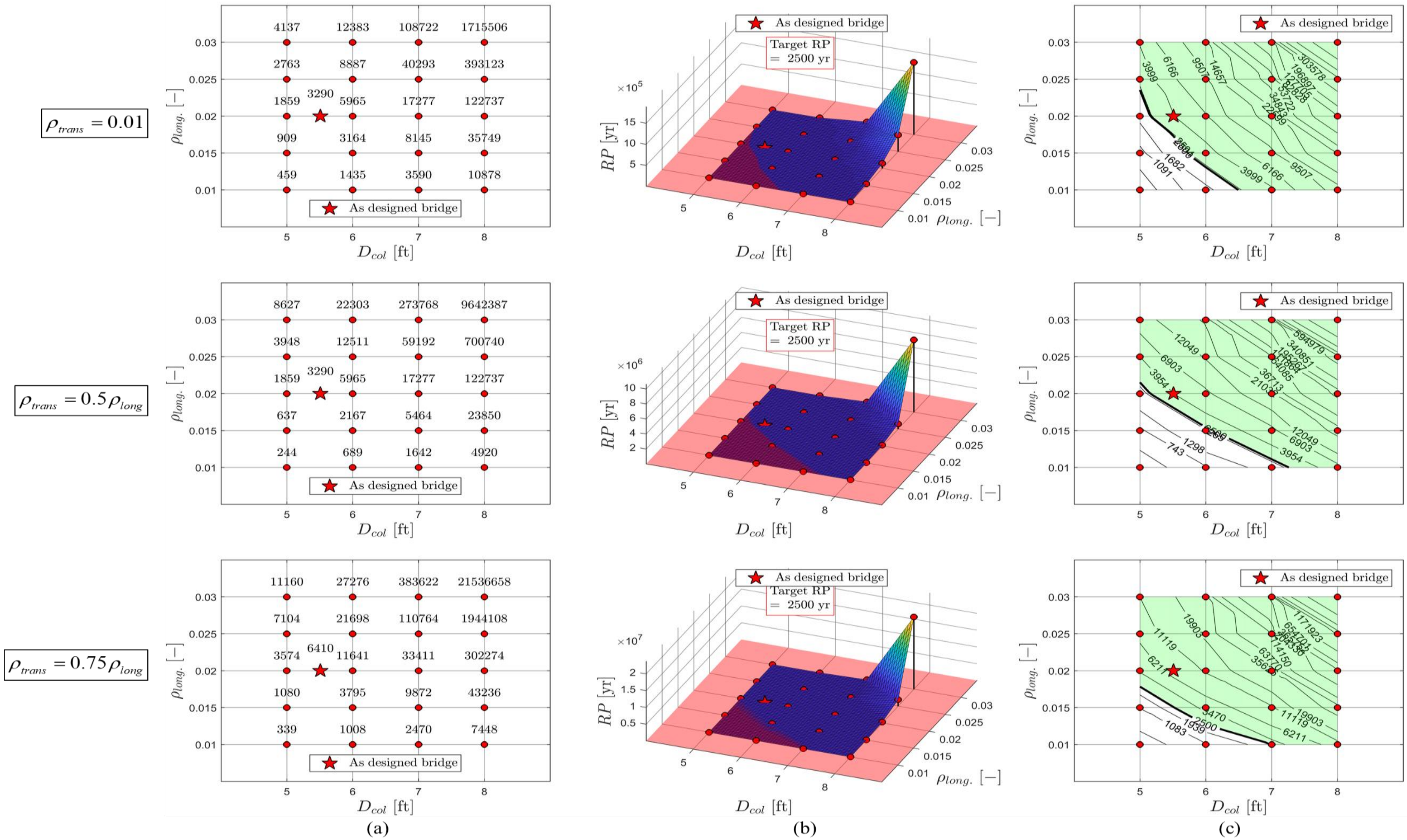

Figure 9.6 Results of parametric probabilistic seismic performance assessment of Bridge A in terms of limit-state 3, i.e., longitudinal rebar fracture: 1st row: $\rho_{trans.} = 0.01$; 2nd row: $\rho_{trans.} = 0.5\rho_{long.}$; 3rd row: $\rho_{trans.} = 0.75\rho_{long.}$; (a) mean RPs (in years) of limit-state exceedance of all design points; (b) fitted mean RP surface; and (c) contours of mean RP surface (target RP contour line in bold) and feasible domain (in green)

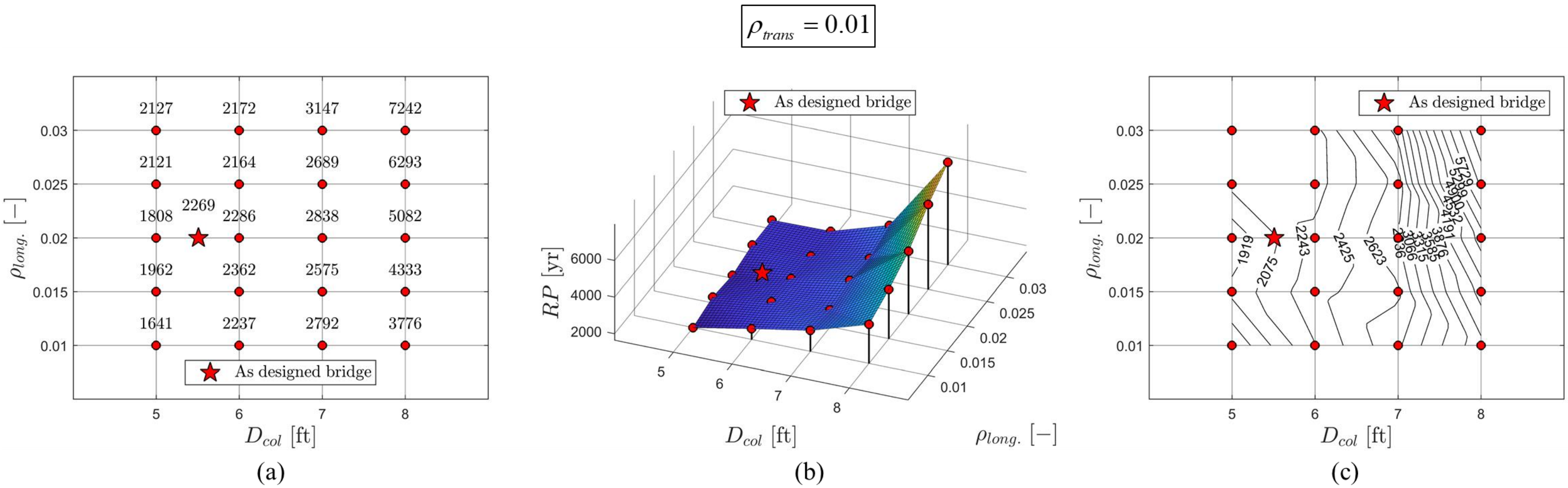

Figure 9.7 Results of parametric probabilistic seismic performance assessment of Bridge A in terms of limit-state 4, i.e., shear key damage: (a) mean RPs (in years) of limit-state exceedance of all design points; (b) fitted mean RP surface; and (c) contours of mean RP surface

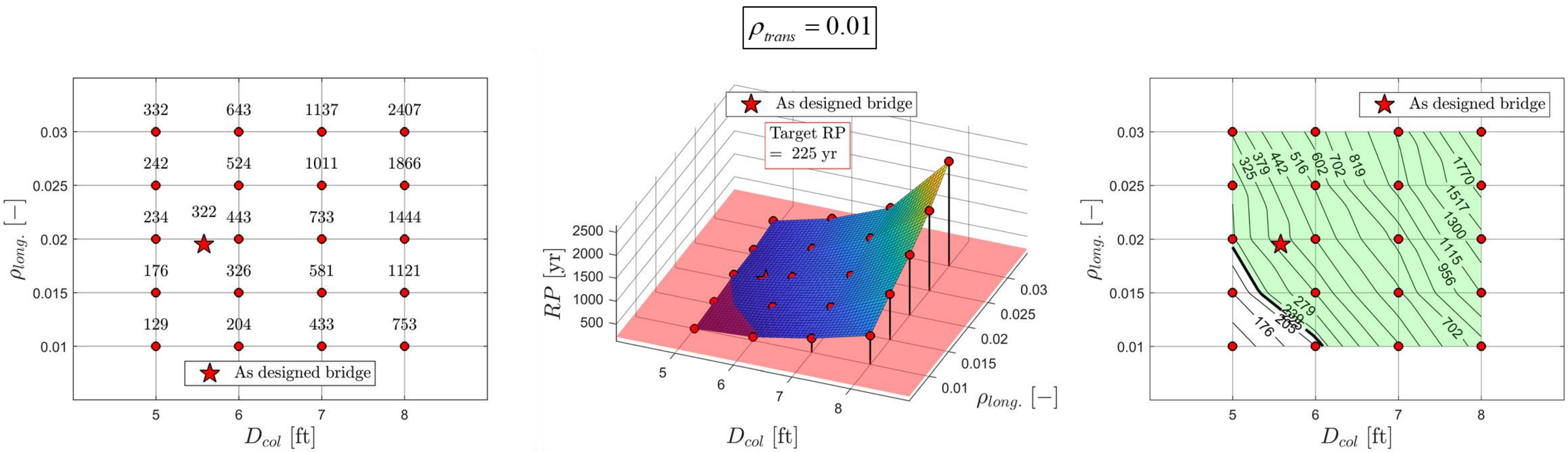

(a) (b) (c)

Figure 9.8 Results of parametric probabilistic seismic performance assessment of Bridge B in terms of limit-state 1, i.e., concrete cover crushing: (a) mean RPs (in years) of limit-state exceedance of all design points; (b) fitted mean RP surface; and (c) contours of mean RP surface (target RP contour line in bold) and feasible domain (in green)

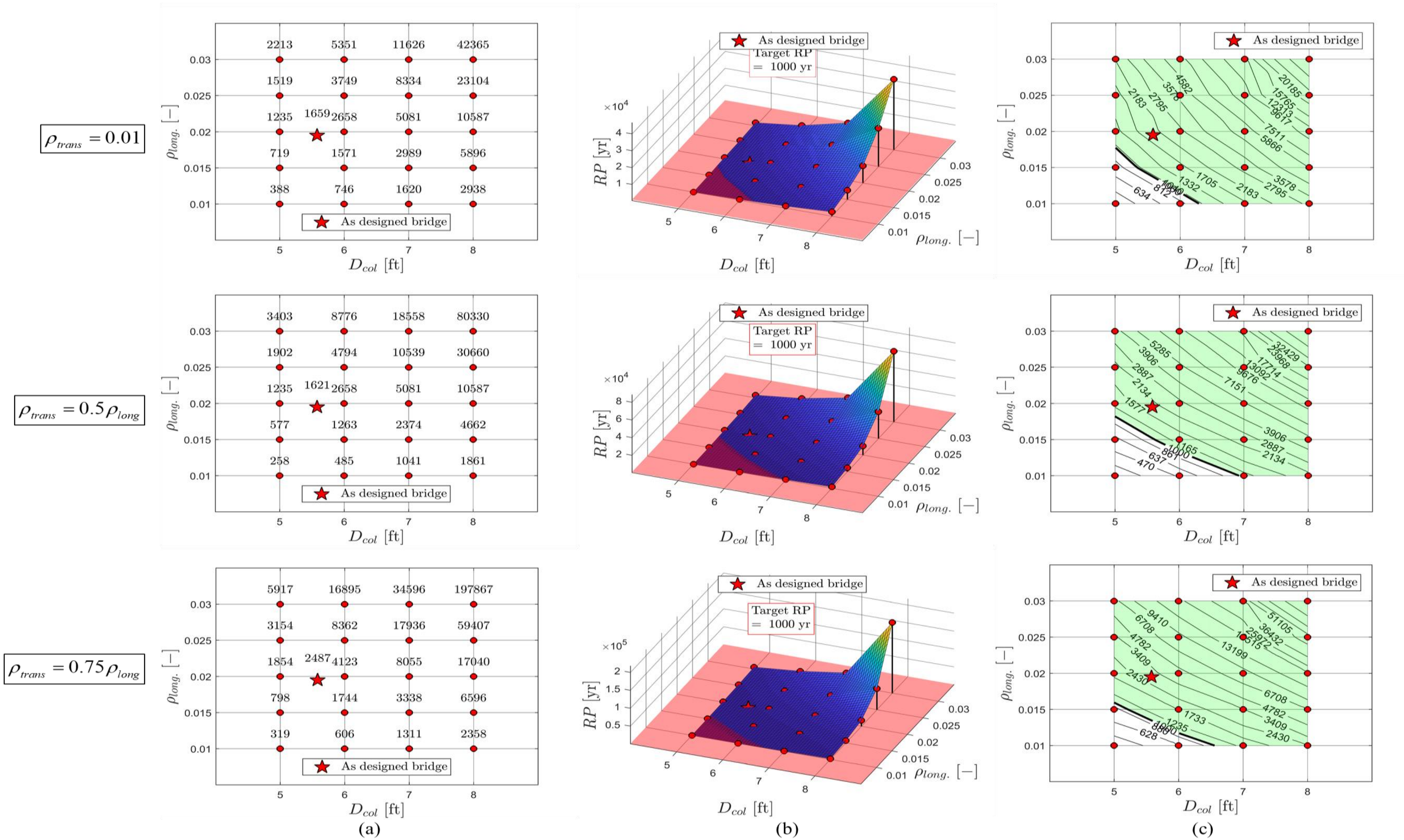

Figure 9.9 Results of parametric probabilistic seismic performance assessment of Bridge B in terms of limit-state 2, i.e., longitudinal rebar buckling: 1st row: $\rho_{trans.} = 0.01$; 2nd row: $\rho_{trans.} = 0.5\rho_{long.}$; 3rd row: $\rho_{trans.} = 0.75\rho_{long.}$; (a) mean RPs (in years) of limit-state exceedance of all design points; (b) fitted mean RP surface; and (c) contours of mean RP surface (target RP contour line in bold) and feasible domain (in green)

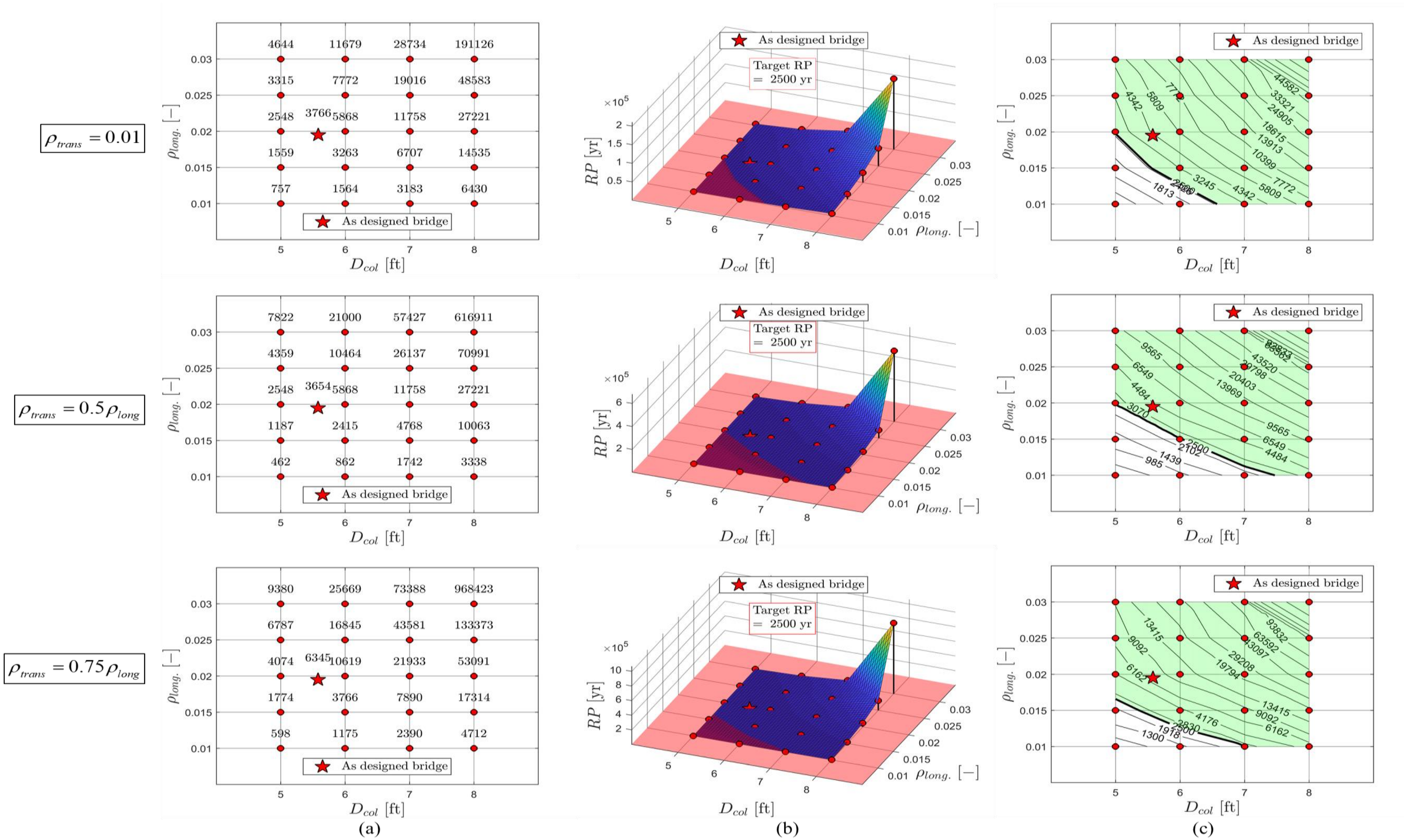

Figure 9.10 Results of parametric probabilistic seismic performance assessment of Bridge B in terms of limit-state 3, i.e., longitudinal rebar fracture: 1st row: $\rho_{trans.} = 0.01$; 2nd row: $\rho_{trans.} = 0.5\rho_{long.}$; 3rd row: $\rho_{trans.} = 0.75\rho_{long.}$; (a) mean RPs (in years) of limit-state exceedance of all design points; (b) fitted mean RP surface; and (c) contours of mean RP surface (target RP contour line in bold) and feasible domain (in green)

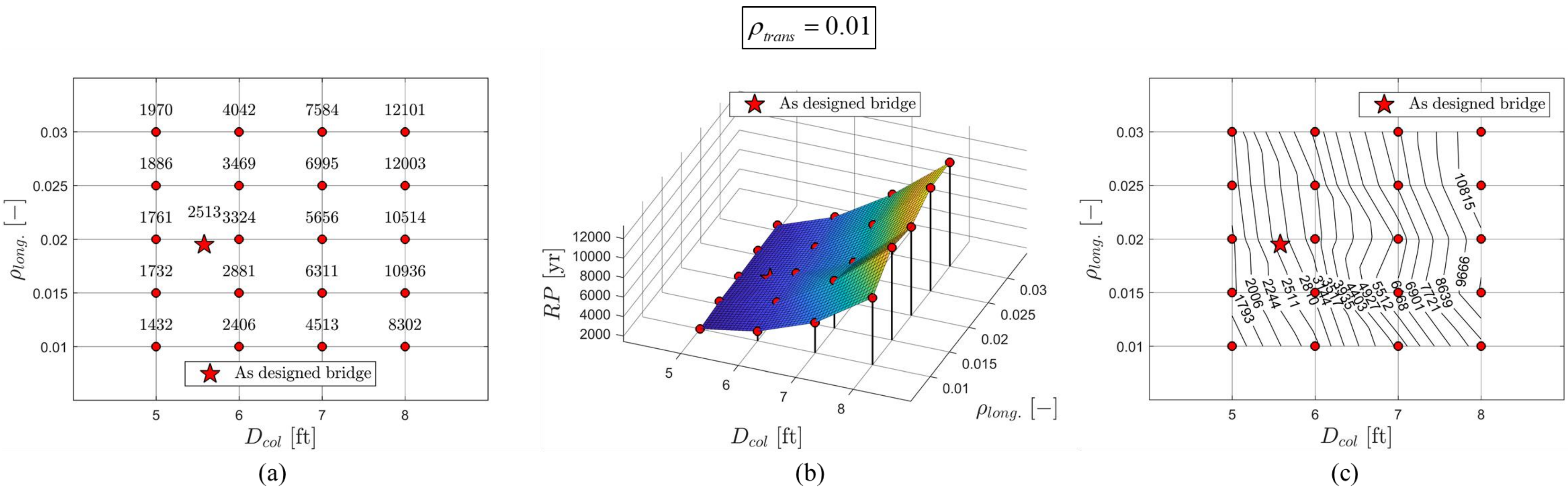

Figure 9.11 Results of parametric probabilistic seismic performance assessment of Bridge B in terms of limit-state 4, i.e., shear key damage: (a) mean RPs (in years) of limit-state exceedance of all design points; (b) fitted mean RP surface; and (c) contours of mean RP surface

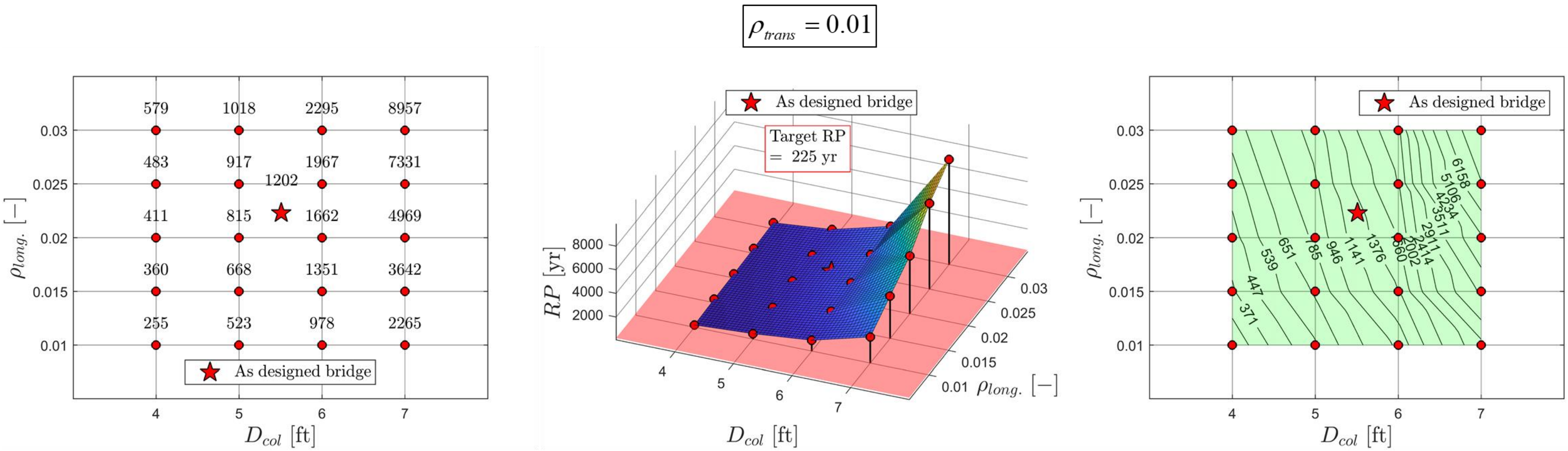

(a) (b) (c)

Figure 9.12 Results of parametric probabilistic seismic performance assessment of Bridge C in terms of limit-state 1, i.e., concrete cover crushing: (a) mean RPs (in years) of limit-state exceedance of all design points; (b) fitted mean RP surface; and (c) contours of mean RP surface (target RP contour line in bold) and feasible domain (in green)

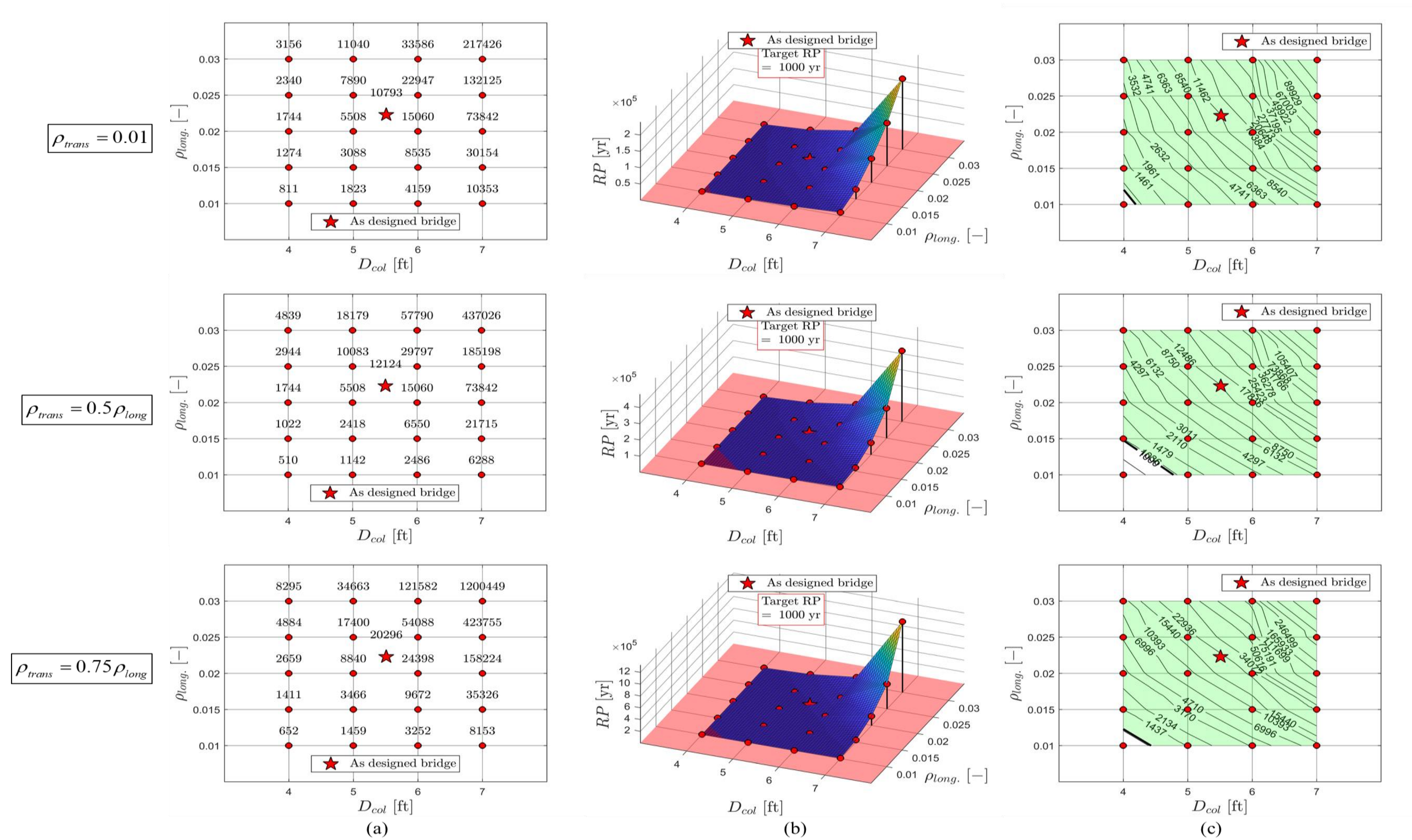

Figure 9.13 Results of parametric probabilistic seismic performance assessment of Bridge C in terms of limit-state 2, i.e., longitudinal rebar buckling: 1st row: $\rho_{trans.} = 0.01$; 2nd row: $\rho_{trans.} = 0.5\rho_{long.}$; 3rd row: $\rho_{trans.} = 0.75\rho_{long.}$; (a) mean RPs (in years) of limit-state exceedance of all design points; (b) fitted mean RP surface; and (c) contours of mean RP surface (target RP contour line in bold) and feasible domain (in green)

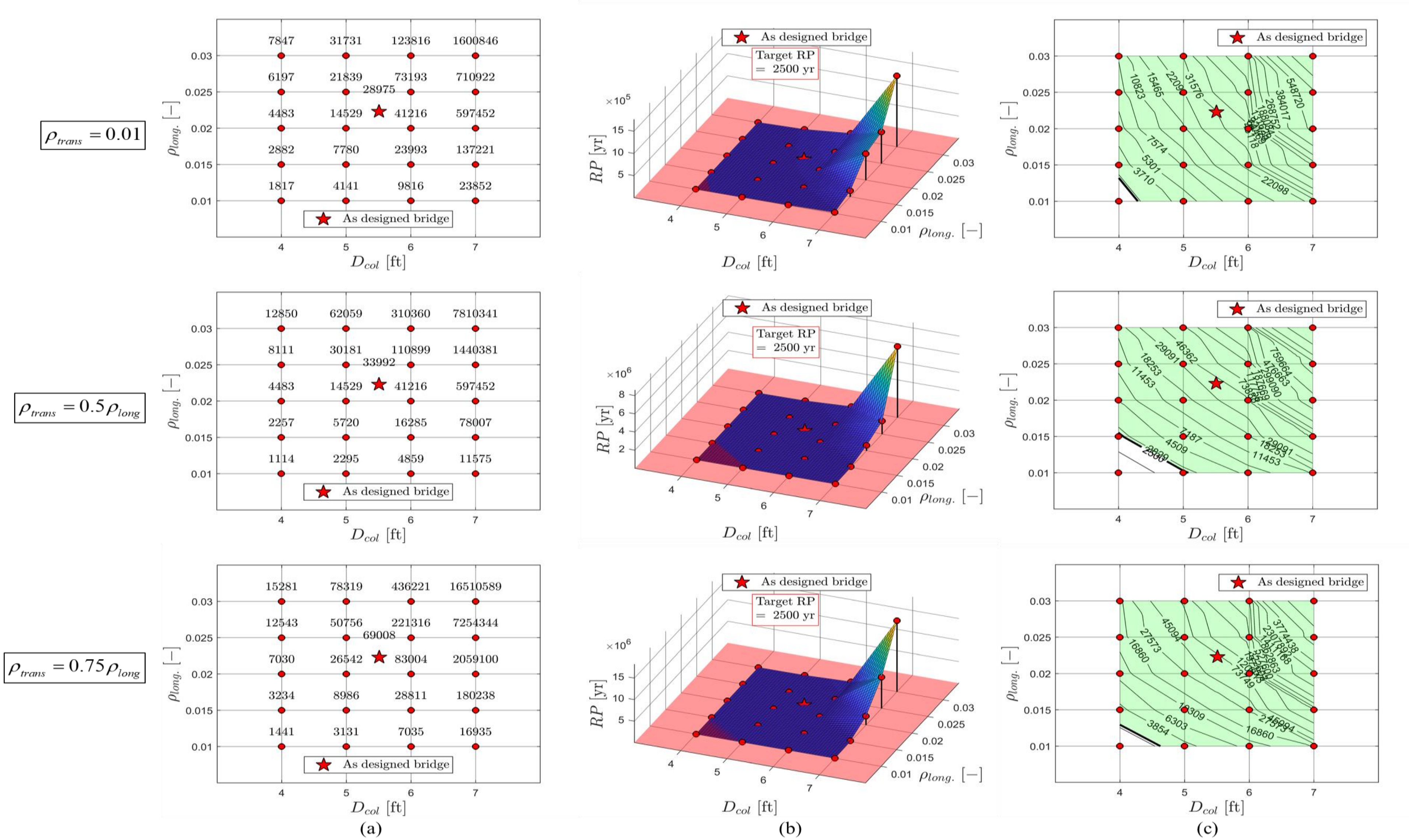

Figure 9.14 Results of parametric probabilistic seismic performance assessment of Bridge C in terms of limit-state 3, i.e., longitudinal rebar fracture: 1st row: $\rho_{trans.} = 0.01$; 2nd row: $\rho_{trans.} = 0.5\rho_{long.}$; 3rd row: $\rho_{trans.} = 0.75\rho_{long.}$; (a) mean RPs (in years) of limit-state exceedance of all design points; (b) fitted mean RP surface; and (c) contours of mean RP surface (target RP contour line in bold) and feasible domain (in green)

$\rho_{trans} = 0.01$

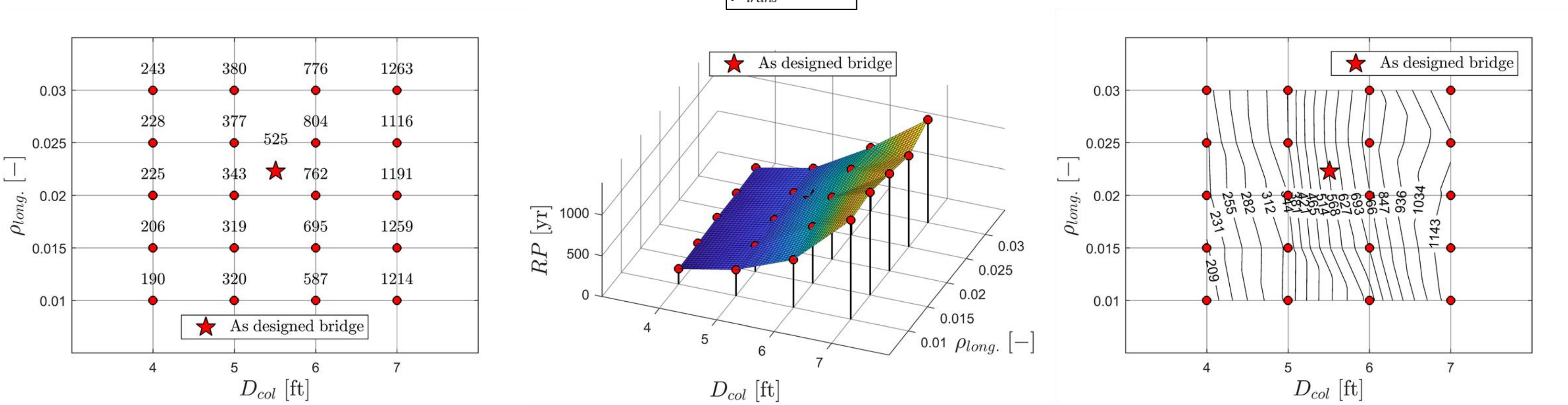

(a) (b) (c)

Figure 9.15 Results of parametric probabilistic seismic performance assessment of Bridge C in terms of limit-state 4, i.e., shear key damage: (a) mean RPs (in years) of limit-state exceedance of all design points; (b) fitted mean RP surface; and (c) contours of mean RP surface

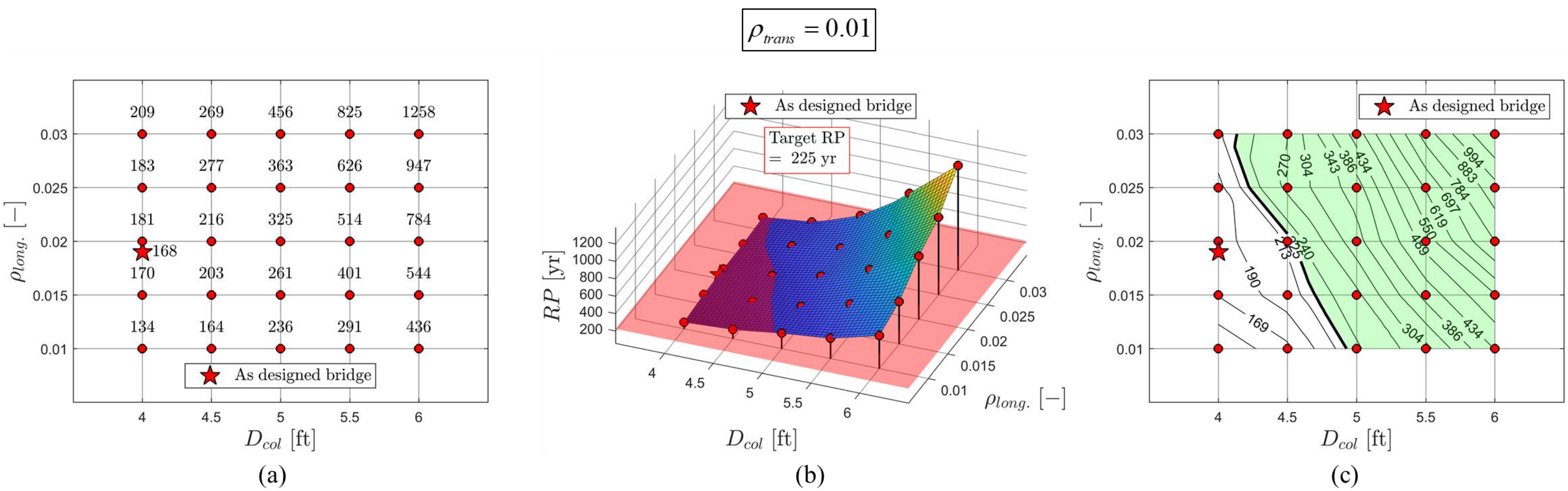

Figure 9.16 Results of parametric probabilistic seismic performance assessment of Bridge MAOC in terms of limit-state 1, i.e., concrete cover crushing: (a) mean RPs (in years) of limit-state exceedance of all design points; (b) fitted mean RP surface; and (c) contours of mean RP surface (target RP contour line in bold) and feasible domain (in green)

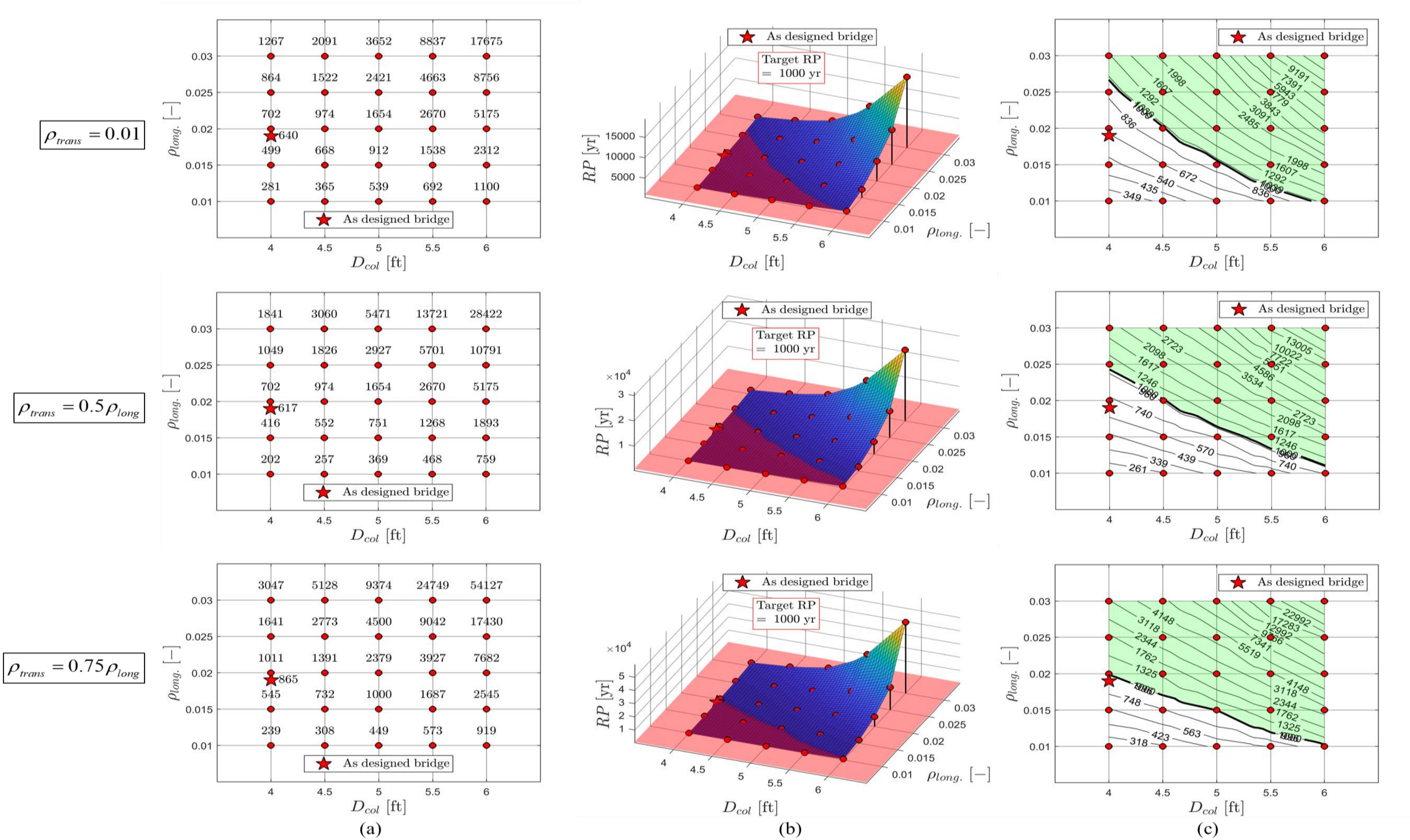

Figure 9.17 Results of parametric probabilistic seismic performance assessment of Bridge MAOC in terms of limit-state 2, i.e., longitudinal rebar buckling: 1st row: $\rho_{trans.} = 0.01$; 2nd row: $\rho_{trans.} = 0.5\rho_{long.}$; 3rd row: $\rho_{trans.} = 0.75\rho_{long.}$; (a) mean RPs (in years) of limit-state exceedance of all design points; (b) fitted mean RP surface; and (c) contours of mean RP surface (target RP contour line in bold) and feasible domain (in green)

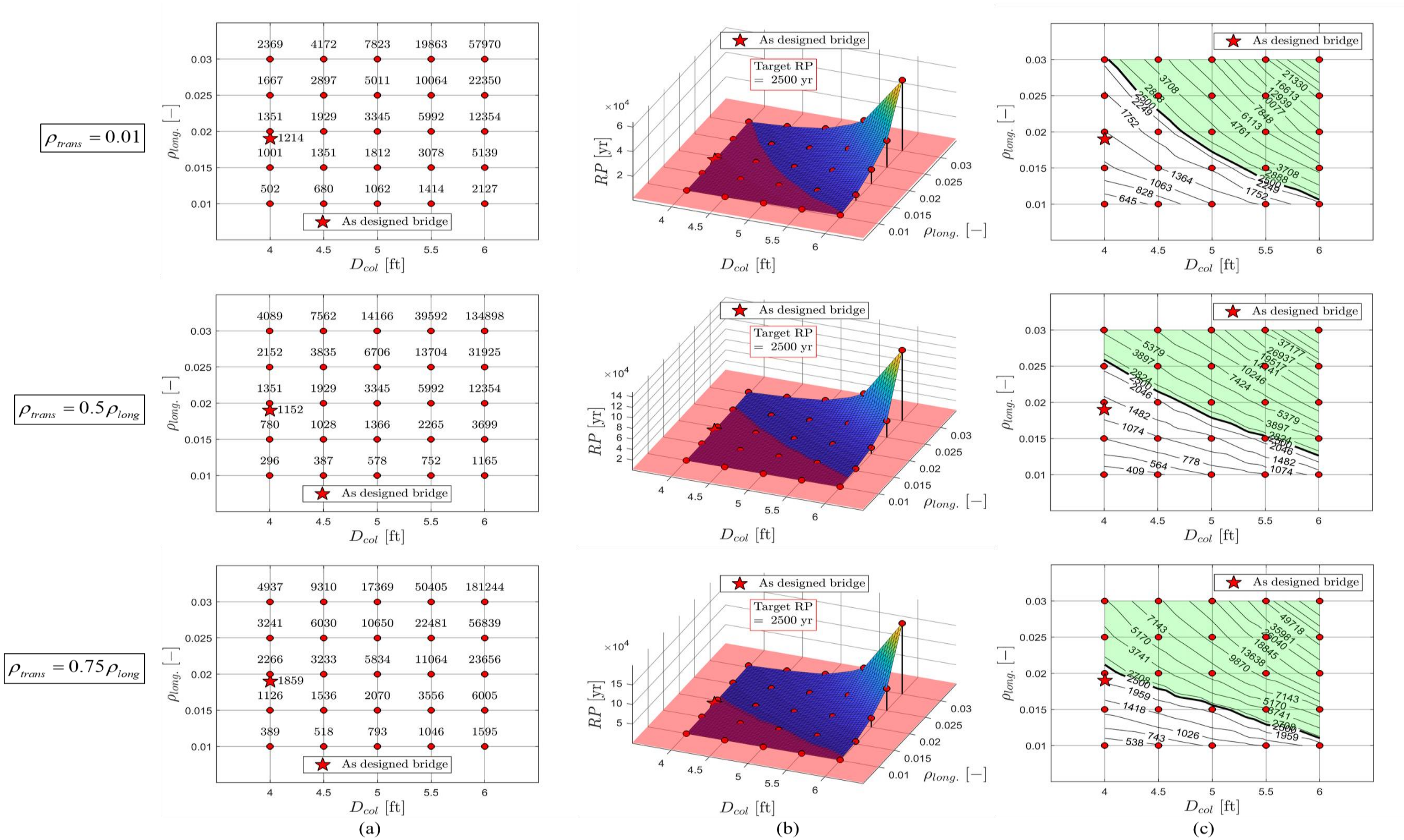

Figure 9.18 Results of parametric probabilistic seismic performance assessment of Bridge MAOC in terms of limit-state 3, i.e., longitudinal rebar fracture: 1st row: $\rho_{trans.} = 0.01$; 2nd row: $\rho_{trans.} = 0.5\rho_{long.}$; 3rd row: $\rho_{trans.} = 0.75\rho_{long.}$; (a) mean RPs (in years) of limit-state exceedance of all design points; (b) fitted mean RP surface; and (c) contours of mean RP surface (target RP contour line in bold) and feasible domain (in green)

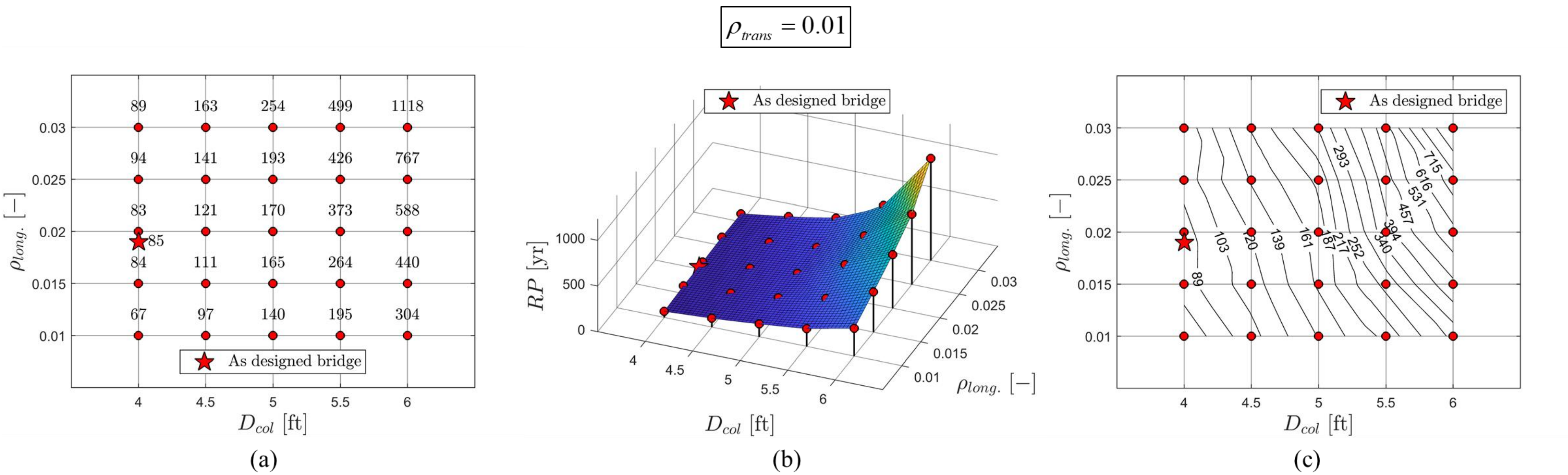

Figure 9.19 Results of parametric probabilistic seismic performance assessment of Bridge MAOC in terms of limit-state 4, i.e., shear key damage: (a) mean RPs (in years) of limit-state exceedance of all design points; (b) fitted mean RP surface; and (c) contours of mean RP surface

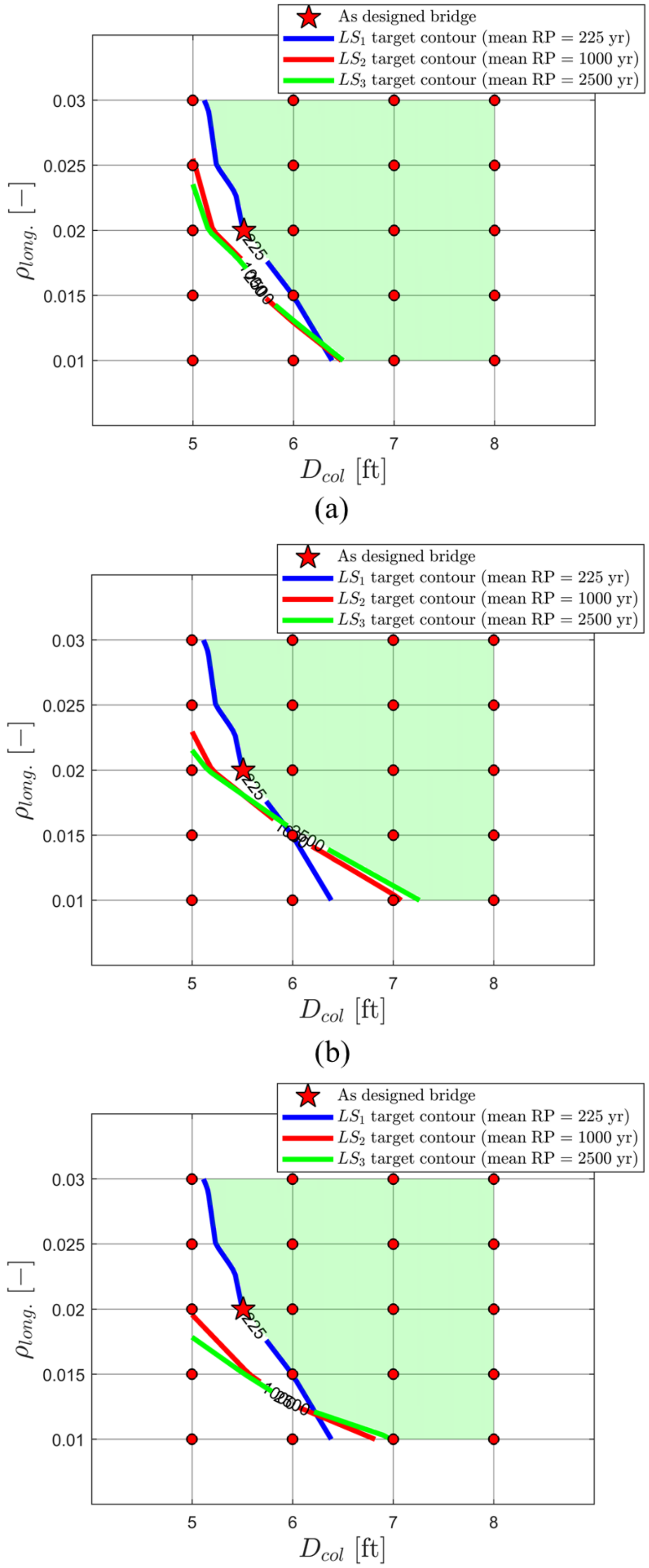

(a)

(b)

(c)

Figure 9.20 Feasible design domains for Bridge A: (a) $\rho_{trans} = 0.01$; (b) $\rho_{trans} = 0.5\rho_{long}$; and (c) $\rho_{trans} = 0.75\rho_{long}$

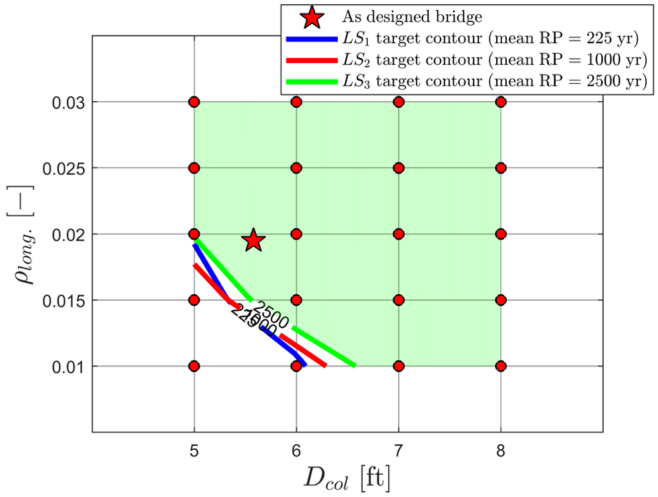

(a)

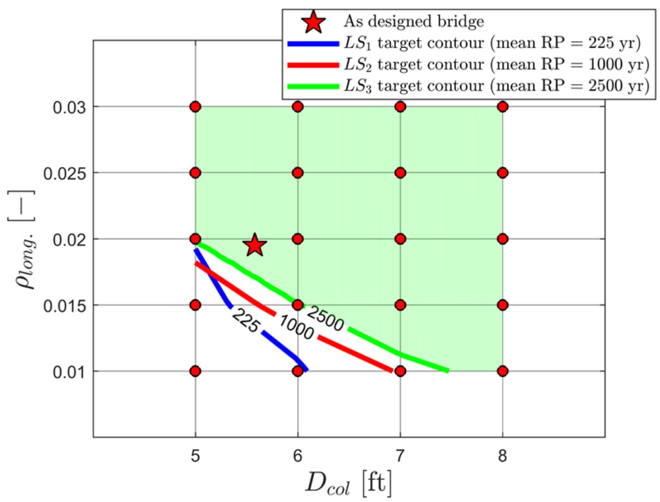

(b)

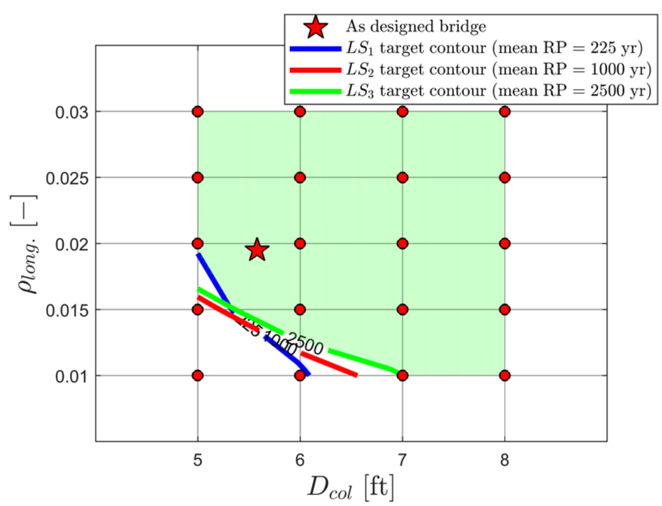

(c)

Figure 9.21 Feasible design domains for Bridge B: (a) $\rho_{trans} = 0.01$; (b) $\rho_{trans} = 0.5\rho_{long}$; and (c) $\rho_{trans} = 0.75\rho_{long}$

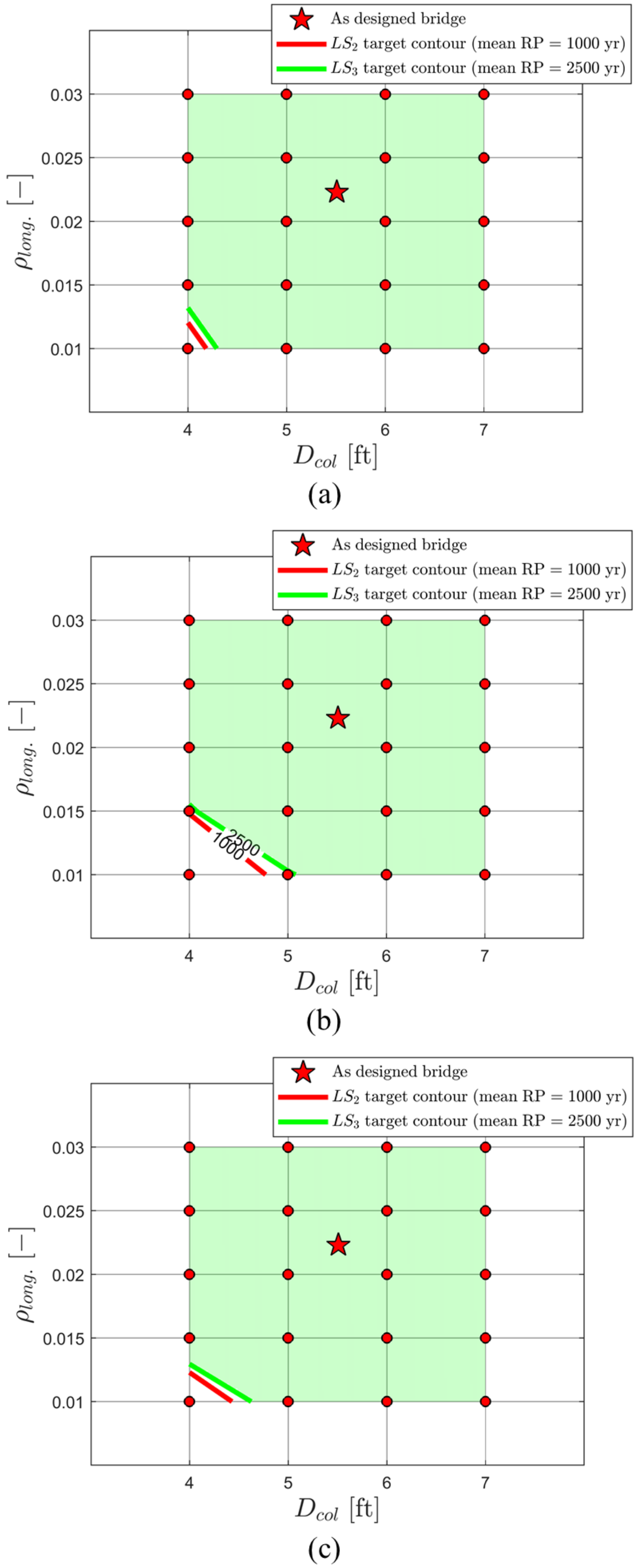

Figure 9.22 Feasible design domains for Bridge C: (a) $\rho_{trans} = 0.01$; (b) $\rho_{trans} = 0.5\rho_{long}$; and (c) $\rho_{trans} = 0.75\rho_{long}$

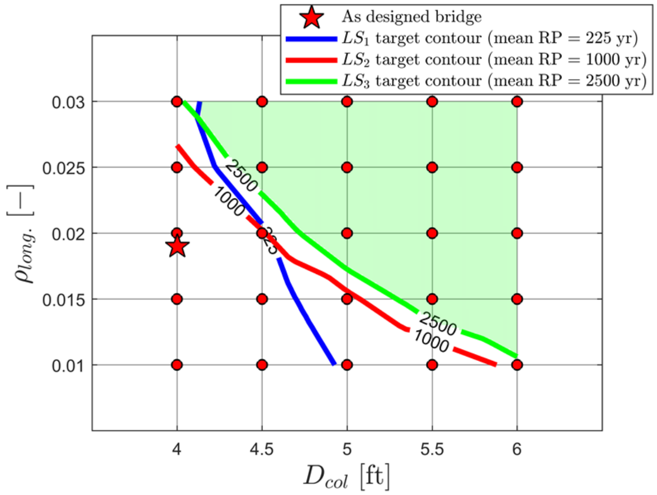

(a)

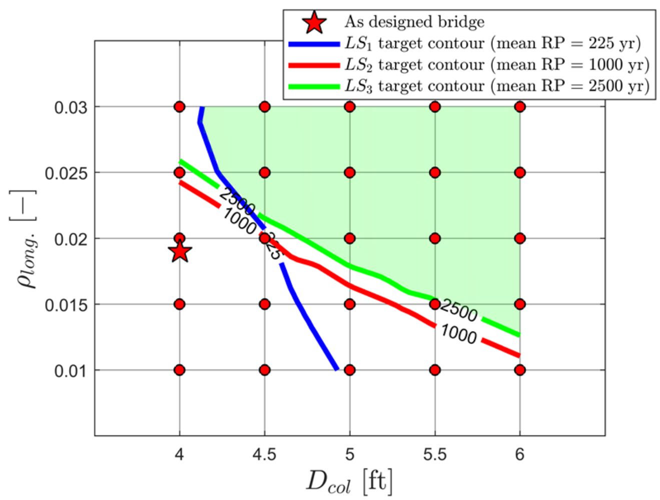

(b)

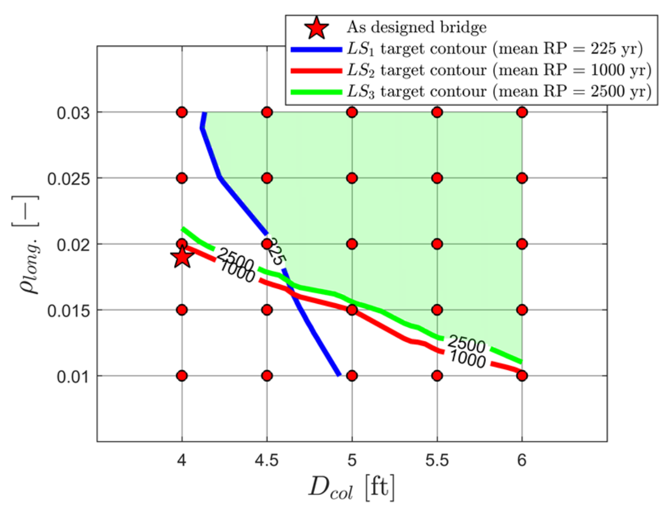

(c)

Figure 9.23 Feasible design domains for Bridge MAOC: (a) $\rho_{trans} = 0.01$; (b) $\rho_{trans} = 0.5\rho_{long}$; and (c) $\rho_{trans} = 0.75\rho_{long}$

9.6 Closed-Form Approximations to Mean Return Periods of Limit-state Exceedances

In the context of performance-based seismic assessment and/or design, closed-form solutions have been derived for the demand hazard curve and the MAR of damage/limit-state exceedance (Cornell et al. 2002; Kumar and Gardoni 2013; Romão et al. 2013; Vamvatsikos 2013). Such closed-form solutions allow an analyst/designer to circumvent the evaluation of probabilistic integrals involved in PSDemHA and PSDamHA steps of the PEER PBEE framework. With an aim to reduce the computational burden of the proposed parametric probabilistic seismic performance assessment framework, potentially to be used for design of new OSBs, a comparative study of the closed-form solutions to the MAR of limit-state exceedance, available in the literature, is conducted. Furthermore, this study is also intended to assess the potential viability of using LRFD-like design formats, based on such closed-form solutions, in the context of a simplified performance-based seismic design (PBSD) methodology to be distilled out of this project.

Cornell et al. (2002) developed a closed-form solution for estimating the MAR of limit-state exceedance as a part of the SAC/FEMA project aimed towards probabilistic performance-based assessment and design of structures. This closed-form solution relies on some restrictive (idealized) assumptions such as:

(1) the seismic hazard curve is assumed to have a power-law form (linear in log space), i.e.,

$$\nu_{IM}(x) = k_0 (x)^{-k_1} \tag{9.1}$$

(2) EDPs are assumed to have a lognormal distribution when conditioned on ,

(3) the median of an EDP, say EDP_k associated with the k^{th} limit-state, conditional on is assumed to have a power-law form, i.e.,

$$\eta_{EDP_k|IM} = a \cdot x^b \tag{9.2}$$

(4) the dispersion of EDP_k conditional on is assumed to be constant, i.e.,

$$\zeta_{EDP_k|IM} = \text{constant} \tag{9.3}$$

(5) the capacity term C_k associated to the k^{th} limit-state is assumed to have a lognormal distribution with median η_{C_k} and dispersion parameter ζ_{C_k}.

Under the above assumptions, the MAR of limit-state exceedance for the k^{th} limit-state can be expressed as (Cornell et al. 2002)

$$\nu_{LS_k} = \nu_{IM}\left(x_{\eta_{C_k}}\right) \cdot e^{\frac{1}{2}\cdot\frac{k_1^2}{b^2}\cdot\left(\zeta^2_{EDP_k|IM} + \zeta^2_{C_k}\right)} \tag{9.4}$$

where $x_{\eta_{C_k}}$ is the value of , conditional on which, the median value of EDP_k, i.e., $a \cdot (x_{\eta_{C_k}})^b$ is equal to the median capacity η_{C_k}. Thus,

$$x_{\eta_{C_k}} = \left(\frac{\eta_{C_k}}{a}\right)^{\frac{1}{b}} \tag{9.5}$$

The above closed-form solution, however, has been criticized for the lack of accuracy (Aslani and Miranda 2005a; Bradley and Dhakal 2008) primarily due to an inadequate, and only locally accurate, power-law fit of the seismic hazard curve. As noted from the disaggregation of damage hazard with respect to , shown in Chapter 8, contribution to a specific level of damage hazard, ν_{LS_k}, can come from a range of possible values that sometimes even spread outside the range of most confidence where EDP_k, given , data is available. An appropriate fit of the seismic hazard curve should therefore be accurate over a wide range of values.

Vamvatsikos (2013) proposed an improved version of the closed-form solution by Cornell et al. (2002) which addresses its main shortcoming of a linear fit of the seismic hazard curve in log space. The improved closed-form solution suggests the use of a second-order polynomial fit of the seismic hazard curve in log-space, i.e.,

$$\nu_{IM}\left(x\right) = k_0 \cdot e^{-k_2(\ln x)^2 - k_1 \ln x} \tag{9.6}$$

Using Eq. (9.6), the curvature of the seismic hazard function can be accurately captured over a wide range of values (see Figure 9.24). Although the actual seismic hazard curve significantly deviates from the proposed fit for small values of , this deviation does not potentially lead to massive errors in the estimation of MARs of damage/limit-state exceedance. As seen from the disaggregation of demand and/or damage hazard, the contribution coming from small values of is negligible owing to small conditional probabilities of EDP and/or limit-state exceedance. With all other assumptions same as before, the MAR of exceeding the k^{th} limit-state can be expressed as (Vamvatsikos 2013)

$$\nu_{LS_k} = \sqrt{\phi}\, k_0^{1-\phi} \left[\nu_{IM}\left(x_{\eta_{C_k}} \right) \right]^{\phi} e^{\frac{1}{2b^2} q k_1^2 \left(\zeta^2_{EDP_k|IM} + \phi \zeta^2_{C_k} \right)} \tag{9.7}$$

where,

$$q = \frac{1}{1 + 2k_2 \dfrac{\zeta^2_{EDP_k|IM}}{b^2}} \tag{9.8}$$

and

$$\phi = \frac{1}{1 + 2k_2 \dfrac{\zeta^2_{EDP_k|IM} + \zeta^2_{C_k}}{b^2}} \tag{9.9}$$

It is to be noted that Eq. (9.7) reduces to Eq. (9.4) when the parameter k_2 is set to zero. The two closed-form solutions given by Eq. (9.4) and Eq. (9.7) are hereafter referred to as closed-form solution 1 and 2 respectively. A visual description of different parameters and assumptions involved in these closed-form solutions is provided in Figure 9.24

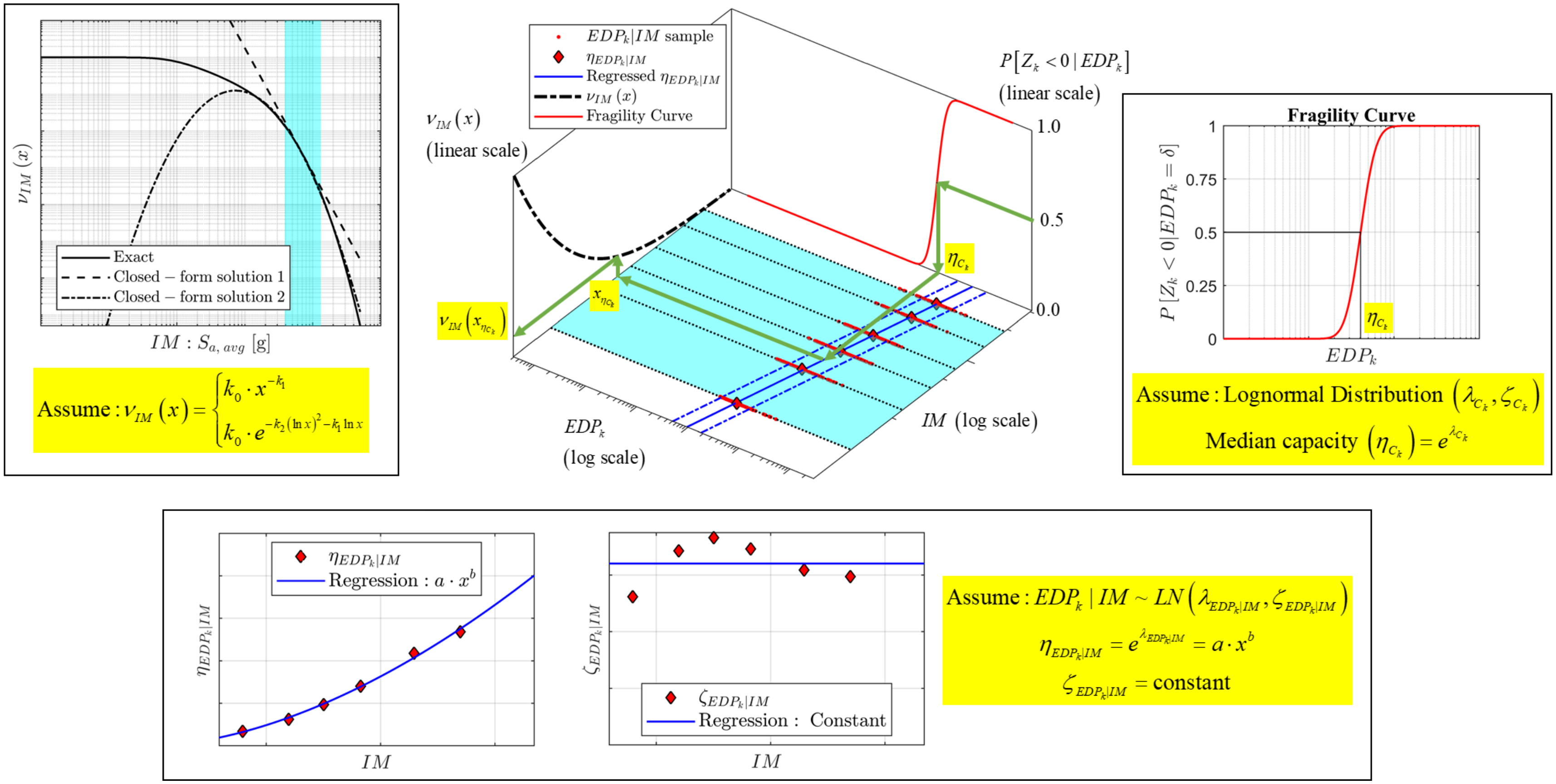

Figure 9.24   General description of parameters and approximations involved in closed-form solutions 1 and 2

9.6.1 Comparison of Numerical Results with Closed-Form Solutions

Mean RPs of limit-state exceedance, obtained (using closed-form solutions 1 and 2) for limit-states 1, 2, and 3 (i.e., concrete cover crushing, longitudinal rebar buckling, and longitudinal rebar fracture, respectively), for each re-design of the considered testbed bridges are shown in Figure 9.25 (a) through Figure 9.36 (a). The piecewise linear surface, for each limit-state, fitted to the mean RPs computed at the re-design points are shown in Figure 9.25 (b) through Figure 9.36Figure 9.19 (b). Contour plots of the mean RP surfaces for individual limit-states and the corresponding feasible domains are shown in Figure 9.25 (c) through Figure 9.36 (c). Finally, the overall feasible design domains for the testbed bridges obtained using closed-form solutions 1 and 2 are compared with the respective numerically obtained feasible design domain in Figure 9.37 through Figure 9.40.

The comparative study does suggest that the closed-form solution by Vamvatsikos (2013) is reasonably accurate (as compared to the numerical solution) and significantly more accurate than the closed-form solution by Cornell et al. (2002). However, the process of delineating a feasible design domain for a testbed bridge using any one of these closed-form solutions still requires almost as much work as the numerical method. Although the use of a closed-form solution evades the rather inexpensive (in terms of computational workload) numerical evaluation of probabilistic demand and damage hazard integrals, the computationally prohibitive step of running ensemble nonlinear time-history analyses for design points cannot be avoided. Moreover, the level of inaccuracy (as compared to the numerical solution) associated with the results of such overly-simplified closed-form solutions are sometimes found to be non-trivial.

Predicated on these findings, formulation of the proposed simplified PBSD methodology, discussed in the next Chapter, does not rely on the use of available closed-form solutions to the MARs, or mean RPs, of limit-states exceedance. The formulation, however, is general and is flexible to the use of both numerical and/or closed-form approaches to probabilistic seismic damage hazard assessment.

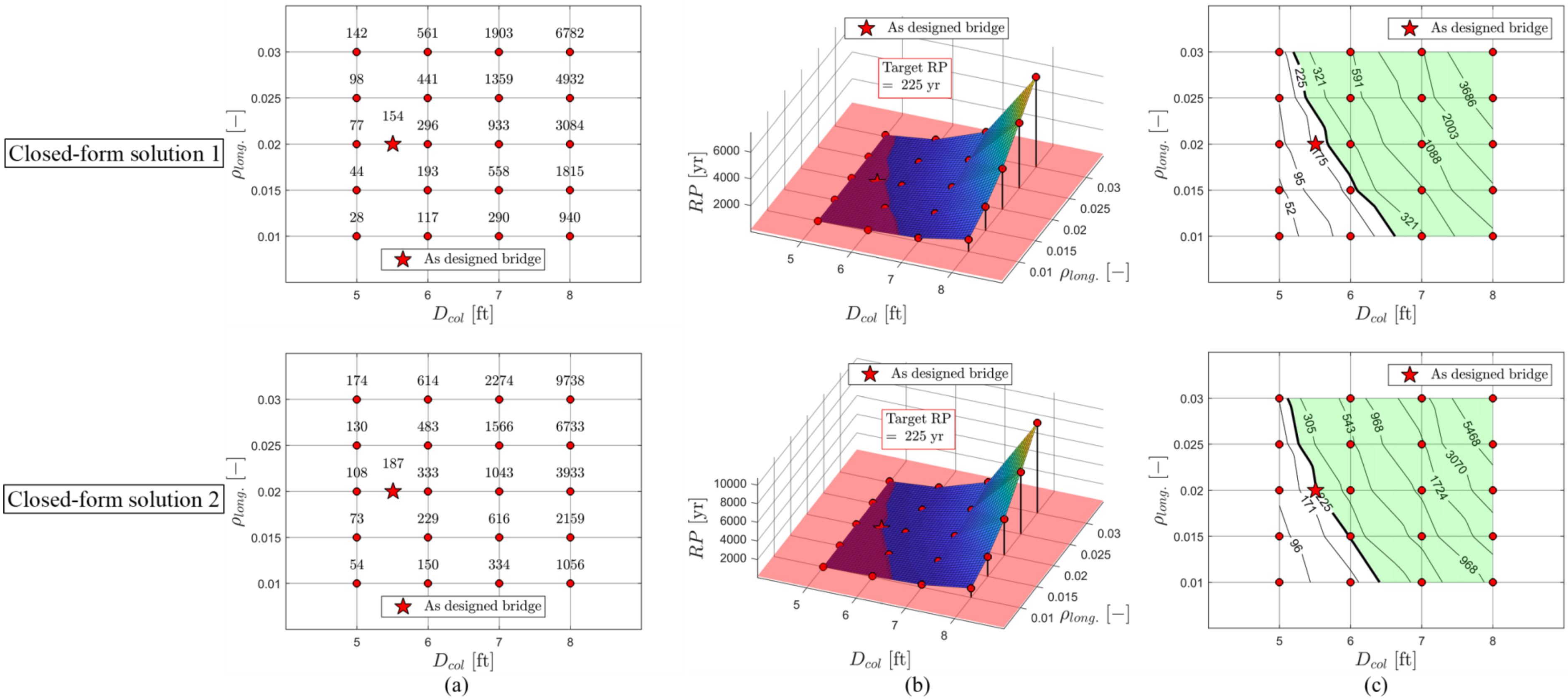

Figure 9.25 Results of parametric probabilistic seismic performance assessment of Bridge A in terms of limit-state 1, i.e., concrete cover crushing: 1st row: Closed-form solution 1; 2nd row: Closed-form solution 2; (a) mean RPs (in years) of limit-state exceedance of all design points; (b) fitted mean RP surface; and (c) contours of mean RP surface (target RP contour line in bold) and feasible domain (in green)

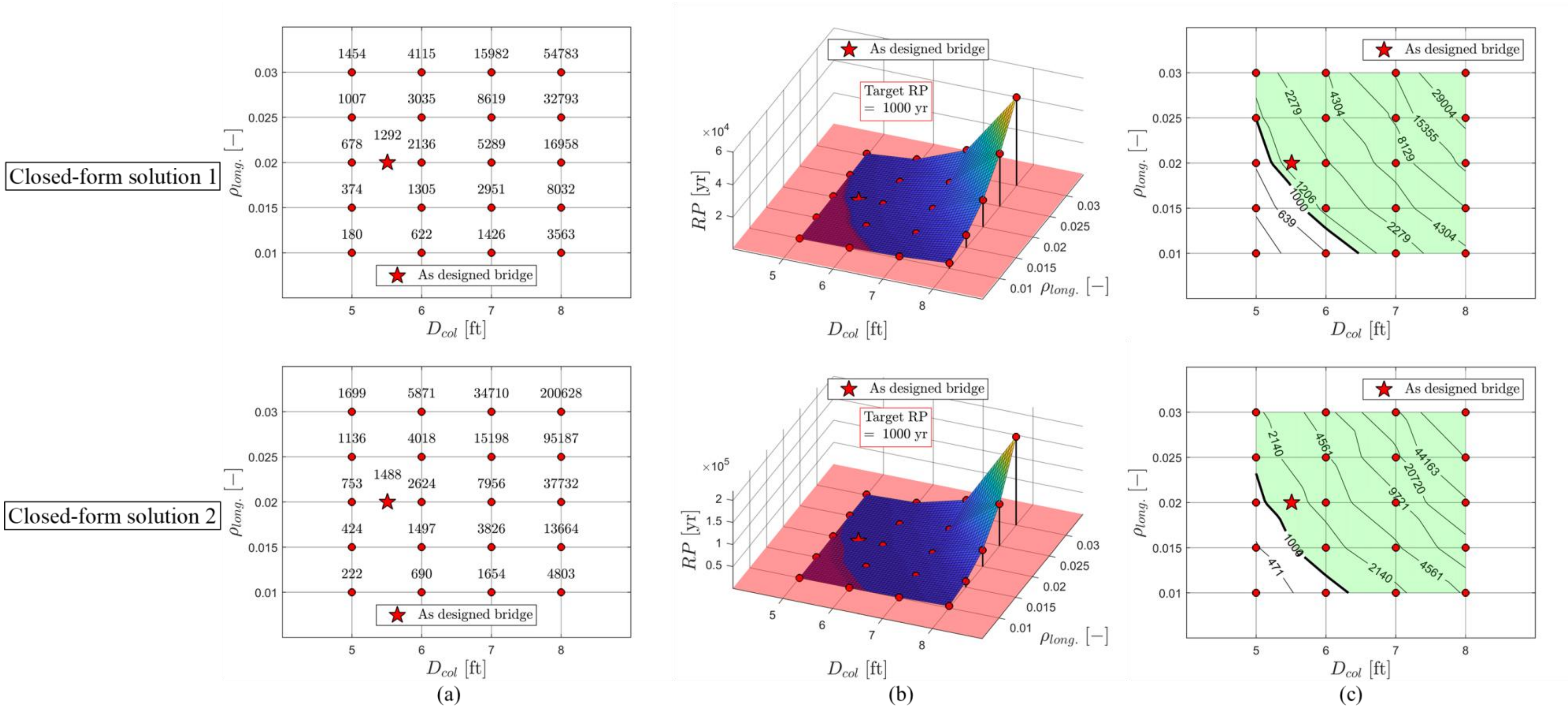

Figure 9.26 Results of parametric probabilistic seismic performance assessment of Bridge A in terms of limit-state 2, i.e., longitudinal rebar buckling: 1st row: Closed-form solution 1; 2nd row: Closed-form solution 2; (a) mean RPs (in years) of limit-state exceedance of all design points; (b) fitted mean RP surface; and (c) contours of mean RP surface (target RP contour line in bold) and feasible domain (in green)

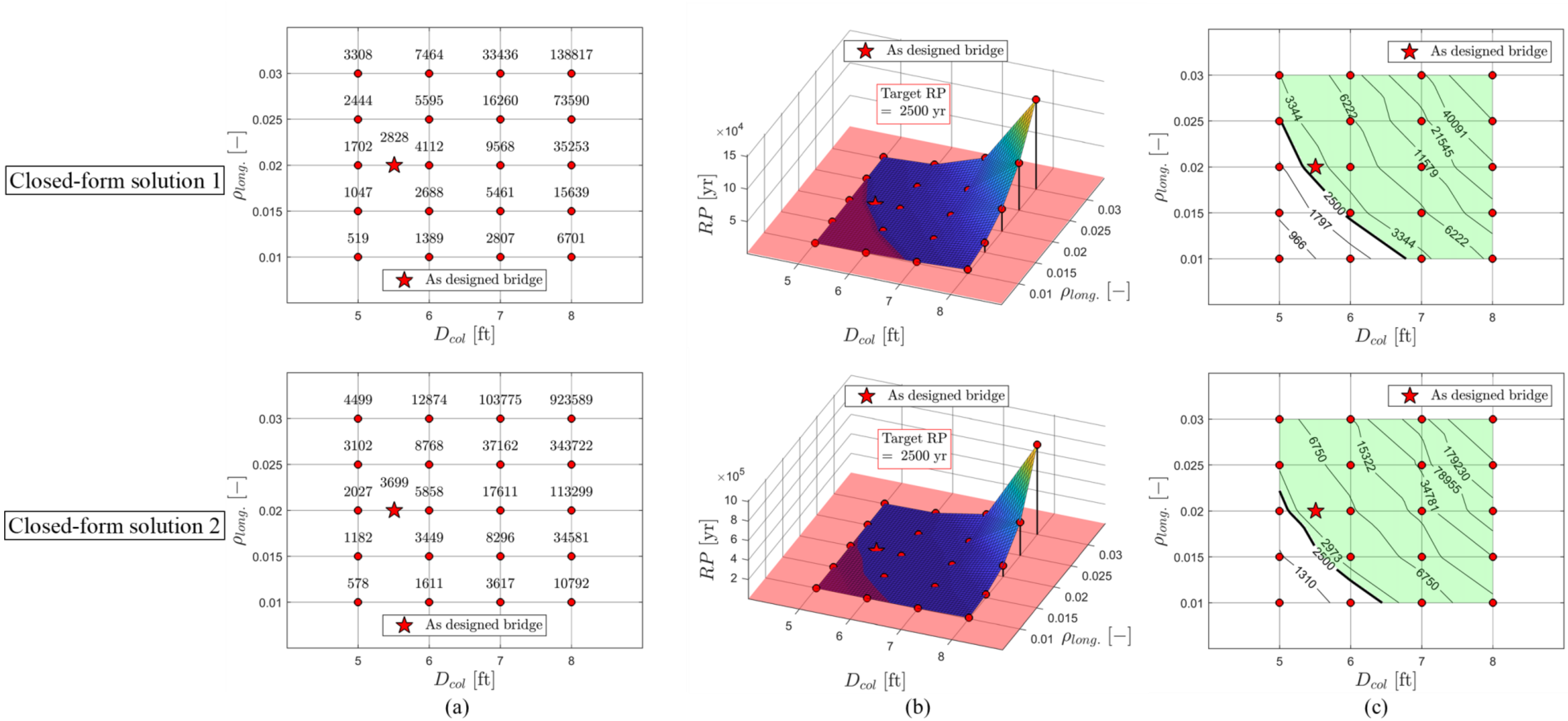

Figure 9.27 Results of parametric probabilistic seismic performance assessment of Bridge A in terms of limit-state 3, i.e., longitudinal rebar fracture: 1st row: Closed-form solution 1; 2nd row: Closed-form solution 2; (a) mean RPs (in years) of limit-state exceedance of all design points; (b) fitted mean RP surface; and (c) contours of mean RP surface (target RP contour line in bold) and feasible domain (in green)

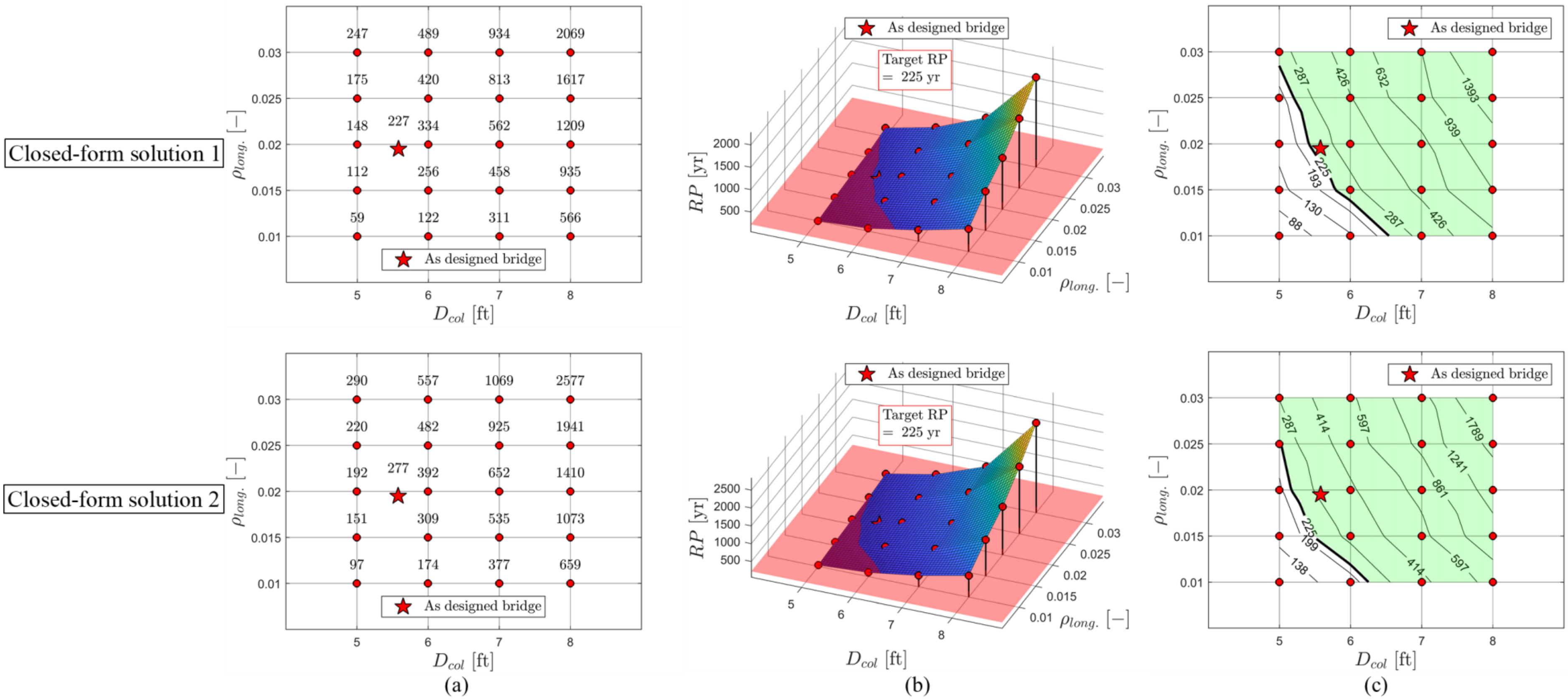

Figure 9.28 Results of parametric probabilistic seismic performance assessment of Bridge B in terms of limit-state 1, i.e., concrete cover crushing: 1st row: Closed-form solution 1; 2nd row: Closed-form solution 2; (a) mean RPs (in years) of limit-state exceedance of all design points; (b) fitted mean RP surface; and (c) contours of mean RP surface (target RP contour line in bold) and feasible domain (in green)

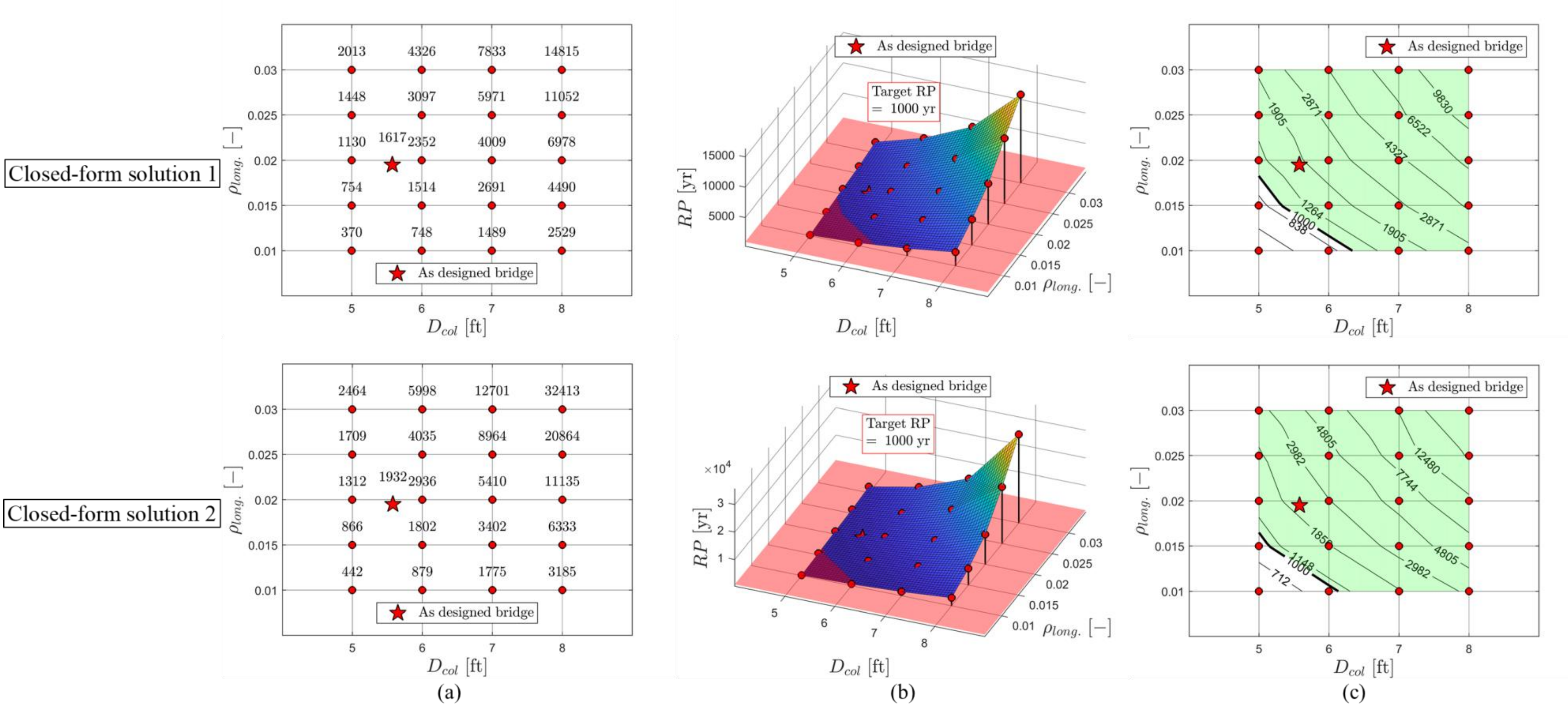

Figure 9.29 Results of parametric probabilistic seismic performance assessment of Bridge B in terms of limit-state 2, i.e., longitudinal rebar buckling: 1st row: Closed-form solution 1; 2nd row: Closed-form solution 2; (a) mean RPs (in years) of limit-state exceedance of all design points; (b) fitted mean RP surface; and (c) contours of mean RP surface (target RP contour line in bold) and feasible domain (in green)

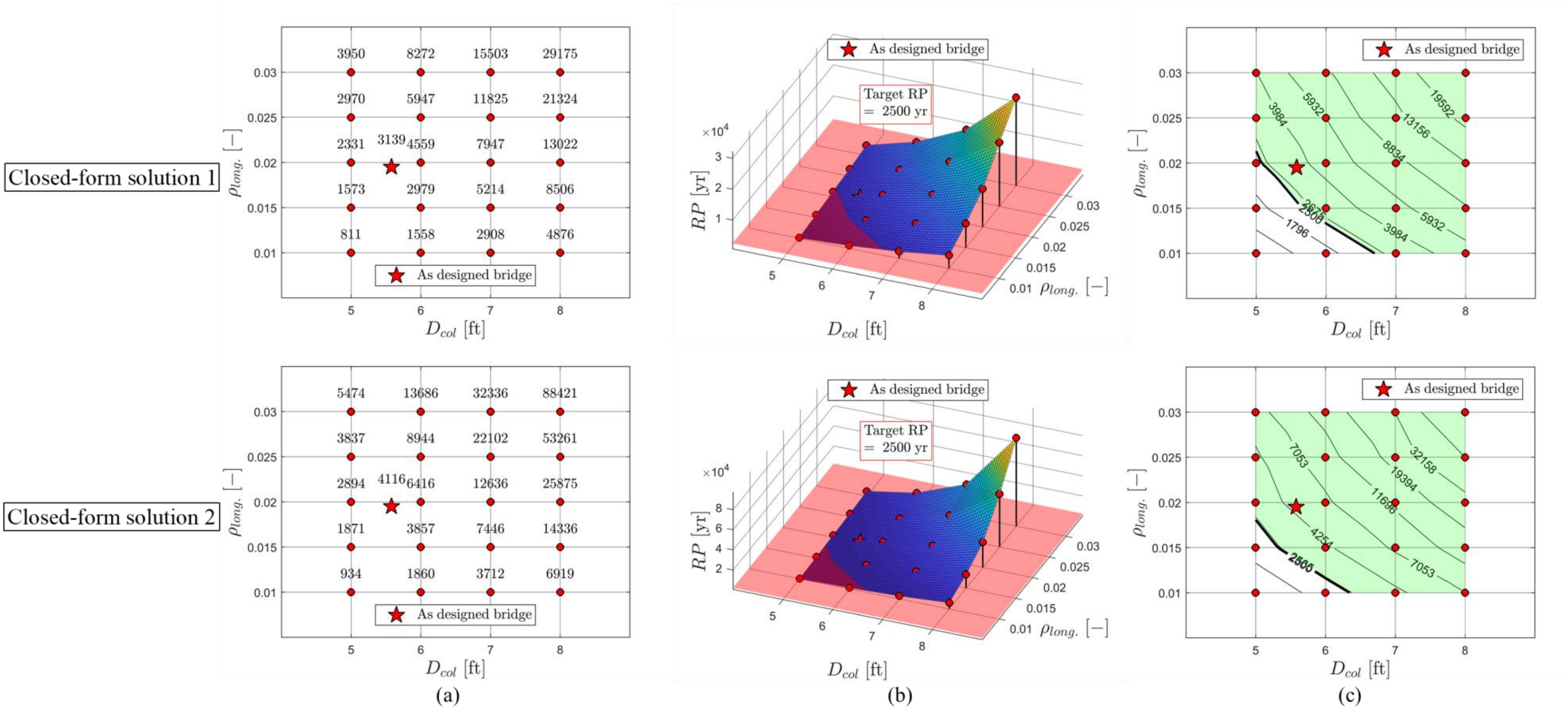

Figure 9.30 Results of parametric probabilistic seismic performance assessment of Bridge B in terms of limit-state 3, i.e., longitudinal rebar fracture: 1st row: Closed-form solution 1; 2nd row: Closed-form solution 2; (a) mean RPs (in years) of limit-state exceedance of all design points; (b) fitted mean RP surface; and (c) contours of mean RP surface (target RP contour line in bold) and feasible domain (in green)

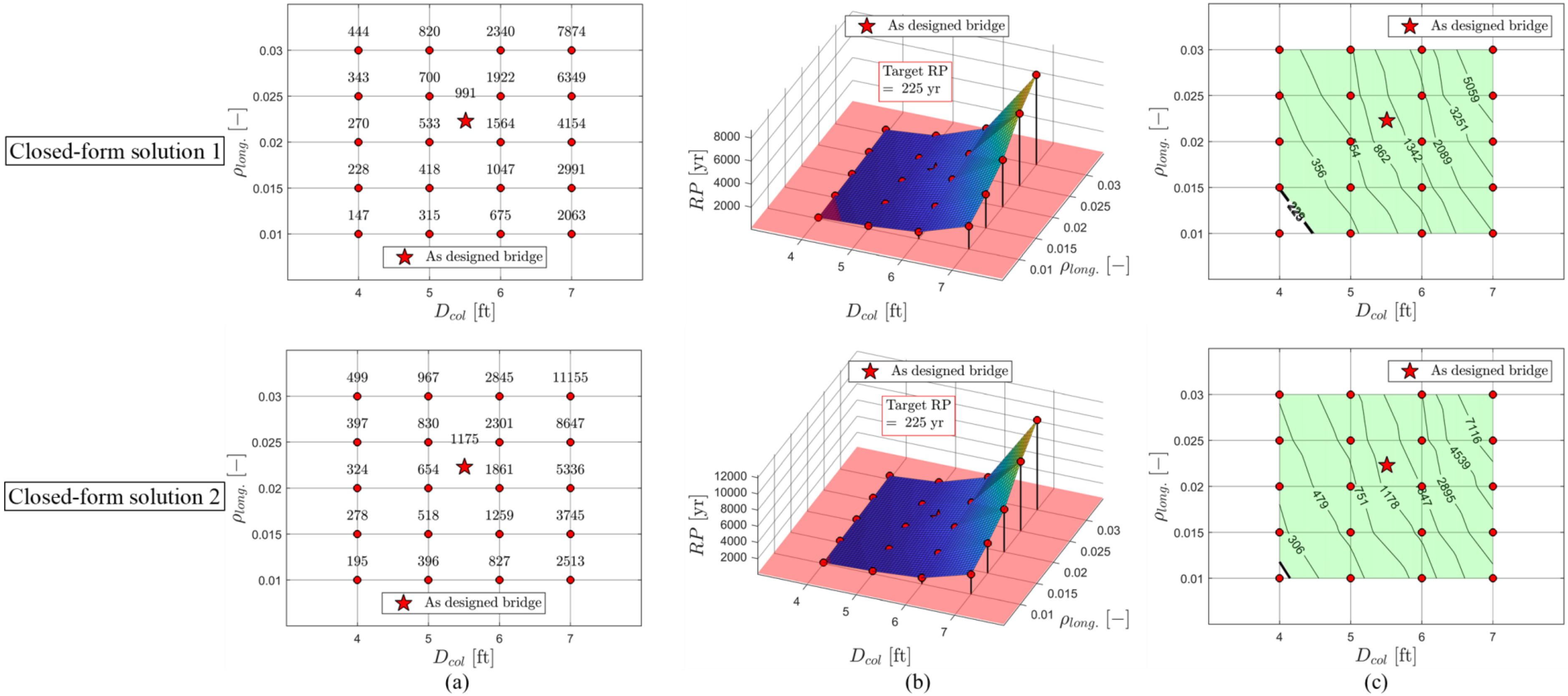

Figure 9.31 Results of parametric probabilistic seismic performance assessment of Bridge C in terms of limit-state 1, i.e., concrete cover crushing: 1st row: Closed-form solution 1; 2nd row: Closed-form solution 2; (a) mean RPs (in years) of limit-state exceedance of all design points; (b) fitted mean RP surface; and (c) contours of mean RP surface (target RP contour line in bold) and feasible domain (in green)

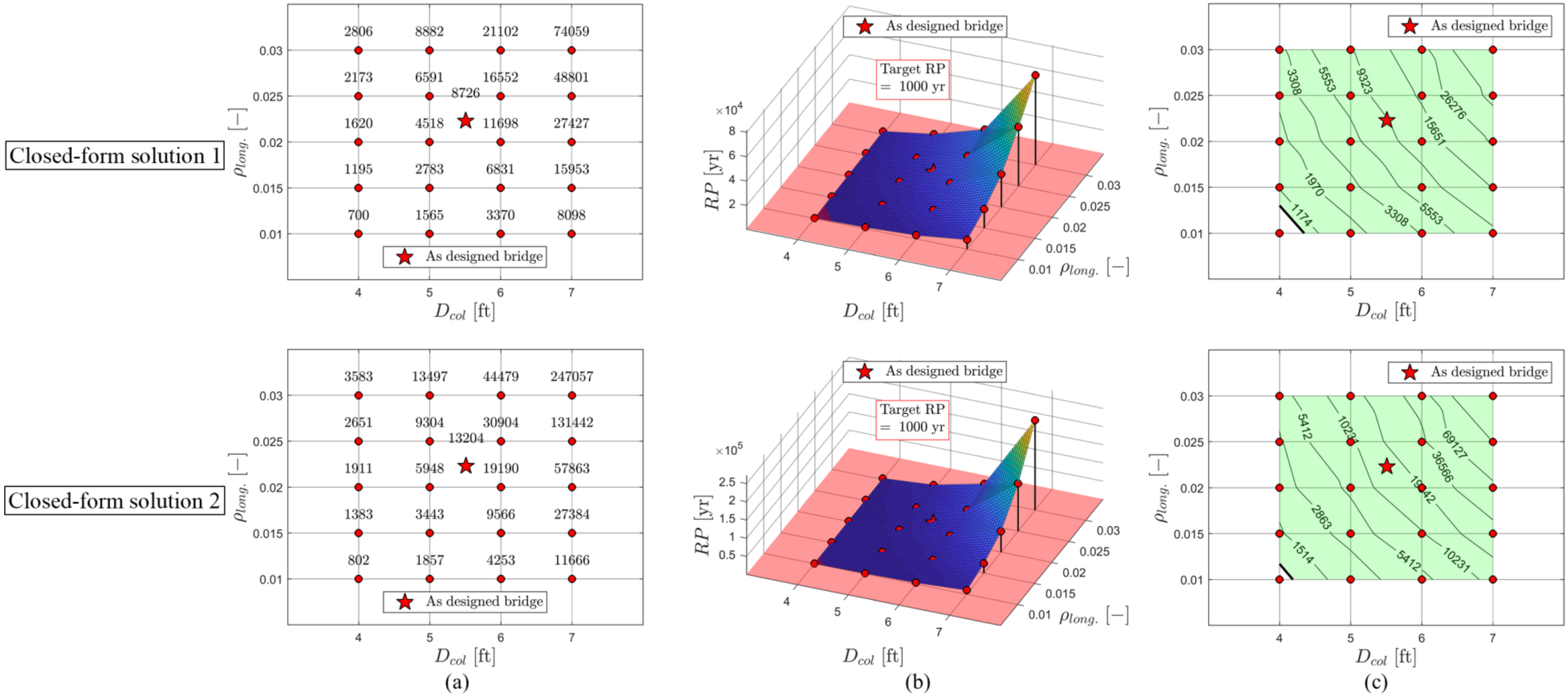

Figure 9.32 Results of parametric probabilistic seismic performance assessment of Bridge C in terms of limit-state 2, i.e., longitudinal rebar buckling: 1st row: Closed-form solution 1; 2nd row: Closed-form solution 2; (a) mean RPs (in years) of limit-state exceedance of all design points; (b) fitted mean RP surface; and (c) contours of mean RP surface (target RP contour line in bold) and feasible domain (in green)

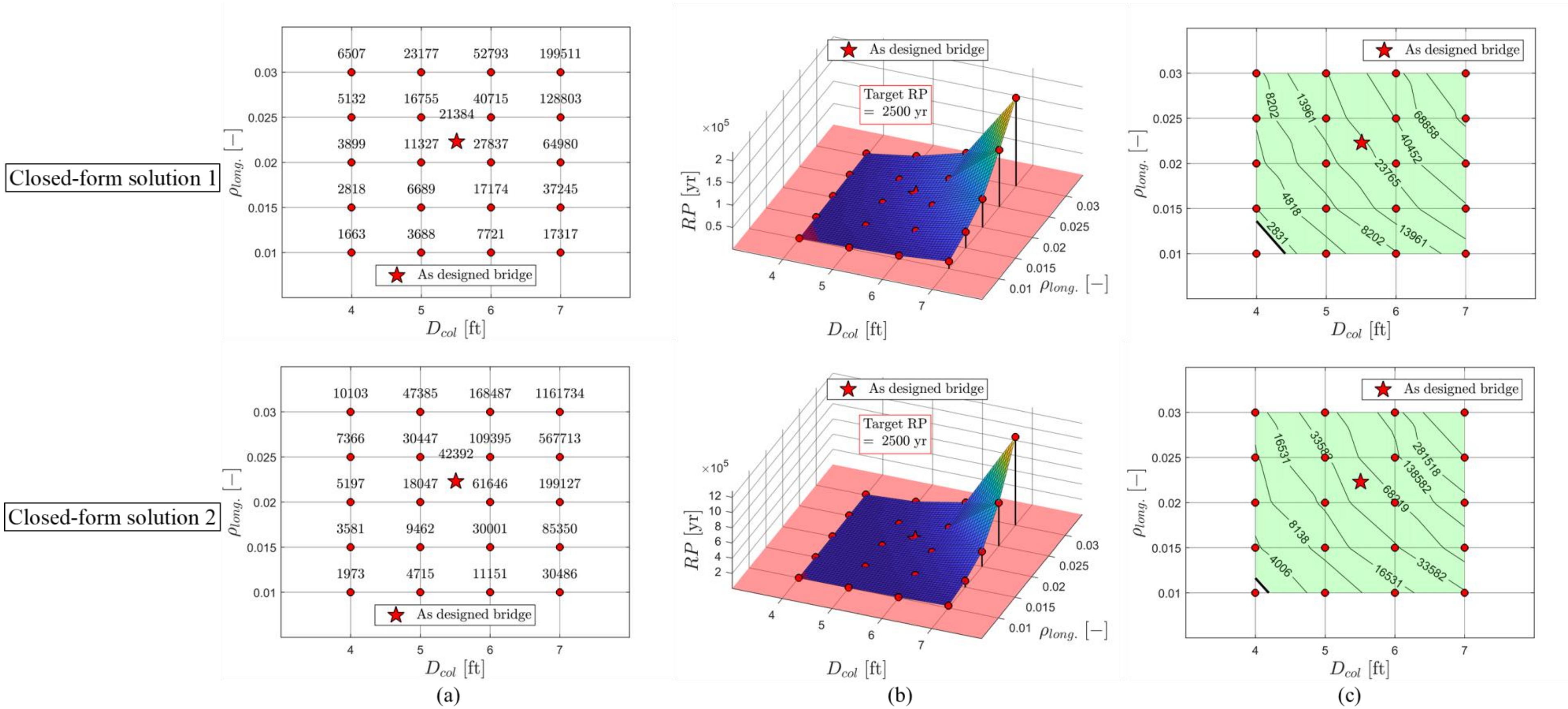

Figure 9.33 Results of parametric probabilistic seismic performance assessment of Bridge C in terms of limit-state 3, i.e., longitudinal rebar fracture: 1st row: Closed-form solution 1; 2nd row: Closed-form solution 2; (a) mean RPs (in years) of limit-state exceedance of all design points; (b) fitted mean RP surface; and (c) contours of mean RP surface (target RP contour line in bold) and feasible domain (in green)

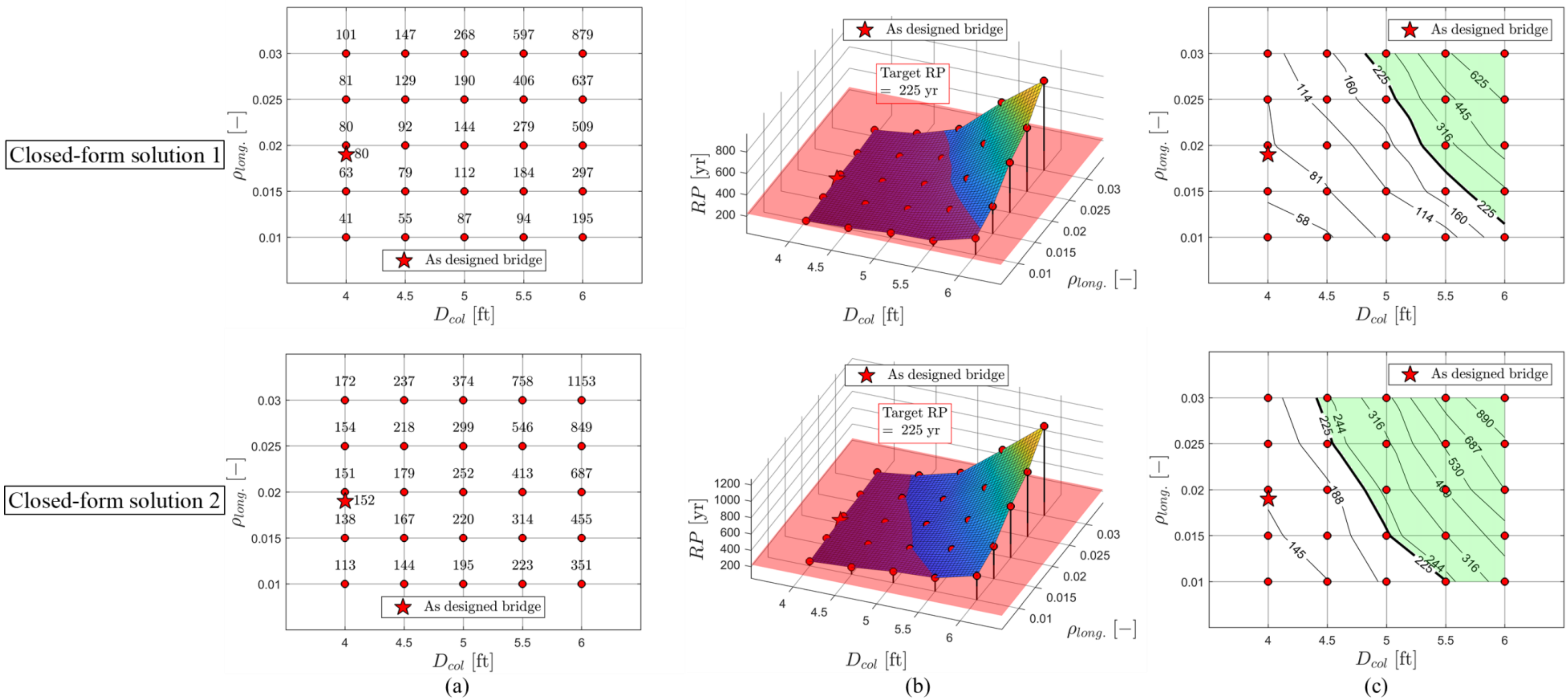

Figure 9.34 Results of parametric probabilistic seismic performance assessment of Bridge MAOC in terms of limit-state 1, i.e., concrete cover crushing: 1st row: Closed-form solution 1; 2nd row: Closed-form solution 2; (a) mean RPs (in years) of limit-state exceedance of all design points; (b) fitted mean RP surface; and (c) contours of mean RP surface (target RP contour line in bold) and feasible domain (in green)

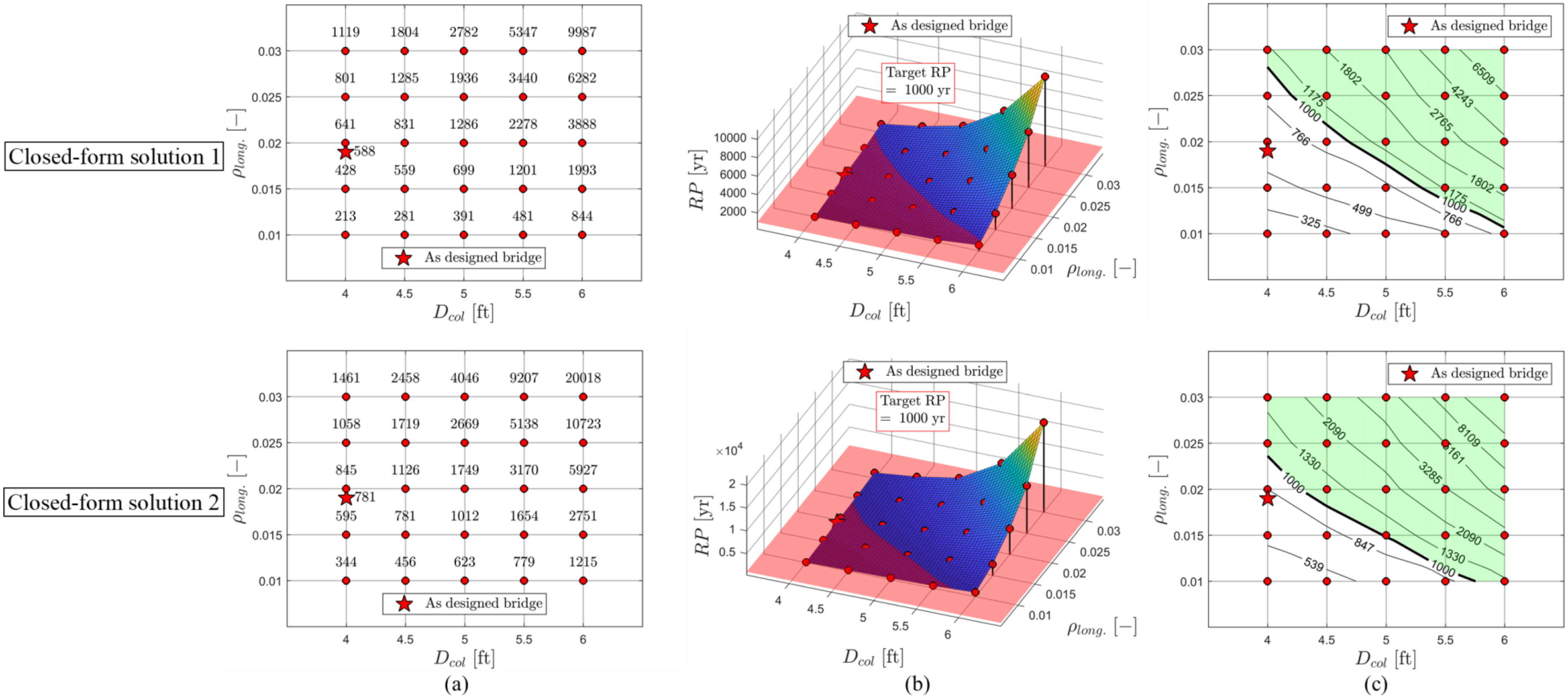

Figure 9.35 Results of parametric probabilistic seismic performance assessment of Bridge MAOC in terms of limit-state 2, i.e., longitudinal rebar buckling: 1st row: Closed-form solution 1; 2nd row: Closed-form solution 2; (a) mean RPs (in years) of limit-state exceedance of all design points; (b) fitted mean RP surface; and (c) contours of mean RP surface (target RP contour line in bold) and feasible domain (in green)

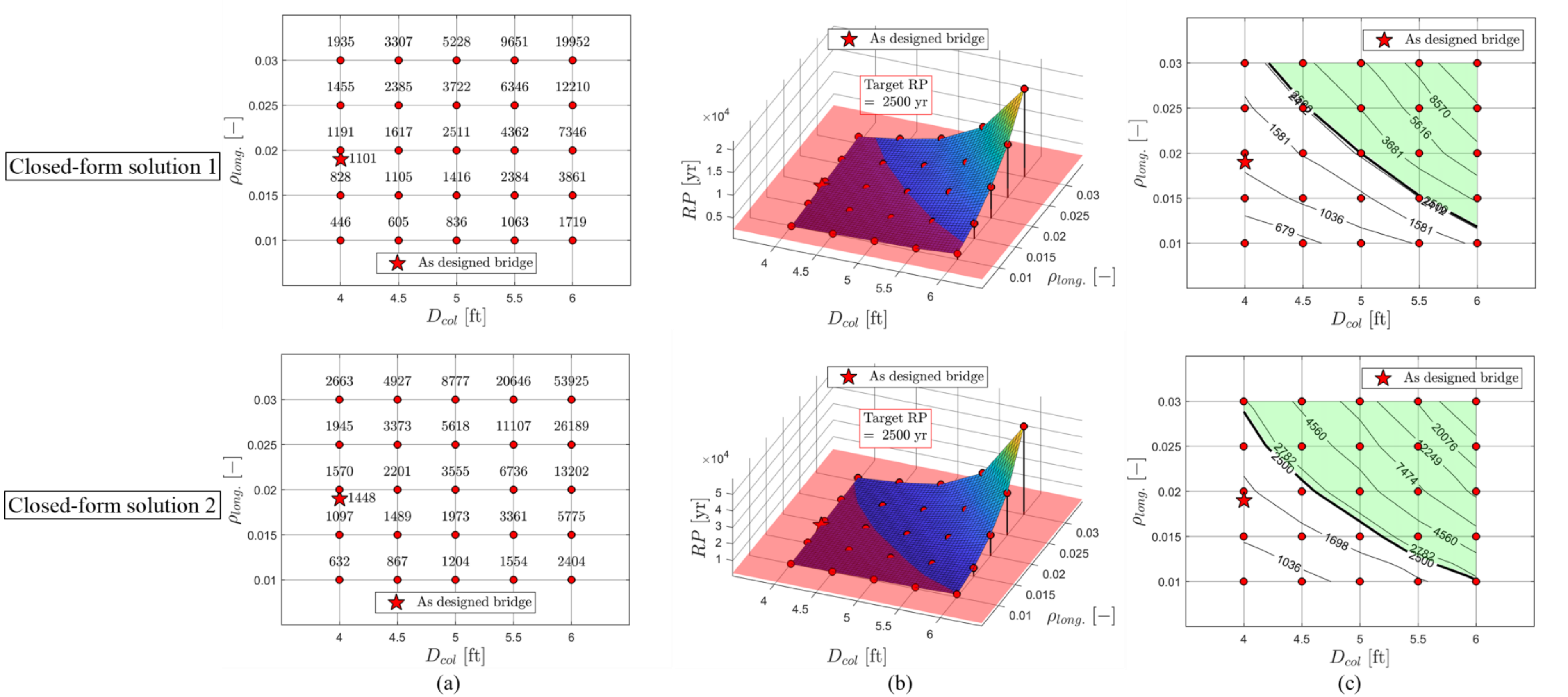

Figure 9.36 Results of parametric probabilistic seismic performance assessment of Bridge MAOC in terms of limit-state 3, i.e., longitudinal rebar fracture: 1st row: Closed-form solution 1; 2nd row: Closed-form solution 2; (a) mean RPs (in years) of limit-state exceedance of all design points; (b) fitted mean RP surface; and (c) contours of mean RP surface (target RP contour line in bold) and feasible domain (in green)

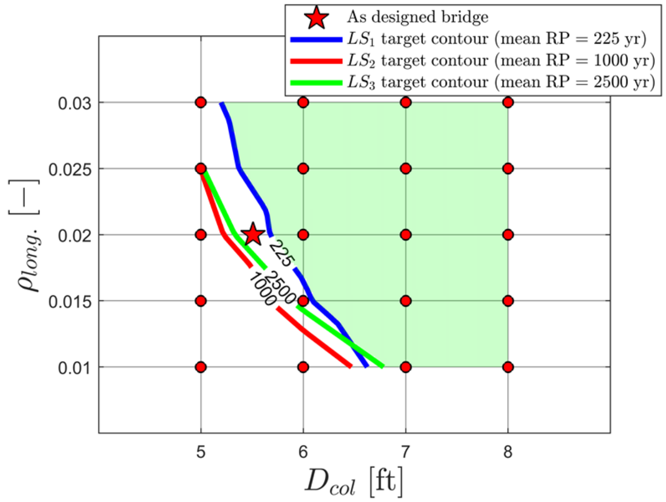

(a)

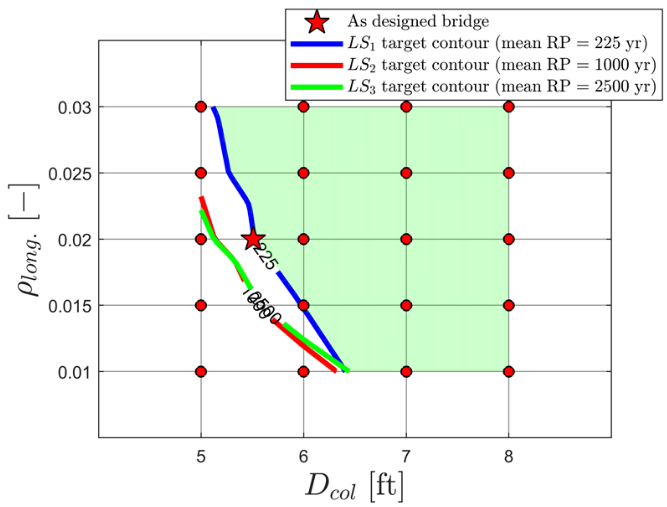

(b)

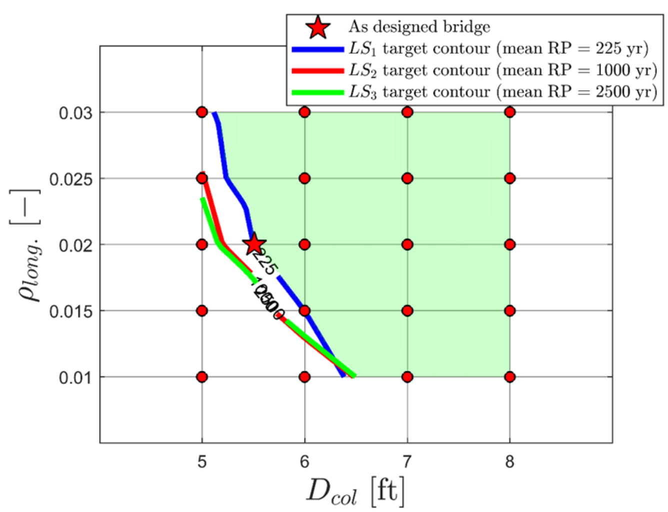

(c)

Figure 9.37 Feasible design domains for Bridge A: (a) Closed-form solution 1; (b) Closed-form solution 2; and (c) Numerical solution

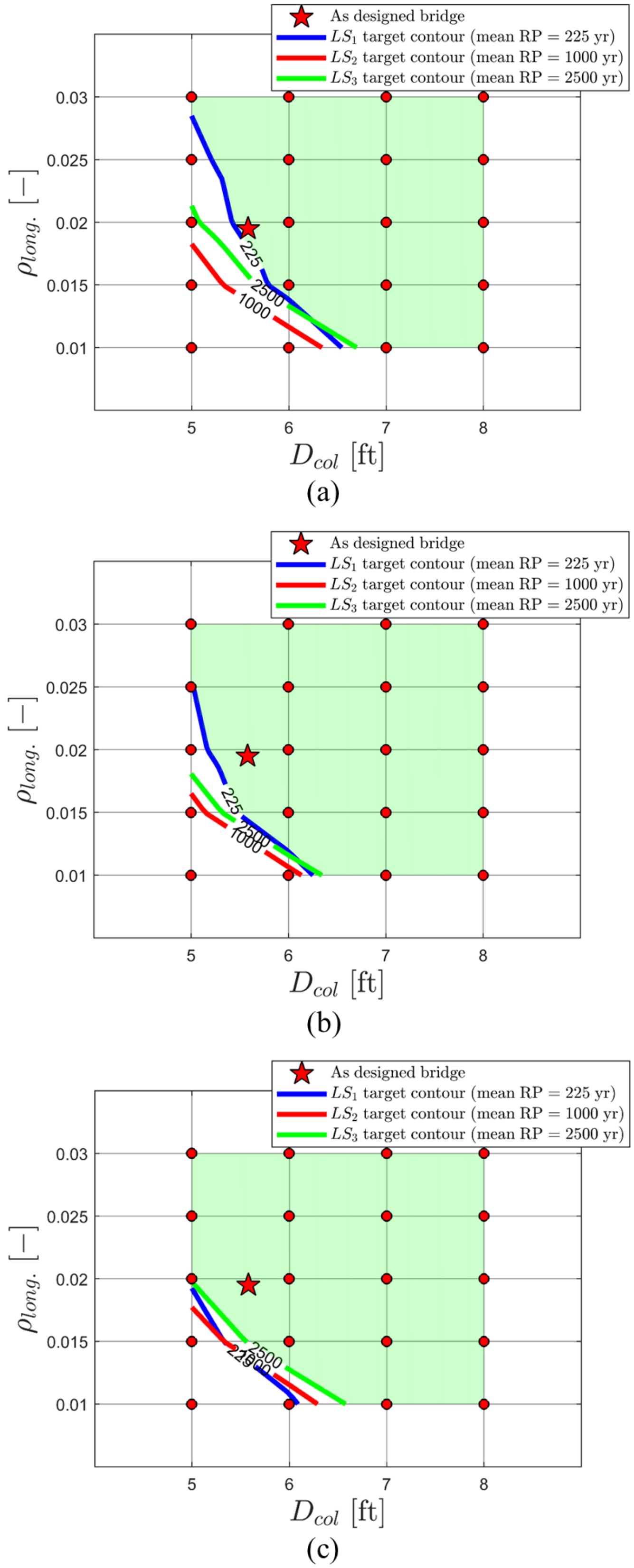

Figure 9.38 Feasible design domains for Bridge B: (a) Closed-form solution 1; (b) Closed-form solution 2; and (c) Numerical solution

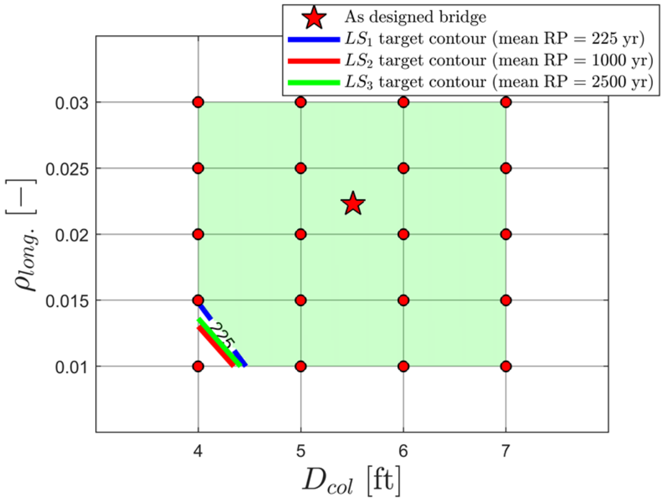

(a)

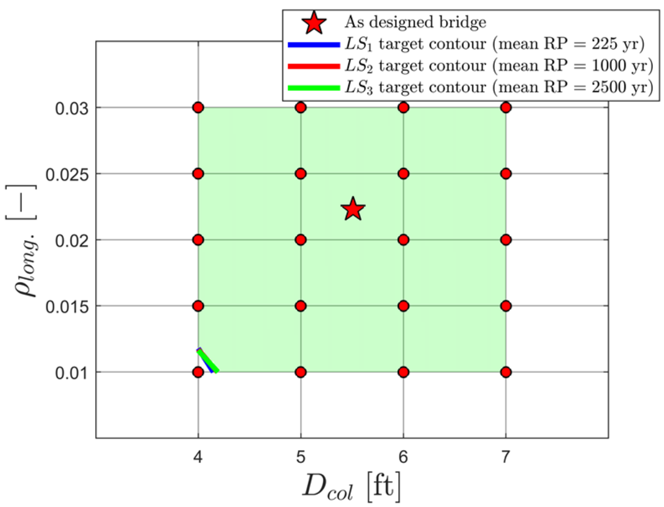

(b)

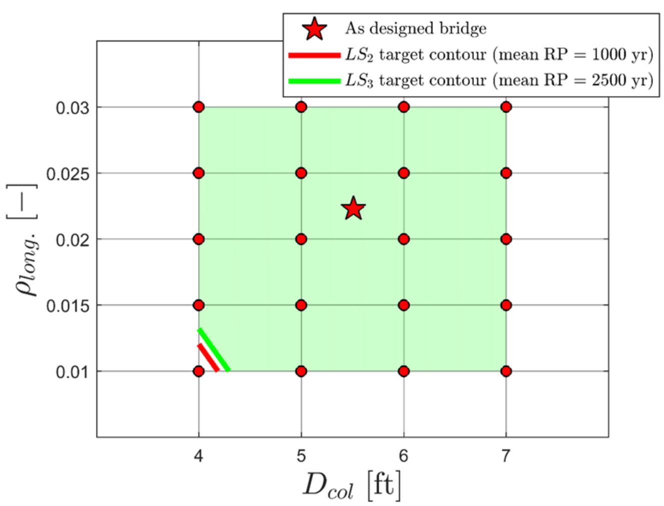

(c)

Figure 9.39 Feasible design domains for Bridge C: (a) Closed-form solution 1; (b) Closed-form solution 2; and (c) Numerical solution

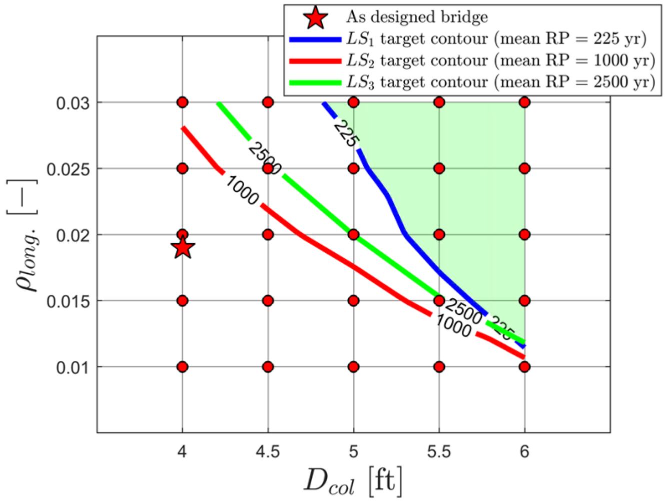

(a)

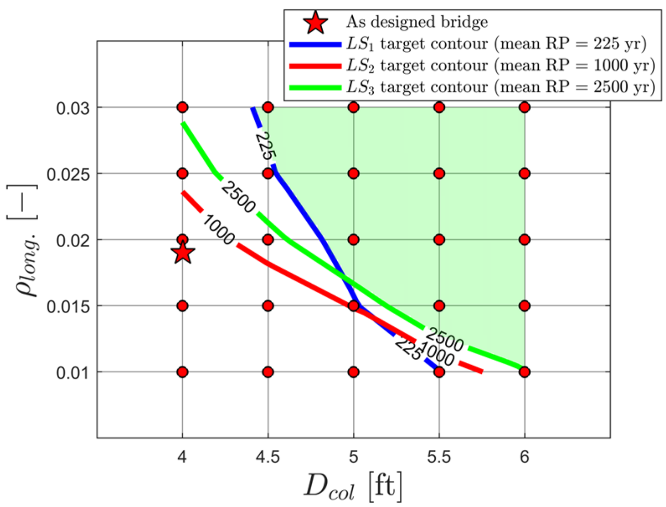

(b)

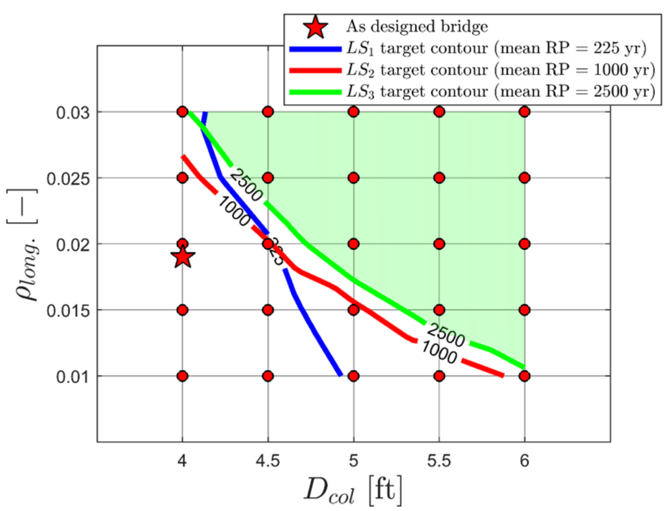

(c)

Figure 9.40 Feasible design domains for Bridge MAOC: (a) Closed-form solution 1; (b) Closed-form solution 2; and (c) Numerical solution

10 Simplified Risk-targeted Performance-based Seismic Design Methodology

10.1 Introduction

A simplified risk-targeted performance-based seismic design methodology is proposed in this chapter in lieu of the full-blown methodology discussed in Chapter 9. The purpose of the simplified methodology is to provide an alternative method to the full-blown parametric probabilistic seismic performance assessment in obtaining a final design point satisfying multiple risk-based objectives along with a feasible design domain in the primary design parameter space but requiring a much lower and practical computational expense. One would adopt the simplified methodology only if the computational expense of the full-blown assessment demands too high a computational load than available. The major sink in computational resource is in running the ensemble nonlinear time-history analyses through a finite element analysis package (OpenSees), rather than the probabilistic computations required. Computational cost, therefore, is directly proportional to the number of ensemble nonlinear time-history analyses carried out. Therefore, the reduction in the computational load for the simplified procedure comes from the following:

- Reduction in the number of design points to be assessed
- Reduction in the number of seismic hazard levels at which ensemble nonlinear time-history analyses are performed
- Reduction in the size of the ensemble, i.e., the number of nonlinear time-history analyses, per seismic hazard level

By implementing a smart combination of the above reductions, the number of nonlinear time-history analyses required to be run to obtain a final design point along with an approximate feasible design domain for a bridge can be greatly reduced. It is important to note that although requiring far fewer nonlinear time-history analyses to be run as compared to the full-blown methodology, the proposed simplified methodology is not compromised in terms of the level of rigor adopted in its formulation.

10.2 Simplified Methodology for Risk-targeted Performance-based Seismic Design

The first step toward a simplified risk-targeted performance-based seismic design methodology is to find a set of primary design parameter values that satisfies multiple risk-based performance objectives. With performance objectives stated in terms of target mean RPs of exceedance for multiple limit-states of interest, the chosen design should be such that the target for one of the limit-states is exactly satisfied while the mean RPs of exceeding the other limit-states are greater than the respective specified targets. To this end, a step-by-step simplified method is outlined based on the findings of the full-blown parametric probabilistic seismic performance assessment of the testbed bridges carried out in Chapter 9.

10.2.1 Simplified Methodology – Step 1: Choosing a Positive Slope Line in the Design Parameter Space for Interpolation

It is noted from the results of Chapter 9 that along any line connecting two or more design points in the primary design parameter space with a positive slope, i.e., along any direction with increasing values of D_{col} and ρ_{long} as shown in Figure 10.1, the growth of mean RP surfaces corresponding to the limit-states of interest can be well-approximated using a piecewise power law/function. A piecewise power function is equivalent to a piecewise linear function in logarithmic space. Thus, with mean RPs of limit-state exceedance evaluated at two or more design points along any positive slope line in the design space of a bridge and given a target mean RP of exceedance for a specific limit-state, a design point along that line that satisfies the specified target can be determined using a piecewise log-linear interpolation.

The first step of the simplified methodology is, therefore, to choose such a positive slope line in the primary design parameter space. To be able to find a design that satisfies a specific target mean RP of exceeding a limit-state along such a line using interpolation, the selected positive slope line should pass through p (≥ 2) arbitrary design points, designated as $[\mathbf{D}_1, \cdots, \mathbf{D}_p]$, for which mean RPs of exceeding that limit-state are known. Having selected such a line, defined as $\overline{\mathbf{D}_1\mathbf{D}_p}$, with a positive slope equal to m ft^{-1}, in the design space, the following unitless quantity, X, representative of continuously increasing values of D_{col} and ρ_{long} along that line is defined:

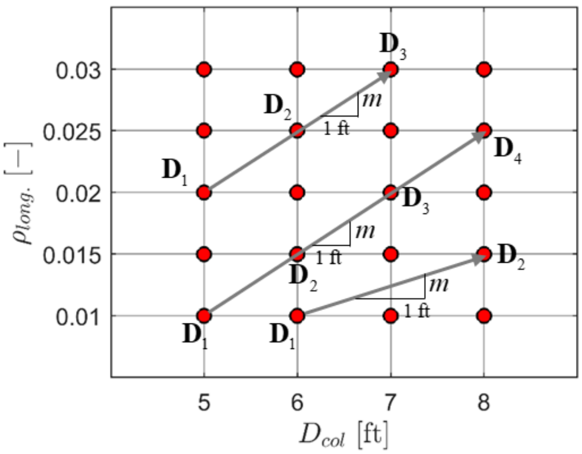

Figure 10.1 Design space of Bridge B showing possible positive slope directions (indicated by arrows) with increasing values of D_{col} and ρ_{long}. Red circles indicate a design point.

$$X[-] = \rho_{long}[-] + \frac{1}{m}\left[\text{ft}^{-1}\right] D_{col}[\text{ft}] \tag{10.1}$$

Mathematically, Eq. (10.1) represents a family of lines with slopes equal to $-\frac{1}{m}$ ft^{-1} which are perpendicular to $\overrightarrow{\mathbf{D}_1\mathbf{D}_p}$ (of slope equal to m ft^{-1}) with different values of X representing the intercepts of these lines along the ρ_{long} axis. The idea is pictorially illustrated in Figure 10.2 where the axes shown are not to scale. From the unit, i.e., ft^{-1}, of slope/slope of a line defined in the design space of a bridge, it is noted that the primary design parameters, D_{col} and ρ_{long}, are assumed to be plotted along the abscissa and ordinate of the design space respectively. To remove any ambiguity of notation, m and $-\frac{1}{m}$ just represent the numerical values of slopes.

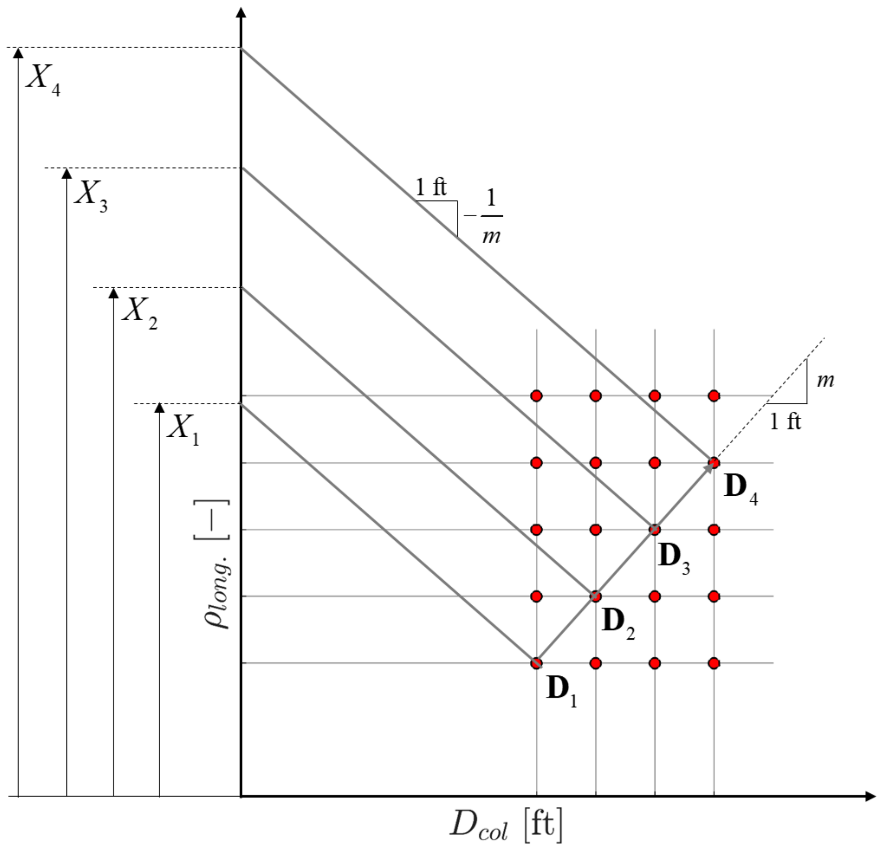

Figure 10.2 Illustration of the quantity X representing design points along the line, $\overrightarrow{\mathbf{D}_1\mathbf{D}_4}$ in this case, having a positive slope equal to m ft^{-1}

A discrete value of X, say X_i, thus, represents an arbitrary design point $\mathbf{D}_i$ with primary design parameters $(D_{col})_i$ and $(\rho_{long})_i$ along $\overrightarrow{\mathbf{D}_1\mathbf{D}_p}$. The mean RP of exceeding limit-state k for any arbitrary design point $\mathbf{D}_i$ lying along $\overrightarrow{\mathbf{D}_1\mathbf{D}_p}$ between points $\mathbf{D}_{i-1}$ and $\mathbf{D}_{i+1}$ can, therefore, be approximated using Eq.(10.2), as follows

$$\left(\text{RP}\right)_i^{LS_k} = \exp\left(\log\left(\text{RP}\right)_{i-1}^{LS_k} + \frac{\log\left(\text{RP}\right)_{i+1}^{LS_k} - \log\left(\text{RP}\right)_{i-1}^{LS_k}}{\log X_{i+1} - \log X_{i-1}} \times \left(\log X_i - \log X_{i-1}\right)\right) \tag{10.2}$$

where $(\text{RP})_i^{LS_k}$ is the mean RP of exceeding limit-state k for the design point represented by X_i. This is shown in Figure 10.3 with the case of Bridge B as an example.

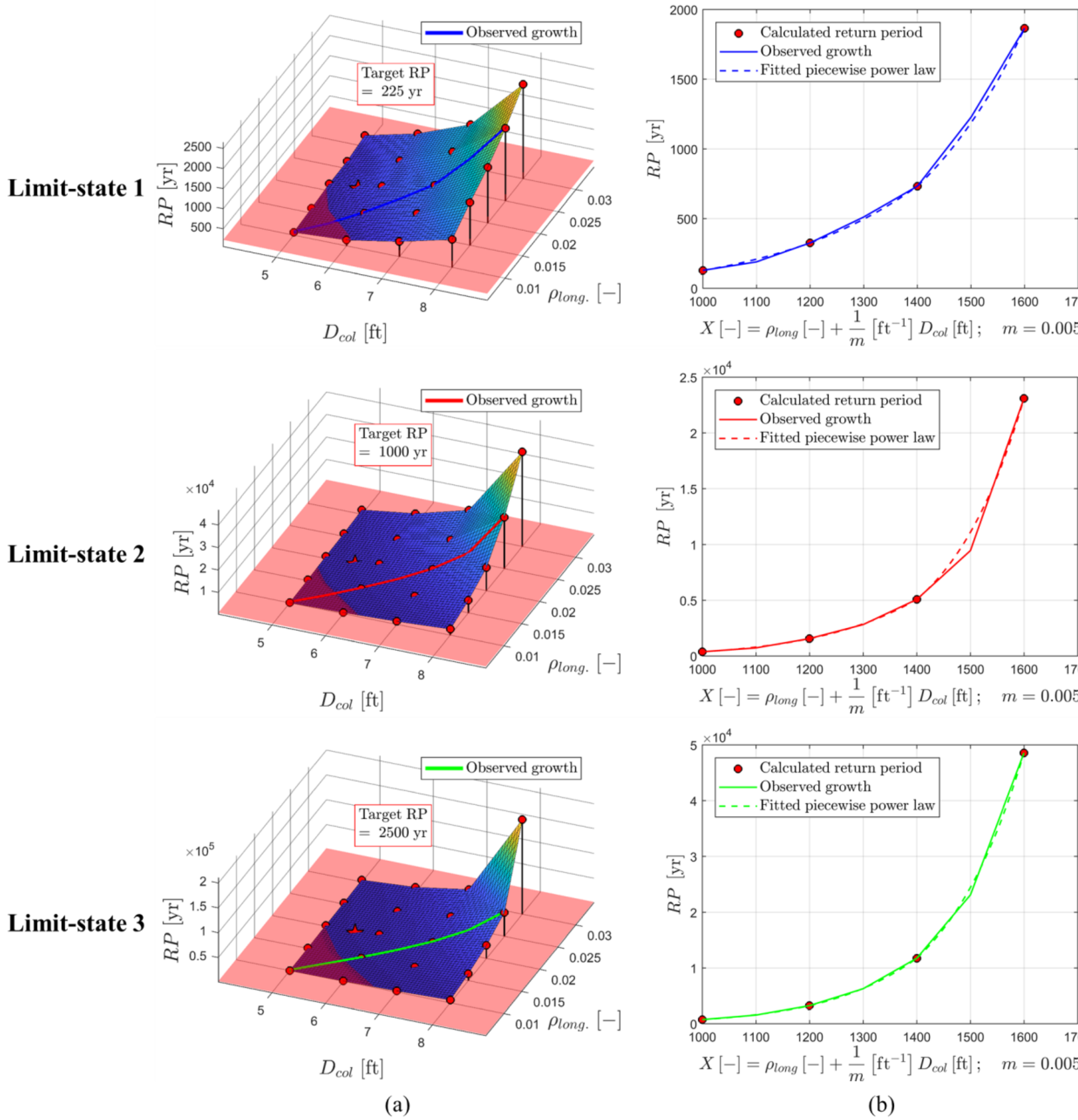

Figure 10.3 Growth of mean RP surfaces for different limit-states along a positive slope line of slope equal to 0.005 ft^{-1} in the design parameter space of Bridge B: 1st row: Limit-state 1; 2nd row: Limit-state 2; 3rd row: Limit-state 3; (a) Mean RP surface with observed growth along the positive slope line. Red circles indicate calculated mean RP for a design point; (b) Fitted piecewise power function to observed growth of mean RP surface along the positive slope line

10.2.2 Simplified Methodology – Step 2a: Selecting Number of Design Points to Assess

With performance objectives stated in terms of target mean RPs of exceedance for a selected set of limit-states, ideally only two extreme design points, say $\mathbf{D}_1$ and $\mathbf{D}_2$ represented by X_1 and X_2 respectively, need to be assessed such that a design satisfying the specified target for a limit-state can be determined through interpolation. In other words, if a very weak design point and a very strong design point were assessed, the design point satisfying the target RP of exceedance for a limit-state will lie somewhere in between these two points. However, if $\mathbf{D}_1$ and $\mathbf{D}_2$, as such, are taken very far apart in order to guarantee that the specified target for a limit-state of interest lies within the evaluated mean RPs for the assessed design points, the fitted power function will contain errors much larger than if the two design points were taken close to each other. Based on the size of the primary design parameter spaces of the four testbed bridges evaluated in this project, it is found that three design points along any positive slope direction are generally required to have a good approximation of the growth of a mean RP surface for a limit-state along that direction. As such, having decided on the size of the primary design parameter space for a bridge, it is recommended that a total of three design points $(p=3)$, $\mathbf{D}_1$, $\mathbf{D}_2$, and $\mathbf{D}_3$, be chosen along a specific positive slope line $\overrightarrow{\mathbf{D}_1\mathbf{D}_3}$ as shown in Figure 10.4. Hence, a two-piecewise power function (a piecewise log-bilinear function) is constructed to approximate the mean RPs along $\overrightarrow{\mathbf{D}_1\mathbf{D}_3}$.

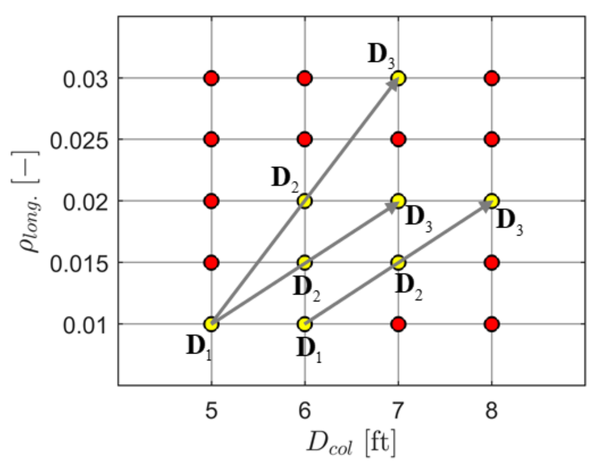

Figure 10.4 Design space of Bridge B showing three possible trios of design points to be assessed (indicated by yellow circles) along three respective positive slope directions. Red circles indicate all other design points

10.2.3 Simplified Methodology – Step 2b: Procedure for Choosing Design Points to Assess

As mentioned earlier, a total of three design points, $\mathbf{D}_1$, $\mathbf{D}_2$, and $\mathbf{D}_3$, are to be chosen along a positive slope line $\overrightarrow{\mathbf{D}_1\mathbf{D}_3}$ in the design space of a bridge. $\mathbf{D}_1$, $\mathbf{D}_2$, and $\mathbf{D}_3$ are named in order of increasing D_{col} and ρ_{long}, i.e., they correspond to increasingly stronger designs. The choice of the three design points to be assessed is not completely arbitrary. Initially a single design point should be chosen somewhere in the middle of the design space and mean RPs of exceeding the selected set of limit-states be evaluated for the first design point. The subsequent design points can be chosen more intelligently based on the results obtained for the first design point:

- if the first design point yields mean RPs of limit-state exceedance all significantly larger than the respective targets, the remaining design points should correspond to weaker designs. The chosen design points in the predefined design space need not necessarily be consecutive.
- if the first design point yields mean RPs of limit-state exceedance all significantly smaller than the respective targets, the remaining design points should correspond to stronger designs. The chosen design points in the predefined design space need not necessarily be consecutive.
- if the first design point yields mean RPs of limit-state exceedance near the respective targets, one of the remaining design points should correspond to a weaker design while the other should correspond to a stronger design. The chosen design points in the predefined design space need not necessarily be consecutive.

The procedure is illustrated in Figure 10.5 with Bridge B as an example.

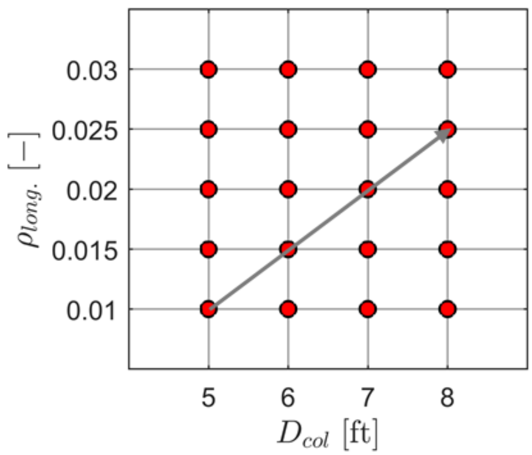

(a) The structure is to be evaluated taking into account limit-states 1, 2, and 3 with target mean RPs of 225 years, 1000 years, and 2500 years respectively. The design space of possible primary design parameters is shown with each design point plotted in red. The positive slope line of slope equal to 0.005 ft^{-1}, along which the parameters D_{col} and ρ_{long} are increasing, is shown as a grey arrow.

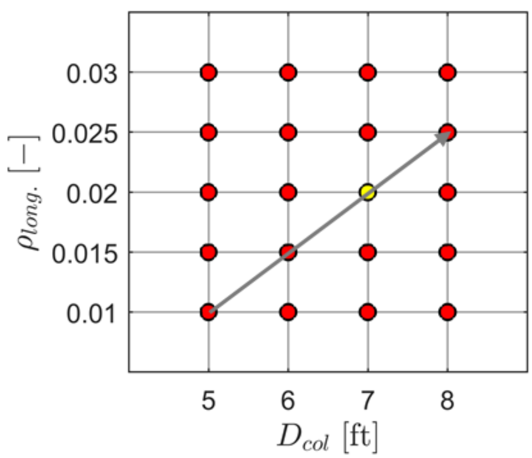

(b) A design point is chosen somewhere near the center of the design space shown in yellow. The point chosen is a design with D_{col} and ρ_{long} of 7 ft and 2% respectively. The mean RPs of exceedance of limit-states 1, 2, and 3 evaluated for this design point are 733 years, 5081 years, and 11758 years respectively, which are much larger than the respective target mean RPs.

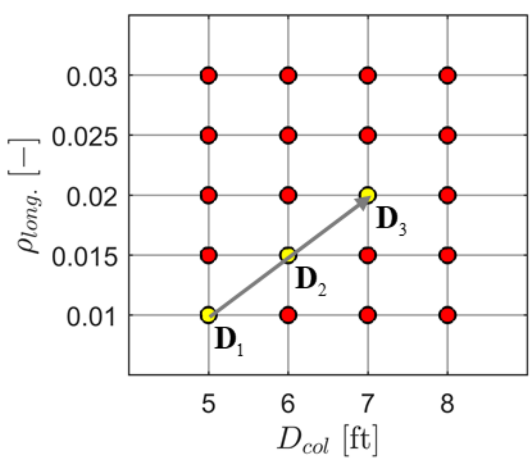

(c) As the calculated mean RPs of limit-state exceedances of the first chosen design point is much larger than the respective targets, additional design points corresponding to weaker designs are chosen. The chosen design points are shown in yellow.

Figure 10.5 Design points selected in the design space of Bridge B for the simplified methodology.

10.2.4 Simplified Methodology – Step 3: Finding Design Point along Positive Slope Line Satisfying Multiple Risk-based Performance Objectives

The seismic performance of three chosen design points, $\mathbf{D}_1$, $\mathbf{D}_2$, and $\mathbf{D}_3$ represented by X_1, X_2, and X_3 respectively, in terms of mean RPs of exceeding the selected set of limit-states are evaluated using the improved version of the PEER PBEE assessment framework assembled as a part of this project. As mentioned earlier, these design points are chosen such that they lie along a positive slope line in the primary design parameter space of a bridge. The equation of this line, $\overrightarrow{\mathbf{D}_1\mathbf{D}_3}$, with D_{col} and ρ_{long} plotted along the abscissa and ordinate of the primary design parameter space, respectively, is given by

$$\rho_{long}\left[-\right] = m\left[\text{ft}^{-1}\right] \cdot D_{col}\left[\text{ft}\right] + \alpha\left[-\right] \tag{10.3}$$

where m, the numerical value of the slope of the line, and α, the intercept of the line along the ρ_{long} axis, can be determined from the coordinates of any two of the chosen design points $\mathbf{D}_1$, $\mathbf{D}_2$, and $\mathbf{D}_3$. The value of X, say $(X^*)^{LS_k}$, satisfying a target value of mean RP of exceedance, say $(\text{RP})_{\text{TARGET}}^{LS_k}$, for the k^{th} limit-state which lies between mean RPs $(\text{RP})_i^{LS_k}$ and $(\text{RP})_{i+1}^{LS_k}$ corresponding to design points represented by X_i and X_{i+1} respectively, is given by Eq. (10.4) according to the piecewise log-linear fit. The index i in Eq. (10.4), for a total of three design points assessed, can take values of 1 and 2.

$$\left(X^*\right)^{LS_k} = \exp\left(\log X_i + \frac{\log X_{i+1} - \log X_i}{\log\left(\text{RP}\right)_{i+1}^{LS_k} - \log\left(\text{RP}\right)_i^{LS_k}} \times \left(\log\left(\text{RP}\right)_{\text{TARGET}}^{LS_k} - \log\left(\text{RP}\right)_i^{LS_k} \right) \right) \tag{10.4}$$

With multiple risk-based performance objectives stated in terms of target mean RPs of exceedance for the selected set of limit-states, a design point per limit-state along $\overrightarrow{\mathbf{D}_1\mathbf{D}_3}$, represented by $(X^*)^{LS_k}$ which exactly satisfies the specified target for limit-state k, can be determined through interpolation as per Eq. (10.4). The value of X, say X^*, representing the design point satisfying multiple targets, i.e., exactly satisfying the target for one limit-state while being on the safer side for the other limit-states, is given by:

$$X^* = \max\left((X^*)^{LS_1}, \cdots, (X^*)^{LS_n} \right) \tag{10.5}$$

where n is the number of limit-states considered, in this case, equal to 3. Once a value of X^* is obtained, Eq. (10.1) can be invoked to write

$$X^* = \rho_{long}^*\left[-\right] + \frac{1}{m}\left[\text{ft}^{-1}\right] D_{col}^*\left[\text{ft}\right] \tag{10.6}$$

where, D_{col}^* and ρ_{long}^* are the primary design parameters of the design point, defined as $\mathbf{D}^*$, along $\overrightarrow{\mathbf{D}_1\mathbf{D}_3}$ that satisfies multiple risk-based performance objectives. Eq. (10.6) basically represents the equation of a line passing through the point $\mathbf{D}^*$ and perpendicular to $\overrightarrow{\mathbf{D}_1\mathbf{D}_3}$. The design point $\mathbf{D}^*$ can therefore be obtained as the point of intersection between the two lines given by Eq. (10.3) and Eq. (10.6), as follows:

$$\mathbf{D}^* = \begin{bmatrix} D_{col}^*\left[\text{ft}\right] \\ \rho_{long}^*\left[-\right] \end{bmatrix} = \begin{bmatrix} \frac{1}{m}\left[\text{ft}^{-1}\right] & 1\left[-\right] \\ -m\left[\text{ft}^{-1}\right] & 1\left[-\right] \end{bmatrix}^{-1} \begin{bmatrix} X^*\left[-\right] \\ \alpha\left[-\right] \end{bmatrix} \tag{10.7}$$

It is to be noted that, in practice, values of D_{col} and ρ_{long} are constrained by various factors such as the availability of existing prefabricated formwork, restrictions on rebar sizes, etc. Thus, exact values of D_{col}^* and ρ_{long}^* obtained may not always be practically realizable. In case, Eq. (10.7) yields a non-feasible value of D_{col}^* and/or ρ_{long}^*, a viable design point nearest to $\mathbf{D}^*$ on the safer side is chosen as the final design.

The procedure is illustrated in Figure 10.6 with Bridge B as an example. In this example, to obtain the mean RPs of limit-state exceedance of limit-states 1, 2, and 3 for the chosen design points, $\mathbf{D}_1$, $\mathbf{D}_2$, and $\mathbf{D}_3$, results of the parametric probabilistic seismic performance assessment of Bridge B, carried out previously in Chapter 9, are directly used. The design point $\mathbf{D}^*$ given by $D_{col}^* = 5.8$ ft and $\rho_{long}^* = 0.014$, is shown in the feasible design domain previously outlined for Bridge B in Chapter 9 using the full-blown methodology. As noted from Figure 10.6 (f), $\mathbf{D}^*$, found to be governed by limit-state 3 in this case, lies just inside the feasible design domain of Bridge B. As noted from the feasible design domain obtained using the full-blown methodology, the governing limit-state in the vicinity of $\overrightarrow{\mathbf{D}_1\mathbf{D}_3}$ in the design space is indeed limit-state 3, thereby validating the simplified method. The already assessed safe design point $\mathbf{D}_2$ lying along $\overrightarrow{\mathbf{D}_1\mathbf{D}_3}$, corresponding to D_{col} and ρ_{long} of 6 ft and 0.015 respectively, qualifies to be the most viable design point in this case.

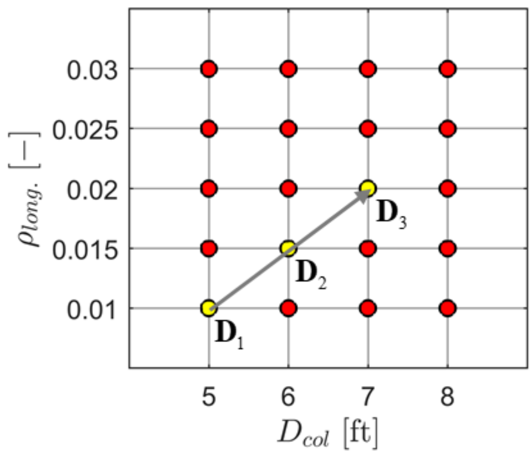

(a) The design points of Bridge B chosen for the simplified methodology (indicated by yellow circles), lying along the line $\overrightarrow{\mathbf{D}_1\mathbf{D}_3}$ (indicated by the grey arrow) are shown. The equation of $\overrightarrow{\mathbf{D}_1\mathbf{D}_3}$ is

$$\rho_{long}\left[-\right]=0.005\left[\text{ft}^{-1}\right]\cdot D_{col}\left[\text{ft}\right]-0.015\left[-\right]$$

The mean RPs of limit-state exceedance of limit-states 1, 2, and 3 are evaluated for the chosen design points

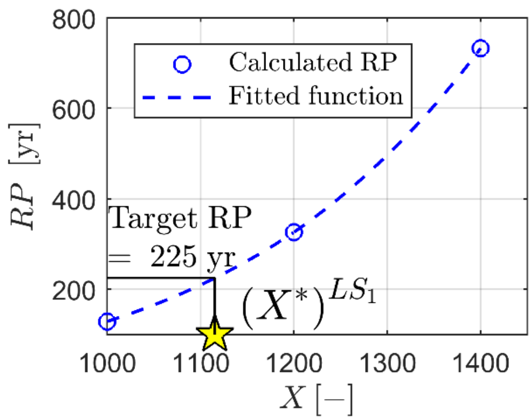

(b) $(X^*)^{LS_1}$ representing the design point along $\overrightarrow{\mathbf{D}_1\mathbf{D}_3}$ in the design space of Bridge B exactly satisfying the target mean RP for limit-state 1 is calculated using Eq. (10.4)

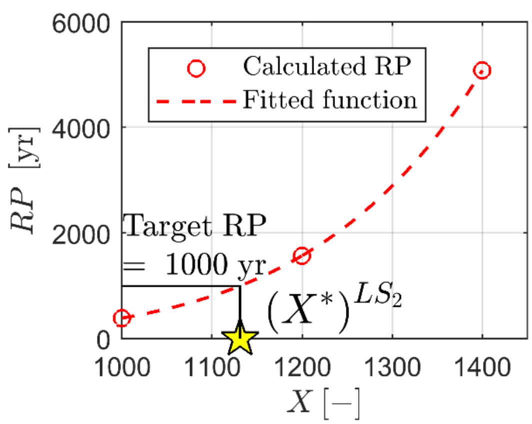

(c) $(X^*)^{LS_2}$ representing the design point along $\overrightarrow{\mathbf{D}_1\mathbf{D}_3}$ in the design space of Bridge B exactly satisfying the target mean RP for limit-state 2 is calculated using Eq. (10.4)

Figure 10.6 Illustration of Steps 1-3 of the simplified methodology applied to Bridge B

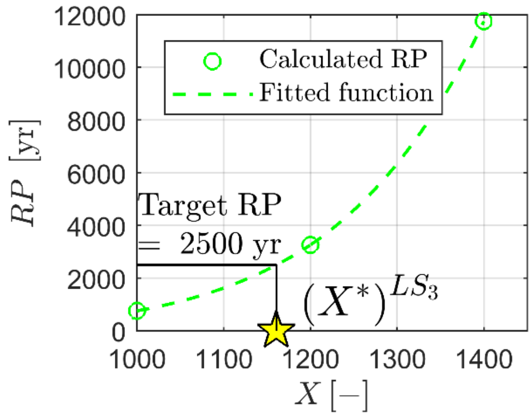

(d) $(X^*)^{LS_3}$ representing the design point along $\overrightarrow{\mathbf{D}_1\mathbf{D}_3}$ in the design space of Bridge B exactly satisfying the target mean RP for limit-state 3 is calculated using Eq. (10.4)

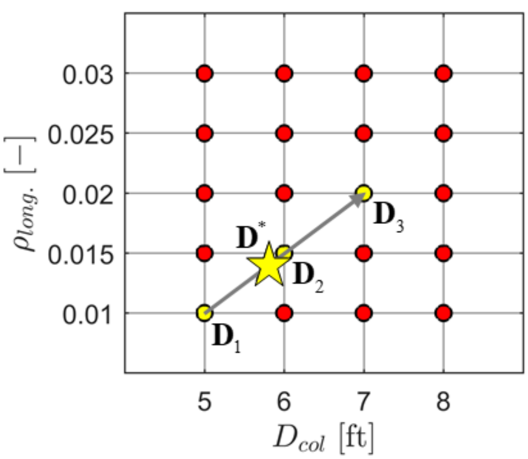

(e) The value of X^* satisfying all three targets and governed by limit-state 3, in this case, is given by

$$X^* = \max\left((X^*)^{LS_1}, (X^*)^{LS_2}, (X^*)^{LS_3}\right)$$
$$= 1160.7885$$

Finally, the design point $\mathbf{D}^*$, along $\overrightarrow{\mathbf{D}_1\mathbf{D}_3}$, with $D^*_{col} = 5.8$ ft and $\rho^*_{long} = 0.014$ is obtained as per Eq. (10.7) and shown as a yellow star in the design space of Bridge B

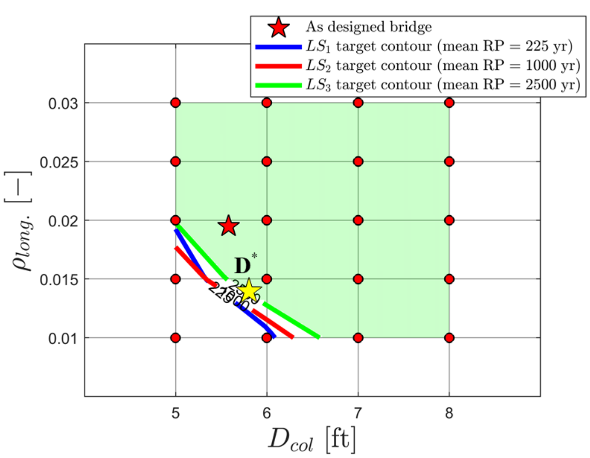

(f) Location of the design point $\mathbf{D}^*$ (indicated by a yellow star) is shown with respect to the feasible design domain for Bridge B. previously obtained in Chapter 9 using the full-blown methodology

Figure 10.6 (contd.) Illustration of Steps 1-3 of the simplified methodology applied to Bridge B

In case a practically unrealizable design point, $\mathbf{D}^*$, is obtained, one might not always come across a situation as favorable as the one encountered in the example illustrated in Figure 10.6. In the example shown, a safe and viable design point, i.e., $\mathbf{D}_2$, lying along the line, $\overrightarrow{\mathbf{D}_1\mathbf{D}_3}$, of already assessed design points happened to be very close to the unrealizable (in terms of D_{col}) design point $\mathbf{D}^*$ in the primary design parameter space. However, it is possible that a relatively more economical and practically realizable design point located away from $\overrightarrow{\mathbf{D}_1\mathbf{D}_3}$ in the design space may actually be closer to $\mathbf{D}^*$, and hence more desirable, than the next viable safe design point lying along $\overrightarrow{\mathbf{D}_1\mathbf{D}_3}$. This is illustrated in Figure 10.7 where the design point $\mathbf{D}^*$ along a chosen line, $\overrightarrow{\mathbf{D}_1\mathbf{D}_3}$, (also shown) in the design space of Bridge MAOC, obtained by using the results of Chapter 9 and following the steps of the simplified methodology outlined so far, is shown. Also shown in Figure 10.7 is the location of the design point $\mathbf{D}^*$ with respect to the feasible design domain previously delineated for Bridge MAOC using the full-blown methodology.

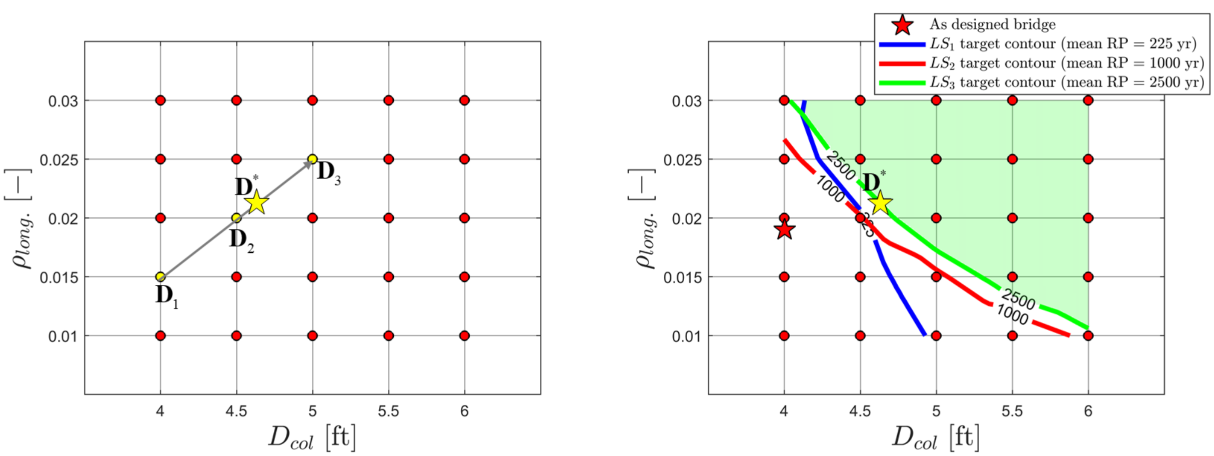

(a) (b)

Figure 10.7 Result of steps 1-3 of the simplified methodology applied to Bridge MAOC. (a) Design point $\mathbf{D}^*$ (indicated by a yellow star) obtained for a specific choice of $\mathbf{D}_1$, $\mathbf{D}_2$, and $\mathbf{D}_3$ (indicated by yellow circles) is show in the design space of Bridge MAOC; (b) Location of the design point $\mathbf{D}^*$ (indicated by a yellow star) obtained is shown with respect to the feasible design domain for Bridge MAOC previously obtained in Chapter 9 using the full-blown methodology

As can be seen from Figure 10.7, the design point corresponding to D_{col} and ρ_{long} of 4.5 ft and 0.025, respectively, or the one corresponding to D_{col} and ρ_{long} of 5 ft and 0.02, respectively, both lying inside the feasible design domain but away from $\overrightarrow{\mathbf{D}_1\mathbf{D}_3}$, are relatively more economical and closer to $\mathbf{D}^*$ as compared to $\mathbf{D}_3$, the next safe and viable design point along $\overrightarrow{\mathbf{D}_1\mathbf{D}_3}$. Hence, these design points qualify, better than $\mathbf{D}_3$, as candidate final designs for Bridge MAOC. Without the knowledge of a feasible design domain, however, such a design decision would not have been well-versed in terms of the associated risk.

The simplified design methodology could have, very well, been concluded at Step 3 thereby engendering a design point $\mathbf{D}^*$ in the primary design parameter space of an OSB satisfying multiple risk-based performance objectives. However, the steps of the simplified design methodology outlined thus far cannot delineate a feasible design domain in the design space of a bridge. The knowledge of a feasible design domain of a bridge in its design space is extremely valuable in the sense that it can be greatly utilized to make risk-informed design decisions thereby leading to safe and economic design of bridges, especially with regard to the earthquake hazard.

The remaining steps of the methodology are primarily aimed towards delineating a feasible design domain in the design space of a bridge using as few design points as possible. Where previously every design point in the primary design parameter space of a testbed bridge was assessed to determine the mean RPs of exceedance of the selected set of limit-states, and hence delineate a feasible design domain, a smarter methodology is employed to reduce the number of design points required to be assessed.

10.2.5 Simplified Methodology – Step 4a: Linear Approximation of Contour Lines of Mean RP Surfaces

Contour lines of the mean RP surfaces, fitted for individual limit-states of interest, corresponding to the respective target mean RPs of exceedance specified for the selected set of limit-states are superimposed in the design space to delineate the overall feasible design domain of a bridge. The next step in the simplified methodology towards obtaining a feasible design domain is, therefore, to approximate the contours of the mean RP surfaces for each limit-state of interest. From observations of the topology of the fitted mean RP surfaces (Chapter 9) for the selected set of limit-states for all testbed bridges considered, the seemingly parallel contours of such a surface in the design space, for a given limit-state, can be reasonably approximated by straight lines having the same slope.

Given a limit-state, the piecewise log-linear relationship fitted along the line $\overrightarrow{\mathbf{D}_1\mathbf{D}_3}$ can be used to approximate different levels of mean RPs of exceedance of that limit-state in the design space. Estimation of the slope of linearized contour lines in the design space corresponding to these mean RP levels requires the seismic performance assessment of an additional design point located away from $\overrightarrow{\mathbf{D}_1\mathbf{D}_3}$. This additional design point, $\mathbf{D}_1^a$, is recommended to correspond to the design with, either the smallest D_{col} and largest ρ_{long}, or the largest D_{col} and smallest ρ_{long}, among all evaluated design points, i.e., $\mathbf{D}_1$, $\mathbf{D}_2$, and $\mathbf{D}_3$, along the line $\overrightarrow{\mathbf{D}_1\mathbf{D}_3}$ in the design space. In other words, assuming $\overrightarrow{\mathbf{D}_1\mathbf{D}_3}$ to be the diagonal of a rectangle passing through vertices $\mathbf{D}_1$ and $\mathbf{D}_3$ in the design space, $\mathbf{D}_1^a$ should be chosen such that it lies at one of the two other vertices of the rectangle. This is to ensure that, for the limit-state in question, the fitted piecewise log-linear relation along $\overrightarrow{\mathbf{D}_1\mathbf{D}_3}$ contains the mean RP of exceedance evaluated for the additional design point, $\mathbf{D}_1^a$. Any other design point enclosed in the above-mentioned rectangle and positioned closer to $\overrightarrow{\mathbf{D}_1\mathbf{D}_3}$ in the design space is not recommended to be chosen as $\mathbf{D}_1^a$. This is because the slope of linearized contours to be determined based on this approximate method is found to become increasingly sensitive to the proximity of this additional design point to $\overrightarrow{\mathbf{D}_1\mathbf{D}_3}$. With the design space of Bridge B as an example, possible choices of the additional design point, $\mathbf{D}_1^a$, given $\overrightarrow{\mathbf{D}_1\mathbf{D}_3}$, are illustrated in Figure 10.8.

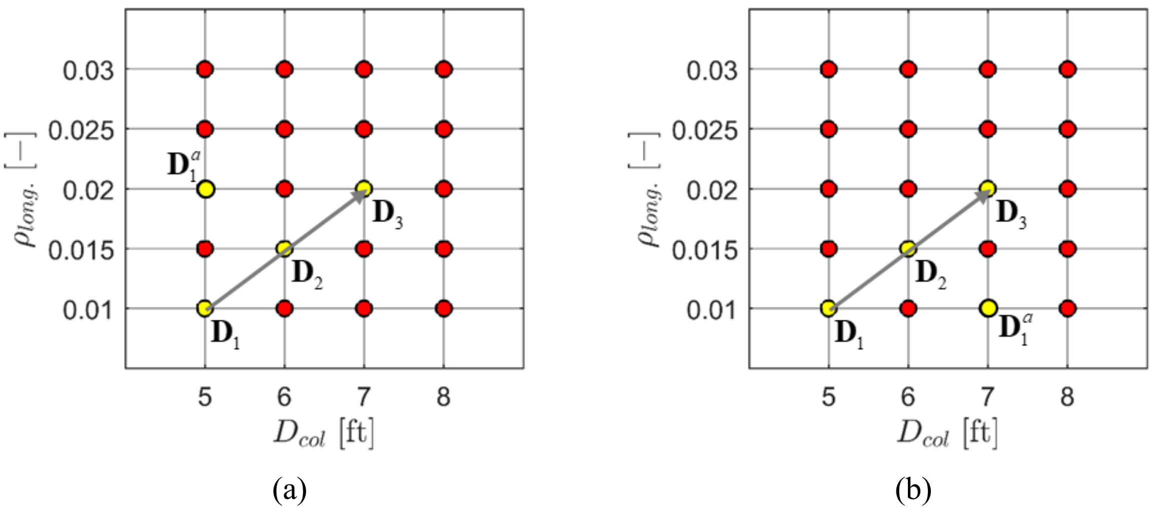

Figure 10.8 Possible choices of the additional design point, $\mathbf{D}_1^a$, given $\overrightarrow{\mathbf{D}_1\mathbf{D}_3}$, in the design space of Bridge B required for Step 4a of the simplified methodology; (a) $D_{col} = 5$ ft, $\rho_{long} = 0.02$; (b) $D_{col} = 7$ ft, $\rho_{long} = 0.01$

The mean RPs of exceeding the selected set of limit-states are evaluated for $\mathbf{D}_1^a$. The mean RP of exceedance of the k^{th} limit-state evaluated for $\mathbf{D}_1^a$ is denoted as $(\text{RP})_{\mathbf{D}_1^a}^{LS_k}$. For the k^{th} limit-state, the design point along $\overrightarrow{\mathbf{D}_1\mathbf{D}_3}$ with the same mean RP of exceedance as that of $\mathbf{D}_1^a$, i.e., $(\text{RP})_{\mathbf{D}_1^a}^{LS_k}$, is determined through interpolation using the piecewise log-linear relationship developed earlier. This new design point along $\overrightarrow{\mathbf{D}_1\mathbf{D}_3}$ is termed $(\mathbf{D}_1^{a\prime})^{LS_k}$. To obtain the coordinates of $(\mathbf{D}_1^{a\prime})^{LS_k}$, the value of X, say $(X_1^{a\prime})^{LS_k}$, along $\overrightarrow{\mathbf{D}_1\mathbf{D}_3}$ representing the design point $(\mathbf{D}_1^{a\prime})^{LS_k}$, and corresponding to a mean RP of exceeding limit-state k equal to $(\text{RP})_{\mathbf{D}_1^a}^{LS_k}$, is first calculated as follows

$$\left(X_1^{a'}\right)^{LS_k} = \exp\left(\log X_i + \frac{\log X_{i+1} - \log X_i}{\log\left(\text{RP}\right)_{i+1}^{LS_k} - \log\left(\text{RP}\right)_i^{LS_k}} \times \left(\log\left(\text{RP}\right)_{\mathbf{D}_1^a}^{LS_k} - \log\left(\text{RP}\right)_i^{LS_k}\right)\right) \quad (10.8)$$

where the index, i, can take values of 1 or 2. X_i and X_{i+1} represent the pair of assessed design points $\mathbf{D}_i$ and $\mathbf{D}_{i+1}$ along $\overrightarrow{\mathbf{D}_1\mathbf{D}_3}$ with mean RPs of exceedance for limit-state k equal to $(\text{RP})_i^{LS_k}$ and $(\text{RP})_{i+1}^{LS_k}$ such that $(\text{RP})_i^{LS_k} < (\text{RP})_{\mathbf{D}_1^a}^{LS_k} < (\text{RP})_{i+1}^{LS_k}$. Hence $(\mathbf{D}_1^{a\prime})^{LS_k}$ can be obtained as

$$\left(\mathbf{D}_1^{a\prime}\right)^{LS_k} = \begin{bmatrix} \dfrac{1}{m}\left[\mathrm{ft}^{-1}\right] & 1[-] \\ -m\left[\mathrm{ft}^{-1}\right] & 1[-] \end{bmatrix}^{-1} \begin{bmatrix} \left(X_1^{a\prime}\right)^{LS_k}[-] \\ \alpha[-] \end{bmatrix} \tag{10.9}$$

where m ft^{-1} and α are the slope and ρ_{long}-axis intercept of $\overrightarrow{\mathbf{D}_1\mathbf{D}_3}$ respectively.

The slope, say m_1^k, of the contour line corresponding to a mean RP of $(\mathrm{RP})_{\mathbf{D}_1^a}^{LS_k}$ in the primary design parameter space can therefore be estimated as the slope of the line connecting the design points $\mathbf{D}_1^a$ and $(\mathbf{D}_1^{a\prime})^{LS_k}$. From observations, the slope of all contour lines for limit-state k in the design space of a bridge can be approximated as m_1^k. Thus, linearized contour lines of the mean RP surface for limit-state k corresponding to different mean RP values (including the respective specified target) encompassed by the piecewise log-linear function fitted along $\overrightarrow{\mathbf{D}_1\mathbf{D}_3}$ can be determined. The procedure is illustrated in Figure 10.9 with the case of Bridge B, as an example. In this example, to obtain the mean RPs of limit-state exceedance of limit-states 1, 2, and 3 for the additional design point, $\mathbf{D}_1^a$, along with $\mathbf{D}_1$, $\mathbf{D}_2$, and $\mathbf{D}_3$, results of the parametric probabilistic seismic performance assessment of Bridge B, carried out previously in Chapter 9, are directly used.

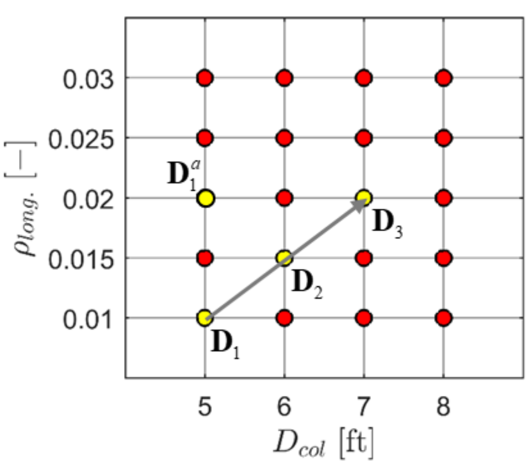

(a) The additional design point, $\mathbf{D}_1^a$, corresponding to $D_{col} = 5$ ft and $\rho_{long} = 0.02$, chosen for assessment is shown. The mean RPs of exceeding limit-states 1-3 are evaluated for this design point.

Figure 10.9 Illustration of Step 4a of the simplified methodology applied to Bridge B

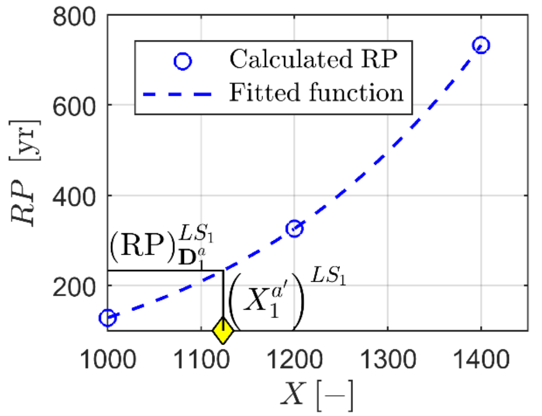

(b) $(\mathrm{RP})^{LS_1}_{\mathbf{D}^a_1}$ is calculated to be 234 years for limit-state 1. $(X^{a'}_1)^{LS_1}$ representing the design point $(\mathbf{D}^{a'}_1)^{LS_1}$ along $\overrightarrow{\mathbf{D}_1\mathbf{D}_3}$ in the design space of Bridge B with mean RP of exceeding limit-state 1 equal to 234 years is calculated using Eq. (10.8)

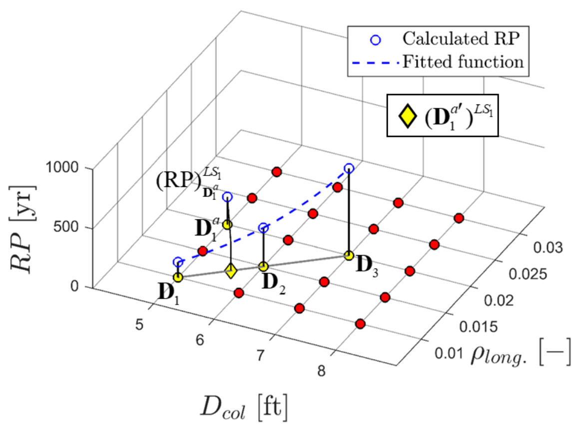

(c) The design point $(\mathbf{D}^{a'}_1)^{LS_1}$ obtained using Eq. (10.9) is shown in the design space of Bridge B. The slope, m^1_1, of all contour lines of the mean RP surface for limit-state 1 can be approximated as the slope of the line joining $\mathbf{D}^a_1$ and $(\mathbf{D}^{a'}_1)^{LS_1}$ in the design space.

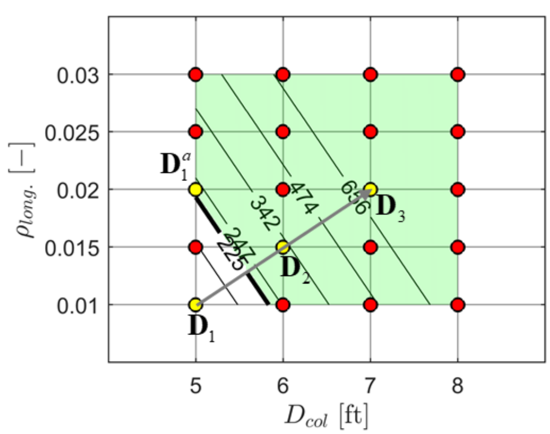

(d) Linearly approximated contours of the mean RP surface for limit-state 1 are shown in the design space of Bridge B with the contour line corresponding to the target mean RP of 225 years for limit-state 1 shown in bold. Green region indicates the feasible domain with regard to limit-state 1.

Figure 10.9 (contd.) Illustration of Step 4a of the simplified methodology applied to Bridge B

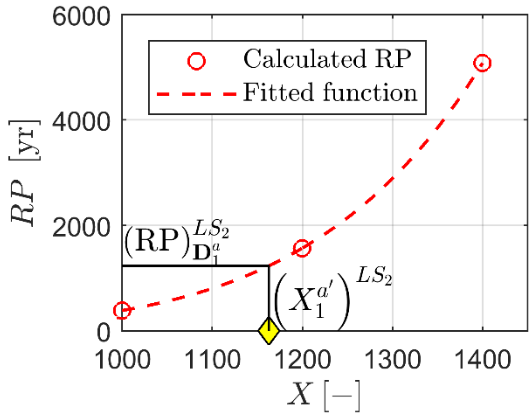

(e) $(\mathrm{RP})^{LS_2}_{\mathbf{D}_1^a}$ is calculated to be 1235 years for limit-state 2. $(X_1^{a'})^{LS_2}$ representing the design point $(\mathbf{D}_1^{a'})^{LS_2}$ along $\overrightarrow{\mathbf{D}_1\mathbf{D}_3}$ in the design space of Bridge B with mean RP of exceeding limit-state 2 equal to 1235 years is calculated using Eq. (10.8)

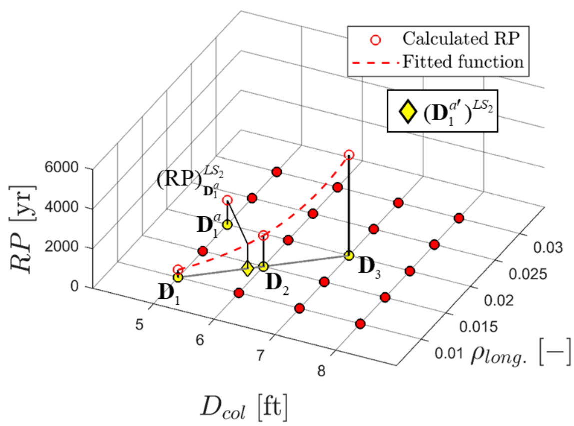

(f) The design point $(\mathbf{D}_1^{a'})^{LS_2}$ obtained using Eq. (10.9) is shown in the design space of Bridge B. The slope, m_1^2, of all contour lines of the mean RP surface for limit-state 2 can be approximated as the slope of the line joining $\mathbf{D}_1^a$ and $(\mathbf{D}_1^{a'})^{LS_2}$ in the design space.

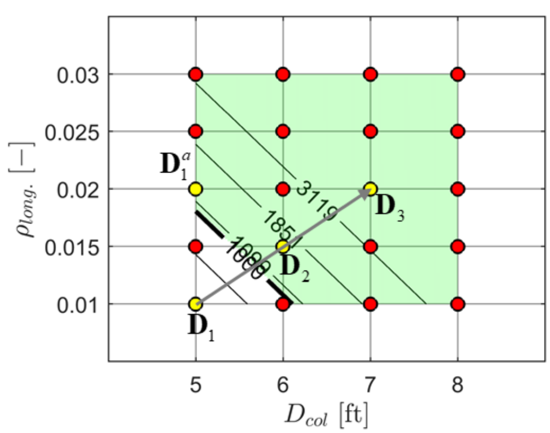

(g) Linearly approximated contours of the mean RP surface for limit-state 2 are shown in the design space of Bridge B with the contour line corresponding to the target mean RP of 1000 years for limit-state 2 shown in bold. Green region indicates the feasible domain with regard to limit-state 2.

Figure 10.9 (contd.) Illustration of Step 4a of the simplified methodology applied to Bridge B

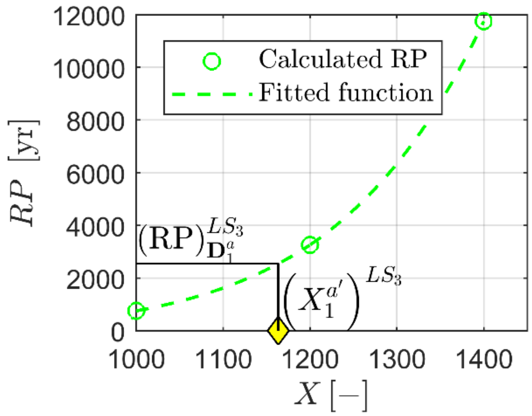

(h) $(\mathrm{RP})^{LS_3}_{\mathbf{D}_1^a}$ is calculated to be 2548 years for limit-state 3. $(X_1^{a\prime})^{LS_3}$ representing the design point $(\mathbf{D}_1^{a\prime})^{LS_3}$ along $\overrightarrow{\mathbf{D}_1\mathbf{D}_3}$ in the design space of Bridge B with mean RP of exceeding limit-state 3 equal to 2548 years is calculated using Eq. (10.8).

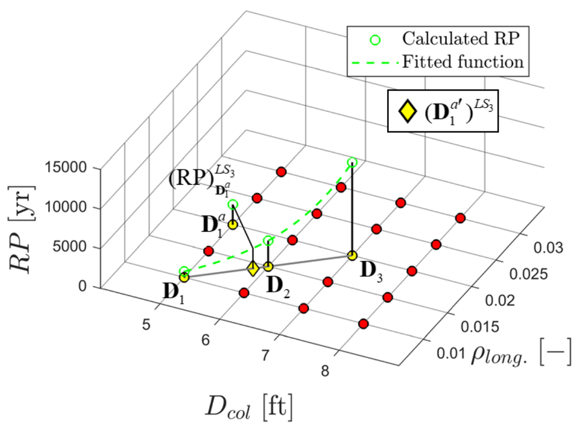

(i) The design point $(\mathbf{D}_1^{a\prime})^{LS_3}$ obtained using Eq. (10.9) is shown in the design space of Bridge B. The slope, m_1^3, of all contour lines of the mean RP surface for limit-state 3 can be approximated as the slope of the line joining $\mathbf{D}_1^a$ and $(\mathbf{D}_1^{a\prime})^{LS_3}$ in the design space.

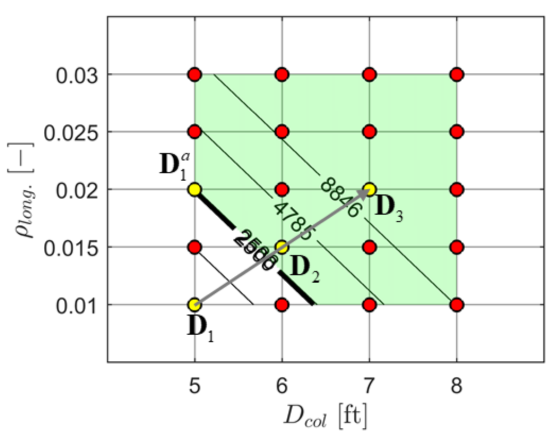

(j) Linearly approximated contours of the mean RP surface for limit-state 3 are shown in the design space of Bridge B with the contour line corresponding to the target mean RP of 2500 years for limit-state 3 shown in bold. Green region indicates the feasible domain with regard to limit-state 3.

Figure 10.9 (contd.) Illustration of Step 4a of the simplified methodology applied to Bridge B

10.2.6 Simplified Methodology – Step 4b (Alternative to Step 4a): Bilinear Approximation of Contour Lines

As an alternative to Step 4a, contours of the mean RP surface for a given limit-state can be better approximated by bilinear parallel lines, rather than linear ones. This requires the seismic performance assessment of two, instead of one, additional design points located away from $\overrightarrow{\mathbf{D}_1\mathbf{D}_3}$. A similar approach, as applied to the choice of $\mathbf{D}_1^a$ only (described earlier in Section 10.2.5), is employed in choosing the other additional design point, $\mathbf{D}_2^a$. Having selected the line $\overrightarrow{\mathbf{D}_1\mathbf{D}_3}$, there are typically two possible choices for the design point $\mathbf{D}_1^a$. Once $\mathbf{D}_1^a$ is selected as per the recommendations stated in Section 10.2.5, $\mathbf{D}_2^a$ just corresponds to the other possible choice for $\mathbf{D}_1^a$. Unlike $\mathbf{D}_1$, $\mathbf{D}_2$, and $\mathbf{D}_3$ referring to designs with increasing D_{col} and ρ_{long}, i.e., increasingly stronger designs, $\mathbf{D}_1^a$ and $\mathbf{D}_2^a$ can interchangeably refer to both additional design points. With the design space of Bridge B as an example, and having selected $\mathbf{D}_1^a$ for the specific choice of $\overrightarrow{\mathbf{D}_1\mathbf{D}_3}$ as shown in the illustrative example in Figure 10.9, the other additional design point, $\mathbf{D}_2^a$, is shown in Figure 10.10.

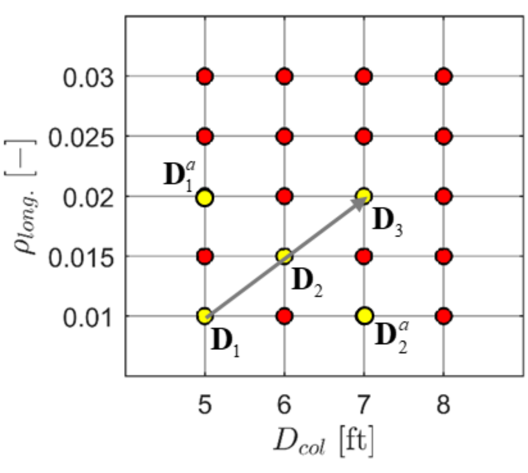

Figure 10.10 Additional design points, $\mathbf{D}_1^a$ and $\mathbf{D}_2^a$, given $\overrightarrow{\mathbf{D}_1\mathbf{D}_3}$, in the design space of Bridge B required for Step 4b of the simplified methodology. $\mathbf{D}_1^a$ corresponds to $D_{col} = 5$ ft, $\rho_{long} = 0.02$ while $\mathbf{D}_2^a$ corresponds to $D_{col} = 7$ ft, $\rho_{long} = 0.01$

Bilinear contour lines, by definition, are therefore split into two segments with respect to $\overrightarrow{\mathbf{D}_1\mathbf{D}_3}$, one corresponding to the region in the design space containing $\mathbf{D}_1^a$, and the other corresponding to that containing $\mathbf{D}_2^a$. Slopes of these two segments of the contours of a mean RP surface for the k^{th} limit-state are denoted by m_1^k and m_2^k respectively. The procedure to evaluate m_1^k is already described in Section 10.2.5. It requires first finding the design point $(\mathbf{D}_1^{a\prime})^{LS_k}$ (using Eq. (10.8) and Eq. (10.9)) along $\overrightarrow{\mathbf{D}_1\mathbf{D}_3}$ having the same mean RP of exceeding limit-state k as that of $\mathbf{D}_1^a$. m_1^k is, thereafter, calculated as the slope of the line in the design space connecting design points $\mathbf{D}_1^a$ and $(\mathbf{D}_1^{a\prime})^{LS_k}$. The other slope, m_2^k, is also evaluated following the same procedure by first locating the design point $(\mathbf{D}_2^{a\prime})^{LS_k}$ along $\overrightarrow{\mathbf{D}_1\mathbf{D}_3}$ having the same mean RP of exceeding limit-state k as that of $\mathbf{D}_2^a$, i.e., $(\text{RP})_{\mathbf{D}_2^a}^{LS_k}$. To obtain the coordinates of $(\mathbf{D}_2^{a\prime})^{LS_k}$, the value of X, say $(X_2^{a\prime})^{LS_k}$, along $\overrightarrow{\mathbf{D}_1\mathbf{D}_3}$ representing the design point $(\mathbf{D}_2^{a\prime})^{LS_k}$, and corresponding to a mean RP of exceeding limit-state k equal to $(\text{RP})_{\mathbf{D}_1^a}^{LS_k}$, is calculated (similar to Eq. (10.8)) as follows

$$\left(X_2^{a'}\right)^{LS_k} = \exp\left(\log X_i + \frac{\log X_{i+1} - \log X_i}{\log\left(\text{RP}\right)_{i+1}^{LS_k} - \log\left(\text{RP}\right)_i^{LS_k}} \times \left(\log\left(\text{RP}\right)_{\mathbf{D}_2^a}^{LS_k} - \log\left(\text{RP}\right)_i^{LS_k}\right)\right) \quad (10.10)$$

where the index, i, can take values of 1 or 2. X_i and X_{i+1} represent the pair of assessed design points $\mathbf{D}_i$ and $\mathbf{D}_{i+1}$ along $\overrightarrow{\mathbf{D}_1\mathbf{D}_3}$ with mean RPs of exceedance for limit-state k equal to $(\text{RP})_i^{LS_k}$ and $(\text{RP})_{i+1}^{LS_k}$ such that $(\text{RP})_i^{LS_k} < (\text{RP})_{\mathbf{D}_2^a}^{LS_k} < (\text{RP})_{i+1}^{LS_k}$. Hence $(\mathbf{D}_2^{a\prime})^{LS_k}$ can be obtained (similar to Eq.(10.9)) as

$$\left(\mathbf{D}_2^{a\prime}\right)^{LS_k} = \begin{bmatrix} \frac{1}{m}\left[\text{ft}^{-1}\right] & 1\left[-\right] \\ -m\left[\text{ft}^{-1}\right] & 1\left[-\right] \end{bmatrix}^{-1} \begin{bmatrix} \left(X_2^{a'}\right)^{LS_k}\left[-\right] \\ \alpha\left[-\right] \end{bmatrix} \quad (10.11)$$

where m ft^{-1} and α are the slope and ρ_{long}-axis intercept of $\overrightarrow{\mathbf{D}_1\mathbf{D}_3}$ respectively. Hence, m_2^k is given by the slope of the line in the design space connecting design points $\mathbf{D}_2^a$ and $(\mathbf{D}_2^{a\prime})^{LS_k}$.

It is to be noted that had the design corresponding to the point $\mathbf{D}_2^a$, in this case, been chosen as the single additional design point, $\mathbf{D}_1^a$, before in Section 10.2.5, m_2^k would have been the approximated slope of linearized parallel contours of the mean RP surface for limit-state k obtained in Section 10.2.5.

Given a limit-state, parallel contour lines of its mean RP surface corresponding to different values of mean RP of exceedance (including the respective specified target) encompassed by the piecewise log-linear function fitted along $\overrightarrow{\mathbf{D}_1\mathbf{D}_3}$, can be approximated as bilinear lines with slopes m_1^k and m_2^k. m_1^k is taken as the contour slope applicable to the portion of the design space, with respect to $\overrightarrow{\mathbf{D}_1\mathbf{D}_3}$, containing $\mathbf{D}_1^a$. The slope m_2^k, on the other hand, is utilized to approximate parallel contours in the portion of the design space, with respect to $\overrightarrow{\mathbf{D}_1\mathbf{D}_3}$, containing $\mathbf{D}_2^a$.

Figure 10.11 shows the results of Step 4b of the simplified methodology applied to Bridge B. These results are obtained by directly using the results of the parametric probabilistic seismic performance assessment of Bridge B, carried out previously in Chapter 9, to calculate the mean RPs of limit-state exceedance of limit-states 1, 2, and 3 for the additional design points, $\mathbf{D}_1^a$ and $\mathbf{D}_2^a$, along with $\mathbf{D}_1$, $\mathbf{D}_2$, and $\mathbf{D}_3$. Bilinear approximations of parallel contour lines corresponding to the mean RP surfaces for limit-states 1, 2, and 3 are shown in Figure 10.11 (a), (b), and (c), respectively. These bilinear contour plots for Bridge B, obtained using Step 4b of the simplified methodology, are the corresponding improved alternatives to the linearized contour plots (shown in Figure 10.9 (d), (g), and (j), respectively) obtained previously, using Step 4a, in the illustrative example considered.

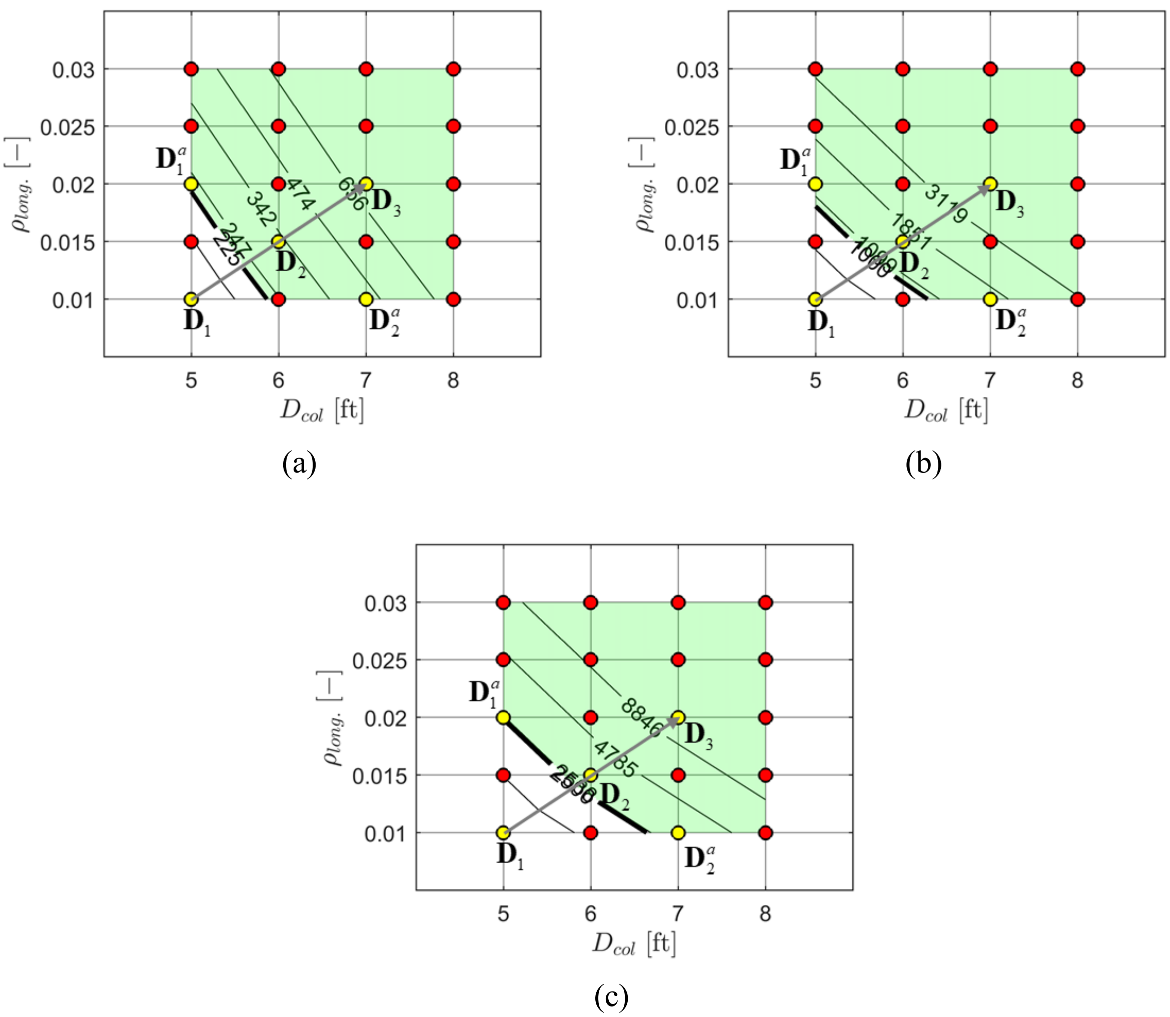

Figure 10.11 Bilinear approximation of parallel contours of the mean RP surfaces obtained for Bridge B corresponding to: (a) limit-state 1; (b) limit-state 2; and (c) limit-state 3. Contour lines corresponding to the respective target mean RPs are shown in bold. Green regions indicate the feasible domains with regard to the respective limit-states

10.2.7 Simplified Methodology – Step 5: Obtaining Feasible Design Domain

Step 4a/4b allows for a linear/bilinear approximation of the target mean RP contour lines corresponding to the respective mean RP surfaces for individual limit-states. In case Step 4a is used, this is done by drawing a line with slope m_1^k passing through the design point along $\overrightarrow{\mathbf{D}_1\mathbf{D}_3}$ satisfying the target mean RP of exceedance specified for the k^{th} limit-state. Step 4b requires drawing two lines, one with slope m_1^k and the other with m_2^k emanating from the design point along $\overrightarrow{\mathbf{D}_1\mathbf{D}_3}$ satisfying the target mean RP of exceedance specified for the k^{th} limit-state. The former line is drawn in the portion of the design space, with respect to $\overrightarrow{\mathbf{D}_1\mathbf{D}_3}$, containing the design point $\mathbf{D}_1^a$, while the latter is drawn in that containing $\mathbf{D}_2^a$. Such approximated target mean RP contour lines of the mean RP surfaces corresponding to individual limit-states can be superimposed in the design space to approximately delineate the overall feasible design domain for a bridge.

For illustration, the approximated contour lines at the target mean RPs specified for limit-states 1-3 and the resulting feasible design domains for Bridge B obtained using both Step 4a and Step 4b are shown in Figure 10.12 (a) and (b) respectively. Also shown in Figure 10.12 (c) is the feasible design domain for Bridge B previously obtained in Chapter 9 using the full-blown methodology wherein every design point in the design space is assessed. Figure 10.13, Figure 10.14, and Figure 10.15, following Figure 10.12 for Bridge B, compare the feasible design domains obtained using Steps 1-5 of the simplified methodology, developed thus far, for the specific choices of $\mathbf{D}_1$, $\mathbf{D}_2$, $\mathbf{D}_3$, $\mathbf{D}_1^a$, and, when applicable, $\mathbf{D}_2^a$ (also shown), for Bridge A, Bridge C, and Bridge MAOC respectively. Note that the usual order of presentation of results corresponding to the considered testbed bridges is altered here. This is because Bridge B was used as a case in point throughout the development of the simplified methodology and results for Bridge B are therefore presented first so as to directly follow the figures from the last two sections. It is also to be noted that results of the simplified methodology presented in Figure 10.12 through Figure 10.15 correspond to the direct use of results of the parametric probabilistic seismic performance assessment of all testbed bridges, carried out previously in Chapter 9, to evaluate the performance of the reduced set of design points required in the simplified methodology.

It can be seen from Figure 10.12 through Figure 10.15 that, for all testbed bridges, the approximated contours at the specified target mean RPs match reasonably well with the corresponding contours obtained using the full-blown methodology. Figure 10.12 through Figure 10.15 also show the location of the respective design point $\mathbf{D}^*$, along $\overrightarrow{\mathbf{D}_1\mathbf{D}_3}$, for a testbed bridge satisfying multiple risk-based performance objectives as obtained from the simplified methodology. As noted from the feasible design domains obtained using the full-blown methodology, the governing limit-state in the vicinity of $\overrightarrow{\mathbf{D}_1\mathbf{D}_3}$ in the design space of a bridge is in agreement with the limit-state dictating the selection of $\mathbf{D}^*$, along $\overrightarrow{\mathbf{D}_1\mathbf{D}_3}$, in the simplified methodology. The simplified methodology, in lieu of the full-blown one, is found to not only generate a valid design solution $\mathbf{D}^*$ satisfying multiple risk-targeted performance objectives, but also provide a comparable approximation of the feasible design domain and governing limit-states in the design space of a bridge, thereby deeming the assumptions made in the formulation of the simplified methodology well founded.

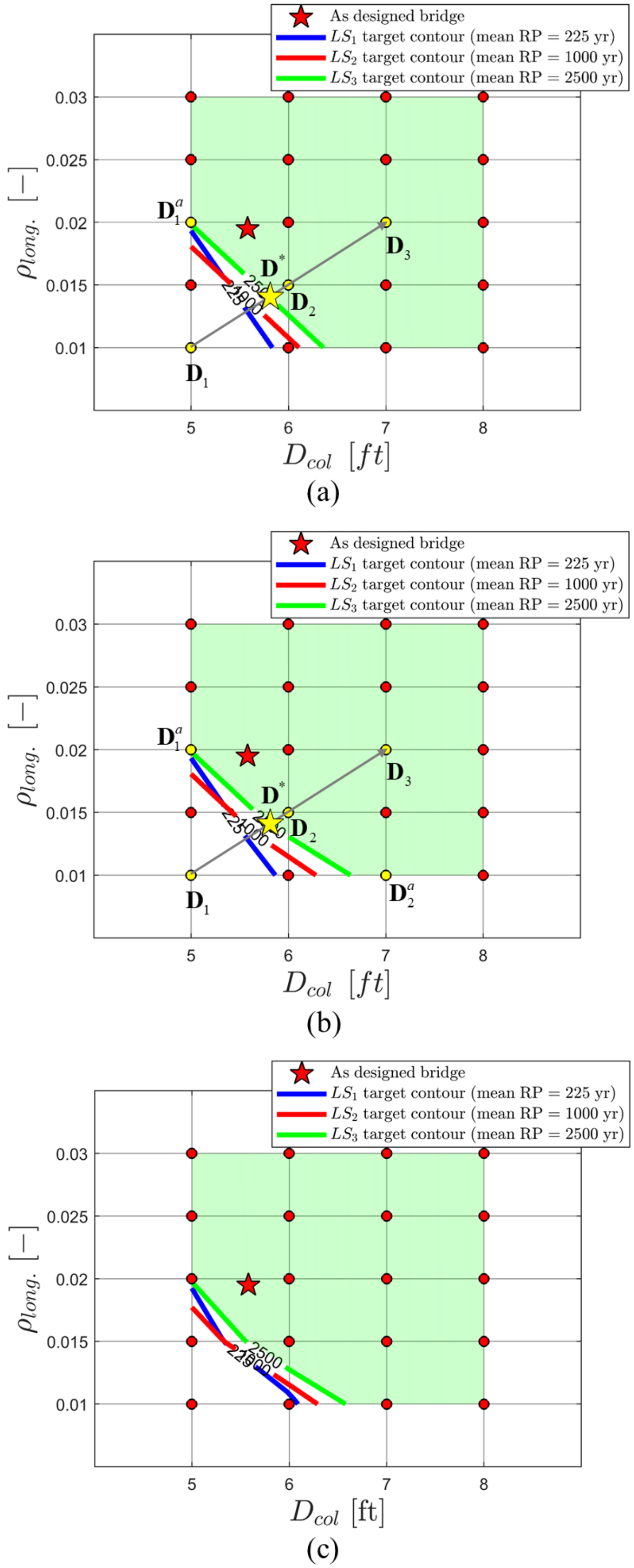

Figure 10.12 Feasible design domains for Bridge B obtained using: (a) simplified method with linear contours (Step 4a); (b) simplified method with bilinear contours (Step 4b); and (c) full-blown method

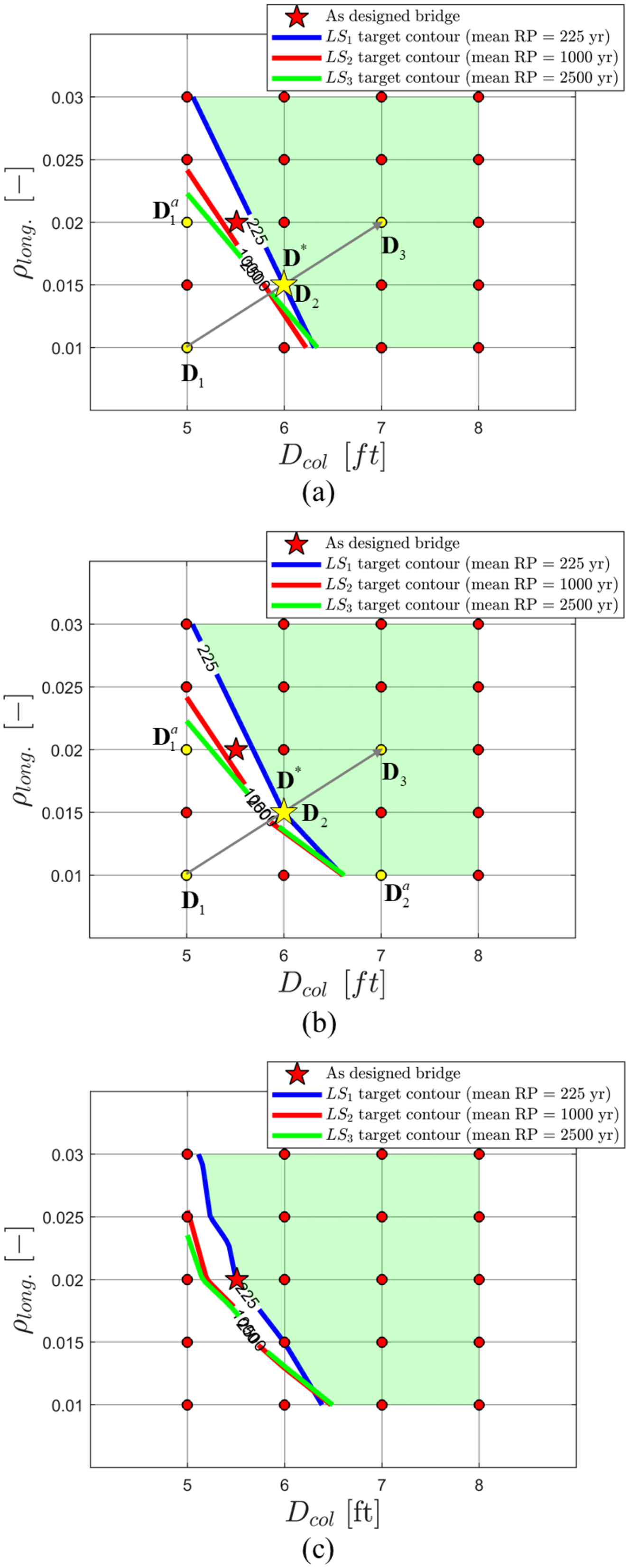

Figure 10.13 Feasible design domains for Bridge A obtained using: (a) simplified method with linear contours (Step 4a); (b) simplified method with bilinear contours (Step 4b); and (c) full-blown method

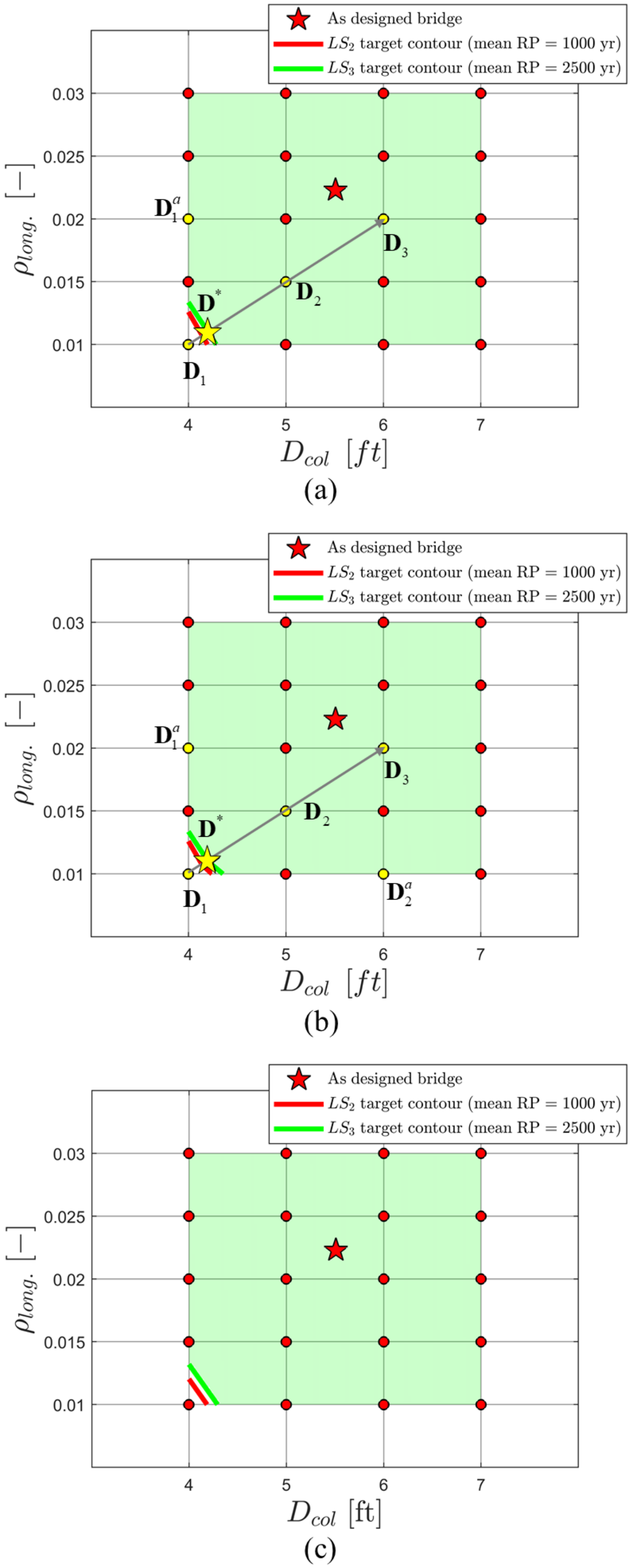

Figure 10.14 Feasible design domains for Bridge C obtained using: (a) simplified method with linear contours (Step 4a); (b) simplified method with bilinear contours (Step 4b); and (c) full-blown method

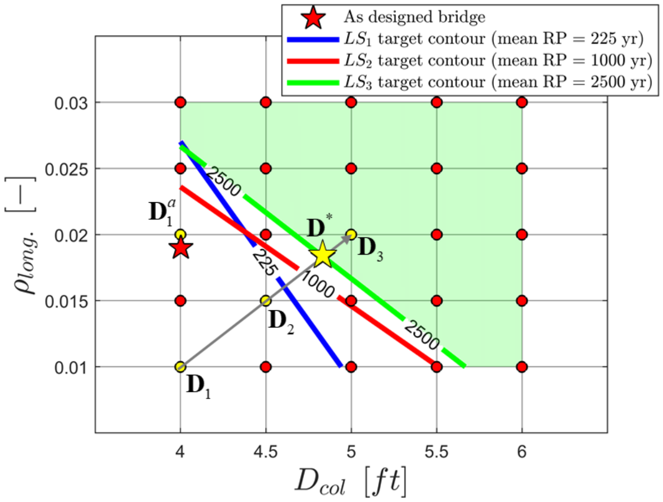

(a)

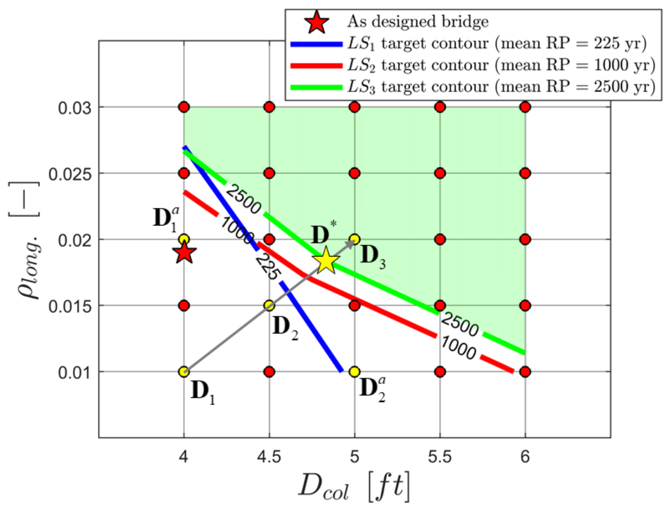

(b)

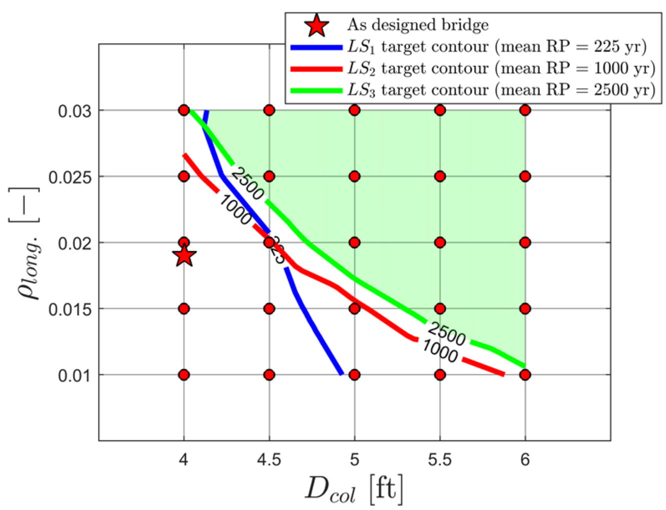

(c)

Figure 10.15 Feasible design domains for Bridge MAOC obtained using: (a) simplified method with linear contours (Step 4a); (b) simplified method with bilinear contours (Step 4b); and (c) full-blown method

10.3 Reduction in Computational Workload

Steps 1 to 5 of the simplified methodology requires the probabilistic performance assessment of only 4 or 5 (depending on whether Step 4a or Step 4b is used) design points. Hence, the simplified methodology, developed thus far, does significantly reduce the computational workload, as compared to the full-blown method, in terms of the number of design points to be assessed towards achieving the goal of finding a design point satisfying multiple risk-based performance objectives and obtaining a feasible design domain in the design space of a bridge. However, in the formulation of the simplified methodology, results of the full-blown parametric probabilistic seismic performance assessment of the testbed bridges carried out in Chapter 9 were used till now to calculate the mean RPs of exceeding the selected set of limit-states for the design points to be assessed. In other words, the workload in terms of the number of seismic hazard levels chosen for performing ensemble nonlinear time-history analyses and the size of the ensemble of ground motion records used per hazard level in the PSDemHA stage of the performance assessment carried out for a single design point was kept the same as before, i.e., 6 hazard levels and 100 ground motion records per hazard levels Therefore, the major sink in available computational resource of running the ensemble nonlinear time-history analyses through a finite element analysis package (OpenSees) for a single design point is not addressed yet.

Computational cost, being directly proportional to the total number of nonlinear time-history analyses performed for a design point, is sought to be further reduced from one or both of the following:

(i) Reduction in the number of seismic hazard levels at which ensemble nonlinear time-history analyses are performed
(ii) Reduction in the size of the ensemble, i.e., the number of nonlinear time-history analyses, per seismic hazard level

The primary goals of the simplified design methodology, formulated thus far, can be summarized as follows:

(i) locating a design point along a chosen positive slope line in the primary design parameter space of a bridge satisfying multiple risk-based performance objectives; and

(ii) delineating a feasible design domain and recognizing its governing/controlling limit-states in the primary design parameter space of a bridge

Without compromising with any one of the above projected goals of the simplified design methodology, it is aimed to reduce the computational workload required for the performance assessment of a single design point of a bridge. It is found that a significant reduction in computational workload, involved in the PSDemHA stage of the performance assessment to be carried out for a single design point, can be achieved while still producing reasonably accurate and consistent approximations of both above-mentioned outcomes for all four testbed bridges considered. While maintaining consistency and accuracy of results, it is possible to reduce the number of hazard levels from 6 up to 3, along with reducing the number of nonlinear time-history analyses performed per hazard level from 100 to, as low as, 20,: The set of three seismic hazard levels to be considered for the performance evaluation of a design point are recommended to be well-spaced in terms of mean RPs of exceedance, e.g., a set of three hazard levels corresponding to mean RPs of 224 years (or 20 percent probability of exceedance in 50 years), 975 years (or 5 percent probability of exceedance in 50 years), and 4975 years (or 1 percent probability of exceedance in 50 years), i.e., previously defined hazard levels II, IV, and VI, can be chosen. With no preference for one over the other and without significantly changing the results, one can also chose a set of three hazard levels corresponding to mean RPs of 72 years (or 50 percent probability of exceedance in 50 years), 475 years (or 10 percent probability of exceedance in 50 years), and 2475 years (or 2 percent probability of exceedance in 50 years), i.e., previously defined hazard levels I, III, and V. It is to be noted that in checking the adequacy of results obtained from using progressively reduced sets of ground motion records per hazard level and arriving at the recommended number, i.e., 30, for the same, new ensembles of ground motion records reselected each time using the site-specific risk-consistent ground motion selection algorithm, previously described, were used. This is because, given a hazard level, the algorithm picks ground motion records from the NGA database that, as an ensemble, match the probability structure of the target spectrum defined for that hazard level. Using reduced sets of ground motion records randomly picked from the originally chosen 100 records per hazard level would, therefore, have disturbed the risk-consistency of such ensembles.

Any further in reduction in workload by using less than 3 seismic hazard levels and/or using ensembles of smaller than 20 ground motion records per hazard level for the performance evaluation of the reduced set of design points in the simplified methodology is not recommended. This is because the accuracy of results past this workload threshold is found to be sensitive to, among other factors, the bridge and its design space, the choice of the reduced set of design points to be assessed, the location of target mean RP contour lines in the chosen design space, the hazard levels considered in the reduced set of three hazard levels, etc.

The reduced workload simplified methodology is re-implemented for the seismic performance-based design of the four testbed bridges, results of which are shown in Figure 10.16 through Figure 10.19 maintaining the usual order of presentation of results pertaining to these bridges. As mentioned earlier, these results correspond to freshly selected ensembles of 20 ground motion records per hazard level for a set of three hazard levels used in the PSDemHA of the specific chosen design points $\mathbf{D}_1$, $\mathbf{D}_2$, $\mathbf{D}_3$. $\mathbf{D}_1^a$, and, if required, $\mathbf{D}_2^a$ (also shown) for each bridge. The set of three hazard levels considered correspond to hazard levels I, III, and V, with mean RPs of exceedance equal to 72 years, 475 years, and 2475 years, respectively. A comparison of the feasible design domain is made between those obtained using the reduced workload simplified methodology (both Step 4a and Step 4b) and the one obtained using the full-blown methodology, the latter involving the seismic performance assessment of all design points in the design space each making use of 6 seismic hazard levels and 100 ground motion records per hazard level in the PSDemHA stage. As can be seen from Figure 10.16 through Figure 10.19, the reduced workload simplified methodology is indeed able to produce results comparable to the full-blown methodology. The reduced workload simplified performance-based design methodology applied to a bridge, not only is able to predict, considerably well, the design $\mathbf{D}^*$ satisfying multiple risk-targeted performance objectives, but also leads to a much cheaper, yet reasonably accurate, delineation of the feasible design domain along with recognition of governing limit-states in the respective design space.

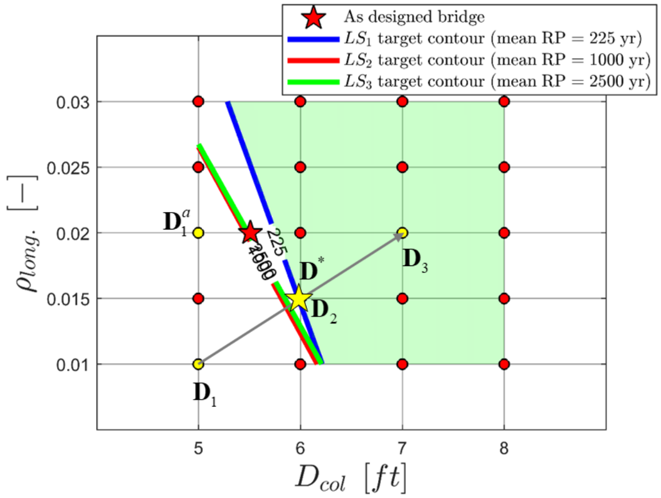

(a)

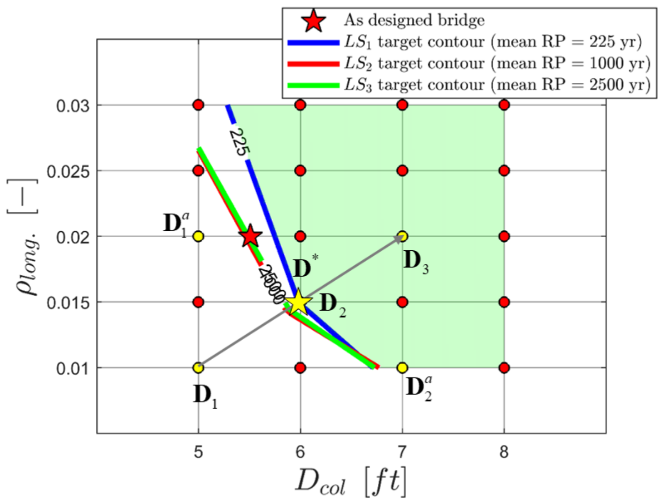

(b)

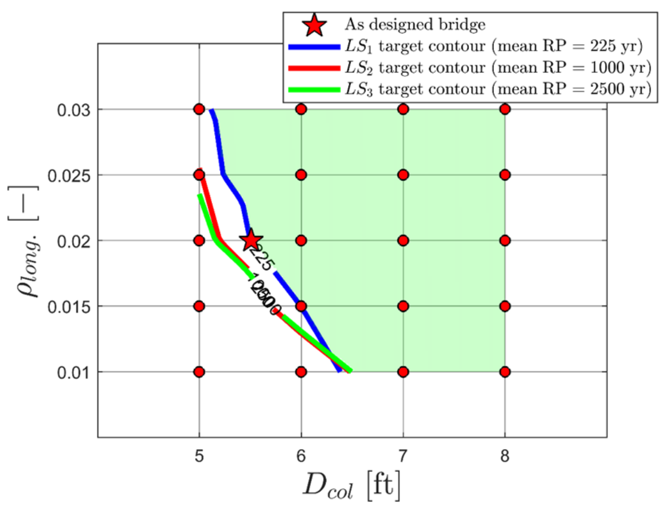

(c)

Figure 10.16 Feasible design domains for Bridge A obtained using: (a) reduced workload simplified method with linear contours (Step 4a); (b) reduced workload simplified method with bilinear contours (Step 4b); and (c) full-blown method

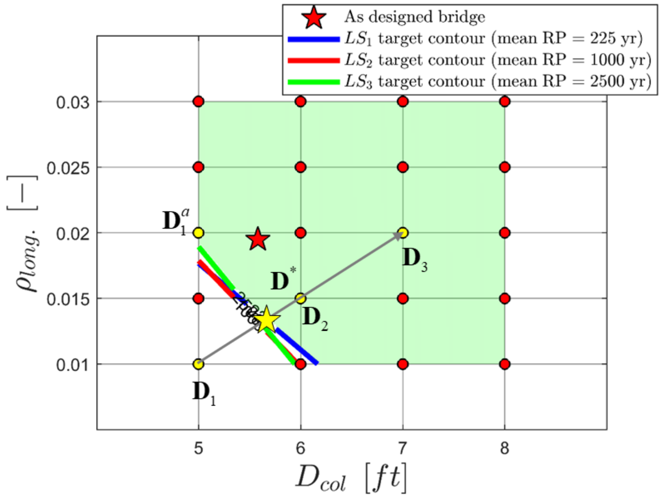

(a)

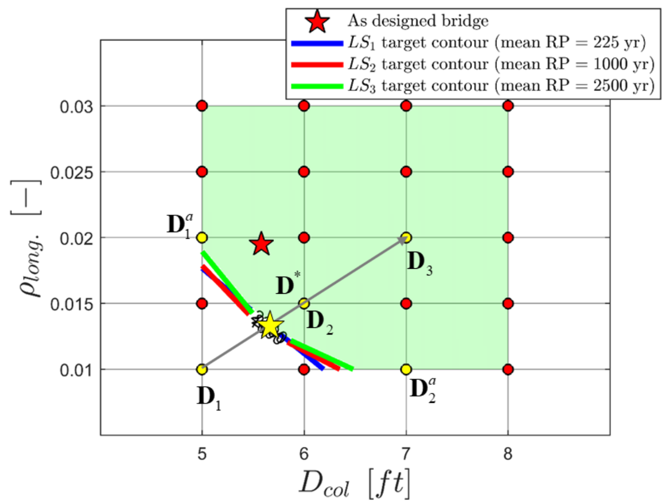

(b)

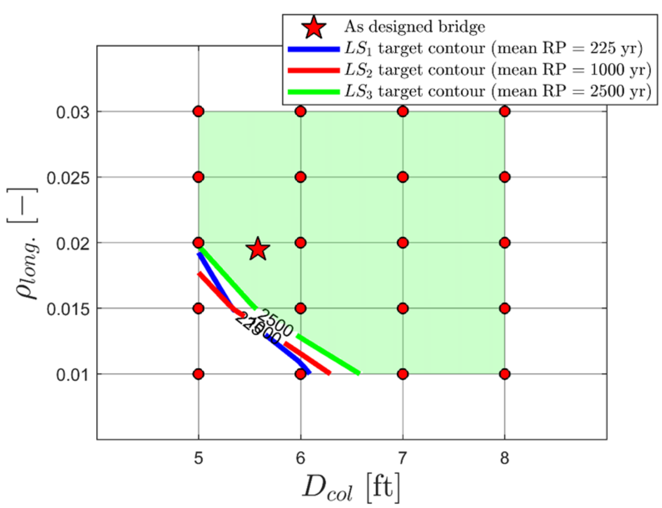

(c)

Figure 10.17 Feasible design domains for Bridge B obtained using: (a) reduced workload simplified method with linear contours (Step 4a); (b) reduced workload simplified method with bilinear contours (Step 4b); and (c) full-blown method

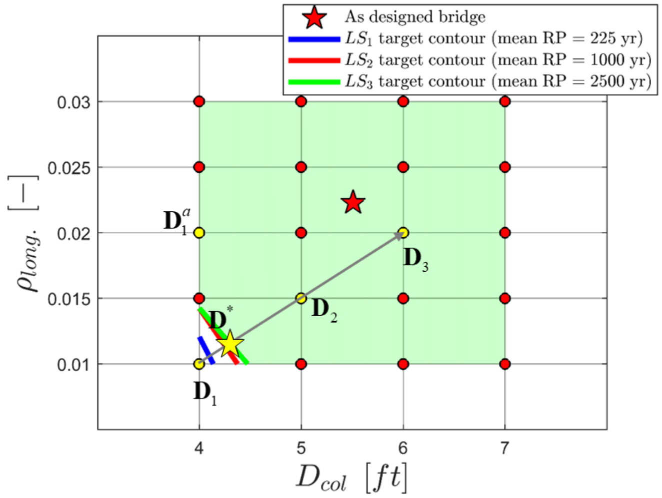

(a)

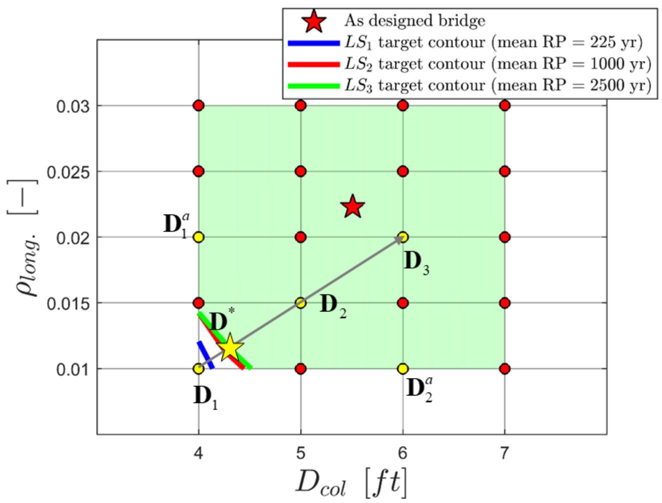

(b)

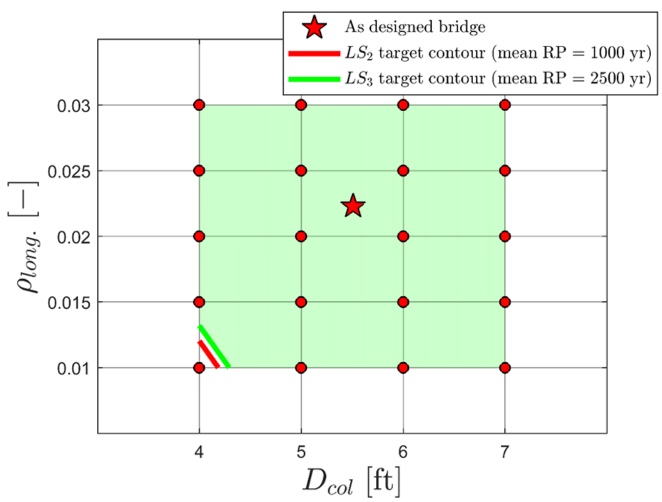

(c)

Figure 10.18 Feasible design domains for Bridge C obtained using: (a) reduced workload simplified method with linear contours (Step 4a); (b) reduced workload simplified method with bilinear contours (Step 4b); and (c) full-blown method

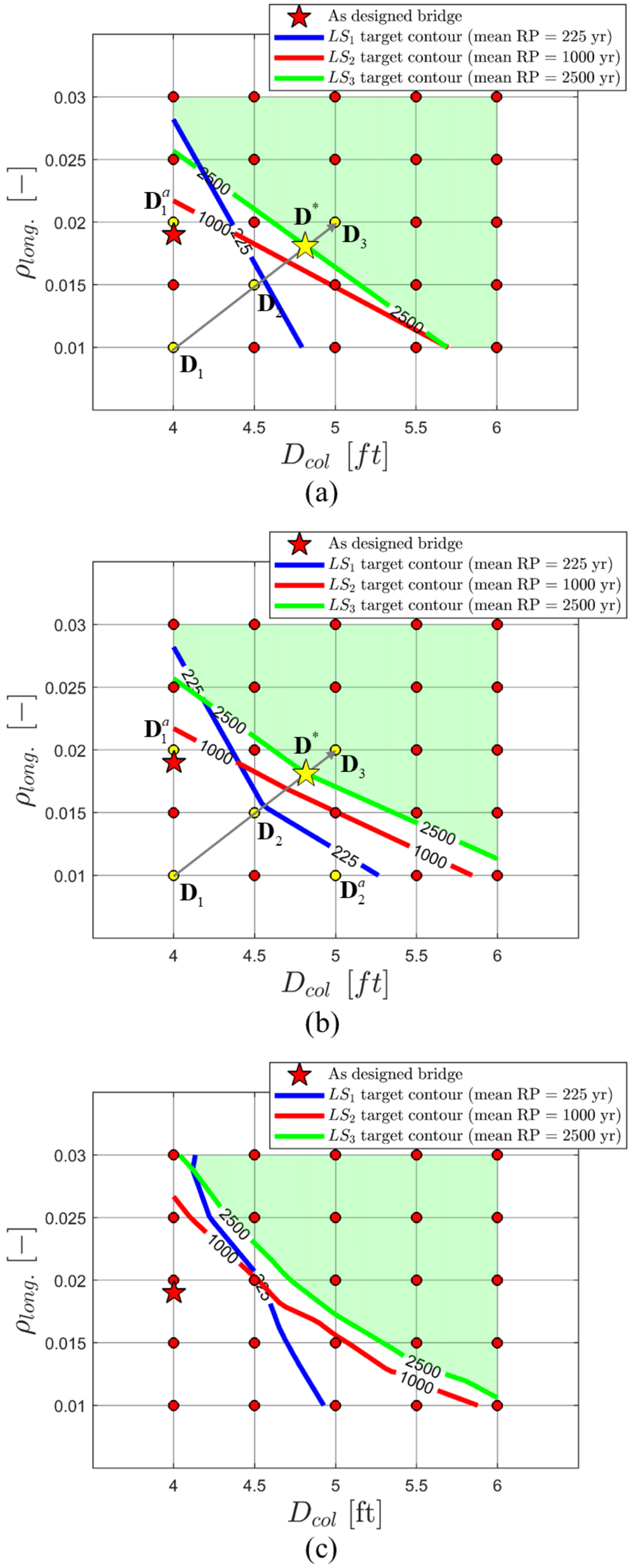

Figure 10.19 Feasible design domains for Bridge MAOC obtained using: (a) reduced workload simplified method with linear contours (Step 4a); (b) reduced workload simplified method with bilinear contours (Step 4b); and (c) full-blown method

10.4 Proposed Simplified Risk-targeted Performance-based Seismic Design Methodology

The proposed simplified risk-targeted performance-based seismic design (PBSD) methodology incorporates the simplified methodology as discussed in Section 10.2 with savings, in terms of computational expense, achieved through a reduction in workload outlined in Section 10.3. The final proposed risk-targeted PBSD procedure for Ordinary Standard Bridges (OSBs) consists of the following preliminary steps, before moving on to an implementation of the simplified methodology subsequently summarized in the form of a flow chart.

(I) Identification of the site and the overall geometry of the bridge to be designed, given available real estate, traffic requirements, etc.

(II) Identification of a set of limit-states of interest and associated engineering demand parameters (EDPs), preferably strain-based, concerning reinforced concrete bridge columns, the primary lateral load resisting component of an OSB. For the chosen limit-states, a set of normalized fragility functions, each giving the probability of a limit-state exceedance given a specific normalized value of the associated EDP, are developed. Normalization of a fragility function, using a deterministic capacity model for the given limit-state, is highly recommended to ensure that fragility curves, constructed using available experimental/numerical data pertaining to specimens/models of varying parameters, can be used for new and specific designs of the considered bridge.

(III) Identification of performance objectives stated in terms of mean return periods (RPs) of exceeding the selected set of limit-states

(IV) Definition of the primary design parameter space of the bridge, a two-dimensional rectangular grid comprising of practically realizable design points, i.e., sets of practically realizable values of the primary design variables, the column diameter, D_{col}, and the column longitudinal reinforcement ratio, ρ_{long}. Based on preliminary column section analyses, the primary design space is recommended not to include designs points exhibiting possible strain softening of section response.

(V) Identification of all relevant secondary design variables (described in Section 9.2.2 of Chapter 9). These variables are preliminarily set to take standardized and/or predetermined values sometimes even dependent on the values of the primary design variables.

(VI) Development of a nonlinear finite element model of the bridge in a finite element analysis package (e.g., OpenSees) allowing appropriate parameterization with respect to the primary design variables while using secondary design variables as determined in Step V.

(VII) Automatization of the following sequential steps involved in the seismic performance evaluation of a bridge design point:

(i) Finite element model generation of the bridge given specific values of the primary design variables.

(ii) Preliminary post-gravity modal analysis to obtain periods of different modes vibration of the bridge, especially the period of the first transverse mode of vibration, i.e., $T_{1,\text{trans}}$.

(iii) Definition of intensity measure (IM), i.e., the spectral acceleration averaged over a period range. Ten discrete points logarithmically spaced within $T_{1,\text{trans}}$ to $2.5T_{1,\text{trans}}$ are used in defining the average (geometric mean) spectral acceleration.

(iv) Probabilistic Seismic Hazard Analysis (PSHA) to obtain seismic hazard curves in terms of mean annual rates (MARs), or equivalently mean RPs (= 1/MAR), of exceeding specific values of the chosen . Details of PSHA are provided in Chapter 5.

(v) Identification of three seismic hazard levels, defined by mean RPs of exceedance, for site-specific risk-consistent ground motion selection and subsequent nonlinear time-history analyses. Chosen seismic hazard levels should be well-spaced in terms of mean RPs of exceedance, e.g., a set of hazard levels corresponding to mean RPs of 224 years, 975 years, and 4975 years, or that corresponding to mean RPs of 72 years,475 years, and 2475 years.

(vi) Site-specific risk-consistent selection of ensembles of 20 ground motions records per hazard level. Details of ground motion selection algorithm are provided in Chapter 5.

(vii) Ensemble nonlinear time-history analyses of the computational model of the bridge at the chosen hazard levels to obtain EDP_k, given , data for the engineering demand parameter associated with the k^{th} limit-state. Multiple-core desktop computers or a supercomputer can be used to run such analyses in parallel. It is recommended not to proceed to the next step without resolving non-collapse related numerical convergence issues encountered in this step.

(viii) Probabilistic Seismic Demand Hazard Analysis (PSDemHA) to obtain demand hazard curves, in terms of MARs or mean RPs of exceeding specific values, of the EDPs associated with the selected set of limit-states. Details of PSDemHA are provided in Chapter 7.

(ix) Denormalization of fragility functions given the specific design of the bridge. Details are provided in Chapter 8.

(x) Probabilistic Seismic Damage Hazard Analysis (PSDamHA) to obtain MARs or mean RPs of exceeding the selected set of limit-states. Details of PSDamHA are provided in Chapter 8.

Having adequately setup the problem, as outlined, the simplified PBSD methodology is initiated to:

(1) locate a design point, $\mathbf{D}^*$, along a chosen positive slope line in the primary design parameter space of a bridge satisfying multiple risk-based performance objectives; and

(2) delineate a feasible design domain and recognize its governing/controlling limit-states in the primary design parameter space of a bridge

Aimed at achieving the above-mentioned goals, the steps involved in the proposed simplified PBSD methodology are summarized in the following flow chart

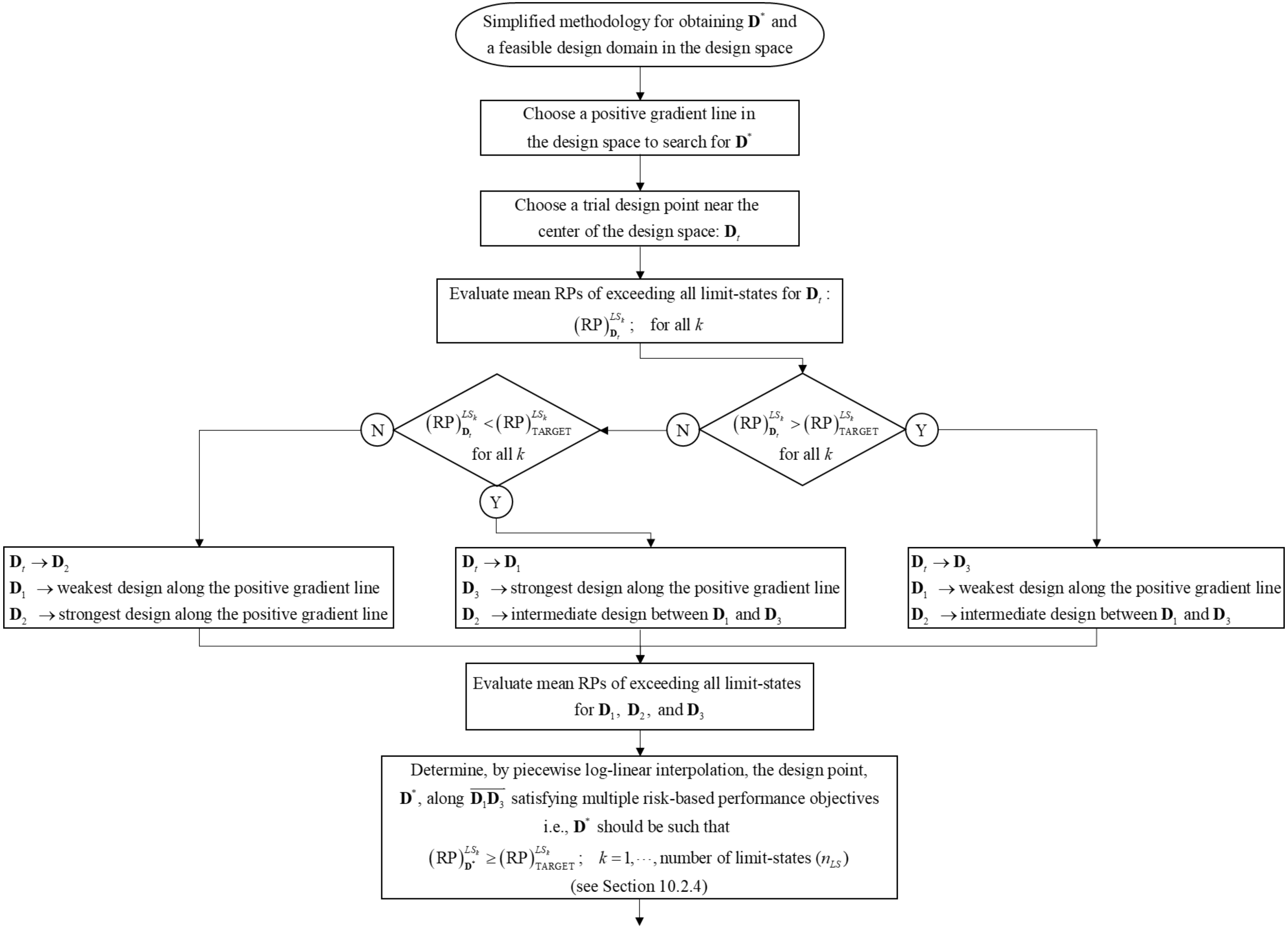
Simplified methodology for obtaining $\mathbf{D}^*$ and a feasible design domain in the design space
Choose a positive gradient line in the design space to search for $\mathbf{D}^*$
Choose a trial design point near the center of the design space: $\mathbf{D}_t$
Evaluate mean RPs of exceeding all limit-states for $\mathbf{D}_t$: $(\mathrm{RP})_{\mathbf{D}_t}^{LS_k}$; for all k
$(\mathrm{RP})_{\mathbf{D}_t}^{LS_k} < (\mathrm{RP})_{\mathrm{TARGET}}^{LS_k}$ for all k
$(\mathrm{RP})_{\mathbf{D}_t}^{LS_k} > (\mathrm{RP})_{\mathrm{TARGET}}^{LS_k}$ for all k
N
Y
N
Y
$\mathbf{D}_t \rightarrow \mathbf{D}_2$
$\mathbf{D}_1$ $\rightarrow$ weakest design along the positive gradient line
$\mathbf{D}_2$ $\rightarrow$ strongest design along the positive gradient line
$\mathbf{D}_t \rightarrow \mathbf{D}_1$
$\mathbf{D}_3$ $\rightarrow$ strongest design along the positive gradient line
$\mathbf{D}_2$ $\rightarrow$ intermediate design between $\mathbf{D}_1$ and $\mathbf{D}_3$
$\mathbf{D}_t \rightarrow \mathbf{D}_3$
$\mathbf{D}_1$ $\rightarrow$ weakest design along the positive gradient line
$\mathbf{D}_2$ $\rightarrow$ intermediate design between $\mathbf{D}_1$ and $\mathbf{D}_3$
Evaluate mean RPs of exceeding all limit-states for $\mathbf{D}_1$, $\mathbf{D}_2$, and $\mathbf{D}_3$
Determine, by piecewise log-linear interpolation, the design point, $\mathbf{D}^*$, along $\overline{\mathbf{D}_1\mathbf{D}_3}$ satisfying multiple risk-based performance objectives
i.e., $\mathbf{D}^*$ should be such that
$(\mathrm{RP})_{\mathbf{D}^*}^{LS_k} \geq (\mathrm{RP})_{\mathrm{TARGET}}^{LS_k}$; $k = 1, \cdots,$ number of limit-states (n_{LS})
(see Section 10.2.4)

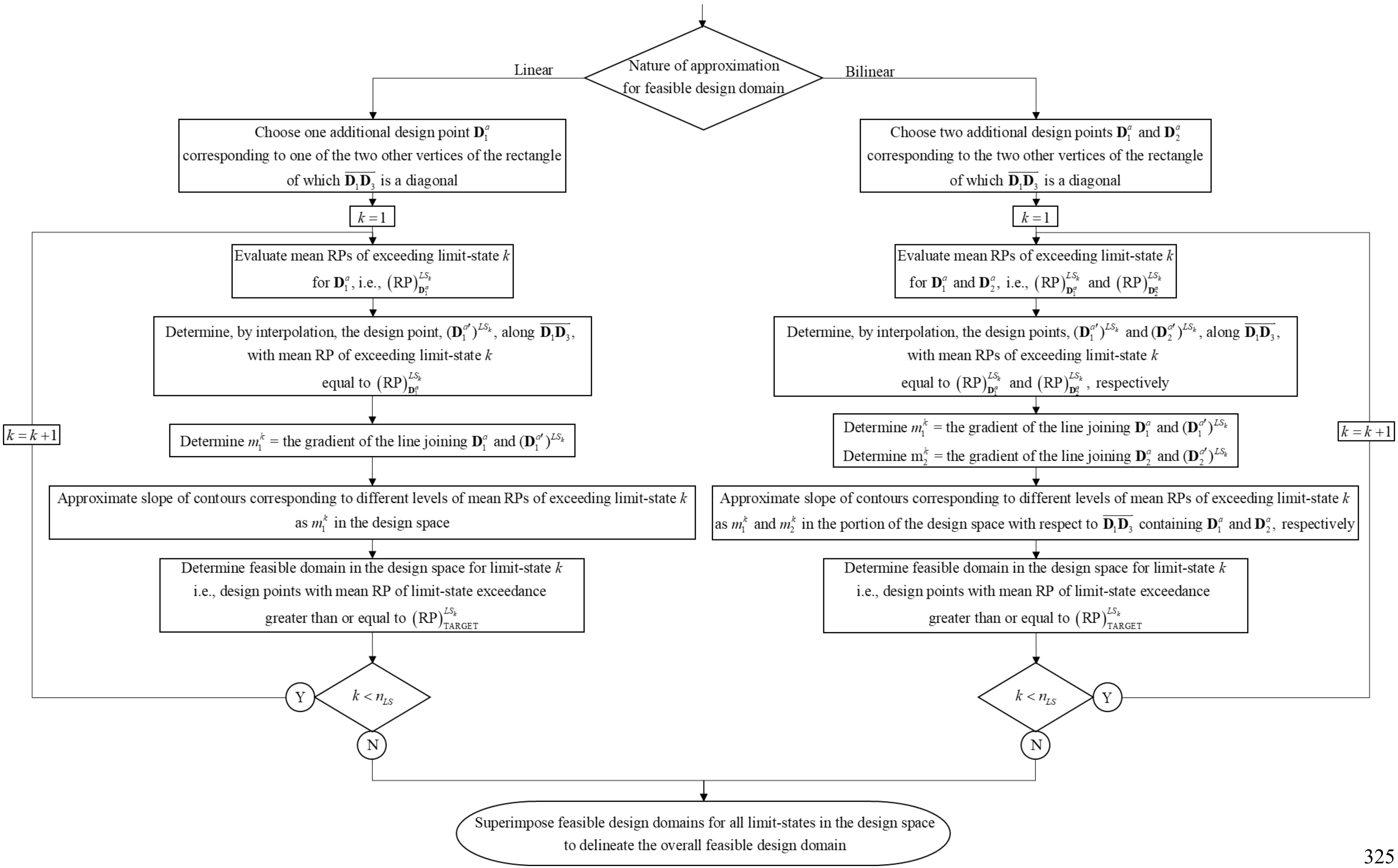
Nature of approximation for feasible design domain
Linear
Bilinear
Choose one additional design point $\mathbf{D}_1^a$ corresponding to one of the two other vertices of the rectangle of which $\overline{\mathbf{D}_1\mathbf{D}_3}$ is a diagonal
Choose two additional design points $\mathbf{D}_1^a$ and $\mathbf{D}_2^a$ corresponding to the two other vertices of the rectangle of which $\overline{\mathbf{D}_1\mathbf{D}_3}$ is a diagonal
$k = 1$
$k = 1$
Evaluate mean RPs of exceeding limit-state k for $\mathbf{D}_1^a$, i.e., $(\mathrm{RP})_{\mathbf{D}_1^a}^{LS_k}$
Evaluate mean RPs of exceeding limit-state k for $\mathbf{D}_1^a$ and $\mathbf{D}_2^a$, i.e., $(\mathrm{RP})_{\mathbf{D}_1^a}^{LS_k}$ and $(\mathrm{RP})_{\mathbf{D}_2^a}^{LS_k}$
Determine, by interpolation, the design point, $(\mathbf{D}_1^{a'})^{LS_k}$, along $\overline{\mathbf{D}_1\mathbf{D}_3}$, with mean RP of exceeding limit-state k equal to $(\mathrm{RP})_{\mathbf{D}_1^a}^{LS_k}$
Determine, by interpolation, the design points, $(\mathbf{D}_1^{a'})^{LS_k}$ and $(\mathbf{D}_2^{a'})^{LS_k}$, along $\overline{\mathbf{D}_1\mathbf{D}_3}$, with mean RPs of exceeding limit-state k equal to $(\mathrm{RP})_{\mathbf{D}_1^a}^{LS_k}$ and $(\mathrm{RP})_{\mathbf{D}_2^a}^{LS_k}$, respectively
$k = k + 1$
Determine m_1^k = the gradient of the line joining $\mathbf{D}_1^a$ and $(\mathbf{D}_1^{a'})^{LS_k}$
Determine m_1^k = the gradient of the line joining $\mathbf{D}_1^a$ and $(\mathbf{D}_1^{a'})^{LS_k}$
Determine m_2^k = the gradient of the line joining $\mathbf{D}_2^a$ and $(\mathbf{D}_2^{a'})^{LS_k}$
$k = k + 1$
Approximate slope of contours corresponding to different levels of mean RPs of exceeding limit-state k as m_1^k in the design space
Approximate slope of contours corresponding to different levels of mean RPs of exceeding limit-state k as m_1^k and m_2^k in the portion of the design space with respect to $\overline{\mathbf{D}_1\mathbf{D}_3}$ containing $\mathbf{D}_1^a$ and $\mathbf{D}_2^a$, respectively
Determine feasible domain in the design space for limit-state k i.e., design points with mean RP of limit-state exceedance greater than or equal to $(\mathrm{RP})_{\mathrm{TARGET}}^{LS_k}$
Determine feasible domain in the design space for limit-state k i.e., design points with mean RP of limit-state exceedance greater than or equal to $(\mathrm{RP})_{\mathrm{TARGET}}^{LS_k}$
Y
$k < n_{LS}$
N
$k < n_{LS}$
Y
N
Superimpose feasible design domains for all limit-states in the design space to delineate the overall feasible design domain

11 Conclusions

11.1 Summary of Research Work

Probability-based design provides the most scientific and rational solution to an earthquake-resistant structural design problem wherein an inherently uncertain structural system needs to be designed such that its performance entails, not only resisting highly uncertain seismic demands, but also meeting reliably societal demands of life safety, economy and resiliency. The classification of structural performance should therefore be predicated on an acceptable risk, defined by the risk tolerance of society as a whole. Fueled by such needs, the structural engineering community, over the last few decades, has moved on towards implementing the philosophy of probabilistic performance-based earthquake engineering (PBEE) in the realm of structural seismic design. Probabilistic performance-based seismic design (PBSD) involves designing a structure to meet more refined and non-traditional performance objectives explicitly stated in terms of the risk associated with the exceedance of critical damage/limit-states or certain tolerable thresholds of monetary loss, downtime, etc. (i.e., probability of limit-state or threshold exceedance in a specified exposure time). The recent advent of PBEE in seismic design practice of buildings motivated this research wherein a simplified risk-targeted PBSD methodology, building on the comprehensive probabilistic PEER PBEE framework, is aimed to be developed for Ordinary Standard Bridges (OSBs) in California. The overarching goal of this project is to address, without any compromise in rigor, the somewhat hindered implementation of the PEER PBEE framework in seismic bridge design practice owing to its all-inclusive nature, pressing computational requirements and inherent theoretical complexity.

A summary of the overall approach taken to arrive at a solution to the formulated problem can be best presented by classifying the entire bulk of the conducted research into three distinct phases:

(I) Implementation of the PEER PBEE assessment framework
(II) Parametric full-blown probabilistic performance assessment
(III) Development of simplified risk-targeted PBSD methodology

The following sections provide a general idea of the work entailed in each of these three phases.

11.1.1 Phase I: Implementation of the PEER PBEE Assessment Framework

At the very outset, the road taken involves a meticulous implementation of the PEER PBEE assessment framework for OSBs which lies at the heart of the proposed PBSD methodology. Improvements from state-of-the-art literature relating to various steps of the PEER PBEE analytical framework are also incorporated. The PEER PBEE framework involves a sequential execution of analytical steps pieced together (integrated) using the Total Probability Theorem (TPT) to arrive at an estimate of a performance measure, e.g., the mean annual rate (MAR) at which a limit-state is exceeded, or the MAR at which a decision variable, say monetary loss, downtime, or death, etc., exceeds a value of interest. The performance measure sought for in this study is the MAR of limit-state exceedance or, equivalently its reciprocal, the mean return period (RP) of limit-state exceedance. The task of probabilistically predicting the future seismic performance of a bridge, in terms of the mean RPs of exceeding a selected set of limit-states, is broken down into three analytical steps, namely: probabilistic seismic hazard analysis (PSHA), probabilistic seismic demand hazard analysis (PSDemHA), and probabilistic seismic damage hazard analysis (PSDamHA).

PSHA aims to identify and quantify the pertinent sources of uncertainty associated with seismic ground motion parameters (i.e., ground motion intensity measures) to rigorously characterize the seismic hazard at the considered site in a probabilistic sense. The essence of PSHA is to identify and aggregate the contribution of all possible seismic events (characterized by pairs of earthquake magnitudes and source-to-site distances that could potentially affect the considered structure) to arrive at an estimate of the mean annual rate (MAR) at which specific values of a ground motion intensity measure (IM) are exceeded. Depending on the results of PSHA, earthquake ground motion records producing desired levels of are selected for probabilistic response assessment of structures subjected to seismic loading. A proper choice of is therefore crucial to have a true picture of structural performance against earthquakes. To this end, an improved earthquake , i.e., average spectral acceleration over a specified period range, is used to account for the following factors deemed important for OSBs, typically not captured by the traditionally used , i.e., elastic 5% damped spectral acceleration at the expected predominant period of the structure:

(a) Lack of certainty in predicting the natural period of the predominant mode of vibration for reinforced concrete structures such as OSBs;

(b) Change in effective natural periods of reinforced concrete structures in going from pristine conditions to cracked states under service loads;

(c) Structural period elongation due to accumulation of damage during an earthquake which leads to higher correlation of structural response with spectral accelerations at longer periods; and

(d) Difference in periods of fundamental modes of vibration in the two orthogonal directions (i.e., longitudinal and transverse) of the bridge.

Owing to the novelty of the chosen , standard PSHA tools do not include seismic hazard assessments in terms of this . Hence, a convenient, yet rigorous, workaround is adopted based on the results of standard PSHA for spectral accelerations at single periods such that the seismic hazard in terms of the average spectral acceleration can be reasonably approximated.

Ground motion record selection serves as the link between PSHA and subsequent probabilistic seismic response assessment of a bridge, thereby imposing a need for hazard- or risk-consistency of earthquake ground motion records to be used for ensemble nonlinear response history analyses of the considered bridge. A ground motion selection algorithm recently developed by Baker and co-workers (Ref.) is implemented for the selection of site-specific risk-consistent ensembles of ground motion records representative of six seismic hazard levels corresponding to the following return periods: 72, 224, … 4,975 years. Given a seismic hazard level, the algorithm employs a conditional mean spectrum-based ground motion selection to pick earthquake records from the NGA database that, as an ensemble, follow the complete probability structure of the target conditional spectrum defined for that hazard level.

The objective of PSDemHA is to characterize probabilistically the seismic demand imposed on the considered bridge, in terms of the MAR at which specific values of seismic response parameters, called engineering demand parameters $(EDPs) LS_1$, are exceeded at the bridge site. This is achieved via a convolution of the conditional probability of EDP exceedance, given , with the site-specific seismic hazard curve for the considered bridge. At this stage, a set of limit-states mainly concerning reinforced concrete bridge columns, the primary lateral load resisting component of an OSB, is defined. These limit-states are selected as: limit-state 1: concrete cover crushing, limit-state 2: a precursor to longitudinal rebar buckling, and limit-state 3: a precursor to longitudinal rebar fracture; they are pertinent to the seismic evaluation of bridge structures and meaningful to practicing engineers. A fourth limit-state corresponding to an abutment exterior shear key reaching its shear strength capacity is also considered. Material strain-based EDPs associated with the limit-states related to the desired failure mode involving bridge columns (i.e., hinging of columns) are defined and used in this project. Strain-based EDPs correlate better to damage than traditionally used displacement based EDPs (e.g., column drift, plastic hinge rotation).

PSDamHA is aimed towards making probabilistic predictions of structural damage/limit-state exceedances in terms of MARs, or mean RPs, associated with these events. This requires a convolution of the fragility function defined for a limit-state (i.e., the conditional probability of limit-state exceedance given EDP) with the corresponding demand hazard curve. Strain-based fragility functions based on reliable experimental data or high-fidelity numerical data are developed or inherited for the considered limit-states through proper identification of relevant test and research programs previously conducted. Fragility functions, typically constructed using experimental or numerical data pertaining to specimens or models with different geometric, material and mechanical characteristics, need to be normalized such that they can be used for structural components of any specified characteristics. Appropriate normalizing deterministic capacity prediction equations are identified and used for this purpose.

The improved version of the PEER PBEE framework assembled is implemented on four California testbed OSBs located in regions with disparate levels of seismicity. The selected testbed bridges also cover a wide range of geometrical parameters such as number of spans, span lengths, number of columns per bent, skew angle, etc. OpenSees Tcl input files for the nonlinear finite element models of these bridges, inherited from previous Caltrans funded projects, are thoroughly revisited and improved based on experimental validation (at the component level) and/or literature review. The Tcl input files are also modified to mitigate the occurrence of non-convergence of the iterative scheme used to integrate the nonlinear equations of motion. In case a non-collapse related numerical convergence issue is encountered, convergence of the numerical solution is ensured through adaptive switching between iterative methods (e.g., Newton, modified-Newton, BFGS, Newton-Krylov) and/or convergence test types and tolerances used to solve the incremental equations of dynamic equilibrium at each time step.

11.1.2 Phase II: Parametric Full-blown Probabilistic Performance Assessment

Using the improved version of the PEER PBEE assessment framework for OSBs assembled and implemented in Phase I, the goal of developing a performance-based seismic design framework is addressed next. At the crux of structural design lies the selection of optimal values of critical design parameters/variables such that predetermined target specifications of certain performance measures are met. The performance measures used in this study are the MARs or mean RPs of exceeding a selected set of limit-states. Hence, a parametric full-blown probabilistic seismic performance assessment of the testbed bridges is carried out to investigate and visualize the effects of varying key structural design parameters on the mean RPs of limit-state exceedances.

A two-dimensional design space is defined in terms of the primary design variables, viz., column diameter (D_{col}) and column longitudinal reinforcement ratio (ρ_{long}), to which the exceedances of the selected set of limit-states are believed to be most sensitive. The chosen design variables pertain to the reinforced concrete bridge columns because they constitute the primary lateral load resisting structural components of an OSB. Moreover, column plastic hinge regions are also meant in a seismic event to act as structural fuses and thereby dissipate energy through inelastic material behavior. All other bridge design parameters to be determined by meeting the requirements of capacity design, minimum ductility capacity, reinforcement ratio restrictions, etc., and/or restricted by the geometry of the bridge, available real estate, traffic requirements, etc. are referred to as secondary design variables. In the parametric study of each of the four testbed bridges, the values of most secondary design variables are taken as per the original design of the as-designed bridge.

A fully automated workflow incorporating an efficient utilization of available computing resources is developed for a smooth and seamless execution of the parametric full-blown probabilistic seismic performance assessment of the considered bridges. The Tcl input files of the OpenSees computational models of these bridges are revisited and parameterized to facilitate the automated generation of models corresponding to multiple re-designed versions of the actual bridges. The seismic performance of such re-designs generated by varying the primary design parameters, subject to practical constraints, are evaluated using the improved PEER PBEE framework described. This involved the extensive parallelization of computationally independent jobs, which was made possible through Stampede2, the flagship supercomputer at the University of Texas at Austin's Texas Advanced Computing Center (TACC). It is noteworthy to mention here that for the sizable number of nonlinear time-history analyses performed for each of the re-designs of the considered testbed bridges, convergence of the numerical integration of the equations of motion over the entire duration of the seismic input is also ensured in an automated fashion.

Finally, for each re-design of a testbed bridge, and for each of the considered limit-states, a piecewise linear surface is fitted in the primary design space to the computed mean RPs of limit-state exceedance. Topologies and contours of these surfaces are explored. Feasible design domains, i.e., collection of design points in the two-dimensional design parameter space with mean RPs of limit-state exceedances higher than or equal to the respective specified targets, are identified. Safety of the as-designed bridges and feasibility of their re-designs are examined.

11.1.3 Phase III: Development of Simplified Risk-targeted PBSD Methodology

The concept of a feasible design domain in the design parameter space can be utilized to make risk-informed design decisions while trying to satisfy multiple risk-based performance objectives. The full-blown parametric probabilistic seismic performance assessment framework can therefore be very well used for the design of a new OSB unless its computational cost is prohibitive for the computational resources available. For reasons of practicability in current bridge design practice, a computationally more economical, simplified, non-traditional, risk-targeted performance-based seismic design procedure is distilled out of this project based on the findings of the full-blown parametric probabilistic seismic performance assessment carried out for the testbed bridges. The proposed simplified design methodology is able to:

(i) find a design point in the primary design parameter space of a bridge being designed for multiple risk-based performance objectives; and
(ii) delineate an approximate, yet sufficiently accurate, feasible design domain and identify the limit-states controlling its boundary in the primary design parameter space of the bridge;

at a computational cost significantly lower than that of the parametric full-blown method.

Upon selection of primary design variables, secondary design variables are to be determined and adjusted to meet requirements of capacity design, code-based minimum ductility capacity and minimum reinforcement, etc., and/or other restrictions imposed by the real estate available, traffic flow, etc. After all primary and secondary design variables have been determined, a final check of structural performance is required to ensure that the final design still satisfies the specified risk-based performance objectives.

11.2 Highlight of Findings

Findings of the present research related to the phases of work described above are grouped accordingly and presented next.

11.2.1 Findings of Phase I: Implementation of the PEER PBEE Assessment Framework

An experimental validation of the finite element modeling technique employed for multiple-column bents of OSBs is carried out. Numerical models of experimental column-bent specimens developed using fiber-section force-based Euler-Bernoulli frame elements are validated by comparing the transverse pushover response of these models with experimental data. This effort revealed the necessity of modeling explicitly the reduced-size section provided at the base of reinforced concrete bridge columns (to mimic a pin connection) instead of modeling this connection as a perfect pin. Numerical models of column-bents with columns perfectly pinned at the base are found to underpredict the transverse pushover resistance of such bents when compared to experimental data for the same imposed lateral displacement time history.

PSDemHA, requiring the convolution of conditional probabilities of EDP exceedance with the site-specific seismic hazard curve of an OSB, calls for a conditional seismic response assessment of the bridge to quantify the conditional probabilities of EDP exceedance given . The demand hazard convolution involves a continuous regression against of the parameters of probability distribution functions fitted to $EDPs$ at discrete levels. An improved functional fit to the conditional lognormal dispersion parameter as a continuous function of , typically taken as a constant, is revealed by the EDP ensembles at discrete values of and proposed in this project.

As expected, the results of PSDamHA of the testbed bridges show that exceedances of increasingly severe limit-states, i.e., limit-states 1 through 3, concerning the reinforced concrete bridge columns for OSBs have increasing values of mean RPs. The as-designed testbed bridges considered, as assessed using the implemented PEER PBEE framework, exhibit a wide range of seismic performance as measured by the mean RPs of exceeding the selected set of limit-states. The mean RPs of exceeding limit-states 1 through 3 are found to cover the gamut of values from 150 to 1,500 years for limit-state 1, 500 to 10,000 years for limit-state 2, and 1,000 to 30,000 years for limit-state 3. The mean RP of exceeding the 4^{th} limit-state, namely that of an abutment exterior shear key reaching its shear strength capacity, is found to range between 80 and 2500 years depending on the type of shear key used in the bridge. Bridges A, B and C, having monolithic non-isolated type abutment shear keys, show high mean RPs of exceeding limit-state 4, while the mean RP of exceedance associated with this limit-state is found to be relatively small (compared to those of Bridges A, B, and C) for Bridge MAOC with sacrificial isolated type shear keys specified in its design. It is also found that the mean RP of abutment shear key limit-state exceedance lies between the mean RPs of exceeding the critical limit-states of rebar buckling and rebar fracture for Bridges A and B. Shear keys of Bridges C and MAOC, on the other hand, are found to exceed this limit-state with mean RPs smaller than the respective mean RPs of exceeding the limit-state of concrete cover crushing.

The implementation of the present improved version of the PEER PBEE framework, developed with painstaking details, is highly advantageous. A design method based on or distilled out of this rigorous assessment framework will be fittingly risk-informed, rational and scientific. The MAR or mean RP of a damage/limit-state exceedance for an OSB, according to the PEER PBEE framework, is computed by aggregating or accounting for the contributions from all seismic hazard levels. As shown by the disaggregation with respect to of the mean RP of exceedance of (or the hazard level associated with) any of the damage/limit-states considered, different levels of (both corresponding to higher and lower mean RPs of exceedance as compared to the specific mean RP of the damage/limit-state exceedance) contribute to the damage/limit-state hazard. This provides a scientific basis to disapprove an incomplete method according to which, for the sake of computational and/or theoretical convenience, one chooses to design a bridge such that specified limit-states are not exceeded (with a specified confidence levels) at specified discrete seismic hazard levels (e.g., earthquake ground motions with a mean return period of IM exceedance of 975 years, 2475 years, etc.).

11.2.2 Findings of Phase II: Parametric Full-Blown Probabilistic Performance Assessment

The improved version of the PEER PBEE assessment framework implemented for OSBs is used to parametrically assess the seismic performance of the testbed bridges considered. A range of possible re-designs of each testbed bridge, corresponding to different values of the primary design variables (i.e., D_{col} and ρ_{long}), are analyzed to investigate the effects of these design parameters on the mean RPs of exceeding the selected set of limit-states.

For each limit-state, a piecewise linear surface is fitted to the mean RPs computed at all the re-design points (located on a regular grid in the 2D primary design space) of a testbed bridge. Although the overall topologies of the fitted mean RP surfaces over the design space are accurate, some topology details are by-products of the fitted surfaces assumed (here piecewise linear). It is important to notice that the limit-state exceedance mean RP results obtained for the as-designed bridges, in each case, are in excellent agreement with the topology of the fitted surfaces despite being excluded from the data used for fitting these surfaces.

Increasing values of the two primary design variables (both related to the design of the bridge columns) result in stronger, and thereby translating to safer designs characterized by lower MAR or higher mean RP of limit-state exceedance. This is found to be especially true for limit-states 1, 2, and 3 related to damage in the bridge columns. The mean RPs of exceeding these limit-states, pertaining to seismic design of OSBs, are found to be indeed sensitive to the chosen primary design variables thereby justifying their choice.

The fitted mean RP surfaces for limit-state 4 (at least one transverse shear key reaching its shear strength capacity) in any of the testbed bridges show low sensitivity to the column longitudinal reinforcement ratio. However, larger column diameters increase the safety of the bridge against shear key failures (i.e., higher mean RP of limit-state exceedance).

Contour lines of the mean RP surfaces for limit-states 1, 2, and 3, corresponding to respectively specified target mean RPs selected based on discussions with and feedback from expert Caltrans engineers, are superimposed in the primary design space to delineate the overall feasible design domains. This also helps identify the governing limit-states along the boundaries of the feasible design domains. The seismic performance of the as-designed version of a testbed bridge is gauged by the location of the corresponding design point in the design parameter space relative to the overall feasible design domain of the bridge (i.e., does the as-designed bridge belong to the feasible design domain and how close is it from its boundary?). The seismic performance of the as-designed testbed bridges is found to show considerable variability. These bridges originally designed following a more traditional (prescriptive) seismic design philosophy, rather than an explicitly performance-based one, are found to exhibit irregular levels of conservativeness. While some of the as-designed testbed bridges are found to be conservative, sometimes too much, with respect to the selected limit-states and corresponding target mean RPs, others are found to lie near the borderline of safety, or clearly in the unsafe domain.

The categorization of an important column design parameter, the transverse reinforcement ratio (ρ_{trans}), for columns with low axial load ratios, typical of OSBs, as a secondary design variable is justifiable. A sensitivity analysis is conducted by repeating the bridge performance evaluation over the grid of re-design points for two additional levels of ρ_{trans} expressed as fractions of ρ_{long}, with the three levels considered spanning a practical range of transverse reinforcement ratio. The observed level of sensitivity of the performance evaluation results with respect to ρ_{trans} is small enough to be ignored for simplicity.

A comparative study is conducted between the closed-form solutions to the MAR of limit-state exceedance, available in the literature, and the numerical results obtained from the full-blown probabilistic performance assessment method used This is done to assess the potential viability of LRFD-like design formats based on such closed-form solutions to be used as the sought PBSD methodology. These closed-form solutions still require the computationally most demanding step of running ensemble nonlinear time-history analyses for a bridge, while circumventing the rather inexpensive numerical evaluation of the demand and damage hazard integrals. Moreover, the results obtained from such simplified closed-form solutions, requiring almost as much computational work as the numerical method, are often inaccurate by a significant margin.

11.2.3 Findings of Phase III: Development of Simplified Risk-targeted PBSD Methodology

The topologies of the mean RP surfaces for limit-states 1, 2, and 3, in the primary design parameter space are explored. These topologies are found to be well-captured by piecewise power functions. Based on this observation, a step-by-step strategy requiring the performance evaluation of only 3 design points is devised that allows locating a design point, which satisfies multiple risk-based performance objectives, in the primary design parameter space of a bridge under design.

Knowledge of the feasible design domain of a bridge in its design space is extremely valuable as it can be utilized to make risk-informed design decisions leading to safe and economic design of bridges. An approximate delineation of the feasible design domain is systematically achieved based on the observation that contours of the mean RP surfaces for the limit-states considered can be approximated by parallel linear/bilinear lines in the primary design space. This however requires the performance evaluation of 1 or 2 additional design points, depending on the choice of linear or bilinear lines in approximating the contours of the mean RP surfaces.

The computational requirement of the full-blown parametric method is therefore significantly reduced by requiring the performance evaluation of only 3 to 5 design points to realize the risk-targeted design objectives. The computational workload is further reduced by drastically curtailing the total number of nonlinear time-history analyses to be run for the performance evaluation of a single design point while still maintaining reasonable levels of accuracy.

Results of the reduced-workload, simplified, non-traditional, risk-targeted, performance-based seismic design procedure applied to the considered testbed bridges are found to tally well with the results of the full-blown parametric method, thereby validating the proposed PBSD methodology.

11.3 Recommendations for Future Research

The completed research work is neither exhaustive nor fully devoid of limitations. A brief account of identified issues, possible solutions, and relevant avenues for further research is presented in this section.

At the heart of performance-based earthquake engineering is the explicit quantification of relevant uncertainties and their consistent propagation through the performance assessment framework. Only sources of uncertainties associated with the seismic hazard, ground motion record-to-record variability, and structural capacity prediction, typically deemed predominant, are considered in this project. Other sources of uncertainties, such as finite element model parameter (e.g., constitutive material model parameters, damping model parameters, etc.) aleatory uncertainty, parameter estimation epistemic uncertainty, and overall modeling epistemic uncertainty, are commonly omitted or neglected in performance-based earthquake engineering. However, recent studies (Bradley 2010; Bradley 2013; Liel et al. 2009; Terzic et al. 2015) have shown that such sources of uncertainties can or are likely to be significant and must be included for a comprehensive seismic performance assessment. This aspect can be enhanced significantly by the inclusion, treatment and propagation of additional pertinent sources of uncertainties associated with various stages of the PEER PBEE assessment framework implemented for OSBs and used to calibrate and validate the simplified PBSD method proposed herein.

Both a scalar for PSHA and a scalar EDP associated with each damage-/limit-state of interest for both PSDemHA and PSDamHA are considered in this project. Vector-valued IMs are found to more accurately characterize/predict, by exhibiting higher levels of "efficiency" and "sufficiency", the seismic demand on structural systems. A single predictive demand parameter can be insufficient to perfectly predict whether a limit-state is reached or exceeded (i.e., other demand parameters may also play a role). A vector of statistically correlated EDPs can therefore be used to more accurately predict the exceedance of damage-/limit-states of interest.

The chosen seismic intensity measure for probabilistic seismic hazard assessment is the average (geometric mean) spectral acceleration over a period range, $S_{a,\,\text{avg}}$. This has already been shown to be superior, in terms of "efficiency" and "sufficiency", as compared to the traditionally used , i.e., spectral acceleration at a single period. Due to the unavailability of seismic hazard assessment results from standard PSHA tools in terms of this rather novel , a simple workaround is developed to estimate the seismic hazard. This involves using the results of standard PSHA tools for spectral accelerations at single periods thereby avoiding the esoteric step of seismic source probabilistic characterization and related calculations. However, the workaround is applicable only if an attenuation relationship independent of the characteristics of the seismic sources/faults (e.g., Boore and Atkinson 2008) is used in PSHA. Such a restriction can be removed by including probabilistic seismic hazard assessments in terms of this easy-to-implement , i.e., $S_{a,\,\text{avg}}$, in available open-source PSHA software tools (e.g., OpenSHA).

Explicit consideration of near fault effects in PSHA and a risk-consistent incorporation of velocity pulses in the selected ensembles of ground motion records are kept beyond the scope of this project. This can lead to an underestimated seismic risk to OSBs as evaluated using the current implementation of the PEER PBEE framework.

The set of three limit-states relating to bridge columns, defined for the development of the proposed PBSD methodology for OSBs, is neither exhaustive nor definitive. The proposed methodology is developed with such limit-state definitions as mere placeholders and is readily able to accommodate more refined (e.g., more mechanics-based) definitions and/or a larger number of limit-states.

The seismic performance measure selected in this study is the MAR of limit-state exceedance or, equivalently, the mean return period (RP) of limit-state exceedance. This can be taken one step further by defining performance measures in terms of the hazard associated with the exceedance of specific values of decision variables, e.g., monetary loss, downtime, deaths, etc., which are more meaningful to stakeholders and/or decision makers (e.g., government officials).

Computational models of OSBs can be improved particularly to model the soil-structure interaction effects at the column foundations and/or at the abutments. Force-deformation relationships assigned to nonlinear springs used to model different components of skewed bridge abutments can be validated using experimental data from reliable sources and/or numerical data from analyses conducted using full-fledged physics-based high-fidelity finite element models.

The proposed simplified PBSD methodology is formulated by retaining the inherent rigor of the PEER PBEE framework lying at its crux. As a result, a rather non-traditional design method is proposed requiring complete probabilistic performance assessments of design iterations (i.e., design points). In this regard, efforts can be channeled to convert the non-traditional method distilled out of this project, without significantly compromising its rigor, into a more traditional design format requiring LRFD-like checks of structural demand-to-capacity ratios.

Having identified the combined values of primary design variables satisfying multiple risk-based performance objectives, the proposed PBSD method recommends determining most secondary design variables (e.g., the ones not restricted by the geometry of the bridge, available real estate, traffic flow requirements, etc.) so as to meet code-based requirements of capacity design, minimum ductility limitations, reinforcement ratio restrictions, etc. These requirements typically involve the use of prescriptive measures and/or safety factors such that undesirable consequences are prevented with some level of confidence. Empirical observations, experience and/or engineering judgment have dictated the prescription of such measures and safety factors in codes of practice. Future research can be directed towards developing a more transparent and more probabilistically explicit determination of these secondary design variables.

Finally, the viability of the proposed simplified PBSD methodology currently relies on a two-dimensional primary design parameter space for OSBs. The possibility of extending the proposed simplified method to accommodate more than two primary design variables, especially for non-ordinary bridges, should be investigated.

12 References

AASHTO (2011). *Guide Specifications for LRFD Seismic Bridge Design*, American Association of State and Highway Transportation Officials, Washington, DC.

AASHTO (2012). *LRFD Bridge Design Specifications*, American Association of State and Highway Transportation Officials, Washington, DC.

Abrahamson, N., and Silva, W. (2008). "Summary of the Abrahamson & Silva NGA Ground-Motion Relations." *Earthquake Spectra*, 24(1), 67-97.

ASCE (2013). *Report Card for America's Infrastructure*, American Society of Civil Engineers.

ASCE-7-02 (2002). *Minimum design loads for buildings and other structures*, American Society of Civil Engineers.

ASCE-7-10 (2010). *Minimum design loads for buildings and other structures*, American Society of Civil Engineers.

ASCE/COPRI (2014). *Seismic Design of Piers and Wharves*, Coasts, Oceans, Ports, and Rivers Institute, American Society of Civil Engineers.

Aslani, H., and Miranda, E. (2005). "Probabilistic earthquake loss estimation and loss disaggregation in buildings." The John A. Blume Earthquake Engineering Center, Stanford University.

Aslani, H., and Miranda, E. (2005a). "Probability-based seismic response analysis." *Engineering Structures*, 27(8), 1151-1163.

ATC (2007). "ATC-58: Guidelines for Seismic Performance Assessment of Buildings."Redwood City.

ATC-3-06 (1978). *Tentative provisions for the development of seismic regulations for buildings: a cooperative effort with the design professions, building code interests, and the research community*, Applied Technology Council, National Bureau of Standards.

Augusti, G., and Ciampoli, M. (2008). "Performance-based design in risk assessment and reduction." *Probabilistic Engineering Mechanics*, 23(4), 496-508.

Baker, J. W. (2007). "Quantitative classification of near-fault ground motions using wavelet analysis." *Bulletin of the Seismological Society of America*, 97(5), 1486-1501.

Baker, J. W. (2011a). "Conditional Mean Spectrum: Tool for Ground-Motion Selection." *Journal of Structural Engineering*, 137(3), 322-331.

Baker, J. W. (2011b). "Software for Ground Motion Selection." *Baker Research Group*.

Baker, J. W., and Cornell, C. A. (2003). *Uncertainty specification and propagation for loss estimation using FOSM method*, Pacific Earthquake Engineering Research Center.

Baker, J. W., and Cornell, C. A. (2004). "Choice of a vector of ground motion intensity measures for seismic demand hazard analysis." *13th World Conference on Earthquake Engineering*.

Baker, J. W., and Cornell, C. A. (2005a). "Vector-valued Ground Motion Intensity Measures for Probabilistic Seismic Demand Analysis." The John A. Blume Earthquake Engineering Center, Stanford University, CA.

Baker, J. W., and Cornell, C. A. (2005b). "A vector-valued ground motion intensity measure consisting of spectral acceleration and epsilon." *Earthquake Engineering & Structural Dynamics*, 34(10), 1193-1217.

Baker, J. W., and Cornell, C. A. (2006a). "Spectral shape, epsilon and record selection." *Earthquake Engineering & Structural Dynamics*, 35(9), 1077-1095.

Baker, J. W., and Cornell, C. A. (2006b). "Which spectral acceleration are you using?" *Earthquake Spectra*, 22(2), 293-312.

Baker, J. W., and Jayaram, N. (2008). "Correlation of Spectral Acceleration Values from NGA Ground Motion Models." *Earthquake Spectra*, 24(1), 299-317.

Barbato, M., Petrini, F., Unnikrishnan, V. U., and Ciampoli, M. (2013). "Performance-based hurricane engineering (PBHE) framework." *Structural Safety*, 45, 24-35.

Barbosa, A. R. (2011). "Simplified vector-valued probabilistic seismic hazard analysis and probabilistic seismic demand analysis: Application to the 13-story NEHRP reinforced concrete frame-wall building design example." Ph.D. Dissertation, UC San Diego.

Bazzurro, P. (1998). "Probabilistic Seismic Demand Analysis." Ph.D. Dissertation, Department of Civil and Environmental Engineering, Stanford University.

Bazzurro, P., and Cornell, C. A. (1994). "Seismic hazard analysis of nonlinear structures. I: Methodology." *Journal of Structural Engineering*, 120(11), 3320-3344.

Bazzurro, P., and Cornell, C. A. (1999). "Disaggregation of seismic hazard." *Bulletin of the Seismological Society of America*, 89(2), 501-520.

Bazzurro, P., and Cornell, C. A. (2002). "Vector-valued probabilistic seismic hazard analysis (VPSHA)." *Proceedings of the 7th US national conference on earthquake engineering*, 21-25.

Bazzurro, P., Tothong, P., and Park, J. (2009). "Efficient approach to vector-valued probabilistic seismic hazard analysis of multiple correlated ground motion parameters." *International Conference; 10th, Structural safety and reliability; Safety, reliability and risk of structures, infrastructures and engineering systems; ICOSSAR2009;*, CRC Press, Osaka, Japan.

Beckwith, F., Restrepo, J. I., and Shing, P.-S. (2015). "Nonlinear Time-History Analysis of Bridges with Varying Skew Angle to Determine the Seismic Demand on Abutment Shear Keys." University of California San Diego.

Berry, M. P., and Eberhard, M. O. (2004). "Performance models for flexural damage in reinforced concrete columns." Pacific Earthquake Engineering Research Center.

Berry, M. P., and Eberhard, M. O. (2005). "Practical performance model for bar buckling." *Journal of Structural Engineering*, 131(7), 1060-1070.

Bianchini, M., Diotallevi, P. P., and Baker, J. W. (2009). "Prediction of inelastic structural response using an average of spectral accelerations." *10th International Conference on Structural Safety and Reliability*Osaka, Japan.

Bojórquez, E., and Iervolino, I. (2011). "Spectral shape proxies and nonlinear structural response." Soil Dynamics and Earthquake Engineering, 996–1008.

Boore, D. M., and Atkinson, G. M. (2008). "Ground-Motion Prediction Equations for the Average Horizontal Component of PGA, PGV, and 5%-Damped PSA at Spectral Periods between 0.01s and 10.0s." *Earthquake Spectra*, 24(1), 99-138.

Bozorgzadeh, A., Megally, S. H., Ashford, S., and Restrepo, J. I. (2007). "Seismic response of sacrificial exterior shear keys in bridge abutments." University of California San Diego.

Bradley, B. A. (2010). "Epistemic uncertainties in component fragility functions." *Earthquake Spectra*, 26(1), 41-62.

Bradley, B. A. (2013). "A critical examination of seismic response uncertainty analysis in earthquake engineering." *Earthquake Engineering & Structural Dynamics*, 42(11), 1717-1729.

Bradley, B. A., and Dhakal, R. P. (2008). "Error estimation of closed-form solution for annual rate of structural collapse." *Earthquake Engineering & Structural Dynamics*, 37(15), 1721-1737.

Caltrans (2000). *Bridge Design Specifications*, California Department of Transportation, Division of Engineering Services.

Caltrans (2006). *Seismic Design Criteria - Version 1.4*, California Department of Transportation, Sacramento, CA.

Caltrans (2013). *Seismic Design Criteria - Version 1.7*, California Department of Transportation, Sacramento, CA.

Charney, F. A. (2008). "Unintended consequences of modeling damping in structures." *Journal of structural engineering*, 134(4), 581-592.

Chiou, B., Darragh, R., Gregor, N., and Silva, W. (2008). "NGA Project Strong-Motion Database." *Earthquake Spectra*, 24(1), 23-44.

Ciampoli, M., and Petrini, F. (2012). "Performance-based Aeolian risk assessment and reduction for tall buildings." *Probabilistic Engineering Mechanics*, 28, 75-84.

Ciampoli, M., Petrini, F., and Augusti, G. (2011). "Performance-based wind engineering: towards a general procedure." *Structural Safety*, 33(6), 367-378.

Clough, R. W., and Penzien, J. (1993). *Dynamics of Structures*, Prentice Hall, New York.

Coleman, J., and Spacone, E. (2001). "Localization issues in force-based frame elements." *Journal of Structural Engineering*, 127(11), 1257-1265.

Conte, J. P., and Zhang, Y. (2007). "Performance-based Earthquake Engineering: Application to an Actual Bridge-Foundation-Ground-System." *Proceedings of the 12th Italian National Conference on Earthquake Engineering*Pisa, Italy.

Cordova, P. P., Deierlein, G. G., Mehanny, S. S. F., and Cornell, C. A. "Development of a two-parameter seismic intensity measure and probabilistic assessment procedure." *Proc., The second US-Japan workshop on performance-based earthquake engineering methodology for reinforced concrete building structures*, 187-206.

Cornell, A. C., and Krawinkler, H. (2000). "Progress and Challenges in Seismic Performance Assessment." *PEER Center News*.

Cornell, C. A. (1968). "Engineering seismic risk analysis." *Bulletin of the seismological society of America*, 58(5), 1583-1606.

Cornell, C. A., Jalayer, F., Hamburger, R. O., and Foutch, D. A. (2002). "Probabilistic basis for 2000 SAC federal emergency management agency steel moment frame guidelines." *Journal of structural engineering*, 128(4), 526-533.

Cornell, C. A., and Newmark, N. M. (1978). "Seismic reliability of nuclear power plants." *Probabilistic analysis of nuclear reactor safety*.

De Biasio, M., Grange, S., Dufour, F., Allain, F., and Petre-Lazar, I. (2014). "A simple and efficient intensity measure to account for nonlinear structural behavior." *Earthquake Spectra*, 30(4), 1403-1426.

De, R. S. (1990). "Offshore Structural System Reliability: Wave-Load modeling, System Behavior, and Analysis." *Reliability of Marine Structures program*, John A. Blume Earthquake Engineering Center Stanford, Calif, USA.

Dodd, L. L., and Restrepo-Posada, J. I. (1995). "Model for Predicting Cyclic Behavior of Reinforcing Steel." *Journal of Structural Engineering*, 121(3).

Duck, D. E., Carreno, R., and Restrepo, J. I. (2018). "Plastic Buckling-Straightening Fatigue of Large Diameter Reinforcing Steel Bars Volume 1." University of California San Diego.

Duncan, J. M., and Mokwa, R. L. (2001). "Passive earth pressures: theories and tests." *Journal of Geotechnical and Geoenvironmental Engineering*, 127(3), 248-257.

Eads, L., Miranda, E., and Lignos, D. G. (2015). "Average spectral acceleration as an intensity measure for collapse risk assessment." *Earthquake Engineering & Structural Dynamics*, 44(12), 2057-2073.

Ellingwood, B. R. (2001). "Earthquake risk assessment of building structures." *Reliability Engineering & System Safety*, 74(3), 251-262.

Ellingwood, B. R. (2008). "Structural reliability and performance-based engineering." *Proceedings of the Institution of Civil Engineers-Structures and Buildings*, 161(4), 199-207.

Ellingwood, B. R., and Ang, A. H. S. (1974). "Risk-based evaluation of design criteria." *Journal of the Structural Division*, 100(Proc. Paper 10778).

Esteva, L., and Ruiz, S. E. (1989). "Seismic failure rates of multistory frames." *Journal of Structural Engineering*, 115(2), 268-284.

Faggella, M. (2008). "Nonlinear modelling, seismic response analysis and probabilistic demand sensitivity of a three-dimensional R/C building." Ph. D. Dissertation, University "G. D'Annunzio" Chieti-Pescara.

Fajfar, P., Vidic, T., and Fischinger, M. (1990). "A measure of earthquake motion capacity to damage medium-period structures." *Soil Dynamics and Earthquake Engineering*, 9(5), 236-242.

FEMA-273 (1997). *NEHRP guidelines for the seismic rehabilitation of buildings*, U.S. Federal Emergency Management Agency.

FEMA-356 (2000). *Pre-standard and commentary for the seismic rehabilitation of buildings*, U.S. Federal Emergency Management Agency.

FEMA-445 (2006). *Next-Generation Performance-Based Seismic Design Guidelines: Program Plan for New and Existing Buildings*, U.S. Federal Emergency Management Agency.

FHWA Retrofit Manual (2006). *Seismic Retrofitting Manual for Highway Structures: Part 1 - Bridges*, Federal Highway Administration, U.S. Department of Transportation, McLean, VA.

Field, E. H., Jordan, T. H., and Cornell, C. A. (2003). "OpenSHA: A developing community-modeling environment for seismic hazard analysis." *Seismological Research Letters*, 74(4), 406-419.

Filippou, F. C., Bertero, V. V., and Popov, E. P. (1983). "Effects of bond deterioration on hysteretic behavior of reinforced concrete joints." Earthquake Engineering Research Center, University of California Berkeley.

Filippou, F. C., and Fenves, G. L. (2004). "Methods of analysis for earthquake-resistant structures." *Earthquake Engineering: From Engineering Seismology to Performance-Based Engineering*, Y. Bozorgnia, and V. V. Bertero, eds., CRC Press, 6-1 - 6-65.

Gobbato, M., Conte, J. P., Kosmatka, J. B., and Farrar, C. R. (2012). "A reliability-based framework for fatigue damage prognosis of composite aircraft structures." *Probabilistic Engineering Mechanics*, 29, 176-188.

Gobbato, M., Kosmatka, J. B., and Conte, J. P. (2014). "A recursive Bayesian approach for fatigue damage prognosis: An experimental validation at the reliability component level." *Mechanical Systems and Signal Processing*, 45(2), 448-467.

Goodnight, J. C., Feng, Y., Kowalsky, M. J., and Nau, J. M. (2015). "The Effects of Load History and Design Variables on Performance Limit States of Circular Bridge Columns Volume 2: Experimental Observations."

Goodnight, J. C., Kowalsky, M. J., and Nau, J. M. (2016). "Strain Limit States for Circular RC Bridge Columns." *Earthquake Spectra*, 32(3).

Guenard, Y. F. (1984). "Application of system reliability analysis to offshore structures." *Reliability of Marine Structures Program*, John A. Blume Earthquake Engineering Center Stanford, Calif, USA.

Günay, S., and Mosalam, K. M. (2013). "PEER Performance-Based Earthquake Engineering Methodology, Revisited." Journal of Earthquake Engineering, 17(6), 829-858.
ICC-PC (2012). International Code Council Performance Code.

Jayaram, N., and Baker, J. W. (2008). "Statistical Tests of the Joint Distribution of Spectral Acceleration Values." Bulletin of the Seismological Society of America, 98(5), 2231-2243.

Jayaram, N., Lin, T., and Baker, J. W. (2011). "A Computationally Efficient Ground-Motion Selection Algorithm for Matching a Target Response Spectrum Mean and Variance." *Earthquake Spectra*, 27(3), 797-815.

Jehel, P., Léger, P., and Ibrahimbegovic, A. (2014). "Initial versus tangent stiffness-based Rayleigh damping in inelastic time history seismic analyses." *Earthquake Engineering & Structural Dynamics*, 43(3), 467-484.

Johnson, G. S., Harn, R., Lai, C., and Jaradat, O. (2013). "The New ASCE Standard for Seismic Design of Piers and Wharves." *Ports 2013: Success through Diversification*, 1345-1354.

Kaviani, P., Zareian, F., and Taciroglu, E. (2012). "Seismic behavior of reinforced concrete bridges with skew-angled seat-type abutments." *Engineering Structures*, 45, 137-150.

Kaviani, P., Zareian, F., and Taciroglu, E. (2014). "Performance-Based Seismic Assessment of Skewed Bridges." Pacific Earthquake Engineering Research Center, University of California, Berkeley.

Kennedy, R. P., Cornell, C. A., Campbell, R. D., Kaplan, S., and Perla, H. F. (1980). "Probabilistic seismic safety study of an existing nuclear power plant." *Nuclear Engineering and Design*, 59(2), 315-338.

Kennedy, R. P., and Ravindra, M. K. (1984). "Seismic fragilities for nuclear power plant risk studies." *Nuclear Engineering and Design*, 79(1), 47-68.

Kennedy, R. P., Short, S. A., Merz, K. L., Tokarz, F. J., Idriss, I. M., Power, M. S., and Sadigh, K. (1984). "Engineering characterization of ground motion. Task I. Effects of characteristics of free-field motion on structural response." U.S. Nuclear Regulatory Commission, Washington, DC.

Kent, D. C., and Park, R. (1971). "Flexural members with confined concrete." *Journal of the Structural Division*.

Keon, D., Pancake, C. M., Steinberg, B., and Yeh, H. (2016). "Performance-Based Tsunami Engineering via a Web-Based GIS Data Explorer." *Journal of Disaster Research*, 11(4), 625.

Kohrangi, M. (2015). "Software for conditional spectrum-based ground motion record selection using average spectral acceleration."

Kohrangi, M., Bazzurro, P., and Vamvatsikos, D. (2016). "Vector and scalar IMs in structural response estimation, Part I: Hazard analysis." *Earthquake Spectra*, 32(3), 1507-1524.

Kohrangi, M., Bazzurro, P., Vamvatsikos, D., and Spillatura, A. (2017). "Conditional spectrum-based ground motion record selection using average spectral acceleration." *Earthquake Engineering & Structural Dynamics*, 46(10), 1667-1685.

Kramer, S. L. (1996). *Geotechnical Earthquake Engineering*, Prentice-Hall.

Krawinkler, H., and Miranda, E. (2004). "Performance-based Earthquake Engineering." *Earthquake Engineering: From Engineering Seismology to Performance-based Engineering*, Y. Bozorgnia, and V. V. Bertero, eds., CRC Press, 9-1 - 9-59.

Kumar, R., and Gardoni, P. (2013). "Second-order Logarithmic formulation for hazard curves and closed-form approximation to annual failure probability." *Structural Safety*, 45, 18-23.

Liel, A. B., Haselton, C. B., Deierlein, G. G., and Baker, J. W. (2009). "Incorporating modeling uncertainties in the assessment of seismic collapse risk of buildings." *Structural Safety*, 31(2), 197-211.

Lin, T., Harmsen, S. C., Baker, J. W., and Luco, N. (2013a). "Conditional spectrum computation incorporating multiple causal earthquakes and ground-motion prediction models." *Bulletin of the Seismological Society of America*, 103(2A), 1103-1116.

Lin, T., Haselton, C. B., and Baker, J. W. (2013b). "Conditional spectrum-based ground motion selection. Part I: Hazard consistency for risk-based assessments." *Earthquake Engineering & Structural Dynamics*, 42(12), 1847-1865.

Luco, N., and Cornell, C. A. (2007). "Structure-specific scalar intensity measures for near-source and ordinary earthquake ground motions." *Earthquake Spectra*, 23(2), 357-392.

Mackie, K., and Stojadinović, B. (2004). "Fragility Curves for Reinforced Concrete Highway Overpass Bridges." *Proceedings of the 13th World Conference on Earthquake Engineering*Vancouver, Canada.

Mackie, K. R., and Stojadinović, B. (2007). "Performance-based seismic bridge design for damage and loss limit states." *Earthquake engineering & structural dynamics*, 36(13), 1953-1971.

Mander, J. B., Priestley, M. J. N., and Park, R. (1988). "Theoretical stress-strain model for confined concrete." *Journal of structural engineering*, 114(8), 1804-1826.

Mander, J. B., Sircar, J., and Damnjanovic, I. (2012). "Direct loss model for seismically damaged structures." *Earthquake Engineering & Structural Dynamics*, 41(3), 571-586.

Marshall, P. W. (1969). "Rick Evaluations for Offshore Structures." *Journal of the Structural Division*, 95(12), 2907-2930.

Masters, F. J., Gurley, K. R., Shah, N., and Fernandez, G. (2010). "The vulnerability of residential window glass to lightweight windborne debris." *Engineering Structures*, 32(4), 911-921.

May, P. J. (2001). "Organizational and societal considerations for performance-based earthquake engineering." Pacific Earthquake Engineering Research Center.

Mazzoni, S., McKenna, F., Scott, M. H., and Fenves, G. L. (2006). "OpenSees command language manual." *Pacific Earthquake Engineering Research (PEER) Center*, 264.

McKenna, F. (2011). "OpenSees: a framework for earthquake engineering simulation." *Computing in Science & Engineering*, 13(4), 58-66.

Megally, S. H., Silva, P. F., and Seible, F. (2002). "Seismic Response of Sacrificial Shear Keys in Bridge Abutments." University of California San Diego.

Mehanny, S. S. F. (2009). "A broad-range power-law form scalar-based seismic intensity measure." *Engineering Structures*, 31(7), 1354-1368.

Menegotto, M., and Pinto, P. E. "Method of analysis for cyclically loaded RC plane frames including changes in geometry and non-elastic behavior of elements under combined normal force and bending." *Proc., Symposium on the Resistance and Ultimate Deformability of Structures Acted on by Well Defined Repeated Loads*, International Association for Bridge and Structural Engineering, 15-22.

Miranda, E., Aslani, H., and Taghavi, S. (2004). "Assessment of seismic performance in terms of economic losses." *Proceedings, International Workshop on Performance-Based Seismic Design: Concepts and Implementation*, Pacific Earthquake Engineering Research (PEER) Center, Bled, Slovenia, 149-160.

Moan, T. (1994). "Reliability and risk analysis for design and operations planning of offshore structures." *ICOSSAR'93 (Innsbruck) Balkema*, 21-43.

Moan, T., and Holand, I. (1981). "Risk assessment of offshore structures: experience and principles." *Structural Safety and Reliability*, T. Moan, and M. Shinozuka, eds., Amsterdam, Oxford, New York: Elsevier, 803-820.

Moehle, J., and Deierlein, G. C. (2004). "A Framework Methodology for Performance-Based Earthquake Engineering." *13th World Conference on Earthquake Engineering*Vancouver, BC, Canada, 2004.

Murcia-Delso, J., Shing, P.-S., Stavridis, A., and Liu, Y. (2013). "Required Embendment Length of Column Reinforcement Exteneded into Type II Shafts."

Nada, H. M., Sanders, D. H., and Saiidi, M. S. (2003). "Seismic performance of RC bridge frames with architectural-flared columns." Center for Earthquake Engineering Research, University of Nevada, Reno.

NCHRP (2013). *Synthesis 440: Performance-Based Seismic Bridge Design, A Synthesis of Highway Practice*, Transportation Research Board of the National Academies, Washington, DC.

Neuenhofer, A., and Filippou, F. C. (1998). "Geometrically nonlinear flexibility-based frame finite element." *Journal of Structural Engineering*, 124(6), 704-711.

Nezamian, A., and Morgan, P. M. (2014). "Performance-based Seismic Design of Fixed Offshore Platforms and Comparison with ISO and API Seismic Design Guidelines." *The Twenty-fourth International Ocean and Polar Engineering Conference*, International Society of Offshore and Polar Engineers.

Nielson, B. G. (2005). "Analytical fragility curves for highway bridges in moderate seismic zones." Ph.D. Thesis, Georgia Institute of Technology.

Omrani, R., Mobasher, B., Liang, X., Gunay, S., Mosalam, K. M., Zareian, F., and Taciroglu, E. (2015). "Guidelines for nonlinear seismic analysis of ordinary bridges: Version 2.0." Caltrans Final Report No. 15-65A0454.

Paulay, T., and Priestley, M. J. N. (1992). *Seismic design of reinforced concrete and masonry buildings*, Wiley New York.

PIANC (2001). *Seismic Design Guidelines for Port Structures*, International Navigation Association.

Port of Long Beach (2009). *Port of Long Beach Wharf Design Criteria*, Port of Long Beach.

Port of Los Angeles (2010). *Code for Seismic Design, Upgrade and Repair of Container Wharves IS*, Port of Los Angeles.

Porter, K. A. (2003). "An overview of PEER's performance-based earthquake engineering methodology." *Proc. Ninth International Conference on Applications of Statistics and Probability in Civil Engineering (ICASP9)*, Civil Engineering Risk and Reliability Association (CERRA), San Francisco, CA.

Priestley, M. J. N., Calvi, G. M., and Kowalsky, M. J. (2007). *Displacement-based seismic design of structures*, IUSS Press, Pavia, Italy.

Riddell, R. (2007). "On ground motion intensity indices." *Earthquake Spectra*, 23(1), 147-173.

Riggs, H. R., Robertson, I. N., Cheung, K. F., Pawlak, G., Young, Y. L., and Yim, S. C. S. (2008). "Experimental simulation of tsunami hazards to buildings and bridges." *Proceedings of the 2008 NSF Engineering Research and Innovation Conference*Knoxville, Tennessee.

Rini, D., and Lamont, S. "Performance based structural fire engineering for modern building design." *Proc., Structures Congress 2008: Crossing Borders*, ASCE, 1-12.

Romão, X., Delgado, R., and Costa, A. (2013). "Alternative closed-form solutions for the mean rate of exceedance of structural limit states." *Earthquake Engineering & Structural Dynamics*, 42(12), 1827-1845.

Saini, A., and Saiidi, M. S. (2014). "Probabilistic Damage Control Approach for Seismic Design of Bridges." University of Nevada, Reno.

Schoettler, M. J., Restrepo, J. I., Guerrini, G., Duck, D. E., and Carrea, F. (2015). "A Full-Scale, Single-Column Bridge Bent Tested by Shake-Table Excitation." Pacific Earthquake Engineering Research Center.

Scott, B. D., Park, R., and Priestley, M. J. N. (1982). "Stress-Strain Behavior of Concrete Confined by Overlapping Hoops at Low and High Strain Rates." *Journal Proceedings*, 79(1), 13-27.

Scott, M. H., and Hamutçuoğlu, O. M. (2008). "Numerically consistent regularization of force-based frame elements." *International journal for numerical methods in engineering*, 76(10), 1612-1631.

SEAOC (1995). *Vision 2000 : Performance-based Seismic Engineering of Buildings*, Structural Engineers Association of California, Sacramento, CA.

Shamsabadi, A., Rollins, K. M., and Kapuskar, M. (2007). "Nonlinear soil–abutment–bridge structure interaction for seismic performance-based design." *Journal of geotechnical and geoenvironmental engineering*, 133(6), 707-720.

Shinozuka, M., Hwang, H., and Reich, M. (1984). "Reliability assessment of reinforced concrete containment structures." *Nuclear Engineering and Design*, 80(2), 247-267.

Shome, N., Cornell, C. A., Bazzurro, P., and Carballo, J. E. (1998). "Earthquakes, records, and nonlinear responses." *Earthquake Spectra*, 14(3), 469-500.

Song, J., and Ellingwood, B. R. (1999a). "Seismic reliability of special moment steel frames with welded connections: I." *Journal of structural engineering*, 125(4), 357-371.

Song, J., and Ellingwood, B. R. (1999b). "Seismic reliability of special moment steel frames with welded connections: II." *Journal of Structural Engineering*, 125(4), 372-384.

Taucer, F., Spacone, E., and Filippou, F. C. (1991). "A fiber beam-column element for seismic response analysis of reinforced concrete structures." Earthquake Engineering Research Center, College of Engineering, University of California, Berkeley.

Terzic, V., Schoettler, M. J., Restrepo, J. I., and Mahin, S. A. (2015). "Concrete column blind prediction contest 2010: outcomes and observations." *PEER Report*, Pacific Earthquake Engineering Research Center.

Tothong, P., and Luco, N. (2007). "Probabilistic seismic demand analysis using advanced ground motion intensity measures." *Earthquake Engineering & Structural Dynamics*, 36(13), 1837-1860.

Trejo, D., Barbosa, A. R., and Link, T. (2014). "Seismic Performance of Circular Reinforced Concrete Bridge Columns Constructed with Grade 80 Reinforcement."

Tsantaki, S., Jäger, C., and Adam, C. (2012). "Improved seismic collapse prediction of inelastic simple systems vulnerable to the P-delta effect based on average spectral acceleration." *15th World Conference on Earthquake Engineering*Lisbon, Portugal.

Tzavelis, C., and Shinozuka, M. (1988). "Seismic reliability of rigid frame structures." *Journal of engineering mechanics*, 114(11), 1953-1972.

Vamvatsikos, D. (2013). "Derivation of new SAC/FEMA performance evaluation solutions with second-order hazard approximation." *Earthquake Engineering & Structural Dynamics*, 42(8), 1171-1188.

Vamvatsikos, D., and Cornell, C. A. (2005). "Developing efficient scalar and vector intensity measures for IDA capacity estimation by incorporating elastic spectral shape information." *Earthquake engineering & structural dynamics*, 34(13), 1573-1600.

van de Lindt, J. W., and Dao, T. N. (2009). "Performance-based wind engineering for wood-frame buildings." *Journal of Structural Engineering*, 135(2), 169-177.

Veletzos, M. J., Panagiotou, M., Van Den Einde, Y., Restrepo, J. I., and Sahs, S. (2008). "Post-Earthquake Assessment of Bridge Columns." *Concrete International*, 30(3).

Vosooghi, A., and Saiidi, M. (2012). "Experimental Fragility Curves for Seismic Response of Reinforced Concrete Bridge Columns." *ACI Structural Journal*, 109(6), 825-834.

Wang, Z., Xie, W.-C., and Pandey, M. D. (2016). "Computationally Efficient Vector-Valued Seismic Risk Analysis of Engineering Structures." *Journal of Structural Engineering*, 142(9), 04016053.

Wen, Y.-K. (2004). "Probabilistic Aspects of Earthquake Engineering." *Earthquake Engineering: From Engineering Seismology to Performance-Based Engineering*, Y. Bozorgnia, and V. V. Bertero, eds., CRC Press, 7-1 - 7-45.

Wen, Y. K. (1995). "Building reliability and code calibration." *Earthquake Spectra*, 11(2), 269-296.

Whittaker, A., Hamburger, R. O., and Mahoney, M. (2003). "Performance-based engineering of buildings and infrastructure for extreme loadings." *Proceedings, AISC-SINY Symposium on Resisting Blast and Progressive Collapse*, American Institute of Steel Construction, New York.

Wilson, P., and Elgamal, A. (2006). "Large scale measurement of lateral earth pressure on bridge abutment back-wall subjected to static and dynamic loading." *Proceedings of New Zealand Workshop on Geotechnical Earthquake Engineering*, 307-315.

Yun, S.-Y., Hamburger, R. O., Cornell, C. A., and Foutch, D. A. (2002). "Seismic performance evaluation for steel moment frames." *Journal of Structural Engineering*, 128(4), 534-545.

Zhang, Y. (2006). "Probabilistic structural seismic performance assessment methodology and application to an actual bridge-foundation-ground system." Ph.D. Thesis, UC San Diego.